DEVELOPMENT OF A STRATEGY TO ADDRESS LOAD POSTED STEEL MULTI-GIRDER BRIDGES THROUGH REDUCTION IN UNCERTAINTY IN LOAD RATINGS

A Thesis

by

MATTHEW WILLIAM STIEGLITZ

Submitted to the Office of Graduate and Professional Studies of
Texas A&M University
in partial fulfillment of the requirements for the degree of

MASTER OF SCIENCE

Chair of Committee,	Mary Beth Hueste
Committee Members,	Stefan Hurlebaus
	John Mander
	Stephanie Paal
	Mohammed Haque
Head of Department,	Robin Autenrieth

December 2019

Major Subject: Civil Engineering

ABSTRACT

Bridges that are posted for load can cause a variety of issues for the people that use them and the entities that manage them. If a truck carrying goods must detour its route because it is too heavy to travel over a posted bridge, this increases its travel time and distance, and therefore costs. Load posted bridges also create issues for the state department of transportation (DOT) officials. Load posted bridges are a part of the inventory that must be more closely monitored and may require more work when conducting inspections or other maintenance. For these reasons, it is desirable for states to have as few load posted bridges in their inventory as possible. This research focuses on steel multi-girder bridges in the state of Texas. Current AASHTO codes and manuals provide procedures that can be used to estimate a bridge's behavior. However, the specifications use simplified methods that provide a conservative analysis that may not represent the true behavior of the bridge. The objective of this research is to explore the potential to improve the load rating of steel multi-girder bridges through three methods; the development of finite element models, the use of partial composite action in the analysis of a non-composite structure, and the use of refined live load distribution factors. This is done through the use of finite element models to more accurately model bridge behavior and through field load testing of a selected bridge to better understand its in-situ behavior. The results of the load test are analyzed through the three previously mentioned methods to observe where improvements in the bridge's load rating could be made. The results of the load test are also used to calibrate the finite element model of the bridge to determine a maximum capacity that the bridge could carry. It was found that the specific bridges tested were able to carry a capacity greater than that of which they are posted, and that the postings are likely not necessary on the bridges.

ACKNOWLEDGEMENTS

I would like to thank my committee chair, Dr. Hueste, and my committee members, Dr. Hurlebaus, Dr. Mander, Dr. Paal, and Dr. Haque, for their guidance and support throughout the course of this research.

I would also like to thank the post-doctoral research associate involved in this study, Dr. Tevfik Terzioglu, and the other Master's student on this study, Nuzhat Kabir, for their help as well.

Thanks also go to my friends and colleagues and the department faculty and staff for making my time at Texas A&M University a great experience.

Finally, thanks to my family for their encouragement and support.

CONTRIBUTORS AND FUNDING SOURCES

Contributors

This work was supervised by a thesis committee consisting of Dr. Mary Beth Hueste, Dr. Stefan Hurlebaus, Dr. John Mander, and Dr. Stephanie Paal of the Zachry Department of Civil and Environmental Engineering and Dr. Mohammed Haque of the Department of Construction Science. Dr. Tevfik Terzioglu, post-doctoral research associate with the Texas A&M Transportation Institute, also provided guidance for this research.

Funding Sources

Graduate study was supported by Texas Department of Transportation Research Project 0-6955, which was administered through the Texas A&M Transportation Institute.

NOMENCLATURE

AASHO	American Association of State Highway Officials
AASHTO	American Association of State Highway and Transportation Officials
ACI	American Concrete Institute
ADT	Average Daily Traffic
ADTT	Average Daily Truck Traffic
AISC	American Institute of Steel Construction
ASCE	American Society of Civil Engineers
ASD	Allowable Stress Design
ASR	Allowable Stress Rating
ASTM	American Society for Testing and Materials
DOT	Department of Transportation
FEM	Finite Element Method
FHWA	Federal Highway Administration
FO	Functionally Obsolete
LFD	Load Factor Design
LFR	Load Factor Rating
LLDF	Live Load Distribution Factor
LRFD	Load and Resistance Factor Design
LRFR	Load and Resistance Factor Rating
MBE	Manual for Bridge Evaluation
MCE	Manual for Condition Evaluation

NBI	National Bridge Inventory
NCHRP	National Highway Cooperative Research Program
NDE	Nondestructive Evaluation
NDT	Nondestructive Testing
RF	Rating Factor
SC	Steel Continuous Multi-Girder
SD	Structurally Deficient
SEI	Structural Engineering Institute
SM	Steel Multi-Girder
SSLO	Sub-Standard for Load Only
TxDOT	Texas Department of Transportation

TABLE OF CONTENTS

Page

LIST OF FIGURES

Page

LIST OF TABLES

Page

1. INTRODUCTION

1.1. GENERAL

Bridges that are posted for load produce a variety of challenges for the people that use them and the entities that manage them. If a truck carrying goods must detour its route because it is too heavy to travel over a posted bridge, this increases its travel time and distance, and therefore costs. Load posted bridges also create issues for the state department of transportation (DOT) officials. Load posted bridges are a part of the inventory that must be more closely monitored and may require more work when conducting inspections or other maintenance. For these reasons, it is desirable for states to have as few load posted bridges in their inventory as possible. This research focuses on steel multi-girder bridges in the state of Texas, which comprise a significant portion of the load posted bridges in the state.

As of the 2016 National Bridge Inventory records, there were 2111 bridges in Texas posted for load. Of that, 969 were classified as Sub-Standard for Load Only (SSLO). This means that the posting is not due to the bridge exhibiting deterioration, and it satisfies the original design criteria. Therefore, these bridges were likely designed using older standards and trucks that are not as heavy as current design vehicles. Of these SSLO bridges, 257 are steel simple-span, multi-girder bridges, accounting for 26.5 percent of the SSLO bridges in Texas. There are also 109 steel continuous, multi-girder SSLO bridges, accounting for 11.2 percent of the SSLO bridges in Texas. As steel multi-girder bridges account for more than one-third of the SSLO bridge inventory in Texas, they were selected for further investigation in this research study.

1.2. OBJECTIVE AND METHODOLOGY

Current American Association of State Highway and Transportation Officials (AASHTO) codes and manuals provide procedures that can be used to estimate the behavior of a bridge. The primary document used to perform a load rating of a bridge is the AASHTO Manual for Bridge Evaluation (MBE) (AASHTO MBE 2018). The AASHTO MBE provides three methods for load rating: (1) the Load and Resistance Factor Rating (LRFR) method, (2) the Allowable Stress Rating (ASR) method, and (3) the Load Factor Rating (LFR) method. However, these methods can be conservative in some cases, with general expressions for load distribution that may not represent to actual in situ behavior of a particular bridge. Therefore, the MBE also provides options to perform refined rating analysis on a bridge. These options include load testing and reference to AASHTO Load and Resistance Factor Design (LRFD) Specifications (AASHTO 2017) Article 4.4, which states, "Any method of analysis that satisfies the requirements of equilibrium and compatibility and utilizes stress-strain relationships for the proposed materials may be used." Therefore, the objective of this research is to explore the potential to improve the load rating of steel multi-girder bridges through three methods: (1) the use of finite element models to capture the actual behavior of the superstructure, (2) consideration of the presence of partial or full composite action in the analysis of structures designed as non-composite, and (3) the development and use of refined live load distribution factors.

The first approach to refine load rating calculations is the use of refined analysis using a finite element model of a specific bridge to estimate the actual behavior of the structure. This will remove the conservatism that could occur when using the general live load distribution factors presented in the AASHTO specifications. Load tests of steel multi-girder bridges will be conducted in the field to verify that the finite element models correctly predict the behavior of the bridges.

The strain in the steel girders during the field load test will be converted to stress and will be compared to the stress obtained from the corresponding finite element model in order to calibrate the model. Additional parameters will also be used for model calibration, such as modal frequencies and measured displacements.

The second method to improve ratings that will be examined is considering the presence of partial or full composite action in steel multi-girder bridges designed as non-composite. The Texas Department of Transportation (TxDOT) currently load rates steel multi-girder bridges with concrete decks as non-composite if they do not have shear studs that allow for the transfer of the shear force between the deck and the girders (TxDOT 2018a). Because the considered bridges were constructed in a non-composite manner, it would seem appropriate to analyze them as fully non-composite structures. However, this analysis may produce conservative results because the coefficient of friction between the deck and the girders is not zero. It could be possible that under service loads, these steel multi-girder bridges will exhibit partially composite behavior, giving them an increased moment capacity than if analyzed as non-composite. Strain gages attached to the steel girders and concrete deck at various depth locations will be used to measure the strain in the girder and the strain in the deck under loading. By comparing the results of these measurements with the known strain diagrams and values of a fully non-composite section and a full composite section, the amount of partial composite action in the steel multi-girder bridge under loading can be determined.

The final method to refine load ratings that is explored is the development of refined live load distribution factors. As will be discussed later in detail, the AASHTO live load distribution factors simplify the bridge system into a linear problem, which does not consider the action of the system as a whole to resist loads. This simplification could possibly lead to conservative live load

distribution factors. If through the field testing of a bridge, the proper load distribution could be determined, updated live load distribution factors for the considered steel multi-girder bridges could be developed to possible improve the load ratings of these bridges, and may indicate similar structures could benefit from a similar analysis. By using strain gages attached to the girders of the steel multi-girder bridge, the amount of moment in each individual girder can be compared to the total applied moment on the bridge. In addition, string potentiometers are used to measure in-span displacements. This will allow the actual live load distribution factor for each girder to be determined.

1.3. OUTLINE OF THIS THESIS

This thesis is structured with nine different chapters. The first chapter provides a background to the research and explains the need for the research to be performed. Chapter 2 discusses the literature review conducted on the history of bridge load rating, current methods that are used nationally and at the state level to load rate, and other research studies that have found new, state-of-the-art ways to rate bridges. Chapter 3 details the three major load rating procedures given in the AASHTO MBE (AASHTO MBE 2018), the ASR method, the LFR method, and the LRFR method. Chapter 4 provides the results for a basic load rating analysis using the three major load rating methods that was performed on a select group of bridges in the Texas SSLO inventory. This was done to help identify areas of possible improvement to load ratings. Chapter 5 and Chapter 6 detail the finite element method (FEM) model development and initial refined analysis of two simple span bridges and one continuous bridge, respectively, selected for further investigation. These models were developed using as built information to investigate live load distribution factors (LLDF)(s) and the effect of composite action. Chapter 7 and Chapter 8 outline the load testing

performed in the field on one simple span bridge and one continuous bridge, respectively. The results from the load tests were used to develop LLDFs, calibrate the previously developed FEM models, and examine partial composite action. The final chapter, Chapter 9 presents the project summary, conclusions and load rating recommendations relevant for the considered bridge types, and recommendations for future work.

2. LITERATURE REVIEW

2.1. INTRODUCTION

Prior to conducting the analysis and testing associated with this study, a review of background information related to bridge load rating and testing was conducted. The ASCE/SEI-AASHTO ad-hoc group (2009) on bridge inspection, rating, rehabilitation, and replacement note that load rating a bridge is a critical process. The load rating must be performed to a level of accuracy required for the intended purposes such as load posting, repairs, etc., and load ratings have to be reliable, uniform, and consistent. Additionally, documenting load ratings for both the bridge and the critical elements provides more value for effective bridge management.

This chapter summarizes a review of the state-of-the-practice and state-of-the-art on load rating of existing bridges. The state-of-the-practice describes historical and current approaches to bridge load rating for the State of Texas, along with national and select international practices. The history of bridge load rating review is focused on the initiation of bridge load rating, the significant contents and procedures in load rating sections of early bridge evaluation manuals, and how these early manuals developed into the current bridge load rating manual. The review of the state-of-the-practice describes the requirements of the current load rating manual, load rating practices that state DOTs currently use, and load rating studies for which states have implemented the results. The state-of-the-art literature review summarizes related research published in journals, conferences, and agency reports and key findings relevant to this study are documented.

2.2. HISTORY OF BRIDGE LOAD RATING

2.2.1. Early Manuals

In 1967, the Silver Bridge collapsed into the Ohio River in Point Pleasant, West Virginia, killing 46 people. Prior to this bridge collapse, inspection of bridges and load rating of bridges were rare. However, the collapse led the United States (U.S.) Congress to add a section requiring a national bridge inspection standard to the Federal Highway Act of 1968. The new National Bridge Inspection Standards (NBIS) required an increased effort and diligence regarding bridge inspections. This led to the creation of three manuals to ensure uniformity in the state bridge inspection procedures (Lichtenstein 1993; Ryan et al. 2012).

Released in 1970, one of these manuals was the American Association of State Highway Officials (AASHO) *Manual for Maintenance Inspection of Bridges* (AASHO 1970). This manual is one of the first to provide over-arching guidelines for bridge load rating. It was based on the concept of working stresses and these stresses caused by loading were not allowed to exceed a specified maximum allowable stress. This maximum allowable stress depended on the level of rating that was being performed. The upper stress level rating was called Operating Rating, in which the allowable stress was usually not allowed to exceed 75 percent of the yield stress of the material. The Operating Rating was defined as the absolute maximum stress level the bridge was allowed to experience. The lower stress level rating was called Inventory Rating, in which the allowable stress was not allowed to exceed 55 percent of the yield stress or the allowable design stress used in the original design of the structure. The Inventory Rating was defined as the load that can travel on the bridge safely for an indefinite period of time. Bridges were evaluated using either the AASHO H design loading, or one of three conventional vehicle types, called the Type 3

Unit, the Type 3S2 Unit, and the Type 3-3 Unit. These three trucks are very similar to the current American Association of State Highway and Transportation Officials (AASHTO) *LRFD Bridge Design Specifications* (AASHTO 2017) legal loads, with minor changes. They are slightly less heavy than the AASHTO legal loads and different amounts of load are distributed to each axle.

AASHO became AASHTO in 1973, and over the next 13 years released three more editions of the *Manual for Maintenance Inspection of Bridges* that were similar in length and layout to the 1970 version, but had some significant changes. The 1974 *Manual for Maintenance Inspection of Bridges* (AASHTO 1974) added the HS design loading to the list of loads required for bridge evaluation. It also introduced rating by Load Factor Design (LFD) methods for use on steel girder bridges. Load Factor Rating (LFR) applied multiples of load or load effects to the bridge. These factors were different for Operating and Inventory Ratings, with the Inventory Rating having an increased live load factor and applying a larger effect to the bridge. The capacity of the bridge was then determined based on the yield strength of steel or ultimate strength of concrete and using different equations depending on the type of structure and element being examined. A Rating Factor (RF) equation was then developed for each type of bridge, using some variation of capacity divided by the live load effect. However, although the Load Factor method of rating bridges was introduced, it was only included in the appendix and the main focus of the 1974 Manual was still load rating using working and allowable stresses.

In the 1978 *Manual for Maintenance Inspection of Bridges* (AASHTO 1978), the working stress and load factor methods for rating were more equally discussed. The load factor method was moved out of the appendix of the manual and into the main load rating section. Use of the load factor method for rating concrete bridges was also briefly introduced, with the tension steel reinforcing assumed to yield. As both methods were now included in the main body of the manual,

the definitions of Operating and Inventory Levels were changed to only be related to the load levels that the bridge was subjected to, with no reference to stresses. Also, while the H and HS loadings were still the design loads, the three legal loads for evaluation were slightly increased and re-distributed among axles to obtain the legal load configurations that are still used currently. The load rating section of the 1983 *Manual for Maintenance Inspection of Bridges* remained essentially the same as the load rating section of the 1978 version, continuing to provide guidelines for both the working stress and load factor methods of rating (AASHTO 1983; TxDOT 2013).

2.2.2. Introduction of Load and Resistance Factor Rating (LRFR) Methods

In 1987, the National Highway Cooperative Research Program (NCHRP) released two reports that helped develop and introduce a new method for rating bridges called Load and Resistance Factor Rating (LRFR). NCHRP Report 292 introduced the use of probabilistic and structural reliability methods to develop load factors used in rating equations for reinforced concrete bridges (Imbsen et al. 1987). NCHRP Report 301 expanded on this to develop load factors that would apply to all types of bridges and proposed a new rating equation that incorporates these factors and Load and Resistance Factor Design (LRFD) principles (Moses and Verma 1987). In 1993, a comprehensive specifications guide for LRFD including calibrated load factors was accepted by AASHTO (Kulicki 1998).

The associated LRFR method is first mentioned in the load rating section of an AASHTO evaluation manual in the 1994 *AASHTO Manual for Condition Evaluation of Bridges* (MCE) (AASHTO 1994). The 1994 MCE was the result of a complete rewrite of the AASHTO evaluation manual and included much more information on load rating with more detail provided than in earlier manuals. However, the LRFR method is only mentioned briefly in the MCE, which notes

that the LRFR method can be used to load rate bridges and that it is described in detail in a document called the *AASHTO Guide Specifications for the Strength Evaluation of Existing Steel and Concrete Bridges* (AASHTO 1994). Otherwise, the 1994 MCE focuses on the working stress and load factor methods, which were given updated titles of Allowable Stress Rating (ASR) and Load Factor Rating (LFR) methods. Besides the addition of a simplified, all-encompassing RF equation to use for both methods, the content is effectively the same as previous manuals, with more detail. The design truck loading was also changed to the HS20 truck in the 1994 MCE, to conform to the *AASHTO LRFD Bridge Design Specifications*.

NCHRP Project 12-46 (Lichtenstein Consulting Engineers 2001) was tasked with developing a new AASHTO manual for load rating that incorporated LRFR methods that was completed in 2001. This led to the publication of the *AASHTO Manual for Condition Evaluation and Load and Resistance Factor Rating of Highway Bridges* (AASHTO 2003). This manual had an entire section on LRFR, introducing it as the main load rating method, including a general RF equation and procedures to find the load factors. The ASR and LFR methods were still included, but as an appendix to the LRFR section titled Alternate Load Rating.

In 2008, AASHTO released the first edition of its *Manual for Bridge Evaluation* (MBE). The MBE combined the material in the 1994 MCE and the 2003 manual to create an all-encompassing evaluation manual for bridges that superseded all previous manuals. The MBE had an entire section dedicated to load rating made up of three parts: one focused on the LRFR method, one on the ASR and LFR methods, and one providing examples of each (AASHTO 2008). The MBE became the required reference for load rating bridges in the U.S.

2.3. CURRENT NATIONAL LOAD RATING PROCEDURES

In 2011, AASHTO released the second edition of the MBE (2011). This, along with revisions made in 2016, contains the current standard procedure to load rate bridges in the United States. Section 6 of the MBE describes different load rating methods and has two parts: Part A covers the LRFR method and Part B covers the ASR and LFR methods. The Federal Highway Administration (FHWA) requires that all bridges constructed after October 1, 2007 be designed using LRFD. This is part of a large push by the industry to go towards the use of LRFD to design bridges and therefore, using LRFR as the accompanying load rating method (CTC & Associates 2009). This effort also requires bridges designed using Allowable Stress Design (ASD) to be re-rated using either LFR or LRFR. Bridges designed using Load Factor Design (LFD) may still be rated using LFR, although load rating using the LRFR method is preferred by the FHWA in all cases (Lwin 2006).

2.3.1. Load and Resistance Factor Rating (LRFR)

The general equation to obtain the bridge RF using the LRFR method is,

$$RF = \frac{C - (\gamma_{DC})(DC) - (\gamma_{DW})(DW) \pm (\gamma_P)(P)}{(\gamma_{LL})(LL + IM)} \tag{2.1}$$

where:

RF = Rating Factor

C = Capacity

DC = Dead load effect due to structural components and attachments

DW = Dead load effect due to wearing surface and utilities

P = Permanent loads other than dead loads

LL = Live load effect

IM = Dynamic load allowance

γ_{DC} = LRFD load factor for structural components and attachments

γ_{DW} = LRFD load factor for wearing surfaces and utilities

γ_P = LRFD load factor for permanent loads other than dead loads = 1.0

γ_{LL} = Evaluation live load factor

For the strength limit states, the capacity is determined as the nominal member resistance multiplied by an LRFD resistance factor ϕ, a system factor ϕ_s, and a condition factor ϕ_c. The product of the condition and system factors is required to be greater than 0.85. An RF is determined for each component of the bridge, and the member that has the lowest RF governs. The RF of the controlling member is then said to be the RF for the entire structure. The limit state that is chosen for determination of the RF gives specific values for γ_{DC}, γ_{DW}, and γ_{LL}. The primary limit state used for the LRFR method is Strength I, however the limit state that is evaluated is dependent on the rating procedure used, as some limit states only apply to specific rating procedures and not to others. LRFR includes three different rating procedures for bridges: (1) Design Load Rating, (2) Legal Load Rating, and (3) Permit Load Rating. Table 2.1 shows the dead load and live load factors for these limit states.

Table 2.1. Load Factors for Load Rating for Various Limit States (Adapted from AASHTO MBE 2018)

Bridge type	Limit State	Dead Load γ_{DC}	Dead Load γ_{DW}	Design Load	
				Inventory	Operating
				γ_{LL}	γ_{LL}
Steel	Strength I	1.25	1.50	1.75	1.35
	Service II	1.00	1.00	1.30	1.00

2.3.1.1. Design Load Rating

Design Load Rating is the first assessment conducted in the LRFR bridge rating procedure and uses the HL-93 load model, which consists of an HS20 truck plus lane load, as defined in the AASHTO LRFD Bridge Design Specifications (AASHTO 2017). The Design Load Rating is split into two separate rating levels: (1) Inventory Rating Level, and (2) Operating Rating Level. The Inventory Rating Level applies a higher live load factor (γ_{LL}) than the Operating Rating Level, which gives an Inventory RF that is lower than the Operating RF. The *Inventory RF* represents the multiple of HL-93 loads that may be applied to the bridge, such that the bridge can be in service for an indefinite period of time. Similarly, the *Operating RF* represents the multiple of HL-93 loads that is the absolute maximum load that can safely travel on the bridge at once. If a bridge has an RF greater than 1.0 at both the Inventory and Operating Levels, it passes the Design Load Rating and does not need to be posted. If a bridge passes at the Operating Level, but not at the Inventory Level, the owner will likely need to post the bridge for its safe load. If a bridge does not pass at either the Inventory or Operating Levels for the Design Load Rating, it will be posted for loads lower than the HL-93 load and therefore must be evaluated for a Legal Load Rating.

2.3.1.2. Legal Load Rating

Many states have legal loads, which are certain axle configurations and weights for trucks specific to their state that are different than the HL-93 load model. These legal loads are applied to the

structure and evaluated to determine the Legal Load Rating. The AASHTO LRFD Bridge Design Specifications (AASHTO 2017) also provide load configurations that are legal throughout the country, called Type 3, Type 3S2, and Type 3-3 trucks, and NRL, SU4, SU5, SU6, and SU7 Specialized Hauling Vehicles. These legal loads produce smaller effects than the HL-93 loading, and are therefore evaluated if the bridge does not pass the Design Load Rating. The LRFR equation (Eqn. 2.1) is still used to determine the RF of the bridge for the group of legal loads. Truck configurations that produce an RF greater than 1.0 are safe to travel on the bridge, while configurations that produce an RF less than 1.0 must be posted. One of the other major differences between the Design Load Rating and Legal Load Rating is the value of the LRFR live load factor, γ_{LL}, which is 1.75 for Inventory Level and 1.35 for Operating Level Design Load Ratings. However, for Legal Load Ratings this value is found through one of two tables that the AASHTO MBE provides based on the truck configuration being evaluated and the Average Daily Truck Traffic (ADTT) on the bridge (Table 2.2).

Table 2.2. Generalized Live Load Factors for Routine Commercial Traffic and Specialized Hauling Vehicles (Adapted from AASHTO 2011)

Traffic Volume (One Direction)	Load Factor for Type 3, Type 3S2, Type 3-3, and Lane Loads	Load Factor for NRL, SU4, SU5, SU6, and SU7 Vehicles
Unknown	1.80	1.60
ADTT ≥ 5000	1.80	1.60
ADTT = 1000	1.65	1.40
ADTT ≤ 100	1.40	1.15

Note: The MBE allows interpolation between ADTT values.

2.3.1.3. Permit Load Rating

Finally, if a bridge passes both the Design Load Rating and the Legal Load Rating, it can be evaluated using the Permit Load Rating procedures. This procedure is used to determine the ability of the bridge to carry a certain load that is over the defined AASHTO or state legal loads. In this case, the bridge is evaluated for a specific load and axle configuration based on a permit request, not a particular family of trucks. Permits are issued as Routine Permits, which are valid for an unlimited number of trips over a specified period of time, or Special Permits, which are valid for only a single trip or limited number of trips. As before, if the bridge has an RF greater than 1.0 when evaluated for the specific permit request, it is rated as safe for that vehicle. However, the LRFR live load factor is also different for Permit Load Rating as compared to the Design or Legal Load Ratings. The live load factor is still dependent on the ADTT for the bridge, but the factors tend to be higher, which will decrease the RF of the structure (see Table 2.3).

2.3.1.4. LRFR Load Factors

The LRFR dead and live load factors for the Design Load Rating were developed as part of NCHRP Project 12-33 (Kulicki 1998). This study was tasked with developing a design and analysis specification that used reliability indices to derive load and resistance factors. The load factors were selected to obtain reliability indices that were close to a target reliability. This target reliability is indirectly related to the probability of failure of the structure.

Table 2.3. Permit Live Load Factors Currently in the AASHTO MBE (Adapted from AASHTO 2011)

Permit Type	Frequency	Loading Conditions	Distribution Factor	ADTT (one direction)	Load Factor by Permit Weight	
					Up to 100 kips	≥ ≥ 150 kips
Routine or Annual	Unlimited Crossings	Mix with traffic (other vehicles may be on the bridge)	Two or more lanes	> 5000	1.80	11.30
				= 1000	1.60	11.20
				< 100	1.40	11.10
					All Weights	
Special or Limited Crossing	Single-Trip	Escorted with no other vehicles on the bridge	One lane	N/A	1.15	
	Single-Trip	Mix with traffic (other vehicles may be on the bridge)	One lane	> 5000	1.50	
				= 1000	1.40	
				< 100	1.35	
	Multiple-Trips (less than 100 crossings)	Mix with traffic (other vehicles may be on the bridge)	One lane	> 5000	1.85	
				= 1000	1.75	
				< 100	1.55	

Note: the MBE allows interpolation between ADTT values.

The live load factors for Legal Load Rating (Table 2.2) and Permit Load Rating (Table 2.3) were developed as part of NCHRP project 12-46 (Moses 2001). This study used essentially the same approach involving reliability indices to determine the necessary live load factors for the legal and permit trucks to keep the target reliability the same.

NCHRP project 12-78 (Mlynarski et al. 2011) followed up on these studies and examined the live load factors that were developed and are in current use in the MBE. In this study researchers analyzed and compared LRFR and LFR ratings of 1500 bridges representing an array of ages, material types, and superstructure types. As part of NCHRP Report 700, released in 2011 and detailing the results of the project, new live load factors were proposed to replace the current ones in the AASHTO MBE (AASHTO 2011). Mlynarski et al. (2011) found that although a reliability index of 2.5 was used to calculate most of the live load factors that are currently in the

MBE, based on their bridge database, those live load factors actually correspond to a reliability index of 3.5. The researchers recalculated the live load factors using their bridge database and a reliability index of 2.5, as they believed that the current MBE live load factors "would result in more bridges not passing the rating under LRFR and [were] thought to be too restrictive." This resulted in the lower live load factors that are shown in Table 2.4 and Table 2.5, compared to those shown in Table 2.2 and Table 2.3. The lower live load factors increased the RFs found using LRFR for the selected database of bridges. While there has been significant research effort using reliability analysis to determine appropriate live load factors, the MBE also provides a procedure in its commentary for determining site-specific live load factors. However, this is geared toward increasing live load factors due to heavier loads in use than those that were considered in the calibration studies. Some states have increased their live load factors using this procedure, while one state has actually decreased their live load factors. This will be discussed later in this chapter.

Table 2.4. Live Load Factors for Routine Commercial Traffic and Specialized Hauling Vehicles Proposed in NCHRP Report 700 (Adapted from Mlynarski et al. 2011)

Traffic Volume (One Direction)	Load Factor for Type 3, Type 3S2, Type 3-3 and Lane Loads	Load Factor for NRL, SU4, SU5, SU6, and SU7 Vehicles
Unknown	~~1.80~~ 1.45	~~1.60~~ 1.45
ADTT ≥ 5000	~~1.80~~ 1.45	~~1.60~~ 1.45
ADTT = 1000	~~1.65~~ 1.30	~~1.40~~ 1.30
ADTT ≤ 100	~~1.40~~ 1.20	~~1.15~~ 1.15

Table 2.5. Live Load Factors for Permit Vehicles Proposed in NCHRP Report 700 (Adapted from Mlynarski et al. 2011)

Permit Type	Frequency	Loading Conditions	Distribution Factor	ADTT (one direction)	Load Factor by Permit Weight	
					Up to 100 kips	1≥ 150 kips
Routine or Annual	Unlimited Crossings	Mix with traffic (other vehicles may be on the bridge)	Two or more lanes	> 5000	~~1.80~~ 1.45	11.30
				= 1000	~~1.60~~ 1.25	11.20
				< 100	~~1.40~~ 1.05	11.10
					All Weights	
Special or Limited Crossing	Single-Trip	Escorted with no other vehicles on the bridge	One lane	N/A	1.15	
	Single-Trip	Mix with traffic (other vehicles may be on the bridge)	One lane	> 5000	~~1.50~~ 1.25	
				= 1000	~~1.40~~ 1.15	
				< 100	~~1.35~~ 1.10	
	Multiple-Trips (less than 100 crossings)	Mix with traffic (other vehicles may be on the bridge)	One lane	> 5000	~~1.85~~ 1.60	
				= 1000	~~1.75~~ 1.50	
				< 100	~~1.55~~ 1.45	

2.3.1.5. Summary

In summary, Part A of the current AASHTO MBE (AASHTO 2011) covers the newest method to load rate bridges, Load and Resistance Factor Rating, which is preferred by the FHWA (Mertz 2015). Within LRFR, bridges are evaluated using possibly three separate procedures. See Figure 2.1 for a load rating procedure flowchart provided in the AASHTO MBE (AASHTO 2011).

- Design Load Rating is the first level evaluation and is broken into Inventory Level Rating, the multiple of HL-93 loads that can travel on the bridge while keeping the structure in sustainable condition for an indefinite period of time, and Operating Level Rating, the multiple of HL-93 loads that is the absolute maximum weight that can travel on the structure. If a bridge has an RF greater than 1.0 for both Inventory Level and Operating Level rating, it passes Design Load Rating and is safe for all AASHTO and state legal truck loads and configurations.

- Legal Load Rating is the second level evaluation that takes place if a bridge does not pass Design Load Rating. This usually means that the bridge will have to be posted for its safe load. In the Legal Load Rating procedure, the bridge is evaluated for all AASHTO and state legal loads, again passing if the RF is greater than 1.0.
- Permit Load Rating is a third level evaluation completed when a bridge passes Design Load Rating and a request is made for a truck heavier than the design HL-93 to travel on it. The specific truck weight and configuration is used and as before, an RF greater than 1.0 indicates that the bridge passes and the vehicle can cross.

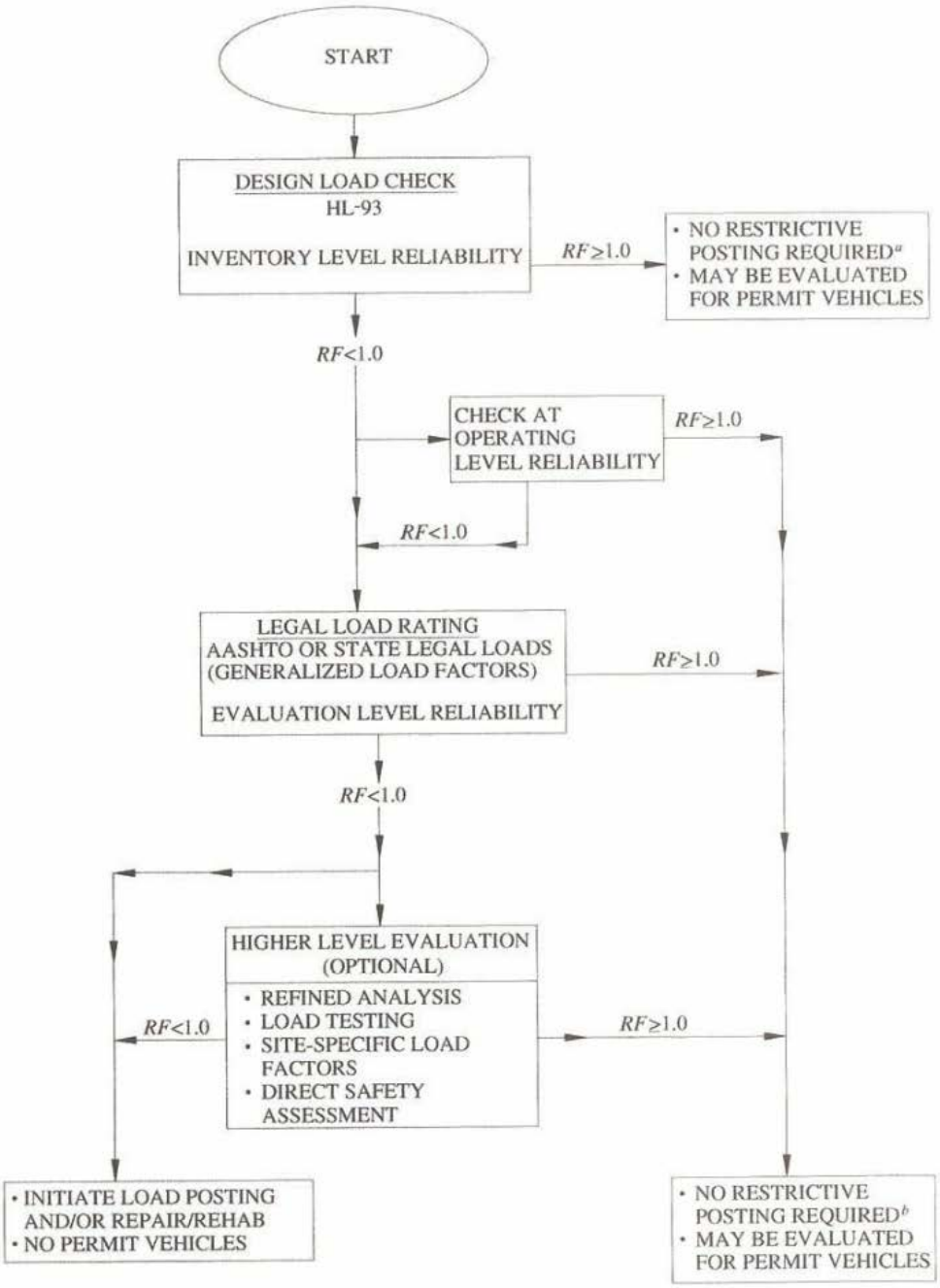

Figure 2.1. MBE LRFR Procedure Flow Chart (Reprinted from AASHTO 2011)

When posting a bridge, the gross weight in tons allowed for specific vehicles is posted on the actual sign. The MBE gives an equation to determine the safe posting load for a bridge if the

RF is between 1.0 and 0.3. If the RF is less than 0.3 the bridge is required to be closed. The safe posting load for a structure is given in Equation (2.2).

$$\text{Safe Posting Load} = \frac{W}{0.7}(RF - 0.3) \tag{2.2}$$

where:

RF = Legal load rating factor

W = Weight of rating vehicle

2.3.2. Allowable Stress Rating (ASR) and Load Factor Rating (LFR)

Part B of the MBE covers the older methods to load rate bridges: Allowable Stress Rating and Load Factor Rating. Both methods use the same general equation to obtain an RF, shown in Equation (2.3).

$$RF = \frac{C - A_1 D}{A_2 L(1 + I)} \tag{2.3}$$

where:

RF = Rating Factor for the live load carrying capacity

C = Capacity of the member

D = Dead load effect on the member

L = Live load effect on the member

I = Impact factor to be used with the live load effect

A_1 = Factor for dead loads

A_2 = Factor for live load

The ASR and LFR do not have the different load rating procedures used for LRFR. The bridge is only evaluated under the design truck load or one of the legal loadings. The A_1 and A_2 factors, which are similar to the dead and live load factors in LRFR, do not change. The design load, and therefore the first loading scenario to be evaluated for ASR and LFR is the HS-20 truck configuration, as opposed to the HL-93 loading used by LRFR. If the bridge passes (has an RF greater than 1.0) for the HS-20 loading it also passes for all of the AASHTO and state legal loads.

For the ASR method, the dead and live load factors, A_1 and A_2, are both always equal to 1.0. The capacity of the member changes depending on whether the bridge is being evaluated at Inventory Level or Operating Level. The MBE has tables and subsections dedicated to finding the capacity for different materials and situations using the ASR method. As the name Allowable Stress Rating suggests, a limit on the maximum stress that a member is allowed to experience is used to determine the capacity. This limit is usually some portion of the yield or ultimate strength of the member and is lower for Inventory Level ratings than Operating Level ratings, therefore producing a smaller Inventory RF.

For the LFR method, the dead load factor, A_1, is 1.3 and the live load factor, A_2, is 2.17 for Inventory Level ratings and 1.3 for Operating Level ratings. This produces higher RFs for Operating Level ratings. Also, unlike the ASR method, the member or component capacity is the same for both Inventory Level and Operating Level ratings. It is calculated using the procedure that is presented in the AASHTO Standard Specifications (AASHTO 2002) and uses relationships corresponding to the component and material being evaluated.

2.3.3. Comparison of Bridge Load Rating Methods

Although having three different rating methods allows engineers to, in some cases, choose to rate using the method they prefer, there are some issues. When a bridge was designed using LFD or ASD, the FHWA gives the engineer the option to rate using LFR or LRFR. This option causes uncertainty and a lack of uniformity among states as to which load rating method produces more accurate ratings. Although LRFR is more recently developed and uses a more rigorous approach, one reason many states are hesitant to switch to it is because of the level of comfort they have in using LFR and the amount of resources they have already invested into it (Bowman and Chou 2014). An Indiana DOT survey and an NCHRP survey, both conducted in 2014, found that more states prefer to use the LFR method over the LRFR method to rate their bridges (Bowman and Chou 2014; Hearn 2014). Another reason that state DOTs seem to be unsure of which method to use is because they do not know the effect switching to LRFR will have on the ratings of their bridge populations. Multiple reports have examined how using a different rating method can significantly affect the RF of the same bridge. NCHRP Report 700 (Mlynarski et al. 2011), titled *A Comparison of AASHTO Bridge Load Rating Methods,* examines this issue and compares the results of load rating 1500 bridges using both the LRFR and LFR methods. The bridge types analyzed include simple span steel girder, simple span prestressed I girder, simple span prestressed box, simple span reinforced concrete T-beam, simple span reinforced concrete slab, continuous steel I-girder, continuous prestressed I-girder, and continuous reinforced concrete slab. When analyzed for flexure at the Design-Load Inventory Level, it was found that almost every bridge exhibited an LFR RF higher than its LRFR RF. This was also the case when the bridges were analyzed using the AASHTO legal loads and numerous state-specific legal loads. For most bridges,

the LRFR RF was 60-80 percent of the LFR RF. The same trend was seen when the bridges were analyzed for shear. In the majority of bridges, the LFR RF was higher than the LRFR RF.

The authors determined two main reasons that the LFR method produced higher RFs than the LRFR method. First, the factored live loads were typically higher for the LRFR method than they were for the LFR method. Second, in the AASHTO Virtis computer program they used, the LRFR method checked for more possible controlling capacity scenarios than was done for the LFR method. This included checking shear in concrete beams and slabs, shear friction resistance between concrete girders and cast-in-place concrete decks, bearing stiffener capacity in steel girder bridges, and the effect of shear on the force in longitudinal reinforcement in concrete beams near the girder ends. Many of these checks that were performed by the LRFR method, but not by the LFR method, controlled the RF of the bridge.

In Task 122 of NCHRP Project 20-07 (Mertz 2005), titled *Load Rating by Load and Resistance Factor Evaluation Method*, 74 example bridges were obtained from New York and Wyoming State Department of Transportation databases. These bridges were load rated using both the LRFR and LFR methods under Design Load Rating procedures and the findings were examined and compared. It was found that for most bridge types examined, the LRFR RF was greater than the LFR RF for Inventory Level ratings. However, for Operating Level ratings, the LRFR RF was less than the LFR RF for most bridge types examined. It was also found that LFR Operating Level ratings were usually approximately 67 percent higher than LFR Inventory Level ratings, but LRFR Operating Level ratings were only about 30 percent higher than LRFR Inventory Level ratings. A comparison of NCHRP Report 700 and NCHRP Project 20-07, Task 122 indicates that the results contradict each other. Report 700 found LFR RFs to be greater than LRFR RFs at the Design-Load, Inventory Level, sometimes quite significantly. Task 122 found the opposite,

that LRFR RFs were slightly greater than LFR RFs at the Design-Load, Inventory Level. One possible explanation for this is that Task 122 used a smaller sample size of bridges (74 bridges from two states) and those bridges tended to perform better using LRFR than bridges nationwide. There may also have been a difference in the LRFR checks included in the two studies. These two studies show that load ratings can be quite different depending on which method is used and the bridge being analyzed.

Task 122 also explores the differences in reliability of LRFR ratings and LFR ratings at the Inventory Level. One million Monte Carlo simulations were run for 26 of the 74 bridges and the failure rate for each of those 26 structures was determined. From this, a reliability index was determined for each bridge, for each rating method. This reliability index was plotted versus the Inventory Level RF of each bridge. This plot is shown in Figure 2.2 and reveals a much greater correlation between the reliability index and Inventory Level rating for bridges rated using LRFR than for those rated using LFR. This shows why there has been a big push to switch to using LRFR methods to calculate load ratings in recent years and why it is the FHWA's preferred method of load rating (Mertz 2015; Mertz 2005).

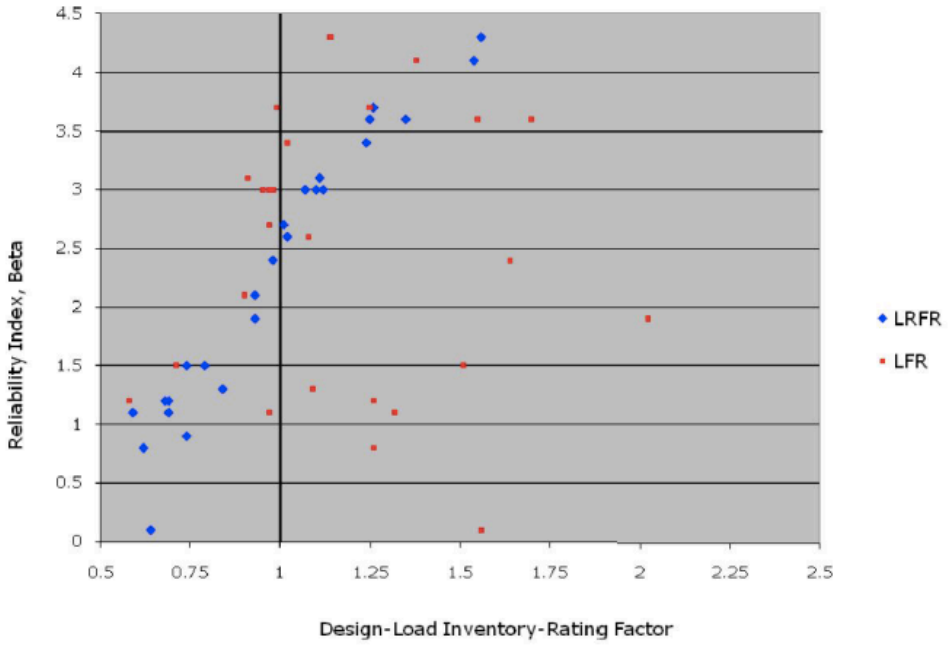

Figure 2.2. Reliability Index vs. Inventory RF for a Database of New York State and Wyoming Bridges (Reprinted from Mertz 2005)

2.3.4. Nondestructive Testing for Bridge Load Rating

The AASHTO MBE (AASHTO 2011) also has a section called Nondestructive Load Testing. Part of this section describes a procedure for load rating a bridge through load testing, using either diagnostic test results or proof test results. A diagnostic test uses loads that are high enough to verify and adjust an analytical model of the bridge. These loads are usually lower than a proof test, in which specific loads are applied to the bridge to determine if the bridge has the capacity to carry these loads without being damaged. Load rating using diagnostic test results is a fairly straightforward procedure. The RF based on test results is the RF found using LRFR methods multiplied by an adjustment factor, *K*. This adjustment factor is affected by other factors that take into account the calculated member strains based on the test vehicle, the member strains observed during the load test, and the ability of the test results to be extrapolated to performance at higher

loads. Proof test results can only be used to find the Operating Level ratings. The RF at Operating Level, RF_O obtained from proof test results is given as,

$$RF_O = \frac{OP}{L_R(1 + IM)} \tag{2.4}$$

where:

OP = Operating level capacity

L_R = Comparable unfactored live load due to the rating vehicle

IM = Dynamic load allowance

The Operating Level capacity, OP, is found as,

$$OP = \frac{k_O L_p}{X_{pA}} \tag{2.5}$$

where:

k_O = 1.0 if the proof load test reached the target load and 0.88 if the proof load test was terminated because of distress in the bridge

L_p = Actual maximum proof live load applied to the bridge

X_{pA} = Target live load factor found using the procedure in Section 8.8.3.3.2 of the MBE (AASHTO 2011)

Although AASHTO gives these procedures to calculate an RF from a load test and load tests are a more refined way to obtain a load rating, load tests are expensive and can be inefficient to run. Load tests can require a significant amount of time and resources to conduct and only give

the RF for one particular structure. For this reason, many states rely on the LRFR, ASR, and LFR methods to load rate bridges and only load test in special circumstances (Hearn 2014).

2.3.5. Material Properties

A large portion of the AASHTO MBE also focuses on material strengths for bridges where the quality of materials used is not known. This could be because the original plans for the bridge either cannot be found or did not specify required material strengths. Because material strengths often play an important role in determining the capacity of the bridge, the MBE gives common values corresponding to time periods of construction.

2.3.5.1. LRFR Material Properties

Table 2.6 through Table 2.9 below contain material strength properties to be used in LRFR when the in-situ strengths are not known. These tables represent some of the material strength information given by the AASHTO MBE (AASHTO 2011). More material strengths for other components are given in Section A of the AASHTO MBE.

Table 2.6. Minimum Compressive Strength of Concrete by Year of Construction (Adapted from AASHTO 2011)

Year of Construction	Compressive Strength, f'_c, ksi
Prior to 1959	2.5
1959 and later	3.0

Table 2.7. Yield Strength of Reinforcing Steel (Adapted from AASHTO 2011)

Type of Reinforcing Steel	Yield Strength, f_y, ksi
Unknown steel constructed prior to 1954	33
Structural grade	36
Billet or intermediate grade, Grade 40, and unknown steel constructed during or after 1954	40
Rail or hard grade, Grade 50	50
Grade 60	60

Table 2.8. Tensile Strength of Prestressing Steel (Adapted from AASHTO 2011)

Year of Construction	Tensile Strength, f_{pu}, ksi
Prior to 1963	232
1963 and Later	250

Table 2.9. Minimum Mechanical Properties of Structural Steel by Year of Construction (Adapted from AASHTO 2011)

Year of Construction	Minimum Yield Point or Minimum Yield Strength, F_y, ksi	Minimum Tensile Strength, F_u, ksi
Prior to 1905	26	52
1905 to 1936	30	60
1936 to 1963	33	66
After 1963	36	66

2.3.5.2. LFR and ASR Material Properties

Table 2.10 and Table 2.11 contain material strength properties to be used in LFR and ASR when the in-situ strengths are not known. These tables represent some of the material strength information given by the AASHTO MBE. More material strengths for other components are given in Section B of the AASHTO MBE.

Table 2.10. Allowable Unit Stresses for Concrete (Adapted from AASHTO 2011)

Year Built	Compressive Strength, f'_c, psi
Prior to 1959	2500
1959 and later	3000

Table 2.11. Allowable Unit Stresses (psi) for Reinforcing Steel (Adapted from AASHTO 2011)

Type of Reinforcing Steel	Inventory Rating	Operating Rating	Yield
Unknown steel constructed prior to 1954	18,000	25,000	33,000
Structural grade	20,000	27,000	36,000
Billet or intermediate grade, Grade 40, and unknown steel constructed during or after 1954	20,000	28,000	40,000
Rail or hard grade, Grade 50	20,000	32,500	50,000
Grade 60	24,000	36,000	60,000

For cases in which the yield strength or allowable stress of other steel members is not specified, the LFR/ASR section of the MBE directs the user to the "date built" column of MBE Tables 6B.6.2.1-1 and 6B.6.2.1-4 for yield strengths, and to Table 10.56A in the AASHTO Standard Specifications (AASHTO 2002) for the maximum strengths of welds, bolts, and rivets. Section 6B.6.3.1 of the MBE also allows for coupon testing to be used to determine the yield strength of a bridge if it is unknown. The yield strength used to determine capacity is taken as the mean test value minus 1.65 standard deviations.

These material strength properties will be examined and discussed in more depth later in this report, as some of them may be able to be refined through laboratory testing of samples obtained from bridges in current use whose load ratings are being evaluated and from available mill certificate information from bridges of interest.

2.3.6. Other Relevant Load Rating Practices

2.3.6.1. National Bridge Inventory and Weight Limits

In addition to the MBE, the FHWA provides further policy for load rating bridges. The FHWA requires states to load rate all of their public bridges longer than 20 feet and report the results

(United States Government 2004). This information along with information about dozens of other characteristics about each bridge is stored in the National Bridge Inventory (NBI) (NBI 2016). This makes it relatively easy to obtain selected bridge information without having to conduct a site visit or rating calculations.

Title 23 of the United States Code (United States Government 1958) provides weight limits for vehicles travelling on the Interstate Highway System and the FHWA summarizes these limits in a guidance pamphlet entitled *Bridge Formula Weights*, which was most recently revised in May 2015 (FHWA 2015). This guide contains a formula to determine the allowable overall gross weight on any group of two or more consecutive axles that is allowed on an Interstate Highway System bridge. This formula is based on the distance between the outer axles in the group and the number of axles in the group. From this formula, a convenient table was produced to show the maximum allowable weights for different numbers of axles and spacing. Even though the table may provide higher allowable weights, the FHWA sets the maximum gross weight allowed for a vehicle to an upper limit of 80,000 lbs, unless the formula gives a lower number (FHWA 2015). Title 23 of the United States Code also sets a limit of 20,000 lbs per axle and 34,000 lbs per tandem axle (United States Government 1958).

2.3.6.2. LRFD Live Load Distribution Factors

Live load distribution factors (LLDFs) are another item of interest when discussing load rating of bridges. Moment LLDFs are focused on in this report as the moment capacity is usually the controlling feature in the capacity of the bridge, as opposed to the shear. Determination of shear LLDFs follows a similar procedure to the determination of moment LLDFs, equations for which can be found in the AASHTO LRFD Bridge Design Specifications (AASHTO 2017). Moment

LLDFs are applied to the live load effect that a member experiences and therefore influence the RF calculated for that member. Currently, for moment on interior beams, LRFD moment LLDFs are calculated through a series of procedures and equations outlined in Section 4 of the AASHTO LRFD Specifications (AASHTO 2017). In almost all cases, depending on the type and cross-section of the superstructure, different equations involving the girder spacing, length of span, and transverse stiffness are given to determine moment LLDFs for interior or exterior girders.

For moment on exterior beams, in most cases, the lever rule is used to determine the LRFD moment distribution factor. The lever rule begins by assuming that the deck of the bridge is hinged at the interior girder closest to the exterior girder for which the moment distribution factor is being analyzed. The truck is then placed with the closest wheel two feet from the barrier or curb. Finally, the reaction on the exterior girder from this loading is to determine the exterior girder moment LLDF (Barth 2015).

These equations and procedures to determine the LRFD LLDFs were first developed and recommended to AASHTO through NCHRP Project 12-26, completed in 1990 (Zokaie et al. 1991). Data from bridge inventories was compiled and average bridges that represented a variety of different bridge types were developed. The average bridges had wheel loads applied to them and their geometric parameters were varied to see how the moment and shear LLDFs changes with those variations. Formulas for the LLDFs were then developed by analyzing each average bridge at three different levels. Bridges were analyzed using simplified analytical methods, graphical analysis methods, and the finite element method (FEM). From this, simplified formulas for the LLDFs were developed. These simplified formulas were compared to the analytical methods and FEM analysis and the formulas that gave the most accurate results were adopted as the pertinent

formulas. With minor adjustments, these formulas are the ones that are included in the *AASHTO LRFD Bridge Design Specifications* (Mertz 2007).

When using the lever rule, the moment LLDF for each girder is multiplied by a multiple presence factor and the overall live load effect to determine the design live load effect for an individual girder. When using one of the simplified equations, the multiple presence factor is included, and therefore the resulting moment LLDF only needs to be multiplied by the overall live load effect. When calculating the RF for an individual member, the LLDF will affect the amount of live load moment or shear that member must resist. The AASHTO MBE (AASHTO 2011) does not specifically mention under which scenarios to use LLDFs and if those factors are modified for load rating. However, in Section 6A.3 it states that "methods of structural analysis suitable for the evaluation of bridges shall be as described in Section 4 of the AASHTO LRFD Bridge Design Specifications." From this statement, it can be inferred that the live load distribution factors that are described in the *AASHTO LRFD Bridge Design Specifications* therefore also apply to the LRFR method of load rating. Figure 2.3 below shows the moment LLDFs for interior beams given in the 2017 edition of the *AASHTO LRFD Bridge Design Specifications*.

Type of Superstructure	Applicable Cross-Section from Table 4.6.2.2.1-1	Distribution Factors	Range of Applicability
Wood Deck on Wood or Steel Beams	a, l	See Table 4.6.2.2.2a-1	
Concrete Deck on Wood Beams	l	One Design Lane Loaded: $S/12.0$ Two or More Design Lanes Loaded: $S/10.0$	$S \le 6.0$
Concrete Deck or Filled Grid, Partially Filled Grid, or Unfilled Grid Deck Composite with Reinforced Concrete Slab on Steel or Concrete Beams; Concrete T-Beams, T- and Double T-Sections	a, e, k and also i, j if sufficiently connected to act as a unit	One Design Lane Loaded: $0.06+\left(\frac{S}{14}\right)^{0.4}\left(\frac{S}{L}\right)^{0.3}\left(\frac{K_g}{12.0Lt_s^3}\right)^{0.1}$ Two or More Design Lanes Loaded: $0.075+\left(\frac{S}{9.5}\right)^{0.6}\left(\frac{S}{L}\right)^{0.2}\left(\frac{K_g}{12.0Lt_s^3}\right)^{0.1}$	$3.5 \le S \le 16.0$ $4.5 \le t_s \le 12.0$ $20 \le L \le 240$ $N_b \ge 4$ $10{,}000 \le K_g \le 7{,}000{,}000$
		use lesser of the values obtained from the equation above with $N_b = 3$ or the lever rule	$N_b = 3$
Cast-in-Place Concrete Multicell Box	d	One Design Lane Loaded: $\left(1.75+\frac{S}{3.6}\right)\left(\frac{1}{L}\right)^{0.35}\left(\frac{1}{N_c}\right)^{0.45}$ Two or More Design Lanes Loaded: $\left(\frac{13}{N_c}\right)^{0.3}\left(\frac{S}{5.8}\right)\left(\frac{1}{L}\right)^{0.25}$	$7.0 \le S \le 13.0$ $60 \le L \le 240$ $N_c \ge 3$ If $N_c > 8$ use $N_c = 8$
Concrete Deck on Concrete Spread Box Beams	b, c	One Design Lane Loaded: $\left(\frac{S}{3.0}\right)^{0.35}\left(\frac{Sd}{12.0L^2}\right)^{0.25}$ Two or More Design Lanes Loaded: $\left(\frac{S}{6.3}\right)^{0.6}\left(\frac{Sd}{12.0L^2}\right)^{0.125}$	$6.0 \le S \le 18.0$ $20 \le L \le 140$ $18 \le d \le 65$ $N_b \ge 3$
		Use Lever Rule	$S > 18.0$
Concrete Beams used in Multibeam Decks	f, g	One Design Lane Loaded: $k\left(\frac{b}{33.3L}\right)^{0.5}\left(\frac{I}{J}\right)^{0.25}$ where: $k = 2.5(N_b)^{-0.2} \ge 1.5$ Two or More Design Lanes Loaded: $k\left(\frac{b}{305}\right)^{0.6}\left(\frac{b}{12.0L}\right)^{0.2}\left(\frac{I}{J}\right)^{0.06}$	$35 \le b \le 60$ $20 \le L \le 120$ $5 \le N_b \le 20$

Type of Superstructure	Applicable Cross-Section from Table 4.6.2.2.1-1	Distribution Factors	Range of Applicability
	h, also i, j if connected only enough to prevent relative vertical displacement at the interface	Regardless of Number of Loaded Lanes: S/D where: $C = K(W/L) \le K$ $D = 11.5 - N_L + 1.4N_L(1-0.2C)^2$ when $C \le 5$ $D = 11.5 - N_L$ when $C > 5$ $K = \sqrt{\frac{(1+\mu)I}{J}}$ for preliminary design, the following values of K may be used: Beam Type — K Nonvoided rectangular beams — 0.7 Rectangular beams with circular voids: — 0.8 Box section beams — 1.0 Channel beams — 2.2 T-beam — 2.0 Double T-beam — 2.0	Skew $\le 45°$ $N_L \le 6$
Open Steel Grid Deck on Steel Beams	a	One Design Lane Loaded: $S/7.5$ If $t_g < 4.0$ $S/10.0$ If $t_g \ge 4.0$ Two or More Design Lanes Loaded: $S/8.0$ If $t_g < 4.0$ $S/10.0$ If $t_g \ge 4.0$	$S \le 6.0$ $S \le 10.5$
Concrete Deck on Multiple Steel Box Girders	b, c	Regardless of Number of Loaded Lanes: $0.05+0.85\frac{N_L}{N_b}+\frac{0.425}{N_L}$	$0.5 \le \frac{N_L}{N_b} \le 1.5$

Figure 2.3. Moment Live Load Distribution Factors per Lane for Interior Beams (Reprinted from AASHTO 2017)

2.3.6.3. LFR and ASR Live Load Distribution Factors

When determining capacity using the LFD method, the LLDFs are calculated using simplified equations that were first introduced by Newmark in 1938 (Newmark 1938) and slightly updated as research became available to increase their accuracy. The factors are given in the form of *S/D*, where *S* is the spacing of the girders and *D* is a factor that changes depending on the type of bridge being analyzed. As can be seen, this formula does not take into account deck stiffness, span length, or skew, which are considered for the LRFD LLDFs. This can make the LFD distribution factors less accurate and too conservative for bridges with characteristics outside of certain ranges (Hueste et al. 2015). Adjusting the LFD distribution factors to make them more accurate is something that could be explored in an effort to improve load ratings. The LFD distribution factors are given in Figure 2.4.

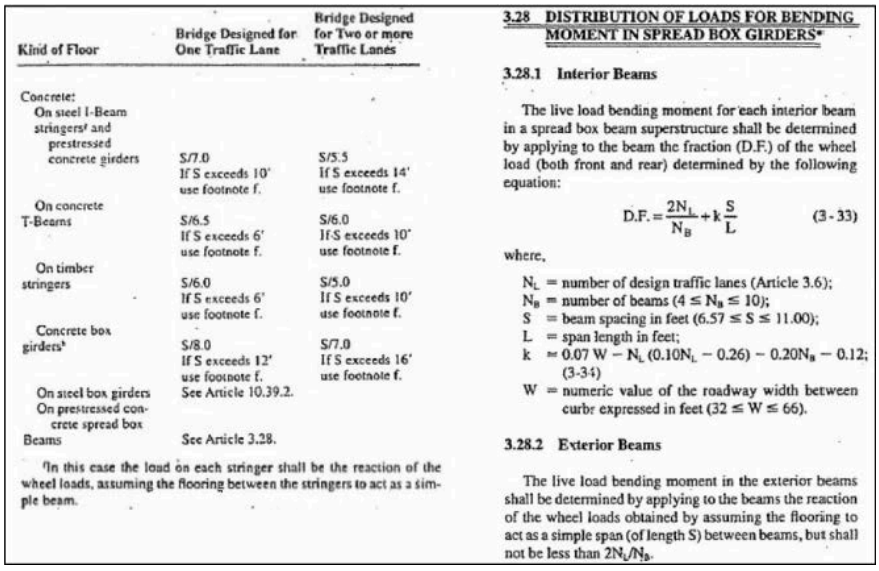

Kind of Floor	Bridge Designed for One Traffic Lane	Bridge Designed for Two or more Traffic Lanes
Concrete: On steel I-Beam stringers[a] and prestressed concrete girders	S/7.0 If S exceeds 10' use footnote f.	S/5.5 If S exceeds 14' use footnote f.
On concrete T-Beams	S/6.5 If S exceeds 6' use footnote f.	S/6.0 If S exceeds 10' use footnote f.
On timber stringers	S/6.0 If S exceeds 6' use footnote f.	S/5.0 If S exceeds 10' use footnote f.
Concrete box girders[b]	S/8.0 If S exceeds 12' use footnote f.	S/7.0 If S exceeds 16' use footnote f.
On steel box girders	See Article 10.39.2.	
On prestressed concrete spread box Beams	See Article 3.28.	

[a]In this case the load on each stringer shall be the reaction of the wheel loads, assuming the flooring between the stringers to act as a simple beam.

3.28 DISTRIBUTION OF LOADS FOR BENDING MOMENT IN SPREAD BOX GIRDERS*

3.28.1 Interior Beams

The live load bending moment for each interior beam in a spread box beam superstructure shall be determined by applying to the beam the fraction (D.F.) of the wheel load (both front and rear) determined by the following equation:

$$D.F. = \frac{2N_L}{N_B} + k\frac{S}{L} \qquad (3-33)$$

where,

N_L = number of design traffic lanes (Article 3.6);
N_B = number of beams ($4 \le N_B \le 10$);
S = beam spacing in feet ($6.57 \le S \le 11.00$);
L = span length in feet;
k = $0.07\,W - N_L(0.10N_L - 0.26) - 0.20N_B - 0.12$; (3-34)
W = numeric value of the roadway width between curbs expressed in feet ($32 \le W \le 66$).

3.28.2 Exterior Beams

The live load bending moment in the exterior beams shall be determined by applying to the beams the reaction of the wheel loads obtained by assuming the flooring to act as a simple span (of length S) between beams, but shall not be less than $2N_L/N_B$.

Figure 2.4. *S/D* Distribution Factors (Reprinted from AASHTO 1996)

2.4. OTHER LOAD RATING PRACTICES IN THE U.S.

In 2014, NCHRP released Synthesis 453, titled *State Bridge Load Posting Processes and Practices* (Hearn 2014). A survey was sent to all fifty states in the U.S. asking a variety of questions about their load rating practices. Out of the 50 states that the survey was sent to, 43 responded and the results were compiled and reported. Out of the 43 responses, 29 states reported that they use LRFR, 39 use LFR, 27 use ASR, 34 use more than one load rating method, and 18 reported using all three load rating methods in practice. It can be seen that although the LRFR method is encouraged by the FHWA, many states still heavily rely on the older methods of load rating. Many of the states that were surveyed also use other methods to load rate besides the basic analytical methods.

2.4.1. Refined Analysis and Improvement of Ratings

Twenty-four states reported using refined analysis methods such as FEM analysis in their load rating practices. Of those, the NCHRP Synthesis 453 report states that 18 reported using refined methods to avoid posting, 14 used them for analyzing complex bridges, and six used refined methods for both of those reasons (Hearn 2014). Other states such as Iowa, Oregon, and Pennsylvania use refined methods or FEM to determine new live load distribution factors to use in analytical methods (Iowa DOT 2013; Oregon DOT 2015; Pennsylvania DOT 2010). West Virginia uses refined analysis methods to compute conversion factors between refined and analytical ratings when new bridges are designed. These conversion factors may then be used to refine future analytical rating calculations (Hearn 2014). The Oregon DOT states in their LRFR Manual that updated material properties may be used if samples from the bridge are obtained and tested. They also allow the LLDFs to be obtained by placing the vehicles in the actual striped lanes of the bridge if it does not initially pass using analytical methods (Oregon DOT 2015). Both the

Oregon and Florida DOTs allow the initial RF calculated using AASHTO's analytical methods to be rounded up by five percent (Florida DOT 2017; Oregon DOT 2015). Florida also allows the AASHTO provided dead load factor of 1.25 to be reduced to 1.15 "when dimensions are thoroughly and accurately field verified" (Florida DOT 2017). These practices are part of the Posting Avoidance step of FDOT's load rating procedures, which is given in their Load Rating Manual as a flowchart, shown in Figure 2.5.

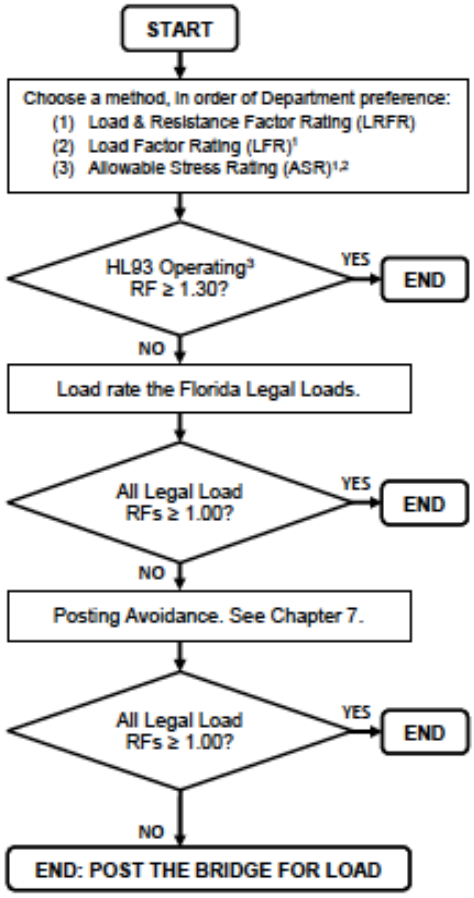

1. LFR and ASR are not permitted among spans exceeding 200 feet.
2. ASR is not permitted for bridges on the National Highway System.
3. At existing bridges, if $RF_{HL93\ Operating} < 1.30$, or if LFR/ASR, assess the Legal Loads.

Figure 2.5. Florida DOT Load Rating Flowchart (Reprinted from Florida DOT 2017)

2.4.2. Field Evaluation and Engineering Judgement

Out of the 43 states that responded to the NCHRP Synthesis 453 survey, 27 reported allowing field evaluation or engineering judgement to be used in load rating bridges. Indiana, Iowa, Pennsylvania, and Wisconsin are among those that allow engineering judgement to be used to rate a reinforced concrete bridge if the reinforcing details are unknown (Indiana DOT 2016; Iowa DOT 2013; Pennsylvania DOT 2010; Wisconsin DOT 2017). The FDOT Bridge Load Rating Manual states that if the bridge with unknown reinforcing details shows no signs of distress, it can be assigned a load rating. However, if it does show signs of distress, the bridge must be load tested (Florida DOT 2017). Although it would seem that numerous state DOTs allow load rating through engineering judgement, some specifically do not. The Massachusetts DOT states in its LRFD Bridge Manual (MassDOT 2013) that using engineering judgement alone is not allowed to load rate. It requires that field measurements, non-destructive testing, and material testing be performed for bridges with unknown structural details.

2.4.3. Load Testing

A total of 19 out of 43 states in the original NCHRP Synthesis 453 reported using load tests to load rate. The Iowa DOT Bridge Rating Manual allows load testing for rating if “deterioration is difficult to quantify, conventional analysis methods are difficult to apply to a unique structural configuration, or there is a public need to allow larger vehicles to cross a bridge than the conventional analysis will allow” (Iowa DOT 2013). A variety of other state DOT load rating manuals specifically allow for load testing to be used on a case-by-case basis, with most following the load testing processes set out in the AASHTO MBE (Michigan DOT 2009; Minnesota DOT

2009; New York State DOT 2005; Oregon DOT 2015; Pennsylvania DOT 2010; Rhode Island DOT 2017; Utah DOT 2014; Wisconsin DOT 2017).

2.5. RESEARCH STUDIES

2.5.1. Research by State DOTs to Improve Load Rating Practices

2.5.1.1. Georgia

In 2006, the Georgia Institute of Technology (Georgia Tech) was tasked by the Georgia Department of Transportation (GDOT) to develop *Recommended Guidelines for Condition Assessment and Evaluation of Existing Bridges in Georgia* by analyzing and load testing four bridges (Ellingwood et al. 2009a; Ellingwood et al. 2009b; Ellingwood et al. 2009c). The bridges selected to test were a straight reinforced concrete T-beam bridge, a skewed reinforced concrete T-beam bridge, a prestressed concrete I-beam bridge, and a non-composite slab on steel I-girder bridge. All of the bridges were simply supported. These bridges were selected because regular and skewed T-beam bridges and steel girder bridges represent a significant population of the bridges in Georgia that are load rated. The prestressed concrete bridge was included because over half of the prestressed concrete bridges in the state that were posted were less than 30 years old and GDOT wanted Georgia Tech to determine why this was the case. A static, diagnostic load test was conducted on each of the four bridges using one, two, three, and four Type 3 trucks, with individual truck weights ranging from 50 kips to almost 70 kips. Dial gauges and potentiometers were used to measure deflections under loading. These field measured deflections were compared to deflections obtained using three-dimensional finite element models of each bridge. The finite element models were constructed using the computer program ABAQUS.

During the load tests, the two concrete T-beam bridges and the steel girder bridge were all loaded significantly above their design or posted limits, and all four bridges remained within their elastic limit. Therefore, the bridges all had significant reserve capacity as compared to the design or posted loads. The researchers also found that in most cases the FEM analysis predicted similar and slightly higher deflections than the field tests produced. In all cases, the measured and computed deflections were similar and the maximum live load deflections all remained less than 50 percent of the *L*/800 limit that the AASHTO LRFD Specifications (AASHTO 2017) provides. As a result of this similarity, the FEM models were used to explore certain characteristics about the bridges that affected their load carrying capacity. The moment LLDFs for interior girders were calculated using the formulas provided in the AASHTO LRFD Specifications (AASHTO 2017) and were determined through the FEM analysis developed for each bridge. For each bridge, the moment LLDFs for interior girders were lower when found using the FEM. This would decrease the live load moment effect for those girders, increasing the RF for them. This increases the live load moment effect on the exterior girders. However, this does not increase their exterior girder LLDF above the AASHTO LRFD LLDF. Therefore, when the FEM LLDFs are used, the controlling moment that affects the RF of the bridge is reduced.

The researchers also conducted what they called a “static pushdown test” using the FEM model of each bridge. In this test, two HS20 trucks were placed side-by-side in a location that maximized the moment effect on the girders. The loads of the trucks, without application of load factors, were systematically increased until an element of the structural system yielded in the model. This allowed the researchers to effectively determine an Operating Level rating from the model, as the lowest moment effect that caused yielding was used as the live load effect in the RF equation. Through this method it was found that each bridge had an operating capacity

substantially higher than the HS-20 truck load. The operating RFs for an HS-20 truck were greater than 4.0 for all four bridges and greater than 5.0 for two of them.

At the conclusion of the research, the research team from Georgia Tech produced *Recommended Guidelines for Condition Assessment, Evaluation, and Rating of Bridges in Georgia*. The main change they suggest for the load rating section of the AASHTO MBE is increasing some material properties based on laboratory tests that were also conducted. The straight T-beam bridge that was field tested was scheduled to be destructed after the field test. Concrete cores were taken from the slab and girders of this bridge and tested under compression. The tests found that the compressive strength of the cores was significantly higher than what was specified when the bridge was constructed. Therefore, some of the concrete compressive strengths that depend on the period of construction were increased and updated. The researchers also provided load rating examples for a straight T-beam bridge, a steel girder bridge, and a prestressed concrete bridge in their recommendations. In each of these examples, the live load distribution factors found using FEM analysis were used to increase the RF for the bridge.

2.5.1.2. Oregon

In a study sponsored by the Oregon Department of Transportation (ODOT) in 2005, researchers used weigh-in-motion (WIM) tests to determine the actual truck weights and configurations that were driving on the roads in Oregon (Pelphrey et al. 2008). They then used this data to develop new live load factors for Legal Loads and Permit Loads and replaced the factors given in Table 6A.4.2.2-1 in the AASHTO MBE.

To obtain WIM data, a pair of loop detectors and sensors were installed directly into one lane on the roadway. They were spaced a certain distance apart longitudinal to the roadway. The

sensors were also offset in the transverse direction so that one sensor covered one half of the lane, and the other sensor further down covered the other half of the lane. When the sensors were run over by a vehicle, they recorded the force applied as an electrical charge. The magnitude of this electrical charge corresponds to the magnitude of the force that was applied. As a result of being offset both transversely and longitudinally within the lane, the sensors could also measure velocity and spacing of axles. Therefore, the axle configurations and weights of any vehicle that passed over the sensors could be determined (Quinley 2010; Shoukry et al. 2008).

The researchers in the Oregon study used four WIM sites on four major roadways in the state to obtain truck weight data that was specific to the state of Oregon. The maximum loading event used to calibrate new factors assumes a legal or permit truck in one lane of the bridge and a random truck, called an alongside truck, in the lane next to it. Using the WIM data, the researchers determined the mean and standard deviation of the top 20 percent of rating vehicle truck weights and alongside vehicle truck weights. Using this data and following the same procedure used in NCHRP Project 12-46 and outlined in NCHRP Report 454 (Moses 2001), new live load factors were calculated as,

$$\gamma_{\mathrm{L}} = 1.8\frac{W_T}{240} \times \frac{72}{W} \tag{2.6}$$

for legal loads,

$$W_T = R_T + A_T \tag{2.7}$$

$$R_T = W^* + t_{ADTT}\sigma^*_{type} \tag{2.8}$$

$$A_T = W^*_{along} + t_{ADTT}\sigma^*_{along} \quad (2.9)$$

for permit loads, Eqn. (2.10) replaces Eqn. (2.8).

$$R_T = P + t_{ADTT}\sigma^*_{along} \quad (2.10)$$

where:

γ_L = Live load factor for the legal or permit vehicle

W = Gross weight of the legal or permit vehicle for which the live load factor is being calculated

W_T = Expected maximum total weight of rating and alongside vehicles

R_T = Rating truck

A_T = Alongside truck

W^* = Mean of the top 20 percent of legal trucks from the group being examined

σ^*_{type} = Standard deviation of the top 20 percent of trucks from the group being examined

t_{ADTT} = Fractal value corresponding to the number of side-by-side events (see NCHRP Report 454)

W^*_{along} = Mean of the top 20 percent of alongside trucks

σ^*_{along} = Standard deviation of the top 20 percent of alongside trucks

P = Weight of permit truck

The researchers found that there were significantly more overloads in the original data used to determine the AASHTO LRFD live load factors than in the Oregon state specific WIM data that was collected. This led them to suggest to ODOT the reduction of some of the live load factors

that depend on average daily truck traffic (ADTT) (Pelphrey et al. 2008). Reducing the live load factor reduces the live load effect on the bridge. As the live load effect is in the denominator of the LRFR RF equation (Eqn. 2.1), reducing it will cause an increase in the RF of the bridge. These new live load factors that were developed are currently being used by ODOT in their LRFR procedures (Oregon DOT 2015). ODOT modifies the load factors from the Routine Commercial Traffic (Type 3, Type 3S2, and Type 3-3) side of Table 2.2 to those in Table 2.12 or Table 2.13, with interpolation allowed between ADTTs.

Table 2.12. Oregon Generalized Live Load Factors for Legal Loads on State-Owned Bridges (Adapted from ODOT 2015)

ADTT (one direction)	Live Load Factor, γ_L
Unknown	1.40
≥ 5000	1.40
= 1500	1.35
≤ 500	1.30

Table 2.13. Oregon Generalized Live Load Factors for Legal Loads on Local Agency Bridges (Adapted from ODOT 2015)

ADTT (one direction)	Live Load Factor, γ_L
Unknown	1.45
≥ 5000	1.45
≤ 1000	1.30

2.5.1.3. Kentucky

In a report published in 2016 (Peiris and Harik 2016), the state of Kentucky load tested a bridge in an effort to increase its rating. Using strain gauges attached at various locations along the span and on the girders, they found that the bridge exhibited unintended composite action for which it was not designed. Through the results of the load test, they were able to increase the operating RF of the bridge from 0.58 to 2.34. Figure 2.6 shows the measured strains at various depths on the girder

and an assumed strain profile developed by the researchers. A fully composite neutral axis can be calculated as approximately 12.28 inches from the bottom of the cross-section. This location is very similar to the location of the measured neutral axis found by the researchers of the Kentucky test. It can therefore be assumed that this bridge was indeed acting in an almost fully composite manner, likely because its top flange is slightly embedded into the concrete deck.

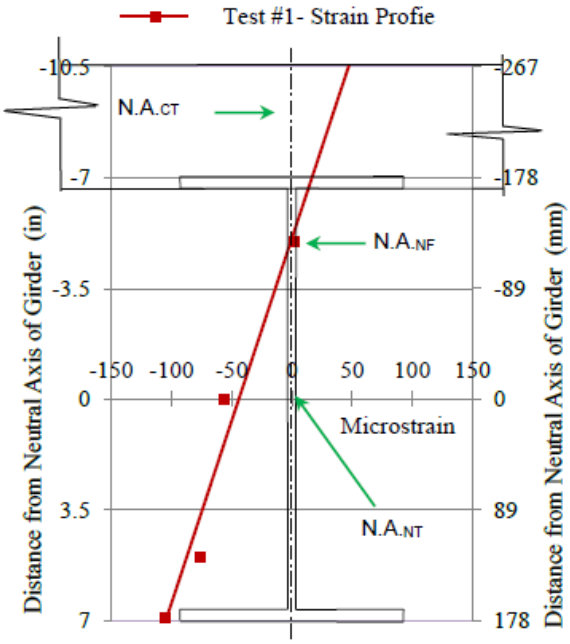

Figure 2.6. Strain Readings at Mid-span for Kentucky Load Test (Reprinted from Peiris and Harik 2016)

2.5.1.4. New York

In three reports published in 2006 (Hag-Elsafi and Kunin 2006a, Hag-Elsafi and Kunin 2006b, Hag-Elsafi and Kunin 2006c), the state of New York conducted static and dynamic load tests on three simply-supported steel multi-girder bridges with concrete decks. The bridges were load tested in an effort to increase load ratings through the investigation of transverse load distribution

and partial composite action. Multiple load paths and patterns were used in an effort to produce the worst possible effects on individual girders. The transverse load distribution, as well as any partial composite action, were determined by analyzing the strain exhibited in each girder during the loading.

For one test, the maximum interior girder live load distribution factor was 0.345 with one truck on the bridge (Hag-Elsafi and Kunin 2006a). This compares to a live load distribution factor of 0.417 found using the AASHTO Standard Specifications, and a live load distribution factor of 0.528 found using the AASHTO LRFD Specifications. In another test, the maximum interior girder live load distribution factor was 0.262 with one truck on the bridge (Hag-Elsafi and Kunin 2006c). This compares to a live load distribution factor of 0.417 found using the AASHTO Standard Specifications, and a live load distribution factor of 0.457 found using the AASHTO LRFD Specifications.

All three of the New York tests also found an increase in girder stiffness due to a higher neutral axis location, likely as a result of partial composite action. One test reported increases in section modulus ranging from 15% to 20%, one test reported increases in section modulus ranging from 15% to 45%, and one test reported increases in moment of inertia ranging from 21% to 67% (Hag-Elsafi and Kunin 2006a, Hag-Elsafi and Kunin 2006c, Hag-Elsafi and Kunin 2006b).

2.5.2. Other Research Conducted to Improve Load Rating Practices

Santini-Bell et al. (2013) conducted a case study highlighting the advantages of a bridge rating procedure incorporating three-dimensional structural modeling and non-destructive testing. Strain gauges were installed on the girders of a three-span, continuous composite steel-girder bridge with a reinforced concrete deck, during fabrication. Prior to opening the bridge to traffic, it

was subjected to a pseudo-static load test. The strain results from this load test were used to calibrate a finite element model of the bridge. The researchers found the rating factor obtained from the calibrated finite element model to be higher than the rating factor calculated using the AASHTO specifications.

In 1997, Chajes et al. (1997) conducted a non-destructive experimental load test on a three-span, load posted, slab-on-steel girder bridge. The bridge was designed as a non-composite structure with three simply supported spans. It was tested using strain transducers placed at varying depths on the cross-section and mainly at midspan of the girders. The results obtained from the strain transducers indicated composite action between the girders and deck. A two-dimensional FEM model was developed using composite section properties and bearing restraints that were calibrated based on the load test data. The results obtained from the model indicated that the bridge had a higher load carrying capacity and that the load posting may not be required.

2.6. LOAD POSTED BRIDGE INVENTORY IN TEXAS

The Federal Highway Administration (FHWA) has two classifications used to describe the condition of a posted bridge. The first is *structurally deficient* (SD), meaning it has severe deterioration or other problems causing extreme reduction in load carrying capacity. The second is *functionally obsolete* (FO), meaning the bridge does not satisfy the original design criteria in some way. TxDOT has a third term used to describe the condition of a posted bridge, *sub-standard for load only* (SSLO). This category describes bridges that have a load carrying capacity below the legal limit, but do not fit into the SD or FO categories. Essentially, SSLO bridges do not have deterioration, and satisfy the original design criteria, they were just designed for less heavy vehicles than the vehicles currently used to design and rate bridges. These SSLO bridges are the

focus of this research study. Ratings for SSLO bridges are more likely to be able to be improved because there is nothing physically wrong with the bridge. Table 2.14 shows the load posted bridges in Texas by their condition classification. On-system bridges are those which are part of a designated highway system and for which TxDOT is responsible for maintenance. Off-system bridges are those which are not part of a highway system and for which another entity, usually a county or city government, is responsible for the maintenance. There are 969 total SSLO bridges in Texas, 78 of which are on-system structures. Both of these values are more than for SD or FO bridges.

Table 2.14. Texas Load Posted Bridges by Condition Classification

Condition Classification	On-System	Off-System	Total
Structurally Deficient (SD)	39	473	512
Functionally Obsolete (FO)	58	572	630
Sub-Standard for Load Only (SSLO)	78	891	969
Total	175	1936	2111

Of the SSLO bridges in Texas, 257 are steel simple-span, multi-girder bridges, accounting for 26.5 percent of the SSLO bridges in Texas. Of the SSLO steel simple-span, multi-girder bridges, 14 are on-system and 243 are off-system. There are also 109 steel continuous, multi-girder SSLO bridges, accounting for 11.2 percent of the SSLO bridges in Texas. Of the SSLO steel continuous, multi-girder bridges, 6 are on-system and 103 are off-system. As steel multi-girder bridges account for more than one-third of the SSLO bridge inventory in Texas, they were selected to investigate further for this research study.

3. LOAD RATING PROCEDURES

3.1. UPDATES IN THE 2018 MANUAL FOR BRIDGE EVALUATION

The American Association of State Highway and Transportation Officials (AASHTO) released the third edition of the Manual for Bridge Evaluation (MBE) in 2018. While the third edition makes no major changes to the general load rating procedures from the second edition, there are some minor changes that do affect load rating. One of these changes is the reduction of the Load and Resistance Factor Rating (LRFR) live load factors for routine commercial traffic, specialized hauling vehicles, and permit vehicles. However, these new load factors only affect Legal Load Rating and Permit Load Rating; the load factors for Design Load Rating remain the same. This research study is focused on the Design Load Rating, so this change does not affect the calculated load ratings provided in this report.

A second change in the third edition AASHTO MBE that could possibly affect this study is the removal of a statement allowing for concrete bridges that have been "carrying normal traffic for an appreciable length of time and show no signs of distress" (AASHTO MBE 2011) to not require a load posting. This is usually applied to concrete bridges in which the reinforcement details are unknown. TxDOT appears to apply this statement for concrete bridges as well as for the concrete decks of steel bridges, as they use an assumed load rating in both cases when drawings are not available. However, the removal of this statement from the third edition MBE could affect TxDOT practices for load rating in these cases. The third edition MBE does not provide an alternate option to load rate a concrete bridge in which the reinforcement details are unknown, and so TxDOT will need to determine whether to continue this as an in-house practice.

3.2. CURRENT LOAD RATING PROCEDURES

3.2.1. Allowable Stress Rating (ASR) and Load Factor Rating (LFR)

Part B of the AASHTO MBE covers the older methods to load rate bridges: Allowable Stress Rating (ASR) and Load Factor Rating (LFR). Both methods use the same general equation to obtain an RF, shown in Eqn. (3.1).

$$RF = \frac{C - A_1 D}{A_2 L(1 + I)} \tag{3.1}$$

where:

RF = Rating factor for the live load carrying capacity

C = Capacity of the member

D = Dead load effect on the member

L = Live load effect on the member

I = Impact factor to be used with live load effect

A_1 = Factor for dead loads

A_2 = Factor for live load

The ASR and LFR methods do not have the different load rating procedures used for LRFR. The bridge is only evaluated under the design truck load or one of the legal loadings. The A_1 and A_2 factors, which are similar to the dead and live load factors in LRFR, do not change. The design load, and therefore the first loading scenario to be evaluated for ASR and LFR is the HS-20 truck configuration, as opposed to the HL-93 loading used by LRFR. If the bridge passes (has an RF greater than 1.0) for the HS-20 loading it also passes for all of the AASHTO and state legal loads.

For the ASR method, the dead and live load factors, A_1 and A_2, are both equal to 1.0. The capacity of the member changes depending on whether the bridge is being evaluated at inventory level or operating level. The MBE has tables and subsections dedicated to finding the capacity for different materials and situations using the ASR method. As the name Allowable Stress Rating suggests, a limit on the maximum stress that a member is allowed to experience is used to determine the capacity. This limit is usually some portion of the yield or ultimate strength of the member and is lower for Inventory Level ratings than Operating Level ratings, therefore producing a smaller Inventory RF.

For the LFR method, the dead load factor, A_1, is 1.3, and the live load factor, A_2, is 2.17 for Inventory Level Ratings and 1.3 for Operating Level Ratings. This produces lower RFs for Inventory Level ratings. Also, unlike the ASR method, the member or component capacity is the same for both Inventory Level and Operating Level ratings. It is calculated using the procedure presented in the AASHTO Standard Specifications (AASHTO 2002) and uses different equations depending on the component and material being evaluated.

3.2.2. Load and Resistance Factor Rating

The general equation to obtain the bridge rating factor (RF) using the LRFR method is shown in Eqn. (3.2).

$$RF = \frac{C - (\gamma_{\mathrm{DC}})(DC) - (\gamma_{DW})(DW) \pm (\gamma_P)(P)}{(\gamma_{LL})(LL + IM)} \tag{3.2}$$

where:

RF = Rating factor

C = Capacity

DC = Dead load effect due to structural components and attachments

DW = Dead load effect due to wearing surface and utilities

P = Permanent loads other than dead loads

LL = Live load effect

IM = Dynamic load allowance

γ_{DC} = LRFD load factor for structural components and attachments

γ_{DW} = LRFD load factor for wearing surfaces and utilities

γ_{P} = LRFD load factor for permanent loads other than dead loads = 1.0

γ_{LL} = Evaluation live load factor

For the strength limit states, the capacity is determined as the nominal member resistance multiplied by an LRFD resistance factor ϕ, a system factor ϕ_s, and a condition factor ϕ_c. The product of the condition and system factors is required to be greater than 0.85. An RF is determined for each structural component of the bridge, and the member that has the lowest RF governs. The RF of the controlling member is then said to be the RF for the entire structure. The limit state that is chosen for determination of the RF gives specific values for γ_{DC}, γ_{DW}, and γ_{LL}. The primary limit state used for the LRFR method is Strength I, however the limit state that is evaluated is dependent on the rating procedure used, as some limit states only apply to specific rating procedures and not to others. The basic load ratings in this report use the Strength I and Service II limit states at the Design Load Rating level for steel bridges and the Strength I limit state at the Design Load Rating level for reinforced concrete bridges. Table 3.1 shows the dead load and live load factors for these limit states.

Table 3.1. Load Factors for Load Rating for Various Limit States (Adapted from AASHTO MBE 2018)

Bridge type	Limit State	Dead Load γ_{DC}	Dead Load γ_{DW}	Design Load	
				Inventory	Operating
				γ_{LL}	γ_{LL}
Steel	Strength I	1.25	1.50	1.75	1.35
	Service II	1.00	1.00	1.30	1.00
Reinforced Concrete	Strength I	1.25	1.50	1.75	1.35

Design Load Rating is the first assessment conducted in the LRFR bridge rating procedure and uses the HL-93 load model, which consists of an HS20 truck plus lane load (AASHTO 2014). The Design Load Rating is split into two separate rating levels, the Inventory Rating Level and the Operating Rating Level. The Inventory Rating Level applies a higher live load factor (γ_{LL}) than the Operating Rating Level. This means that the inventory RF will be lower than the operating RF. The inventory RF represents the multiple of HL-93 loads that may be applied to the bridge, such that the bridge can be in service for an indefinite period of time. Similarly, the operating RF represents the multiple of HL-93 loads that is the absolute maximum load that can safely travel on the bridge at once. Figure 3.1 provides a load rating procedure flowchart included in the AASHTO MBE (AASHTO MBE 2018).

When load posting a bridge, the MBE leaves much of the decision making up to the owner of the bridge. However, for Legal Loads such as the AASHTO Type 3, 3S2, and 3-3 trucks, the MBE gives a suggested equation to determine the safe posting load for a bridge if the RF is between 0.3 and 1.0. If the RF is less than 0.3 the bridge is required to be closed. The safe posting load for a structure is given by Eqn. (3.3).

$$Safe\ Posting\ Load = \frac{W}{0.7}(RF - 0.3) \tag{3.3}$$

where:

RF = Legal Load rating factor

W = Weight of rating vehicle

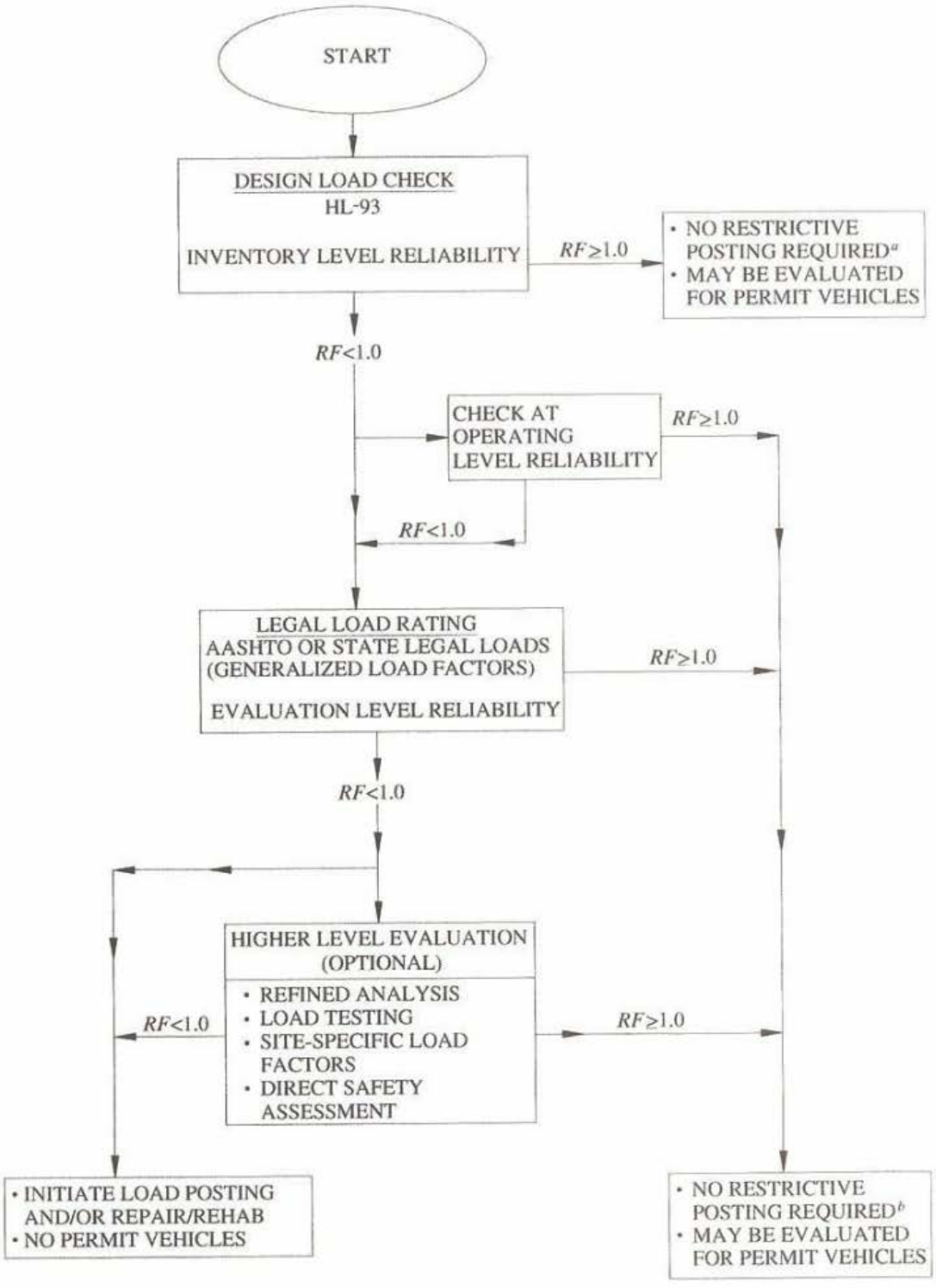

Figure 3.1. AASHTO MBE Load Rating Procedure Flowchart (Reprinted from AASHTO MBE 2018)

3.2.3. Current TxDOT Practices

Currently TxDOT uses the LRFR method to evaluate all bridges designed using Load and Resistance Factor Design (LRFD). The Federal Highway Administration (FHWA) requires all bridges on which preliminary engineering was initiated after October 1, 2007 to be designed using LRFD. Most of the bridges that was built after 2007 using LRFD guidelines do not require load posting. All selected load posted bridges in Texas were built before 2007 and therefore TxDOT analyzes them using either the ASR or LFR methods. TxDOT requires the use of LFR for analysis of all on-system bridges and allows all off-system bridges to be analyzed using either ASR or LFR. When load rating, TxDOT seems to follow the practice of rating all on-system bridges using LFR and all off-system bridges using ASR in most cases. The bridges are analyzed using an H-15 truck and an HS-15 truck, and then one of three flowcharts are followed to determine the posting of the bridge. For on-system bridges the flowchart shown in Figure 3.2 is followed, for off-system bridges the flowchart shown in Figure 3.3 is applied, and for concrete bridges with no plans the flowchart shown in Figure 3.4 is used. In the charts, Item 58 is the Deck Condition Rating in the NBI, Item 59 is the Superstructure Condition Rating in the NBI, Item 60 is the Substructure Condition Rating in the NBI, and Item 62 is the Culvert Condition Rating. In the Figures, I.F. stands for Inspection Frequency. Figure 3.5 shows the simplified load posting procedure that TxDOT uses to determine the actual posting that goes on the sign. The calculated posting loads in pounds are rounded to the nearest load increment, no matter if it is above or below the computed value.

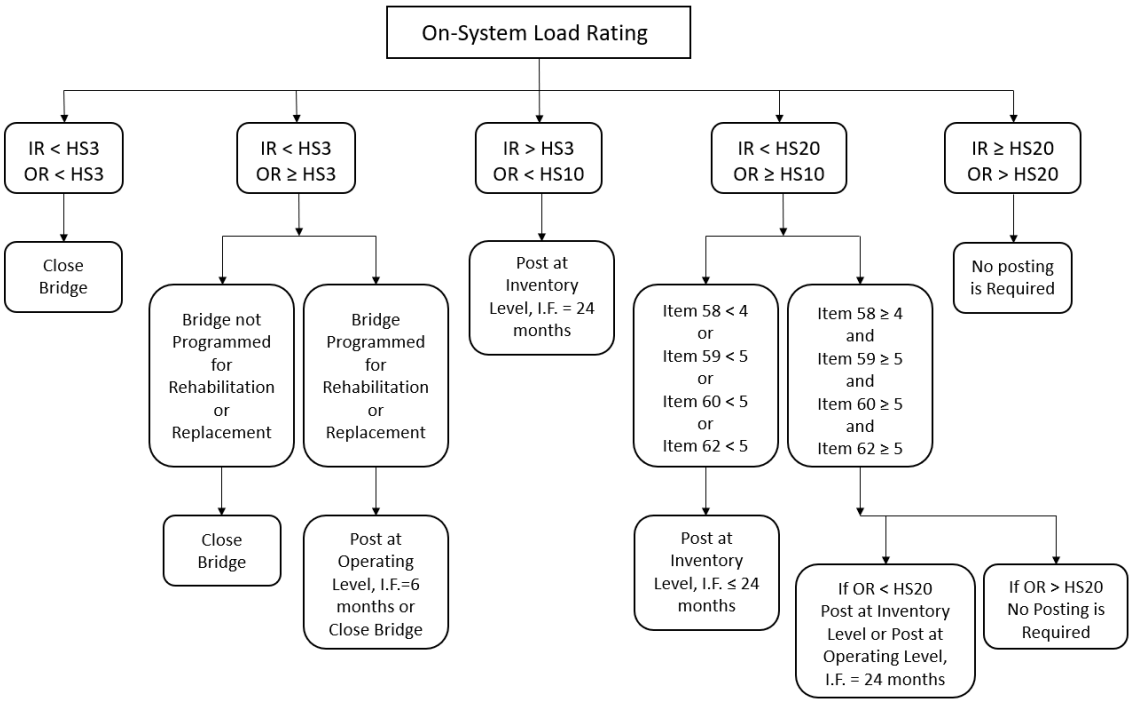

Figure 3.2. TxDOT On-System Load Rating Flowchart (Adapted from TxDOT 2018a)

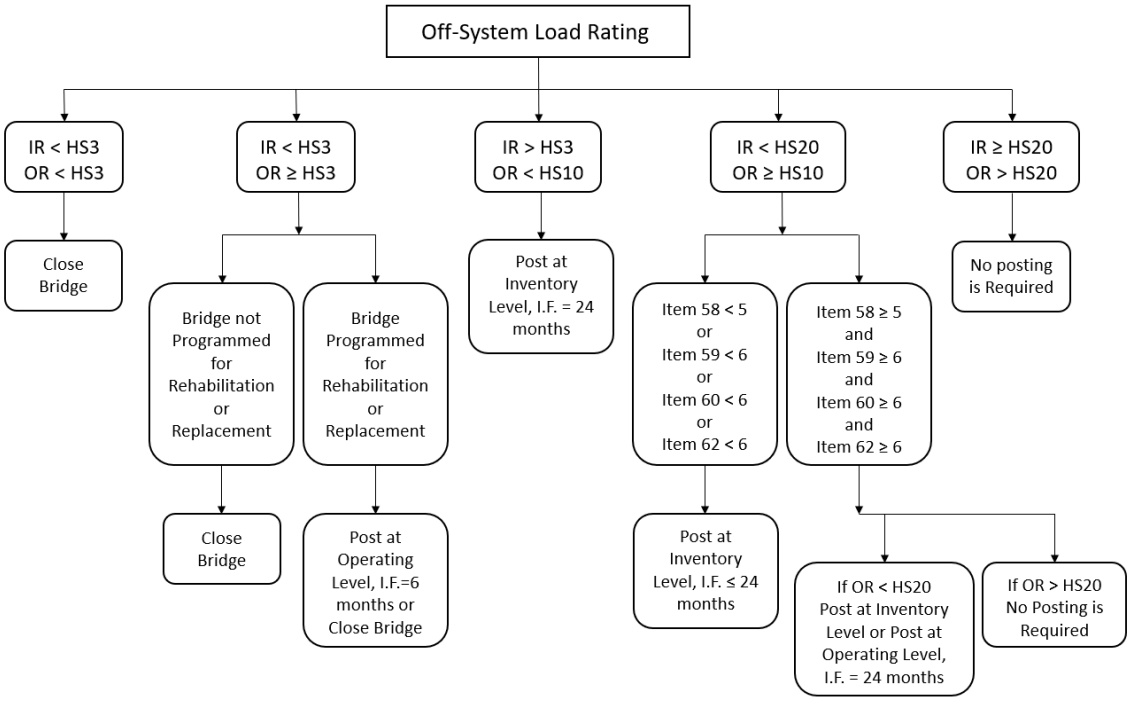

Figure 3.3. TxDOT Off-System Load Rating Flowchart (Adapted from TxDOT 2018a)

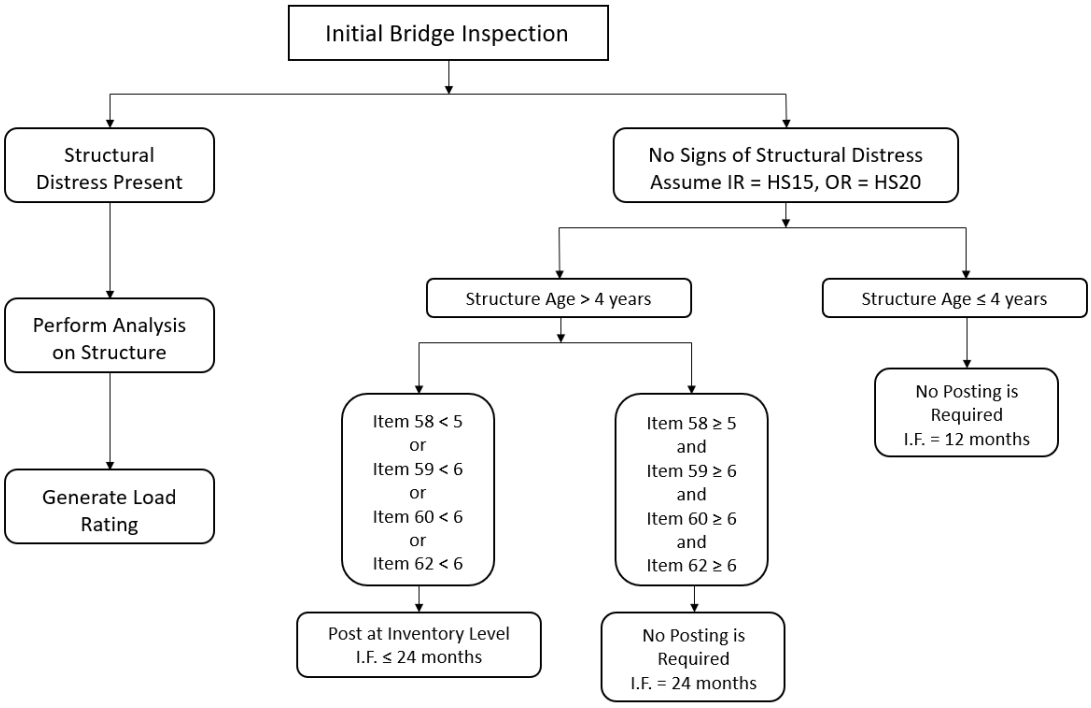

Figure 3.4. TxDOT Load Rating Flowchart for Concrete Bridges and Bridge Decks with No Plans (Adapted from TxDOT 2018a)

SIMPLIFIED LOAD POSTING PROCEDURE

This procedure is appropriate for computing posting loads equivalent to the inventory rating. Approximations are involved which make this procedure unacceptable at load levels higher than the Inventory Rating.

The posting load in pounds is the product of the RATING MULTIPLIER and the INVENTORY RATING in tons for the standard "H" truck. In selecting the RATING MULTIPLIER from the table use the longest simple span length or 80% of the longest continuous span length, whichever gives the longest span length for the bridge. If the resulting span length is 160' or greater, then the bridge should receive an analysis more exact than this procedure.

The recommended posting increments are listed below. Round off to the nearest increment listed.

Post axle and gross load for span lengths 40' and greater. Post axle load only for span lengths 39' and less. Weight limit signs should conform to the Texas Manual on Uniform Traffic Control Devices. The recommended signs are R12-2Tb or R12-4Tb except if the axle load is noted "*" use signs R12-2Tc or R12-4Tc.

EXAMPLE 1
35' Simple Span Slab & Girder Bridge, H14 Rating
Axle = 14 x 1,450 = 20,300 lbs.
Post 21,000 tandem axle (Signs R12-2Tc)

EXAMPLE 2
120' Pony Truss, H7 Rating
Axle = 7 x 1,450 = 10,100 lbs.
Gross = 7 x 2,300 = 16,100 lbs.
Post 10,000 lbs. Axle or tandem and 16,000 lbs. Gross (sign R12-4Tb)

EXAMPLE 3
30'-40'-30' Continuous Slab Bridge with
25' slab approach spans, H10 Rating.
0.80 x 40' = 32'>25' = Use 32' span
Axle = 10 x 1,480 = 14,800 lbs.
Post 15,000 lbs. Axle or tandem (Sign R12-2Tb)

EXAMPLE 4
25' Simple Span Timber Bridge, H2 Rating
Axle = 1,550 x 2 = 3,100 lbs.
Recommendation: Close bridge until repair increases capacity.

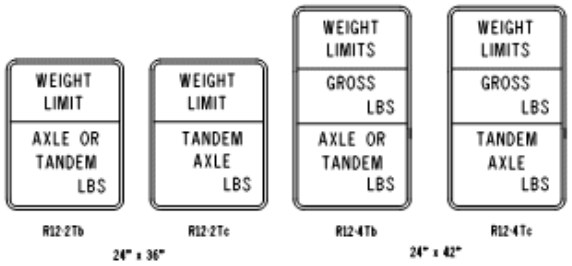

SPAN	RATING MULTIPLIER	
	AXLE OR TANDEM	GROSS
FEET	LBS. H-TON	LBS. H-TON
≤ 20	1,600	
25	1,550	
30	1,500	
35	1,450	
40	1,450	3,100
45	1,450	2,950
50	1,450	2,800
60	1,450	2,600
70	1,450	2,500
80	1,450	2,450
90	1,450	2,400
100	1,450	2,350
120	1,450	2,300
140	1,450	2,250
160	1,450	2,200

LOAD INCREMENTS FOR AXLE OR TANDEM LBS.	LOAD INCREMENTS FOR GROSS LBS.
5,000	8,000
7,500	10,000
10,000	12,000
12,500	14,000
15,000	16,000
17,500	20,000
21,000*	24,000
24,000*	28,000
28,000*	32,000
32,000*	36,000
	40,000
	44,000
	48,000
	52,000
	60,000
	68,000
	76,000

*Axle load exceeds 20,000 lbs. Single axle limit, therefore post for tandem axle (Signs R12-2Tc or R12-4Tc).

Figure 3.5. TxDOT Simplified Load Posting Procedure Guide (Reprinted from TxDOT 2018a)

Based on their inspections and using the described load rating methods, TxDOT has determined the superstructure operating ratings, superstructure inventory ratings, and condition ratings shown in Table 3.2 and Table 3.3 for each selected SSLO bridge, along with the calculated operating and inventory level HS-20 RFs. The load rating in tons is calculated by multiplying the RF by 20. This research task focused on the superstructure of the bridges. In some instances, the superstructure is not the controlling component of the rating. In many cases, TxDOT also seems to assume or does not calculate a rating factor for the substructure, concrete deck, and in some cases for a concrete bridge's main load carrying component, based on the flowchart shown in Figure 3.4. The following tables show the load ratings for the "superstructure" component of the considered bridges.

As can be seen, a number of the selected SSLO bridges have operating RFs greater than 1.0, meaning the operating load rating is greater than an HS-20 truck. Along with condition ratings greater than or equal to 6 (Satisfactory), these bridges should not be posted according to TxDOT's on-system and off-system posting flowcharts shown in Figure 3.2 and Figure 3.3. Some of these bridges are likely posted due to a lower substructure rating, while others may be posted for other reasons such as continuation of a previous posting.

Table 3.2. TxDOT Superstructure Load Ratings and Condition Ratings for Selected SSLO Simple-Span Steel Multi-Girder Bridges (Data from NBI 2016)

ID	On/Off System	Condition Rating			Rating Method	Controlling Component	Tonnage Rating (US tons)		HS20 RF	
		Deck	Superstr.	Substr.			Inv.	Oper.	Inv.	Oper.
SM-1	On	6	6	7	LFR	Superstructure	7	11	0.33	0.55
SM-2	On	6	6	6	LFR	Superstructure	7	11	0.34	0.56
SM-3	On	6	6	6	LFR	Superstructure	9	16	0.48	0.80
SM-4	On	6	6	7	N/A	Superstructure	8	11	0.39	0.56
SM-5	On	7	6	7	LFR	Superstructure	9	15	0.47	0.79
SM-6	Off	6	6	7	ASR	Superstructure	15	20	0.89	1.39
SM-7	On	6	5	5	LFR	Superstructure	12	19	0.57	0.95
SM-8	On	6	6	6	LFR	Superstructure	9	14	0.41	0.69
SM-9	Off	7	6	6	ASR	Assumed Deck	15	20	0.82	1.27
SM-10	Off	5	5	6	ASR	Assumed Deck	15	24	0.77	1.20
SM-11	On	6	6	5	LFR	Superstructure	14	24	0.73	1.22
SM-12	Off	6	6	5	LFR	Superstructure	10	17	0.51	0.86
SM-13	Off	5	5	6	ASR	Superstructure	13	20	0.67	1.00
SM-14	Off	7	6	7	ASR	Superstructure	8	15	0.41	0.75
SM-15	On	7	6	6	LFR	Superstructure	10	17	0.51	0.85
SM-16	Off	7	6	7	ASR	Superstructure	16	24	0.82	1.24
SM-17	Off	7	5	5	ASR	Superstructure	11	18	0.55	0.89
SM-18	Off	6	5	7	ASR	Superstructure	12	19	0.59	0.95
SM-19	Off	7	6	5	ASR	Superstructure	10	14	0.71	1.04
SM-20	Off	6	6	5	ASR	Superstructure	11	18	0.56	0.91
SM-21	Off	8	7	7	ASR	Assumed Deck	14	20	1.35	2.02
SM-22	Off	7	6	6	ASR	Superstructure	7	17	0.38	0.87
SM-23	Off	8	6	6	ASR	Superstructure	10	18	0.51	0.88
SM-24	Off	8	5	5	ASR	Superstructure	12	19	0.60	0.99
SM-25	Off	7	6	5	ASR	Assumed Substructure	15	20	3.37	4.77

Condition Ratings:
0 = Failed Condition
1 = "Imminent" Failure Condition
2 = Critical Condition
3 = Serious Condition
4 = Poor Condition
5 = Fair Condition
6 = Satisfactory Condition
7 = Good Condition
8 = Very Good Condition
9 = Excellent Condition

N/A means that TxDOT did not perform load ratings for this bridge and it is therefore most likely posted based on precedent.

Table 3.3. TxDOT Superstructure Load Ratings and Condition Ratings for Selected SSLO Continuous Steel Multi-Girder Bridges (Data from NBI 2016)

ID	On/Off System	Condition Rating			TxDOT Rating Method	Controlling Component	Tonnage Rating (US tons)		HS20 RF	
		Deck	Superstr.	Substr.			Inv.	Oper.	Inv.	Oper.
SC-1	Off	6	5	6	ASR	Superstructure	7	11	0.37	0.56
SC-2	Off	5	6	5	ASR	Superstructure	8	14	0.42	0.72
SC-3	Off	5	6	7	ASR	Substructure	13	21	0.99	1.46
SC-4	Off	5	6	6	ASR	Substructure	12	20	1.09	1.61
SC-5	Off	5	6	6	ASR	Superstructure	12	18	0.58	0.89
SC-6	Off	5	6	5	ASR	Assumed Deck	15	21	1.08	1.53
SC-7	Off	7	6	5	ASR	Superstructure	15	20	0.84	1.23
SC-8	On	7	6	5	LFR	Superstructure	11	18	0.56	0.93
SC-9	Off	6	6	6	ASR	Superstructure	11	18	0.56	0.93
SC-10	On	6	5	6	LFR	Superstructure	12	19	0.58	0.96
SC-11	Off	6	5	6	ASR	Superstructure	8	12	0.40	0.61
SC-12	On	6	7	7	LFR	Superstructure	10	18	0.55	0.93
SC-13	On	6	6	6	LFR	Superstructure	12	19	0.73	1.22
SC-14	Off	6	6	5	ASR	Substructure	8	12	0.48	0.73
SC-15	Off	7	7	6	ASR	Substructure	11	18	0.56	0.94
SC-16	Off	7	6	6	ASR	Superstructure	7	11	0.34	0.56

Condition Ratings:
0 = Failed Condition
1 = “Imminent” Failure Condition
2 = Critical Condition
3 = Serious Condition
4 = Poor Condition
5 = Fair Condition
6 = Satisfactory Condition
7 = Good Condition
8 = Very Good Condition
9 = Excellent Condition

4. BASIC LOAD RATINGS FOR SSLO STEEL BRIDGE WITH CONCRETE DECKS

4.1. SIMPLE-SPAN STEEL MULTI-GIRDER BRIDGES

4.1.1. Introduction

Twenty-five simple-span steel multi-girder (SM) bridges with concrete decks were selected from the entire SSLO bridge inventory of Texas for further analysis. Table 4.1 summarizes these bridges and their main characteristics. Some SM bridges have multiple spans with varying lengths, girder types, or other properties. The information shown in the table contains the characteristics that pertain to the controlling span of the bridge. The girder spacing shown is the largest interior girder spacing in the span if all girders are not equally spaced. Some of the girder cross-sections are historical sections and are named accordingly. A girder named W##x## or S##x## is a current cross section in the 14th edition of the *AISC Steel Construction Manual* (AISC 2013). A girder named ##WFx##, CB##x##, or B##x## is a historic section found in AISC's *Historic Record, Dimensions and Properties, Rolled Shapes, Steel and Wrought Iron Beams & Columns* (AISC 1953). Detailed characteristics for the selected bridges were compiled from the TxDOT inspection database into a master spreadsheet to efficiently review the relevant information for conducting basic load rating analysis.

Table 4.1. Selected SSLO Simple-Span Steel Multi-Girder Bridges and Characteristics

ID	On/Off System	Year Built	Max. Span Length (ft)	Deck Width (ft)	Steel Yield Strength[2] (ksi)	Interior Girder Section	Exterior Girder Section	Interior Girder Spacing (ft)	Concrete Deck Thickness (in.)	Wearing Surface Thickness (in.)
SM-1	On	1931	39	25	30	CB211x58	B18x47	4'-5"	5.50	1.5
SM-2	On	1931	39	25	30	CB211x58	B18x47	4'-5"	5.50	1.5
SM-3	On	1938	30	25	33	21WFx63	21WFx63	7'-1"	8.00	1.0
SM-4	On	1938	30	25	33	21WFx63	21WFx63	7'-1"	6.75	2.0
SM-5	On	1938	41	24	33	S15x42.9	S15x42.9	1'-11"	6.00	1.0
SM-6	Off	1940	24	22	33	S15x42.9	S15x42.9	3'-4.5"	5.50	5.0
SM-7	On	1940	30	23	33	S12x31.8	S12x31.8	1'-10.5"	6.50	2.0
SM-8	On	1940	69	27	33	CB141x34	CB141x34	4'-5"	7.00	4.0
SM-9	Off	1941	40	16	33	21WFx59	B26x91	4'-11"	6.00	0.0
SM-10	Off	1945	29	22	33	S18x54.7	S18x54.7	4'-4"	6.00	1.0
SM-11	On	1947	40	46	33	30WFx108	PC[3]	7'-8"	7.25	2.0
SM-12	Off	1955	30	22	33	W18x50	W18x50	6'-0"	6.00	0.0
SM-13	Off	1958	14	26	33	S12x31.8	B64x48	4'-10"	7.00	4.0
SM-14	Off	1960	38	16	33	S15x42.9	C15x33.9	2'-4"	7.50	0.0
SM-15	On	1961	43	26	33	30WFx116	30WFx116	9'-6"	7.00	2.0
SM-16[1]	Off	1965	36	30	50	W21x55	W21x55	5'-10"	7.00	0.0
SM-17	Off	1970	30	16	33	S12x31.8	C12x20.7	2'-0"	3.50	3.0
SM-18	Off	1977	33	15	27	S18x54.7	S18x54.7	2'-9.5"	5.50	1.0
SM-19	Off	1982	21	14	36	S10x25.4	S10x25.4	2'-8"	4.00	0.0
SM-20	Off	1986	54	24	33	W24x68	W24x68	2'-11"	5.50	0.0
SM-21	Off	1990	53	25	33	W33x130	W33x130	4'-0"	6.00	1.0
SM-22	Off	1990	55	24	36	W33x118	W33x130	6'-8.5"	8.00	5.0
SM-23	Off	1992	48	17	36	W21x44	W21x44	2'-5.5"	6.00	0.5
SM-24	Off	1995	29	14	36	W8x35	W8x35	1'-9.25"	8.00	12.0
SM-25	Off	2000	28	21	36	W24x68	W24x68	2'-7"	7.50	1.0

Notes:
1. SM-16 is the only bridge in this group that is specifically noted as composite in TxDOT's inspection records.
2. Steel yield strength is the value used by TxDOT for load rating calculations, which typically matches the value given in the TxDOT Bridge Inspection Manual (TxDOT 2018a) and AASHTO MBE (AASHTO MBE 2018), unless additional information is available.
3. PC = Prestressed Concrete

4.1.2. Basic Load Rating Analysis

4.1.2.1. General

Each selected steel multi-girder bridge was analyzed using the three rating methods defined in the AASHTO MBE: Allowable Stress Rating (ASR), Load Factor Rating (LFR), and Load and Resistance Factor Rating (LRFR). All three rating methods follow a similar general procedure. For the flexure rating factors, the following steps are used:

1. Modified section properties are calculated if the girder has a cover plate in the positive moment region or if it is a composite girder. Composite section properties are calculated using the same procedure as in Example A1 in MBE Appendix A (AASHTO MBE 2018). This procedure finds two different transformed section moduli: one using the width of the transformed concrete deck based on the modular ratio of the steel to concrete elastic moduli ($n=E_s/E_c$), and one using the width of the transformed concrete deck based on $3n$. The section properties based on n are used when considering the live load on the structure, and the section properties based on $3n$ are used when considering the superimposed dead load on the structure. This is practiced in the rating factor equations for each method.
2. The appropriate live load distribution factors are determined. For ASR and LFR, these are given as the girder spacing over a number based on the number of lanes for interior girders. For exterior girders, the lever rule is used. For LRFR, the distribution factors are determined as a function of the spacing of the girders and have a range of applicability based on the spacing of the girders, span length, thickness of the slab, and number of girders, or by using the lever rule. Skew adjustments are also considered.

3. The live load distribution factor, along with the appropriate impact factor, are applied to the live load moment that is extracted from MBE Tables E6A-1 and C6B-1 (AASHTO MBE 2018) to get the final maximum girder live load moment for the load being considered. For ASR and LFR the impact factor is given in Article 3.8.2.1 of the AASHTO Standard Specifications and is a function of the span length. For LRFR the impact factor is always 33 percent. Table E6A-1 gives the HL93 live load moment based on span length and Table C6B-1 gives the HS20 live load moment based on span length. Both interior and exterior girders are examined and analyzed.
4. The dead load moments are found by calculating a tributary distributed load for each girder.
5. The non-composite or composite moment capacity for both the interior and exterior girders is calculated. Consideration is given to whether the section is compact or noncompact, following the requirements in the respective AASHTO specifications. For ASR, this capacity is given in the form of a stress, as a percentage of the yield stress, from the AASHTO MBE. For the LFR capacity, if the section meets the compact requirements, Eqn. (4.1) is used. If the section does not meet the compact requirements, but does meet the noncompact requirements, Eqn. (4.2) is used. If the section meets neither the compact or noncompact requirements, Eqn. (4.3) is used. For LRFR, if the section meets the compact requirements, Eqn. (4.4) is used. If the section does not meet the compact requirements, but does meet the noncompact requirements, Eqn. (4.6) is used. The section is also checked using equations based on the braced length of the span. For a composite section for both methods, the plastic neutral axis is determined and the moments caused by the components are summed about the plastic neutral axis.

6. Load rating is conducted based on the three load rating procedures (ASR, LFR, and LRFR) at the operating and inventory levels considering both the interior girder and exterior girder moment demands at the strength and service limit states.

$$M_u = F_y \times Z \tag{4.1}$$

where:

M_u = Maximum bending strength

F_y = Specified minimum yield strength of steel

Z = Plastic section modulus

$$M_u = F_y \times S_{xt} \tag{4.2}$$

where:

M_u = Maximum bending strength

F_y = Specified minimum yield strength of steel

S_{xt} = Elastic section modulus with respect to the tension flange

$$M_u = M_r \times R_b \tag{4.3}$$

where:

M_u = Maximum bending strength

M_r = Moment capacity – not allowed to exceed yield moment or lateral torsional buckling moment

R_b = Bending capacity reduction factor

$$M_n = M_y \times R_b \times R_h \tag{4.4}$$

where:

M_n = Nominal flexural resistance of the section

M_y = Yield moment

R_b = Web load-shedding factor

R_h = Hybrid factor

$$M_n = \left[1 - \left(1 - \frac{0.7M_y}{R_h M_y}\right)\left(\frac{\lambda_f - \lambda_{pf}}{\lambda_{rf} - \lambda_{pf}}\right)\right] R_b R_h M_y \quad (4.5)$$

where:

M_n = Nominal flexural resistance of the section

M_y = Yield moment

R_b = Web load-shedding factor

R_h = Hybrid factor

λ_f = Slenderness ratio for the compression flange

λ_{pf} = Limiting slenderness ratio for a compact flange

λ_{rf} = Limiting slenderness ratio for a noncompact flange

For the shear rating factors, the following steps are used:

1. As the web of the steel section is the shear resisting component, section properties such as web thickness, web height, and web area are found and calculated.
2. The appropriate live load distribution factors are determined. For ASR and LFR, these are given as the girder spacing over a number based on the number of lanes for interior girders. For exterior girders the lever rule is used. For LRFR, these are determined as a function of the spacing of the girders and have a range of applicability based on the spacing of the

girders, span length, thickness of the slab, and number of girders, or by using the lever rule. Skew adjustments are also considered.

3. The live load distribution factor, along with the appropriate impact factor, are applied to the live load shear that is extracted from MBE Table E6B-1 (AASHTO MBE 2018) to get the final maximum live load shears applied to the bridge for the load being analyzed. For ASR and LFR the impact factor is given in Article 3.8.2.1 of the AASHTO Standard Specifications and is a function of the span length. For LRFR the impact factor is always 33 percent. Table E6B-1 gives the HS20 live load shear based on span length. For LRFR, the lane load shear was added to this based on statics. Both interior and exterior girders are examined and analyzed.
4. The dead load shears are found by calculating a tributary distributed load for each girder.
5. The web buckling coefficient is determined, and the shear capacity is determined using Eqn. (4.6).
6. Load rating is conducted based on the three load rating procedures (ASR, LFR, and LRFR) at the operating and inventory levels considering both the interior girder and exterior girder shear demands at the strength limit state.

$$V_u = C \times 0.58 \times F_y \times D \times t_w \tag{4.6}$$

where:

V_u = Maximum shear force

C = Web buckling coefficient

F_y = Specified minimum yield strength of steel

D = Clear unsupported distance between flange components

t_w = Web thickness

4.1.2.2. ASR and LFR

The ASR and LFR calculations follow the AASHTO *Standards Specifications for Highway Bridges* (AASHTO 2002). The live load distribution factors for ASR and LFR are calculated according to Article 3.23.2 of the AASHTO Standard Specifications.

The non-composite moment capacity is calculated based on the compactness of the section by checking the compact section requirements given in Articles 10.48.1 through 10.48.4 of the AASHTO Standard Specifications. For the composite moment capacity, first the location of the plastic neutral axis is determined by equating the compressive and tensile forces in the fully plastic slab and steel section. The plastic moment capacity is found by summing the moments of each component about the plastic neutral axis. Article 10.50.1 of the AASHTO Standard Specifications is followed to determine the final composite moment capacity as a value between the plastic moment capacity and elastic moment capacity based on the location of the plastic neutral axis. The service capacities, which are provided as a percentage of the yield strength in Articles 10.57.1 and 10.57.2 of the AASHTO Standard Specifications, are also checked. The shear coefficients and capacities are calculated using Equations 10-113 through 10-117 in Article 10.48.8 of the AASHTO Standard Specifications, as no selected bridge is transversely stiffened.

The ASR inventory and operating capacities for both flexure and shear are determined from Tables 6B.5.2.1-1 and 6B5.2.1-2 in the AASHTO MBE. The dead load moments and live load moments previously found are converted to stresses by dividing by the section modulus. The dead load moments and live load shears previously found are converted to stresses by dividing by the

area of the web of the steel section. Then, ASR is conducted for the strength limit state for interior and exterior girders in moment and shear at the inventory and operating levels.

Finally, LFR is conducted for the strength and serviceability limit states for interior and exterior girders in moment and shear at the inventory and operating levels. The procedure for the serviceability limit state for composite sections follows that shown in Example A1 of MBE Appendix A (AASHTO MBE 2018) and involves considering the dead load moment and superimposed dead load moment under different transformed sections for the member.

For both LFR and ASR methods the controlling RFs are multiplied by the weight of the truck being analyzed to determine a gross weight of that truck allowed on the bridge.

4.1.2.3. LRFR

The LRFR calculations follow the AASHTO *LRFD Bridge Design Specifications* (AASHTO LRFD Specifications) (AASHTO 2014). The live load distribution factors are found according to Article 4.6.2.2 of the AASHTO LRFD Specifications. These distribution factors are adjusted appropriately accounting for skew through Table 4.6.2.2.1-1 in the AASHTO LRFD Specifications.

When determining non-composite moment capacity, the slenderness parameters and web plastification, web load-shedding, and hybrid factors are first calculated. Then, if the skew of the bridge is less than twenty degrees, the non-composite moment capacity is calculated using Sections A6.1 through A6.3 of the AASHTO LRFD Specifications. If the skew is over 20 degrees, the non-composite moment capacity is calculated using Article 6.10.8.2 of the AASHTO LRFD Specifications. The composite moment capacity is found using the same procedure as is used in

the ASR/LFR section and Article 6.10.7 of the AASHTO LRFD Specifications. The appropriate capacity is then chosen based on whether the bridge is classified as composite or non-composite.

The shear coefficient and capacity are found using Article 6.10.9.2 of the AASHTO LRFD Specifications, as no selected bridge is transversely stiffened. The service capacities are found through Article 6.10.4.2 of the AASHTO LRFD Specifications as a percentage of the yield strength.

Finally, LRFR rating is conducted at the Strength I and Service II limit states, checking interior and exterior girders in moment and shear at the inventory and operating levels. The controlling LRFR RFs are found at the inventory and operating levels and are also multiplied by the weight of the truck being analyzed to determine a gross weight of that truck allowed on the bridge using the LRFR method.

4.1.3. Calculated Load Rating Results

Each of the 25 selected simple-span, steel multi-girder bridges with concrete decks was rated using each of the three rating methods. The bridges were rated for an HS-20 truck for ASR and LFR, as that is the truck TxDOT uses when reporting to the NBI, and the HL-93 design load was used for LRFR. The bridges were examined and rated for interior girder flexure, exterior girder flexure, interior girder shear, and exterior girder shear. The bridges were initially rated by following the procedures laid out in the AASHTO MBE, AASHTO Standard Specifications, and AASHTO LRFD Specifications.

4.1.3.1. Interior Girder Flexure Analysis

The flexure RFs found for the design loads using each method for the interior girders of each SM bridge are shown in Table 4.2 and Figure 4.1.

Table 4.2. Interior Girder Flexure RFs for SM Bridges

Bridge ID	Inventory HS20 RF			Operating HS20 RF		
	ASR	LFR	LRFR	ASR	LFR	LRFR
SM-1	0.35	0.41	0.35	0.62	0.69	0.45
SM-2	0.38	0.44	0.37	0.66	0.73	0.46
SM-3	0.41	0.45	0.40	0.72	0.75	0.52
SM-4	0.42	0.46	0.41	0.73	0.76	0.53
SM-5	0.46	0.48	0.32	0.78	0.81	0.42
SM-6	0.78	0.75	0.47	1.21	1.25	0.60
SM-7	0.51	0.53	0.27	0.85	0.88	0.35
SM-8	0.34	0.39	0.27	0.63	0.65	0.35
SM-9	0.88	0.89	0.77	1.37	1.49	1.01
SM-10	0.74	0.73	0.53	1.17	1.22	0.68
SM-11	0.61	0.67	0.67	1.01	1.11	0.87
SM-12	0.32	0.35	0.30	0.56	0.58	0.39
SM-13	0.60	0.57	0.48	0.92	0.95	0.62
SM-14	0.38	0.48	0.30	0.72	0.81	0.39
SM-15	0.40	0.46	0.52	0.73	0.76	0.68
SM-16	0.86	1.20	0.99	1.43	1.99	1.29
SM-17	0.54	0.58	0.29	0.88	0.97	0.38
SM-18	0.76	0.75	0.49	1.20	1.25	0.63
SM-19	0.69	0.63	0.33	1.02	1.06	0.43
SM-20	0.52	0.58	0.43	0.88	0.97	0.56
SM-21	1.33	1.25	1.08	2.02	2.08	1.41
SM-22	0.16	0.35	0.38	0.55	0.59	0.50
SM-23	0.42	0.49	0.34	0.78	0.81	0.45
SM-24	0.40	0.51	0.25	0.81	0.85	0.33
SM-25	2.53	2.22	1.39	3.61	3.71	1.81
Average	0.63	0.66	0.50	1.03	1.11	0.64
Std. Dev.	0.46	0.39	0.28	0.62	0.65	0.36

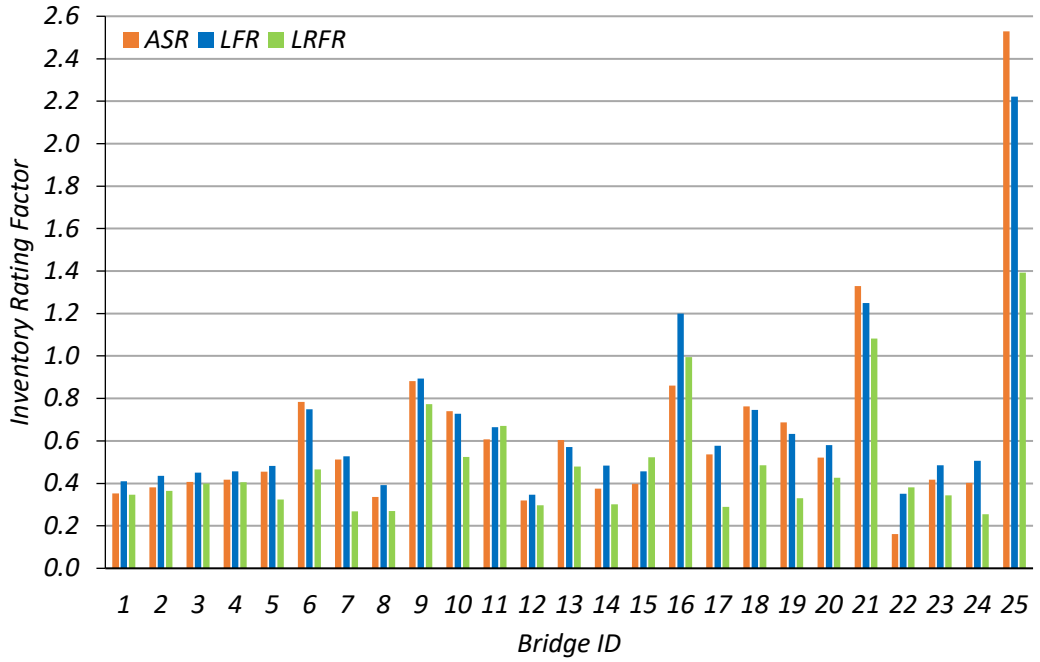

(a) Inventory RFs

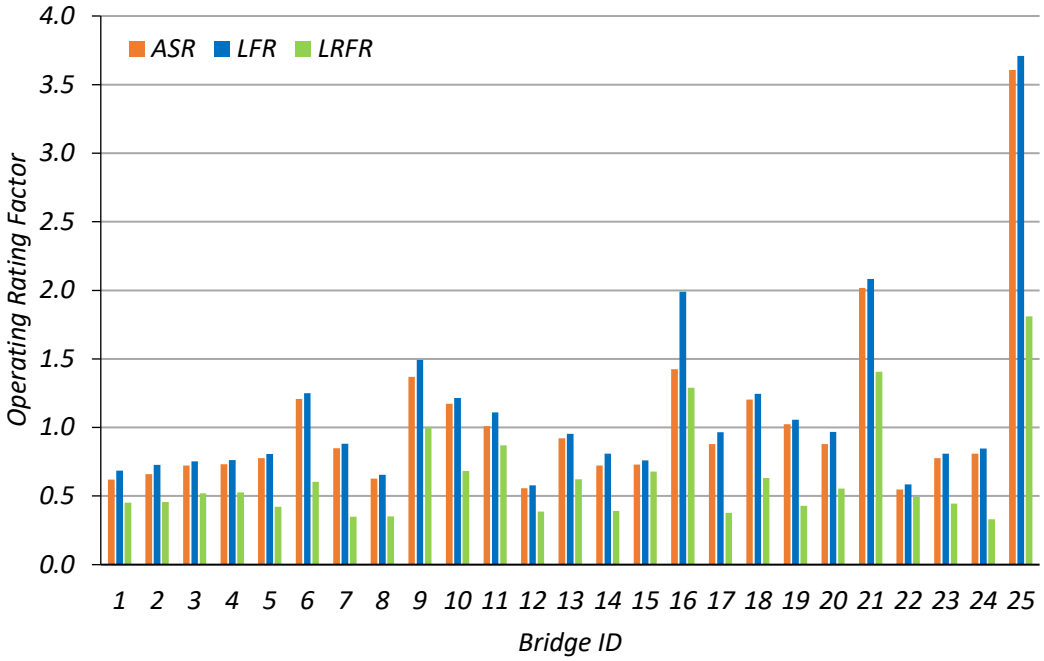

(b) Operating RFs

Figure 4.1. Interior Girder Flexure RFs for SM Bridges

For the interior girder flexure of the selected SM bridges, the LFR method produced a higher average inventory RF (0.66) than the ASR method (0.63), which produced a higher average inventory RF than the LRFR method (0.50). The LFR method also produced a higher average operating RF (1.11) than the ASR method (1.03), which produced a higher average operating RF than the LRFR method (0.64).

Of the 25 bridges whose interior girders were analyzed, two were found to have HS-20 inventory ratings at or above 1.0 and nine were found to have HS-20 operating ratings at or above 1.0 using the ASR method. Three were found to have HS-20 inventory ratings at or above 1.0 and nine were found to have HS-20 operating ratings at or above 1.0 using the LFR method. Two were found to have HL-93 inventory ratings at or above 1.0 and four were found to have HL-93 operating ratings at or above 1.0 using the LRFR method. Bridges SM-21 and SM-25 were the only SM bridges that had operating and inventory design-level ratings at or above 1.0 using all three methods. SM-16 was the only bridge in addition to these two that also had both operating and inventory design-level ratings at or above 1.0 using the LFR method. The three bridges that were found to have operating RFs greater than 1.0 using all three rating methods were bridges SM-16, SM-21, and SM-25.

4.1.3.2. Exterior Girder Flexure Analysis

The exterior girders of the bridges were rated separately for this study. It should be noted that the TxDOT practice appears to rate the superstructure of SM bridges based on the interior girders only. Each SM bridge was analyzed in this study considering the exterior girders and the related AASHTO requirements, which mainly resulted in differences in distribution factors. Table 4.3 and Figure 4.2 show the exterior girder flexure RFs found using each rating method for each simple-

span SM bridge. Note that an exterior girder RF was not determined for Bridge SM-11 because it was widened, and the new exterior girder is a prestressed concrete I-girder instead of a steel section.

Table 4.3. Exterior Girder Flexure RFs for SM Bridges

Bridge ID	Inventory HS20 RF			Operating HS20 RF		
	ASR	LFR	LRFR	ASR	LFR	LRFR
SM-1	0.64	0.63	0.30	0.96	1.04	0.39
SM-2	0.68	0.66	0.31	1.01	1.10	0.40
SM-3	0.51	0.52	0.44	0.84	0.87	0.57
SM-4	0.52	0.53	0.44	0.85	0.88	0.57
SM-5	0.53	0.53	0.35	0.86	0.89	0.46
SM-6	0.93	0.84	0.52	1.36	1.40	0.67
SM-7	0.51	0.53	0.27	0.85	0.88	0.35
SM-8	0.52	0.50	0.34	0.81	0.84	0.44
SM-9	0.79	0.76	0.84	1.18	1.27	1.09
SM-10	0.71	0.65	0.59	1.05	1.08	0.77
SM-11	-	-	-	-	-	-
SM-12	0.36	0.37	0.32	0.60	0.62	0.41
SM-13	1.73	1.50	1.31	2.43	2.50	1.69
SM-14	0.28	0.29	0.25	0.47	0.49	0.32
SM-15	0.54	0.58	0.54	0.93	0.97	0.70
SM-16	1.02	1.12	0.99	1.56	1.87	1.29
SM-17	0.26	0.26	0.18	0.42	0.43	0.23
SM-18	0.21	0.22	0.19	0.36	0.37	0.25
SM-19	0.60	0.54	0.35	0.87	0.90	0.46
SM-20	0.64	0.65	0.48	1.00	1.09	0.62
SM-21	1.48	1.34	1.16	2.17	2.24	1.50
SM-22	0.46	0.57	0.58	0.91	0.96	0.76
SM-23	0.46	0.46	0.40	0.75	0.78	0.52
SM-24	0.42	0.46	0.29	0.74	0.77	0.38
SM-25	2.58	2.23	1.44	3.62	3.72	1.87
Average	0.72	0.70	0.54	1.11	1.16	0.70
Std. Dev.	0.52	0.44	0.35	0.71	0.73	0.45

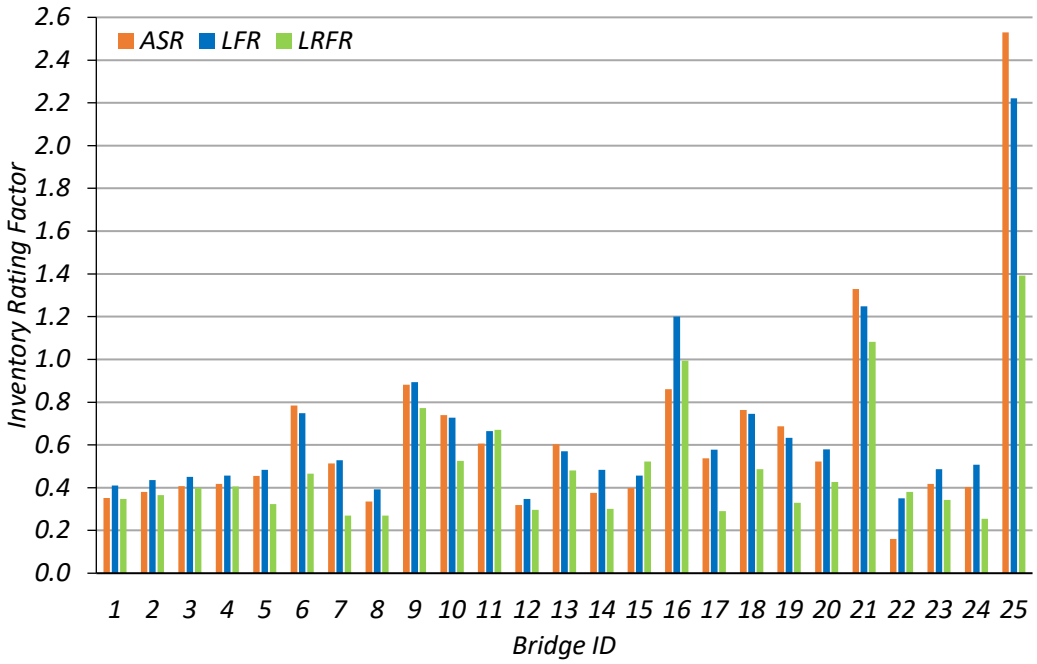

(a) Inventory RFs

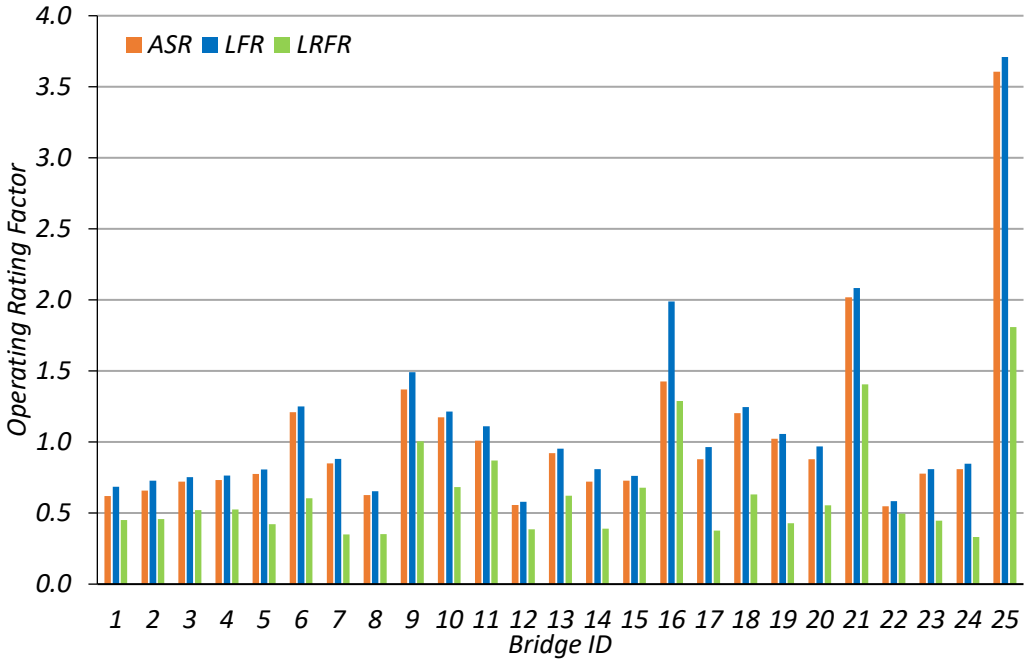

(b) Operating RFs

Figure 4.2. Exterior Girder Flexure RFs for SM Bridges

For the exterior girder flexure of the selected SM bridges, the ASR method produced a higher average inventory RF (0.72) than the LFR method (0.70), which produced a higher average inventory RF than the LRFR method (0.54). However, the LFR method produced a higher average operating RF (1.16) than the ASR method (1.11), which produced a higher average operating RF than the LRFR method (0.70).

The exterior girder was found to control the rating for seven of the considered SM bridges. Table 4.4 and Figure 4.3 show the calculated operating and inventory design-level RFs for the interior and exterior girders of these bridges. It should be noted, however, that the results obtained when considering an exterior girder may be overly conservative. For these seven bridges (SM-10, SM-14, SM-17, SM-19, SM-23, and SM-24), the exterior girder controls due to restrictions in Article 3.23.2.3.1.5 of the AASHTO Standard Specifications. This article puts a minimum on the exterior girder live load distribution factor determined using the lever rule. Without this minimum, the exterior girder would not control. However, in order to follow the AASHTO Standard Specifications as closely as possible, this article was considered.

Table 4.4. SM Bridges Controlled by Exterior Girder Flexure RFs

ID	TxDOT Rating Method	Interior Girder Rating		Exterior Girder Rating		Exterior Rating/ Interior Rating	
		Inventory	Operating	Inventory	Operating	Inventory	Operating
SM-10	ASR	0.74	1.17	0.71	1.05	0.96	0.90
SM-14	ASR	0.38	0.72	0.28	0.47	0.74	0.65
SM-17	ASR	0.54	0.88	0.26	0.42	0.48	0.48
SM-18	ASR	0.76	1.20	0.21	0.36	0.28	0.30
SM-19	ASR	0.69	1.02	0.60	0.87	0.87	0.85
SM-23	ASR	0.42	0.78	0.42	0.75	1.00	0.96
SM-24	ASR	0.40	0.81	0.40	0.74	1.00	0.91
Average		0.56	0.94	0.41	0.67	0.76	0.72

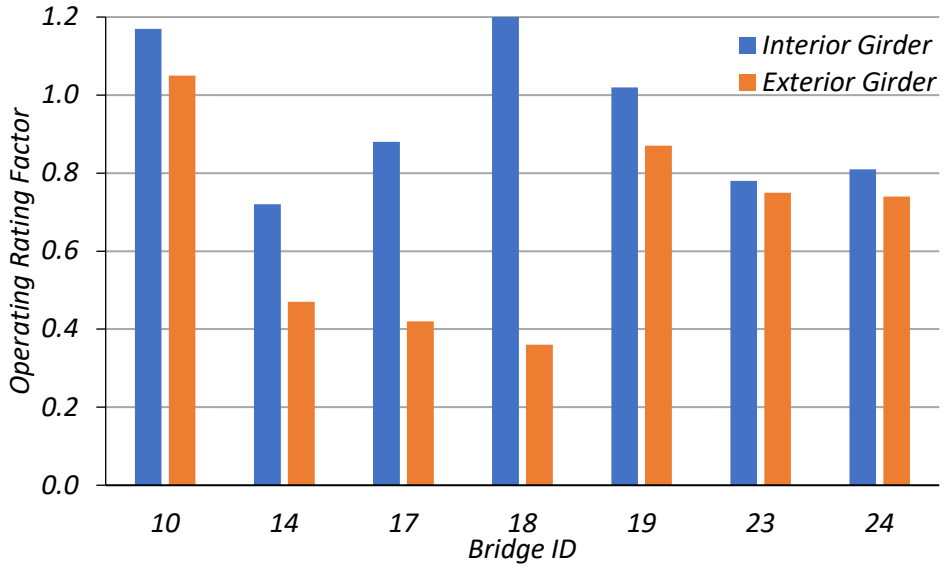

Figure 4.3. Interior Girder and Exterior Girder RFs for Select SM Bridges

4.1.3.3. Interior Girder Shear Analysis

Table 4.5 and Figure 4.4 show the shear RFs calculated for the design loads on the interior girders for each selected simple-span, steel multi-girder bridge.

Table 4.5. Interior Girder Shear RFs for SM Bridges

ID	Inventory HS20 RF			Operating HS20 RF		
	ASR	LFR	LRFR	ASR	LFR	LRFR
SM-1	2.16	1.81	1.58	3.05	3.02	2.05
SM-2	2.18	1.83	1.60	3.09	3.06	2.07
SM-3	1.81	1.54	1.57	2.60	2.57	2.03
SM-4	1.82	1.55	1.57	2.61	2.58	2.04
SM-5	4.58	3.78	1.75	6.37	6.31	2.27
SM-6	3.13	2.60	1.90	4.37	4.33	2.46
SM-7	3.53	2.93	1.14	4.93	4.89	1.48
SM-8	1.45	1.25	0.99	2.11	2.09	1.28
SM-9	2.99	2.50	1.84	4.21	4.17	2.38
SM-10	3.91	3.24	2.10	5.46	5.41	2.73
SM-11	2.97	2.49	2.30	4.19	4.16	2.99
SM-12	1.60	1.35	1.30	2.27	2.25	1.68
SM-13	2.01	1.69	0.92	2.84	2.82	1.19
SM-14	4.78	3.96	1.70	6.68	6.62	2.20
SM-15	2.34	1.99	2.17	3.35	3.32	2.81
SM-16	2.97	2.48	2.14	4.18	4.14	2.77
SM-17	4.21	3.47	1.26	5.85	5.80	1.63
SM-18	4.69	3.87	1.72	6.53	6.47	2.23
SM-19	2.97	2.45	1.13	4.12	4.08	1.47
SM-20	4.64	3.84	2.38	6.47	6.41	3.09
SM-21	6.68	5.51	4.31	9.29	9.20	5.58
SM-22	3.64	3.12	2.95	5.25	5.20	3.82
SM-23	5.79	4.79	2.08	8.07	8.00	2.70
SM-24	2.74	2.33	0.77	3.93	3.89	0.99
SM-25	7.13	5.84	3.49	9.84	9.75	4.52
Average	3.47	2.89	1.87	4.87	4.82	2.42
Std. Dev.	1.51	1.23	0.79	2.07	2.05	1.02

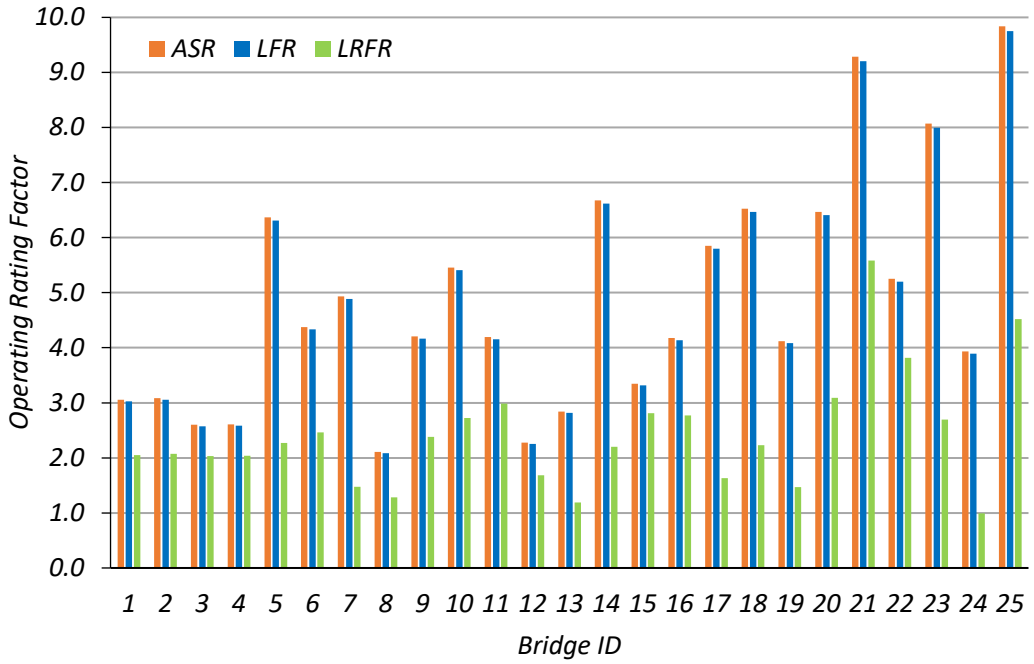

Figure 4.4. Interior Girder Shear Operating RFs for SM Bridges

For the interior girder shear of the selected SM bridges, the ASR method produced a higher average inventory RF (3.47) than the LFR method (2.89), which produced a higher average inventory RF than the LRFR method (1.87). The ASR method also produced a higher average operating RF (4.87) than the LFR method (4.82), which produced a higher average operating RF than the LRFR method (1.02).

For all bridges, both the ASR method and the LFR method produced operating and inventory interior girder shear RFs greater than or equal to 1.0. There were only two bridges, SM-8 and SM-24, for which the LRFR method did not produce inventory RFs greater than 1.0. The LRFR method produced operating RFs greater than or equal to 1.0 for all bridges except for one, SM-24, which had an RF of 0.99. None of the interior girder shear RFs control over the corresponding interior girder flexure RFs.

4.1.3.4. Exterior Girder Shear Analysis

Table 4.6 and Figure 4.5 show the shear RFs calculated for the design loads using each method for the exterior girders of all selected simple-span steel multi-girder bridges.

Table 4.6. Exterior Girder Shear RFs for SM Bridges

ID	Inventory HS20 RF			Operating HS20 RF		
	ASR	LFR	LRFR	ASR	LFR	LRFR
SM-1	15.50	12.74	1.38	21.46	21.27	1.79
SM-2	15.66	12.87	1.40	21.68	21.48	1.81
SM-3	2.47	2.08	1.60	3.50	3.47	2.08
SM-4	2.48	2.08	1.61	3.51	3.48	2.08
SM-5	16.18	13.31	1.77	22.42	22.22	2.29
SM-6	5.37	4.41	1.94	7.42	7.36	2.52
SM-7	12.04	9.98	1.14	16.81	16.66	1.48
SM-8	2.26	1.89	1.05	3.18	3.15	1.37
SM-9	6.43	5.28	2.90	8.90	8.82	3.76
SM-10	7.22	5.93	2.15	9.98	9.90	2.79
SM-11	-	-	-	-	-	-
SM-12	2.05	1.72	1.32	2.90	2.87	1.71
SM-13	6.04	4.96	1.64	8.35	8.27	2.13
SM-14	16.06	13.19	1.69	22.21	22.01	2.19
SM-15	2.81	2.37	2.20	3.99	3.95	2.85
SM-16	5.44	4.50	2.19	7.58	7.51	2.84
SM-17	9.98	8.19	1.04	13.79	13.66	1.35
SM-18	1.52	1.26	1.10	2.12	2.10	1.43
SM-19	3.36	2.75	1.15	4.63	4.59	1.49
SM-20	6.51	5.36	2.42	9.03	8.95	3.14
SM-21	9.91	8.13	4.37	13.70	13.58	5.66
SM-22	4.50	3.80	3.19	6.40	6.34	4.14
SM-23	20.76	17.08	2.11	28.77	28.51	2.74
SM-24	7.19	6.05	0.79	10.20	10.10	1.02
SM-25	15.46	12.63	3.52	21.26	21.07	4.57
Average	8.22	6.77	1.90	11.41	11.31	2.47
Std. Dev.	5.57	4.56	0.86	7.68	7.61	1.11

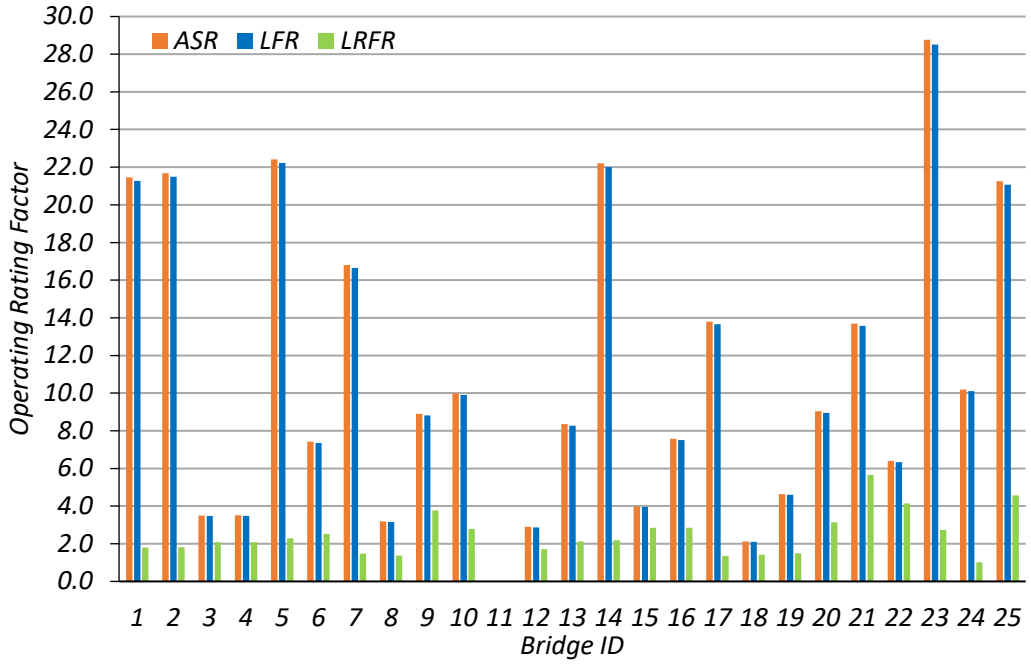

Figure 4.5. Exterior Girder Shear Operating RF for SM Bridges

For the exterior girder shear of the selected SM bridges, the ASR method produced a higher average inventory RF (8.22) than the LFR method (6.77), which produced a higher average inventory RF than the LRFR method (1.90). The LRFR shear RFs are significantly lower than the ASR and LFR RFs because the LRFR live load distribution factors for shear are much higher than the corresponding ASR and LFR live load distribution factors. The ASR method also produced a higher average operating RF (11.41) than the LFR method (11.31), which produced a higher average operating RF than the LRFR method (2.47). Bridge SM-11 does not have an exterior girder shear RF because it was widened, and the exterior girder is now a prestressed concrete I-beam instead of a steel cross-section.

For all bridges, both the ASR method and the LFR method produced inventory and operating exterior girder shear RFs greater than or equal to 1.0. The LRFR method produced

operating RFs greater than or equal to 1.0 for all bridges, and an inventory RF less than 1.0 for only one bridge, SM-24, which had an inventory RF of 0.79. None of the exterior girder shear RFs control over the corresponding exterior girder flexure RFs.

4.1.3.5. Comparison of SM Bridge Interior Girder Flexure and Shear RFs

After calculating the flexure and shear RFs for the selected SM bridges, the RFs were compared to determine if girder flexure or girder shear was the controlling limit state for each bridge. Table 4.7 and Figure 4.6 show the interior girder inventory and operating flexure and shear RFs found using the same method TxDOT uses in analysis. For every SM bridge, the flexure RF controlled the interior girder rating at both the inventory and operating level.

Table 4.7. Interior Girder Flexure and Shear RFs for SM Bridges

ID	TxDOT Rating Method	Inventory HS20 RF		Operating HS20 RF	
		Flexure	Shear	Flexure	Shear
SM-1	LFR	0.41	1.81	0.69	3.02
SM-2	LFR	0.44	1.83	0.73	3.06
SM-3	LFR	0.45	1.54	0.75	2.57
SM-4	ASR	0.42	1.82	0.73	2.61
SM-5	LFR	0.48	3.78	0.81	6.31
SM-6	ASR	0.78	3.13	1.21	4.37
SM-7	LFR	0.53	2.93	0.88	4.89
SM-8	LFR	0.39	1.25	0.65	2.09
SM-9	ASR	0.88	2.99	1.37	4.21
SM-10	ASR	0.74	3.91	1.17	5.46
SM-11	LFR	0.67	2.49	1.11	4.16
SM-12	LFR	0.35	1.35	0.58	2.25
SM-13	ASR	0.60	2.01	0.92	2.84
SM-14	ASR	0.38	4.78	0.72	6.68
SM-15	LFR	0.46	1.99	0.76	3.32
SM-16	ASR	0.86	2.97	1.43	4.18
SM-17	ASR	0.54	4.21	0.88	5.85
SM-18	ASR	0.76	4.69	1.20	6.53
SM-19	ASR	0.69	2.97	1.02	4.12
SM-20	ASR	0.52	4.64	0.88	6.47
SM-21	ASR	1.33	6.68	2.02	9.29
SM-22	ASR	0.16	3.64	0.55	5.25
SM-23	ASR	0.42	5.79	0.78	8.07
SM-24	ASR	0.40	2.74	0.81	3.93
SM-25	ASR	2.53	7.13	3.61	9.84
Avg.		0.65	3.32	1.05	4.85
Std. Dev.		0.45	1.58	0.61	2.08

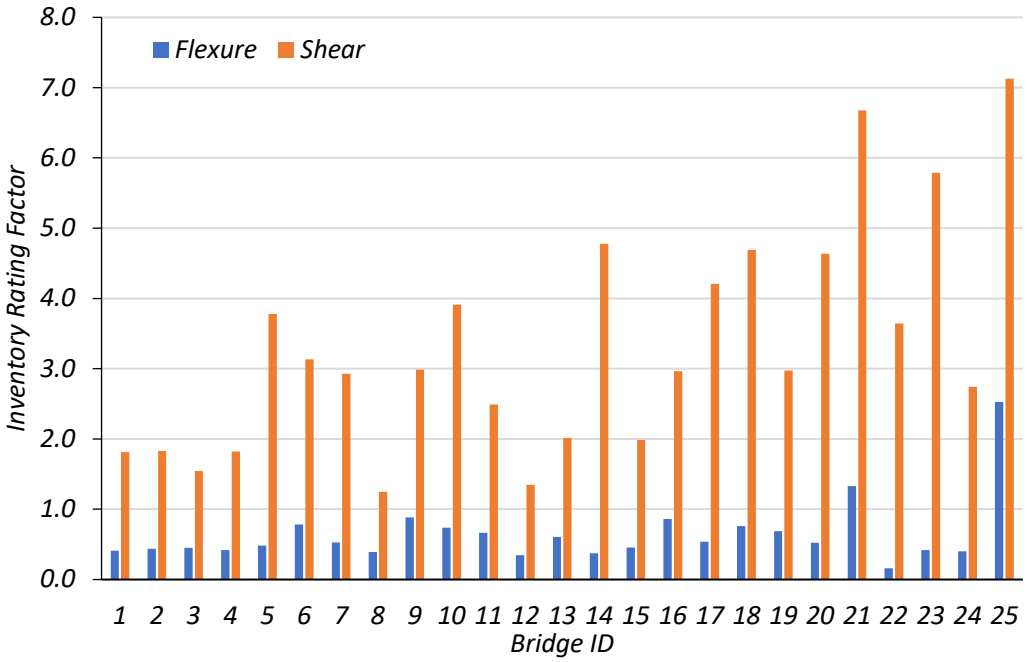

(a) Inventory RFs

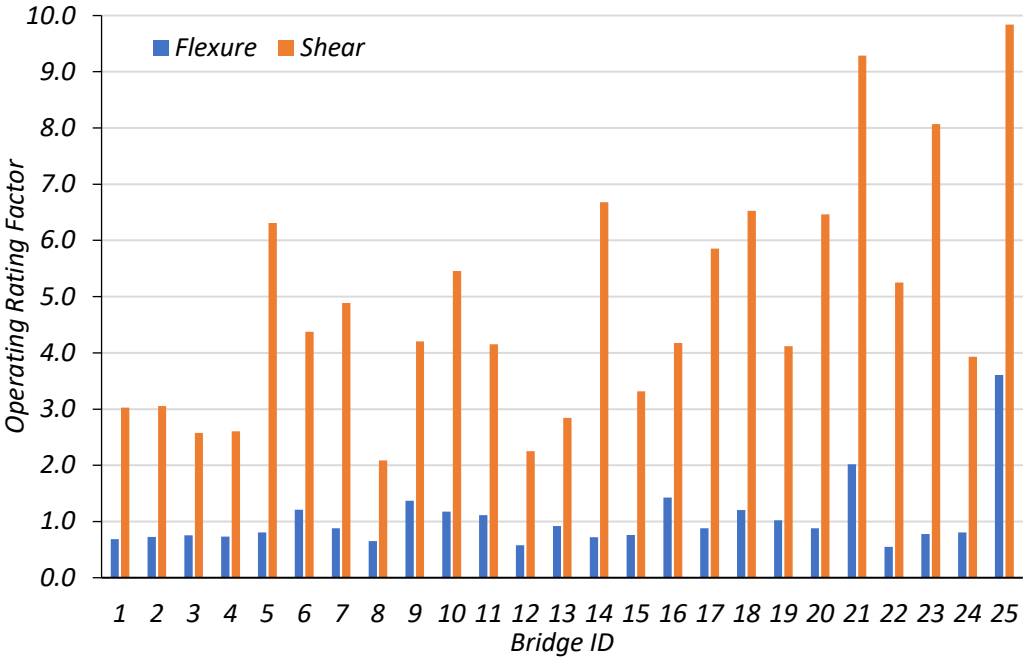

(b) Operating RFs

Figure 4.6. Comparison of Interior Girder Flexure and Shear RFs for SM Bridges

4.1.4. Check of SM Bridge Calculations

After conducting the rating analysis of each bridge, a check was conducted to confirm that the load rating process followed the AASHTO MBE and TxDOT practices. Therefore, for each bridge, the input characteristics were changed to match TxDOT's values where differences were noted and the same standard practices employed by TxDOT were used. Any differences within five percent could be attributed to slight rounding difference. Table 4.8 shows the corresponding results for each selected SM bridge.

There were only two SM bridges for which changing the input characteristics did not produce a result within five percent of TxDOT's rating. For Bridge SM-2 this was due to the calculated capacity being slightly higher than TxDOT's capacity for the same steel cross-section. The underlying reason behind this seems to be that TxDOT does not have an entry for this shape in their rating program and therefore section properties are calculated based on flange and web dimensions instead of taking them directly from a shape table. For Bridge SM-4, as previously mentioned, TxDOT does not provide rating calculations, so there were no results to compare. Through this exercise, the calculated ratings were found to be close to TxDOT's ratings, confirming that the process used in the rating calculations for this study.

Table 4.8. Interior Girder RFs for SM Bridges with Adjusted Characteristics

Bridge ID	Rating Method	Revised Calculations HS20 RF		Revised Calculations RF/ TxDOT RF	
		Inventory	Operating	Inventory	Operating
SM-1	LFR	0.35	0.58	1.05	1.05
SM-2	LFR	0.36	0.60	1.07	1.08
SM-3	LFR	0.48	0.81	1.02	1.02
SM-4	ASR	0.43	0.73	1.11	1.31
SM-5	LFR	0.49	0.82	1.04	1.04
SM-6	ASR	0.94	1.46	1.05	1.05
SM-7	LFR	0.57	0.95	1.00	1.00
SM-8	LFR	0.41	0.68	0.99	0.99
SM-9	ASR	0.85	1.32	1.05	1.04
SM-10	ASR	0.79	1.22	1.02	1.02
SM-11	LFR	0.72	1.21	0.99	0.99
SM-12	LFR	0.51	0.85	1.00	0.99
SM-13	ASR	0.63	0.95	0.95	0.95
SM-14	ASR	0.42	0.76	1.02	1.02
SM-15	LFR	0.48	0.80	0.95	0.95
SM-16	ASR	0.80	1.22	0.99	0.99
SM-17	ASR	0.58	0.92	1.05	1.04
SM-18	ASR	0.59	0.94	1.01	0.99
SM-19	ASR	0.71	1.05	1.00	1.00
SM-20	ASR	0.57	0.93	1.02	1.02
SM-21	ASR	1.37	2.06	1.02	1.02
SM-22	ASR	0.36	0.85	0.96	0.99
SM-23	ASR	0.48	0.85	0.95	0.96
SM-24	ASR	0.59	1.00	1.00	1.01
SM-25	ASR	3.24	4.61	0.96	0.97
Avg.		0.71	1.13	1.01	1.02
Std. Dev.		0.56	0.77	0.04	0.07

4.1.5. Comparison of Calculated Ratings with TxDOT Ratings

4.1.5.1. General

After confirming the rating process, the original calculated RFs were compared to the RFs that TxDOT documents in the NBI (NBI 2016). The exterior girder was ignored in this analysis in order to compare corresponding calculated RFs to the TxDOT RFs, as TxDOT does not seem to analyze exterior girders in the rating calculations provided in their inspection reports.

Table 4.9 and Figure 4.7 show the TxDOT RFs for each bridge, the method they used, and the calculated RF (from this study) based on the same rating method (ASR, LRF or LRFR). The only bridge that did not have a rating method reported in the NBI was Bridge SM-4. In the NBI it was reported as "no rating analysis performed" and in TxDOT's inspection report, a note is written that says, "Original posting recommendation. No calculations to verify ratings." For this bridge, the calculated ASR RF was used for the comparison.

Of the 25 bridges whose interior girders were analyzed using the same method as TxDOT, seven had inventory and operating design-level ratings that were greater than or equal to TxDOT's rating, and eight had operating design-level ratings that were greater than or equal to TxDOT's rating. Of the bridges that were found to have lower design-level ratings than TxDOT's at the both the inventory and operating level, twelve had inventory and operating design-level ratings that were within ten percent of TxDOT's rating. For these bridges, the difference in ratings can usually be attributed to rounding differences or differences in the consideration of certain aspects related to loads. Of the bridges that were found to have lower design-level ratings than TxDOT's at both the inventory and operating levels, 14 had inventory and operating design-level ratings that were

within 20 percent of TxDOT's rating. In addition, four bridges had inventory or operating design-level ratings with more than a 20 percent difference relative to the TxDOT RF values.

Table 4.9. Comparison of Interior Girder Flexure RFs to TxDOT RFs for SM Bridges

ID	Calculated HS20 RF		TxDOT HS20 RF		Rating Method	Calculated/TxDOT	
	Inventory	Operating	Inventory	Operating		Inventory	Operating
SM-1	0.41	0.69	0.33	0.55	LFR	1.24	1.25
SM-2	0.44	0.73	0.34	0.56	LFR	1.30	1.31
SM-3	0.45	0.75	0.48	0.80	LFR	0.95	0.95
SM-4	0.42	0.73	0.39	0.56	N/A (ASR)	1.19	1.32
SM-5	0.48	0.81	0.47	0.79	LFR	1.03	1.02
SM-6	0.78	1.21	0.89	1.39	ASR	0.88	0.87
SM-7	0.53	0.88	0.57	0.95	LFR	0.93	0.93
SM-8	0.39	0.65	0.41	0.69	LFR	0.96	0.95
SM-9	0.88	1.37	0.82	1.27	ASR	1.08	1.08
SM-10	0.74	1.17	0.77	1.20	ASR	0.96	0.98
SM-11	0.67	1.11	0.73	1.22	LFR	0.91	0.91
SM-12	0.35	0.58	0.51	0.86	LFR	0.68	0.68
SM-13	0.60	0.92	0.67	1.00	ASR	0.91	0.92
SM-14	0.38	0.72	0.41	0.75	ASR	0.92	0.96
SM-15	0.46	0.76	0.51	0.85	LFR	0.90	0.90
SM-16	0.86	1.43	0.82	1.24	ASR	1.06	1.15
SM-17	0.54	0.88	0.55	0.89	ASR	0.98	0.99
SM-18	0.76	1.20	0.59	0.95	ASR	1.30	1.27
SM-19	0.69	1.02	0.71	1.04	ASR	0.97	0.98
SM-20	0.52	0.88	0.56	0.91	ASR	0.93	0.97
SM-21	1.33	2.02	1.35	2.02	ASR	0.99	1.00
SM-22	0.16	0.55	0.38	0.87	ASR	0.43	0.63
SM-23	0.42	0.78	0.51	0.88	ASR	0.82	0.88
SM-24	0.40	0.81	0.60	0.99	ASR	0.68	0.82
SM-25	2.53	3.61	3.37	4.77	ASR	0.75	0.76
Avg.	0.65	1.05	0.71	1.12	-	0.95	0.98
Std. Dev.	0.45	0.61	0.58	0.81	-	0.19	0.17

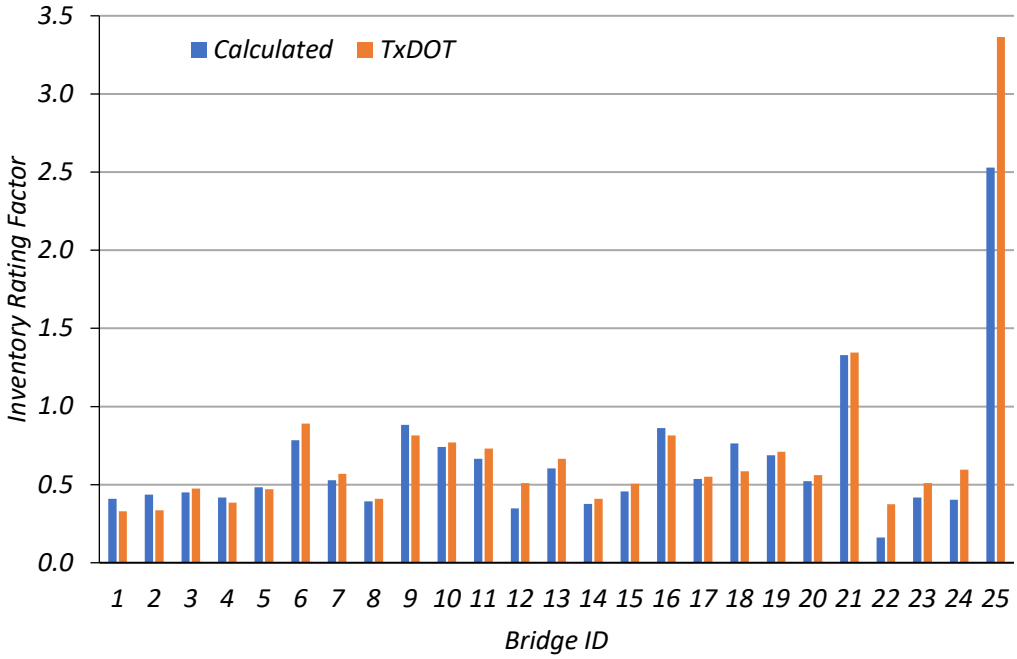

(a) Inventory RFs

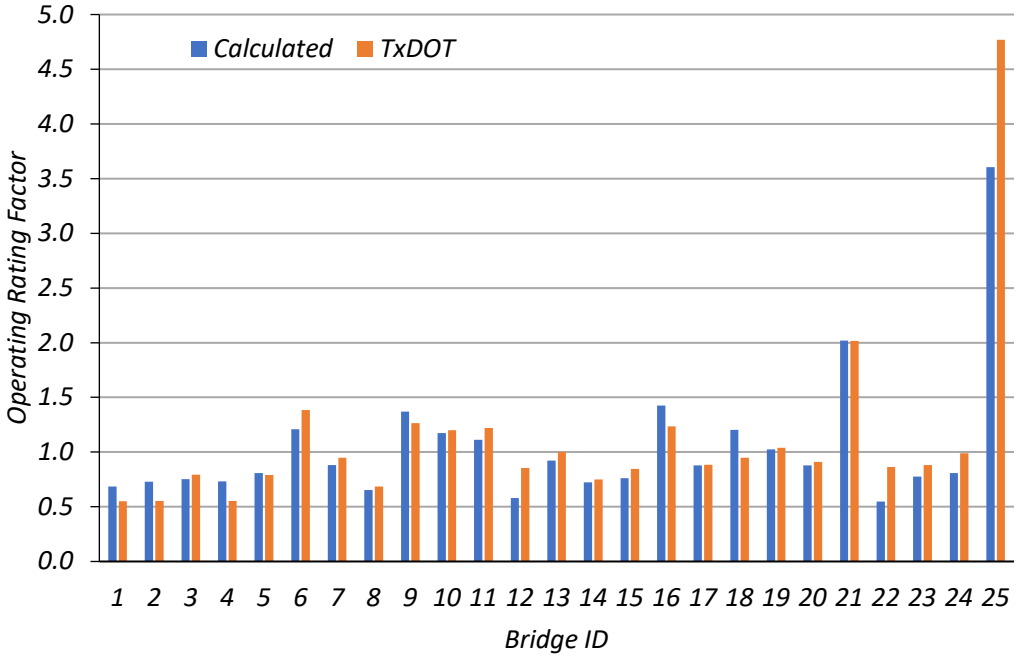

(b) Operating RFs

Figure 4.7. Calculated RF vs. TxDOT RF for Interior Girder Flexure of SM Bridges

After the selected SM bridges were rated, the interior girder flexure RF for each bridge was analyzed to determine the source of any difference with respect to the RFs in the NBI (NBI 2016). The load rating calculations were compared with the TxDOT calculations as closely as possible, given that in some cases the inspection records did not have complete calculations. The interior girder RFs that were obtained from the calculations were used for comparison, as TxDOT's ratings seem to be based on the interior girder.

For every bridge that exhibited a calculated RF lower than the TxDOT RF, the consideration of certain dead load components played into the difference. TxDOT seems to only consider the girders, concrete deck, and wearing surface in most of the dead load calculations. Some of these bridges have significant concrete curbs, lateral bracing members, or railings that are considered in the calculations developed in this study. The rating calculations include a best estimate of the weight of these components and distribute them to the girders according to the AASHTO MBE. Although these are not major components of the dead load of the structure, this produced a higher dead load moment for almost every bridge. This difference affected every bridge overall and is the main reason for slight differences in the calculated and TxDOT RFs. This reason was in some cases paired with another reason to further increase the difference. This difference still applied to bridges that exhibited higher calculated RFs than the TxDOT RFs, however some other difference in the calculations outweighed this item.

Another reason for differences in RFs for many of the bridges involves the braced length used for the non-composite moment capacity of the steel girder. In Article 6A.6.9.3 of the LRFR section of the MBE, AASHTO allows the top flange of a girder to be assumed to be fully braced if it is "fully in contact with the deck and no sign of cracking, rust, or separation along the steel-concrete interface is evident" (AASHTO MBE 2018). However, no such clause exists in the

ASR/LFR section of the MBE, and in Article 10.48.1.1 of the LFR part of the AASHTO Standard Specifications, which addresses compact section moment capacity, it states that “the required lateral bracing shall be provided by braces capable of preventing lateral displacement and twisting of the main members or by embedment of the top and sides of the compression flange in concrete.” No such article requiring embedment of the top flange exists in the ASR section for the girder to be fully braced. TxDOT seems to assume the girder to be fully braced by the deck when using ASR. In consideration of these articles, each bridge was analyzed considering the braced lengths provided by lateral members for LFR and assumed to be fully braced for ASR and LRFR. TxDOT, on the other hand, seems to assume the deck provides full bracing in almost all cases. This difference causes TxDOT ratings to use a slightly higher moment capacity for LFR ratings, however it does not affect the controlling rating for any of the bridges for which LFR is used by TxDOT because the serviceability limit state controls the rating.

4.1.6. Conclusion

The girders of 25 simple-span steel bridges with concrete decks were analyzed according to the AASHTO MBE, AASHTO Standard Specifications, and AASHTO LRFD Specifications. The exterior girder was initially not considered in order to compare RFs of the same structural components to TxDOT. The LFR and ASR methods produced significantly higher RFs than the LRFR method, with the LFR method being slightly higher than the ASR method. Most bridges were calculated to have RFs within ten percent of the corresponding TxDOT RFs, the differences being contributed to differences in the dead loads considered for analysis. These differences are described. For the bridges that exhibited calculated RFs having greater than a ten percent difference with the TxDOT RFs, the reason for this discrepancy was examined further. These

reasons were expanded upon and justified. Based on the analysis performed on the selected simple-span bridges, possible areas for improvement to load posting are identified and elaborated upon in Section 4.3 of this report.

4.2. CONTINUOUS STEEL MULTI-GIRDER BRIDGES

4.2.1. Introduction

Sixteen continuous steel multi-girder (SC) bridges with concrete decks were selected from the SSLO bridge inventory of Texas for further analysis. Table 4.10 summarizes these bridges and their main characteristics. The information shown in this table contains the characteristics that pertain to the controlling span of the bridge. In order to obtain comparable ratings, this same process was used in the calculated rating. In this table, the girder spacing shown is the largest interior girder spacing in the span, if all girders are not equally spaced. Some of the girder cross-sections are historical sections and are named accordingly. A girder named W##x##, S##x##, or C#x## is a current cross section in the 14th edition of the *AISC Steel Construction Manual* (AISC 2013). A girder named ##WFx## is a historic section found in AISC's *Historic Record, Dimensions and Properties, Rolled Shapes, Steel and Wrought Iron Beams & Columns* (AISC 1953). Detailed characteristics for the selected bridges were compiled from the TxDOT inspection database into a master spreadsheet. This enabled the efficient collection of bridge properties and other relevant information so that the basic load ratings could be conducted.

Table 4.10. Selected SSLO Continuous Steel Multi-Girder Bridges and Characteristics

ID	On/Off System	Year Built	Span Lengths (ft)	Deck Width (ft)	Steel Yield Strength[2] (ksi)	Interior Girder Section	Exterior Girder Section	Interior Girder Spacing (ft)	Concrete Deck Thickness (in.)	Wearing Surface Thickness (in.)
SC-1[1]	Off	1910	19' – 18'	19	30	S6x17.25	W6x9	2'-4"	5.50	0.0
SC-2	Off	1925	26' – 26'	14	30	S12x31.8	S12x31.8	3'-7"	3.00	0.0
SC-3	Off	1935	18' – 18'	18	30	S10x25.4	S10x25.4	1'-11.5"	4.00	5.0
SC-4	Off	1937	18' – 15'	18	33	S10x25.4	S10x25.4	2'-2"	4.75	5.8
SC-5[1]	Off	1940	21' – 21'	23	33	S10x25.4	S10x25.4	5'-6.5"	6.25	0.0
SC-6	Off	1942	23' – 22'	24	33	S12x31.8	B15x39	2'-10.5"	5.50	0.0
SC-7	Off	1943	12' – 11'	24	30	S9x21.8	C9x13.4	2'-5"	7.00	7.0
SC-8	On	1949	60' – 70' – 60'	26	33	30WFx108	30WFx108	7'-0"	6.00	1.0
SC-9	Off	1950	11' – 11'	21	33	S6x12.5	S6x12.5	2'-0"	6.00	0.0
SC-10[3]	On	1950	21'	34	33	27WFx94	27WFx94	10'-0"	7.50	0.0
SC-11	Off	1955	15' – 19' – 19'	21	33	S6x12.5	C6x8.2	1'-8"	5.50	0.0
SC-12	On	1959	60' – 75' – 60'	26	33	30WFx108	30WFx108	6'-8"	6.00	2.0
SC-13	On	1965	60' – 75' – 60'	28	36	W30x108	W30x108	7'-0"	6.50	0.0
SC-14	Off	1970	36' – 19'	14	30	S9x21.8	S9x21.8	2'-8"	6.00	0.0
SC-15	Off	1997	24' – 24'	24	36	16WFx88	16WFx88	4'-3.5"	6.00	0.0
SC-16	Off	1999	39' – 37'	20	36	W27x94	W27x94	3'-3"	10.00	0.0

1. SC-1 and SC-5 are the only bridges in this group that is specifically noted as composite in TxDOT's inspection records.
2. Steel yield strength is the value used by TxDOT for load rating calculations, which typically matches the value given in the TxDOT Bridge Inspection Manual (TxDOT 2018a) and AASHTO MBE (AASHTO MBE 2018), unless additional information is available.
3. Floor beam characteristics are shown for SC-10.

4.2.2. Basic Load Rating Analysis

4.2.2.1. General

All the selected continuous steel multi-girder bridges were rated using ASR, LFR, and LRFR. All three methods follow the same general procedure as described in Section 4.1.2. For the flexure rating factors, the following steps are used:

1. Modified section properties are calculated if the girder has a cover plate in the positive moment region or if it is a composite girder. Composite section properties are calculated using the same procedure as in Example A1 in MBE Appendix A (AASHTO MBE 2018). This procedure finds two different transformed section moduli: one using the width of the transformed concrete deck based on the modular ratio of the steel to concrete elastic moduli ($n=E_s/E_c$), and one using the width of the transformed concrete deck based on 3n. The section properties based on n are used when considering the live load on the structure, and the section properties based on 3n are used when considering the superimposed dead load on the structure. This is practiced in the rating factor equations for each method.
2. The appropriate live load distribution factors are determined for both the positive and negative moment regions. For ASR and LFR, these are given as the girder spacing over a number based on the number of lanes for interior girders. For exterior girders the lever rule is used. For LRFR, these are determined as a function of the spacing of the girders and have a range of applicability based on the spacing of the girders, span length, thickness of the slab, and number of girders, or by using the lever rule. For LRFR the average distribution factor for adjacent spans is used as the negative moment distribution factor. Skew adjustments are also considered.

3. The live load distribution factor, along with the appropriate impact factor, are applied to the positive and negative live load moments that are obtained for a single-girder of the bridge. For ASR and LFR the impact factor is given in Article 3.8.2.1 of the AASHTO Standard Specifications and is a function of the span length. For LRFR the impact factor is always 33 percent. Both interior and exterior girders are examined and analyzed.
4. The dead load moments are found by calculating a tributary distributed load for each girder and applying the continuous beam coefficients based on the number of spans and maximum span length (AISC 2013).
5. The appropriate non-composite or composite moment capacity for positive and negative flexure for both the interior and exterior girders is calculated. Consideration is given to whether the section is compact or noncompact, following the requirements in the respective AASHTO specifications. For ASR, this capacity is given in the form of a stress, as a percentage of the yield stress, from the AASHTO MBE. For the LFR capacity, if the section meets the compact requirements, Eqn. (4.1) is used. If the section does not meet the compact requirements, but does meet the noncompact requirements, Eqn. (4.2) is used. If the section meets neither the compact or the noncompact requirements, Eqn. (4.3) is used. For LRFR, if the section meets the compact requirements, Eqn. (4.4) is used. If the section does not meet the compact requirements, but does meet the noncompact requirements, Eqn. (4.6) is used. The section is also checked using equations based on the braced length of the span. For a composite section for both methods, the plastic neutral axis is determined and the moments caused by the components are summed about the plastic neutral axis.

6. Load rating is conducted based on the three load rating procedures (ASR, LFR, and LRFR) at the operating and inventory levels considering both the interior girder and exterior girder positive and negative moment demands at the strength and service limit states.

For the shear rating factors, the following steps are used:

1. As the web of the steel section is the shear resisting component, section properties such as web thickness, web height, and web area are found and calculated.
2. The appropriate live load distribution factors are determined. For ASR and LFR, these are given as the girder spacing over a number based on the number of lanes for interior girders. For exterior girders the lever rule is used. For LRFR, these are determined as a function of the spacing of the girders and have a range of applicability based on the spacing of the girders, span length, thickness of the slab, and number of girders, or by using the lever rule. Skew adjustments are also considered.
3. The live load distribution factor, along with the appropriate impact factor, are applied to the live load shear that is obtained for the bridge. For ASR and LFR the impact factor is given in Article 3.8.2.1 of the AASHTO Standard Specifications and is a function of the span length. For LRFR the impact factor is always 33 percent. Both interior and exterior girders are examined and analyzed.
4. The dead load shears are found by calculating a tributary distributed load for each girder and applying the approximate continuous beam coefficients based on the number of spans and maximum span length (AISC 2013).
5. The web buckling coefficient is determined, and the shear capacity is determined using Eqn. (4.6).

6. Load rating is conducted based on the three load rating procedures (ASR, LFR, and LRFR) at the operating and inventory levels considering both the interior girder and exterior girder shear demands at the strength limit state.

Some bridges had special considerations that had to be made when conducting the load rating analysis. Bridges SC-1 and SC-5 have their top flanges embedded into the concrete deck making them composite sections. Their composite section properties were calculated based on provided structural drawings. However, TxDOT seems to assume that the neutral axis was located at the surface of the top flange and ignored the part of concrete below the top surface of the flange when calculating moment capacity. The moment capacity calculations use the same approach to have comparable ratings. However, when the ASR method and the LFR and LRFR serviceability limit states are checked, the section modulus used to find stresses must be the actual section modulus of the cross-section and for consistency the same procedure that is used in Example A1 in MBE Appendix A (AASHTO MBE 2018) is used. Therefore, the composite section moduli for SC-1 and SC-5 were calculated separately and used for these ratings. Bridge SC-10 involved the analysis of a floorbeam and not the girders of the bridge. Bridges SC-12 and SC-13 have top and bottom cover plates in the negative moment region for which extra section property calculations were conducted. Bridge SC-14 is labeled as continuous, however it contains two different sized steel cross-sectional shapes that are spliced and bolted at the interior support. TxDOT in their rating calculations say this is not a true moment connection and analyze the bridge as a simple span. For this reason, the bridge was analyzed as a simple-span bridge in the calculations. Finally, bridges SC-15 and SC-16 each have one or more girders that do not touch the interior support and are therefore act as simply supported over the entire bridge length. TxDOT analyzes both of these

bridges as a single simply supported span, and therefore the project calculations analyzed them in the same way.

4.2.2.2. Allowable Stress Rating and Load Factor Rating

The capacities of continuous steel multi-girder bridges were determined using the same process as for the capacity calculations for the simple-span (SC) bridges, with the addition of the negative moment capacity calculations. For a non-composite bridge, the negative moment capacity is taken as the same as the non-composite positive moment capacity, unless the bridge has a negative moment region cover plate. For a composite bridge, the AASHTO Standard Specifications allow the rebar contribution to be considered in the negative moment region, per Article 10.50.2.1 (AASHTO 2002). Therefore, for composite cross-sections a composite negative moment section modulus and moment capacity were calculated and used in determination of the negative moment region RFs. The RFs are calculated in the same way as the simple-span RFs, with the consideration of the negative moment region as well.

4.2.2.3. Load and Resistance Factor Rating

As with the ASR and LFR continuous calculations, the LRFR continuous calculations determined the capacities using the same process as for the simple-span bridges with the addition of the negative moment region moment capacity calculations. However, the AASHTO LRFD Specifications do not have a clause allowing for the consideration of composite rebar in the negative moment region, so this was not included. Also, for negative moment region live load distribution factors, the AASHTO LRFD Specifications require the averaging of the two adjacent span lengths when calculating the distribution factors. This process was conducted in the LRFR continuous bridge rating calculations.

4.2.3. Calculated Load Rating Results

Each of the 16 selected continuous, steel multi-girder (SC) bridges with concrete decks was rated using each of the three rating methods. The bridges were rated for an HS-20 truck for ASR and LFR, as that is the truck TxDOT uses when reporting to the NBI, and for the HL-93 design load for LRFR. They were examined and rated for interior girder flexure, exterior girder flexure, interior girder shear, and exterior girder shear. The bridges were initially rated by following the procedures laid out in the AASHTO MBE, AASHTO Standard Specifications, and AASHTO LRFD Specifications as closely as possible.

4.2.3.1. Interior Girder Flexure Analysis

The flexure RFs found for the design loads using each method for the interior girders of each bridge are shown in Table 4.11 and Figure 4.8. In the interior girder flexure analysis, for all of the selected bridges except SC-2, the LFR method produced a higher operating RF than the ASR method. For all of the selected bridges, the LFR method produced a higher operating RF than the LRFR method.

Table 4.11. Interior Girder Flexure RFs for SC Bridges

ID	Inventory HS20 RF			Operating HS20 RF		
	ASR	LFR	LRFR	ASR	LFR	LRFR
SC-1	0.32	0.44	0.09	0.53	0.74	0.11
SC-2	0.07	0.25	0.19	0.39	0.42	0.25
SC-3	1.21	1.13	0.29	1.83	1.89	0.37
SC-4	1.12	1.02	0.25	1.66	1.71	0.33
SC-5	0.17	0.34	0.15	0.37	0.57	0.20
SC-6	1.18	1.03	0.61	1.67	1.72	0.79
SC-7	0.95	0.84	0.39	1.37	1.41	0.51
SC-8	0.42	0.50	0.43	0.80	0.84	0.55
SC-9	0.58	0.50	0.23	0.82	0.84	0.29
SC-10	1.38	1.27	1.42	1.97	2.12	1.84
SC-11	0.25	0.31	0.08	0.49	0.51	0.10
SC-12	0.59	0.55	0.60	0.89	0.92	0.78
SC-13	0.64	0.60	0.76	0.98	1.01	0.99
SC-14	0.47	0.49	0.14	0.74	0.81	0.19
SC-15	0.38	0.46	0.39	0.69	0.76	0.50
SC-16	0.04	0.32	0.27	0.49	0.54	0.35
Average	0.61	0.63	0.39	0.98	1.05	0.51
Std. Dev.	0.42	0.31	0.33	0.52	0.52	0.43

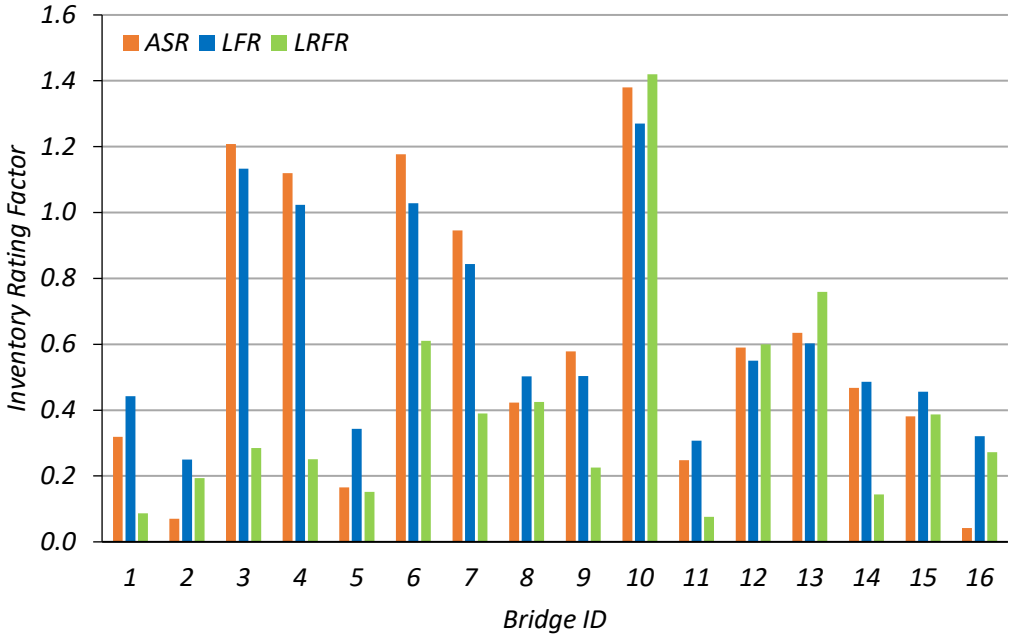

(a) Inventory RFs

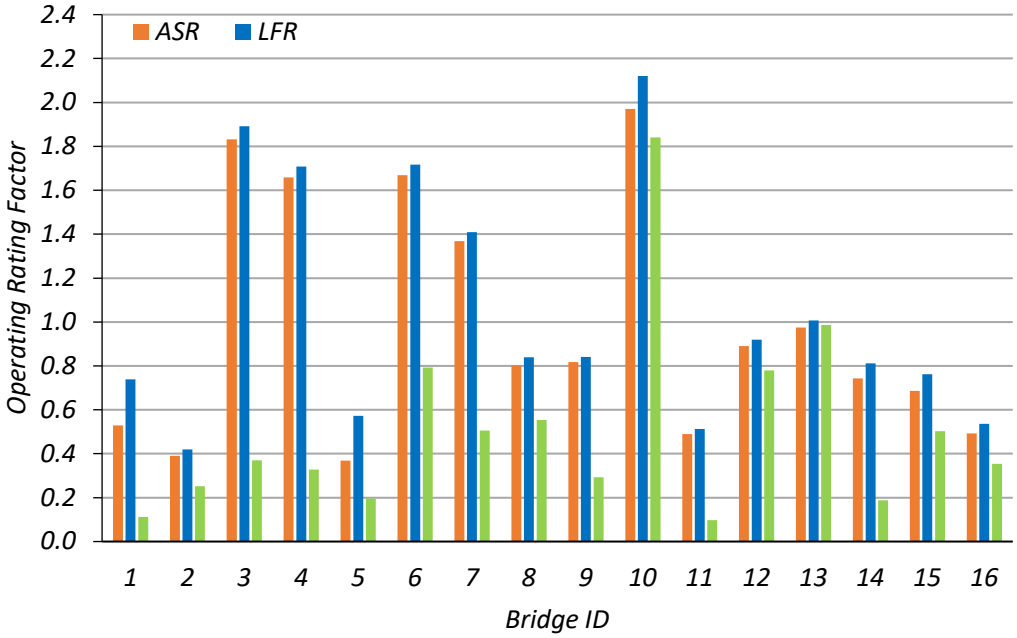

(b) Operating RFs

Figure 4.8. Interior Girder Flexure RFs for SC Bridges

For the interior girder flexure of the selected SC bridges, the LFR method produced a higher average inventory RF (0.63) than the ASR method (0.61), which produced a higher average inventory RF than the LRFR method (0.39). The LFR method also produced a higher average operating RF (1.05) than the ASR method (0.98), which produced a higher average operating RF than the LRFR method (0.51).

Of the 16 bridges whose interior girders were analyzed, four were found to have HS-20 inventory ratings at or above 1.0 and five were found to have HS-20 operating ratings at or above 1.0 using both the ASR method and the LFR method. One was found to have an HL-93 inventory rating at or above 1.0 and the same one was found to have an HL-93 operating rating at or above 1.0 using the LRFR method. This bridge was SC-10. Three bridges along with this one had both operating and inventory ratings above 1.0 using both the ASR and LFR method. These bridges were SC-3, SC-4, and SC-6.

4.2.3.2. Exterior Girder Flexure Analysis

As with the simple-span bridges, the exterior girders of the continuous bridges were rated separately, as it appears that the TxDOT practice is to rate the SC bridges based on the interior girders only. However, each bridge was analyzed again, this time considering the exterior girders and the AASHTO articles relevant to them, with the main differences again being the live load distribution factors. Table 4.12 and Figure 4.9 show the exterior girder flexure RFs found using each rating method for each continuous SC bridge. As the rating for Bridge SC-10 consisted of only analyzing a floorbeam, the exterior girder RF shown is the same as the interior girder RF, which is the singular RF for the floorbeam.

For the exterior girder flexure of the selected SC bridges, the ASR method produced a higher average inventory RF (0.58) than the LFR method (0.57), which produced a higher average inventory RF than the LRFR method (0.41). However, the LFR method produced a higher average operating RF (0.95) than the ASR method (0.89), which produced a higher average operating RF than the LRFR method (0.53).

There were seven continuous bridges for which the exterior girder was found to control the rating. Table 4.13 and Figure 4.10 show the operating and inventory design-level RFs found for each of these bridges when the exterior was not considered and when it was considered, and the difference between the two RFs.

Table 4.12. Exterior Girder Flexure RFs for SC Bridges

ID	Inventory HS20 RF			Operating HS20 RF		
	ASR	LFR	LRFR	ASR	LFR	LRFR
SC-1	0.20	0.27	0.05	0.32	0.45	0.07
SC-2	0.34	0.37	0.33	0.59	0.61	0.43
SC-3	1.09	0.96	0.30	1.55	1.60	0.39
SC-4	0.72	0.64	0.25	1.04	1.07	0.33
SC-5	0.25	0.38	0.21	0.45	0.63	0.27
SC-6	1.23	1.06	0.63	1.72	1.77	0.82
SC-7	0.53	0.47	0.22	0.77	0.79	0.28
SC-8	0.53	0.58	0.48	0.93	0.96	0.63
SC-9	0.42	0.37	0.23	0.60	0.61	0.29
SC-10	1.38	1.27	1.42	1.97	2.12	1.84
SC-11	0.06	0.09	0.04	0.15	0.15	0.05
SC-12	0.75	0.67	0.70	1.08	1.12	0.91
SC-13	0.77	0.69	0.71	1.11	1.14	0.92
SC-14	0.45	0.43	0.16	0.66	0.72	0.21
SC-15	0.45	0.50	0.42	0.75	0.83	0.55
SC-16	0.35	0.44	0.46	0.71	0.74	0.59
Average	0.58	0.57	0.41	0.89	0.95	0.53
Std. Dev.	0.36	0.29	0.32	0.48	0.49	0.42

It should be noted, however, that the results obtained when considering an exterior girder may be overly conservative. For bridges SC-1, SC-3, SC-7, SC-11, and SC-14 the exterior girder controls due to restrictions in Article 3.23.2.3.1.5 of the AASHTO Standard Specifications. As mentioned with the simple-span bridges, this article puts a minimum on the exterior girder live load distribution factor, therefore decreasing the exterior girder rating. For bridges SC-4, SC-9, and SC-13, the lever rule produces higher exterior distribution factors that outweigh the reduction in dead load the exterior girder experiences. Nevertheless, the bridges were analyzed according to the AASHTO Standard Specifications and the lever rule.

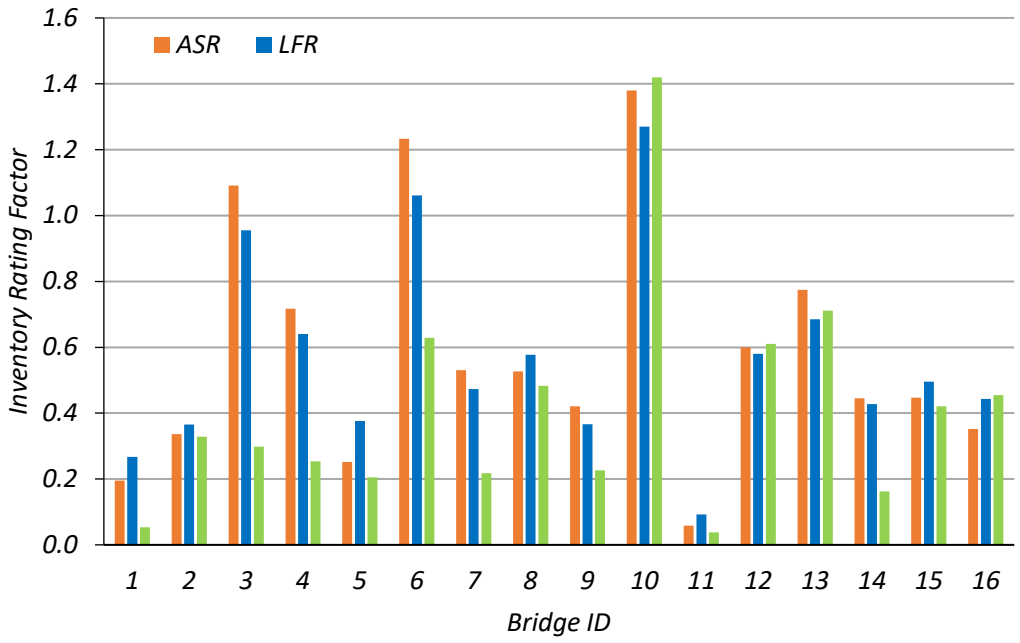

(a) Inventory RFs

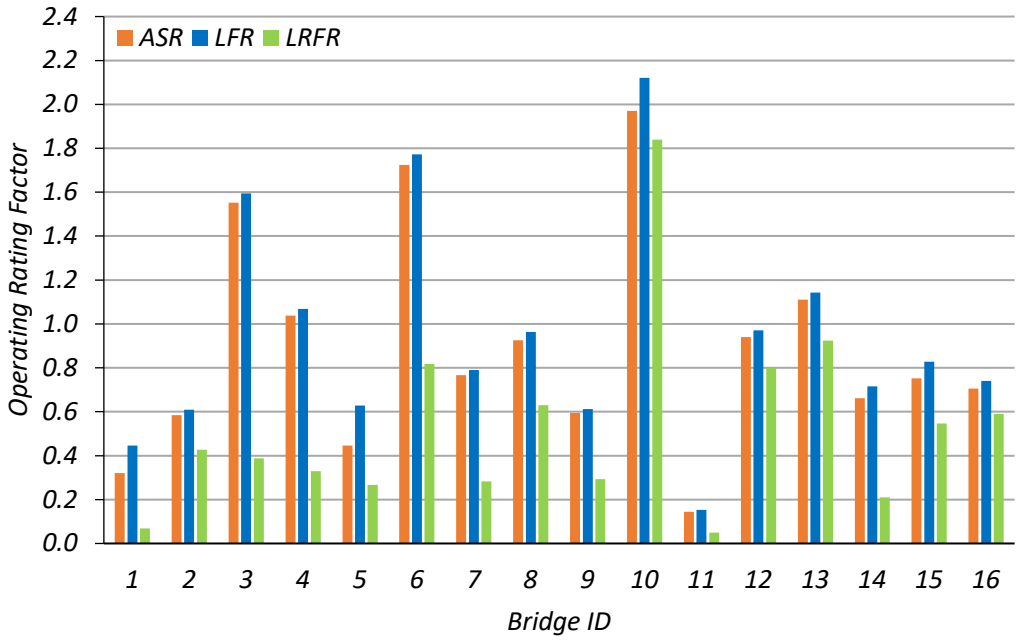

(b) Operating RFs

Figure 4.9. Exterior Girder Flexure RFs for SC Bridges

Table 4.13. SC Bridges Controlled by Exterior Girder Flexure RFs

ID	TxDOT Rating Method	Interior Girder Rating		Exterior Girder Rating		Exterior Rating/ Interior Rating	
		Inv.	Oper.	Inv.	Oper.	Inv.	Oper.
SC-1	ASR	0.32	0.53	0.20	0.32	0.61	0.61
SC-3	ASR	1.21	1.83	1.09	1.55	0.90	0.85
SC-4	ASR	1.12	1.66	0.72	1.04	0.64	0.63
SC-7	ASR	0.95	1.37	0.53	0.77	0.56	0.56
SC-9	ASR	0.58	0.82	0.42	0.60	0.73	0.73
SC-11	ASR	0.25	0.49	0.06	0.15	0.23	0.30
SC-14	ASR	0.47	0.74	0.45	0.66	0.95	0.89
Average		0.70	1.06	0.49	0.73	0.66	0.65

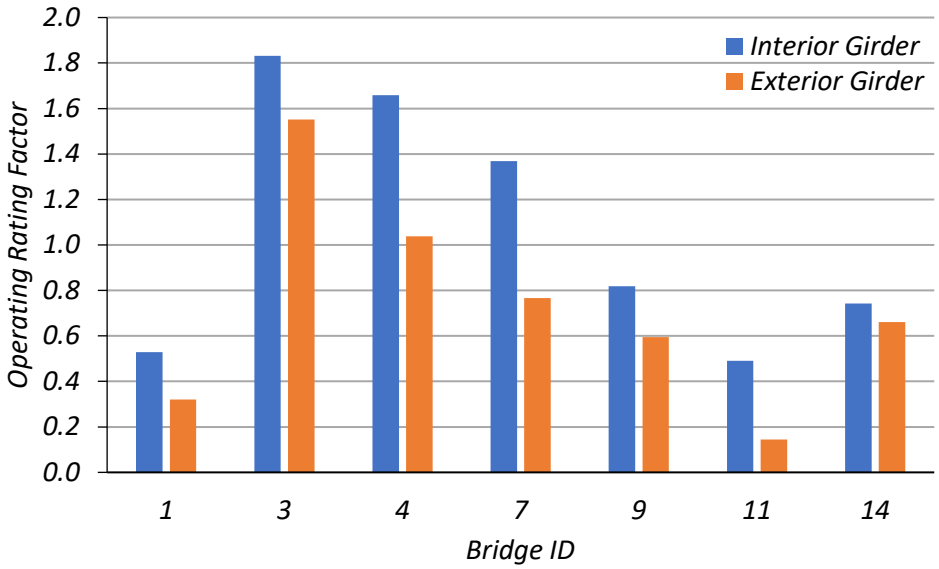

Figure 4.10. Interior Girder and Exterior Girder RFs for Select SC Bridges

4.2.3.3. Interior Girder Shear Analysis

The shear RFs found for the design loads using each method for the interior girders of each continuous bridge are shown in Table 4.14 and Figure 4.11. In the interior girder shear analysis,

for all of the selected bridges, the ASR method produced a higher operating RF than both the LFR and LRFR methods.

Table 4.14. Interior Girder Shear RFs for SC Bridges

ID	Inventory HS20 RF			Operating HS20 RF		
	ASR	LFR	LRFR	ASR	LFR	LRFR
SC-1	1.94	1.61	0.70	2.72	2.69	0.91
SC-2	1.79	1.56	0.87	2.63	2.60	1.13
SC-3	3.89	3.24	0.94	5.45	5.40	1.21
SC-4	3.13	2.62	0.94	4.41	4.37	1.22
SC-5	0.78	0.69	0.59	1.17	1.15	0.76
SC-6	2.41	2.00	1.21	3.37	3.33	1.57
SC-7	2.17	1.84	0.68	3.10	3.07	0.88
SC-8	2.71	2.32	2.11	3.91	3.87	2.74
SC-9	1.66	1.38	0.50	2.32	2.30	0.64
SC-10	3.94	3.26	3.83	5.48	5.43	4.97
SC-11	1.98	1.67	0.42	2.81	2.78	0.55
SC-12	2.96	2.52	2.10	4.25	4.21	2.73
SC-13	3.20	2.69	2.28	4.53	4.49	2.95
SC-14	2.24	1.87	0.79	3.15	3.12	1.03
SC-15	2.61	2.19	1.79	3.69	3.66	2.32
SC-16	6.98	5.88	2.92	9.91	9.82	3.79
Average	2.77	2.33	1.42	3.93	3.89	1.84
Std. Dev.	1.34	1.13	0.96	1.90	1.88	1.24

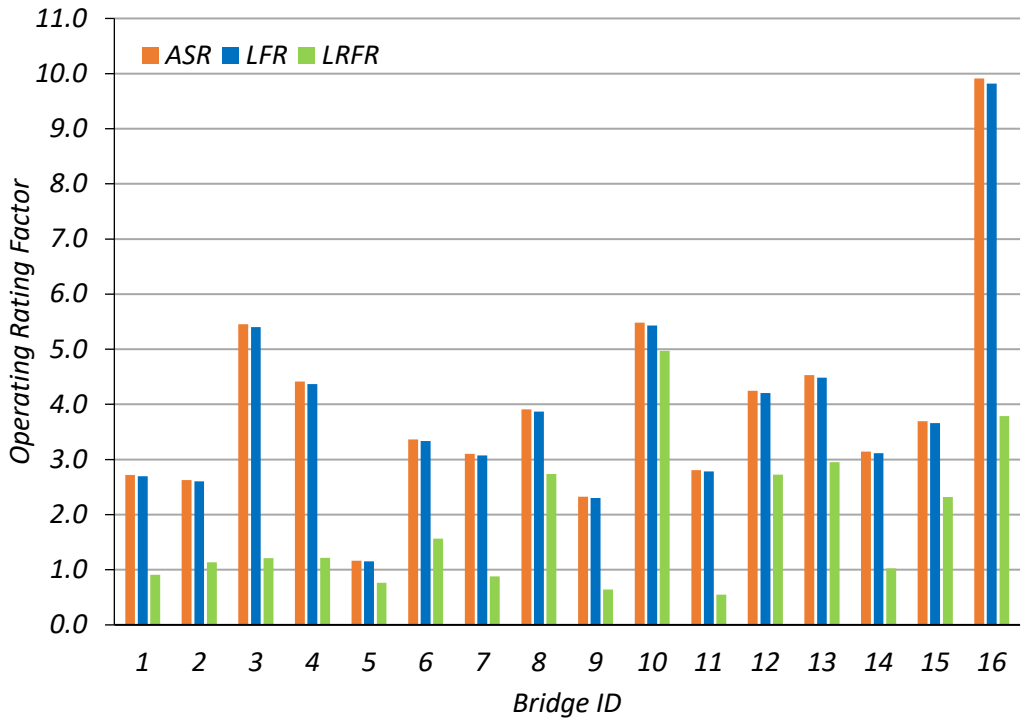

Figure 4.11. Interior Girder Shear Operating RFs for SC Bridges

For the interior girder shear of the selected SC bridges, the ASR method produced a higher average inventory RF (2.89) than the LFR method (2.42), which produced a higher average inventory RF than the LRFR method (1.47). The ASR method also produced a higher average operating RF (4.07) than the LFR method (4.03), which produced a higher average operating RF than the LRFR method (1.90).

For all but one continuous bridge, SC-5, both the ASR method and the LFR method produced inventory and operating interior girder shear RFs greater than or equal to 1.0. The LRFR method produced operating RFs greater than or equal to 1.0 for 11 of the continuous bridges. There were nine SC bridges for which the LRFR method did not produce inventory RFs greater than 1.0. None of the interior girder shear RFs control over the corresponding interior girder flexure RFs.

4.2.3.4. Exterior Girder Shear Analysis

The shear RFs found for the design loads using each method for the exterior girders of each bridge are shown in Table 4.15 and Figure 4.12. In the exterior girder shear analysis, for all of the selected bridges, the ASR method produced a higher operating RF than both the LFR and LRFR methods.

Table 4.15. Exterior Girder Shear RFs for SC Bridges

ID	Inventory HS20 RF			Operating HS20 RF		
	ASR	LFR	LRFR	ASR	LFR	LRFR
SC-1	1.38	1.17	0.26	1.97	1.95	0.33
SC-2	2.22	1.87	0.95	3.14	3.11	1.23
SC-3	11.29	9.30	0.96	15.67	15.53	1.24
SC-4	1.96	1.63	0.95	2.75	2.72	1.23
SC-5	1.80	1.54	0.63	2.60	2.58	0.81
SC-6	3.65	3.00	1.35	5.05	5.00	1.76
SC-7	8.18	6.83	0.57	11.50	11.40	0.74
SC-8	3.55	3.01	2.15	5.07	5.02	2.79
SC-9	1.21	1.00	0.50	1.69	1.67	0.64
SC-10	3.94	3.26	3.83	5.48	5.43	4.97
SC-11	4.20	3.51	0.37	5.91	5.86	0.48
SC-12	3.30	2.80	2.12	4.73	4.68	2.75
SC-13	3.16	2.66	2.27	4.48	4.44	2.95
SC-14	2.36	1.95	0.81	3.28	3.25	1.05
SC-15	2.67	2.24	1.82	3.77	3.73	2.36
SC-16	10.23	8.50	3.03	14.32	14.19	3.93
Average	4.07	3.39	1.41	5.71	5.66	1.83
Std. Dev.	2.98	2.46	1.00	4.15	4.11	1.30

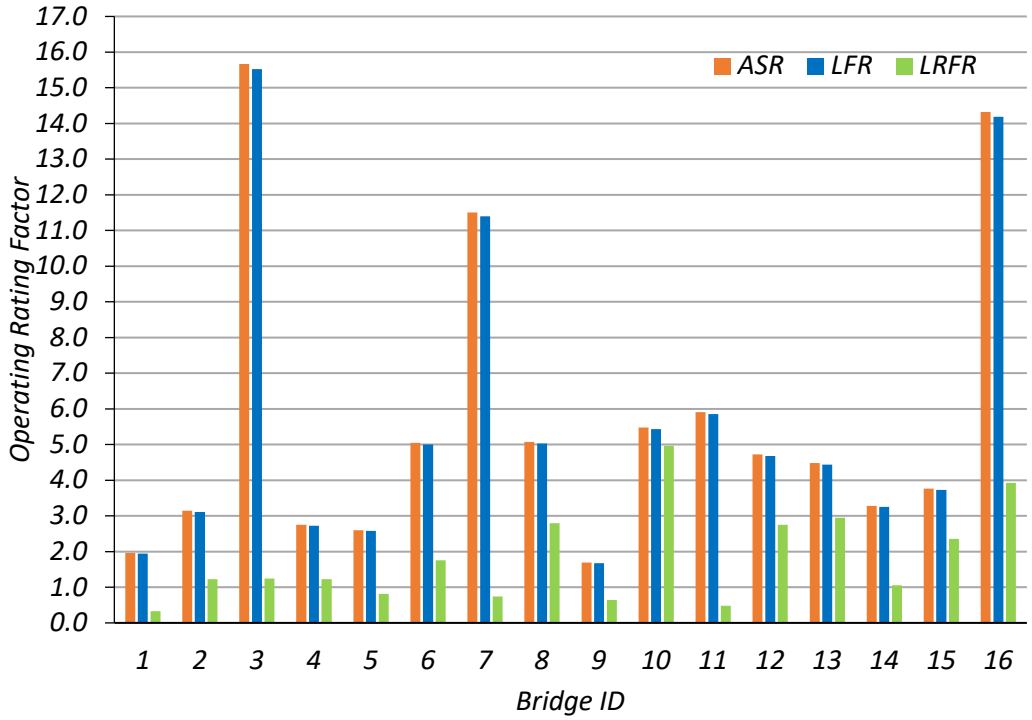

Figure 4.12. Exterior Girder Shear Operating RFs for SC Bridges

For the exterior girder shear of the selected SC bridges, the ASR method produced a higher average inventory RF (4.20) than the LFR method (3.49), which produced a higher average inventory RF than the LRFR method (1.46). The ASR method also produced a higher average operating RF (5.88) than the LFR method (5.82), which produced a higher average operating RF than the LRFR method (1.89).

Again, the interior girder and exterior girder ratings for Bridge SC-10 are the same; the singular rating for the floorbeam. For all bridges, both the ASR method and the LFR method produced inventory and operating exterior girder shear RFs greater than or equal to 1.0. The LRFR method produced an inventory RF greater than or equal to 1.0 for seven SC bridges and operating RFs greater than or equal to 1.0 for eleven SC bridges. None of the exterior girder shear RFs control over the corresponding exterior girder flexure RFs.

4.2.3.5. Comparison of SC Bridge Interior Girder Flexure and Shear RFs

After calculating the flexure and shear RFs for the selected SC bridges, the RFs were compared to determine if girder flexure or girder shear was the controlling limit state for each bridge. Table 4.16 and Figure 4.13 show the interior girder inventory and operating flexure and shear RFs found using the same method TxDOT uses in analysis. For every SC bridge, the flexure RF controlled the interior girder rating at both the inventory and operating level.

Table 4.16. Interior Girder Flexure and Shear RFs for SC Bridges

ID	TxDOT Rating Method	Inventory HS20 RF		Operating HS20 RF	
		Flexure	Shear	Flexure	Shear
SC-1	ASR	0.32	1.94	0.53	2.72
SC-2	ASR	0.07	1.79	0.39	2.63
SC-3	ASR	1.21	3.89	1.83	5.45
SC-4	ASR	1.12	3.13	1.66	4.41
SC-5	ASR	0.17	0.78	0.37	1.17
SC-6	ASR	1.18	2.41	1.67	3.37
SC-7	ASR	0.95	2.17	1.37	3.10
SC-8	LFR	0.50	2.32	0.84	3.87
SC-9	ASR	0.58	1.66	0.82	2.32
SC-10	LFR	1.27	3.26	2.12	5.43
SC-11	ASR	0.25	1.98	0.49	2.81
SC-12	LFR	0.64	2.52	1.07	4.21
SC-13	LFR	0.60	2.69	1.01	4.49
SC-14	ASR	0.47	2.24	0.74	3.15
SC-15	ASR	0.38	2.61	0.69	3.69
SC-16	ASR	0.04	6.98	0.49	9.91
Avg.		0.61	2.65	1.01	3.92
Std. Dev.		0.40	1.31	0.54	1.89

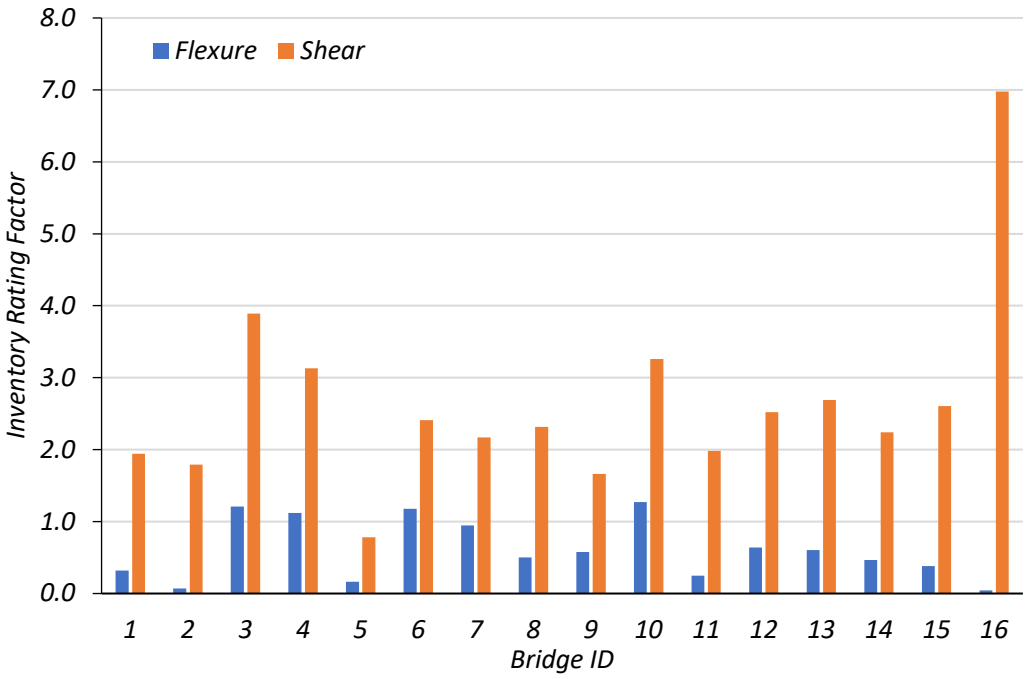

(c) Inventory RFs

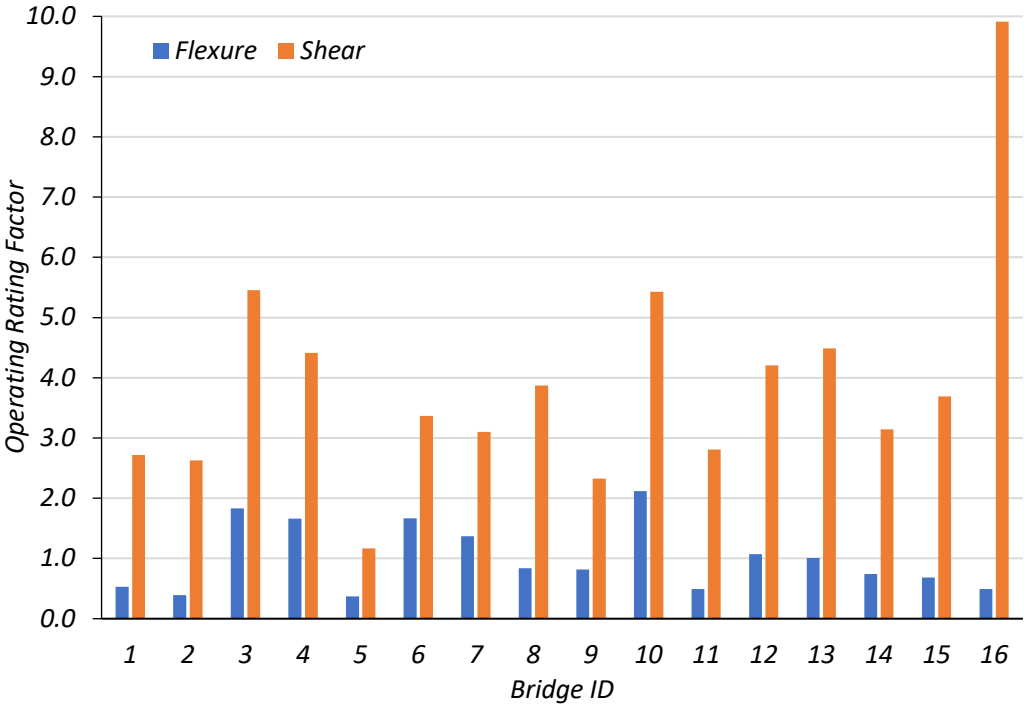

(d) Operating RFs

Figure 4.13. Comparison of Interior Girder Flexure and Shear RFs for SC Bridges

4.2.4. Check of SC Bridge Calculations

After conducting the rating analysis of each bridge, a check was conducted to confirm that the load rating process followed the AASHTO MBE and TxDOT practices. Therefore, for each bridge, the input characteristics were changed to match TxDOT's values where differences were noted and the same standard practices employed by TxDOT were used. Any differences within five percent could be attributed to slight rounding differences, especially with choosing the span length. Table 4.17 shows the results of this procedure for each selected SC bridge.

There was only one SC bridge for which changing the input characteristics did not produce a result within five percent of TxDOT's rating. For Bridge SC-13, as previously mentioned, TxDOT uses the pan girder ratings as the ratings for the overall bridge, instead of the steel multi-girder ratings which control the ratings according to both TxDOT RFs and the calculated RFs. Through this approach, the calculated ratings were found to be close or the same as the TxDOT ratings, confirming the process used in the rating calculations.

Table 4.17. Interior Girder Results for SC Bridges with Adjusted Characteristics

Bridge ID	Rating Method	Adjusted Calculations HS20 RF		Adjusted Calculations RF/ TxDOT RF	
		Inventory	Operating	Inventory	Operating
SC-1	ASR	0.38	0.59	1.05	1.05
SC-2	ASR	0.43	0.75	1.04	1.04
SC-3	ASR	0.98	1.46	0.99	1.00
SC-4	ASR	1.08	1.60	0.99	1.00
SC-5	ASR	0.58	0.84	0.99	0.95
SC-6	ASR	1.13	1.61	1.05	1.05
SC-7	ASR	0.86	1.25	1.03	1.02
SC-8	LFR	0.53	0.89	0.96	0.97
SC-9	ASR	0.56	0.89	1.01	0.96
SC-10	LFR	0.60	1.01	1.04	1.05
SC-11	ASR	0.38	0.60	0.97	0.98
SC-12	LFR	0.56	0.93	1.01	1.00
SC-13	LFR	0.59	0.99	0.81	0.82
SC-14	ASR	0.50	0.76	1.04	1.04
SC-15	ASR	0.56	0.94	1.00	1.00
SC-16	ASR	0.33	0.56	0.99	1.00
Avg.	-	0.63	0.98	1.00	1.00
Std. Dev.	-	0.24	0.33	0.06	0.06

4.2.5. Comparison of Calculated Ratings with TxDOT Ratings

4.2.5.1. General

After confirming the rating process, the originally calculated RFs were then compared to the RFs provided by TxDOT in the NBI (NBI 2016). The exterior girder RFs are note considered in this comparison, as TxDOT does not seem to analyze exterior girders in the rating calculations provided in their inspection reports. For each selected SC bridge, Table 4.18 and Figure 4.14 show the TxDOT RFs, the rating method used by TxDOT, and the ratio of calculated RF to TxDOT RF using the same rating method.

Of the 16 SC bridges whose interior girders were analyzed for flexure using the same method as TxDOT, five had inventory and operating design-level ratings that were greater than or equal to the TxDOT ratings. Of the bridges that were found to have lower design-level ratings than TxDOT's at the both the inventory and operating level, three had inventory and operating design-level ratings that were within ten percent of the TxDOT ratings. For these bridges, the difference in ratings can usually be attributed to rounding differences or differences in the consideration of certain aspects of loads. Of the bridges that were found to have lower design-level ratings than TxDOT's at both the inventory and operating levels, three had inventory and operating design-level ratings that were within twenty percent of the corresponding TxDOT ratings. There were five bridges that had inventory or operating design-level ratings with more than a 20 percent difference relative to the TxDOT ratings.

After the selected SC bridges were rated, the interior girder flexure RF for each bridge was analyzed to determine the source of any difference with respect to the RFs in the NBI (NBI 2016). The load rating calculations were compared with the TxDOT calculations as closely as possible, given that in some cases the inspection records did not have complete calculations. The interior girder RFs that were obtained from the calculations were used for comparison, as TxDOT's ratings seem to be based on the interior girder.

Table 4.18. Comparison of Interior Girder Flexure RFs for SC Bridges to TxDOT RFs Using the Same Rating Method

ID	Calculated HS20 RF		HS20 RF (TxDOT)		TxDOT Rating Method	Calculated/TxDOT	
	Inv.	Oper.	Inv.	Oper.		Inv.	Oper.
SC-1	0.32	0.53	0.37	0.56	ASR	0.87	0.94
SC-2	0.07	0.39	0.42	0.72	ASR	0.17	0.54
SC-3	1.21	1.83	1.00	1.46	ASR	1.21	1.26
SC-4	1.12	1.66	1.09	1.61	ASR	1.03	1.03
SC-5	0.17	0.37	0.58	0.89	ASR	0.28	0.41
SC-6	1.18	1.67	1.08	1.53	ASR	1.09	1.09
SC-7	0.95	1.37	0.84	1.23	ASR	1.13	1.11
SC-8	0.50	0.84	0.56	0.92	LFR	0.91	0.92
SC-9	0.58	0.82	0.56	0.93	ASR	1.04	0.88
SC-10	1.27	2.12	0.58	0.96	LFR	2.19	2.21
SC-11	0.25	0.49	0.40	0.61	ASR	0.63	0.81
SC-12	0.55	0.92	0.55	0.93	LFR	1.00	0.99
SC-13	0.60	1.01	0.73	1.22	LFR	0.83	0.83
SC-14	0.47	0.74	0.48	0.73	ASR	0.99	1.02
SC-15	0.38	0.69	0.56	0.94	ASR	0.69	0.73
SC-16	0.04	0.49	0.34	0.56	ASR	0.13	0.88
Average	0.61	1.01	0.63	0.99	-	0.90	0.99
Std. Dev.	0.40	0.54	0.24	0.32	-	0.47	0.38

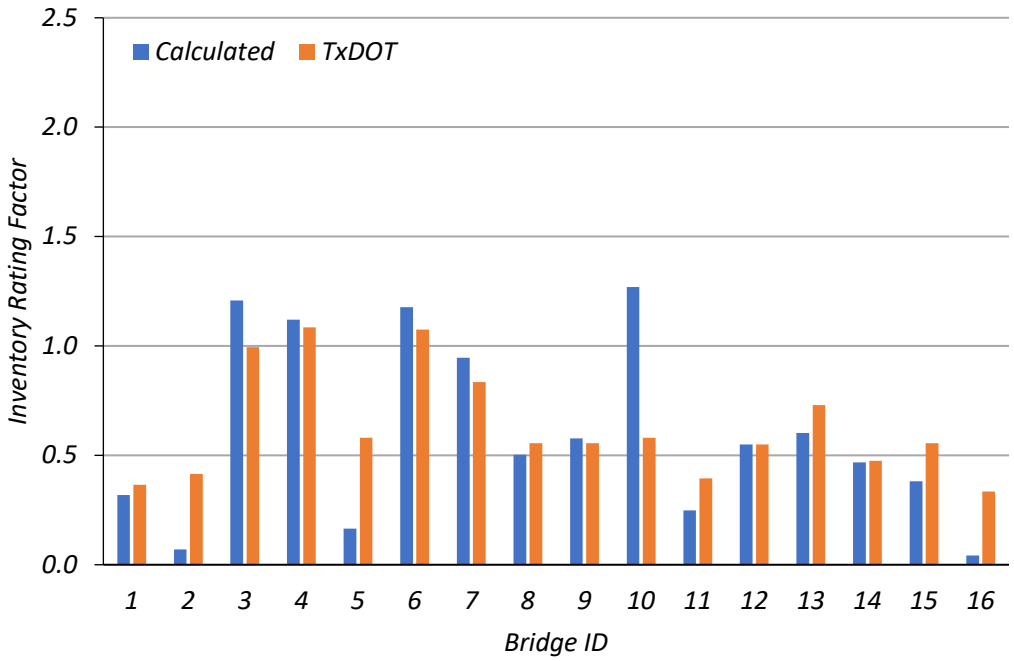

(a) Inventory RFs

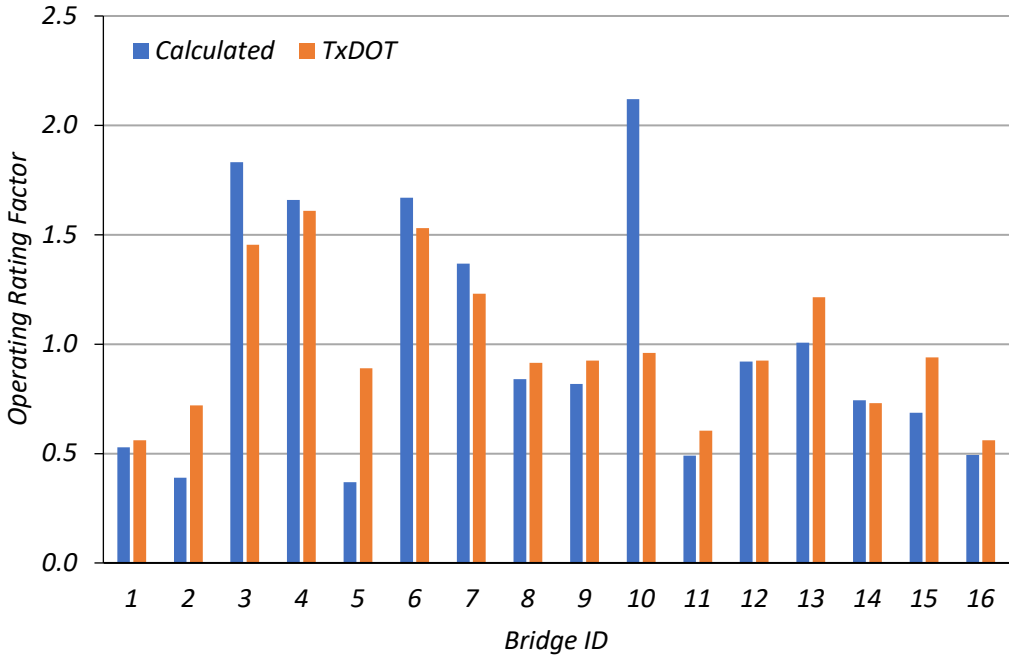

(b) Operating RFs

Figure 4.14. Calculated RF vs. TxDOT RF for Interior Girder Flexure for SC Bridges

For every bridge that exhibited a calculated RF lower than the TxDOT RF, the consideration of certain dead load components played into the difference. TxDOT seems to only consider the girders, concrete deck, and wearing surface in most of their dead load calculations. Some of these bridges have significant concrete curbs, lateral bracing members, or railings that are considered in the calculations developed in this study. The rating calculations include a best estimate of the weight of these components and distribute them to the girders according to the AASHTO MBE. Although these are not major components of the dead load of the structure, this produced a higher dead load moment for almost every bridge. This difference affected each SM bridge overall and is the main reason for slight differences in the calculated RFs and the TxDOT RFs. This reason was in some cases paired with another reason to increase the difference. This difference also applies to bridges that exhibited higher calculated RFs than the TxDOT RF, however some other difference in the calculations outweighed this item, causing a higher RF to be calculated.

Another difference between the calculations and TxDOT load rating is that TxDOT does not seem to analyze off-system continuous bridges in negative flexure when using the ASR method. These bridges are assumed to have an equivalent simple-span with a length usually between 70 percent and 90 percent of the actual bearing support to bearing support length. Then they analyze the bridge as they would any other simple-span in positive flexure. However, the calculations for this study evaluate these off-system bridges in both the negative and positive moment regions. The calculated RFs determine the live load moments acting on the continuous bridge using analytical tools, whereas TxDOT seems to use an approximate method for their ASR analysis. This approximate method uses the moment values from the MBE with the determined

equivalent simple span length. This is another source of slight differences in ratings of all continuous bridges analyzed using ASR.

One final difference between the project calculations and TxDOT ratings is related to the braced length of the girders. First, the project calculations analyze each bridge considering the braced lengths provided by lateral members for LFR and assumed to be fully braced for ASR and LRFR. However, TxDOT seems to assume the deck provides full bracing for both LFR and LRFR. This gives them a slightly higher capacity for the LFR method in some cases, however the serviceability limit state controls for these bridges.

4.2.6. Conclusion

The girders of 16 continuous steel bridges with concrete decks were analyzed according to the AASHTO MBE, AASHTO Standard Specifications, and AASHTO LRFD Specifications. The exterior girder was initially not considered in order to compare RFs of the same structural components to TxDOT. The ASR and LFR methods produced significantly higher RFs than the LRFR method, with the LFR method being slightly higher than the ASR method. Most bridges were calculated to have RFs within ten percent of the corresponding TxDOT RFs, the differences attributed to the dead loads considered for analysis. For the bridges that exhibited calculated RFs with more than a ten percent difference as compared to the TxDOT RFs, the reason for these differences were examined further. The associated contributing factors were identified and discussed. Based on the analysis performed for the selected steel continuous (SC) bridges, possible areas for improvement to load posting are identified and elaborated upon in Section 4.3 of this report.

4.3. AREAS OF POSSIBLE IMPROVEMENT FOR STEEL BRIDGES

4.3.1. Partial Composite Action

It is well known that a composite slab-girder bridge exhibits a higher moment capacity than a non-composite bridge. This was observed in the rating calculations conducted for this study, as both the composite and non-composite capacities of the bridge girders were determined and then the appropriate value was selected for the load rating analysis. The composite moment capacity was, for most bridges, significantly higher than the non-composite capacity. Bridges without shear studs or embedded girders may not be able to be analyzed as fully composite; however, as Chajes (1997) showed, non-composite bridges do exhibit some amount of partial composite behavior. Chajes (1997) instrumented and load tested a simply-supported, three-span, non-composite steel multi-girder and concrete slab bridge. Based on the strains obtained from the load test, they were able to determine that the bridge was acting as partially composite and then calculate new section properties. These properties were then used in a finite element model of the bridge that was developed. A similar procedure could be used for any of the selected bridges, which could increase the section modulus, increase the capacity, and improve the rating of the bridge.

To examine the effects of applying partial composite action, two steel bridges that have been identified as possible candidates for further investigation were re-analyzed. Bridge SM-5 was analyzed using full composite action, because its flange is embedded 0.5 in. into the concrete deck according to TxDOT records. Bridge SC-12 was analyzed as being 50 percent composite by taking the average of the fully composite and non-composite section properties and moment capacities. Table 4.19 shows the results of this procedure in the form of a ratio of revised RF to initially calculated RF. This procedure increased the RF of SM-5 by more than double the amount of the

originally calculated factor and increased the RF of SC-12 by almost 50 percent of the originally calculated value.

Table 4.19. Effect of Composite Behavior on Interior Girder Ratings

Bridge ID	Rating Method	TxDOT HS20 RF		Non-composite HS20 RF		Composite HS20 RF		Composite RF/ Non-composite RF	
		Inv.	Oper.	Inv.	Oper.	Inv.	Oper.	Inv.	Oper.
SM-5	LFR	0.47	0.79	0.48	0.81	1.01	1.69	2.09	2.09
SC-12	LFR	0.55	0.93	0.55	0.92	0.87	1.46	1.58	1.59
Note: SM-5 was analyzed as fully composite due to flange embedment SC-12 was analyzed as partially (50%) composite									

4.3.2. Number of Lanes

TxDOT is already considering the option of reducing the number of lanes in some cases, but could expand upon and continue to practice this approach as appropriate. One-lane distribution factors are lower than two-lane distribution factors, meaning that by using one-lane distribution factors, the applied live load moment on the bridge can be decreased, and the rating can be increased. This was shown for many of the selected simple-span and continuous steel bridges, as TxDOT calculated higher RFs than the project calculations for this reason. If a bridge is observed to have only one set of wheel-lines shown on the wearing surface, indicating vehicles are using it as a one-lane bridge, or if an engineering decision is made that the bridge is too narrow to carry two lanes, the bridge could be converted into a one-lane bridge if deemed appropriate.

The effects of applying a reduction to the number of lanes was not performed for the two bridges selected for further investigation because both bridges are on major routes with high Average Daily Traffic (ADT). It would not be practical, or even possible, for TxDOT to reduce the number of lanes on these bridges. This option was tested however for a few bridges that

exhibited narrow deck widths. Table 4.20 shows the effect of reducing the number of lanes to one lane for selected bridges that have a deck width smaller than 24 ft, and currently carry two lanes according to the NBI. This approach increased the RFs for bridges analyzed using the LFR method by 35 percent of the originally calculated factor, and improved the RFs for bridges analyzed using the ASR method by 27 percent of the originally calculated value.

Table 4.20. The Effect of Number of Design Lanes to Interior Girder Ratings for Two-Lane Bridges with Deck Widths Below 24 ft

Bridge ID	Rating Method	TxDOT HS20 RF		Two-Lanes HS20 RF		One-Lane HS20 RF		One-Lane RF/ Two-Lanes RF	
		Inv.	Oper.	Inv.	Oper.	Inv.	Oper.	Inv.	Oper.
SM-7	LFR	0.57	0.95	0.53	0.88	0.71	1.19	1.35	1.35
SM-12	LFR	0.51	0.86	0.35	0.58	0.47	0.78	1.35	1.35
SM-25	ASR	3.37	4.77	2.53	3.61	3.22	4.59	1.27	1.27
SC-6	ASR	1.08	1.53	1.18	1.67	1.50	2.12	1.27	1.27
SC-9	ASR	0.56	0.93	0.58	0.82	0.74	1.04	1.27	1.27

4.3.3. Material Properties

As shown for Bridge SM-16, the steel yield strength used in analysis can significantly affect the rating of a bridge. For Bridge SM-16, TxDOT used a yield strength of 36 ksi. The project calculations use a yield strength of 50 ksi, as it was stated in the TxDOT bridge inventory record file that city records state that the bridge has 50 ksi steel. This increase in yield strength caused the calculations to produce a higher RF than the TxDOT value. If steel coupons from steel bridges were to be tested in tension, these tests could reveal yield strengths to be higher than the tabulated values that TxDOT is currently using for older bridges in which the actual yield strength is unknown. Increasing the steel yield strength would lead to an increased capacity, and therefore an increased rating.

To examine the effects of applying improved material properties, the two bridges selected for further investigation were re-analyzed. Both were analyzed assuming an approximately 20 percent increase in yield strength, from the assumed value of 33 ksi to 40 ksi. Table 4.21 shows the results of this procedure in the form of a ratio of revised RF to initially calculated RF. This procedure improved the RF of SM-5 by 33 percent of the originally calculated factor and increased the RF of SC-12 by 25 percent of the originally calculated value.

Table 4.21. The Effect of Yield Strength to Interior Girder Ratings

Bridge ID	Rating Method	TxDOT HS20 RF		HS20 RF for f_y = 33 ksi		HS20 RF for f_y = 40 ksi		RF with f_y = 40 ksi / RF with f_y = 33 ksi	
		Inv.	Oper.	Inv.	Oper.	Inv.	Oper.	Inv.	Oper.
SM-5	LFR	0.47	0.79	0.48	0.81	0.64	1.07	1.33	1.33
SC-12	LFR	0.55	0.93	0.55	0.92	0.71	1.18	1.29	1.28

4.3.4. Live Load Distribution Factors

The current live load distribution factors found in the AASHTO Standard Specifications and AASHTO LRFD Specifications are simple equations that have been found to be accurate for certain bridges of certain types and characteristics, and less accurate and too conservative for others (Hueste et al. 2015). If a bridge was to be modelled using finite element software, it could more accurately show the distribution of the live load to the girders. These changes to the distribution factors could then possibly be applied to all bridges exhibiting certain characteristics. In a study conducted by researchers at Georgia Institute of Technology (Ellingwood et al. 2009c), this approach was taken and the change in live load distribution factors was used to help increase the RF of bridges that were analyzed. Other states around the country including Iowa, Oregon, and

Pennsylvania practice this approach as well (Iowa Department of Transportation 2013; ODOT 2015; Pennsylvania Department of Transportation 2010).

To examine the effects of applying improved live load distribution factors, the two bridges selected for further investigation were re-analyzed. Both were analyzed assuming a new live load distribution factor reduced to 75 percent of the initially calculated value. Table 4.22 shows the results of this procedure in the form of a ratio of revised RF to initially calculated RF. This procedure improved the RF of both SM-5 and SC-12 by 33 percent of the originally calculated RFs.

Table 4.22. The Effect of Live Load Distribution Factors to Interior Girder Ratings

Bridge ID	Rating Method	TxDOT HS20 RF		Calculated HS20 RF		Revised Calculated HS20 RF		Revised Calculated RF/ Calculated RF	
		Inv.	Oper.	Inv.	Oper.	Inv.	Oper.	Inv.	Oper.
SM-5	LFR	0.47	0.79	0.48	0.81	0.65	1.08	1.34	1.34
SC-12	LFR	0.55	0.93	0.55	0.92	0.73	1.22	1.33	1.33

4.3.5. Refined Analysis Models

Load ratings could be increased for some bridges through refined analysis methods such as the use of the finite element method (FEM). Current analysis methods given in AASHTO's manuals and standards are simplified procedures that are meant to be fairly quick to complete and straightforward to understand. However, this means that they can incorporate simplifying assumptions that may reduce the accuracy of the results, erring on the side of conservatism. FEM models can be tailored to a particular bridge, and reduce the need for simplifying assumptions as they are designed to be more representative of the actual, in-situ condition of the bridge. As a

result, the outcomes of loading a finite element model of a bridge should be more accurate in terms of how the bridge will actually react under the design loads. That being said, finite element models take a considerable amount of time to develop and can be inaccurate if incorrect modeling parameters are used. Analyzing every bridge in an inventory would be an onerous task. However, if a number of typical bridges were analyzed using finite element models, a practice could possibly be developed for bridges of one type based on representative models. If these changes increased capacity or decreased the load effect through refined live load distribution factors, RFs for a group of bridges could be increased.

The effect of using refined analysis models was not evaluated in the basic load rating task, but will be examined in the next task of the project. As discussed for bridges SC-15 and SC-16, the current method of analysis TxDOT uses is intended to be on the conservative side. An in-depth analysis of these bridges, whether it be using computer models to examine load distribution or to determine the behavior of continuous bridges where some girders are not in contact with an interior support, would more than likely produce higher load ratings than TxDOT currently applies.

4.3.6. Rating Method

As shown by the results of the basic loading rating, for both simple-span and continuous steel bridges with concrete decks, the ASR method produced a higher average RF for the analysis limit states performed on the selected SM and SC bridges in most cases. However, the LFR method produced higher RFs for more individual bridges than the ASR and LRFR method. TxDOT has rated some of the selected bridges using LFR already, however many of them were rated using ASR as well. Although the improvement of rating using LFR over rating using ASR was not very

significant, rating using LFR instead of ASR could be a practice that is used to slightly increase ratings in situations where it is appropriate.

The effect of using a different rating method was not analyzed for the selected bridges for Tasks 4 and 5, because TxDOT already uses the LFR method for both bridges. Previously in this report it was observed that the LFR method produced higher flexure rating factors than the ASR and LRFR methods.

4.3.7. Partial Fixity at Supports

Consideration of partial fixity at supports may be in appropriate for some bridges. Chajes (1997) load tested an existing simply-supported, three-span, non-composite steel multi-girder and concrete slab bridge and found that although the bridge was a simple-span, it exhibited some degree of support restraint. This restraint was also included in the finite element model of the bridge. If a simple-span bridge can be load tested and demonstrated to show partial fixity at the supports, this would lower the maximum positive live load and dead load moments near the middle of the span, and therefore increase the rating. This could be established for bridges with certain characteristics and potentially applied to similar bridges exhibiting that characteristic. However, this means that a negative moment will then be induced at the support, and the negative moment region should then be checked when determining the controlling RF. The effect of partial support fixity will be examined in the refined analysis task of the project.

5. FEM ANALYSIS OF SIMPLE-SPAN STEEL MULTI-GIRDER BRIDGES

In the previous tasks a detailed review and synthesis of the population of load-posted bridges in Texas was conducted, and 25 simple-span steel multi-girder bridges were selected from the inventory of SSLO simple-span steel multi-girder bridges in Texas for basic load rating evaluation. This basic load rating analysis helped identify several areas of opportunity for refined load rating analysis. The refined load rating analysis used in this study investigated the effect of the identified parameters using three-dimensional finite element models that can more accurately capture the bridge behavior. The main objectives of the refined analysis of the simple-span steel multi-girder bridges can be summarized as: (1) create a model of the bridge superstructure that can more accurately predict the live load distribution and (2) investigate the effect of partial composite action on the load distribution behavior of the bridge under service loads.

5.1. INTRODUCTION

Two typical load posted simple-span steel multi-girder (SM) bridges were selected as representative structures of this type to further investigate the identified objectives. Table 5.1 lists some of the key parameters for the two SM bridges, and for the average SSLO simple-span steel multi-girder bridge in Texas. In this table, the *Operating HS-20 RF* represents the multiple of HS-20 truck loads that is the absolute maximum load that can safely travel on the bridge. The posting evaluation represents the degree to which the operating rating of the bridge is below the maximum legal load. A value of 5 indicates that the operating rating is equal to or above the legal load. The

values 0-4 represent varying degrees that the operating rating is below the legal load, with 4 denoting within 10% of the legal load and 0 indicating 40% or greater below the legal load.

Three-dimensional linear FEM models were developed using the commercial software package CSiBridge (Computers and Structures 2019), which has the capability to model and analyze complex bridge superstructures while also providing user-friendly pre- and post-processing tools for bridge structures. The following sections provide the geometric and material properties of the selected simple-span steel multi-girder bridges, describe the FEM modeling approach, and summarize the analysis results.

Table 5.1. Selected SSLO SM Bridges and Average Characteristics (Data from NBI 2016)

ID	Route Prefix	Year Built	ADT	Max. Span Length (ft)	Deck Width (ft)	Condition Rating			Operating HS-20 Rating Factor	Posting Eval.
						Deck	Super-structure	Sub-structure		
Avg.	-	1974	-	36	20	6	6	6	0.83	3
SM-5	3	1938	300	41	24	7	6	7	0.77	2
SM-21	4	1990	550	53	25	8	7	7	0.99	5

Route Prefix: 3=On-System, 4=Off-System
Condition Ratings: 6=Satisfactory, 7=Good, 8=Very Good
Posting Evaluation: 2=20-29.9% below legal load, 3=10-19.9% below legal load, 5=equal to or above legal load

The models were analyzed with HS-20 truck and designated HL-93 load simulations to obtain deflection profiles, modal properties, and moment and shear values. The deflection and modal property analysis were conducted for comparison to the measured behavior of the bridges in the future field tests. The deflection values and modal characteristics allow for calibration of the FEM models based on the field test results. For the moment and shear analysis, the main bridge characteristic of interest is the LLDFs. The LLDFs found using the FEM model are to be compared to those determined through the field testing and values from the procedures in the AASHTO

Standard Specifications (AASHTO 2002) and AASHTO LRFD Specifications (AASHTO 2017). LLDFs can be calculated as the moment or shear force of an individual girder divided by the sum of moments or shear forces in all of the girders for a one-lane loaded case. This can be expressed as,

$$g = m\frac{F_{girder}}{F_{total}} \tag{5.1}$$

where:

g = Live load distribution factor

F_{girder} = Moment or shear force in the individual girder

F_{total} = Total moment or shear force on the entire section for one-lane loading

m = Multiple presence factor per the AASHTO LRFD Specifications (AASHTO 2017), 1.2 for one-lane loading and 1.0 for two-lane loading.

5.2. DESCRIPTION OF SELECTED BRIDGES

5.2.1. Bridge SM-5

Simple-span Bridge SM-5 has a 41'-4" total length and 40'-2" center-to-center of bearing span length. The total width of the bridge is 24'-0", with a roadway width of 23'-6". The girder spacing for SM-5 is 23 in. and lateral bracing is provided at third points along the span. The deck thickness is 6 in. The steel yield strength and the 28-day concrete compressive strength are taken as 33 ksi and 2.5 ksi, respectively based on values prescibed in the AASHTO MBE (AASHTO MBE 2018).

The bridge carries two lanes, one in each direction, and has an average daily traffic of 300 vehicles. These properties are tabulated in Table 5.2. Also of note, this bridge has a girder flange embedment of approximately 0.5 in. into the deck.

Table 5.2. Geometric and Material Properties of SM-5

Characteristic	Measurement
Total Length	41'-4"
Span Length	40'-2"
Deck Width	24'-0"
Roadway Width	23'-6"
Girder Spacing	1'-11"
Lateral Bracing Spacing	13'-5"
Steel Cross-Section Shape	S15x42.9
Steel Yield Strength	33 ksi
Deck Thickness	6 in.
28-day Concrete Compressive Strength	2.5 ksi
Number of Lanes	2

Bridge SM-5 has a deck condition rating of 7 (Good), a superstructure condition rating of 6 (Satisfactory) with 2% beam section loss due to corrosion, and a substructure condition rating of 7 (Good). The steel girder flexure controls the rating of the bridge, which has an inventory gross loading of 17 US tons and an operating gross loading of 28 US tons. Table 5.3 shows the posted loads of Bridge SM-5 for different axle and vehicle configurations. Figure 5.1 shows an elevation view of Bridge SM-5 and a view of the underside of the superstructure. Figure 5.2 shows a transverse section detail of Bridge SM-5.

Table 5.3. Bridge SM-5 Postings

Configuration	Posting (lbs)
Single Axle	20,000
Tandem Axle	34,000
Single Vehicle	47,000
Combination Vehicle	74,000

(a) Elevation view

(b) Underside view

Figure 5.1. Photographs of Bridge SM-5

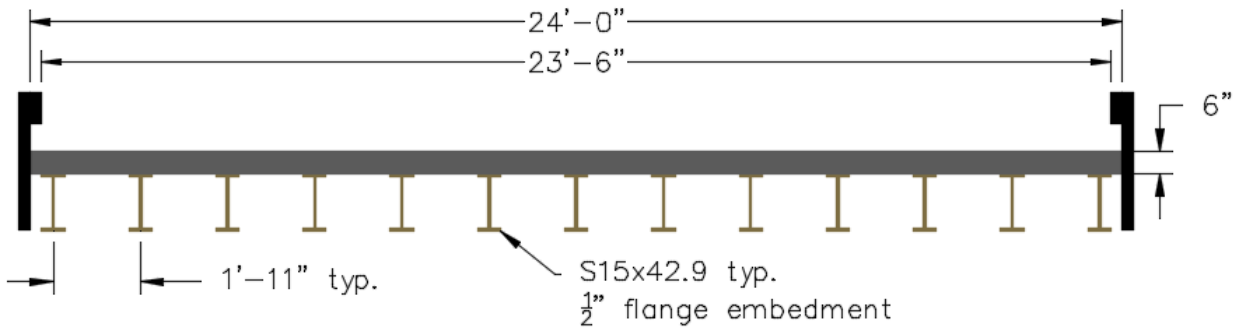

Figure 5.2. Transverse Section of Bridge SM-5 (Adapted from TxDOT 2018b)

5.2.2. Bridge SM-21

A second steel simple-span bridge was selected for refined analysis to provide a girder spacing that is more typical when compared to the group of bridges for which basic load rating analysis was conducted. The average girder spacing value for this group of bridges, including both simple span and steel continuous steel multi-girder bridges, is 4'-0.5". Bridge SM-5 has a girder spacing of 1'-11" and Bridge SC-12, discussed later, has a girder spacing of 6'-8". Therefore, Bridge SM-21, with a girder spacing of 4'-0", was chosen to consider a typical girder spacing.

Bridge SM-21 has a total length of 54'-0" and center-to-center of bearing span length of 52'-10". The total width of the bridge is 25'-0", with a roadway width of 24'-0". The girder spacing of SM-21 is 4'-0" and lateral bracing is provided at third points along the span. The deck thickness is 6 in. The steel yield strength and the 28-day concrete compressive strength are taken as 33 ksi and 2.5 ksi, respectively, based on values prescribed by the AASHTO MBE (AASHTO MBE 2018). The bridge carries two lanes, one in each direction, and has an average daily traffic of 550 vehicles. These properties are tabulated in Table 5.4.

Table 5.4. Geometric and Material Properties of SM-21

Characteristic	Measurement
Total Length	54'-0"
Span Length	52'-10"
Deck Width	25'-0"
Roadway Width	24'-0"
Girder Spacing	4'-0"
Lateral Bracing Spacing	17'-7"
Steel Cross-Section Shape	W33x130
Steel Yield Strength	33 ksi
Deck Thickness	6 in.
28-day Concrete Compressive Strength	2.5 ksi
Number of Lanes	2

Bridge SM-21 has a deck condition rating of 8 (Very Good), a superstructure condition rating of 7 (Good) with 2% beam section loss due to corrosion, and a substructure condition rating of 7 (Good). The assumed deck rating controls the rating of the bridge, which has an inventory gross loading of 25 US tons and an operating gross loading of 36 US tons. The bridge was once posted for a 28,000-pound tandem axle and a 52,000-pound gross vehicle; however, it is no longer posted. Figure 5.3 shows transverse section details of Bridge SM-21.

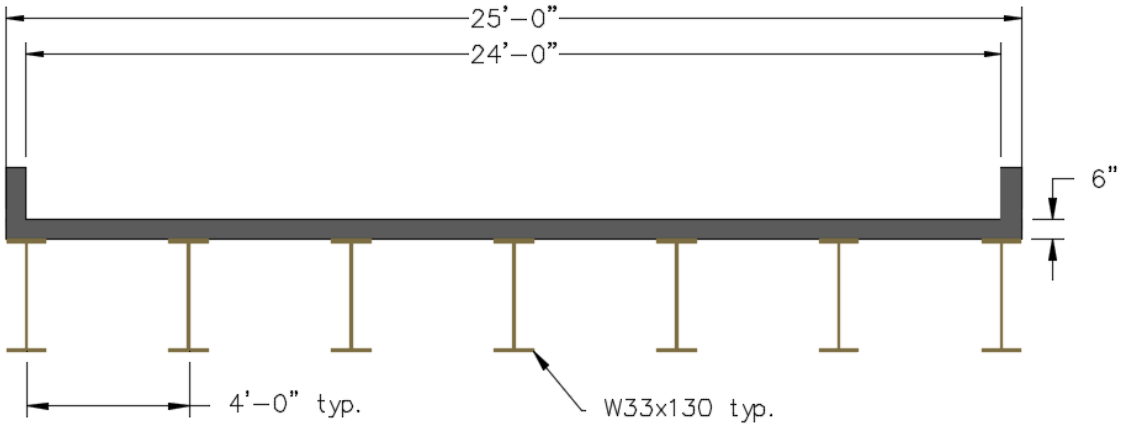

Figure 5.3. Transverse Section of Bridge SM-21 (Adapted from TxDOT 2018b)

5.3. FEM MODEL DEVELOPMENT

Three-dimensional linear FEM models of the selected simple-span steel multi-girder bridges, SM-5 and SM-21, were developed using the commercial CSiBridge software (Computers and Structures 2019). The geometry of the bridges was modeled based on information provided in the design drawings and inspection reports for each bridge. The geometric information relevant to the development of the FEM models of these two bridges was presented in the previous sections of this chapter. The following subsection describes the FEM modeling approach, finite element types, and material properties. The next subsection presents the results of the mesh sensitivity study and selection of mesh size. The last subsection provides details about boundary conditions, which is critical for accurately capturing the behavior of the bridge.

5.3.1. Bridge Model Description

The superstructure of a slab-on-girder bridge can be modeled using a variety of finite element types, most of which are available in the CSiBridge software. There is a significant amount of information in the literature providing guidelines for developing FEM models for slab-on-girder steel bridges (Barnard et al. 2010; Hurlebaus et al. 2018; Puckett et al. 2011). Based on the recommendations provided in the literature and engineering judgement, the FEM models of the selected SM bridges were developed using a combination of four-node linear quadrilateral shell elements and two-node linear beam elements (frame elements). The superstructures of the selected SM bridges consist of steel I-girders and a reinforced concrete deck. The reinforced concrete deck was modeled using four-node linear shell elements. Table 5.5 shows the relevant material properties for the steel girders and concrete deck used in the FEM models of both bridges, which match the material strength values noted in the TxDOT load rating calculations. Deck

reinforcement is not modeled because the linear elastic model will be analyzed under service level loads only and the superstructure is expected to remain in the linear elastic range. The steel girder webs were also modeled using four-node linear shell elements. Top and bottom flanges of the steel girder and the diaphragms were modeled using two-node linear beam/frame elements. Figure 5.4 shows the meshed FEM model of SM-21 with the components of the model labeled. When creating a meshed analytical model, CSiBridge first partitions the deck along the centerlines of the girders, and then meshes based on the selected maximum mesh size. The maximum mesh size is 6 in. for the FEM model of Bridge SM-21 shown in Figure 5.4. Bridge SM-5 was meshed in a very similar manner.

The default option for modeling a steel multi-girder bridge with a concrete deck in the CSiBridge software considers the deck and girders as fully composite. In order to model non-composite behavior, an edge release was applied to the bottom surface of the concrete deck. This option removes interface shear restraint between the deck and the girders, thereby creating fully non-composite behavior. Both bridges were modeled and analyzed as fully composite and fully non-composite to allow comparison of the results.

Table 5.5. FEM Model Material Properties

Material	Density (pcf)	Modulus of Elasticity (ksi)	Poisson's Ratio	28-Day Concrete Compressive Strength (ksi)	Steel Yield Strength (ksi)
Steel	490	29,000	0.3	-	33
Concrete	150	2850	0.2	2.5	-

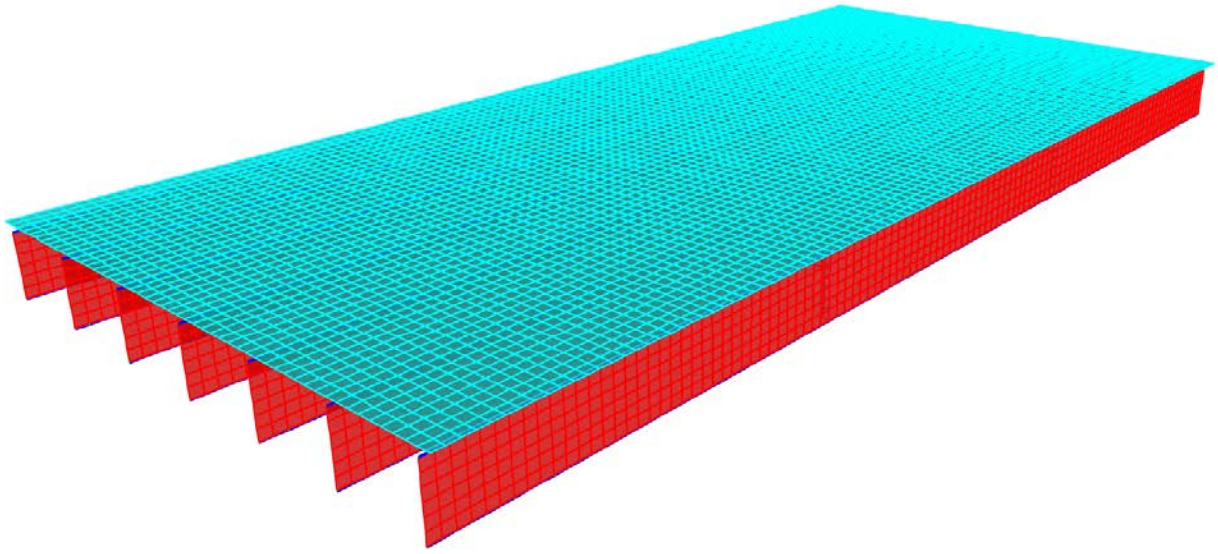

(a) Fully Meshed Superstructure

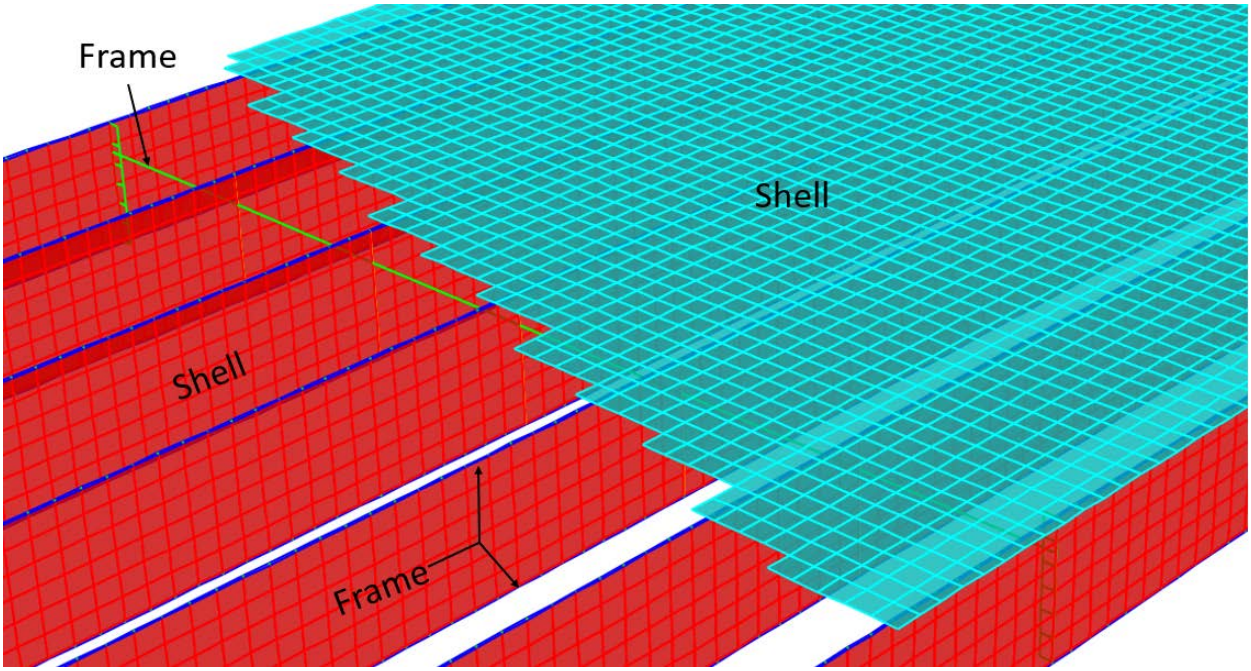

(b) Finite Element Types

Figure 5.4. FEM Model of the SM-21 Bridge (6 in. mesh)

For Bridge SM-5, the CSiBridge models for the composite analysis and for the non-composite analysis were slightly different in an attempt to accurately model the actual geometry of the bridge. The bridge has a 6 in. thick deck with girder flanges embedded 0.5 in. into the deck. Limitations with the CSiBridge software do not allow the modeling of flange embedment. Therefore, for the composite bridge, the model consists of a 5.5 in. thick deck on top of the steel girders. This results in calculated fully composite centroids, moments of inertia, and section moduli for the entire bridge, an interior girder, and an exterior girder that are very close to values of those properties calculated for the actual bridge cross section assuming fully composite behavior. For the non-composite bridge, a 6 in. thick deck was used on top of the steel girders. This will best represent the load distribution by the deck to the bridge girders assuming fully non-composite behavior, because the actual bridge deck thickness is 6 in.

5.3.2. Mesh Sensitivity Analysis

To determine the most efficient mesh size to use in the FEM models of each SM bridge, the effect of different mesh sizes on the calculated shear force, moment, and bottom flange bending stress was examined. A model of each bridge was created using maximum mesh sizes of 4 in., 6 in., 12 in., and 18 in. Figure 5.5 shows these different mesh sizes when applied to Bridge SM-5. Each bridge was analyzed using a static multi-step analysis of one HS-20 truck driving across it with the interior wheel line two feet away from the centerline of the bridge (shown as PATH 3 in Figure 5.12(a) and Figure 5.13(a)).The maximum forces and stresses in the bridge cross-section for each model with different mesh sizes were then compared.

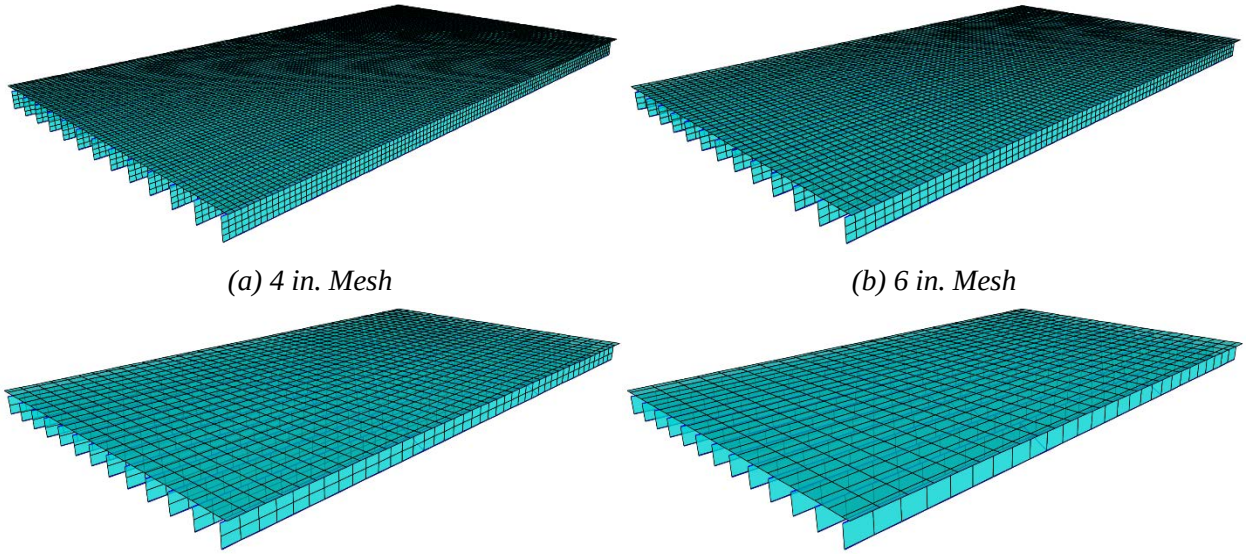

(a) 4 in. Mesh *(b) 6 in. Mesh*

(c) 12 in. Mesh *(d) 18 in. Mesh*

Figure 5.5. FEM Models Showing Different Mesh Sizes for the SM-5 Bridge

Table 5.6 and Table 5.7 show the results of the mesh sensitivity analysis for Bridge SM-5 and SM-21, respectively. There was no difference in the results for the models using a 12 in. mesh and an 18 in. mesh. There was only minimal difference in the results for the models with a 4 in. mesh and a 6 in. mesh, and this difference was deemed to not justify the added computation time. However, there was a noticeable difference in the results between using a 6 in. mesh and a 12 in. mesh. The 6 in. mesh produces more refined results, and for the reasons noted, a 6 in. mesh size was chosen to be used for Bridge SM-5. Figure 5.6 shows the final meshed CSiBridge models that were used for the analysis of the SM-5 and SM-21 bridges.

Table 5.6. Mesh Sensitivity Analysis for Bridge SM-5

Mesh Size (in.)	Maximum Moment in Girder 11 (kip-ft)	Maximum Shear in Girder 11 (kip)	Maximum Bottom Flange Stress in Girder 11 (ksi)
4	64.61	13.68	8.10
6	63.87	13.68	8.07
12	63.62	12.21	7.91
18	63.14	12.10	7.89

Table 5.7. Mesh Sensitivity Analysis for Bridge SM-21

Mesh Size (in.)	Maximum Moment in Girder 6 (kip-ft)	Maximum Shear in Girder 6 (kip)	Maximum Bottom Flange Stress in Girder 6 (ksi)
4	177.97	19.71	4.03
6	177.76	19.59	4.03
12	174.93	19.45	3.98
18	174.21	19.21	3.97

5.3.3. Boundary Conditions

In the absence of more accurate information, the boundary conditions at the supports are defined as pins and rollers. The boundary conditions for both SM bridges were modeled to represent a simply supported condition in which both ends of all of the girders, except one end of one of the girders, are modeled as roller supports. A roller support releases all three rotational degrees of freedom as well as two translational degrees of freedom in the horizontal plane (two orthogonal in-plane directions parallel to the bridge superstructure), and fully restrains the translational degree of freedom in the vertical direction (perpendicular to the plane of the bridge superstructure). Only one girder was pinned at one end in order to resist any horizontal forces that develop. A pin support releases all three rotational degrees of freedom and restrains all three translational degrees of freedom.

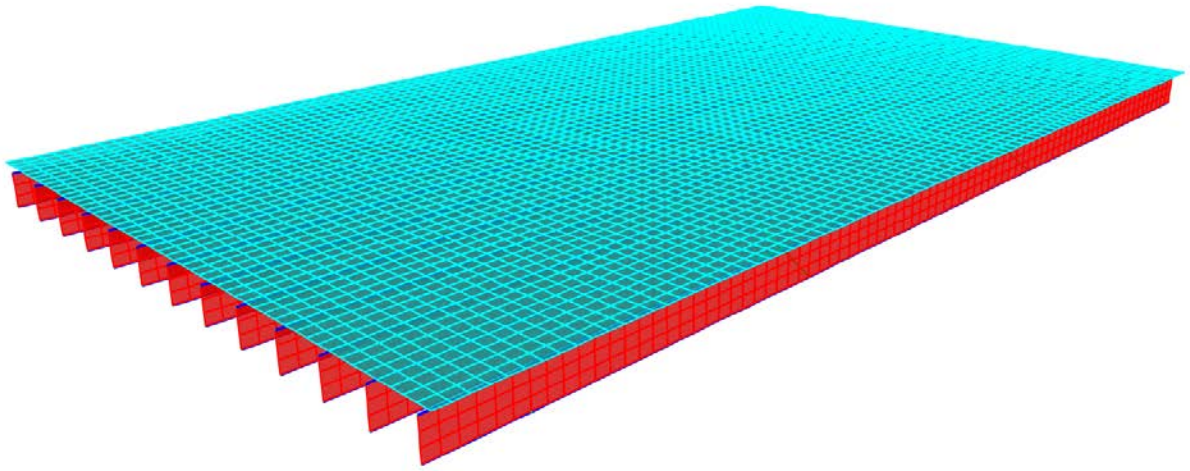

(a) SM-5 Bridge

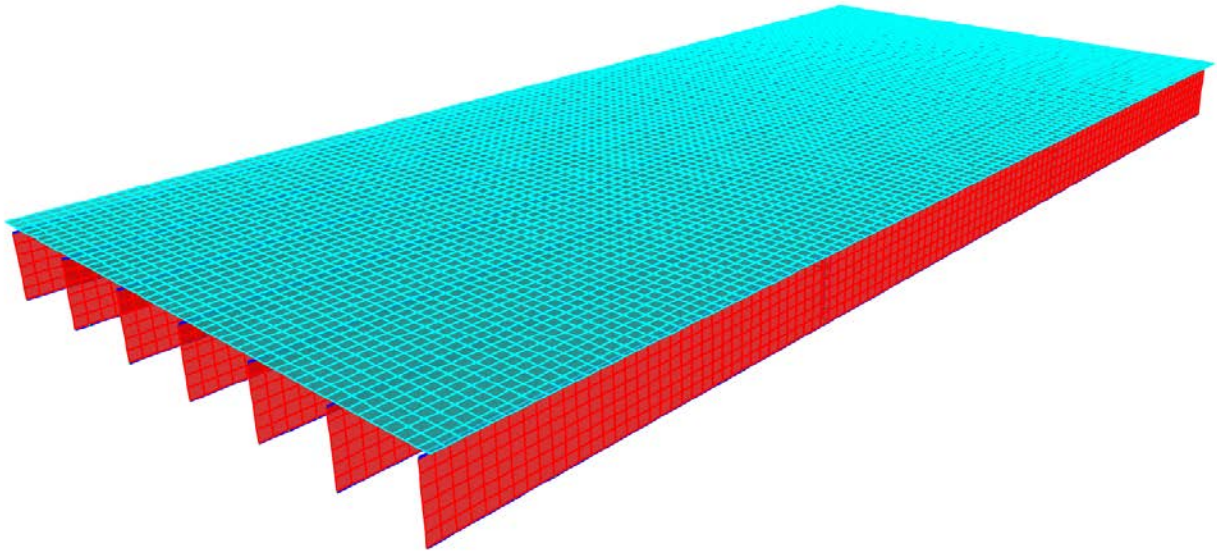

(b) SM-21 Bridge

Figure 5.6. Selected Meshed CSiBridge Models (6 in. mesh)

Accurately modeling the boundary conditions may have a significant effect on the overall behavior of the bridge. Although the boundary conditions are initially modeled as simply supported, the restraint of the supports will be evaluated based on field testing results during the

next phase of this study. Unintended partial fixity may develop at the supports due to the bearing detail at the supports and/or friction between the bottom surface of the bridge girders and the bearing surface. The presence of partial fixity will be verified through field testing.

5.4. BASIC VERIFICATION OF FEM MODELS

Some basic loading conditions were simulated to verify that the CSiBridge models were developed correctly. These basic checks were conducted by investigating maximum deflections under uniformly distributed dead load, and absolute maximum moments and support reactions under HS-20 design truck and designated HL-93 loading.

Figure 5.7 shows the characteristics of the HS-20 design truck as specified in the AASHTO LRFD Specifications (AASHTO 2017). The front axle has an 8-kip total load and is 14 ft in front of the middle axle, which has a 32-kip total load. The spacing between the middle axle and the rear axle, which also carries a 32-kip total load, varies between 14 ft and 30 ft depending on which distance produces the maximum effect for the force being investigated. The vehicular live load model in the AASHTO Standard Specifications (AASHTO 2002) also considers an alternative loading scheme consisting of a uniformly distributed 0.64 kips per linear foot of load lane and a concentrated load of 18 kips when checking moment or 26 kips when checking shear, which should be used if it controls over the HS-20 design truck loading.

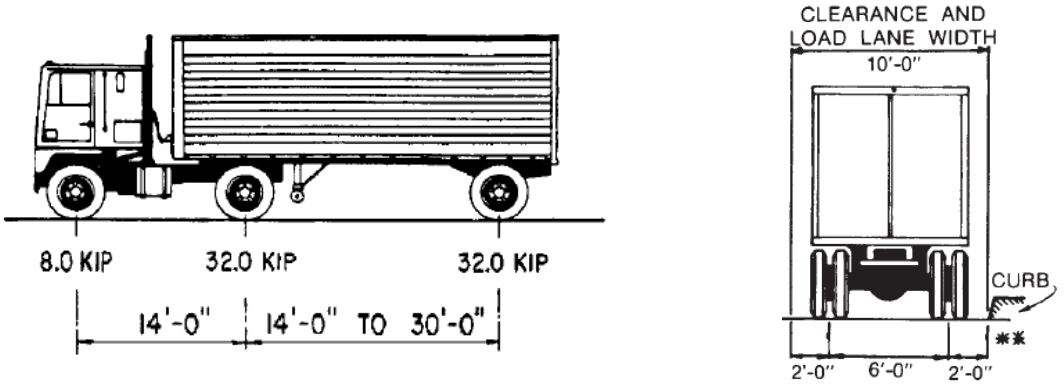

(a) Truck Axle Loadings and Longitudinal Spacings *(b) Truck Transverse Spacing*

Figure 5.7. HS-20 Truck Loading (Reprinted from AASHTO 2002; AASHTO 2017)

Figure 5.8 shows the designated HL-93 loading with HS-20 truck and tandem loads. The designated HL-93 loading consists of the design truck or design tandem coincident with the design lane load. The design lane load consists of a 0.64 kip per linear foot uniformly distributed load that is evenly distributed over a 10 ft width. The design truck or design tandem is used depending on which will create the maximum force effects on the span. Figure 5.8(a) shows the HS-20 design truck and the design lane load. The design tandem consists of two 25-kip axle loads spaced 4 ft apart in the longitudinal direction and 6 ft apart in the transverse direction. Figure 5.8(b) shows the design tandem loading with the lane load.

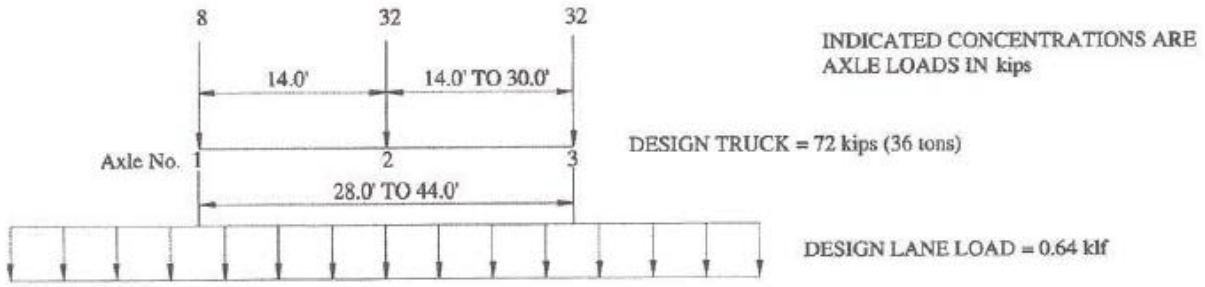

(a) Design Truck and Lane Load

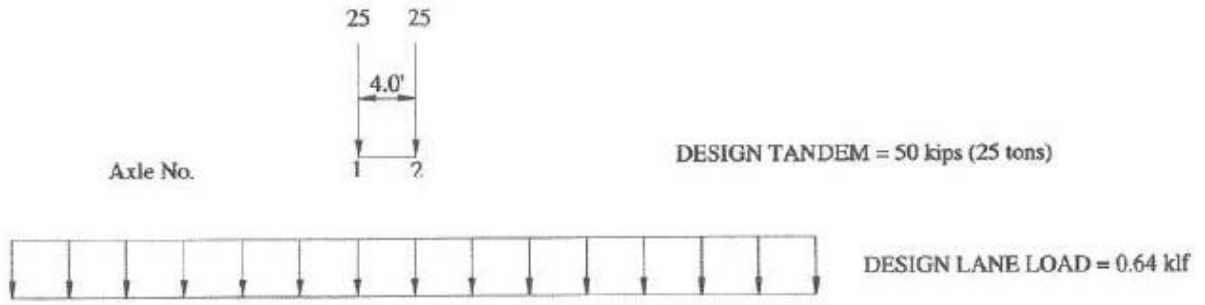

(b) Design Tandem and Lane Load

Figure 5.8. Designated HL-93 Load Model (Reprinted from AASHTO MBE 2018)

5.4.1. Verification of Maximum Deflection

To verify that the structure had been modeled correctly, maximum deflections for the composite and non-composite bridge superstructure under uniform distributed dead load were verified against the deflections obtained from theoretical structural analysis. The model was analyzed as both composite and non-composite under dead loads and the deflection of an interior girder was obtained. The estimated deflection values from FEM analysis were compared to the calculated deflection of an interior girder with tributary width of the deck using theoretical structural analysis. For Bridge SM-5 assuming fully non-composite action, the equivalent distributed load was

calculated as the sum of the weight of the girder, the deck, and the wearing surface. The total uniform distributed weight can be found as,

$$w = w_g + w_d + w_{ws} = 0.209 \text{ kip/ft} \tag{5.2}$$

in which:

w_g = weight of the girder = 0.0429 kip/ft

$$w_d = (\gamma_c)(t_d)(s) = 0.144 \text{ kip/ft} \tag{5.3}$$

$$w_{ws} = (\gamma_{ws})(t_{ws})(s) = 0.0224 \text{ kip/ft} \tag{5.4}$$

where:

w_d	=	Weight of the deck (kip/ft)
γ_c	=	Unit weight of concrete = 0.15 kip/ft^3
t_d	=	Thickness of the concrete deck (ft)
s	=	Spacing of the steel girders (ft)
w_{ws}	=	Weight of the wearing surface (kip/ft)
γ_{ws}	=	Unit weight of the wearing surface = 0.14 kip/ft^3
t_{ws}	=	Thickness of the wearing surface (ft)

When the section is assumed to be non-composite, the stiffness EI of each component is linearly added for the deflection calculation. The total deflection of the non-composite section under dead

loads can be calculated using the Eqn. (5.5) for maximum deflection of a simply-supported beam under uniformly distributed load.

$$\Delta_{non-composite} = \frac{5wL^4}{384(E_s I_g + E_c I_d)} = 0.866 \text{ in.} \quad (5.5)$$

where:

I_g = Moment of inertia of the steel girder = 446 in^4

I_d = Moment of inertia of the deck = 414 in^4

E_s = Modulus of elasticity of steel = 29,000 ksi

E_c = Modulus of elasticity of concrete = $57{,}000\sqrt{f'_c}$ = 2850 ksi

To determine the fully composite deflection of Bridge SM-5, the moment of inertia of the composite section with transformed deck width, I_{tr}, was calculated about the horizontal axis at the centroid of the composite section. The width of the transformed deck, $b_{tr} = 2.3$ in., was determined by dividing the effective width of the deck by the modular ratio, which is approximately 10.

$$I_{tr} = I_g + A_g(y_{bc} - y_b)^2 + I_{d_{tr}} + A_d(y_{bc} - y_d)^2 = 1214 \text{ in}^4 \quad (5.6)$$

where:

A_g = Cross-sectional area of the steel girder = 12.6 in^2

y_{bc} = Distance from the bottom of girder to the centroid of the composite section

= 12.99 in.

y_b = Distance from the bottom of girder to the centroid of the steel girder = 7.5 in.

$I_{d_{tr}}$ = Moment of inertia of the transformed deck about its own centroidal axis = 41.4 in^4

A_d = Area of the transformed deck = 13.8 in^2

y_d = Distance from the bottom of girder to the centroid of the transformed deck = 18 in.

Finally, the maximum composite deflection can be found using the same deflection equation and replacing the non-composite moment of inertia with the transformed section moment of inertia.

$$\Delta_{composite} = \frac{5wL^4}{384E_sI_{tr}} = 0.348 \text{ in.} \quad (5.7)$$

A similar analysis was performed for Bridge SM-21, allowing the maximum vertical non-composite and composite deflections due to dead load to be determined. Table 5.8 shows the deflections calculated using each method and the percent difference between them. The CSiBridge deflections matched very closely to the calculated deflections.

Table 5.8. Dead Load Deflection Comparison for Modeled SM Bridges

Bridge ID	Composite/ Non-Composite	CSiBridge Deflection (in.)	Calculated Deflection (in.)	Percent Difference
SM-5	Non-Composite	0.865	0.866	0.12
	Composite	0.349	0.348	0.29
SM-21	Non-Composite	0.427	0.424	0.71
	Composite	0.226	0.221	2.24

5.4.2. Verification of Absolute Maximum Moment

The live load moments obtained from FEM analysis were compared to the moment values obtained from basic structural analysis to verify that the truck loadings were modeled correctly. The following calculations show the analysis for obtaining the absolute maximum moment due to moving loads in a simple span.

5.4.2.1. Maximum Moment due to HS-20 Design Truck Loading

For a simple span bridge, a 14-ft spacing between the rear and middle axles produces the maximum moment for the HS-20 design truck loading. Three cases can be considered for a bridge under HS-20 truck loading depending on the span length.

1. The first case is placing only the rear axle at the center of the span to produce the maximum moment at the center of the span. This loading governs for spans smaller than 24 ft. The absolute maximum moment at midspan can be calculated as,

$$M = \frac{PL}{4} = 8L \tag{5.8}$$

2. The second case is the application of the rear and middle axles on the span to produce the maximum moment on the span. Figure 5.9(a) show the general loading diagram to determine the location of the truck that produces the maximum moment.

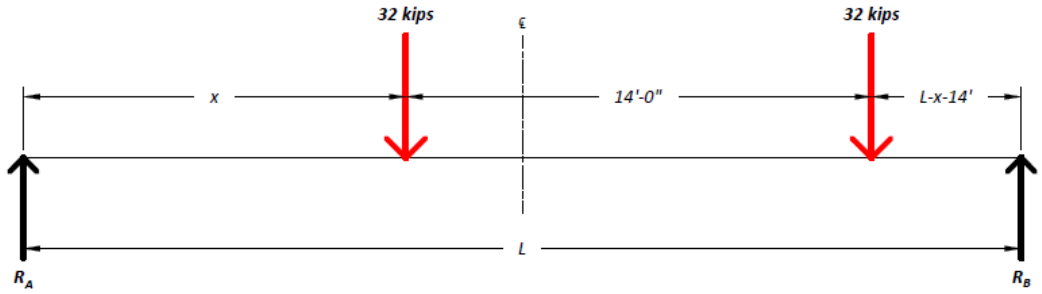

(a) Diagram of Loading Scheme

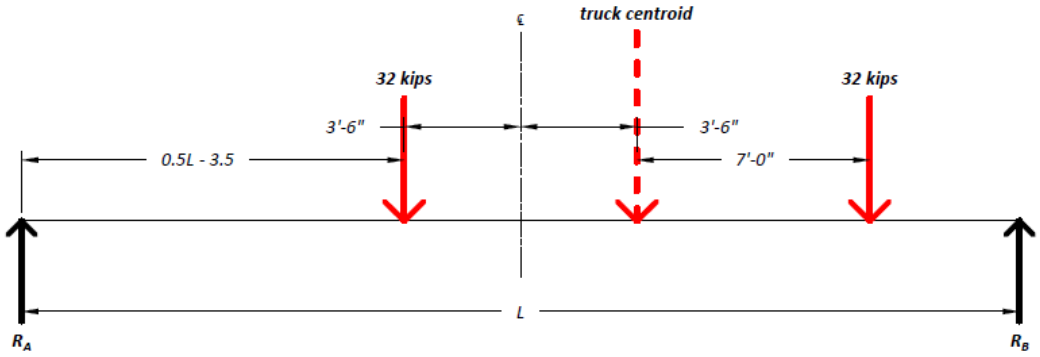

(b) Location of Axles for Maximum Moment

Figure 5.9. Positioning of HS-20 Truck for Maximum Moment for Case 2

The maximum moment occurs under one of the axles when it is located at a distance x from the support. The support reaction and the maximum moment can be calculated as shown in Eqns. (5.9) and (5.10),

$$R_A = 32\left(\frac{L-x}{L}\right) + 32\left(\frac{L-x-14}{L}\right) = 64 - \frac{64x}{L} - \frac{448}{L} \tag{5.9}$$

$$M_{at\,x} = R_A \cdot x \tag{5.10}$$

The distance x to produce the absolute maximum moment can then be computed by setting the first derivative of the moment equation to zero and solving for x.

$$x = \frac{L}{2} - 3.5 \tag{5.11}$$

By substituting this value for *x* in Equation (5.10), the value for the absolute maximum moment on the span due to the HS-20 truck loading for Case 2 can be found as,

$$M_{max} = (16L) - 224 + \frac{784}{L} \tag{5.12}$$

Note that the maximum moment occurs under one of the axles when this axle and the resultant of the load group are placed equidistant from the centerline of the span. Figure 5.9(b) shows a diagram of this moment critical position of the two 32-kip axle loading. This loading case governs for span lengths between 24 ft and 34 ft.

3. The third case is the application of the full HS-20 design truck on the span to produce the maximum moment on the span. Figure 5.10(a) shows the loading diagram that can be used to determine the location of the truck position that will produce the maximum moment.

The maximum moment occurs under the middle axle when it is located at a distance $x +$ 14 ft from the support. The support reaction and the maximum moment can be calculated as shown in Equations (5.13) and (5.14),

$$R_A = 32\left(\frac{L-x}{L}\right) + 32\left(\frac{L-x-14}{L}\right) + 8\left(\frac{L-x-28}{L}\right) = 72 - \frac{72x}{L} - \frac{672}{L} \tag{5.13}$$

$$M_{at\ (x+14)} = (R_A \cdot x) + (R_A - 32) \times 14 \tag{5.14}$$

The distance x to produce the absolute maximum moment can then be computed by setting the first derivative of the moment equation to zero and solving for x.

$$x = \frac{L}{2} - 11.67 \tag{5.15}$$

By substituting this value for x in Equation (5.14), the value for the maximum moment on the span due to the HS-20 truck loading can be found as,

$$M_{max} = (18L) - 280 + \frac{392}{L} \tag{5.16}$$

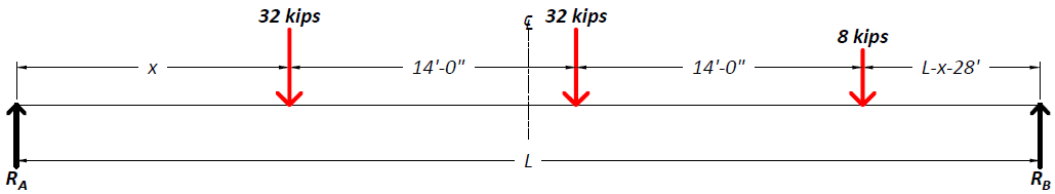

(a) Diagram of loading scheme

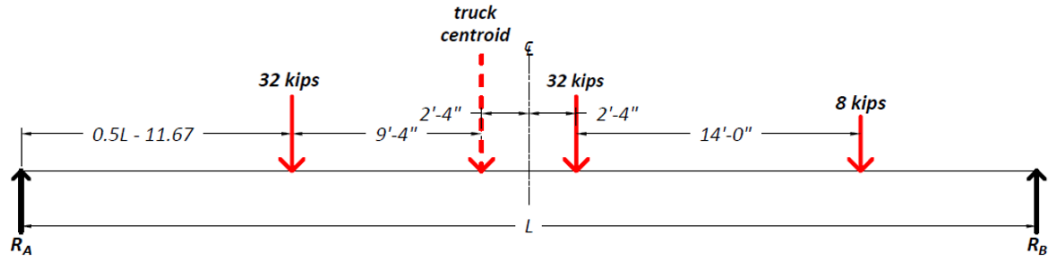

(b) Location of axles for maximum moment

Figure 5.10. Positioning of HS-20 Truck for Maximum Moment for Case 3

Note that the maximum moment occurs under the middle axle when the middle axle and the resultant of the load group are placed equidistant from the centerline of the span. Figure 5.10(b) shows a diagram of this moment critical position of the three-axle loading for the HS-20 truck. This loading case governs for span lengths longer than 34 ft.

Both the SM-5 and SM-21 bridges are longer than 34 ft. Therefore, the absolute maximum moment values due to one-lane-loaded case was computed using the equation derived for Case 3 above. The absolute moment values calculated from basic structural analysis and the maximum moment results obtained for the total section from FEM analysis are compared in Table 5.9.

5.4.2.2. Maximum Moment due to Designated HL-93 Loading

The designated HL-93 load model considers the HS-20 design truck or design tandem coincident with uniformly distributed design lane load. The absolute maximum moment for a simple span due to combined truck plus lane and tandem plus lane loading was calculated.

1. For the combined loading of the HS-20 design truck and lane loading, shown in Figure 5.11(a), the absolute maximum moment that occurs under the middle axle and the corresponding longitudinal position of the combined loading is calculated by first finding the reaction at support A and the maximum moment, shown in Equation (5.20) and (5.21).

$$R_A = \left[72 - \frac{72x}{L} - \frac{672}{L}\right] + 0.32L \tag{5.17}$$

$$M_{at\ (x+14)} = \left(72 - \frac{72x}{L} - \frac{672}{L}\right)x + \left(40 - \frac{72x}{L} - \frac{672}{L}\right) \times 14 + 0.32L(x + 14) \tag{5.18}$$

$$-0.32(x + 14)^2$$

The distance x to produce the absolute maximum moment can then be computed by setting the first derivative of the moment equation to zero and solving for x.

$$x = \frac{L^2 + 197L - 5250}{2L + 450} \tag{5.19}$$

By substituting this value for x in Equation (5.21), the value for maximum moment on the span due to the HL-93 design truck and lane loading can be found.

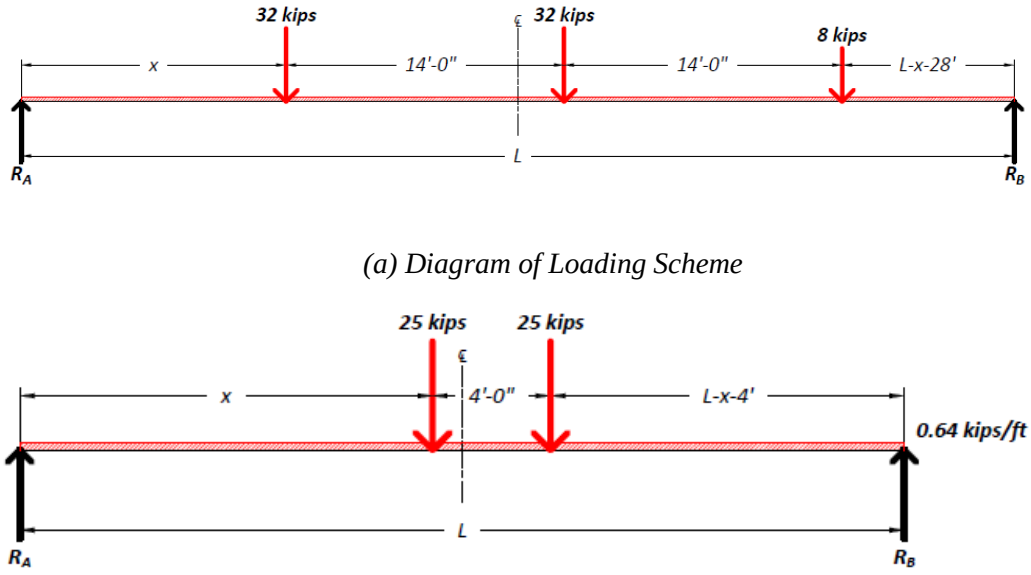

(a) Diagram of Loading Scheme

(b) Location of Axles for Maximum Moment

Figure 5.11. Positioning of HL-93 Tandem for Maximum Moment

2. For the combined loading of design tandem and lane loading, shown in Figure 5.11(b), the absolute maximum moment that occurs under the middle axle and the corresponding longitudinal position of the combined loading is calculated by first finding the reaction at support A and the maximum moment, shown in Equation (5.20) and (5.21).

$$R_A = \left[50 - \frac{50x}{L} - \frac{100}{L}\right] + 0.32L \tag{5.20}$$

$$M_{at\ x} = \left(50 - \frac{50x}{L} - \frac{100}{L}\right)x + 0.32Lx - 0.32x^2 \tag{5.21}$$

The distance x to produce the absolute maximum moment can then be computed by setting the first derivative of the moment equation to zero and solving for x.

$$x = \frac{4L^2 + 625L - 1250}{8L + 1250} \tag{5.22}$$

By substituting this value for x in Equation (5.21), the value for maximum moment on the span due to the HL-93 design tandem and lane combined loading can be found.

Table 5.9 shows the live load moments calculated using this method, the CSiBridge calculated moments, and the percent difference between them. The CSiBridge live load moments match very closely to the expected live load moments.

Table 5.9. Comparison of Live Load Moment on Composite Section for SM Bridges

Bridge ID	Applied Load	CSiBridge one-lane Moment on Total Section (kip-ft)	Expected one-lane Moment on Total Section (kip-ft)	Percent Difference
SM-5	HS-20	452.4	452.8	0.09
	HL-93	581.9	582.1	0.03
SM-21	HS-20	676.7	678.6	0.28
	HL-93	899.3	900.3	0.11
Note: All calculated moments are without the application of the Impact factor.				

5.4.3. Verification of Maximum Shears

The maximum shears were also verified to ensure that the load models were developed correctly. The CSiBridge models use step-by-step loading for the moving load analysis. The step size of the moving load was adjusted such that the first step with the rear axle of the vehicle on the bridge placed the rear axle approximately one member depth away from the support. The resulting shears from this loading were obtained from the FEM model. These were compared with the shears found using classical structural analysis methods by placing the rear axle one foot away from the support. Table 5.10 shows the live load shears calculated using this method, the CSiBridge calculated shears, and the percent difference between them. The CSiBridge live load shears matched up very closely to the expected live load shears.

Table 5.10. Comparison of Live Load Shears on Composite Section for SM Bridges

Bridge ID	Applied Load	CSiBridge one-lane Shear on Total Section (kips)	Expected one-lane Shear on Total Section (kips)	Percent Difference
SM-5	HS-20	53.5	53.5	0.01
	HL-93	59.0	59.1	0.26
SM-21	HS-20	57.9	57.9	0.00
	HL-93	74.7	74.8	0.21
Note: All calculated shears are without the application of the impact factor.				

5.5. SIMULATING VEHICLE LOADS

5.5.1. Simulating HS-20 Truck Loading

The HS-20 truck-loads were placed transversely on the SM bridges per the AASHTO Standard Specifications (AASHTO 2002). Both SM bridges are two-lane bridges.

5.5.1.1. Bridge SM-5

Bridge SM-5 has a lane width of 11'-9". For a one-lane-loaded case based on the Standard Specifications, the truck was first placed so that the exterior wheel line was 2 ft away from the edge of the barrier. For each separate load case, the truck was moved transversely 1 ft closer to the interior of the bridge. The third and final load case was only moved 9 in. closer to the centerline of the bridge in order to keep the interior wheel line 2 ft away from the interior edge of the lane. This created three different one-lane-loaded cases shown in Figure 5.12(a): one with the exterior wheel line 2 ft from the barrier (Path 1), one with the exterior wheel line 3 ft from the barrier (Path 2), and one with the exterior wheel line 3'-9" from the barrier (Path 3).

For the two-lane-loaded case, the first truck was positioned in the same way as for each one-lane-loaded case. A second truck was placed in the second lane of the bridge with the interior wheel line 2 ft away from the interior edge of the lane for each load case. This created three separate two-lane-loaded cases: Path 1 + Path 4, Path 2 + Path 4, and Path 3 + Path 4, as shown in Figure 5.12(b).

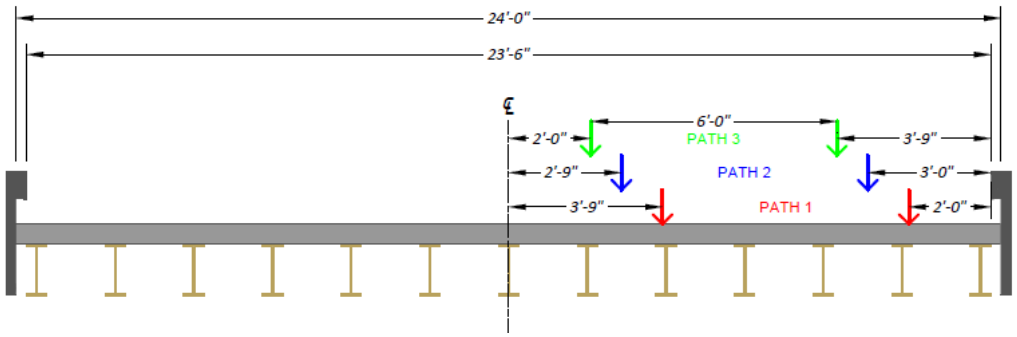

(a) One-Lane Loading Paths

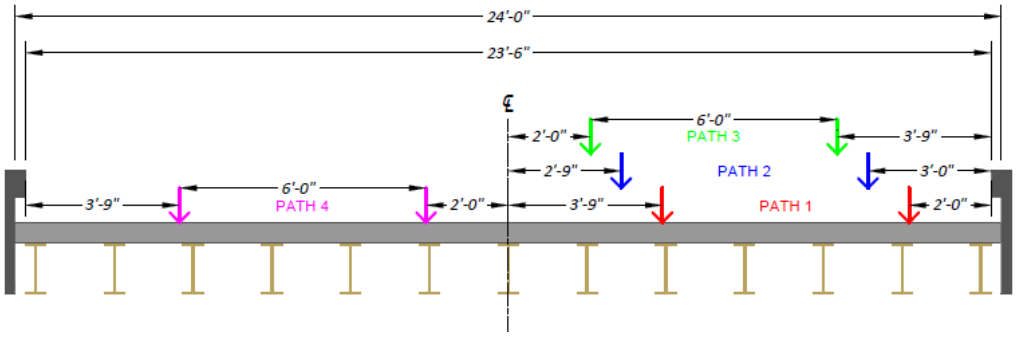

(b) Two-Lane Loading Paths

Figure 5.12. HS-20 Loading Cases for Bridge SM-5

5.5.1.2. Bridge SM-21

Bridge SM-21 has a lane width of 12 ft. For a one-lane-loaded case based on the AASHTO Standard Specifications (AASHTO 2002), the HS-20 design truck was placed at three transverse positions within the first lane similar to Bridge SM-5. Figure 5.13(a) shows the exact transverse positions of the three paths of the truck in the first lane. The two-lane-loaded cases were also created similarly to Bridge SM-5, which created three separate two-lane-loaded cases for the bridge, Path 1 + Path 4, Path 2 + Path 4, and Path 3 + Path 4, as shown in Figure 5.13(b).

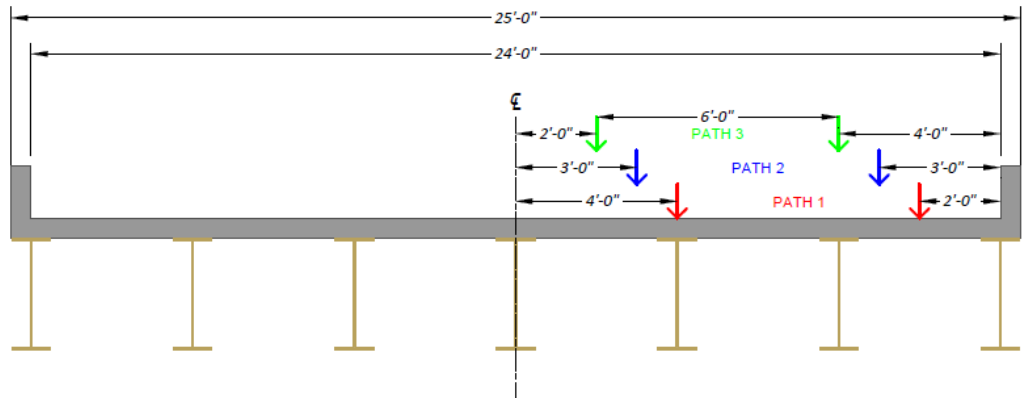

(a) One-Lane Loading Paths

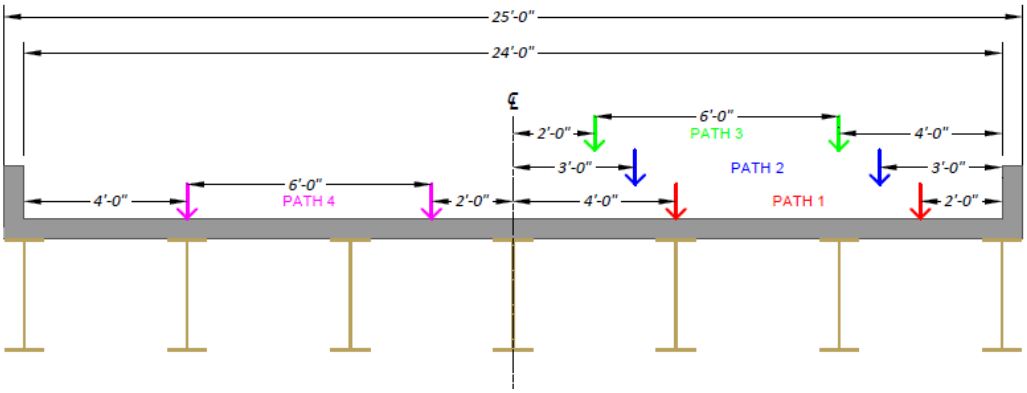

(b) Two-Lane Loading Paths

Figure 5.13. HS-20 Loading Cases for Bridge SM-21

5.5.2. Simulating HL-93 Loading

The HL-93 load model was also placed at different transverse locations on the SM bridges per the AASHTO LRFD Specifications (AASHTO 2017).

5.5.2.1. Bridge SM-5

Bridge SM-5 has a lane width of 11'-9" and a span length of approximately 40'-2". As the tandem load configuration controls for spans shorter than 40'-6", the tandem plus lane load was used for

the HL-93 loading of SM-5. The design tandem was placed transversely in the same manner as described for the HS-20 load. The lane load was added so that the exterior edge of the lane load in Path 1 was immediately adjacent to the railing of the bridge. The exterior edge of the lane load in Path 2 was placed 1 ft away from the railing, and the interior edge of the lane load in Path 3 was placed immediately adjacent to the interior edge of the lane. A total of three different one-lane-loaded cases were created in the first lane as shown in Figure 5.14(a): (1) one with the exterior wheel line of the tandem 2 ft from the railing and the exterior edge of the lane load against the railing (Path 1), (2) one with the exterior wheel line of the tandem three ft. from the railing and the exterior edge of the lane load 1 ft from the railing (Path 2), and (3) one with the exterior wheel line of the tandem 3'-9" from the railing and the interior edge of the lane load adjacent to the interior edge of the lane (Path 3).

For a two-lane-loaded case, the tandem and lane loads were positioned in the same way as for each one-lane-loaded case. A second tandem was placed in the second lane of the bridge with the interior wheel line 2 feet away from the interior edge of the lane for each load case. A second lane load was placed with its right edge against the interior edge of the lane in the second lane. This created three separate two-lane-loaded cases for the bridge, Path 1 + Path 4, Path 2 + Path 4, and Path 3 + Path 4, as shown in Figure 5.14(b).

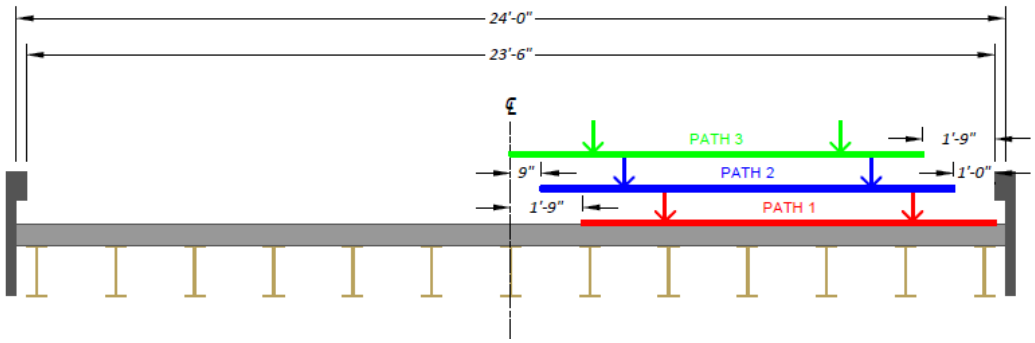

(a) One-Lane Loading Paths

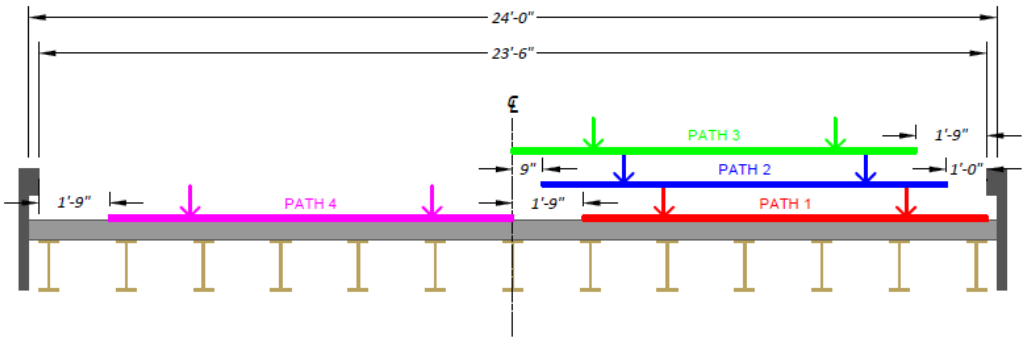

(b) Two-Lane Loading Paths

Figure 5.14. HL-93 Loading Cases for Bridge SM-5

5.5.2.2. Bridge SM-21

Bridge SM-21 has a lane width of 12'-0" and a span length of approximately 52'-10". The HS-20 truck configuration was now used along with the lane load, as the tandem no longer controls for span lengths above 40'-6". For a one-lane-loaded case based on the AASHTO LRFD Specifications (AASHTO 2017), the HL-93 loading scheme was placed at three transverse positions within the first lane similar to the SM-5 bridge. Figure 5.15(a) shows the exact transverse positions of the three paths of the truck and lane load in the first lane. Two-lane-loaded cases were also created

similarly to the SM-5 Bridge, which created three separate two-lane-loaded cases for the bridge, Path 1 + Path 4, Path 2 + Path 4, and Path 3 + Path 4, as shown in Figure 5.15(b).

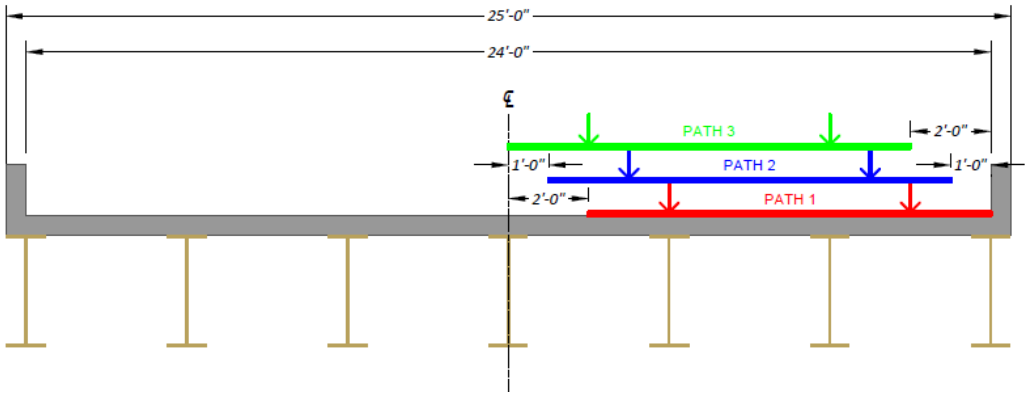

(a) One-Lane Loading Paths

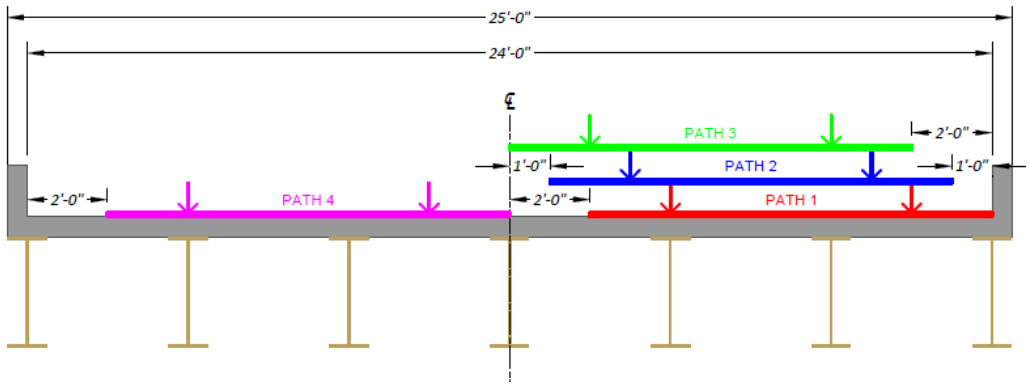

(b) Two-Lane Loading Paths

Figure 5.15. HL-93 Loading Cases for Bridge SM-21

5.6. FEM RESULTS FOR BRIDGE SM-5

Bridge SM-5 was analyzed using the CSiBridge software under the loading scenarios provided in Figure 5.12 thru Figure 5.15. Girder displacement profiles were obtained for the load cases that represent the field testing plans. Modal analyses were conducted for both composite and non-

composite conditions to determine estimated modal frequencies and mode shapes. Live load moment and shear values were also extracted and analyzed to compare the expected LLDFs with the LLDFs prescribed in AASHTO Standard Specifications (AASHTO 2002) and AASHTO LRFD Specifications (AASHTO 2017).

The AASHTO Standard Specifications (AASHTO 2002) Article 3.23.2.3.1.4 states that "In no case shall an exterior stringer have less carrying capacity than an interior stringer." The AASHTO LRFD Specifications (AASHTO 2017) Article 2.5.2.7.1 also states that, "Unless future widening is virtually inconceivable, the load carrying capacity of exterior beams shall not be less than the load carrying capacity of an interior beam." In some cases for bridges SM-5 and SM-21, the moment LLDF determined through AASHTO Standard and AAHTO LRFD for the exterior girder is smaller than moment LLDF for the interior girder. Therefore, interior girder moment LLDFs were used when calculating the exterior girder moment demands to account for any potential future widening of the bridge.

5.6.1. Modal Properties

The first two modes of Bridge SM-5 were identified as the first longitudinal bending mode and the first torsional mode. The frequencies of the non-composite bridge were determined to be 4.04 Hz and 4.70 Hz, respectively. Figure 5.16(a) shows the amplitude contours of the first longitudinal bending mode shape and the normalized amplitudes along the span for non-composite condition. Figure 5.16(b) shows the amplitude contours for the first torsional mode shape and the normalized amplitudes transverse to the span for the non-composite condition. The frequencies of the longitudinal bending and torsional modes for the composite bridge were determined to be 6.27 Hz and 7.12 Hz, respectively. Figure 5.17(a) shows the amplitude contours of the first longitudinal

bending mode shape and the normalized amplitudes along the span for the composite condition. Figure 5.17(b) shows the amplitude contours resulting from the first torsional mode and the normalized amplitudes transverse to the span for composite analysis.

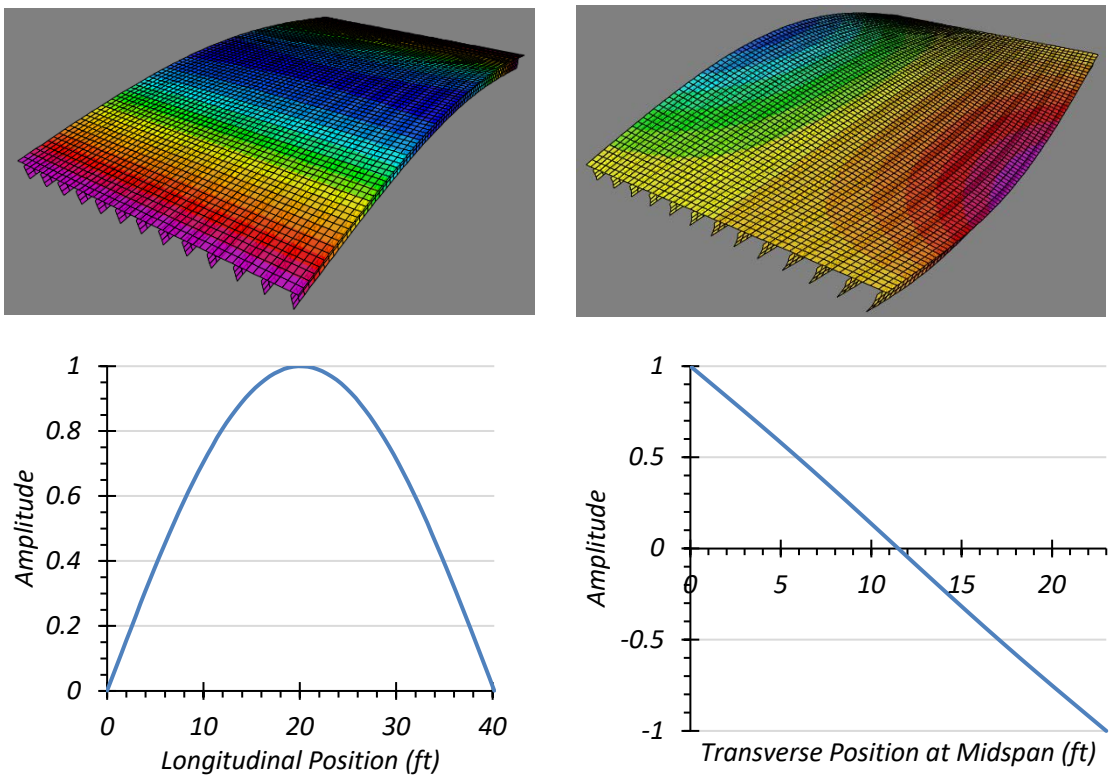

(a) Longitudinal bending Mode (f=4.04 Hz) *(b) Torsional Mode (f=4.69 Hz)*

Figure 5.16. First Two Mode Shapes of Non-Composite Bridge SM-5

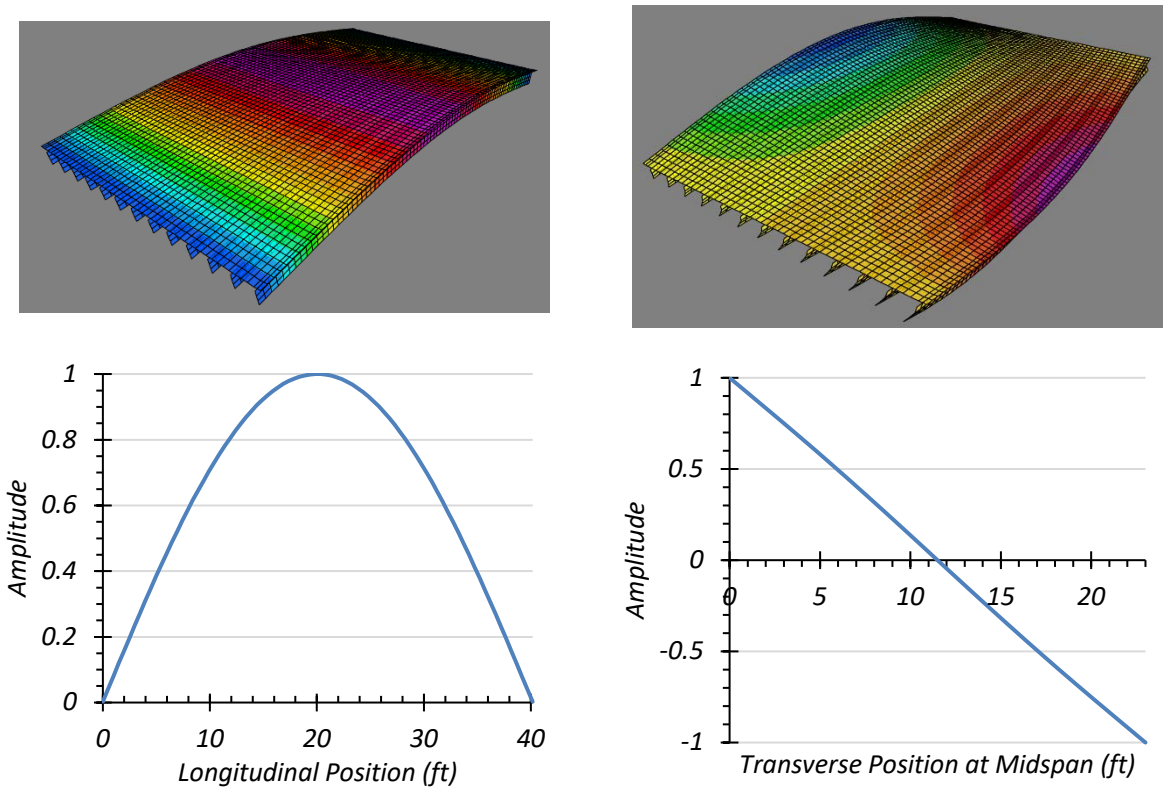

(a) Longitudinal bending Mode (f=6.27 Hz) *(b) Torsional Mode (f=7.12 Hz)*

Figure 5.17. First Two Mode Shapes of Composite Bridge SM-5

5.6.2. HS-20 Live Load Analysis

Bridge SM-5 was first analyzed using the HS-20 design truck presented in the AASHTO Standard Specifications (AASHTO 2002). The bridge was analyzed for one-lane and two-lane-loaded cases along four transverse paths as shown in Figure 5.12. Deflection, moment, and shear results were obtained.

5.6.2.1. Deflection Results

Figure 5.18 shows the estimated girder deflection profiles and contours along the span for one-lane HS-20 loading along Path 1 and Path 4 when the bridge is analyzed as fully non-composite.

Table 5.11 shows the corresponding maximum deflections for each girder assuming non-composite action. Load paths 1 and 4 are the only ones shown as these are expected to be the load paths used in future field load tests, as they were selected to maximize the forces on an interior girder and on an exterior girder

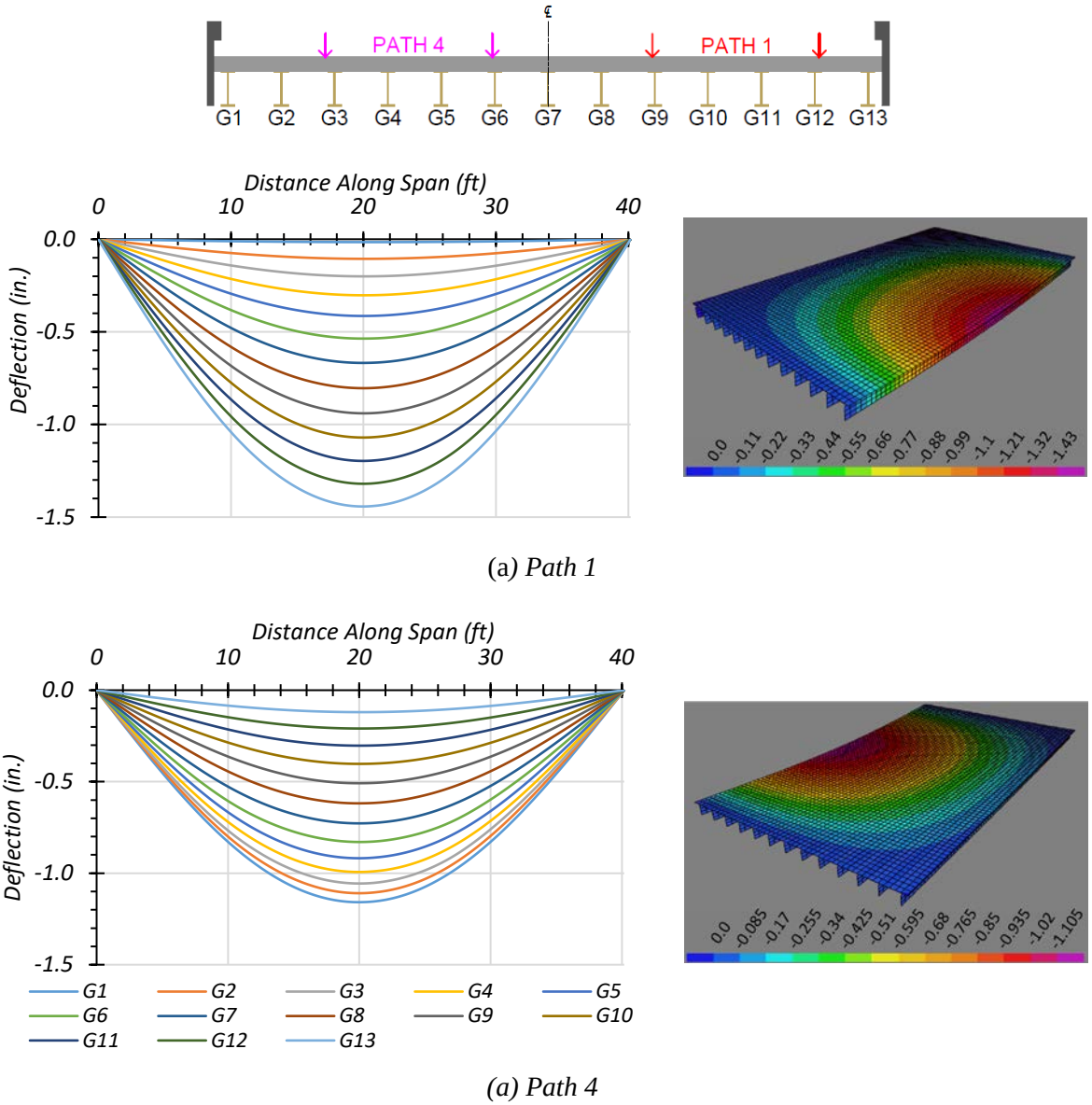

(a) *Path 1*

(a) Path 4

Figure 5.18. Deflection Profiles for Non-Composite Bridge SM-5 with HS-20 Loading

Table 5.11. Maximum Deflections for Non-Composite Bridge SM-5 with HS-20 Loading

Loading	G1	G2	G3	G4	G5	G6	G7	G8	G9	G10	G11	G12	G13
Path 1	-0.016	-0.106	-0.200	-0.302	-0.414	-0.536	-0.668	-0.804	-0.940	-1.070	-1.197	-1.320	-1.442
Path 4	-1.158	-1.109	-1.056	-0.993	-0.918	-0.829	-0.728	-0.618	-0.508	-0.402	-0.303	-0.209	-0.120
Note: G = girder, paths indicate transverse loading positions as shown, deflections have inch units													

Figure 5.19 shows the estimated girder deflection profiles and contours along the span for one-lane HS-20 loading along Path 1 and Path 4 when the bridge is analyzed as fully composite. Table 5.12 shows the corresponding maximum deflections for each girder assuming fully composite action. Load paths 1 and 4 are the only ones shown as these are expected to be the load paths used in future field load tests, as they were selected to maximize the forces on an interior girder and on an exterior girder

For both non-composite and composite cases, the maximum deflections were obtained in Girder 13 when the HS-20 truck was run along Path 1. The estimated deflections were 1.442 in. and 0.691 in. for the non-composite and composite cases, respectively. This result indicates that the composite bridge is 70.4 percent stiffer in flexure than the non-composite bridge. The maximum deflections obtained when the HS-20 truck was run along Path 4 were in Girder 1 for both the non-composite and composite case. The estimated deflections were 1.158 in. and 0.527 in. for the non-composite and composite cases, respectively. This result indicates that the composite bridge is 74.9 percent stiffer in flexure than the non-composite bridge. The slightly different values of relative stiffness suggest that the relative girder deflection depends on the location of loading and corresponding load distribution.

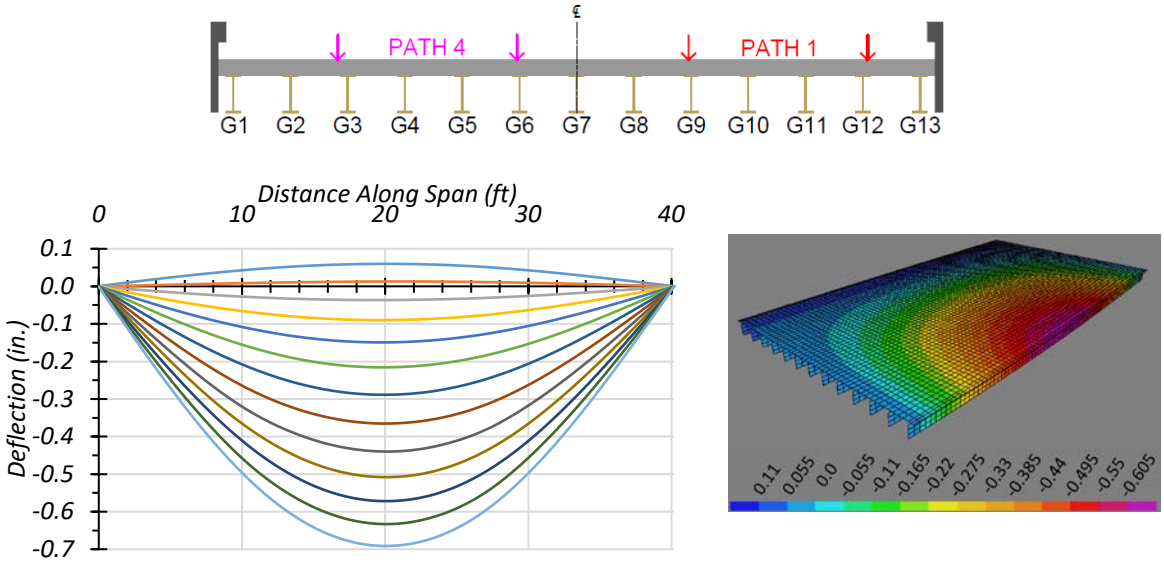

(a) Path 1

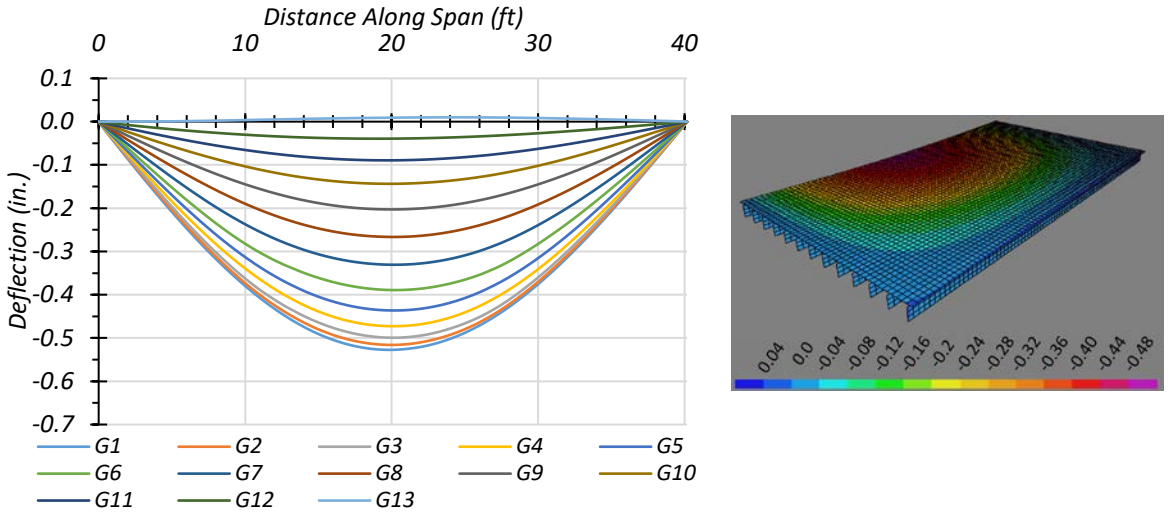

(b) Path 4

Figure 5.19. Deflection Profiles for Composite Bridge SM-5 with HS-20 Loading

Table 5.12. Maximum Deflections for Composite Bridge SM-5 with HS-20 Loading

Loading	G1	G2	G3	G4	G5	G6	G7	G8	G9	G10	G11	G12	G13
Path 1	0.060	0.013	-0.037	-0.090	-0.149	-0.216	-0.289	-0.365	-0.440	-0.508	-0.572	-0.633	-0.691
Path 4	-0.527	-0.516	-0.499	-0.473	-0.436	-0.389	-0.331	-0.266	-0.203	-0.144	-0.089	-0.039	0.014
Note: G = girder, paths indicate transverse loading positions as shown, deflections have inch units													

5.6.2.2. Moment Results

5.6.2.2.1. One-Lane Loading

Figure 5.20 shows the individual girder moments and moment LLDF results for the non-composite Bridge SM-5 under simulated moving HS-20 loading along three one-lane loading paths. Table 5.13 provides the corresponding maximum moment values of each girder for each loading path. The moment LLDF values are calculated using the estimated moment results from FEM analysis. Table 5.15 shows the governing moment LLDFs found using the FEM analysis and compares them to the AASHTO LLDF values. Compared to the FEM results, the governing moment LLDF value computed using the approximate equations in the AASHTO Standard Specifications (AASHTO 2002) is slightly unconservative for interior girders with a g^m_{AASHTO}/g^m_{FEM} ratio of 0.90, while being conservative for exterior girders with a g^m_{AASHTO}/g^m_{FEM} ratio of 1.12.

Figure 5.21 shows the individual girder moments and moment LLDF results for the fully composite Bridge SM-5 under simulated moving HS-20 loading along three one-lane loading paths. Table 5.14 provides the corresponding maximum moment values of each girder for each loading path. The moment LLDF values are calculated using the estimated moment results from the FEM analysis. Compared to the FEM results, the governing moment LLDF value computed using the approximate equations in the AASHTO Standard Specifications (AASHTO 2002) is unconservative for interior girders with a g^m_{AASHTO}/g^m_{FEM} ratio of 0.80, while being conservative for exterior girders with a g^m_{AASHTO}/g^m_{FEM} ratio of 1.12.

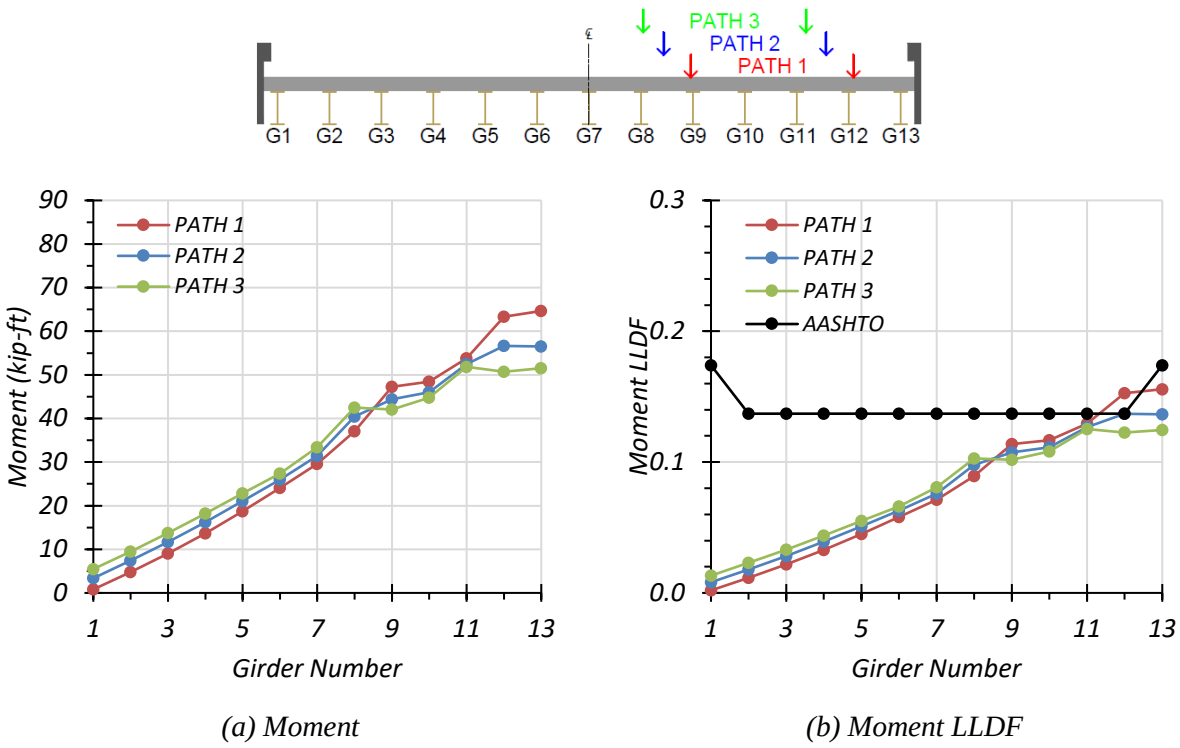

(a) Moment *(b) Moment LLDF*

Figure 5.20. Moment Results for Non-Composite Bridge SM-5 with One-Lane HS-20 Loading

Table 5.13. Maximum Moments for Non-Composite Bridge SM-5 with One-Lane HS-20 Loading

Loading	G1	G2	G3	G4	G5	G6	G7	G8	G9	G10	G11	G12	G13
Path 1	0.8	4.8	9.1	13.7	18.7	24.1	29.6	37.0	47.3	48.4	53.8	63.4	64.7
Path 2	3.4	7.4	11.7	16.2	21.1	26.0	31.4	40.5	44.4	46.0	52.5	56.6	56.5
Path 3	5.5	9.5	13.7	18.2	22.8	27.4	33.4	42.5	42.1	44.8	51.8	50.7	51.5
Note: G = girder, paths indicate transverse loading positions as shown, moments have kip-ft units													

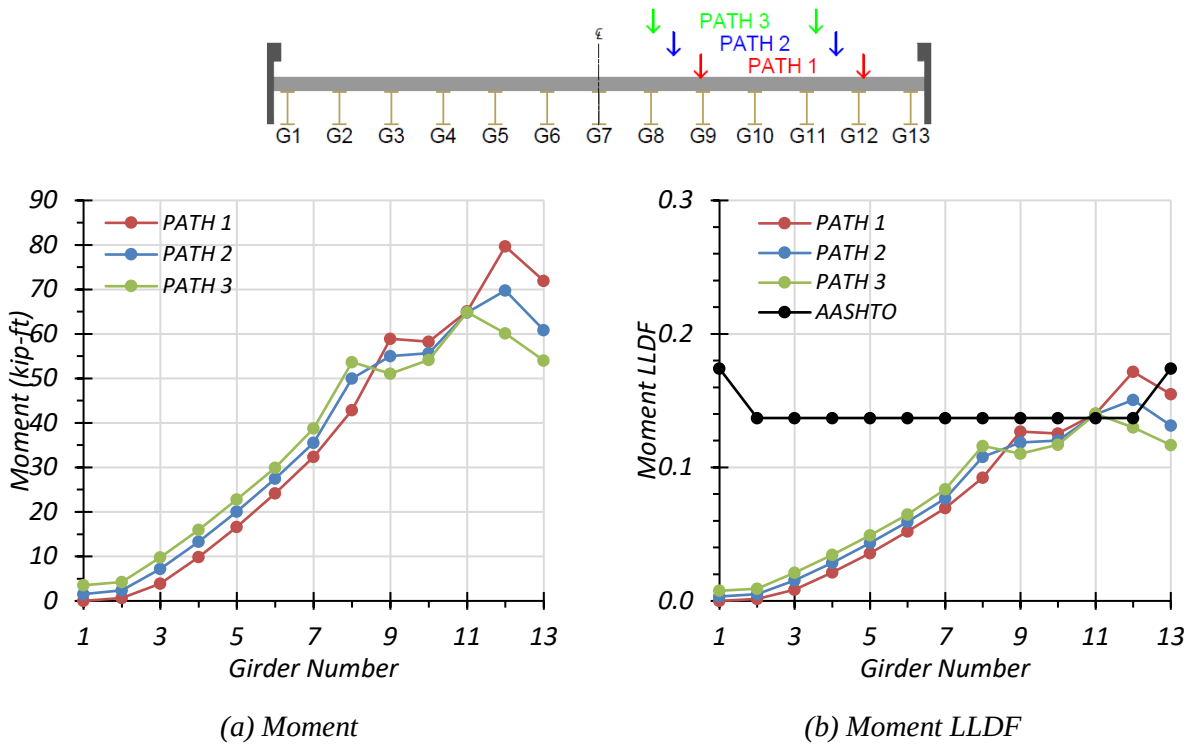

(a) Moment *(b) Moment LLDF*

Figure 5.21. Moment Results for Composite Bridge SM-5 with One-Lane HS-20 Loading

Table 5.14. Maximum Moments for Composite Bridge SM-5 with One-Lane HS-20 Loading

Loading	G1	G2	G3	G4	G5	G6	G7	G8	G9	G10	G11	G12	G13
Path 1	0.0	0.6	3.9	9.9	16.6	24.2	32.3	42.9	58.9	58.3	65.1	79.7	72.0
Path 2	1.5	2.4	7.2	13.3	20.1	27.5	35.5	50.0	55.0	55.7	64.8	69.8	60.9
Path 3	3.5	4.2	9.8	16.0	22.8	29.9	38.8	53.7	51.0	54.2	64.9	60.1	54.0
Note: G = girder, paths indicate transverse loading positions as shown, moments have kip-ft units													

Comparison of governing moment LLDF values computed from FEM results for the composite and non-composite cases reveals that the maximum moment LLDF in an interior girder for the composite bridge is higher than the one for the non-composite bridge with a $g^m_{composite}/g^m_{non-composite}$ ratio of 1.12. Whereas, the maximum moment LLDF in an exterior

girder for the composite bridge is almost the same as that for the non-composite bridge with a $g^m_{composite}/g^m_{non-composite}$ ratio of 0.99.

Table 5.15. Governing Moment LLDFs for Bridge SM-5 with One-Lane HS-20 Loading

Type	Girder Location	AASHTO (g^m_{AASHTO})	FEM (g^m_{FEM})	g^m_{AASHTO}/g^m_{FEM}
Non-Composite	Interior	0.137	0.153	0.90
	Exterior	0.174	0.156	1.12
Composite	Interior	0.137	0.172	0.80
	Exterior	0.174	0.155	1.12

5.6.2.2.2. Two-Lane Loading

Figure 5.22 shows the individual girder moments and moment LLDF results for the non-composite Bridge SM-5 under simulated moving HS-20 loading along three two-lane loading paths. Table 5.16 provides the corresponding maximum moment values of each girder for each loading path. The moment LLDF values are calculated using the estimated moment results from FEM analysis. Table 5.18 shows the governing moment LLDFs found using the FEM analysis and compares them to the AASHTO LLDF values. Compared to the FEM results, the governing moment LLDF value computed using the approximate equations in the AASHTO Standard Specifications (AASHTO 2002) is almost the same for interior girders with a g^m_{AASHTO}/g^m_{FEM} ratio of 0.99, while being slightly conservative for exterior girders with a g^m_{AASHTO}/g^m_{FEM} ratio of 1.03.

Figure 5.23 shows the individual girder moments and moment LLDF results for the fully composite Bridge SM-5 under simulated moving HS-20 loading along three two-lane loading paths. Table 5.17 provides the corresponding maximum moment values of each girder for each loading path. The moment LLDF values are calculated using the estimated moment results from

the FEM analysis. Compared to the FEM results, the governing moment LLDF value computed using the approximate equations in the AASHTO Standard Specifications (AASHTO 2002) is slightly unconservative for interior girders with a g^m_{AASHTO}/g^m_{FEM} ratio of 0.96, while being conservative for exterior girders with a g^m_{AASHTO}/g^m_{FEM} ratio of 1.12.

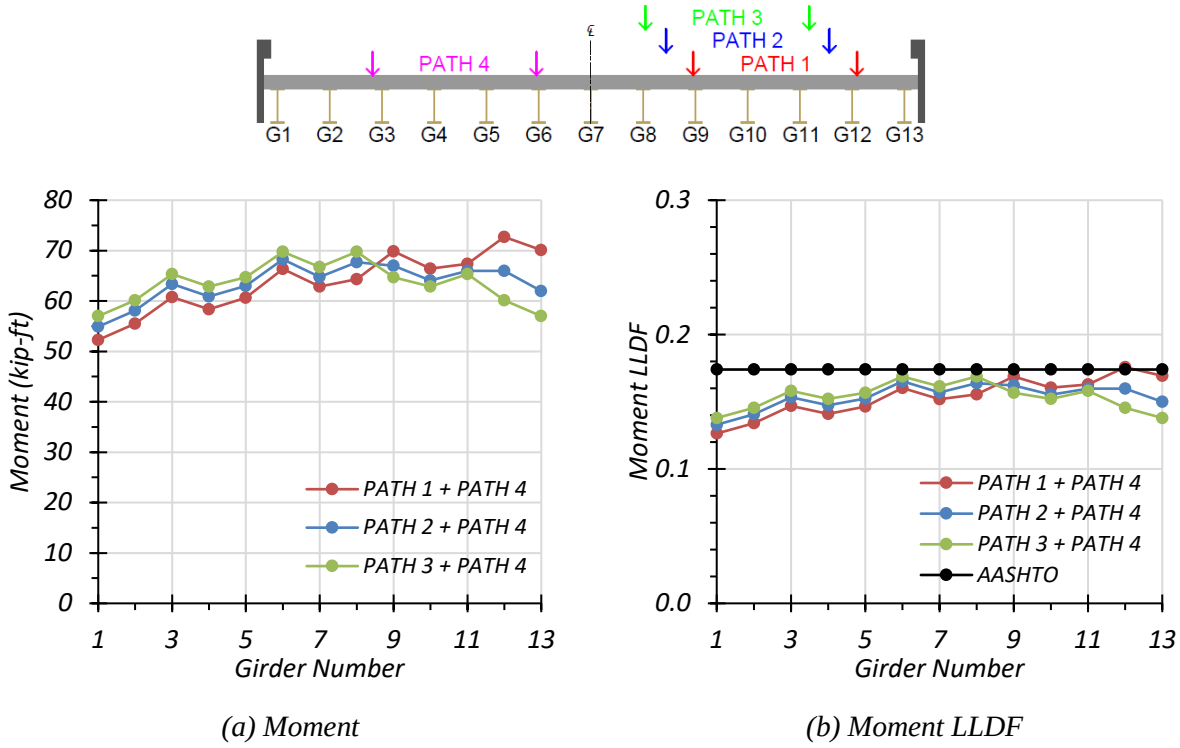

(a) Moment *(b) Moment LLDF*

Figure 5.22. Moment Results for Non-Composite Bridge SM-5 with Two-Lane HS-20 Loading

Table 5.16. Maximum Moments for Non-Composite Bridge SM-5 with Two-Lane HS-20 Loading

Loading	G1	G2	G3	G4	G5	G6	G7	G8	G9	G10	G11	G12	G13
Path 1 + Path 4	52.3	55.5	60.8	58.4	60.6	66.3	62.9	64.3	69.9	66.4	67.3	72.7	70.1
Path 2 + Path 4	54.9	58.1	63.4	60.9	63.0	68.3	64.8	67.7	67.0	64.1	66.0	66.0	62.0
Path 3 + Path 4	57.0	60.1	65.4	62.8	64.7	69.8	66.7	69.8	64.7	62.8	65.4	60.1	57.0
Note: G = girder, paths indicate transverse loading positions as shown, moments have kip-ft units													

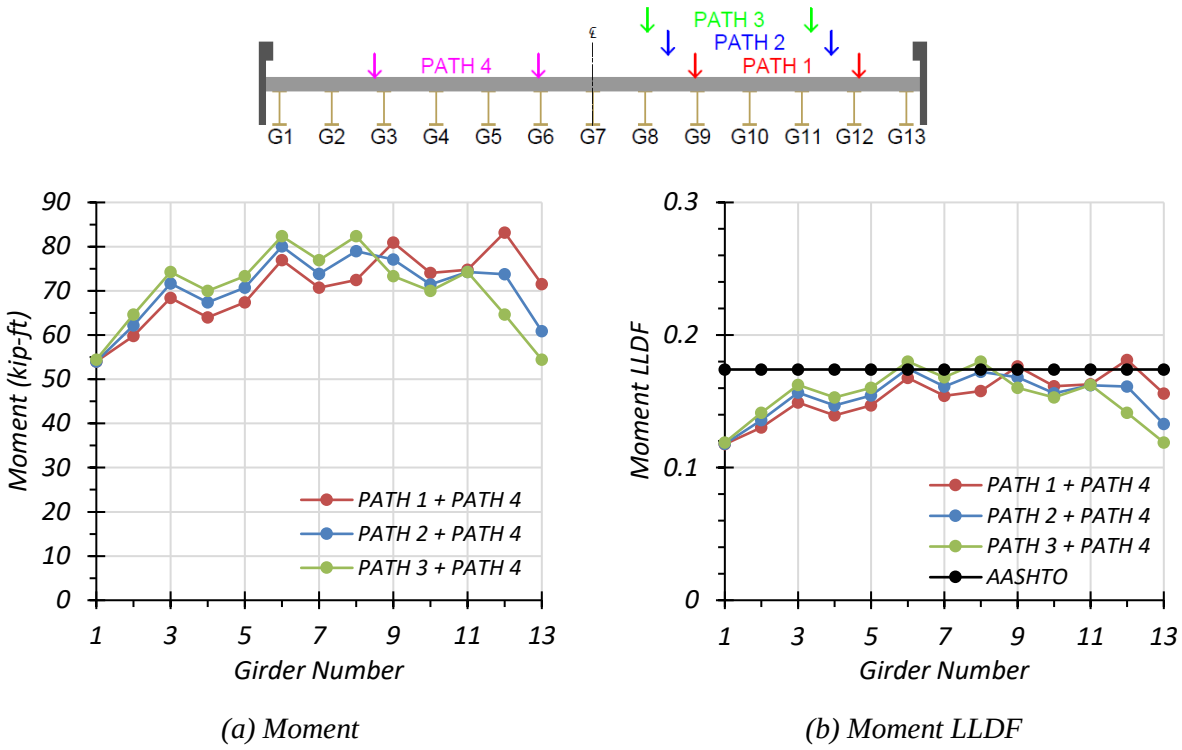

(a) Moment *(b) Moment LLDF*

Figure 5.23. Moment Results for Composite Bridge SM-5 with Two-Lane HS-20 Loading

Table 5.17. Maximum Moments for Composite Bridge SM-5 with Two-Lane HS-20 Loading

Loading	G1	G2	G3	G4	G5	G6	G7	G8	G9	G10	G11	G12	G13
Path 1 + Path 4	54.0	60.1	68.6	63.9	67.4	77.5	70.9	72.6	81.5	74.1	74.7	83.6	72.0
Path 2 + Path 4	54.0	61.6	71.8	67.3	70.9	80.9	74.3	79.7	77.6	71.5	74.3	73.7	60.9
Path 3 + Path 4	54.1	64.0	74.4	70.0	73.6	83.4	77.5	83.4	73.6	70.0	74.4	64.0	54.1
Note: G = girder, paths indicate transverse loading positions as shown, moments have kip-ft units													

Comparison of governing moment LLDF values computed from FEM results for the composite and non-composite cases reveals that the maximum moment LLDF in an interior girder for the composite bridge is higher than the one for the non-composite bridge with a $g^m_{composite}/g^m_{non-composite}$ ratio of 1.03. Whereas, the maximum moment LLDF in an exterior

girder for the composite bridge is lower than that for the non-composite bridge with a $g^m_{composite}/g^m_{non-composite}$ ratio of 0.92.

Table 5.18. Governing Moment LLDFs for Bridge SM-5 with Two-Lane HS-20 Loading

Type	Girder Location	AASHTO (g^m_{AASHTO})	FEM (g^m_{FEM})	g^m_{AASHTO}/g^m_{FEM}
Non-Composite	Interior	0.174	0.176	0.99
	Exterior	0.174	0.169	1.03
Composite	Interior	0.174	0.182	0.96
	Exterior	0.174	0.156	1.12

5.6.2.3. Shear Results

5.6.2.3.1. One-Lane Loading

Figure 5.24 shows the individual girder shears and shear LLDF results for the non-composite Bridge SM-5 under simulated moving HS-20 loading along three one-lane loading paths. Table 5.19 provides the corresponding maximum shear values of each girder for each loading path. The shear LLDF values are calculated using the estimated shear results from the FEM analysis. Table 5.21 shows the governing shear LLDFs found using the FEM analysis and compares them to the AASHTO LLDF values. Compared to the FEM results, the governing shear LLDF value computed using the approximate equations in the AASHTO Standard Specifications (AASHTO 2002) is unconservative for interior girders with a g^v_{AASHTO}/g^v_{FEM} ratio of 0.75, while being conservative for exterior girders with a g^v_{AASHTO}/g^v_{FEM} ratio of 1.21.

Figure 5.25 shows the individual girder shears and shear LLDF results for the fully composite Bridge SM-5 under simulated moving HS-20 loading along three one-lane loading

paths. Table 5.20 provides the corresponding maximum shear values of each girder for each loading path. The shear LLDF values are calculated using the estimated shear results from the FEM analysis. Compared to the FEM results, the governing shear LLDF value computed using the approximate equations in the AASHTO Standard Specifications (AASHTO 2002) is very unconservative for interior girders with a g^v_{AASHTO}/g^v_{FEM} ratio of 0.59, while being very conservative for exterior girders with a g^v_{AASHTO}/g^v_{FEM} ratio of 1.31.

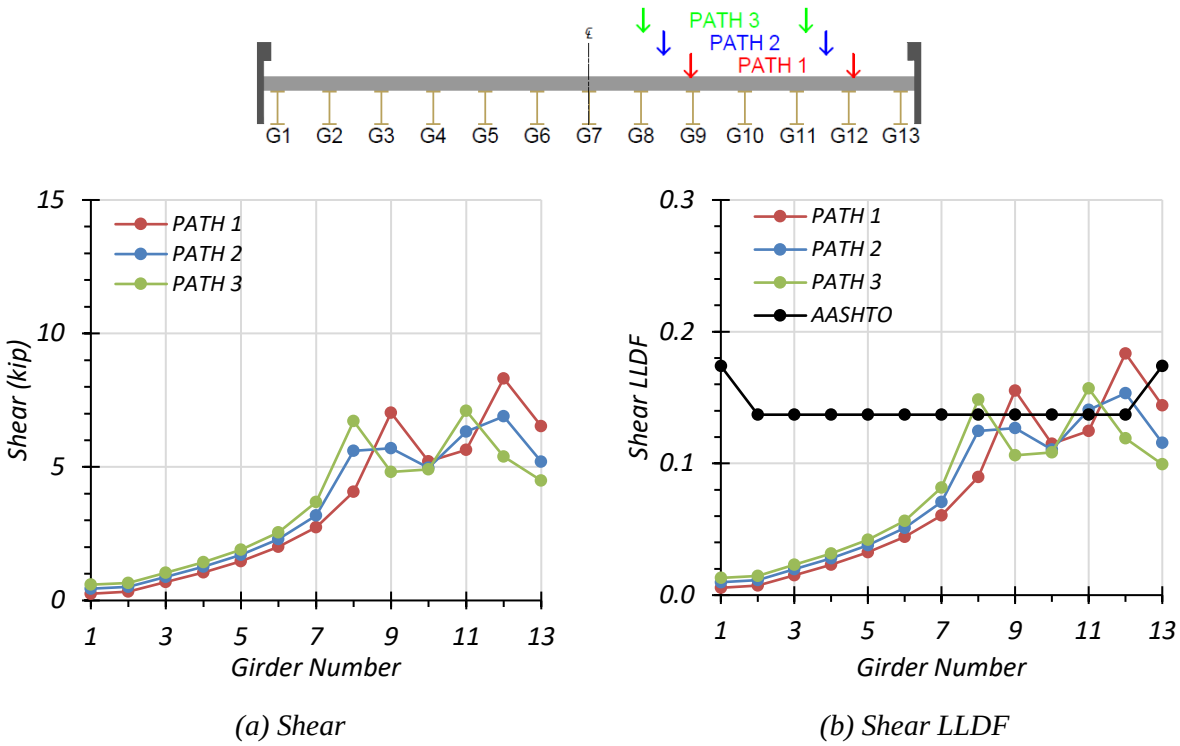

(a) Shear *(b) Shear LLDF*

Figure 5.24. Shear Results for Non-Composite Bridge SM-5 with One-Lane HS-20 Loading

Table 5.19. Maximum Shears for Non-Composite Bridge SM-5 with One-Lane HS-20 Loading

Loading	G1	G2	G3	G4	G5	G6	G7	G8	G9	G10	G11	G12	G13
Path 1	0.3	0.3	0.7	1.0	1.5	2.0	2.7	4.1	7.0	5.2	5.6	8.3	6.5
Path 2	0.4	0.5	0.9	1.3	1.7	2.3	3.2	5.6	5.7	5.0	6.3	6.9	5.2
Path 3	0.6	0.7	1.0	1.4	1.9	2.6	3.7	6.7	4.8	4.9	7.1	5.4	4.5
Note: G = girder, paths indicate transverse loading positions as shown, shears have kip units													

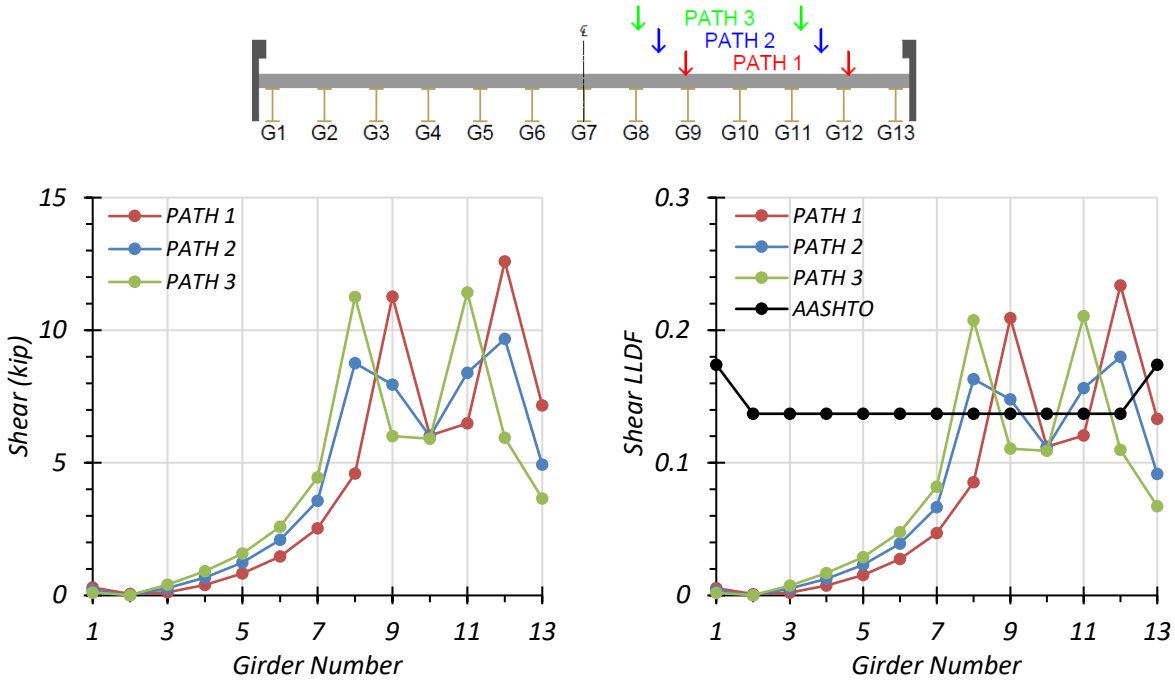

(a) Shear *(b) Shear LLDF*

Figure 5.25. Shear Results for Composite Bridge SM-5 with One-Lane HS-20 Loading

Table 5.20. Maximum Shears for Composite Bridge SM-5 with One-Lane HS-20 Loading

Loading	G1	G2	G3	G4	G5	G6	G7	G8	G9	G10	G11	G12	G13
Path 1	0.3	0.1	0.1	0.4	0.8	1.5	2.5	4.6	11.3	6.0	6.5	12.6	7.2
Path 2	0.2	0.0	0.3	0.7	1.2	2.1	3.6	8.8	7.9	6.0	8.4	9.7	4.9
Path 3	0.1	0.0	0.4	0.9	1.6	2.6	4.4	11.3	6.0	5.9	11.4	6.0	3.7
Note: G = girder, paths indicate transverse loading positions as shown, shears have kip units													

Comparison of governing shear LLDF values computed from FEM results for the composite and non-composite cases reveals that the maximum shear LLDF in an interior girder for the composite bridge is higher than the one for the non-composite bridge with a $g^v_{composite}/g^v_{non-composite}$ ratio of 1.28. Whereas, the maximum shear LLDF in an exterior girder for the composite bridge is lower than that for the non-composite bridge with a $g^v_{composite}/g^v_{non-composite}$ ratio of 0.92.

Table 5.21. Governing Shear LLDFs for Bridge SM-5 with One-Lane HS-20 Loading

Type	Girder Location	AASHTO (g^v_{AASHTO})	FEM (g^v_{FEM})	g^v_{AASHTO}/g^v_{FEM}
Non-Composite	Interior	0.137	0.183	0.75
	Exterior	0.174	0.144	1.21
Composite	Interior	0.137	0.234	0.59
	Exterior	0.174	0.133	1.31

5.6.2.3.2. Two-Lane Loading

The same procedure was conducted for two-lane loading. Figure 5.26 shows the individual girder shears and shear LLDF results for the non-composite Bridge SM-5 under simulated moving HS-20 loading along three two-lane loading paths. Table 5.22 provides the corresponding maximum shear values of each girder for each loading path. The shear LLDF values are calculated using the estimated shear results from the FEM analysis. Table 5.24 shows the governing shear LLDFs found using the FEM analysis and compares them to the AASHTO LLDF values. Compared to the FEM results, the governing shear LLDF value computed using the approximate equations in the AASHTO Standard Specifications (AASHTO 2002) is unconservative for interior girders with

a g^v_{AASHTO}/g^v_{FEM} ratio of 0.84, while being conservative for exterior girders with a g^v_{AASHTO}/g^v_{FEM} ratio of 1.12.

Figure 5.27 shows the individual girder shears and shear LLDF results for the fully composite Bridge SM-5 under simulated moving HS-20 loading along three one-lane loading paths. Table 5.23 provides the corresponding maximum shear values of each girder for each loading path. The shear LLDF values are calculated using the estimated shear results from the FEM analysis. Compared to the FEM results, the governing shear LLDF value computed using the approximate equations in the AASHTO Standard Specifications (AASHTO 2002) is very unconservative for interior girders with a g^v_{AASHTO}/g^v_{FEM} ratio of 0.68, while being very conservative for exterior girders with a g^v_{AASHTO}/g^v_{FEM} ratio of 1.31.

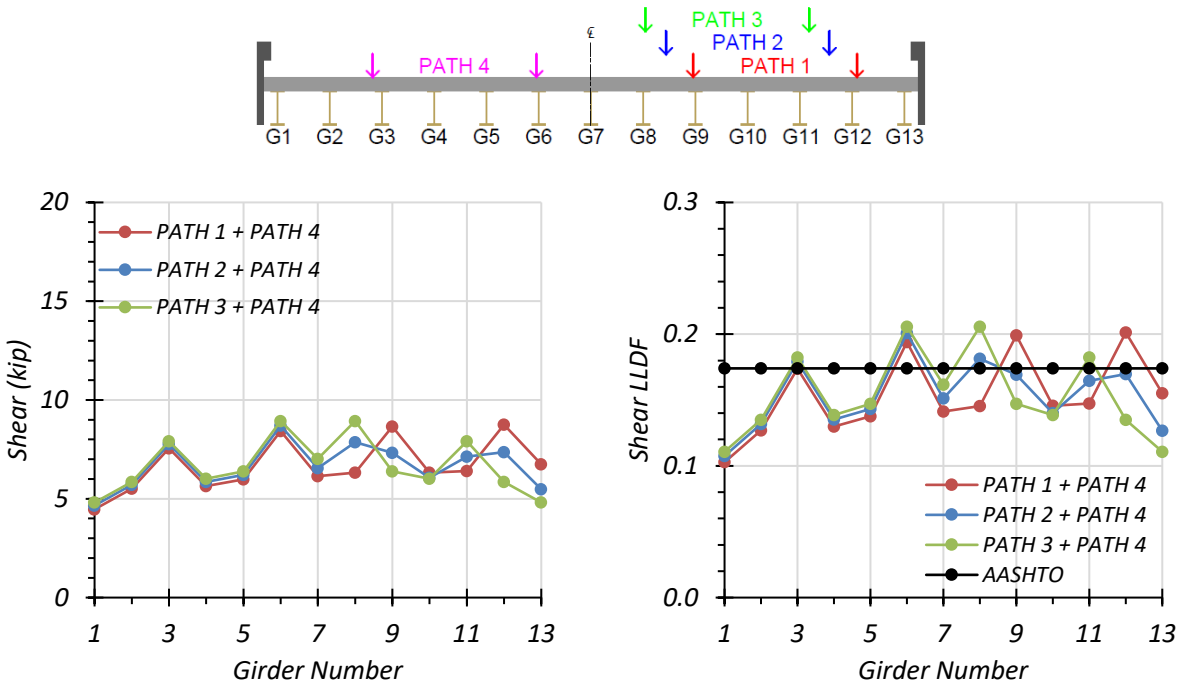

(a) Shear *(b) Shear LLDF*

Figure 5.26. Shear Results for Non-Composite Bridge SM-5 with Two-Lane HS-20 Loading

Table 5.22. Maximum Shears for Non-Composite Bridge SM-5 with Two-Lane HS-20 Loading

Loading	G1	G2	G3	G4	G5	G6	G7	G8	G9	G10	G11	G12	G13
Path 1 + Path 4	4.5	5.5	7.6	5.6	6.0	8.4	6.1	6.3	8.7	6.3	6.4	8.8	6.7
Path 2 + Path 4	4.7	5.7	7.8	5.9	6.2	8.7	6.6	7.9	7.3	6.1	7.1	7.4	5.5
Path 3 + Path 4	4.8	5.9	7.9	6.0	6.4	8.9	7.0	8.9	6.4	6.0	7.9	5.9	4.8
Note: G = girder, paths indicate transverse loading positions as shown, shears have kip units													

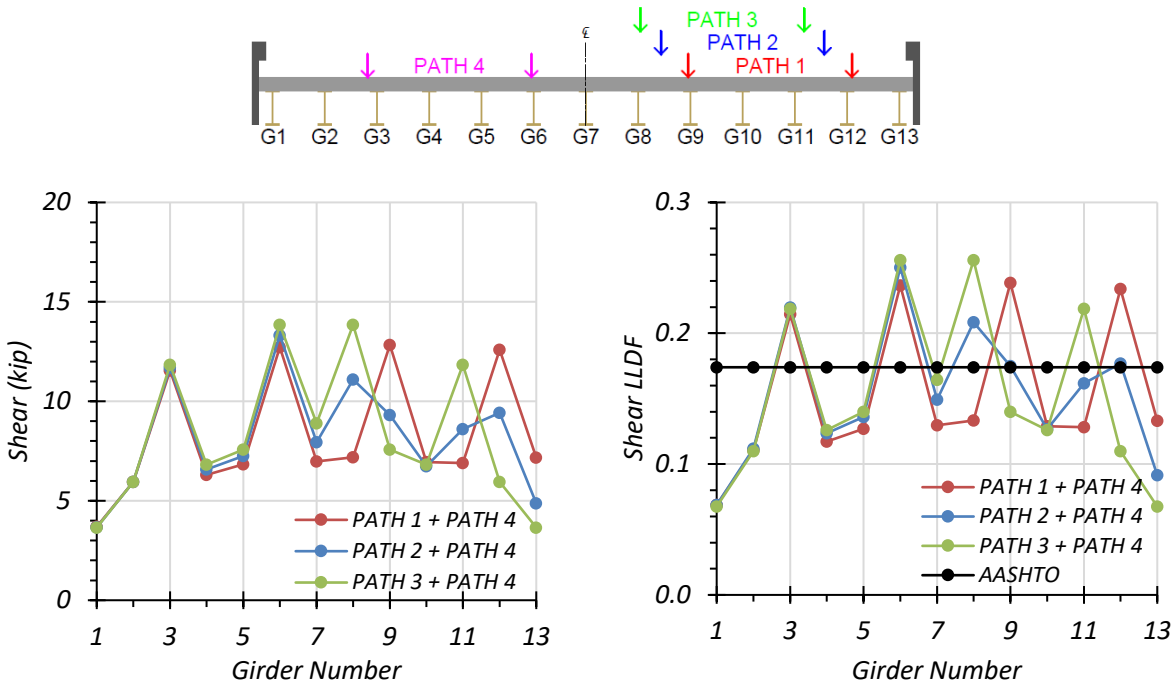

(a) Shear *(b) Shear LLDF*

Figure 5.27. Shear Results for Composite Bridge SM-5 with Two-Lane HS-20 Loading

Table 5.23. Maximum Shears for Composite Bridge SM-5 with Two-Lane HS-20 Loading

Loading	G1	G2	G3	G4	G5	G6	G7	G8	G9	G10	G11	G12	G13
Path 1 + Path 4	3.7	6.0	11.5	6.3	6.8	12.7	7.0	7.2	12.8	6.9	6.9	12.6	7.2
Path 2 + Path 4	3.7	6.0	11.7	6.6	7.2	13.3	7.9	11.1	9.3	6.7	8.6	9.4	4.9
Path 3 + Path 4	3.7	6.0	11.8	6.8	7.6	13.8	8.9	13.8	7.6	6.8	11.8	6.0	3.7
Note: G = girder, paths indicate transverse loading positions as shown, shears have kip units													

Comparison of governing shear LLDF values computed from FEM results for the composite and non-composite cases reveals that the maximum shear LLDF in an interior girder for the composite bridge is higher than the one for the non-composite bridge with a $g^{v}_{composite}/g^{v}_{non-composite}$ ratio of 1.24. Whereas, the maximum shear LLDF in an exterior girder

for the composite bridge is lower than that for the non-composite bridge with a $g^v_{composite}/g^v_{non-composite}$ ratio of 0.86.

Table 5.24. Governing Shear LLDFs for Bridge SM-5 with Two-Lane HS-20 Loading

Type	Girder Location	AASHTO (g^v_{AASHTO})	FEM (g^v_{FEM})	g^v_{AASHTO}/g^v_{FEM}
Non-Composite	Interior	0.174	0.206	0.84
	Exterior	0.174	0.155	1.12
Composite	Interior	0.174	0.256	0.68
	Exterior	0.174	0.133	1.31

5.6.3. HL-93 Live Load Analysis

Bridge SM-5 was also analyzed using the HL-93 design loading presented in the AASHTO LRFD Specifications (AASHTO 2017). The bridge was analyzed for one-lane and two-lane-loaded cases along four transverse paths as shown in Figure 5.14. Deflection, moment, and shear results were obtained.

5.6.3.1. Deflection Results

Figure 5.28 shows the estimated girder deflection profiles and contours along the span for one-lane HL-93 loading along Path 1 and Path 4 when the bridge is analyzed as fully non-composite. Table 5.25 shows the corresponding maximum deflections for each girder assuming non-composite action. Load paths 1 and 4 are the only ones shown as these are expected to be the load paths used in future field load tests, as they were selected to maximize the forces on an interior girder and on an exterior girder.

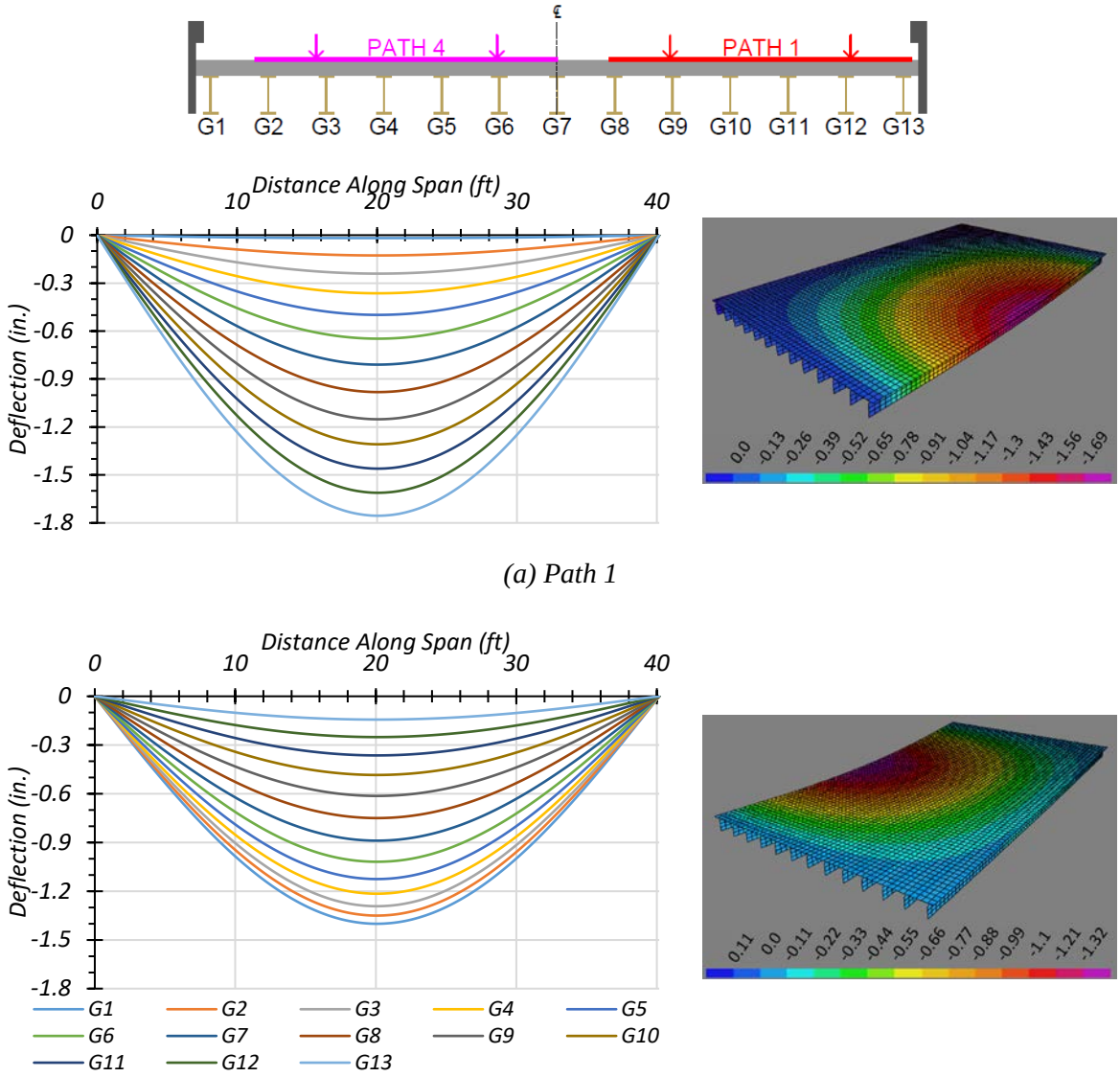

Figure 5.28. Deflection Profiles for Non-Composite Bridge SM-5 with HL-93 Loading

Table 5.25. Maximum Deflections for Non-Composite Bridge SM-5 with HL-93 Loading

Loading	G1	G2	G3	G4	G5	G6	G7	G8	G9	G10	G11	G12	G13
Path 1	-0.018	-0.127	-0.241	-0.364	-0.499	-0.647	-0.810	-0.981	-1.151	-1.308	-1.460	-1.611	-1.755
Path 4	-1.401	-1.350	-1.292	-1.215	-1.125	-1.019	-0.889	-0.750	-0.613	-0.484	-0.364	-0.251	-0.143
Note: G = girder, paths indicate transverse loading positions as shown, deflections have inch units													

Figure 5.29 shows the estimated girder deflection profiles and contours along the span for one-lane HL-93 loading along Path 1 and Path 4 when the bridge is analyzed as fully composite. Table 5.26 shows the corresponding maximum deflections for each girder assuming fully composite action. Load paths 1 and 4 are the only ones shown as these are expected to be the load paths used in future field load tests, as they were selected to maximize the forces on an interior girder and on an exterior girder.

For both non-composite and composite cases, the maximum deflections were obtained in Girder 13 when the HL-93 truck was run along Path 1. The estimated deflections were 1.755 in. and 0.840 in. for the non-composite and composite cases, respectively. This result indicates that the composite bridge is 70.5 percent stiffer than the non-composite bridge. The maximum deflections obtained when the HL-93 truck was run along Path 4 were in Girder 1 for both the non-composite and composite case. The estimated deflections were 1.401 in. and 0.635 in. for the non-composite and composite cases, respectively. This result indicates that the composite bridge is 75.2 percent stiffer than the non-composite bridge. The slightly different values of relative stiffness suggest that the relative girder deflection depends on the location of loading and corresponding load distribution.

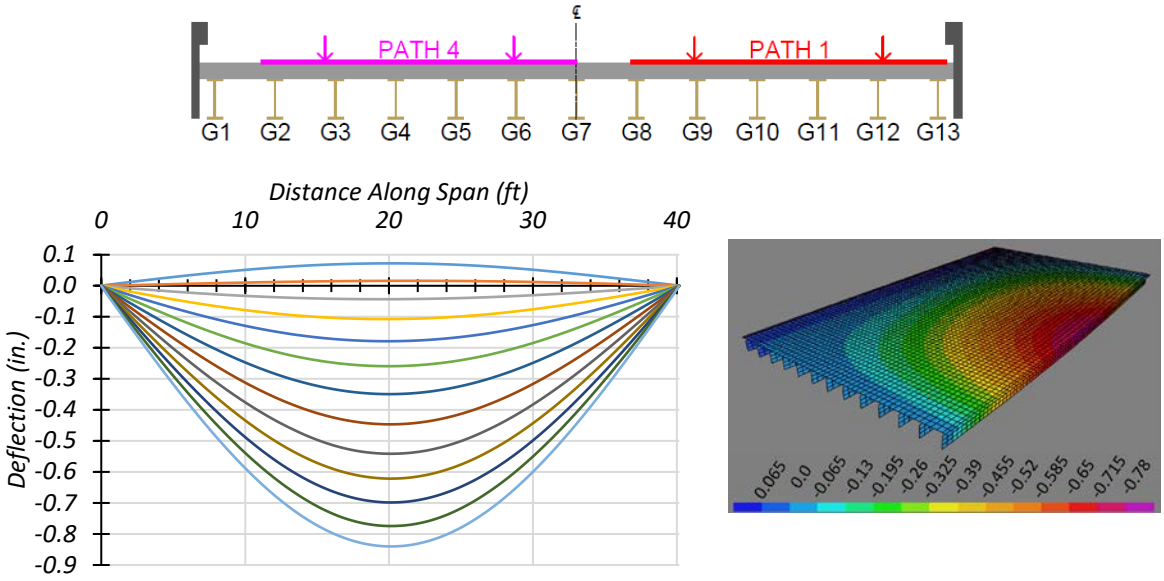

(a) Path 1

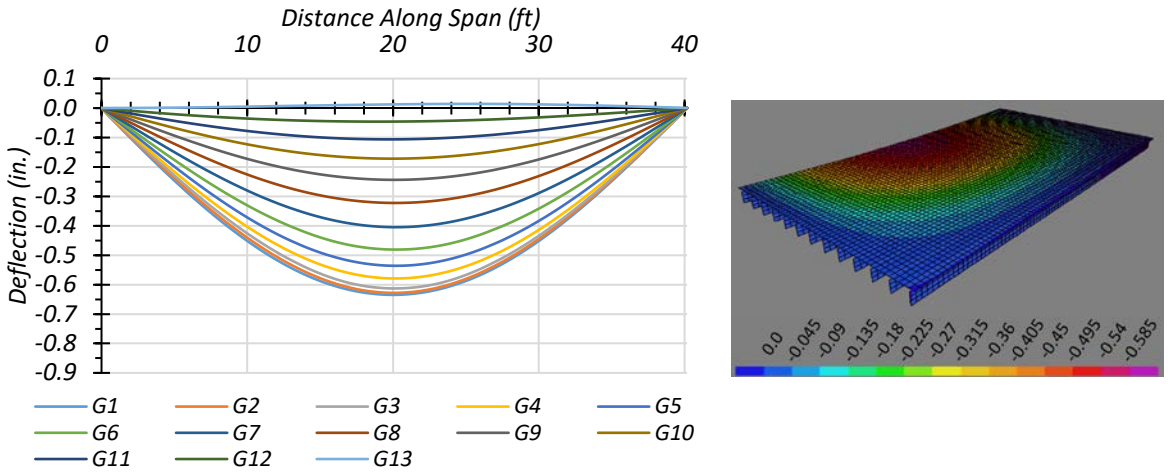

(b) Path 4

Figure 5.29. Deflection Profiles for Composite Bridge SM-5 with HL-93 Loading

Table 5.26. Maximum Deflections for Composite Bridge SM-5 with HL-93 Loading

Loading	G1	G2	G3	G4	G5	G6	G7	G8	G9	G10	G11	G12	G13
Path 1	0.072	0.016	-0.043	-0.107	-0.179	-0.259	-0.349	-0.447	-0.541	-0.621	-0.698	-0.774	-0.840
Path 4	-0.635	-0.628	-0.613	-0.579	-0.536	-0.481	-0.405	-0.323	-0.244	-0.172	-0.107	-0.046	0.014
Note: G = girder, paths indicate transverse loading positions as shown, deflections have inch units													

5.6.3.2. Moment Results

5.6.3.2.1. One-Lane Loading

Figure 5.30 shows the individual girder moments and moment LLDF results for the non-composite Bridge SM-5 under simulated moving HL-93 loading along three one-lane loading paths. Table 5.27 provides the corresponding maximum moment values of each girder for each loading path. The moment LLDF values are calculated using the estimated moment results from the FEM analysis. Table 5.29 shows the governing moment LLDFs found using the FEM analysis and compares them to the AASHTO LLDF values. The first AASHTO LLDF value is calculated using the simplified stiffness parameter. The second AASHTO LLDF value is calculated using the analytical stiffness parameter calculated for the specific bridge. Compared to the FEM results, the governing moment LLDF value computed using the approximate equations and the simplified stiffness parameter in AASHTO LRFD Specifications (AASHTO 2017) is quite conservative for interior girders with a $g^m_{AASHTO\_S}/g^m_{FEM}$ ratio of 1.36, and is conservative for exterior girders a g^m_{AASHTO}/g^m_{FEM} ratio of 1.28. Compared to the FEM results, the governing moment LLDF value computed using the approximate equations and the analytical stiffness parameter in AASHTO LRFD Specifications (AASHTO 2017) is conservative for interior girders with a $g^m_{AASHTO\_K}/g^m_{FEM}$ ratio of 1.18, and is slightly conservative for exterior girders with a $g^m_{AASHTO\_K}/g^m_{FEM}$ ratio of 1.10.

Figure 5.31 shows the individual girder moments and moment LLDF results for the fully composite Bridge SM-5 under simulated moving HL-93 loading along three one-lane loading paths. Table 5.28 provides the corresponding maximum moment values of each girder for each loading path. The moment LLDF values are calculated using the estimated moment results from the FEM analysis. Compared to the FEM results, the governing moment LLDF value computed

using the approximate equations and the simplified stiffness parameter in AASHTO LRFD Specifications (AASHTO 2017) is conservative for both interior and exterior girders with a $g^m_{AASHTO\_S}/g^m_{FEM}$ ratio of 1.22 and 1.29, respectively. Compared to the FEM results, the governing moment LLDF value computed using the approximate equations and the analytical stiffness parameter in AASHTO LRFD Specifications (AASHTO 2017) is slightly conservative for interior girders with a $g^m_{AASHTO\_K}/g^m_{FEM}$ ratio of 1.05, and conservative for exterior girders with a $g^m_{AASHTO\_K}/g^m_{FEM}$ ratio of 1.12.

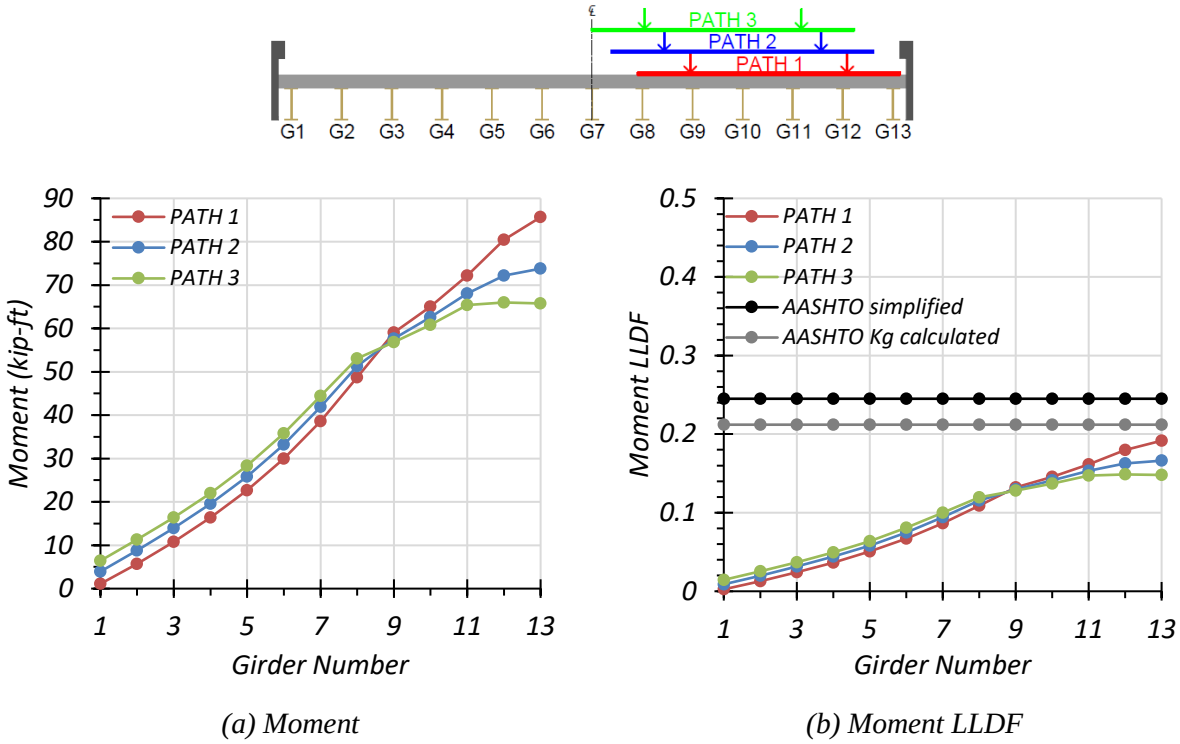

(a) Moment *(b) Moment LLDF*

Figure 5.30. Moment Results for Non-Composite Bridge SM-5 with One-Lane HL-93 Loading

Table 5.27. Maximum Moments for Non-Composite Bridge SM-5 with One-Lane HL-93 Loading

Loading	G1	G2	G3	G4	G5	G6	G7	G8	G9	G10	G11	G12	G13
Path 1	1.1	5.7	10.8	16.4	22.7	30.0	38.6	48.8	59.1	65.1	72.2	80.4	85.7
Path 2	3.9	8.8	13.9	19.5	25.8	33.2	41.9	51.3	57.7	62.6	68.0	72.2	73.8
Path 3	6.4	11.3	16.4	22.0	28.4	35.8	44.4	53.1	56.8	60.9	65.4	66.0	65.8
Note: G = girder, paths indicate transverse loading positions as shown, moments have kip-ft units													

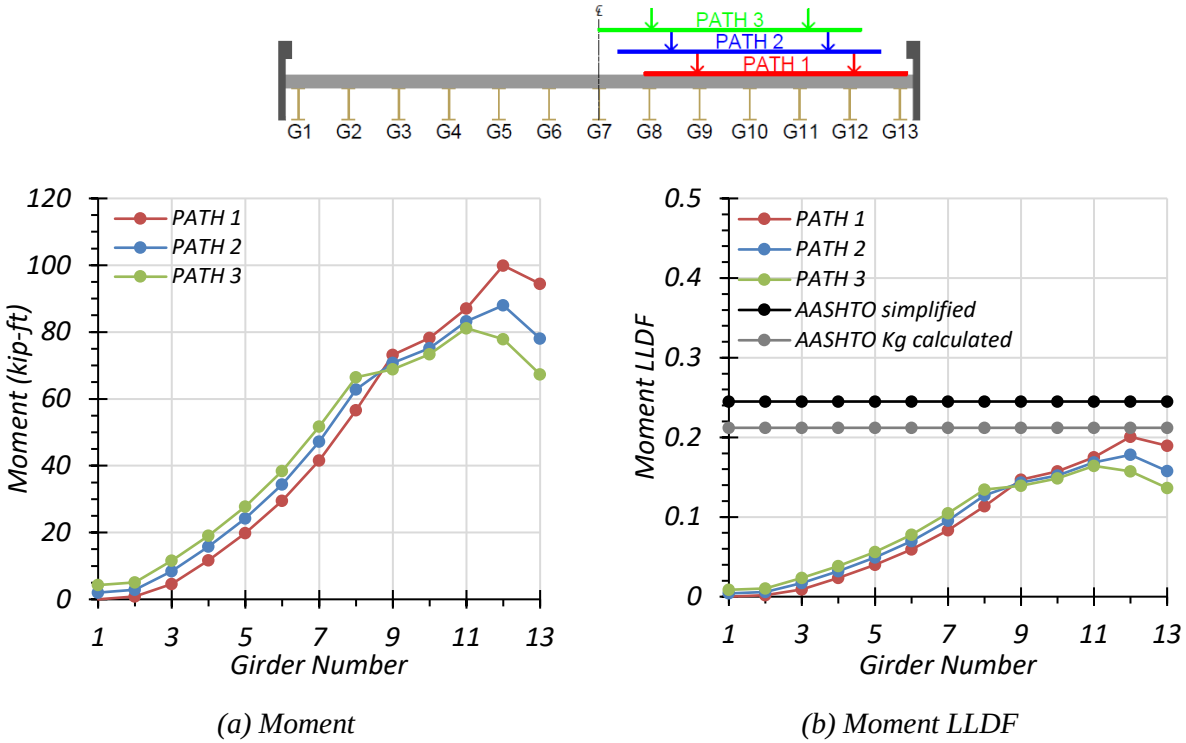

(a) Moment *(b) Moment LLDF*

Figure 5.31. Moment Results for Composite Bridge SM-5 with One-Lane HL-93 Loading

Table 5.28. Maximum Moments for Composite Bridge SM-5 with One-Lane HL-93 Loading

Loading	G1	G2	G3	G4	G5	G6	G7	G8	G9	G10	G11	G12	G13
Path 1	0.0	0.9	4.6	11.7	19.9	29.5	41.6	56.6	73.1	78.2	87.0	99.9	94.4
Path 2	2.0	2.8	8.4	15.8	24.3	34.4	47.2	62.8	70.8	75.2	83.2	88.0	78.0
Path 3	4.3	5.1	11.5	19.1	27.8	38.4	51.7	66.5	68.9	73.4	81.2	77.9	67.4
Note: G = girder, paths indicate transverse loading positions as shown, moments have kip-ft units													

Comparison of governing moment LLDF values computed from FEM results for the composite and non-composite cases reveals that the maximum moment LLDF in an interior girder for the composite bridge is higher than the one for the non-composite bridge with a $g^m_{composite}/g^m_{non-composite}$ ratio of 1.12. Whereas, the maximum moment LLDF in an exterior girder for the composite bridge is almost the same as that for the non-composite bridge with a $g^m_{composite}/g^m_{non-composite}$ ratio of 0.99.

Table 5.29. Governing Moment LLDFs for Bridge SM-5 with One-Lane HL-93 Loading

Type	Girder Location	AASHTO Simplified ($g^m_{AASHTO\_S}$)	AASHTO K_g Calculated ($g^m_{AASHTO\_K}$)	FEM (g^m_{FEM})	$g^m_{AASHTO\_S}/g^m_{FEM}$	$g^m_{AASHTO\_K}/g^m_{FEM}$
Non-Composite	Interior	0.245	0.212	0.180	1.36	1.18
	Exterior	0.245	0.212	0.192	1.28	1.10
Composite	Interior	0.245	0.212	0.201	1.22	1.05
	Exterior	0.245	0.212	0.190	1.29	1.12

5.6.3.2.2. Two-Lane Loading

Figure 5.32 shows the individual girder moments and moment LLDF results for the non-composite Bridge SM-5 under simulated moving HL-93 loading along three two-lane loading paths. Table 5.30 provides the corresponding maximum moment values of each girder for each loading path. The moment LLDF values are calculated using the estimated moment results from the FEM analysis. Table 5.32 shows the governing moment LLDFs found using the FEM analysis and compares them to the AASHTO LLDF values. The first AASHTO LLDF value is calculated using the simplified stiffness parameter. The second AASHTO LLDF value is calculated using the analytical stiffness parameter calculated for the specific bridge. Compared to the FEM results, the

governing moment LLDF value computed using the approximate equations and the simplified stiffness parameter in AASHTO LRFD Specifications (AASHTO 2017) is quite conservative for both interior and exterior girders with a $g^m_{AASHTO\_S}/g^m_{FEM}$ ratio of 1.67 for both. Compared to the FEM results, the governing moment LLDF value computed using the approximate equations and the analytical stiffness parameter in AASHTO LRFD Specifications (AASHTO 2017)is quite conservative for both interior and exterior girders with a $g^m_{AASHTO\_K}/g^m_{FEM}$ ratio of 1.45 for both.

Figure 5.33 shows the individual girder moments and moment LLDF results for the fully composite Bridge SM-5 under simulated moving HL-93 loading along three two-lane loading paths. Table 5.31 provides the corresponding maximum moment values of each girder for each loading path. The moment LLDF values are calculated using the estimated moment results from the FEM analysis. Compared to the FEM results, the governing moment LLDF value computed using the approximate equations and the simplified stiffness parameter in AASHTO LRFD Specifications (AASHTO 2017) is quite conservative for both interior and exterior girders with a $g^m_{AASHTO\_S}/g^m_{FEM}$ ratio of 1.62 and 1.80, respectively. Compared to the FEM results, the governing moment LLDF value computed using the approximate equations and the analytical stiffness parameter in AASHTO LRFD Specifications (AASHTO 2017) is quite conservative for both interior and exterior girders with a $g^m_{AASHTO\_K}/g^m_{FEM}$ ratio of 1.40 and 1.56, respectively.

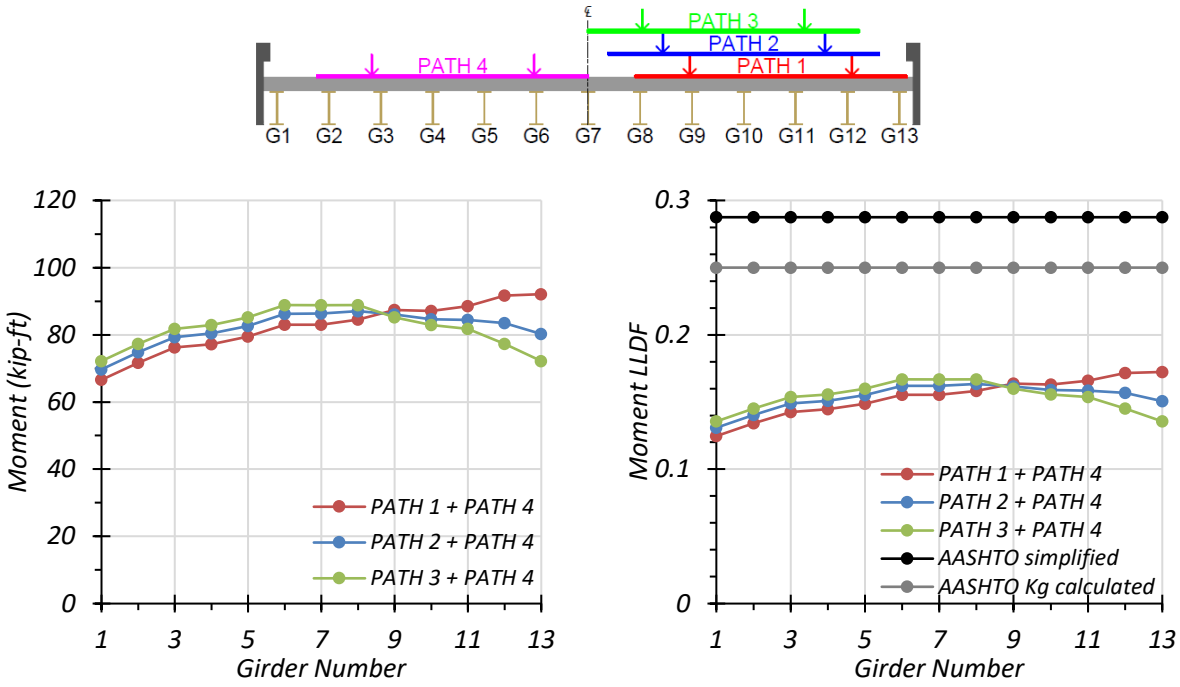

(a) Moment *(b) Moment LLDF*

Figure 5.32. Moment Results for Non-Composite Bridge SM-5 with Two-Lane HL-93 Loading

Table 5.30. Maximum Moments for Non-Composite Bridge SM-5 with Two-Lane HL-93 Loading

Loading	G1	G2	G3	G4	G5	G6	G7	G8	G9	G10	G11	G12	G13
Path 1 + Path 4	66.6	71.7	76.2	77.2	79.5	83.0	83.0	84.5	87.4	87.1	88.6	91.7	92.1
Path 2 + Path 4	69.7	74.8	79.3	80.4	82.7	86.3	86.3	87.0	86.0	84.6	84.4	83.5	80.2
Path 3 + Path 4	72.2	77.3	81.8	82.9	85.2	88.9	88.8	88.9	85.2	82.9	81.8	77.3	72.2
Note: G = girder, paths indicate transverse loading positions as shown, moments have kip-ft units													

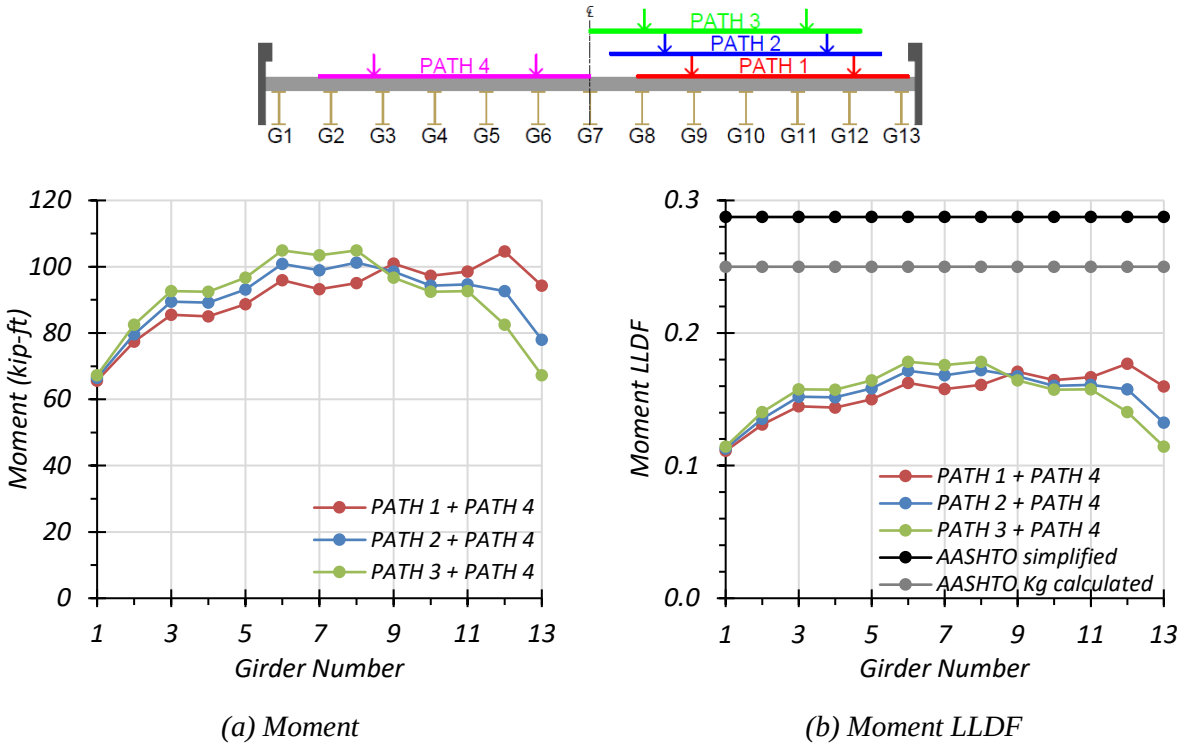

(a) Moment *(b) Moment LLDF*

Figure 5.33. Moment Results for Composite Bridge SM-5 with Two-Lane HL-93 Loading

Table 5.31. Maximum Moments for Composite Bridge SM-5 with Two-Lane HL-93 Loading

Loading	G1	G2	G3	G4	G5	G6	G7	G8	G9	G10	G11	G12	G13
Path 1 + Path 4	65.7	77.4	85.5	85.0	88.7	96.0	93.3	95.0	100.9	97.3	98.5	104.6	94.3
Path 2 + Path 4	66.5	79.6	89.5	89.2	93.1	100.9	99.0	101.2	98.5	94.3	94.7	92.6	77.9
Path 3 + Path 4	67.3	82.5	92.6	92.5	96.7	104.9	103.4	104.9	96.7	92.5	92.6	82.5	67.3
Note: G = girder, paths indicate transverse loading positions as shown, moments have kip-ft units													

Comparison of governing moment LLDF values computed from FEM results for the composite and non-composite cases reveals that the maximum moment LLDF in an interior girder for the composite bridge is higher than the one for the non-composite bridge with a $g^m_{composite}/g^m_{non-composite}$ ratio of 1.03. Whereas, the maximum moment LLDF in an exterior

girder for the composite bridge is lower than that for the non-composite bridge with a $g^m_{composite}/g^m_{non-composite}$ ratio of 0.93.

Table 5.32. Governing Moment LLDFs for Bridge SM-5 with Two-Lane HL-93 Loading

Type	Girder Location	AASHTO Simplified ($g^m_{AASHTO\_S}$)	AASHTO K_g Calculated ($g^m_{AASHTO\_K}$)	FEM (g^m_{FEM})	$g^m_{AASHTO\_S}/g^m_{FEM}$	$g^m_{AASHTO\_K}/g^m_{FEM}$
Non-Composite	Interior	0.288	0.250	0.172	1.67	1.45
	Exterior	0.288	0.250	0.172	1.67	1.45
Composite	Interior	0.288	0.250	0.178	1.62	1.40
	Exterior	0.288	0.250	0.160	1.80	1.56

5.6.3.3. Shear Results

5.6.3.3.1. One-Lane Loading

Figure 5.34 shows the individual girder shears and shear LLDF results for the non-composite Bridge SM-5 under simulated moving HL-93 loading along three one-lane loading paths. Table 5.33 provides the corresponding maximum shear values of each girder for each loading path. The shear LLDF values are calculated using the estimated shear results from the FEM analysis. Table 5.35 shows the governing shear LLDFs found using the FEM analysis and compares them to the AASHTO LLDF values. Compared to the FEM results, the governing shear LLDF value computed using the approximate equations in AASHTO LRFD Specifications (AASHTO 2017) is quite conservative for both interior and exterior girders with a g^v_{AASHTO}/g^v_{FEM} ratio of 2.14 and 2.46, respectively.

Figure 5.35 shows the individual girder shears and shear LLDF results for the fully composite Bridge SM-5 under simulated moving HL-93 loading along three one-lane loading

paths. Table 5.34 provides the corresponding maximum shear values of each girder for each loading path. The shear LLDF values are calculated using the estimated shear results from the FEM analysis. Compared to the FEM results, the governing shear LLDF value computed using the approximate equations in AASHTO LRFD Specifications (AASHTO 2017) is quite conservative for both interior and exterior girders with a $g^{v}_{AASHTO}/g^{v}_{FEM}$ ratio of 1.71 and 2.68, respectively.

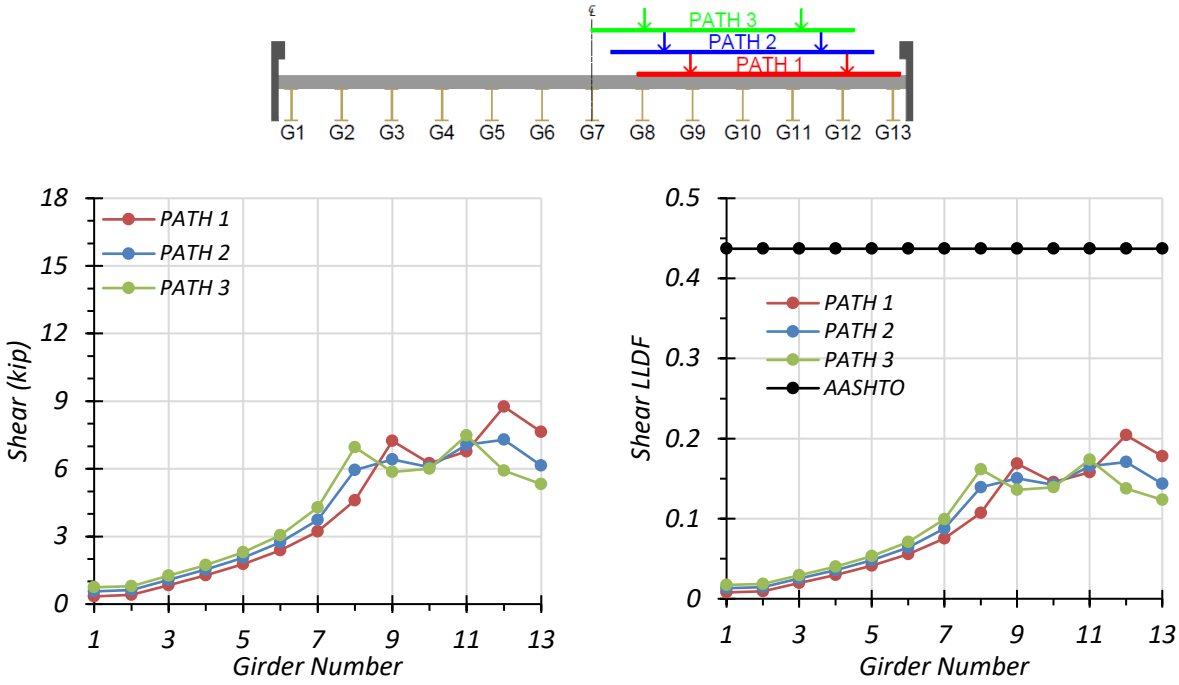

(a) Shear *(b) Shear LLDF*

Figure 5.34. Shear Results for Non-Composite Bridge SM-5 with One-Lane HL-93 Loading

Table 5.33. Maximum Shears for Non-Composite Bridge SM-5 with One-Lane HL-93 Loading

Loading	G1	G2	G3	G4	G5	G6	G7	G8	G9	G10	G11	G12	G13
Path 1	0.3	0.4	0.8	1.3	1.8	2.4	3.2	4.6	7.2	6.2	6.8	8.8	7.6
Path 2	0.6	0.6	1.1	1.5	2.1	2.7	3.7	6.0	6.4	6.1	7.1	7.3	6.1
Path 3	0.7	0.8	1.3	1.7	2.3	3.1	4.3	7.0	5.9	6.0	7.5	5.9	5.3
Note: G = girder, paths indicate transverse loading positions as shown, shears have kip units													

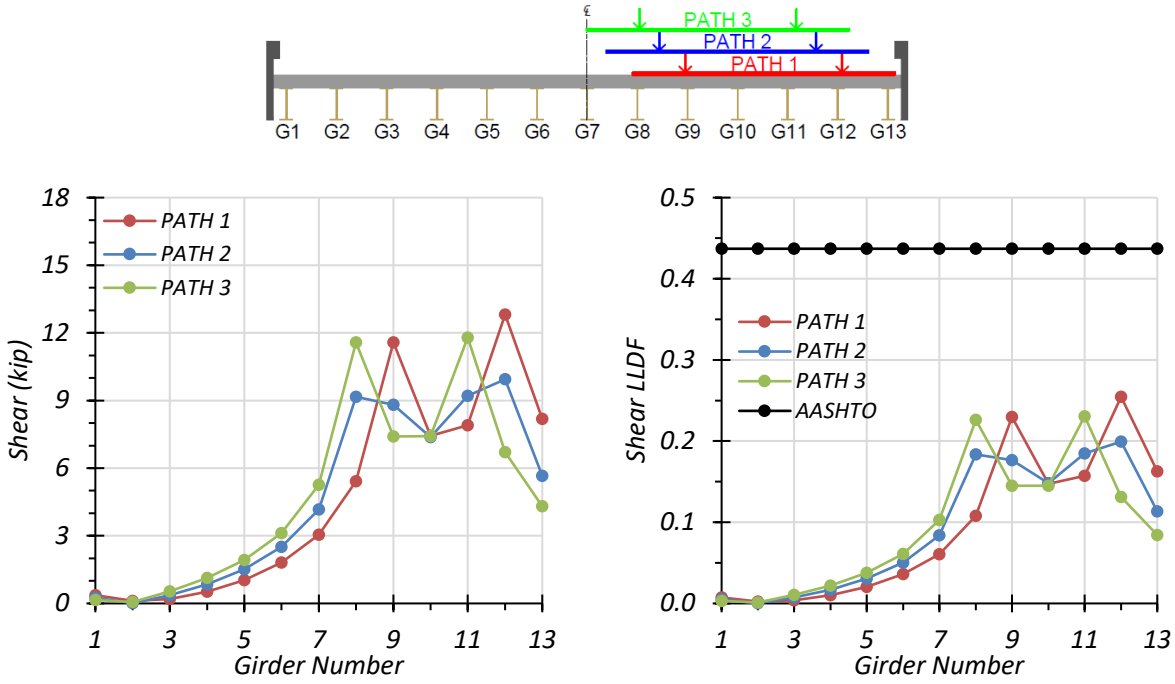

(a) Shear *(b) Shear LLDF*

Figure 5.35. Shear Results for Composite Bridge SM-5 with One-Lane HL-93 Loading

Table 5.34. Maximum Shears for Composite Bridge SM-5 with One-Lane HL-93 Loading

Loading	G1	G2	G3	G4	G5	G6	G7	G8	G9	G10	G11	G12	G13
Path 1	0.4	0.1	0.2	0.5	1.0	1.8	3.0	5.4	11.6	7.4	7.9	12.8	8.2
Path 2	0.2	0.0	0.4	0.8	1.5	2.5	4.2	9.2	8.8	7.4	9.2	9.9	5.7
Path 3	0.2	0.1	0.5	1.1	1.9	3.1	5.3	11.6	7.4	7.4	11.8	6.7	4.3
Note: G = girder, paths indicate transverse loading positions as shown, shears have kip units													

Comparison of governing shear LLDF values computed from FEM results for the composite and non-composite cases reveals that the maximum shear LLDF in an interior girder for the composite bridge is higher than the one for the non-composite bridge with a $g^v_{composite}/g^v_{non-composite}$ ratio of 1.25. Whereas, the maximum shear LLDF in an exterior girder for the composite bridge is lower than that for the non-composite bridge with a $g^v_{composite}/g^v_{non-composite}$ ratio of 0.92.

Table 5.35. Governing Shear LLDFs for Bridge SM-5 with One-Lane HL-93 Loading

Type	Girder Location	AASHTO (g^v_{AASHTO})	FEM (g^v_{FEM})	g^v_{AASHTO}/g^v_{FEM}
Non-Composite	Interior	0.437	0.204	2.14
	Exterior	0.437	0.178	2.46
Composite	Interior	0.437	0.255	1.71
	Exterior	0.437	0.163	2.68

5.6.3.3.2. Two-Lane Loading

The same procedure was conducted for two-lane loading. Figure 5.36 shows the individual girder shears and shear LLDF results for the non-composite Bridge SM-5 under simulated moving HL-93 loading along three two-lane loading paths. Table 5.36 provides the corresponding maximum shear values of each girder for each loading path. The shear LLDF values are calculated using the estimated shear results from the FEM analysis. Table 5.38 shows the governing shear LLDFs found using the FEM analysis and compares them to the AASHTO LLDF values. Compared to the FEM results, the governing shear LLDF value computed using the approximate equations in AASHTO LRFD Specifications (AASHTO 2017) is quite conservative for both interior and exterior girders with a g^v_{AASHTO}/g^v_{FEM} ratio of 2.25 and 2.71, respectively.

Figure 5.37 shows the individual girder shears and shear LLDF results for the fully composite Bridge SM-5 under simulated moving HL-93 loading along three one-lane loading paths. Table 5.37 provides the corresponding maximum shear values of each girder for each loading path. The shear LLDF values are calculated using the estimated shear results from the FEM analysis. Compared to the FEM results, the governing shear LLDF value computed using the approximate equations in AASHTO LRFD Specifications (AASHTO 2017) is quite conservative for both interior and exterior girders with a g^v_{AASHTO}/g^v_{FEM} ratio of 1.82 and 3.24, respectively.

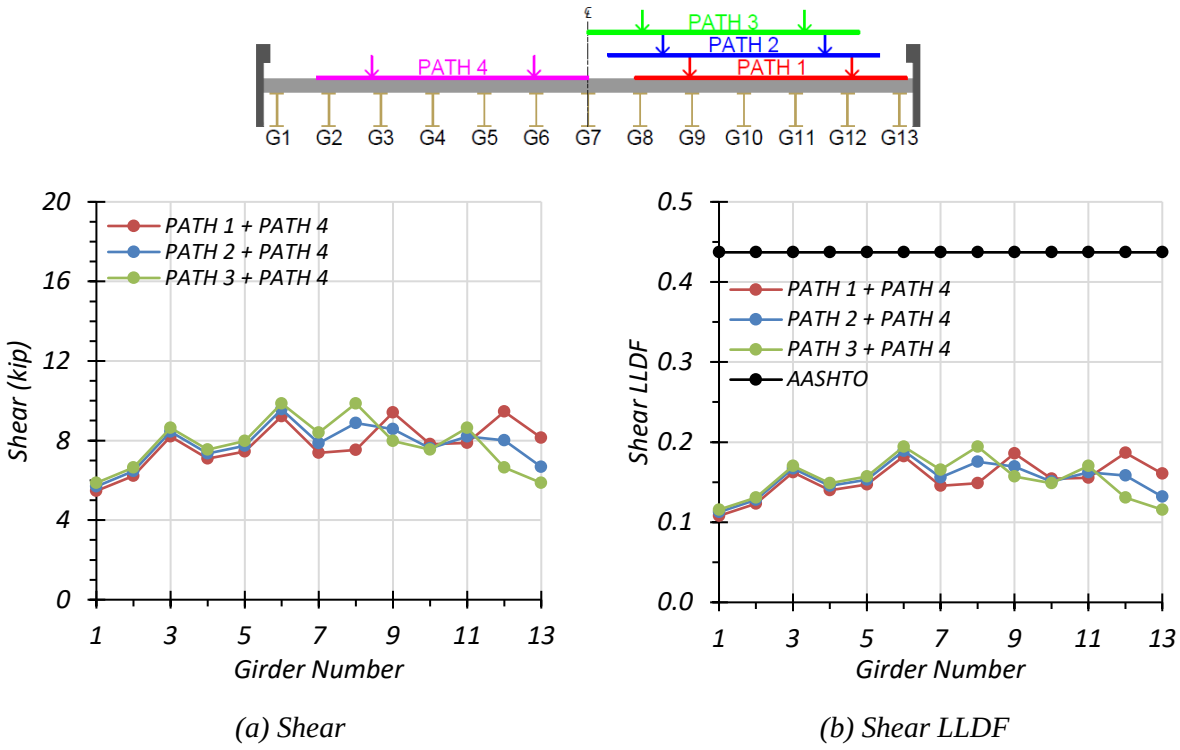

(a) Shear *(b) Shear LLDF*

Figure 5.36. Shear Results for Non-Composite Bridge SM-5 with Two-Lane HL-93 Loading

Table 5.36. Maximum Shears for Non-Composite Bridge SM-5 with Two-Lane HL-93 Loading

Loading	G1	G2	G3	G4	G5	G6	G7	G8	G9	G10	G11	G12	G13
Path 1 + Path 4	5.5	6.2	8.2	7.1	7.5	9.2	7.4	7.5	9.4	7.8	7.9	9.5	8.1
Path 2 + Path 4	5.7	6.5	8.5	7.3	7.7	9.6	7.9	8.9	8.6	7.6	8.2	8.0	6.7
Path 3 + Path 4	5.9	6.6	8.6	7.6	8.0	9.9	8.4	9.9	8.0	7.6	8.6	6.6	5.9
Note: G = girder, paths indicate transverse loading positions as shown, shears have kip units													

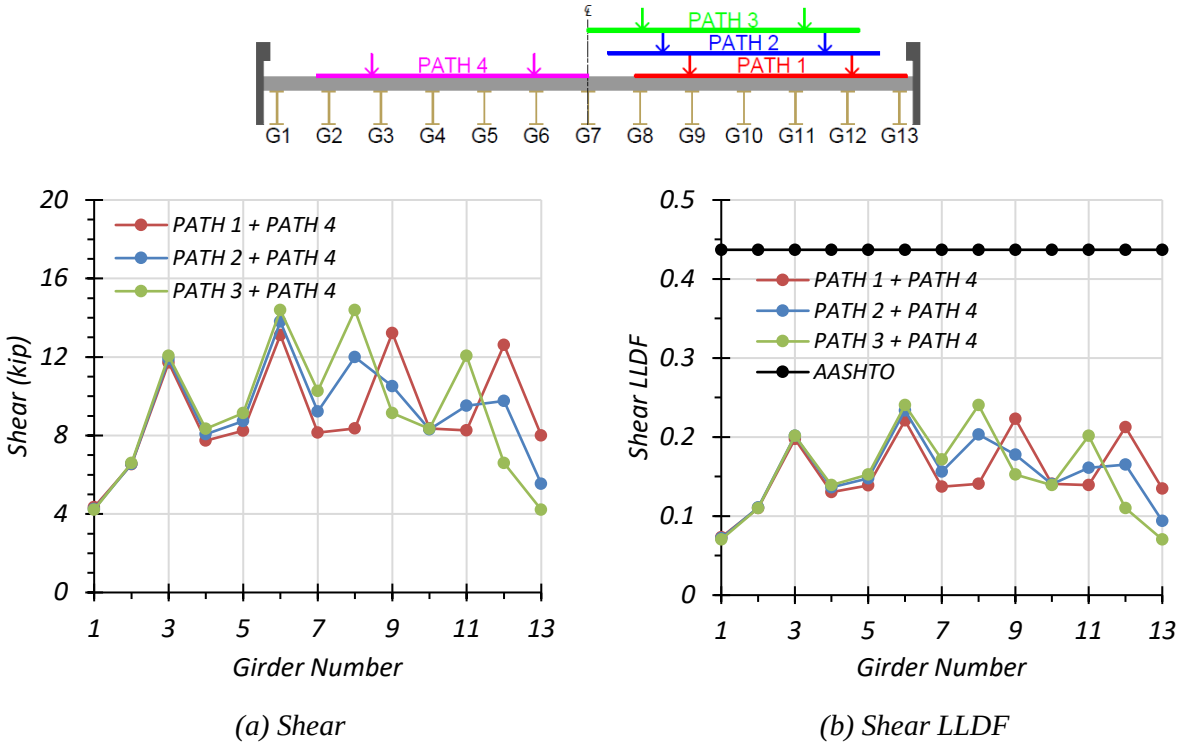

(a) Shear *(b) Shear LLDF*

Figure 5.37. Shear Results for Composite Bridge SM-5 with Two-Lane HL-93 Loading

Table 5.37. Maximum Shears for Composite Bridge SM-5 with Two-Lane HL-93 Loading

Loading	G1	G2	G3	G4	G5	G6	G7	G8	G9	G10	G11	G12	G13
Path 1 + Path 4	4.3	6.5	11.7	7.7	8.2	13.1	8.1	8.4	13.2	8.4	8.3	12.6	8.0
Path 2 + Path 4	4.3	6.5	11.9	8.1	8.7	13.8	9.2	12.0	10.5	8.3	9.5	9.8	5.5
Path 3 + Path 4	4.2	6.6	12.1	8.3	9.1	14.4	10.3	14.4	9.1	8.3	12.1	6.6	4.2
Note: G = girder, paths indicate transverse loading positions as shown, shears have kip units													

Comparison of governing shear LLDF values computed from FEM results for the composite and non-composite cases reveals that the maximum shear LLDF in an interior girder for the composite bridge is higher than the one for the non-composite bridge with a $g^v_{composite}/g^v_{non-composite}$ ratio of 1.24. The maximum shear LLDF in an exterior girder for the composite bridge is also lower than that for the non-composite bridge with a $g^v_{composite}/g^v_{non-composite}$ ratio of 0.84.

Table 5.38. Governing Shear LLDFs for Bridge SM-5 with Two-Lane HL-93 Loading

Type	Girder Location	AASHTO (g^v_{AASHTO})	FEM (g^v_{FEM})	g^v_{AASHTO}/g^v_{FEM}
Non-Composite	Interior	0.437	0.194	2.25
	Exterior	0.437	0.161	2.71
Composite	Interior	0.437	0.240	1.82
	Exterior	0.437	0.135	3.24

5.7. FEM RESULTS FOR BRIDGE SM-21

Bridge SM-21 was analyzed using the CSiBridge software under the loading scenarios provided in Figure 5.12 thru Figure 5.15. Girder displacement profiles were obtained for the load cases that represent the field load testing plans. Modal analyses were conducted for both composite and non-

composite conditions to determine estimated modal frequencies and mode shapes. Live load moment and shear values were also extracted and analyzed to compare the expected LLDFs with the LLDFs prescribed in AASHTO Standard Specifications (AASHTO 2002) and AASHTO LRFD Specifications (AASHTO 2017).

As stated for Bridge SM-5, because of articles in the AASHTO Standard Specifications (AASHTO 2002) and AASHTO LRFD Specifications (AASHTO 2017) and the way in which they are interpreted, in some cases for Bridge SM-21 the LLDF determined through AASHTO for the exterior girder is controlled by the LLDF determined for the interior girder.

5.7.1. Modal Properties

The first two modes of Bridge SM-21 were identified as the first longitudinal bending mode and the first torsional mode. The frequencies of longitudinal bending and torsional modes for the non-composite bridge were determined to be 6.29 Hz and 6.41 Hz, respectively. Figure 5.38(a) shows the amplitude contours of the first longitudinal bending mode shape and the normalized amplitudes along the span for the non-composite condition. Figure 5.38(b) shows the amplitude contours for the first torsional mode shape and the normalized amplitudes transverse to the span for non-composite condition. The frequencies of the longitudinal bending and torsional modes of the composite bridge were determined to be 8.04 Hz and 8.33 Hz, respectively. Figure 5.39(a) shows the amplitude contours of the first longitudinal bending mode shape and the normalized amplitudes along the span for the composite condition. Figure 5.39(b) shows the amplitude contours resulting from the first torsional mode and the normalized amplitudes transverse to the span for composite analysis.

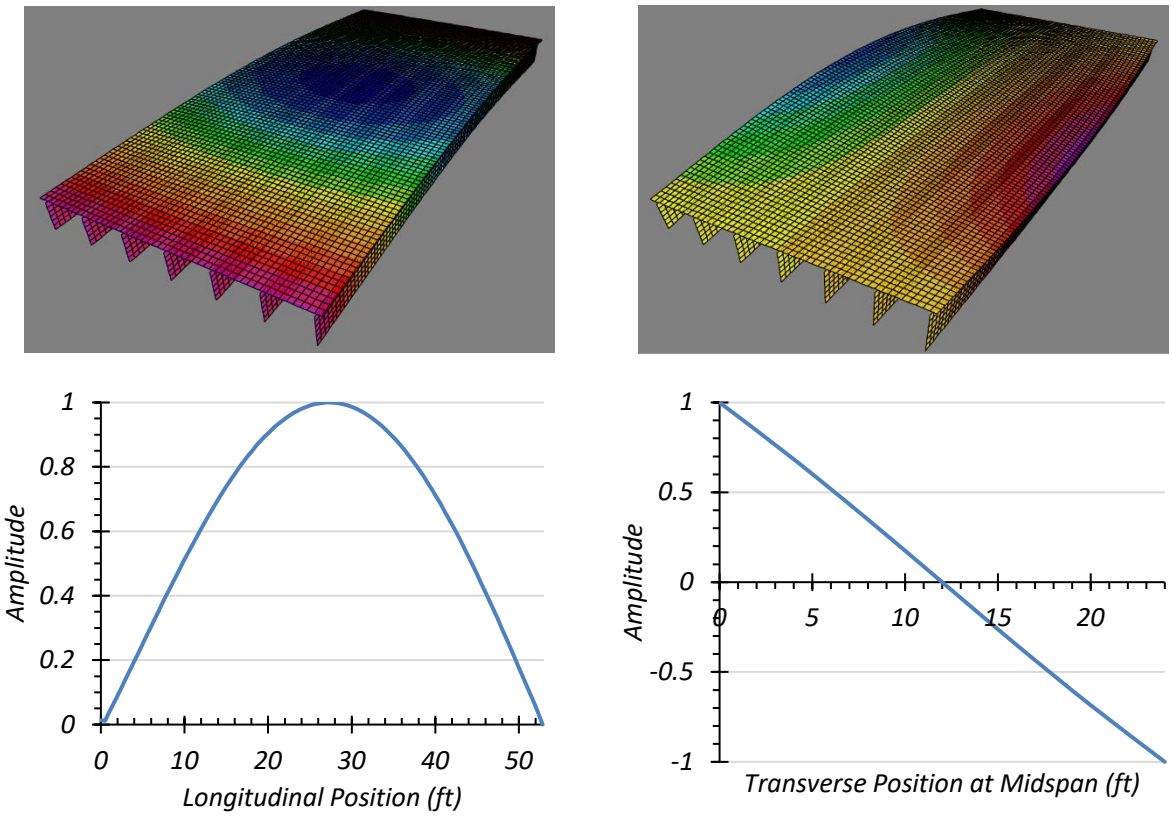

(a) Longitudinal bending Mode (f=6.29 Hz) *(b) Torsional Mode (f=6.41 Hz)*

Figure 5.38. First Two Mode Shapes of Non-Composite Bridge SM-21

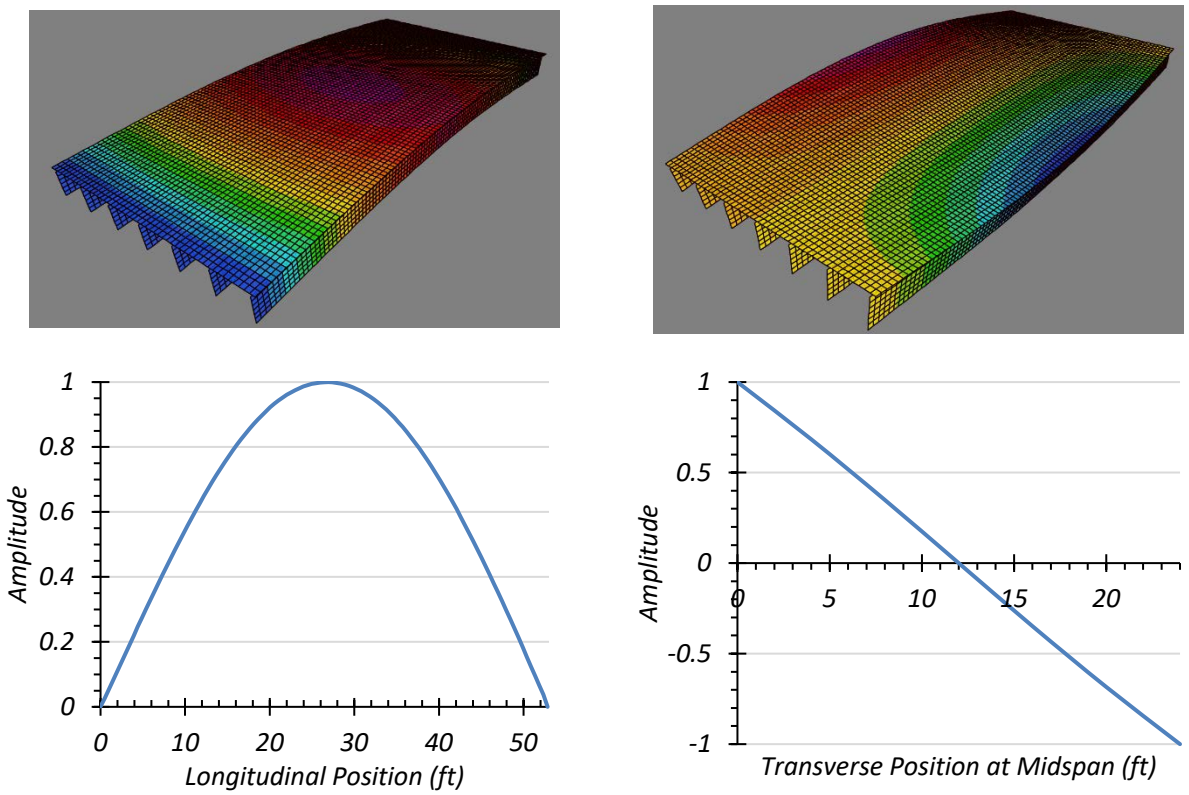

(a) Longitudinal bending Mode (f=8.04 Hz) *(b) Torsional Mode (f=8.33 Hz)*

Figure 5.39. First Two Mode Shapes of Composite Bridge SM-21

5.7.2. HS-20 Live Load Analysis

Bridge SM-21 was first analyzed using the HS-20 design truck presented in the AASHTO Standard Specifications (AASHTO 2002). The bridge was analyzed for one-lane and two-lane-loaded cases along four transverse paths as shown in Figure 5.12. Deflection, moment, and shear results were obtained.

5.7.2.1. Deflection Results

Figure 5.40 shows the estimated girder deflection profiles and contours along the span for one-lane HS-20 loading along Path 1 and Path 4 when the bridge is analyzed as fully non-composite.

Table 5.39 shows the corresponding maximum deflections for each girder assuming non-composite action. Load paths 1 and 4 are the only ones shown as these are expected to be the load paths used in future field load tests, as they were selected to maximize the forces on an interior girder and on an exterior girder.

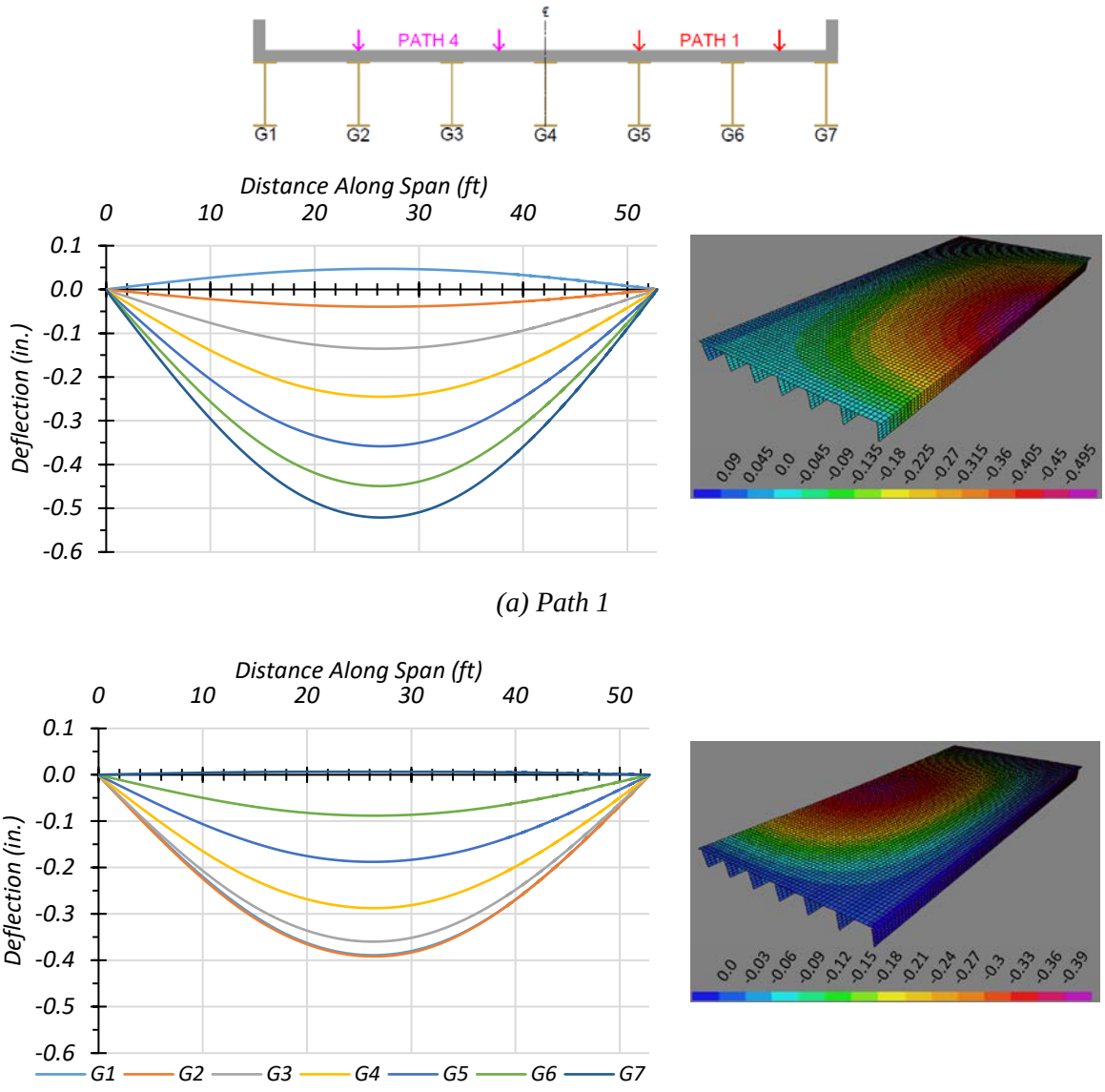

(a) Path 1

(a) Path 4

Figure 5.40. Deflection Profiles for Non-Composite Bridge SM-21 with HS-20 Loading

Table 5.39. Maximum Deflections for Non-Composite Bridge SM-21 with HS-20 Loading

Loading	G1	G2	G3	G4	G5	G6	G7
Path 1	0.047	-0.039	-0.135	-0.245	-0.358	-0.449	-0.521
Path 4	-0.453	-0.421	-0.361	-0.267	-0.162	-0.063	0.007
Note: G = girder, paths indicate transverse loading positions as shown, deflections have inch units							

Figure 5.41 shows the estimated girder deflection profiles and contours along the span for one-lane HS-20 loading along Path 1 and Path 4 when the bridge is analyzed as fully composite. Table 5.40 shows the corresponding maximum deflections for each girder assuming fully composite action. Load paths 1 and 4 are the only ones shown as these are expected to be the load paths used in future field load tests, as they were selected to maximize the forces on an interior girder and on an exterior girder.

For both non-composite and composite cases, the maximum deflections were obtained in Girder 7 when the HS-20 truck was run along Path 1. The estimated deflections were 0.521 in. and 0.297 in. for non-composite and composite cases, respectively. This result indicates that the composite bridge is 54.8 percent stiffer than the non-composite bridge. The maximum deflections obtained when the HS-20 truck was run along Path 4 were in Girder 1 for both the non-composite and composite case. The estimated deflections were 0.453 in. and 0.225 in. for non-composite and composite cases, respectively. This result indicates that the composite bridge is 67.7 percent stiffer than the non-composite bridge. The slightly different values of relative stiffness suggest that the relative girder deflection depends on the location of loading and corresponding load distribution.

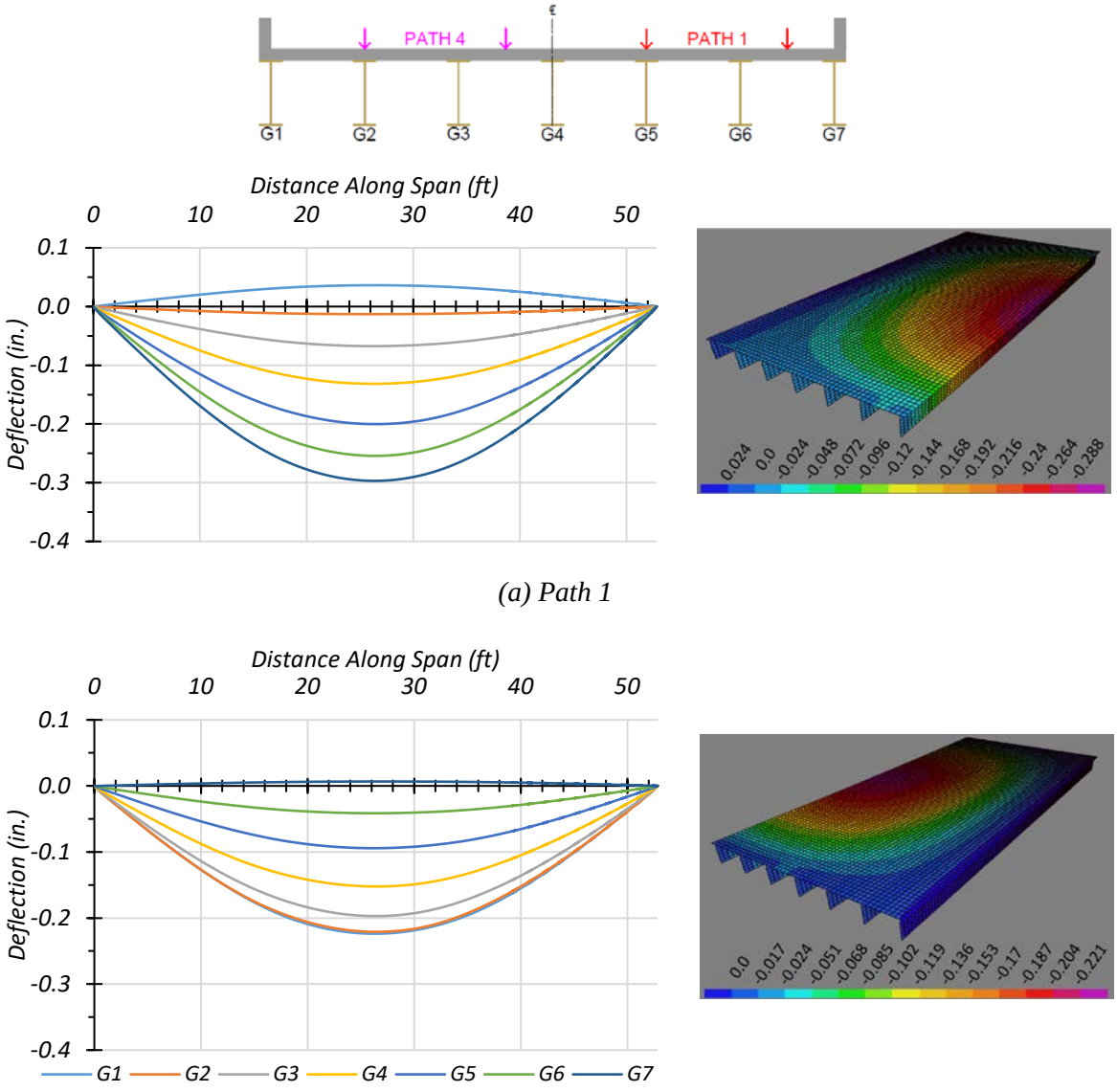

(a) Path 1

(b) Path 4

Figure 5.41. Deflection Profiles for Composite Bridge SM-21 with HS-20 Loading

Table 5.40. Maximum Deflections for Composite Bridge SM-21 with HS-20 Loading

Loading	G1	G2	G3	G4	G5	G6	G7
Path 1	0.036	-0.013	-0.067	-0.132	-0.200	-0.254	-0.297
Path 4	-0.224	-0.221	-0.197	-0.152	-0.094	-0.041	0.007
Note: G = girder, paths indicate transverse loading positions as shown, deflections have inch units							

5.7.2.2. Moment Results

5.7.2.2.1. One-Lane Loading

Figure 5.42 shows the individual girder moments and moment LLDF results for the non-composite Bridge SM-21 under simulated moving HS-20 loading along three one-lane loading paths. Table 5.41 provides the corresponding maximum moment values of each girder for each loading path. The moment LLDF values are calculated using the estimated moment results from FEM analysis. Table 5.43 shows the governing moment LLDFs found using the FEM analysis and compares them to the AASHTO LLDF values. Compared to the FEM results, the governing moment LLDF value computed using the approximate equations in the AASHTO Standard Specifications (AASHTO 2002) is slightly conservative for interior girders with a g^m_{AASHTO}/g^m_{FEM} ratio of 1.10, and is conservative for exterior girders with a g^m_{AASHTO}/g^m_{FEM} ratio of 1.25.

Figure 5.43 shows the individual girder moments and moment LLDF results for the fully composite Bridge SM-21 under simulated moving HS-20 loading along three one-lane loading paths. Table 5.42 provides the corresponding maximum moment values of each girder for each loading path. The moment LLDF values are calculated using the estimated moment results from the FEM analysis. Compared to the FEM results, the governing moment LLDF value computed using the approximate equations in the AASHTO Standard Specifications (AASHTO 2002) is slightly conservative for interior girders with a g^m_{AASHTO}/g^m_{FEM} ratio of 1.03, and is quite conservative for exterior girders with a g^m_{AASHTO}/g^m_{FEM} ratio of 1.34.

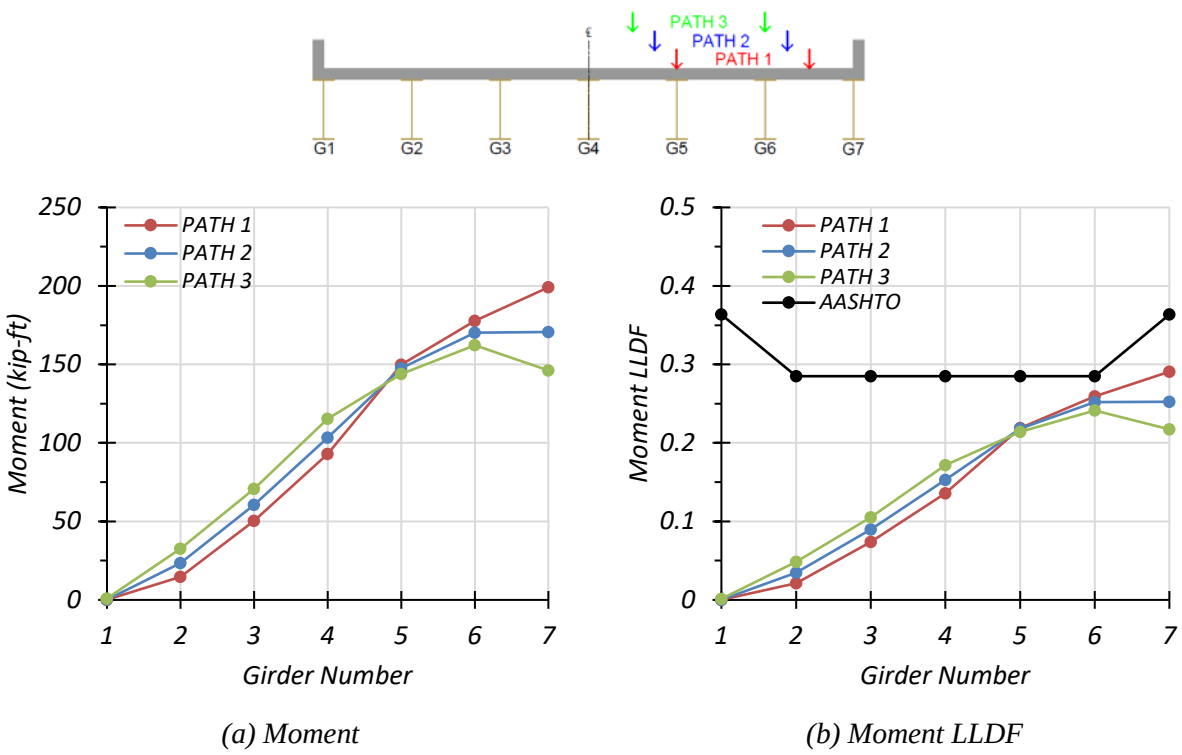

(a) Moment *(b) Moment LLDF*

Figure 5.42. Moment Results for Non-Composite Bridge SM-21 with One-Lane HS-20 Loading

Table 5.41. Maximum Moments for Non-Composite Bridge SM-21 with One-Lane HS-20 Loading

Loading	G1	G2	G3	G4	G5	G6	G7
Path 1	0.1	14.6	50.5	93.0	149.8	177.7	199.1
Path 2	0.1	23.5	60.6	103.3	147.5	170.3	170.6
Path 3	0.9	32.7	70.8	115.5	144.0	162.2	146.1
Note: G = girder, paths indicate transverse loading positions as shown, moments have kip-ft units							

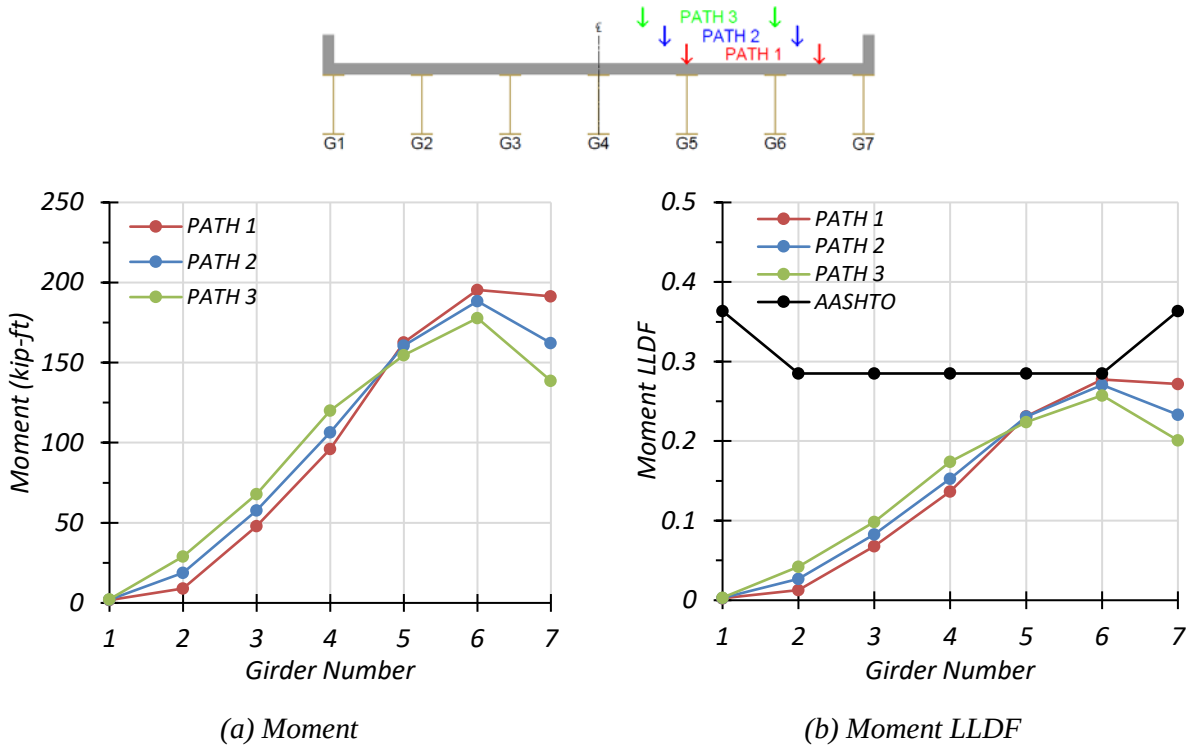

(a) Moment *(b) Moment LLDF*

Figure 5.43. Moment Results for Composite Bridge SM-21 with One-Lane HS-20 Loading

Table 5.42. Maximum Moments for Composite Bridge SM-21 with One-Lane HS-20 Loading

Loading	G1	G2	G3	G4	G5	G6	G7
Path 1	1.8	9.0	47.9	96.1	162.7	195.4	191.4
Path 2	2.0	18.7	57.7	106.4	160.7	188.3	162.2
Path 3	2.3	29.0	68.0	120.0	154.6	177.8	138.7
Note: G = girder, paths indicate transverse loading positions as shown, moments have kip-ft units							

Comparison of governing moment LLDF values computed from FEM results for the composite and non-composite cases reveals that the maximum moment LLDF in an interior girder for the composite bridge is higher than the one for the non-composite bridge with a $g^m_{composite}/g^m_{non-composite}$ ratio of 1.07. Whereas, the maximum moment LLDF in an exterior

girder for the composite bridge is lower than that for the non-composite bridge with a $g^m_{composite}/g^m_{non-composite}$ ratio of 0.93.

Table 5.43. Governing Moment LLDFs for Bridge SM-21 with One-Lane HS-20 Loading

Type	Girder Location	AASHTO (g^m_{AASHTO})	FEM (g^m_{FEM})	g^m_{AASHTO}/g^m_{FEM}
Non-Composite	Interior	0.285	0.259	1.10
	Exterior	0.364	0.291	1.25
Composite	Interior	0.285	0.277	1.03
	Exterior	0.364	0.272	1.34

5.7.2.2.2. Two-Lane Loading

Figure 5.44 shows the individual girder moments and moment LLDF results for the non-composite Bridge SM-21 under simulated moving HS-20 loading along three two-lane loading paths. Table 5.44 provides the corresponding maximum moment values of each girder for each loading path. The moment LLDF values are calculated using the estimated moment results from FEM analysis. Table 5.46 shows the governing moment LLDFs found using the FEM analysis and compares them to the AASHTO LLDF values. Compared to the FEM results, the governing moment LLDF value computed using the approximate equations in the AASHTO Standard Specifications (AASHTO 2002) is slightly conservative for interior girders with a g^m_{AASHTO}/g^m_{FEM} ratio of 1.06, and is conservative for exterior girders with a g^m_{AASHTO}/g^m_{FEM} ratio of 1.24.

Figure 5.45 shows the individual girder moments and moment LLDF results for the fully composite Bridge SM-21 under simulated moving HS-20 loading along three two-lane loading paths. Table 5.45 provides the corresponding maximum moment values of each girder for each loading path. The moment LLDF values are calculated using the estimated moment results from

the FEM analysis. Compared to the FEM results, the governing moment LLDF value computed using the approximate equations in the AASHTO Standard Specifications (AASHTO 2002) is slightly conservative for interior girders with a g^m_{AASHTO}/g^m_{FEM} ratio of 1.04, and is quite conservative for exterior girders with a g^m_{AASHTO}/g^m_{FEM} ratio of 1.32.

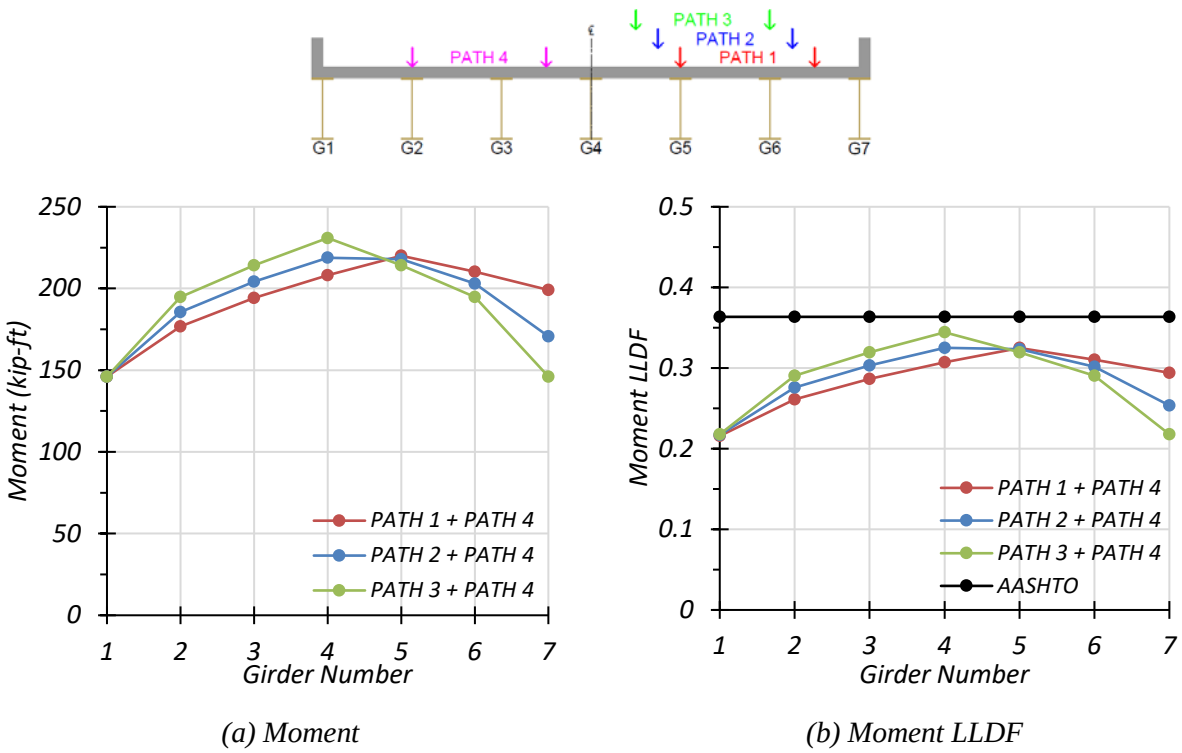

(a) Moment *(b) Moment LLDF*

Figure 5.44. Moment Results for Non-Composite Bridge SM-21 with Two-Lane HS-20 Loading

Table 5.44. Maximum Moments for Non-Composite Bridge SM-21 with Two-Lane HS-20 Loading

Loading	G1	G2	G3	G4	G5	G6	G7
Path 1 + Path 4	146.1	176.8	194.2	208.2	220.0	210.3	199.1
Path 2 + Path 4	146.1	185.6	204.1	218.8	217.8	202.9	170.6
Path 3 + Path 4	146.1	194.8	214.3	230.9	214.3	194.8	146.1
Note: G = girder, paths indicate transverse loading positions as shown, moments have kip-ft units							

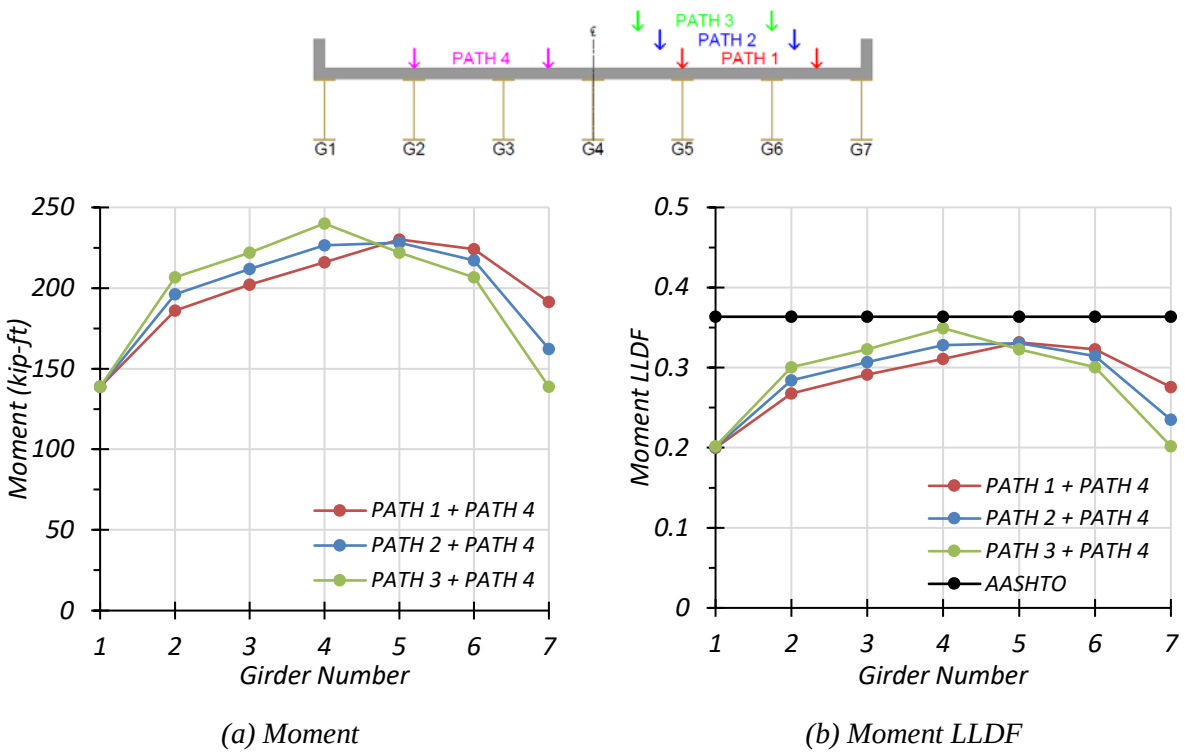

(a) Moment *(b) Moment LLDF*

Figure 5.45. Moment Results for Composite Bridge SM-21 with Two-Lane HS-20 Loading

Table 5.45. Maximum Moments for Composite Bridge SM-21 with Two-Lane HS-20 Loading

Loading	G1	G2	G3	G4	G5	G6	G7
Path 1 + Path 4	138.7	186.0	202.2	215.9	230.1	224.2	191.4
Path 2 + Path 4	138.7	196.1	211.8	226.4	228.1	217.1	162.2
Path 3 + Path 4	138.7	206.6	222.0	240.1	222.0	206.6	138.7
Note: G = girder, paths indicate transverse loading positions as shown, moments have kip-ft units							

Comparison of governing moment LLDF values computed from FEM results for the composite and non-composite cases reveals that the maximum moment LLDF in an interior girder for the composite bridge almost the same as the one for the non-composite bridge with a $g^m_{composite}/g^m_{non-composite}$ ratio of 1.01. Whereas, the maximum moment LLDF in an exterior

girder for the composite bridge is lower than that for the non-composite bridge with a $g^m_{composite}/g^m_{non-composite}$ ratio of 0.94.

Table 5.46. Governing Moment LLDFs for Bridge SM-21 with Two-Lane HS-20 Loading

Type	Girder Location	AASHTO (g^m_{AASHTO})	FEM (g^m_{FEM})	g^m_{AASHTO}/g^m_{FEM}
Non-Composite	Interior	0.364	0.344	1.06
	Exterior	0.364	0.294	1.24
Composite	Interior	0.364	0.349	1.04
	Exterior	0.364	0.276	1.32

5.7.2.3. Shear Results

5.7.2.3.1. One-Lane Loading

Figure 5.46 shows the individual girder shears and shear LLDF results for the non-composite Bridge SM-21 under simulated moving HS-20 loading along three one-lane loading paths. Table 5.47 provides the corresponding maximum shear values of each girder for each loading path. The shear LLDF values are calculated using the estimated shear results from the FEM analysis. Table 5.49 shows the governing shear LLDFs found using the FEM analysis and compares them to the AASHTO LLDF values. Compared to the FEM results, the governing shear LLDF value computed using the approximate equations in the AASHTO Standard Specifications (AASHTO 2002) is almost the same for interior girders with a g^v_{AASHTO}/g^v_{FEM} ratio of approximately 1.00, while being very conservative for exterior girders with a g^v_{AASHTO}/g^v_{FEM} ratio of 1.44.

Figure 5.47 shows the individual girder shears and shear LLDF results for the fully composite Bridge SM-21 under simulated moving HS-20 loading along three one-lane loading

paths. Table 5.48 provides the corresponding maximum shear values of each girder for each loading path. The shear LLDF values are calculated using the estimated shear results from the FEM analysis. Compared to the FEM results, the governing shear LLDF value computed using the approximate equations in the AASHTO Standard Specifications (AASHTO 2002) is slightly unconservative for interior girders with a g^v_{AASHTO}/g^v_{FEM} ratio of 0.91, while being very conservative for exterior girders with a g^v_{AASHTO}/g^v_{FEM} ratio of 1.44.

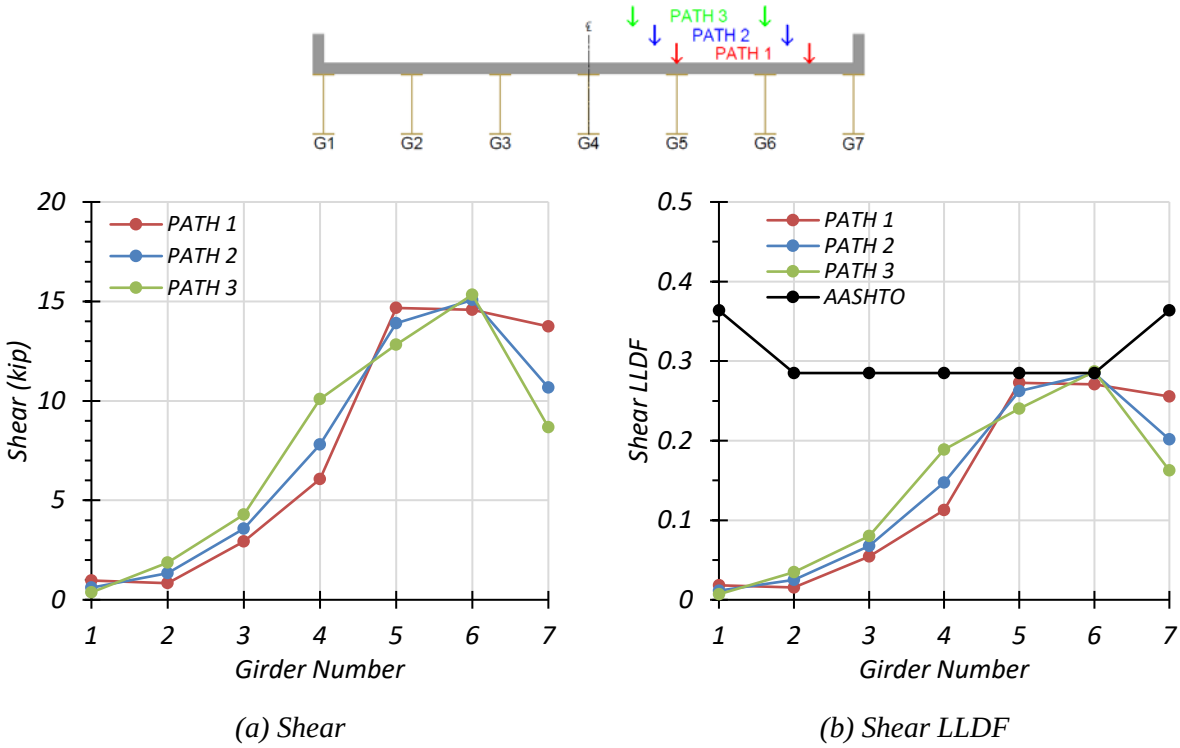

(a) Shear *(b) Shear LLDF*

Figure 5.46. Shear Results for Non-Composite Bridge SM-21 with One-Lane HS-20 Loading

Table 5.47. Maximum Shears for Non-Composite Bridge SM-21 with One-Lane HS-20 Loading

Loading	G1	G2	G3	G4	G5	G6	G7
Path 1	1.4	0.8	2.9	6.1	14.7	14.6	13.7
Path 2	1.0	1.3	3.6	7.8	13.9	15.1	10.7
Path 3	0.6	1.9	4.3	10.1	12.8	15.3	8.7
Note: G = girder, paths indicate transverse loading positions as shown, shears have kip units							

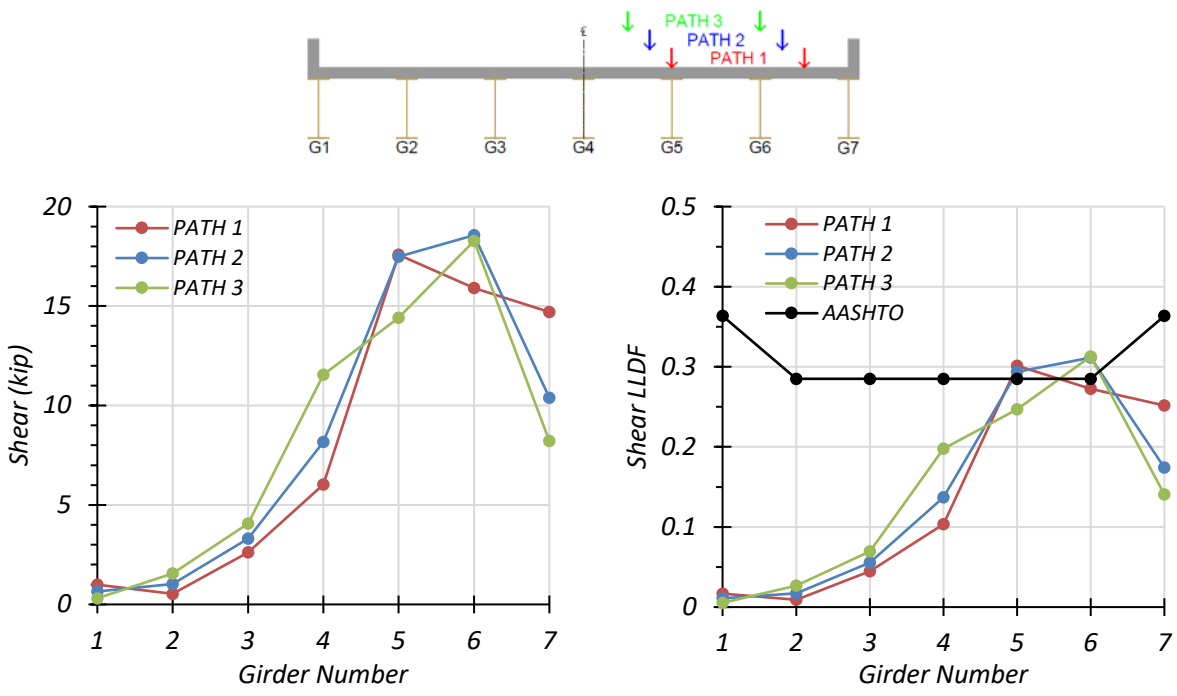

(a) Shear *(b) Shear LLDF*

Figure 5.47. Shear Results for Composite Bridge SM-21 with One-Lane HS-20 Loading

Table 5.48. Maximum Shears for Composite Bridge SM-21 with One-Lane HS-20 Loading

Loading	G1	G2	G3	G4	G5	G6	G7
Path 1	1.0	0.5	2.6	6.0	17.6	15.9	14.7
Path 2	0.7	1.0	3.3	8.2	17.5	18.6	10.4
Path 3	0.4	1.6	4.1	11.6	14.4	18.3	8.2
Note: G = girder, paths indicate transverse loading positions as shown, shears have kip units							

Comparison of governing shear LLDF values computed from FEM results for the composite and non-composite cases reveals that the maximum shear LLDF in an interior girder for the composite bridge is higher than the one for the non-composite bridge with a $g^v_{composite}/g^v_{non-composite}$ ratio of 1.09. Whereas, the maximum shear LLDF in an exterior girder for the composite bridge is about the same as that for the non-composite bridge with a $g^v_{composite}/g^v_{non-composite}$ ratio of 1.00.

Table 5.49. Governing Shear LLDFs for Bridge SM-21 with One-Lane HS-20 Loading

Type	Girder Location	AASHTO (g^v_{AASHTO})	FEM (g^v_{FEM})	g^v_{AASHTO}/g^v_{FEM}
Non-Composite	Interior	0.285	0.286	1.00
	Exterior	0.364	0.253	1.44
Composite	Interior	0.285	0.313	0.91
	Exterior	0.364	0.252	1.44

5.7.2.3.2. Two-Lane Loading

The same procedure was conducted for two-lane loading. Figure 5.48 shows the individual girder shears and shear LLDF results for the non-composite Bridge SM-21 under simulated moving HS-20 loading along three two-lane loading paths. Table 5.50 provides the corresponding maximum shear values of each girder for each loading path. The shear LLDF values are calculated using the estimated shear results from the FEM analysis. Table 5.52 shows the governing shear LLDFs found using the FEM analysis and compares them to the AASHTO LLDF values. Compared to the FEM results, the governing shear LLDF value computed using the approximate equations in the AASHTO Standard Specifications (AASHTO 2002) is slightly unconservative for interior

girders with a g^v_{AASHTO}/g^v_{FEM} ratio of 0.96, while being very conservative for exterior girders with a g^v_{AASHTO}/g^v_{FEM} ratio of 1.40.

Figure 5.49 shows the individual girder shears and shear LLDF results for the fully composite Bridge SM-21 under simulated moving HS-20 loading along three one-lane loading paths. Table 5.51 provides the corresponding maximum shear values of each girder for each loading path. The shear LLDF values are calculated using the estimated shear results from the FEM analysis. Compared to the FEM results, the governing shear LLDF value computed using the approximate equations in the AASHTO Standard Specifications (AASHTO 2002) is slightly unconservative for interior girders with a g^v_{AASHTO}/g^v_{FEM} ratio of 0.91, while being very conservative for exterior girders with a g^v_{AASHTO}/g^v_{FEM} ratio of 1.43.

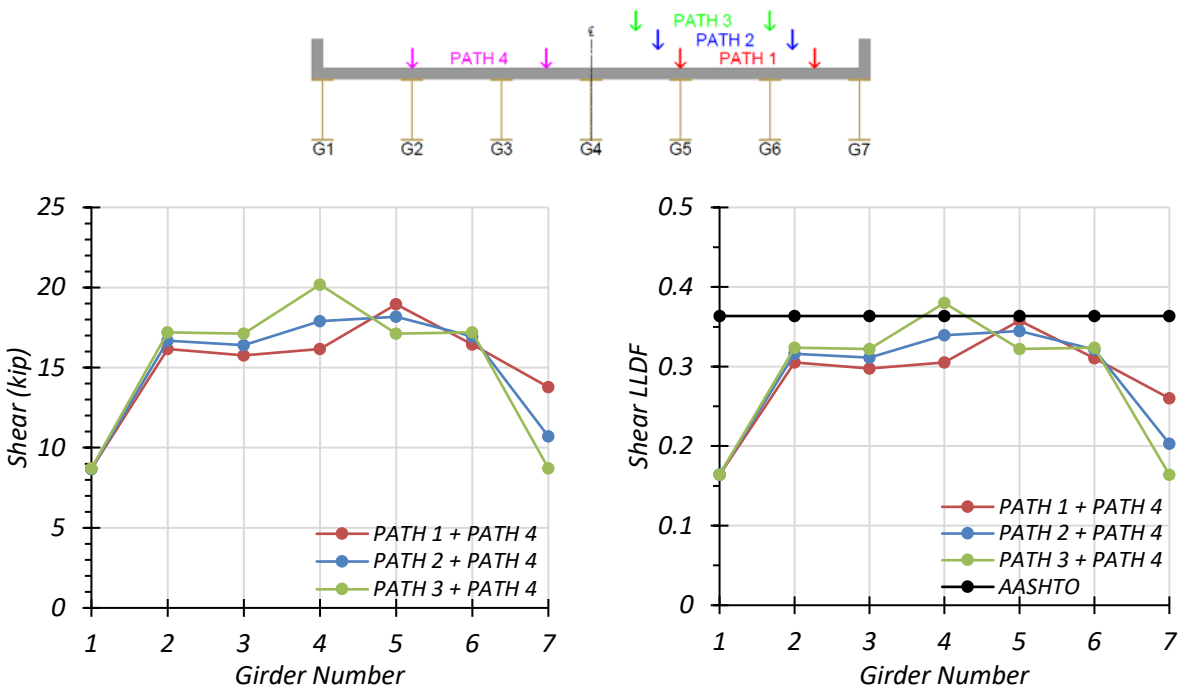

(a) Shear *(b) Shear LLDF*

Figure 5.48. Shear Results for Non-Composite Bridge SM-21 with Two-Lane HS-20 Loading

Table 5.50. Maximum Shears for Non-Composite Bridge SM-21 with Two-Lane HS-20 Loading

Loading	G1	G2	G3	G4	G5	G6	G7
Path 1 + Path 4	8.7	16.2	15.8	16.2	19.0	16.4	13.8
Path 2 + Path 4	8.7	16.7	16.4	17.9	18.2	16.9	10.7
Path 3 + Path 4	8.7	17.2	17.1	20.2	17.1	17.2	8.7
Note: G = girder, paths indicate transverse loading positions as shown, shears have kip units							

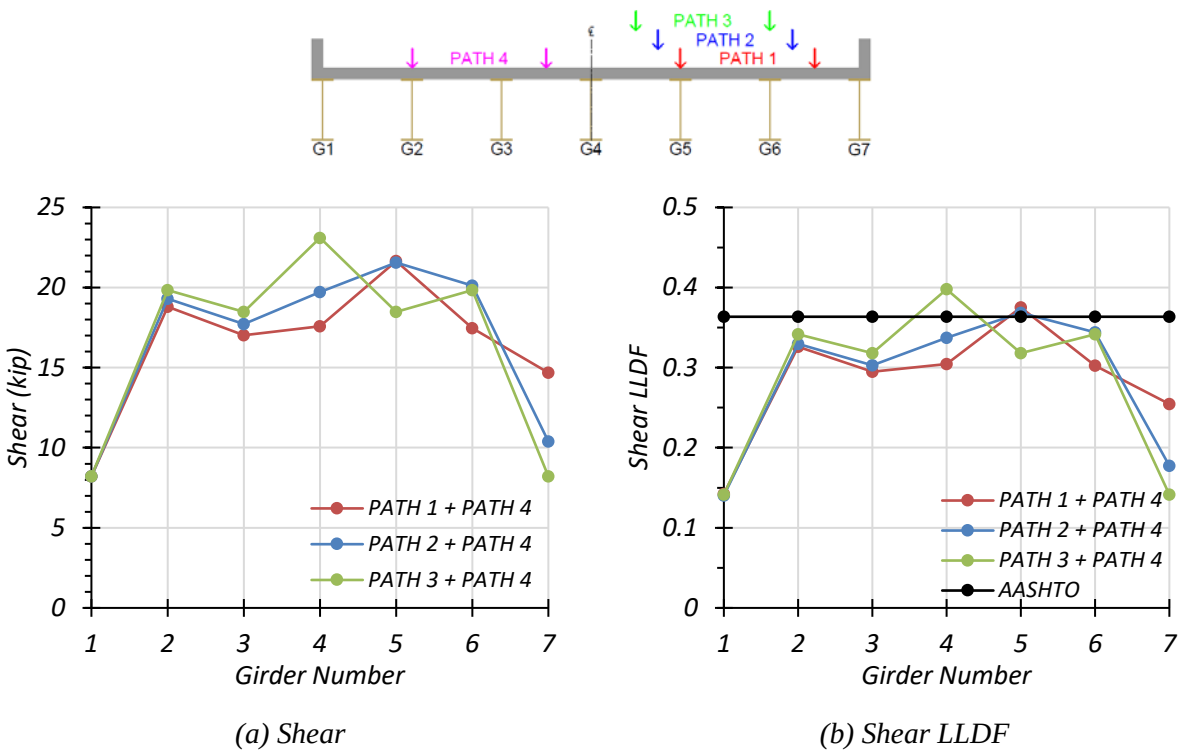

(a) Shear *(b) Shear LLDF*

Figure 5.49. Shear Results for Composite Bridge SM-21 with Two-Lane HS-20 Loading

Table 5.51. Maximum Shears for Composite Bridge SM-21 with Two-Lane HS-20 Loading

Loading	G1	G2	G3	G4	G5	G6	G7
Path 1 + Path 4	8.2	18.8	17.0	17.6	21.6	17.5	14.7
Path 2 + Path 4	8.2	19.3	17.7	19.7	21.6	20.1	10.4
Path 3 + Path 4	8.2	19.8	18.5	23.1	18.5	19.8	8.2
Note: G = girder, paths indicate transverse loading positions as shown, shears have kip units							

Comparison of governing shear LLDF values computed from FEM results for the composite and non-composite cases reveals that the maximum shear LLDF in an interior girder for the composite bridge is higher than the one for the non-composite bridge with a $g^{v}_{composite}/g^{v}_{non-composite}$ ratio of 1.05. Whereas, the maximum shear LLDF in an exterior girder for the composite bridge is almost the same as that for the non-composite bridge with a $g^{v}_{composite}/g^{v}_{non-composite}$ ratio of 0.98.

Table 5.52. Governing Shear LLDFs for Bridge SM-21 with Two-Lane HS-20 Loading

Type	Girder Location	AASHTO (g^v_{AASHTO})	FEM (g^v_{FEM})	g^v_{AASHTO}/g^v_{FEM}
Non-Composite	Interior	0.364	0.380	0.96
	Exterior	0.364	0.260	1.40
Composite	Interior	0.364	0.398	0.91
	Exterior	0.364	0.255	1.43

5.7.3. HL-93 Live Load Analysis

Bridge SM-5 was also analyzed using the HL-93 design loading presented in the AASHTO LRFD Specifications (AASHTO 2017). The bridge was analyzed for one-lane and two-lane-loaded cases along four transverse paths as shown in Figure 5.14. Deflection, moment, and shear results were obtained.

5.7.3.1. Deflection Results

Figure 5.50 shows the estimated girder deflection profiles and contours along the span for one-lane HL-93 loading along Path 1 and Path 4 when the bridge is analyzed as fully non-composite. Table 5.53 shows the corresponding maximum deflections for each girder assuming non-composite action. Load paths 1 and 4 are the only ones shown as these are expected to be the load paths used in future field load tests, as they were selected to maximize the forces on an interior girder and on an exterior girder.

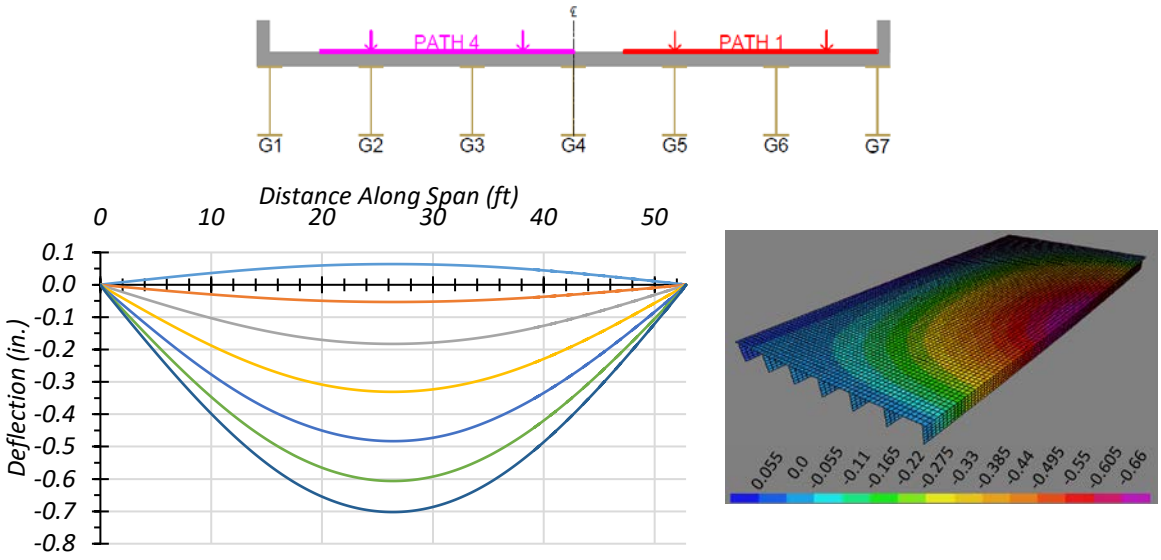

(a) Path 1

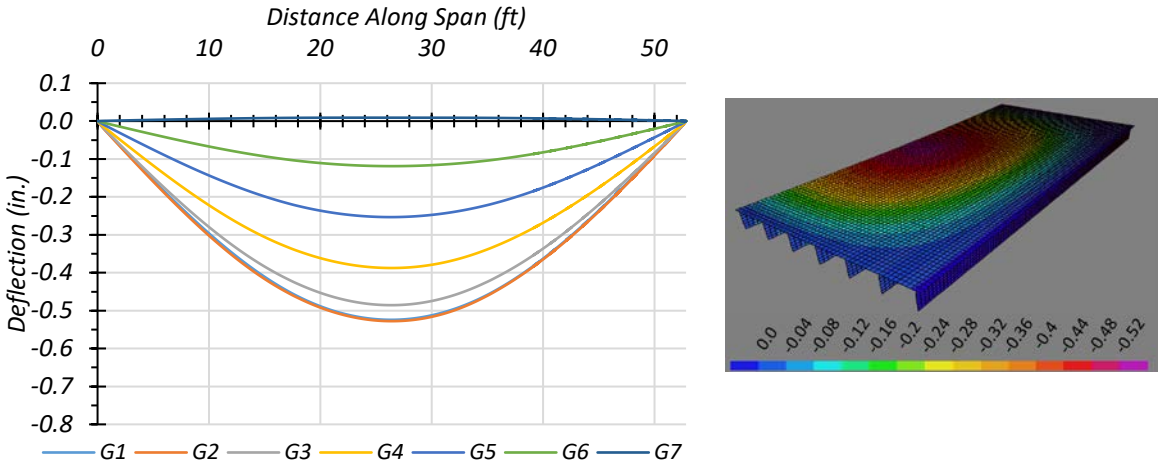

(a) Path 4

Figure 5.50. Deflection Profiles for Non-Composite Bridge SM-21 with HL-93 Loading

Table 5.53. Maximum Deflections for Non-Composite Bridge SM-21 with HL-93 Loading

Loading	G1	G2	G3	G4	G5	G6	G7
Path 1	0.064	-0.053	-0.183	-0.331	-0.483	-0.606	-0.702
Path 4	-0.524	-0.528	-0.486	-0.388	-0.253	-0.119	0.009
Note: G = girder, paths indicate transverse loading positions as shown, deflections have inch units							

Figure 5.51 shows the estimated girder deflection profiles and contours along the span for one-lane HL-93 loading along Path 1 and Path 4 when the bridge is analyzed as fully composite. Table 5.54 shows the corresponding maximum deflections for each girder assuming fully composite action. Load paths 1 and 4 are the only ones shown as these are expected to be the load paths used in future field load tests, as they were selected to maximize the forces on an interior girder and on an exterior girder.

For both non-composite and composite cases, the maximum deflections were obtained in Girder 7 when the HL-93 truck was run along Path 1. The estimated deflections were 0.702 in. and 0.400 in. for the non-composite and composite cases, respectively. This result indicates that the composite bridge is 54.8 percent stiffer than the non-composite bridge. The maximum deflections obtained when the HL-93 truck was run along Path 4 were in Girder 1 for both the non-composite and composite case. The estimated deflections were 0.524 in. and 0.302 in. for the non-composite and composite cases, respectively. This result indicates that the composite bridge is 50.1 percent stiffer than the non-composite bridge. The slightly different values of relative stiffness suggest that the relative girder deflection depends on the location of loading and corresponding load distribution.

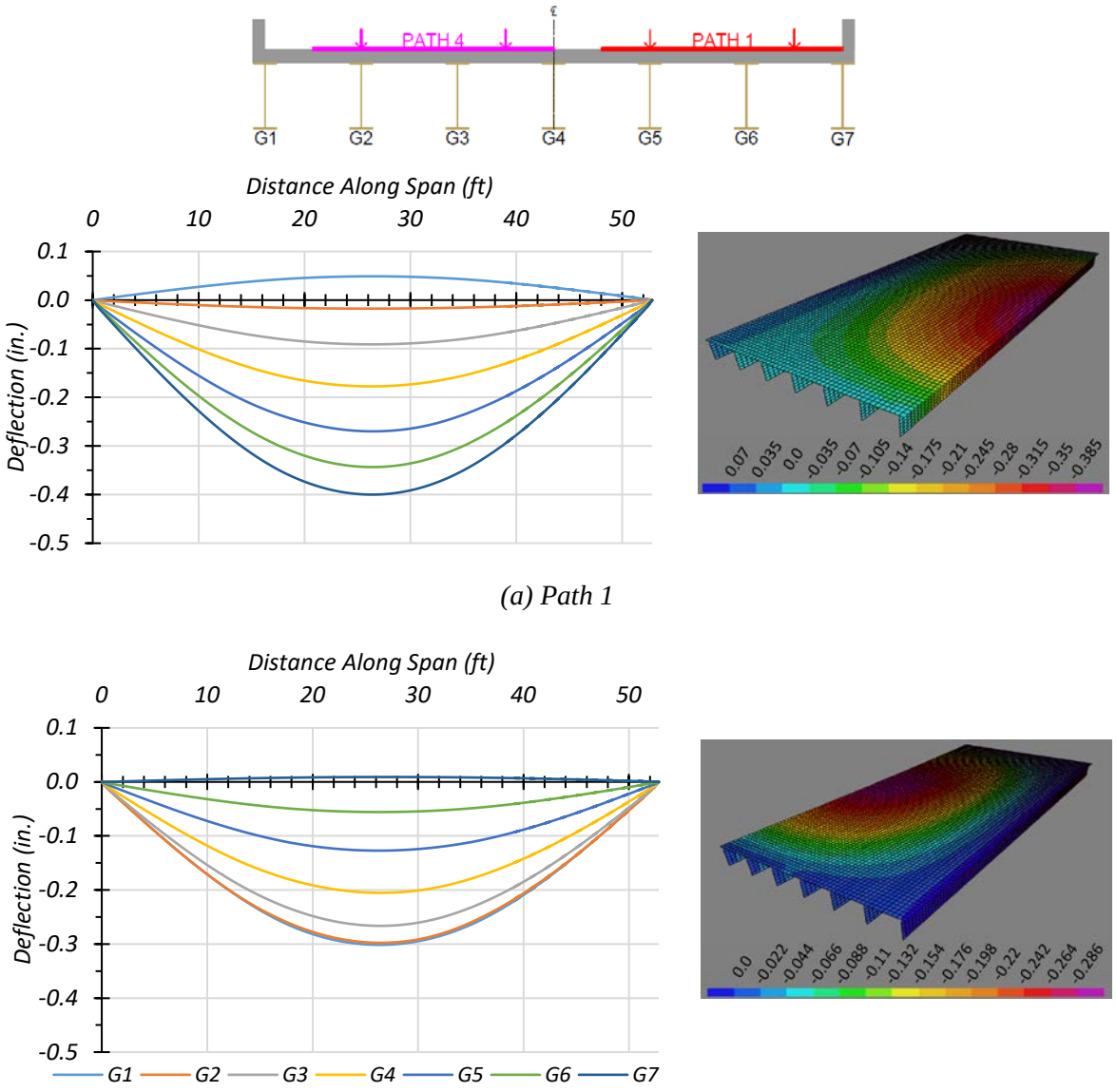

(a) Path 1

(b) Path 4

Figure 5.51. Deflection Profiles for Composite Bridge SM-21 with HL-93 Loading

Table 5.54. Maximum Deflections for Composite Bridge SM-21 with HL-93 Loading

Loading	G1	G2	G3	G4	G5	G6	G7
Path 1	0.049	-0.017	-0.091	-0.177	-0.270	-0.343	-0.400
Path 4	-0.302	-0.298	-0.266	-0.205	-0.127	-0.056	0.009
Note: G = girder, paths indicate transverse loading positions as shown, deflections have inch units							

5.7.3.2. Moment Results

5.7.3.2.1. One-Lane Loading

Figure 5.52 shows the individual girder moments and moment LLDF results for the non-composite Bridge SM-21 under simulated moving HL-93 loading along three one-lane loading paths. Table 5.55 provides the corresponding maximum moment values of each girder for each loading path. The moment LLDF values are calculated using the estimated moment results from the FEM analysis. Table 5.57 shows the governing moment LLDFs found using the FEM analysis and compares them to the AASHTO LLDF values. The first AASHTO LLDF value is calculated using the simplified stiffness parameter. The second AASHTO LLDF value is calculated using the analytical stiffness parameter calculated for the specific bridge. Compared to the FEM results, the governing moment LLDF value computed using the approximate equations and the simplified stiffness parameter in AASHTO LRFD Specifications (AASHTO 2017) is conservative for interior girders with a $g^m_{AASHTO\_S}/g^m_{FEM}$ ratio of 1.11, and is also conservative for exterior girders with a $g^m_{AASHTO\_S}/g^m_{FEM}$ ratio of 1.10. Compared to the FEM results, the governing moment LLDF value computed using the approximate equations and the analytical stiffness parameter in AASHTO LRFD Specifications (AASHTO 2017) is conservative for both interior and exterior girders with a $g^m_{AASHTO\_K}/g^m_{FEM}$ ratio of 1.13 and 1.12, respectively.

Figure 5.53 shows the individual girder moments and moment LLDF results for the fully composite Bridge SM-21 under simulated moving HL-93 loading along three one-lane loading paths. Table 5.56 provides the corresponding maximum moment values of each girder for each loading path. The moment LLDF values are calculated using the estimated moment results from the FEM analysis. Compared to the FEM results, the governing moment LLDF value computed

using the approximate equations and the simplified stiffness parameter in AASHTO LRFD Specifications (AASHTO 2017) is slightly conservative for both interior and exterior girders with a $g^m_{AASHTO\_S}/g^m_{FEM}$ ratio of 1.04 and 1.06, respectively. Compared to the FEM results, the governing moment LLDF value computed using the approximate equations and the analytical stiffness parameter in AASHTO LRFD Specifications (AASHTO 2017) is slightly conservative for both interior and exterior girders with a $g^m_{AASHTO\_K}/g^m_{FEM}$ ratio of 1.06 and 1.08, respectively.

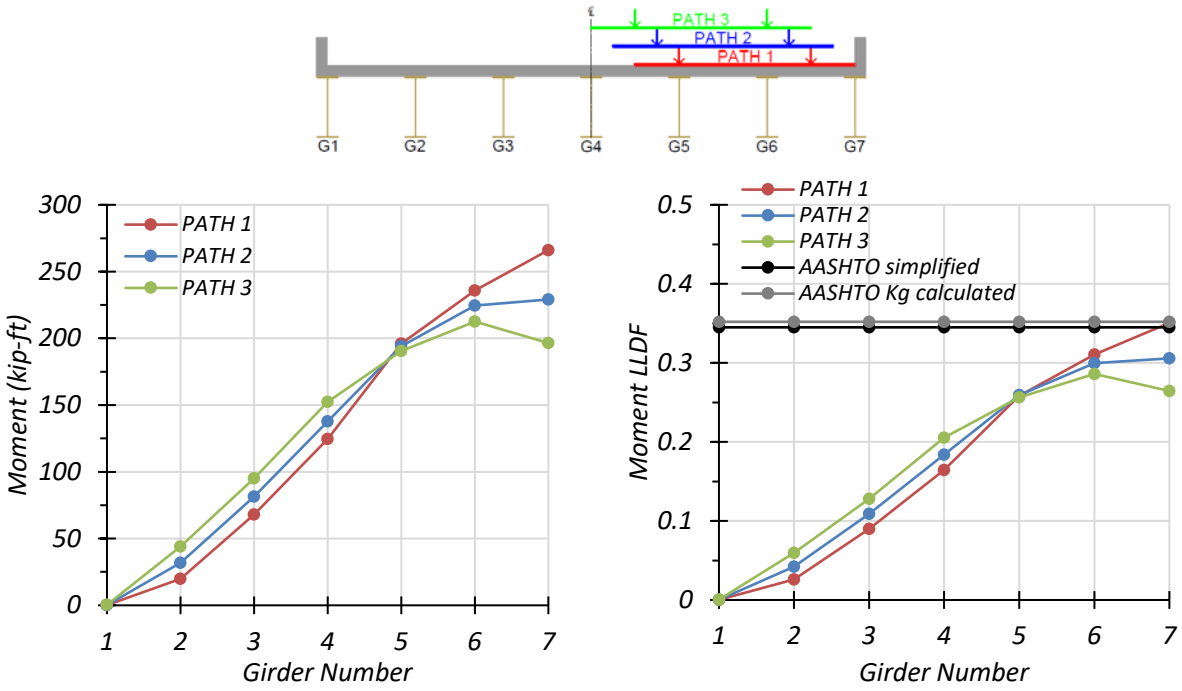

(a) Moment *(b) Moment LLDF*

Figure 5.52. Moment Results for Non-Composite Bridge SM-21 with One-Lane HL-93 Loading

Table 5.55. Maximum Moments for Non-Composite Bridge SM-21 with One-Lane HL-93 Loading

Loading	G1	G2	G3	G4	G5	G6	G7
Path 1	0.2	19.8	68.1	124.7	196.0	235.8	266.1
Path 2	0.4	44.2	95.1	152.5	190.5	212.5	196.5
Path 3	0.2	31.7	81.5	137.8	194.1	224.7	229.1
Note: G = girder, paths indicate transverse loading positions as shown, moments have kip-ft units							

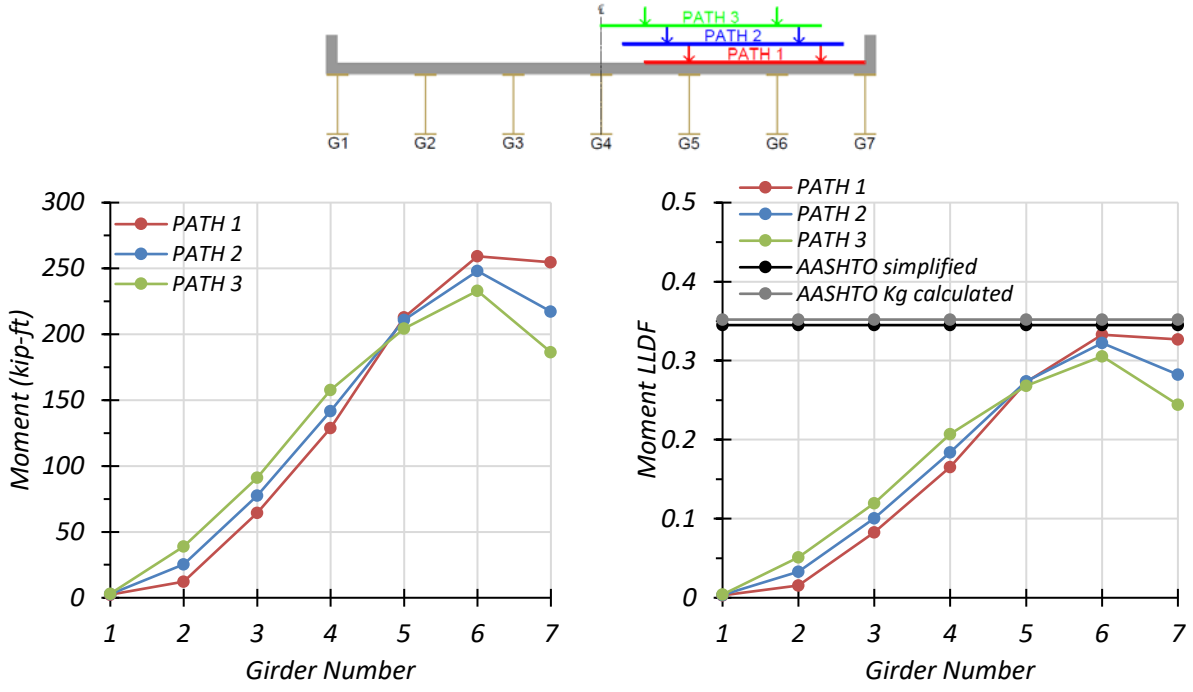

(a) Moment *(b) Moment LLDF*

Figure 5.53. Moment Results for Composite Bridge SM-21 with One-Lane HL-93 Loading

Table 5.56. Maximum Moments for Composite Bridge SM-21 with One-Lane HL-93 Loading

Loading	G1	G2	G3	G4	G5	G6	G7
Path 1	2.4	12.2	64.5	128.9	212.8	259.2	254.7
Path 2	2.8	25.2	77.6	141.7	210.9	248.1	217.3
Path 3	3.1	39.0	91.2	157.8	204.4	233.0	186.4
Note: G = girder, paths indicate transverse loading positions as shown, moments have kip-ft units							

Comparison of governing moment LLDF values computed from FEM results for the composite and non-composite cases reveals that the maximum moment LLDF in an interior girder for the composite bridge is higher than the one for the non-composite bridge with a $g^m_{composite}/g^m_{non-composite}$ ratio of 1.07. The maximum moment LLDF in an exterior girder for the composite bridge is also higher than that for the non-composite bridge with a $g^m_{composite}/g^m_{non-composite}$ ratio of 1.04.

Table 5.57. Governing Moment LLDFs for Bridge SM-21 with One-Lane HL-93 Loading

Type	Girder Location	AASHTO Simplified ($g^m_{AASHTO\_S}$)	AASHTO K_g Calculated ($g^m_{AASHTO\_K}$)	FEM (g^m_{FEM})	$g^m_{AASHTO\_S}/g^m_{FEM}$	$g^m_{AASHTO\_K}/g^m_{FEM}$
Non-Composite	Interior	0.345	0.352	0.311	1.11	1.13
	Exterior	0.345	0.352	0.315	1.10	1.12
Composite	Interior	0.345	0.352	0.333	1.04	1.06
	Exterior	0.345	0.352	0.327	1.06	1.08

5.7.3.2.2. Two-Lane Loading

Figure 5.54 shows the individual girder moments and moment LLDF results for the non-composite Bridge SM-21 under simulated moving HL-93 loading along three two-lane loading paths. Table 5.58 provides the corresponding maximum moment values of each girder for each loading path. The moment LLDF values are calculated using the estimated moment results from the FEM analysis. Table 5.60 shows the governing moment LLDFs found using the FEM analysis and compares them to the AASHTO LLDF values. The first AASHTO LLDF value is calculated using the simplified stiffness parameter. The second AASHTO LLDF value is calculated using the analytical stiffness parameter calculated for the specific bridge. Compared to the FEM results, the

governing moment LLDF value computed using the approximate equations and the simplified stiffness parameter in AASHTO LRFD Specifications (AASHTO 2017) is conservative for interior girders with a $g^m_{AASHTO\_S}/g^m_{FEM}$ ratio of 1.27, and is quite conservative for exterior girders with a g^m_{AASHTO}/g^m_{FEM} ratio of 1.48. Compared to the FEM results, the governing moment LLDF value computed using the approximate equations and the analytical stiffness parameter in AASHTO LRFD Specifications (AASHTO 2017) is quite conservative for both interior and exterior girders with a $g^m_{AASHTO\_K}/g^m_{FEM}$ ratio of 1.30 and 1.51, respectively.

Figure 5.55 shows the individual girder moments and moment LLDF results for the fully composite Bridge SM-21 under simulated moving HL-93 loading along three two-lane loading paths. Table 5.59 provides the corresponding maximum moment values of each girder for each loading path. The moment LLDF values are calculated using the estimated moment results from the FEM analysis. Compared to the FEM results, the governing moment LLDF value computed using the approximate equations and the simplified stiffness parameter in AASHTO LRFD Specifications (AASHTO 2017) is conservative for interior girders with a $g^m_{AASHTO\_S}/g^m_{FEM}$ ratio of 1.26, and is quite conservative for exterior girders with a g^m_{AASHTO}/g^m_{FEM} ratio of 1.58. Compared to the FEM results, the governing moment LLDF value computed using the approximate equations and the analytical stiffness parameter in AASHTO LRFD Specifications (AASHTO 2017) is conservative for interior girders with a $g^m_{AASHTO\_K}/g^m_{FEM}$ ratio of 1.29, and is quite conservative for exterior girders with a g^m_{AASHTO}/g^m_{FEM} ratio of 1.61.

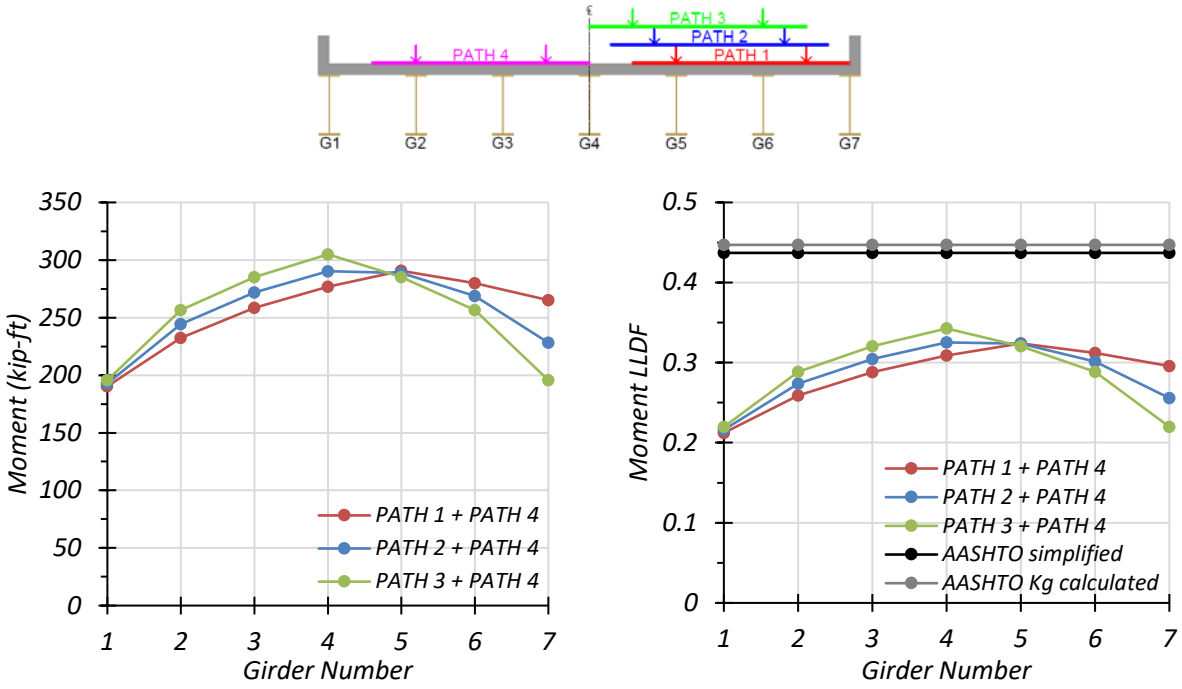

(a) Moment *(b) Moment LLDF*

Figure 5.54. Moment Results for Non-Composite Bridge SM-21 with Two-Lane HL-93 Loading

Table 5.58. Maximum Moments for Non-Composite Bridge SM-21 with Two-Lane HL-93 Loading

Loading	G1	G2	G3	G4	G5	G6	G7
Path 1 + Path 4	190.4	232.3	258.5	276.9	290.6	279.9	265.3
Path 2 + Path 4	192.9	244.2	271.8	290.3	288.8	268.8	228.3
Path 3 + Path 4	195.7	256.6	285.2	305.0	285.2	256.6	195.7
Note: G = girder, paths indicate transverse loading positions as shown, moments have kip-ft units							

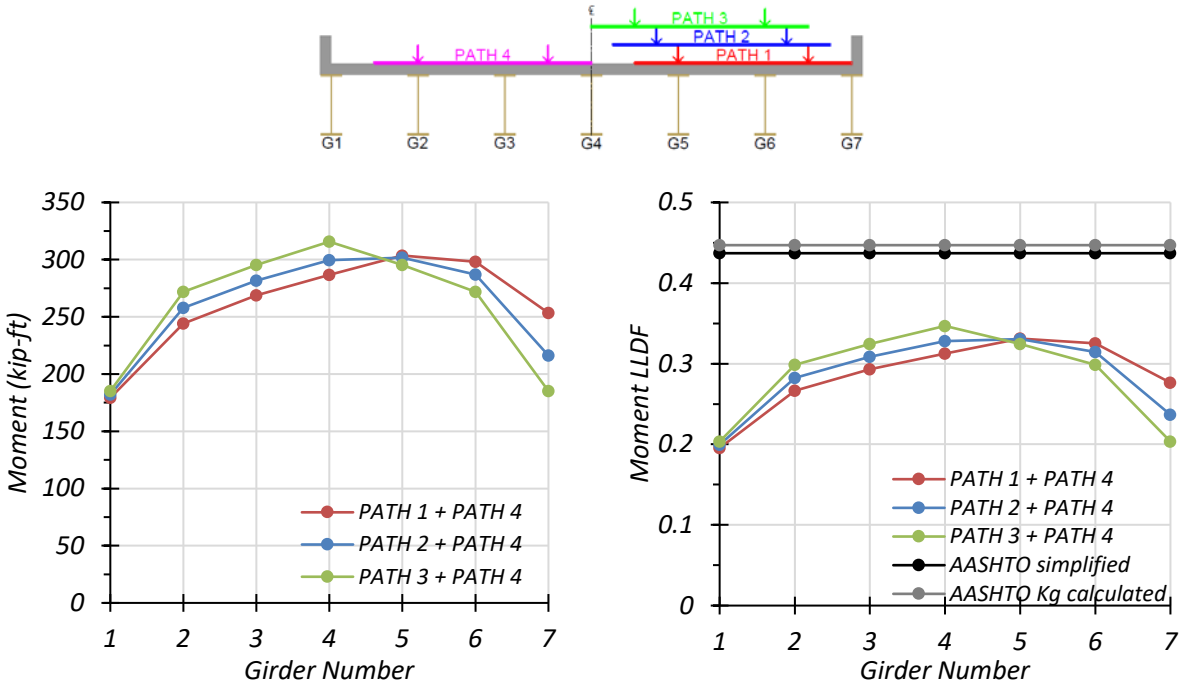

(a) Moment *(b) Moment LLDF*

Figure 5.55. Moment Results for Composite Bridge SM-21 with Two-Lane HL-93 Loading

Table 5.59. Maximum Moments for Composite Bridge SM-21 with Two-Lane HL-93 Loading

Loading	G1	G2	G3	G4	G5	G6	G7
Path 1 + Path 4	179.2	244.2	268.7	286.6	303.6	298.1	253.5
Path 2 + Path 4	182.1	257.8	281.7	299.5	301.7	287.0	216.2
Path 3 + Path 4	185.2	271.9	295.3	315.7	295.3	271.9	185.2
Note: G = girder, paths indicate transverse loading positions as shown, moments have kip-ft units							

Comparison of governing moment LLDF values computed from FEM results for the composite and non-composite cases reveals that the maximum moment LLDF in an interior girder for the composite bridge is almost the same as the one for the non-composite bridge with a $g^m_{composite}/g^m_{non-composite}$ ratio of 1.01. Whereas, the maximum moment LLDF in an exterior

girder for the composite bridge is lower than that for the non-composite bridge with a $g^m_{composite}/g^m_{non-composite}$ ratio of 0.96.

Table 5.60. Governing Moment LLDFs for Bridge SM-21 with Two-Lane HL-93 Loading

Type	Girder Location	AASHTO Simplified ($g^m_{AASHTO\_S}$)	AASHTO K_g Calculated ($g^m_{AASHTO\_K}$)	FEM (g^m_{FEM})	$g^m_{AASHTO\_S}/g^m_{FEM}$	$g^m_{AASHTO\_K}/g^m_{FEM}$
Non-Composite	Interior	0.437	0.447	0.343	1.27	1.30
	Exterior	0.437	0.447	0.296	1.48	1.51
Composite	Interior	0.437	0.447	0.347	1.26	1.29
	Exterior	0.437	0.447	0.277	1.58	1.61

5.7.3.3. Shear Results

5.7.3.3.1. One-Lane Loading

Figure 5.56 shows the individual girder shears and shear LLDF results for the non-composite Bridge SM-5 under simulated moving HL-93 loading along three one-lane loading paths. Table 5.61 provides the corresponding maximum shear values of each girder for each loading path. The shear LLDF values are calculated using the estimated shear results from the FEM analysis. Table 5.63 shows the governing shear LLDFs found using the FEM analysis and compares them to the AASHTO LLDF values. Compared to the FEM results, the governing shear LLDF value computed using the approximate equations in AASHTO LRFD Specifications (AASHTO 2017) is quite conservative for both interior and exterior girders with a g^v_{AASHTO}/g^v_{FEM} ratio of 1.57 and 1.68, respectively.

Figure 5.57 shows the individual girder shears and shear LLDF results for the fully composite Bridge SM-21 under simulated moving HL-93 loading along three one-lane loading

paths. Table 5.62 provides the corresponding maximum shear values of each girder for each loading path. The shear LLDF values are calculated using the estimated shear results from the FEM analysis. Compared to the FEM results, the governing shear LLDF value computed using the approximate equations in AASHTO LRFD Specifications (AASHTO 2017) is quite conservative for both interior and exterior girders with a $g^{v}_{AASHTO}/g^{v}_{FEM}$ ratio of 1.43 and 1.69, respectively.

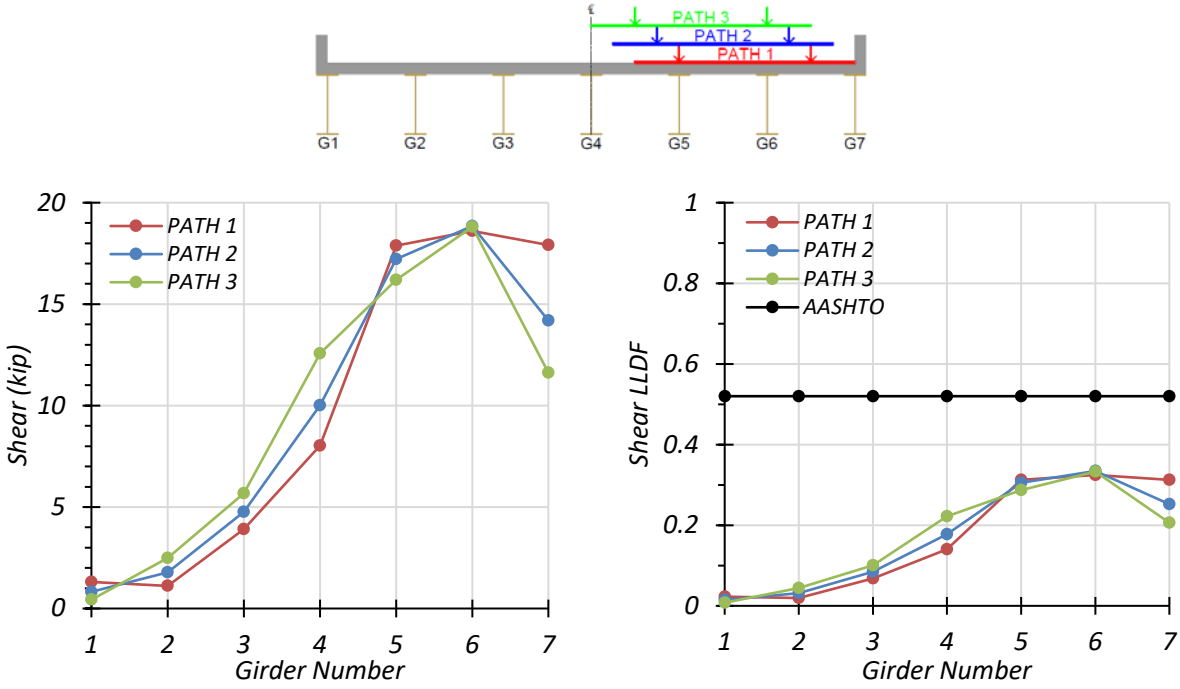

(a) Shear *(b) Shear LLDF*

Figure 5.56. Shear Results for Non-Composite Bridge SM-21 with One-Lane HL-93 Loading

Table 5.61. Maximum Shears for Non-Composite Bridge SM-21 with One-Lane HL-93 Loading

Loading	G1	G2	G3	G4	G5	G6	G7
Path 1	1.9	1.1	3.9	8.0	17.9	18.6	17.9
Path 2	0.8	2.5	5.7	12.6	16.2	18.8	11.6
Path 3	1.4	1.8	4.8	10.0	17.2	18.9	14.2
Note: G = girder, paths indicate transverse loading positions as shown, shears have kip units							

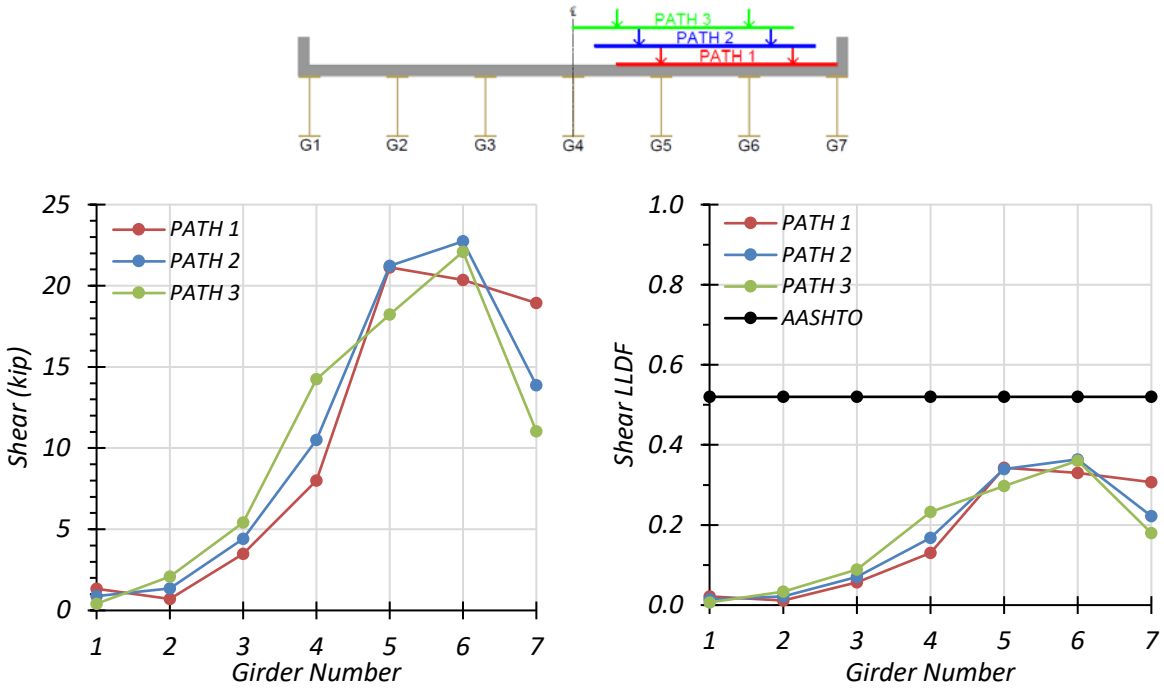

(a) Shear *(b) Shear LLDF*

Figure 5.57. Shear Results for Composite Bridge SM-21 with One-Lane HL-93 Loading

Table 5.62. Maximum Shears for Composite Bridge SM-21 with One-Lane HL-93 Loading

Loading	G1	G2	G3	G4	G5	G6	G7
Path 1	1.3	0.7	3.5	8.0	21.1	20.4	18.9
Path 2	0.9	1.4	4.4	10.5	21.2	22.7	13.9
Path 3	0.4	2.1	5.4	14.2	18.2	22.1	11.0
Note: G = girder, paths indicate transverse loading positions as shown, shears have kip units							

Comparison of governing shear LLDF values computed from FEM results for the composite and non-composite cases reveals that the maximum shear LLDF in an interior girder for the composite bridge is higher than the one for the non-composite bridge with a $g^v_{composite}/g^v_{non-composite}$ ratio of 1.10. Whereas, the maximum shear LLDF in an exterior girder for the composite bridge is almost the same as that for the non-composite bridge with a $g^v_{composite}/g^v_{non-composite}$ ratio of 0.99.

Table 5.63. Governing Shear LLDFs for Bridge SM-21 with One-Lane HL-93 Loading

Type	Girder Location	AASHTO (g^v_{AASHTO})	FEM (g^v_{FEM})	g^v_{AASHTO}/g^v_{FEM}
Non-Composite	Interior	0.520	0.332	1.57
	Exterior	0.520	0.310	1.68
Composite	Interior	0.520	0.364	1.43
	Exterior	0.520	0.307	1.69

5.7.3.3.2. Two-Lane Loading

The same procedure was conducted for two-lane loading. Figure 5.58 shows the individual girder shears and shear LLDF results for the non-composite Bridge SM-21 under simulated moving HL-93 loading along three two-lane loading paths. Table 5.64 provides the corresponding maximum shear values of each girder for each loading path. The shear LLDF values are calculated using the estimated shear results from the FEM analysis. Table 5.66 shows the governing shear LLDFs found using the FEM analysis and compares them to the AASHTO LLDF values. Compared to the FEM results, the governing shear LLDF value computed using the approximate equations in AASHTO LRFD Specifications (AASHTO 2017) is quite conservative for both interior and exterior girders with a g^v_{AASHTO}/g^v_{FEM} ratio of 1.39 and 1.95, respectively.

Figure 5.59 shows the individual girder shears and shear LLDF results for the fully composite Bridge SM-21 under simulated moving HL-93 loading along three one-lane loading paths. Table 5.65 provides the corresponding maximum shear values of each girder for each loading path. The shear LLDF values are calculated using the estimated shear results from the FEM analysis. Compared to the FEM results, the governing shear LLDF value computed using the approximate equations in AASHTO LRFD Specifications (AASHTO 2017) is quite conservative for both interior and exterior girders with a g^v_{AASHTO}/g^v_{FEM} ratio of 1.33 and 2.01, respectively.

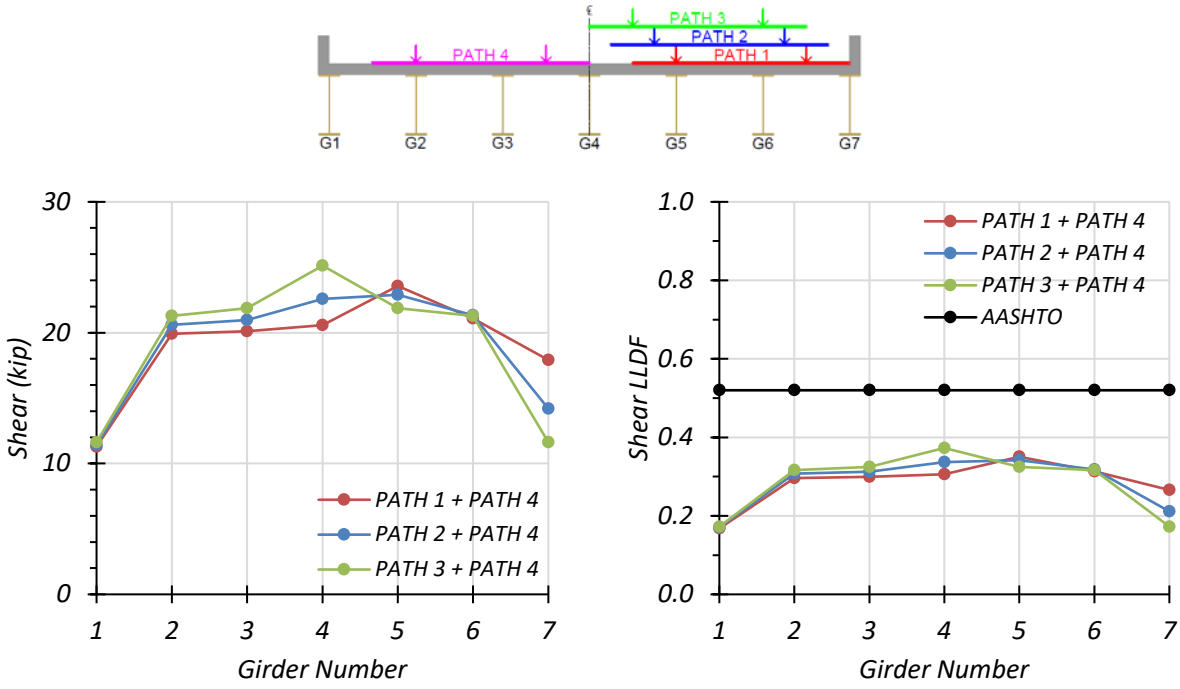

(a) Shear *(b) Shear LLDF*

Figure 5.58. Shear Results for Non-Composite Bridge SM-21 with Two-Lane HL-93 Loading

Table 5.64. Maximum Shears for Non-Composite Bridge SM-21 with Two-Lane HL-93 Loading

Loading	G1	G2	G3	G4	G5	G6	G7
Path 1 + Path 4	11.3	19.9	20.1	20.6	23.6	21.1	17.9
Path 2 + Path 4	11.4	20.6	21.0	22.6	22.9	21.3	14.2
Path 3 + Path 4	11.6	21.3	21.9	25.1	21.9	21.3	11.6
Note: G = girder, paths indicate transverse loading positions as shown, shears have kip units							

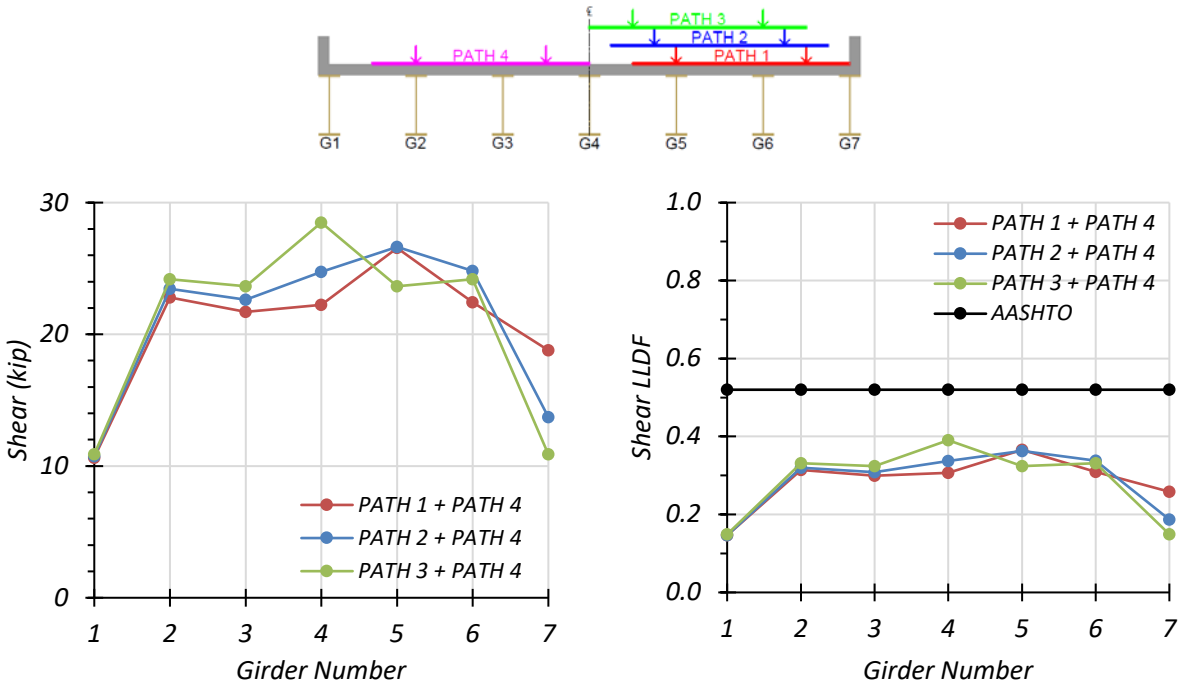

(a) Shear *(b) Shear LLDF*

Figure 5.59. Shear Results for Composite Bridge SM-21 with Two-Lane HL-93 Loading

Table 5.65. Maximum Shears for Composite Bridge SM-21 with Two-Lane HL-93 Loading

Loading	G1	G2	G3	G4	G5	G6	G7
Path 1 + Path 4	10.6	22.8	21.7	22.2	26.6	22.4	18.8
Path 2 + Path 4	10.8	23.5	22.6	24.7	26.6	24.8	13.7
Path 3 + Path 4	10.9	24.2	23.6	28.5	23.6	24.2	10.9
Note: G = girder, paths indicate transverse loading positions as shown, shears have kip units							

Comparison of governing shear LLDF values computed from FEM results for the composite and non-composite cases reveals that the maximum shear LLDF in an interior girder for the composite bridge is higher than the one for the non-composite bridge with a $g^v_{composite}/g^v_{non-composite}$ ratio of 1.05. Whereas, the maximum shear LLDF in an exterior girder for the composite bridge is slightly lower than that for the non-composite bridge with a $g^v_{composite}/g^v_{non-composite}$ ratio of 0.97.

Table 5.66. Governing Shear LLDFs for Bridge SM-21 with Two-Lane HL-93 Loading

Type	Girder Location	AASHTO (g^v_{AASHTO})	FEM (g^v_{FEM})	g^v_{AASHTO}/g^v_{FEM}
Non-Composite	Interior	0.520	0.373	1.39
	Exterior	0.520	0.266	1.95
Composite	Interior	0.520	0.390	1.33
	Exterior	0.520	0.259	2.01

5.8. CONCLUSIONS

5.8.1. Live Load Distribution Factors

5.8.1.1. AASHTO Standard Specification LLDFs

The FEM analysis of the selected simple-span steel multi-girder bridges has shown that, in general, the current LLDF equations given in the AASHTO Standard Specifications (AASHTO 2002) provide accurate, slightly conservative LLDF values in flexure for the selected bridges. The g_{AASHTO}/g_{FEM} ratio for flexure ranges from 0.80 to 1.34, however in most cases it is slightly above 1.0. This result will likely not significantly affect the rating of this bridge type.

Meanwhile, for the shear LLDF values obtained from the FEM analysis, the g_{AASHTO}/g_{FEM} ratio for shear ranges from 0.59 to 1.44, producing a larger variation in results. In order to better capture the wide range, the shear LLDFs could be changed, however, the shear RFs for the larger group of selected bridges are already quite high, as shown in Technical Memorandum 3, and changing the LLDF is not expected to significantly change RFs and corresponding load postings.

5.8.1.2. AASHTO LRFD Specification LLDFs

The FEM analysis of the selected simple-span steel multi-girder bridges has shown that, in general, the current LLDF equations given in the AASHTO LRFD Specifications (AASHTO 2017) provide conservative, with some variability in accuracy, LLDF values in flexure for the selected bridges. The g_{AASHTO}/g_{FEM} ratio for flexure using the simplified stiffness parameter ranges from 1.04 to 1.80, and in every case is above 1.0. The g_{AASHTO}/g_{FEM} ratio for flexure using the calculated stiffness parameter ranges from 1.05 to 1.61, and in every case is above 1.0. These LLDFs are accurate and only slightly conservative for one-lane loaded cases. However, for two-lane loaded cases they are significantly conservative. Using more accurate LLDFs for two-lane HL-93 loading cases would likely help increase LRFR ratings.

For the shear LLDF values obtained from the FEM analysis, the g_{AASHTO}/g_{FEM} ratio for shear ranges from 1.31 to 3.24, again producing very conservative results. As with the LRFD flexure LLDFs, the shear LLDFs could be modified in order to improve the LRFR shear RFs of bridges.

5.8.2. Composite Action

When examining the effect of analyzing the bridge as fully composite or fully non-composite on the LLDFs, the FEM analysis did not find a significant difference. For the most part, the LLDFs found were very similar, however, the non-composite bridge seemed to produce more uniform LLDF profiles across the bridge transverse section.

When examining HS-20 loading, the $g_{composite}/g_{non-composite}$ ratio for flexure ranged from 0.92 to 1.12 and the $g_{composite}/g_{non-composite}$ ratio for shear ranged from 0.86 to 1.28. The $g_{composite}/g_{non-composite}$ ratio for an interior girder was always above 1.0, while it was always below 1.0 for an exterior girder except for in one case, one-lane shear for Bridge SM-21.

When examining HL-93 loading, the $g_{composite}/g_{non-composite}$ ratio for flexure ranged from 0.93 to 1.12 and the $g_{composite}/g_{non-composite}$ ratio for shear ranged from 0.84 to 1.25. The $g_{composite}/g_{non-composite}$ ratio for an interior girder was always above 1.0, while it was always below 1.0 for an exterior girder except in one case, one-lane flexure for Bridge SM-21. Between the HS-20 loading and the HL-93 loading, the ratios did not significantly change for the same number of lanes loaded and force being examined.

In terms of LLDFs, composite action does not seem to have a major effect, however, it is known that composite action or partial composite action significantly affects the capacity of the bridge. This was noticed in the FEM analysis through the stress values computed for the girders. The effect of partial composite action on load rating will be further explored in the next task, where any partial composite measured during field testing will be used to help calibrate the FEM models, which will be used to develop a more refined load rating of the bridge.

5.8.3. End Fixity

During the FEM modeling process, it was noted that partial fixity springs can be added to the girder supports in the model. If any partial fixity is measured during the field testing to take place during the next task, it will be accounted for in the calibrated model. Partial end fixity would help improve the load rating by reducing the applied positive moment in the span.

5.8.4. Additional Comments

Additional results from the FEM modeling will be used to calibrate the FEM model after field testing is complete. The results presented in this report for deflections and dynamic characteristics will be compared to those found in the field to determine if the girders are acting compositely or non-compositely.

6. FEM ANALYSIS OF A CONTINUOUS STEEL MULTI-GIRDER BRIDGE

In the previous tasks a detailed review and synthesis of the population of load-posted bridges in Texas was conducted, and 16 continuous steel multi-girder bridges were selected from the inventory of SSLO continuous steel multi-girder bridges in Texas for basic load rating evaluation. This basic load rating analysis helped identify several areas of opportunity for refined load rating analysis. The refined load rating analysis used in this study investigated the effect of the identified parameters using three-dimensional finite element models that can more accurately capture the bridge behavior. The main objectives of FEM analysis of the continuous steel multi-girder bridge can be summarized as: (1) create a model of the bridge superstructure that can more accurately predict the live load distribution, (2) investigate the effect of partial composite action on the load distribution behavior of the bridge under service loads, and (3) evaluate the effect of deck cracking over the negative moment region.

6.1. INTRODUCTION

A typical load posted continuous steel multi-girder (SC) bridge was selected as a representative structure of this type to further investigate the identified objectives. Table 6.1 lists some of the key parameters for the selected continuous steel multi-girder bridge (SC-12), and for the average SSLO continuous steel multi-girder bridge in Texas. In this table, the *Operating HS-20 RF* represents the multiple of HS-20 truck loads that is the absolute maximum load that can safely travel on the bridge. The posting evaluation represents the degree to which the operating rating of the bridge is below the maximum legal load.

A three-dimensional linear FEM model was developed using the commercial software package CSiBridge (Computers and Structures 2019), which has the capability to model and analyze complex bridge superstructures while also providing user-friendly pre- and post-processing tools for bridge structures. The following sections provide the geometric and material properties of the selected continuous steel multi-girder bridge, describe the FEM modeling approach, and summarize the analysis results.

Table 6.1. Selected SSLO SC Bridge and Average Characteristics (Data from NBI 2016)

ID	Route Prefix	Year Built	ADT	Max. Span Length (ft)	Deck Width (ft)	Condition Rating			Operating HS-20 Rating Factor	Posting Eval.
						Deck	Super-structure	Sub-structure		
Avg.	-	1962	-	25	20	6	6	6	0.85	3
SC-12	3	1959	260	75	26	6	7	7	0.88	4
Route Prefix: 3=On-System Condition Ratings: 6=Satisfactory, 7=Good Posting Evaluation: 3=10-19.9% below legal load, 4=0.1-9.9% below legal load										

The models were analyzed with HS-20 truck and designated HL-93 load simulations to obtain deflection profiles, modal properties, and moment and shear values. The deflection and modal property analysis were conducted for comparison to the measured behavior of the bridges in the future field tests. The deflection values and modal characteristics allow for calibration of the FEM models based on the field test results. For the moment and shear analysis, the main bridge characteristic of interest is the LLDFs. The LLDFs found using the FEM model are to be compared to those determined through the field testing and values from the procedures in the AASHTO Standard Specifications (AASHTO 2002) and AASHTO LRFD Specifications (AASHTO 2017). LLDFs can be calculated as the moment or shear force of an individual girder divided by the sum

of moments or shear forces in all of the girders for a one-lane loaded case, as shown in Eqn. (5.1) in Chapter 1

6.2. DESCRIPTION OF SELECTED BRIDGE

The selected continuous steel multi-girder bridge to be modeled has a total length of 195'-0" consisting of three continuous spans. The center-to-center of bearing $_{span}$ length of the middle span is 75'-0", which controls the load ratings. The length of both end spans is 60'-0". The total width of the bridge is 25'-6", with a roadway width of 24'-0" and a 6 in. thick deck. The girder spacing is 6'-8" and lateral bracing is provided at quarter points of each span. The steel yield strength and the 28-day concrete compressive strength are taken as 33 ksi and 2.5 ksi, respectively based on values prescribed by the AASHTO MBE (AASHTO MBE 2018). The bridge carries two lanes, one in each direction, and has an average daily traffic of 260 vehicles. These properties are tabulated in Table 6.2.

Table 6.2. Load Rating Characteristics for SC-12

Characteristic	**Measurement**
Total Length	195'-0"
Controlling Span Length	75'-0"
Deck Width	25'-6"
Roadway Width	24'-0"
Girder Spacing	6'-8"
Lateral Bracing Spacing	18'-9"
Steel Cross-Section Shape	W30x108
Steel Yield Strength	33 ksi
Deck Thickness	6 in.
28-day Concrete Compressive Strength	2.5 ksi
Number of Lanes	2

Bridge SC-12 has a deck condition rating of 6 (Satisfactory), a superstructure condition rating of 7 (Good) without beam section loss due to corrosion, and a substructure condition rating of 7 (Good). The girder flexure controls the rating of the bridge, which has an inventory gross loading of 19 US tons and an operating gross loading of 32 US tons. Table 6.3 shows the posted loads of Bridge SC-12 for different axle and vehicle configurations. Figure 6.1 shows an elevation view of Bridge SC-12 and a view of the underside of the superstructure. Figure 6.2 shows transverse section details of Bridge SC-12.

Table 6.3. Bridge SC-12 Postings

Configuration	**Posting (lbs)**
Single Axle	20,000
Tandem Axle	34,000
Single Vehicle	58,000
Combination Vehicle	75,000

(a) Elevation view

(b) Underside view

Figure 6.1. Photographs of Bridge SC-12

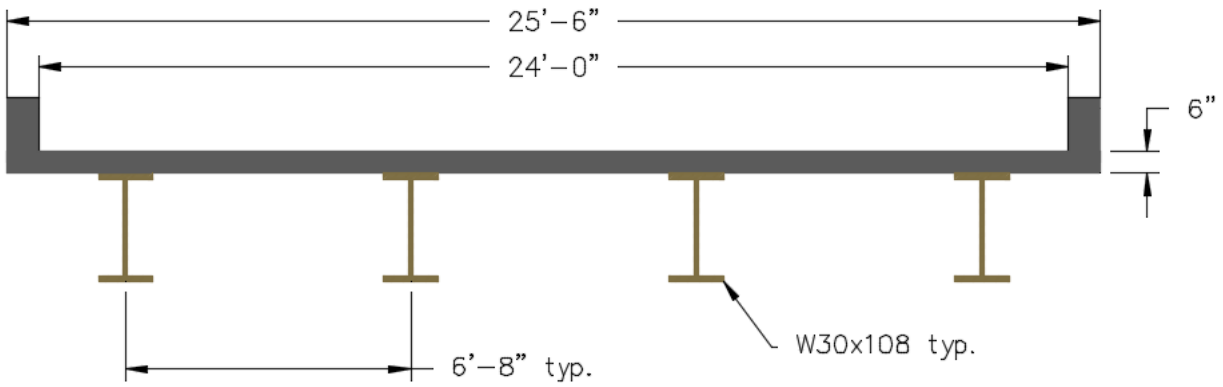

Figure 6.2. Bridge SC-12 Transverse Section (Adapted from TxDOT 2018b)

6.3. FEM MODEL DEVELOPMENT

A three-dimensional linear FEM model of the selected continuous steel multi-girder bridge, SC-12, was developed using the commercial CSiBridge software (Computers and Structures 2019). The geometry of the bridge was modeled based on information provided in the design drawings and inspection reports. The geometric information relevant to the development of the FEM model was presented in the previous section of this chapter. The following subsection describes the FEM modeling approach, finite element types, and material properties. The next subsection describes selection of mesh size. The last subsection provides details about boundary conditions, which is critical for accurately capturing the behavior of the bridge.

6.3.1. Bridge Model Description

The superstructure of a slab-on-girder bridge can be modeled using a variety of finite element types, most of which are available in the CSiBridge software. There is a significant amount of information in the literature providing guidelines for developing FEM models for slab-on-girder steel bridges (Barnard et al. 2010; Hurlebaus et al. 2018; Puckett et al. 2011) Based on the

recommendations provided in the literature and engineering judgement, the FEM models of the selected SC bridge was developed using a combination of four-node linear quadrilateral shell elements and two-node linear beam elements (frame elements). The superstructure of the selected SC bridge consists of steel I-girders and a reinforced concrete deck. The reinforced concrete deck was modeled using four-node linear shell elements. Table 6.4 shows the relevant material properties for the steel girders and concrete deck used in the FEM models of the bridge, which match the material strength values noted in the TxDOT load rating calculations. Deck reinforcement is not modeled because the linear elastic model will be analyzed under service level loads only and the superstructure is expected to remain in the linear elastic range. The steel girder webs were also modeled using four-node linear shell elements. Top and bottom flanges of the steel girders and the diaphragms were modeled using two-node linear beam/frame elements. Figure 6.3 shows the meshed FEM model of SC-12 with the components of the model labeled. When creating a meshed analytical model, CSiBridge first partitions the deck along the centerlines of the girders, and then meshes based on the selected maximum mesh size. The maximum mesh size is 6 in. for the FEM model of Bridge SC-12 shown in Figure 6.3.

The default option for modeling a steel multi-girder bridge with a concrete deck in CSiBridge software considers the deck and girders as fully composite. In order to model non-composite behavior, an edge release was applied to the bottom surface of the concrete deck. This option removes interface shear restraint between the deck and the girders, thereby creating fully non-composite behavior. Bridge SC-12 was modeled and analyzed as fully composite and fully non-composite to allow comparison of the results.

Table 6.4. FEM Model Material Properties

Material	Density (pcf)	Modulus of Elasticity (ksi)	Poisson's Ratio	28-Day Concrete Compressive Strength (ksi)	Steel Yield Strength (ksi)
Steel	490	29,000	0.3	-	33
Concrete	150	2850	0.2	2.5	-

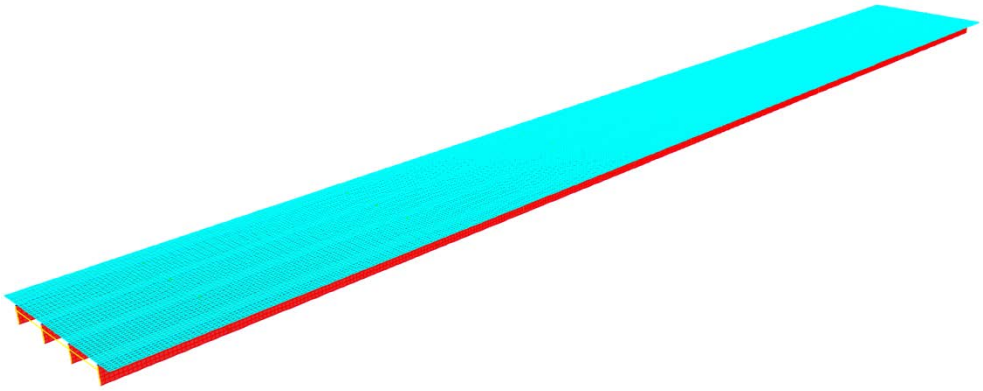

(a) Fully Meshed Superstructure

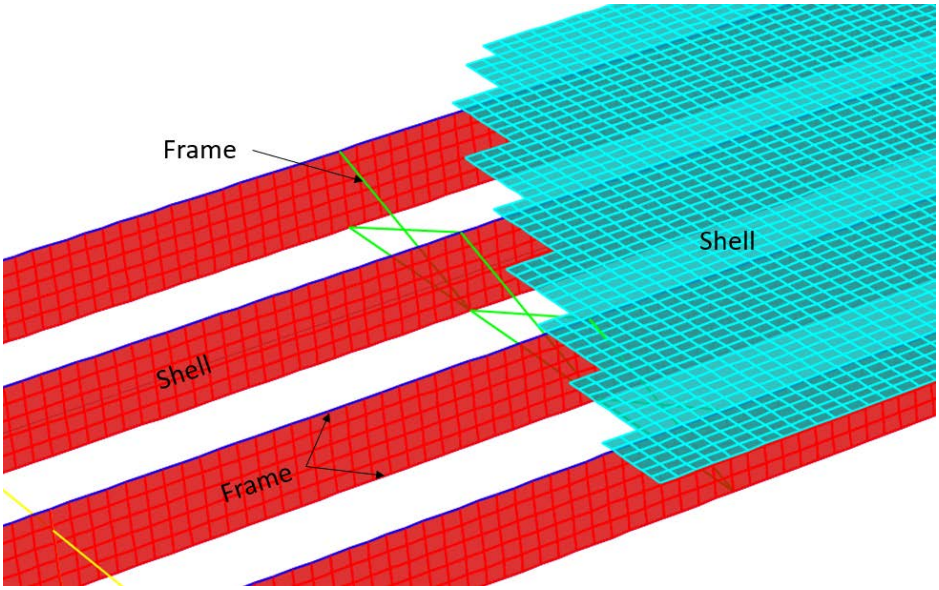

(b) Finite Element Types

Figure 6.3. FEM Model of the SC-12 Bridge (6 in. mesh)

6.3.2. Mesh Sensitivity Analysis

A mesh sensitivity analysis was conducted on the SM bridges and is presented in the first chapter of this report. This analysis found that a 6-in. mesh was the optimal mesh size to use. Mesh sensitivity analysis for Bridge SC-12 is not expected to produce different results from the previous analysis performed for the SM bridges. Therefore, a mesh size of 6 in. was chosen for the FEM analysis of Bridge SC-12.

6.3.3. Boundary Conditions

In the absence of more accurate information, the boundary conditions at the supports are defined as pins and rollers. The boundary conditions for Bridge SC-12 was modeled to represent a three-span continuous condition. Roller supports were used under the girders for all exterior and interior supports except for one exterior support on one girder, which was modeled as a pin support. A roller support releases all three rotational degrees of freedom as well as two translational degrees of freedom in the horizontal plane (two orthogonal in-plane directions parallel to the bridge superstructure), and fully restrains the translational degree of freedom in the vertical direction (perpendicular to the plane of the bridge superstructure). Only one girder was pinned at one end in order to resist any horizontal forces that develop. A pin support releases all three rotational degrees of freedom and restrains all three translational degrees of freedom.

Accurately modeling the boundary conditions has significant effect on the overall behavior of the bridge. Although the boundary conditions are initially modeled as simply supported, the restraint of the supports will be evaluated based on field testing results during the next phase of this study. Unintended partial fixity may develop at the end supports due to the bearing detail at

the supports and/or friction between the bottom surface of the bridge girders and the bearing surface. The presence of partial fixity will be verified through field testing.

6.4. BASIC VERIFICATION OF FEM MODELS

The three-span continuous FEM model of Bridge SC-12 was verified through a comparison with a single beam analysis conducted in RISA 3D software (RISA Tech 2016). The bridge was modeled as a single beam in RISA 3D, with three spans and continuous over the interior supports. For verification of HS-20 loading, the HS-20 truck configuration was moved along the beam using static step loading at 6 in. increments. A similar loading approach was used for HL-93 loading verification with the addition of the lane load onto the appropriate spans to obtain the maximum moment and shear reactions. To obtain maximum moment and shear the lane load was applied to the center span, while for the negative moment the HS-20 truck train was used, and the lane load was applied to the center span and one adjacent span. When using the truck train, both the trucks and lane load were multiplied by a factor of 0.9, per the AASHTO LRFD Specifications (AASHTO 2017).

6.4.1. Verification of Absolute Maximum Moment

Table 6.5 shows the live load moments calculated using the RISA verification model, the CSiBridge calculated moments, and the percent difference between them. The CSiBridge live load moments matches up very closely to the expected live load moments obtained from RISA.

Table 6.5. Comparison of Live Load Moment on Composite Section for Bridge SC-12

Bridge ID	Positive/ Negative Moment	Applied Load	CSiBridge One-Lane Moment on Total Section (kip-ft)	Expected One-Lane Moment on Total Section (kip-ft)	Percent Difference
SC-12	Positive	HS-20	658.7	664.0	0.8
	Positive	HL-93	901.7	909.2	0.8
SC-12	Negative	HS-20	441.3	438.3	0.7
	Negative	HL-93	892.6	887.6	0.6
Note: All calculated moments are without the application of the impact factor.					

6.4.2. Verification of Shear Forces

The maximum shear force was also verified to ensure that the load models were developed correctly. The CSiBridge models use step-by-step loading for the moving load analysis. The step size of the moving load was adjusted such that the first step with the rear axle of the vehicle on the bridge placed the rear axle 3 ft away from the support, which is equivalent to one member depth. The resulting shear forces at 3 ft away from the support were obtained from the FEM model. These were compared with the shear forces found using RISA by placing the rear axle 3 ft away from the support. Table 6.6 shows the live load shears calculated using the RISA verification model, the CSiBridge calculated shears, and the percent difference between them. The CSiBridge live load shears match very closely to the expected live load shears.

Table 6.6. Comparison of Live Load Shear Forces on Composite Section for Bridge SC-12

Bridge ID	Applied Load	CSiBridge one-lane Shear on Total Section (kips)	Expected one-lane Shear on Total Section (kips)	Percent Difference
SC-12	HS-20	61.9	61.8	0.2
	HL-93	85.6	85.7	0.1
Note: All calculated shears are without the application of the impact factor.				

6.5. SIMULATING VEHICLE LOADS

6.5.1. Simulating HS-20 Truck Loading

The HS-20 truck loads were placed transversely on the SC bridge per the AASHTO Standard Specifications (AASHTO 2002). Bridge SC-12 is a two-lane bridge with a lane width of 12'-0". For a one-lane-loaded case based on the Standard Specifications, the truck was first placed so that the exterior wheel line was 2 ft away clear of the edge of the barrier. For each separate load case, the truck was moved transversely 1 ft toward the centerline of the bridge. For the third and final load case the interior wheel line was placed 2 ft away from the interior edge of the lane. This created three different one-lane-loaded cases shown in Figure 6.4(a): one with the exterior wheel line 2 ft from the barrier (Path 1), one with the exterior wheel line 3 ft from the barrier (Path 2), and one with the exterior wheel line 4 ft from the barrier (Path 3).

For the two-lane-loaded case, the first truck was positioned in the same way as for each one-lane-loaded case. A second truck was placed in the second lane of the bridge with the interior wheel line 2 ft away from the interior edge of the lane for each load case. This created three separate two-lane-loaded cases: Path 1 + Path 4, Path 2 + Path 4, and Path 3 + Path 4, as shown in Figure 6.4(b).

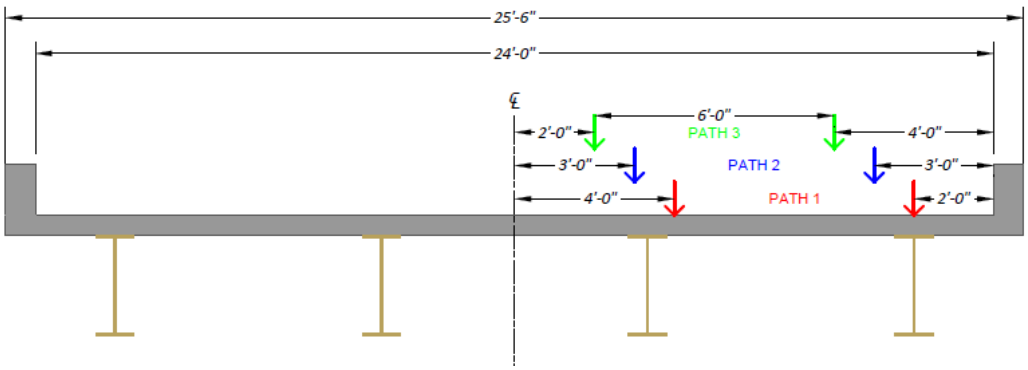

(a) One-Lane Loading Paths

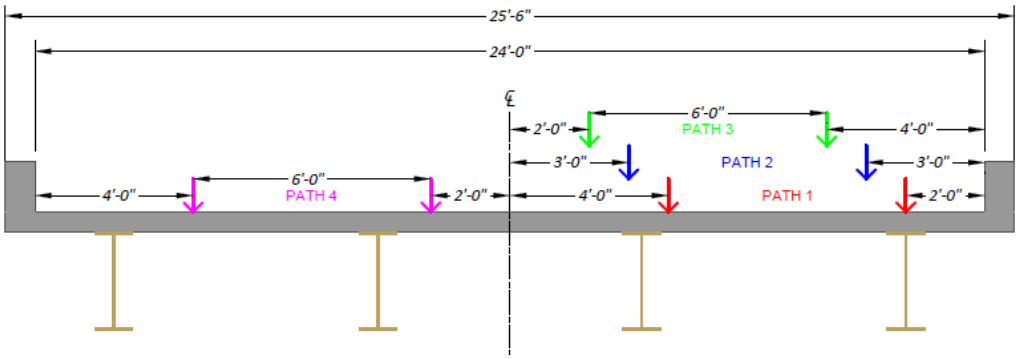

(b) Two-Lane Loading Paths

Figure 6.4. HS-20 Loading Cases for Bridge SC-12

6.5.2. Simulating HL-93 Loading

The HL-93 load model was also placed at different transverse locations on the SC bridge per the AASHTO LRFD Specifications (AASHTO 2017). It has a lane width of 12'-0" and a maximum span length in the center span of approximately 75'-0". As the truck load configuration controls for spans longer than 40'-6", the truck plus lane load was used for the HL-93 loading of Bridge SC-12. The design truck was placed transversely in the same manner as described for the HS-20 load. The lane load was added so that the exterior edge of the lane load in Path 1 was against the

railing of the bridge. The exterior edge of the lane load in Path 2 was placed 1 ft away from the railing, and the interior edge of the lane load in Path 3 was placed against the interior edge of the lane. A total of three different one-lane-loaded cases were created in the first lane as shown in Figure 6.5(a): (1) one with the exterior wheel line of the truck 2 ft from the railing and the exterior edge of the lane load immediately adjacent to the railing (Path 1), (2) one with the exterior wheel line of the truck 3 ft from the railing and the exterior edge of the lane load 1 ft away from the railing (Path 2), and (3) one with the exterior wheel line of the truck 4 ft from the railing and the interior edge of the lane load immediately adjacent to the interior edge of the lane (Path 3).

For a two-lane-loaded case, the tandem and lane loads were positioned in the same way as for each one-lane-loaded case. A second truck was placed in the second lane of the bridge with the interior wheel line 2 ft away from the interior edge of the lane for each load case. A second lane load was placed with its right edge against the interior edge of the lane in the second lane. This created three separate two-lane-loaded cases for the bridge: Path 1 + Path 4, Path 2 + Path 4, and Path 3 + Path 4, as shown in Figure 6.5(b).

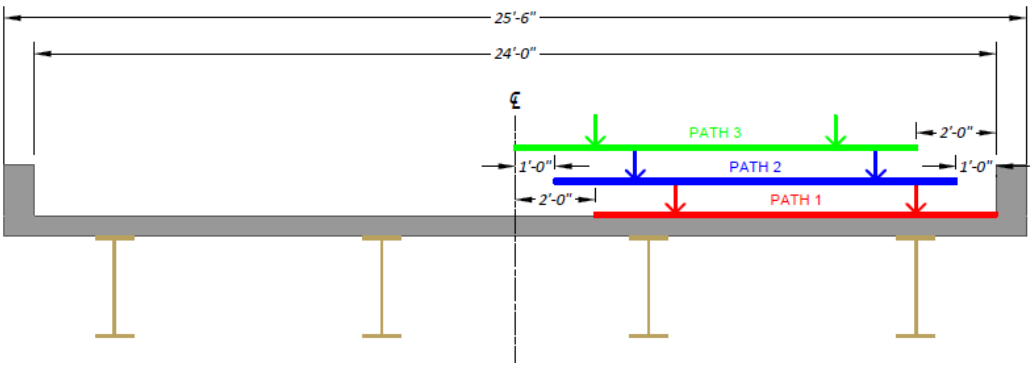

(a) One-Lane Loading Paths

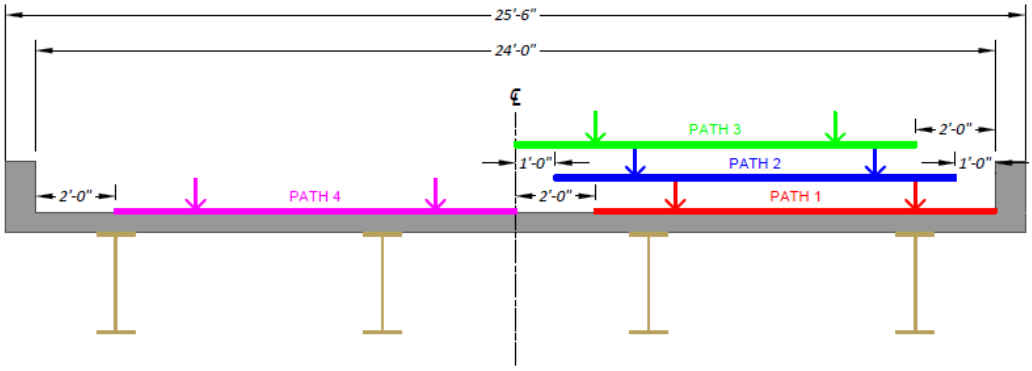

(b) Two-Lane Loading Paths

Figure 6.5. HL-93 Loading Cases for Bridge SC-12

6.6. FEM RESULTS FOR BRIDGE SC-12

Bridge SC-12 was analyzed using the CSiBridge software under the loading scenarios provided in Figure 6.4 and Figure 6.5. Girder displacement profiles were obtained for the load cases that represent the field load testing plans. Modal analyses were conducted for both composite and non-composite conditions to determine estimated modal frequencies and mode shapes. Live load moment and shear values were also extracted and analyzed to compare the expected LLDFs with

the LLDFs prescribed in the AASHTO Standard Specifications (AASHTO 2002) and the AASHTO LRFD Specifications (AASHTO 2017).

The AASHTO Standard Specifications (AASHTO 2002) Article 3.23.2.3.1.4 states that "In no case shall an exterior stringer have less carrying capacity than an interior stringer." The AASHTO LRFD Specifications (AASHTO 2017) Article 2.5.2.7.1 also states that, "Unless future widening is virtually inconceivable, the load carrying capacity of exterior beams shall not be less than the load carrying capacity of an interior beam." In most cases for Bridge SC-12 the moment LLDF determined through the AASHTO Standard Specifications and AAHTO LRFD Specifications for the exterior girder is smaller than the moment LLDF for the interior girder. Therefore, interior girder moment LLDFs were used when calculating the exterior girder moment demands.

It is also important to note that for calculation of the negative moment LLDFs, Table 4.6.2.2.1-2 in the AASHTO LRFD Specifications (AASHTO 2017) prescribes the use of the average length of the two adjacent spans over the support of interest to be used as the variable *L* in the LLDF equations.

6.6.1. Modal Properties

The first two modes of the Bridge SC-12 were identified as the first longitudinal bending mode and the first torsional mode. The frequencies of the longitudinal and torsional modes for the non-composite bridge were determined to be 2.31 Hz and 2.72 Hz, respectively. Figure 6.6(a) shows the amplitude contours of the first longitudinal bending mode shape for half of the bridge length and the normalized amplitudes along the span for the non-composite condition. Figure 6.6(b)

shows the amplitude contours for the first torsional mode shape for half of the bridge length and the normalized amplitudes transverse to the center span for the non-composite condition.

The frequencies of the first longitudinal bending and the first torsional modes of the composite bridge were determined to be 3.23 Hz and 3.41 Hz, respectively. Figure 6.7(a) shows the amplitude contours of the first longitudinal bending mode shape for half of the bridge and the normalized amplitudes along the span for the composite condition. Figure 6.7(b) shows the amplitude contours resulting from the first torsional mode for half of the bridge and the normalized amplitudes transverse to the center span for composite analysis.

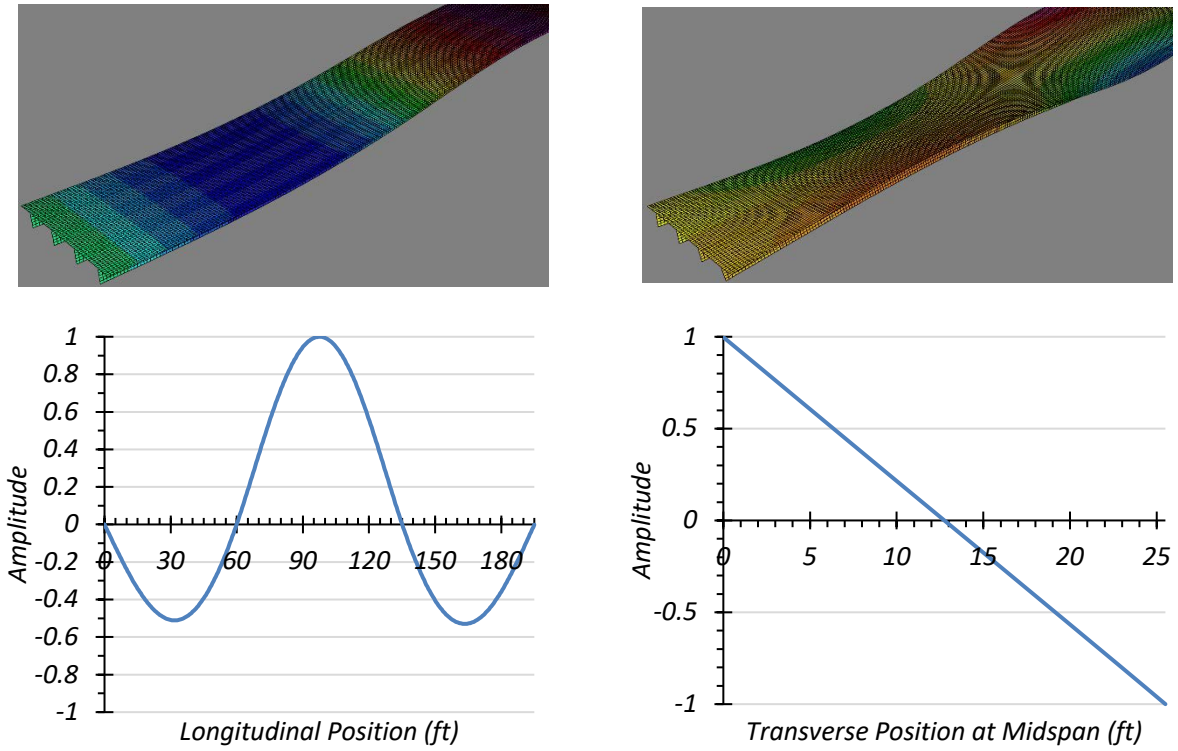

(a) Longitudinal bending Mode (f=2.31 Hz) *(b) Torsional Mode (f=2.72 Hz)*

Figure 6.6. First Two Mode Shapes of Non-Composite Bridge SC-12

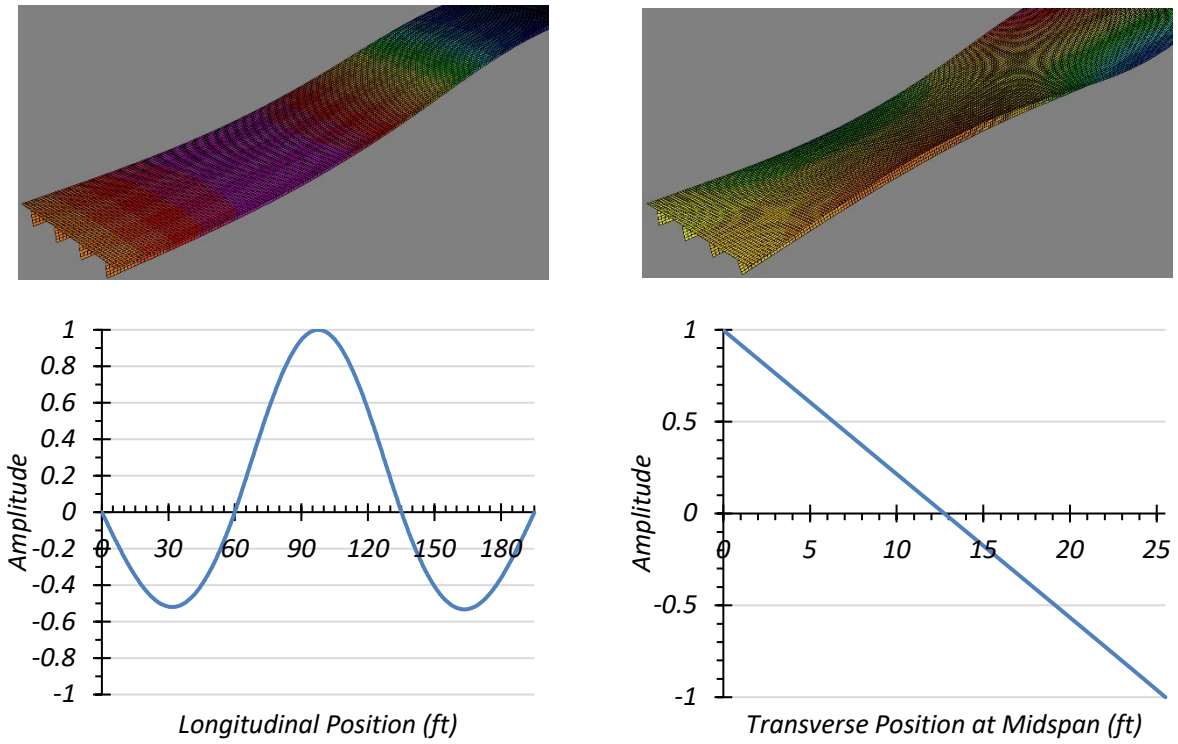

(a) Longitudinal bending Mode (f=3.23 Hz) *(b) Torsional Mode (f=3.41 Hz)*

Figure 6.7. First Two Mode Shapes of Composite Bridge SC-12

6.6.2. HS-20 Live Load Analysis

Bridge SC-12 was first analyzed using the HS-20 design truck presented in the AASHTO Standard Specifications (AASHTO 2002). The bridge was analyzed for one-lane and two-lane-loaded cases along four transverse paths as shown in Figure 6.4. Deflection, moment, and shear results were obtained.

6.6.2.1. Deflection Results

Figure 6.8 shows the estimated girder deflection profile envelopes for the full length of the bridge and contours of the half length of the bridge for one-lane HS-20 loading along Path 1 and Path 4 when the bridge is analyzed as fully non-composite. Table 6.7 shows the corresponding positive

(downward) and negative (upward) deflections for each girder assuming non-composite action. Load paths 1 and 4 are the only ones shown as these are expected to be the load paths used in future field load tests, and were selected to maximize the forces on an interior girder and on an exterior girder.

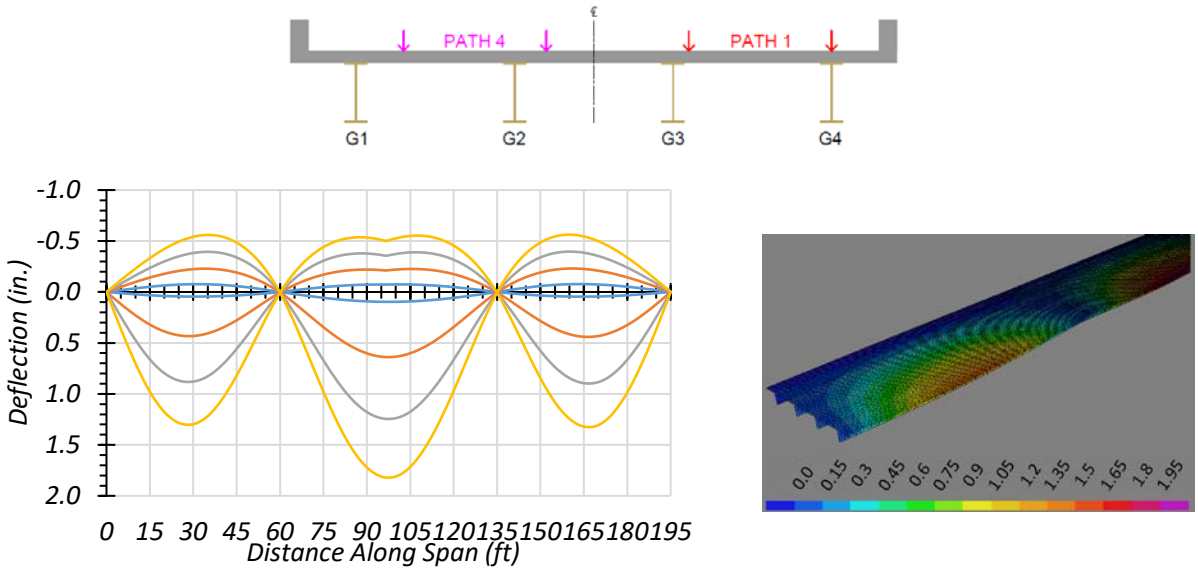

(a) Path 1

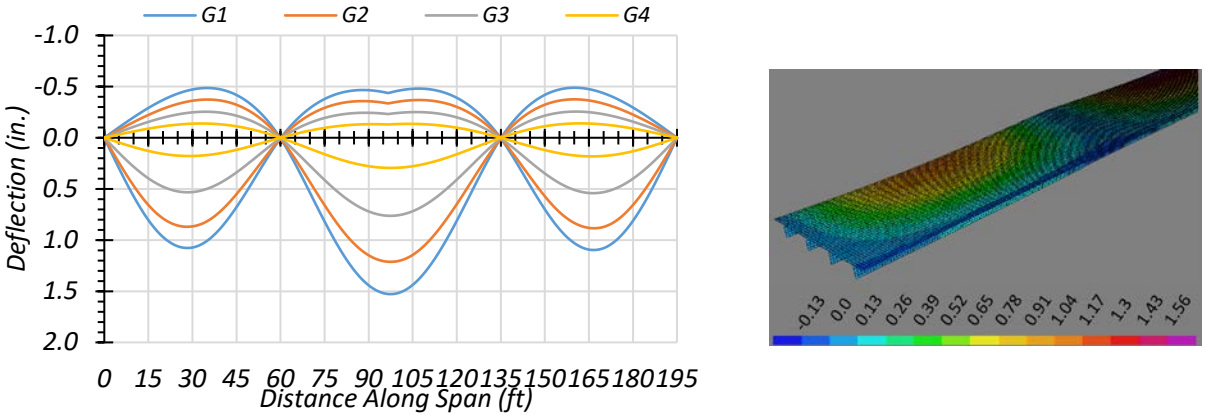

(a) Path 4

Figure 6.8. Deflection Profiles for Non-Composite Bridge SC-12 with HS-20 Loading

Table 6.7. Maximum Deflections for Non-Composite Bridge SC-12 with HS-20 Loading

Loading	Deflection Positive/Negative	G1	G2	G3	G4
Path 1	Positive	0.097	0.639	1.246	1.822
Path 1	Negative	-0.077	-0.230	-0.396	-0.562
Path 4	Positive	1.528	1.212	0.763	0.295
Path 4	Negative	-0.489	-0.375	-0.256	-0.141
Note: G = girder, paths indicate transverse loading positions as shown, deflections have inch units					

Figure 6.9 shows the estimated girder deflection profile envelopes for the full length of the bridge and contours of the half length of the bridge for one-lane HS-20 loading along Path 1 and Path 4 when the bridge is analyzed as fully composite. Table 6.8 shows the corresponding positive (downward) and negative (upward) deflections for each girder assuming fully composite action. Load paths 1 and 4 are the only ones shown as these are expected to be the load paths used in future field load tests, and were selected to maximize the forces on an interior girder and on an exterior girder.

For both non-composite and composite cases, the maximum negative deflections were obtained in Girder 4 when the HS-20 truck was run along Path 1. The estimated deflections were 1.82 in. and 0.84 in. for the non-composite and composite cases, respectively. This result indicates that the composite bridge is 74 percent stiffer than the non-composite bridge. The maximum deflections obtained in Girder 1 when the HS-20 truck was run along Path 4 for both the non-composite and composite case. The estimated deflections were 1.53 in. and 0.69 in. for the non-composite and composite cases, respectively. This result indicates that the composite bridge is 76 percent stiffer than the non-composite bridge. The slightly different values of relative stiffness suggest that the relative girder deflection depends on the location of loading and corresponding load distribution.

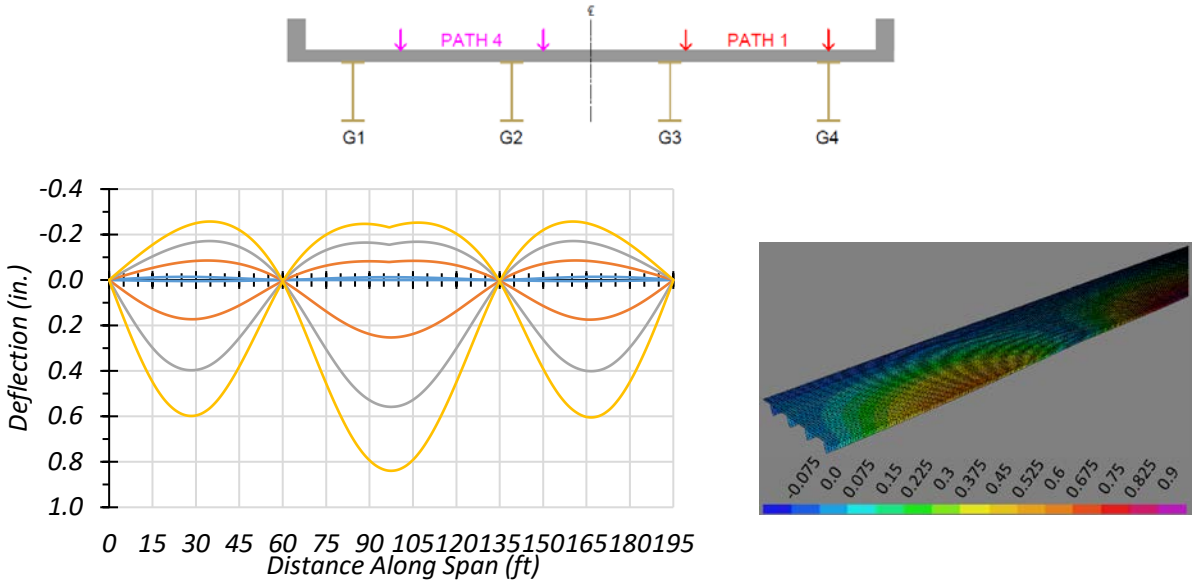

(a) Path 1

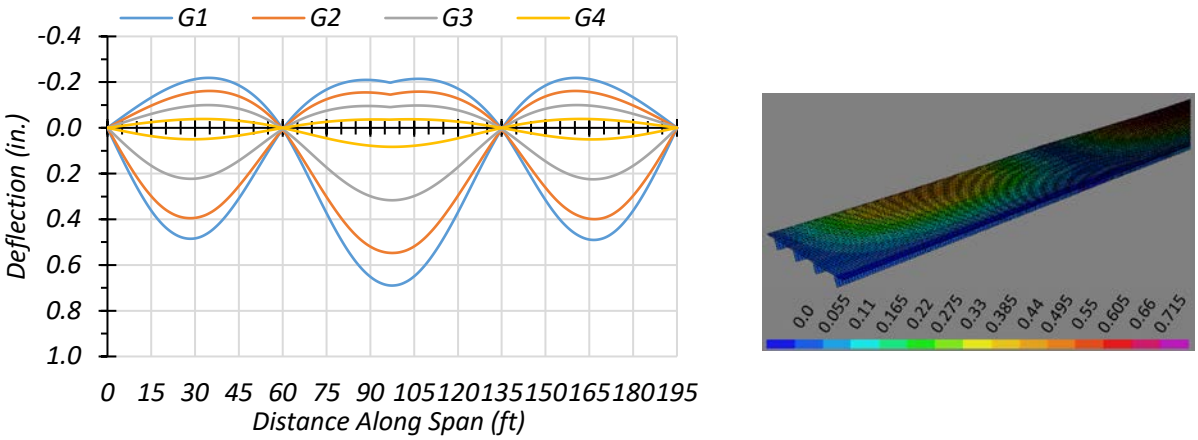

(b) Path 4

Figure 6.9. Deflection Profiles for Composite Bridge SC-12 with HS-20 Loading

Table 6.8. Maximum Deflections for Composite Bridge SC-12 with HS-20 Loading

Loading	Deflection Positive/Negative	G1	G2	G3	G4
Path 1	Positive	0.005	0.253	0.558	0.839
Path 1	Negative	-0.014	-0.086	-0.171	-0.257
Path 4	Positive	0.690	0.547	0.317	0.083
Path 4	Negative	-0.219	-0.161	-0.100	-0.039
Note: G = girder, paths indicate transverse loading positions as shown, deflections have inch units					

6.6.2.2. Positive Moment Results

6.6.2.2.1. One-Lane Loading

Figure 6.10 shows the individual girder positive moment and positive moment LLDF results for the non-composite Bridge SC-12 under simulated moving HS-20 loading along three one-lane loading paths. Table 6.9 provides the corresponding maximum positive moment values of each girder for each loading path. The positive moment LLDF values are calculated using the estimated positive moment results from the FEM analysis. Table 6.11 shows the governing positive moment LLDFs found using the FEM analysis and compares them to the AASHTO LLDF values. Compared to the FEM results, the governing positive moment LLDF value computed using the approximate equations in the AASHTO Standard Specifications (AASHTO 2002) is quite conservative for interior with a g^m_{AASHTO}/g^m_{FEM} ratio of 1.43, and is conservative for exterior girders with a g^m_{AASHTO}/g^m_{FEM} ratio of 1.22.

Figure 6.11 shows the individual girder positive moment and positive moment LLDF results for the fully composite Bridge SC-12 under simulated moving HS-20 loading along three one-lane loading paths. Table 6.10 provides the corresponding maximum positive moment values of each girder for each loading path. The positive moment LLDF values are calculated using the estimated positive moment results from the FEM analysis. Compared to the FEM results, the governing positive moment LLDF value computed using the approximate equations in the AASHTO Standard Specifications (AASHTO 2002) is quite conservative for interior girders with a g^m_{AASHTO}/g^m_{FEM} ratio of 1.31, and is conservative for exterior girders with a g^m_{AASHTO}/g^m_{FEM} ratio of 1.19.

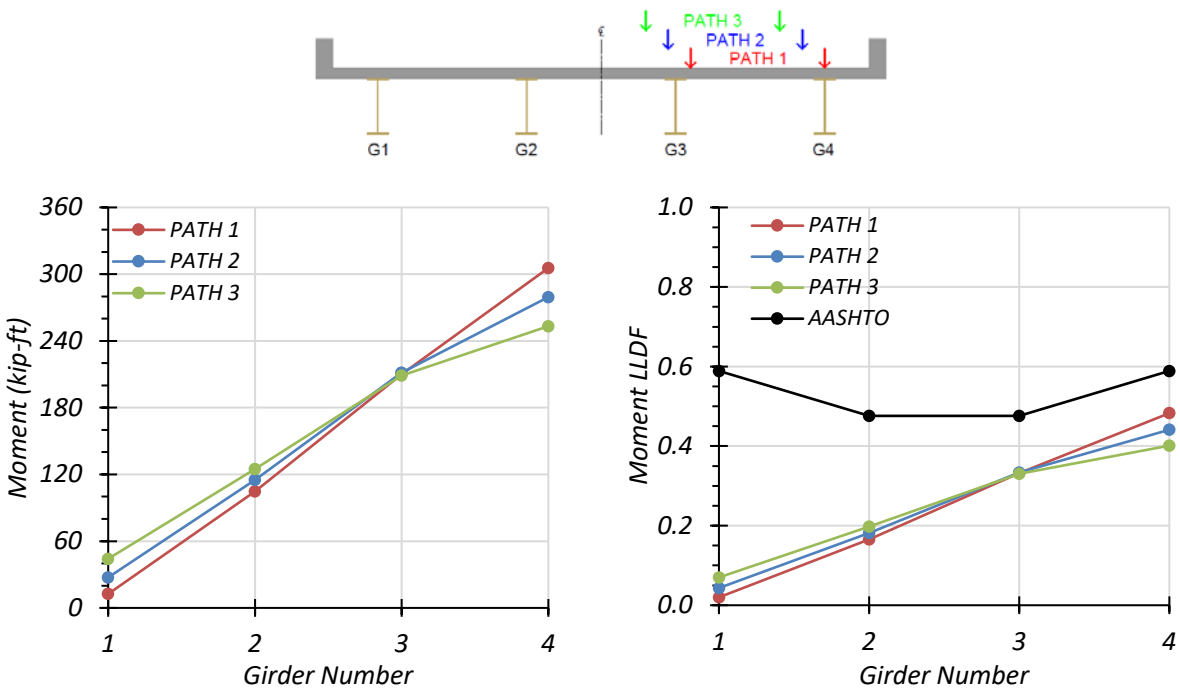

(a) Moment *(b) Moment LLDF*

Figure 6.10. Positive Moment Results for Non-Composite Bridge SC-12 with One-Lane HS-20 Loading

Table 6.9. Maximum Positive Moments for Non-Composite Bridge SC-12 with One-Lane HS-20 Loading

Loading	G1	G2	G3	G4
Path 1	12.6	104.8	209.9	305.6
Path 2	27.4	115.1	211.5	279.4
Path 3	44.2	125.0	208.8	253.2
Note: G = girder, paths indicate transverse loading positions as shown, moments have kip-ft units				

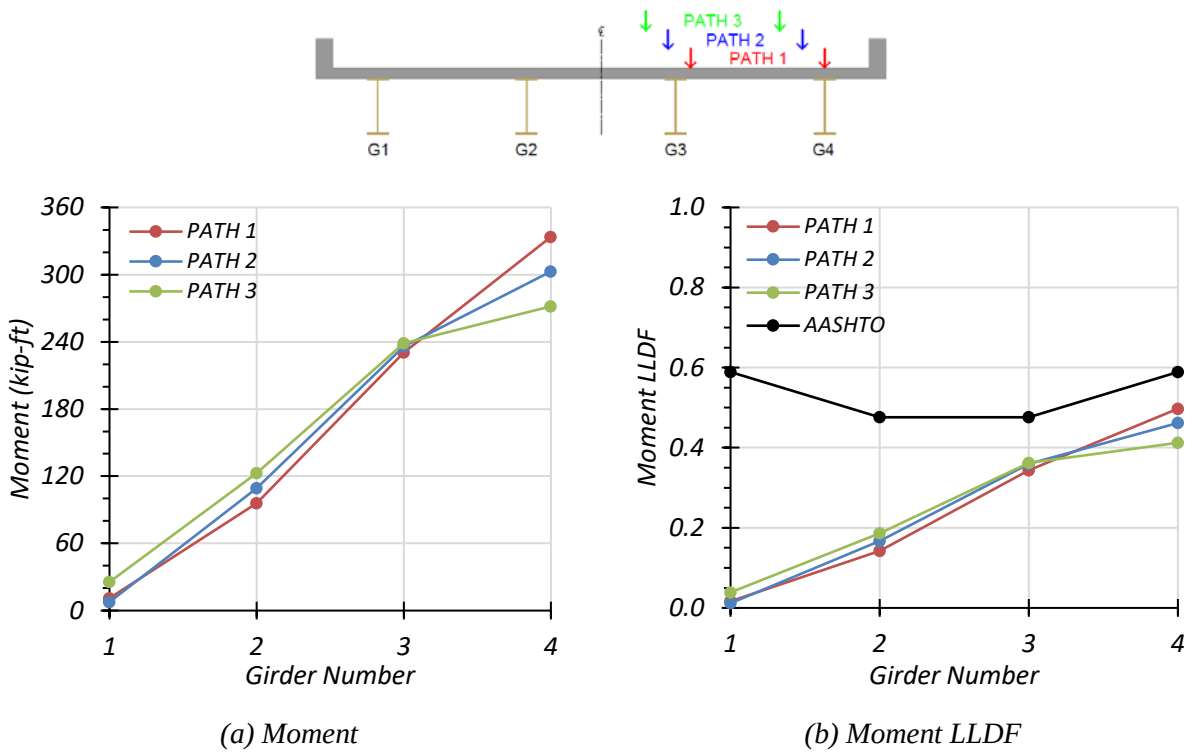

(a) Moment *(b) Moment LLDF*

Figure 6.11. Positive Moment Results for Composite Bridge SC-12 with One-Lane HS-20 Loading

Table 6.10. Maximum Positive Moments for Composite Bridge SC-12 with One-Lane HS-20 Loading

Loading	G1	G2	G3	G4
Path 1	11.1	95.7	230.4	333.7
Path 2	7.7	109.4	236.0	302.8
Path 3	25.5	122.8	238.7	271.7
Note: G = girder, paths indicate transverse loading positions as shown, moments have kip-ft units				

Comparison of governing positive moment LLDF values computed from FEM results for the composite and non-composite cases reveals that the maximum positive moment LLDF in an interior girder for the composite bridge is slightly higher than the one for the non-composite bridge with a $g^m_{composite}/g^m_{non-composite}$ ratio of 1.08. The maximum positive moment LLDF in an

exterior girder for the composite bridge is also slightly higher than that for the non-composite bridge with a $g^m_{composite}/g^m_{non-composite}$ ratio of 1.03.

Table 6.11. Governing Positive Moment LLDFs for Bridge SC-12 with One-Lane HS-20 Loading

Type	Girder Location	AASHTO (g^m_{AASHTO})	FEM (g^m_{FEM})	g^m_{AASHTO}/g^m_{FEM}
Non-Composite	Interior	0.476	0.334	1.43
	Exterior	0.589	0.483	1.22
Composite	Interior	0.476	0.362	1.31
	Exterior	0.589	0.497	1.19

6.6.2.2.2. Two-Lane Loading

Figure 6.12 shows the individual girder positive moments and positive moment LLDF results for the non-composite Bridge SC-12 under simulated moving HS-20 loading along three two-lane loading paths. Table 6.12 provides the corresponding maximum positive moment values of each girder for each loading path. The positive moment LLDF values are calculated using the estimated positive moment results from the FEM analysis. Table 6.14 shows the governing positive moment LLDFs found using the FEM analysis and compares them to the AASHTO LLDF values. Compared to the FEM results, the governing positive moment LLDF value computed using the approximate equations in the AASHTO Standard Specifications (AASHTO 2002) is conservative for interior girders with a g^m_{AASHTO}/g^m_{FEM} ratio of 1.14, and is slightly conservative for exterior girders with a g^m_{AASHTO}/g^m_{FEM} ratio of 1.09.

Figure 6.13 shows the individual girder positive moments and positive moment LLDF results for the fully composite Bridge SC-12 under simulated moving HS-20 loading along three

two-lane loading paths. Table 6.13 provides the corresponding maximum positive moment values of each girder for each loading path. The positive moment LLDF values are calculated using the estimated positive moment results from the FEM analysis. Compared to the FEM results, the governing positive moment LLDF value computed using the approximate equations in the AASHTO Standard Specifications (AASHTO 2002) is conservative for interior girders with a g^m_{AASHTO}/g^m_{FEM} ratio of 1.11, and is also conservative for exterior girders with a g^m_{AASHTO}/g^m_{FEM} ratio of 1.10.

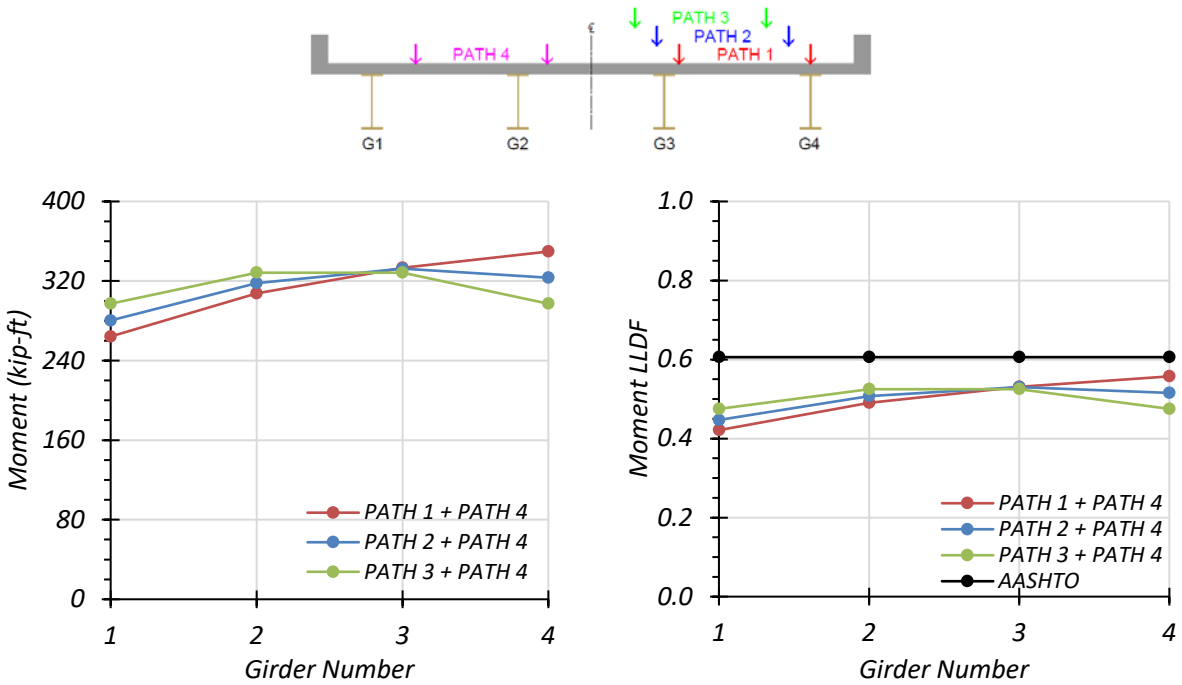

(a) Moment *(b) Moment LLDF*

Figure 6.12. Positive Moment Results for Non-Composite Bridge SC-12 with Two-Lane HS-20 Loading

Table 6.12. Maximum Positive Moments for Non-Composite Bridge SC-12 with Two-Lane HS-20 Loading

Loading	G1	G2	G3	G4
Path 1 + Path 4	264.2	307.5	333.3	349.6
Path 2 + Path 4	280.3	318.0	332.5	323.4
Path 3 + Path 4	297.2	328.4	328.4	297.2
Note: G = girder, paths indicate transverse loading positions as shown, moments have kip-ft units				

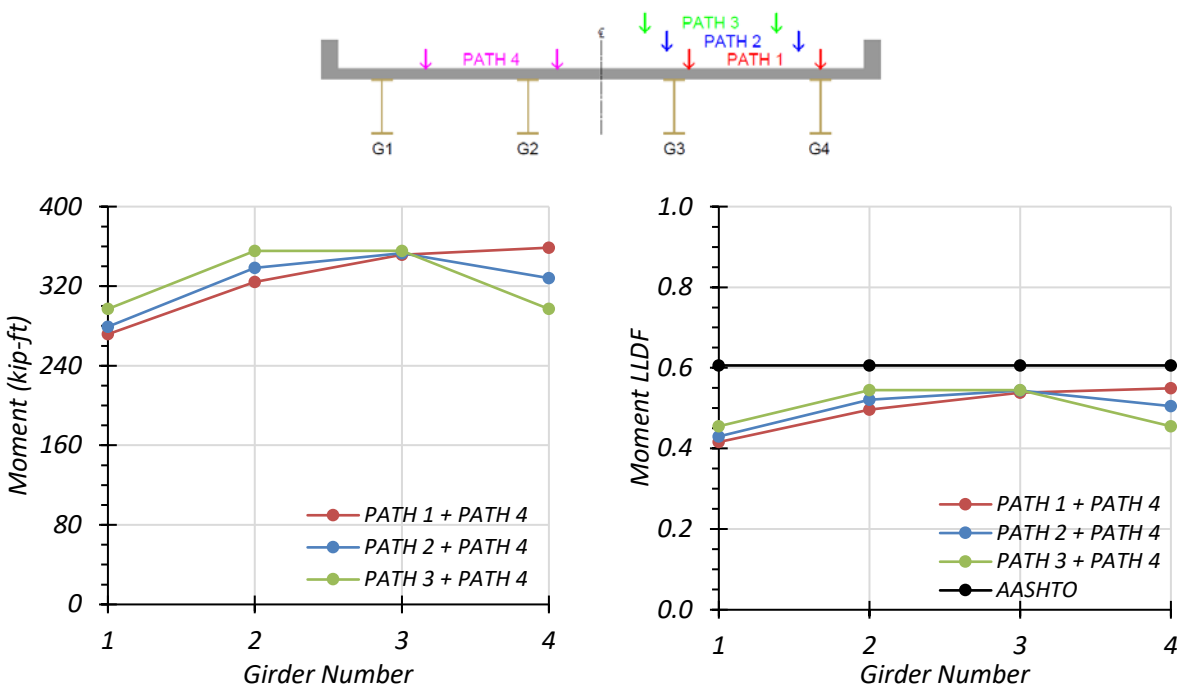

(a) Moment *(b) Moment LLDF*

Figure 6.13. Positive Moment Results for Composite Bridge SC-12 with Two-Lane HS-20 Loading

Table 6.13. Maximum Positive Moments for Composite Bridge SC-12 with Two-Lane HS-20 Loading

Loading	G1	G2	G3	G4
Path 1 + Path 4	271.7	324.1	351.6	358.7
Path 2 + Path 4	279.2	338.5	353.1	328.2
Path 3 + Path 4	297.1	355.6	355.6	297.1
Note: G = girder, paths indicate transverse loading positions as shown, moments have kip-ft units				

Comparison of governing positive moment LLDF values computed from FEM results for the composite and non-composite cases reveals that the maximum positive moment LLDF in an interior girder for the composite bridge is higher than the one for the non-composite bridge with a $g^m_{composite}/g^m_{non-composite}$ ratio of 1.03. The maximum positive moment LLDF in an exterior girder for the composite bridge is slightly lower than that for the non-composite bridge with a $g^m_{composite}/g^m_{non-composite}$ ratio of 0.96.

Table 6.14. Governing Positive Moment LLDFs for Bridge SC-12 with Two-Lane HS-20 Loading

Type	Girder Location	AASHTO (g^m_{AASHTO})	FEM (g^m_{FEM})	g^m_{AASHTO}/g^m_{FEM}
Non-Composite	Interior	0.606	0.531	1.14
	Exterior	0.606	0.557	1.09
Composite	Interior	0.606	0.545	1.11
	Exterior	0.606	0.549	1.10

6.6.2.3. Negative Moment Results

6.6.2.3.1. One-Lane Loading

Figure 6.14 shows the individual girder negative moment and negative moment LLDF results for the non-composite Bridge SC-12 under simulated moving HS-20 loading along three one-lane loading paths. Table 6.15 provides the corresponding maximum negative moment values of each girder for each loading path. The negative moment LLDF values are calculated using the estimated negative moment results from FEM analysis. Table 6.17 shows the governing negative moment LLDFs found using the FEM analysis and compares them to the AASHTO LLDF values. Compared to the FEM results, the governing negative moment LLDF value computed using the approximate equations in the AASHTO Standard Specifications (AASHTO 2002) is quite

conservative for interior girders with a g^m_{AASHTO}/g^m_{FEM} ratio of 1.40, and is conservative for exterior girders with a g^m_{AASHTO}/g^m_{FEM} ratio of 1.19.

Figure 6.15 shows the individual girder negative moment and negative moment LLDF results for the fully composite Bridge SC-12 under simulated moving HS-20 loading along three one-lane loading paths. The HS20 design truck with 14-ft axle spacing between 32-kip axles was used for the analyses, as this was found to control the negative moment for the bridge. Table 6.16 provides the corresponding maximum negative moment values of each girder for each loading path. The negative moment LLDF values are calculated using the estimated negative moment results from the FEM analysis. Compared to the FEM results, the governing negative moment LLDF value computed using the approximate equations in the AASHTO Standard Specifications (AASHTO 2002) is conservative for both interior and exterior girders with a g^m_{AASHTO}/g^m_{FEM} ratio of 1.27 and 1.16, respectively.

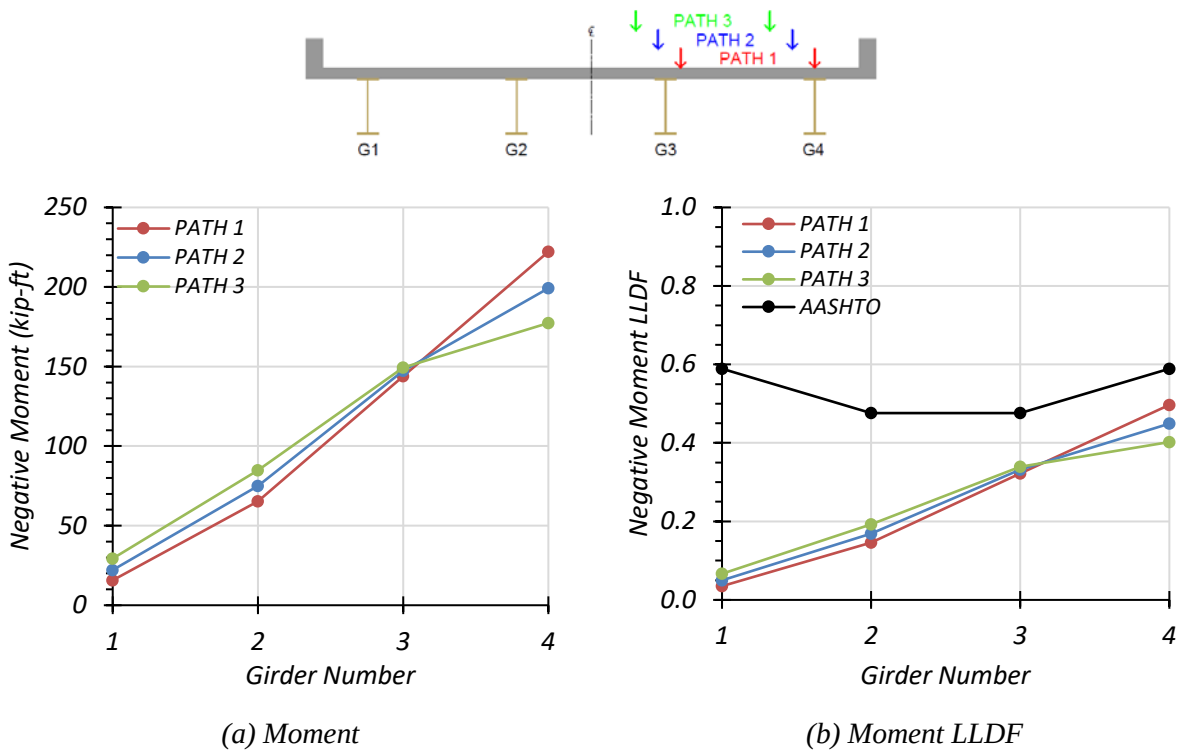

(a) Moment *(b) Moment LLDF*

Figure 6.14. Negative Moment Results for Non-Composite Bridge SC-12 with One-Lane HS-20 Loading

Table 6.15. Maximum Negative Moments for Non-Composite Bridge SC-12 with One-Lane HS-20 Loading

Loading	G1	G2	G3	G4
Path 1	15.7	65.3	144.0	222.2
Path 2	22.1	74.9	147.3	199.2
Path 3	29.4	84.8	149.4	177.3
Note: G = girder, paths indicate transverse loading positions as shown, moments have kip-ft units				

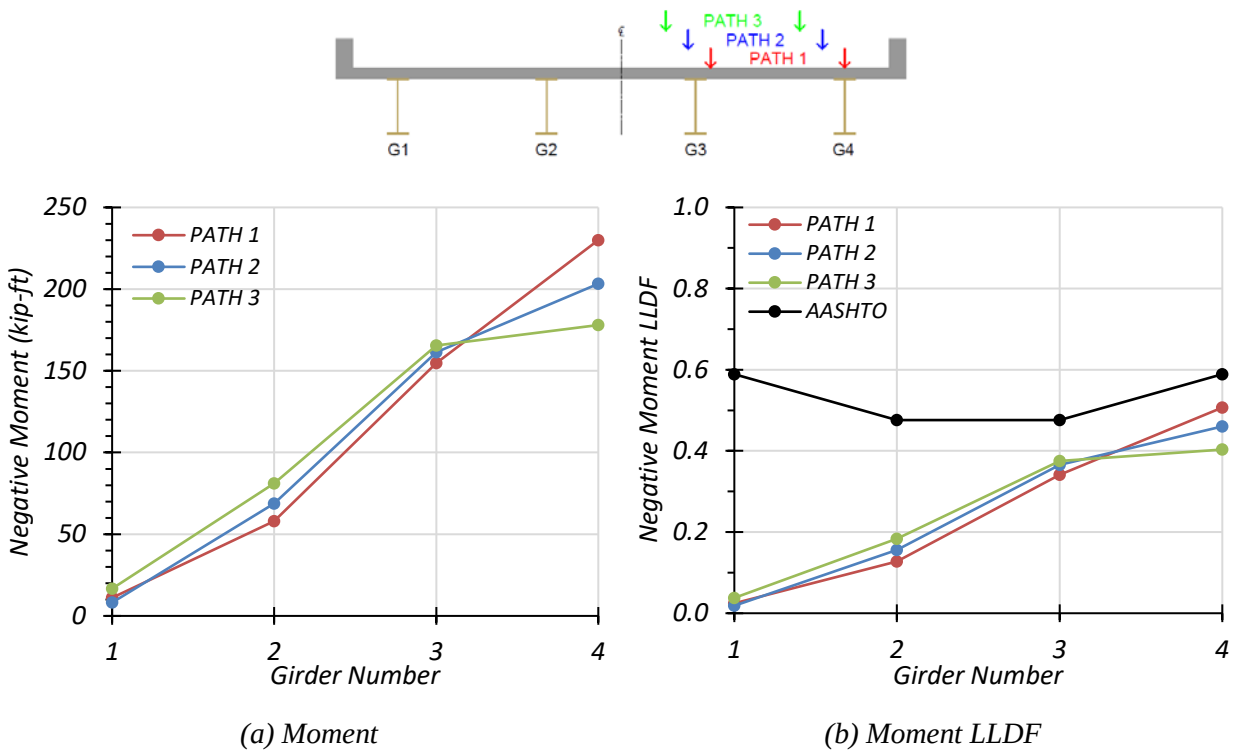

(a) Moment *(b) Moment LLDF*

Figure 6.15. Negative Moment Results for Composite Bridge SC-12 with One-Lane HS-20 Loading

Table 6.16. Maximum Negative Moments for Composite Bridge SC-12 with One-Lane HS-20 Loading

Loading	G1	G2	G3	G4
Path 1	11.1	57.9	154.8	230.0
Path 2	8.2	68.8	161.3	203.3
Path 3	16.7	81.1	165.5	178.0
Note: G = girder, paths indicate transverse loading positions as shown, moments have kip-ft units				

Comparison of governing negative moment LLDF values computed from FEM results for the composite and non-composite cases reveals that the maximum negative moment LLDF in an interior girder for the composite bridge is higher than the one for the non-composite bridge with a $g^m_{composite}/g^m_{non-composite}$ ratio of 1.11. The maximum negative moment LLDF in an exterior

girder for the composite bridge is also slightly higher than that for the non-composite bridge with a $g^m_{composite}/g^m_{non-composite}$ ratio of 1.02.

Table 6.17. Governing Negative Moment LLDFs for Bridge SC-12 with One-Lane HS-20 Loading

Type	Girder Location	AASHTO (g^m_{AASHTO})	FEM (g^m_{FEM})	g^m_{AASHTO}/g^m_{FEM}
Non-Composite	Interior	0.476	0.339	1.40
	Exterior	0.589	0.497	1.19
Composite	Interior	0.476	0.375	1.27
	Exterior	0.589	0.507	1.16

6.6.2.3.2. Two-Lane Loading

Figure 6.16 shows the individual girder negative moment and negative moment LLDF results for the non-composite Bridge SC-12 under simulated moving HS-20 loading along three two-lane loading paths. Table 6.18 provides the corresponding maximum negative moment values of each girder for each loading path. The negative moment LLDF values are calculated using the estimated negative moment results from the FEM analysis. Table 6.20 shows the governing negative moment LLDFs found using the FEM analysis and compares them to the AASHTO LLDF values. Compared to the FEM results, the governing negative moment LLDF value computed using the approximate equations in the AASHTO Standard Specifications (AASHTO 2002) is conservative for interior girders with a g^m_{AASHTO}/g^m_{FEM} ratio of 1.11, and is slightly conservative for exterior girders with a g^m_{AASHTO}/g^m_{FEM} ratio of 1.09.

Figure 6.17 shows the individual girder negative moment and negative moment LLDF results for the fully composite Bridge SC-12 under simulated moving HS-20 loading along three

different two-lane loading paths. Table 6.19 provides the corresponding maximum negative moment values of each girder for each loading path. The negative moment LLDF values are calculated using the estimated negative moment results from the FEM analysis. Compared to the FEM results, the governing negative moment LLDF value computed using the approximate equations in the AASHTO Standard Specifications (AASHTO 2002) is slightly conservative for interior girders with a g^m_{AASHTO}/g^m_{FEM} ratio of 1.07, and is conservative for exterior girders with a g^m_{AASHTO}/g^m_{FEM} ratio of 1.11.

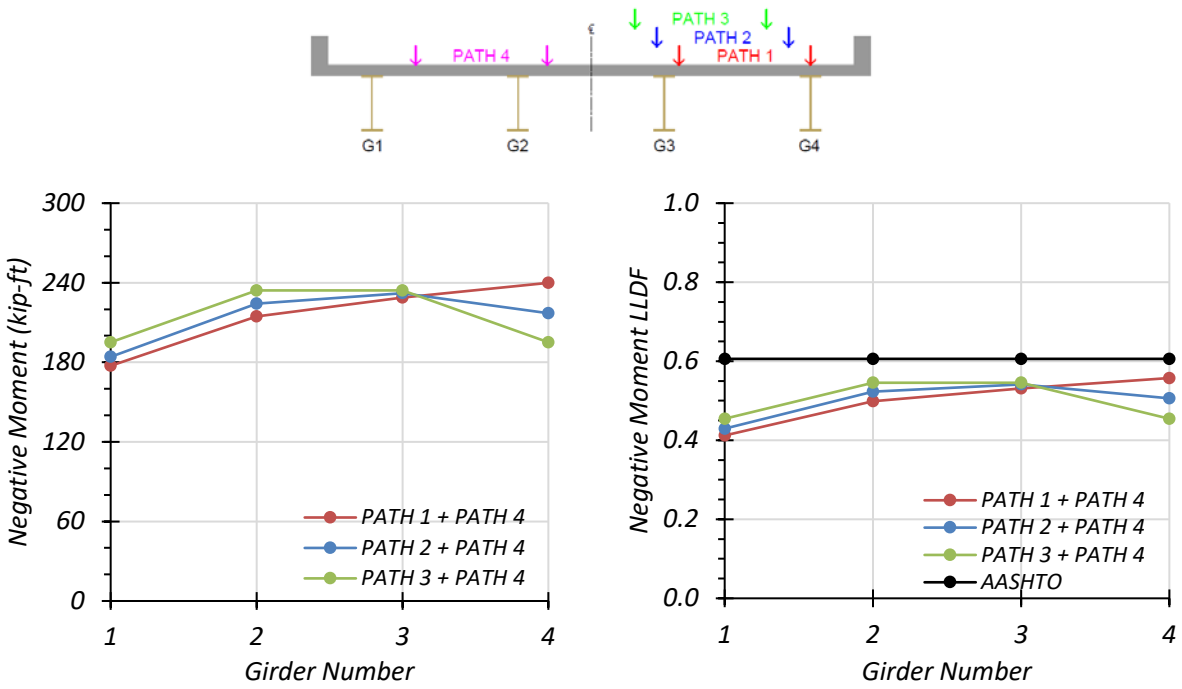

(a) Moment *(b) Moment LLDF*

Figure 6.16. Negative Moment Results for Non-Composite Bridge SC-12 with Two-Lane HS-20 Loading

Table 6.18. Maximum Negative Moments for Non-Composite Bridge SC-12 with Two-Lane HS-20 Loading

Loading	G1	G2	G3	G4
Path 1 + Path 4	177.3	214.7	228.8	239.9
Path 2 + Path 4	184.1	224.3	232.1	217.0
Path 3 + Path 4	195.1	234.2	234.2	195.1
Note: G = girder, paths indicate transverse loading positions as shown, moments have kip-ft units				

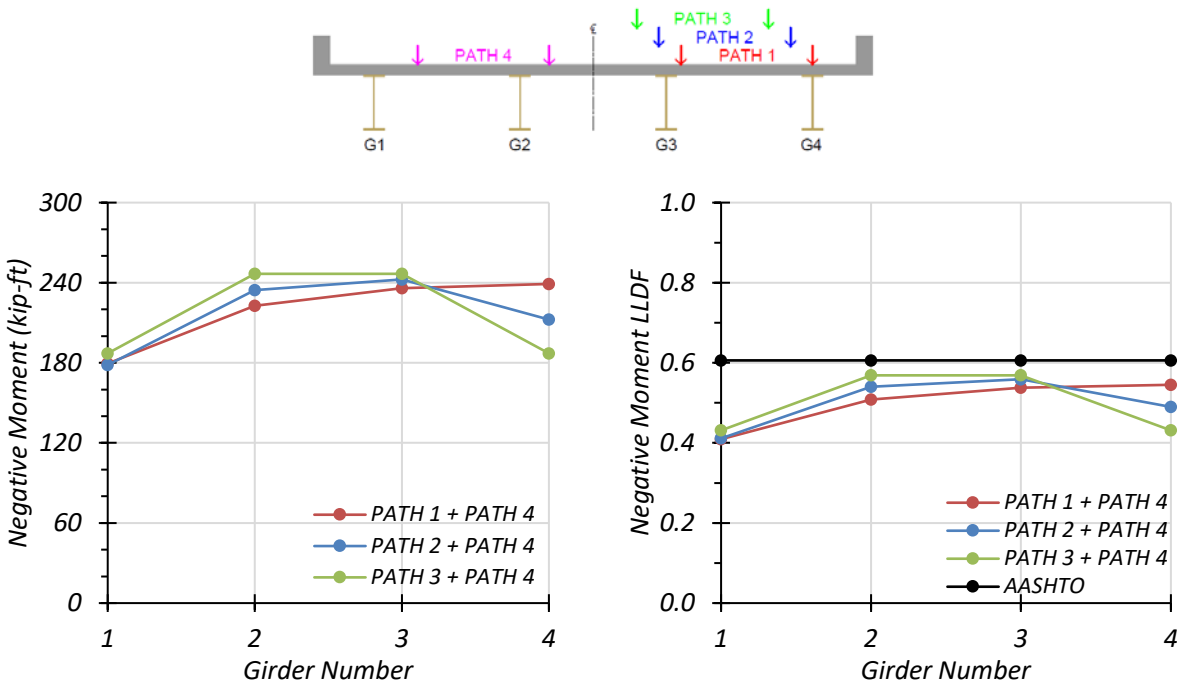

(a) Moment *(b) Moment LLDF*

Figure 6.17. Negative Moment Results for Composite Bridge SC-12 with Two-Lane HS-20 Loading

Table 6.19. Maximum Negative Moments for Composite Bridge SC-12 with Two-Lane HS-20 Loading

Loading	G1	G2	G3	G4
Path 1 + Path 4	179.5	222.7	235.9	239.1
Path 2 + Path 4	178.4	234.3	242.4	212.3
Path 3 + Path 4	187.1	246.7	246.7	187.1
Note: G = girder, paths indicate transverse loading positions as shown, moments have kip-ft units				

Comparison of governing negative moment LLDF values computed from FEM results for the composite and non-composite cases reveals that the maximum negative moment LLDF in an interior girder for the composite bridge is higher than the one for the non-composite bridge with a $g^m_{composite}/g^m_{non-composite}$ ratio of 1.04. Whereas, the negative moment LLDF in an exterior girder for the composite bridge is slightly lower than that for the non-composite bridge with a $g^m_{composite}/g^m_{non-composite}$ ratio of 0.98.

Table 6.20. Governing Negative Moment LLDFs for Bridge SC-12 with Two-Lane HS-20 Loading

Type	Girder Location	AASHTO (g^m_{AASHTO})	FEM (g^m_{FEM})	g^m_{AASHTO}/g^m_{FEM}
Non-Composite	Interior	0.606	0.546	1.11
	Exterior	0.606	0.557	1.09
Composite	Interior	0.606	0.569	1.07
	Exterior	0.606	0.545	1.11

6.6.2.4. Shear Results

6.6.2.4.1. One-Lane Loading

Figure 6.18 shows the individual girder shear forces and shear LLDF results for the non-composite Bridge SC-12 under simulated moving HS-20 loading along three one-lane loading paths. Table 6.21 provides the corresponding maximum shear values of each girder for each loading path. The shear LLDF values are calculated using the estimated shear results from the FEM analysis. Table 6.23 shows the governing shear LLDFs found using the FEM analysis and compares them to the AASHTO LLDF values. Compared to the FEM results, the governing shear LLDF value computed using the approximate equations in the AASHTO Standard Specifications (AASHTO 2002) is

conservative for both interior and exterior girders with a g^v_{AASHTO}/g^v_{FEM} ratio of 1.15 and 1.17, respectively.

Figure 6.19 shows the individual girder shears and shear LLDF results for the fully composite Bridge SC-12 under simulated moving HS-20 loading along three one-lane loading paths. Table 6.22 provides the corresponding maximum shear values of each girder for each loading path. The shear LLDF values are calculated using the estimated shear results from the FEM analysis. Compared to the FEM results, the governing shear LLDF value computed using the approximate equations in the AASHTO Standard Specifications (AASHTO 2002) is slightly conservative for interior girders with a g^v_{AASHTO}/g^v_{FEM} ratio of 1.06, and is conservative for exterior girders with a g^v_{AASHTO}/g^v_{FEM} ratio of 1.15.

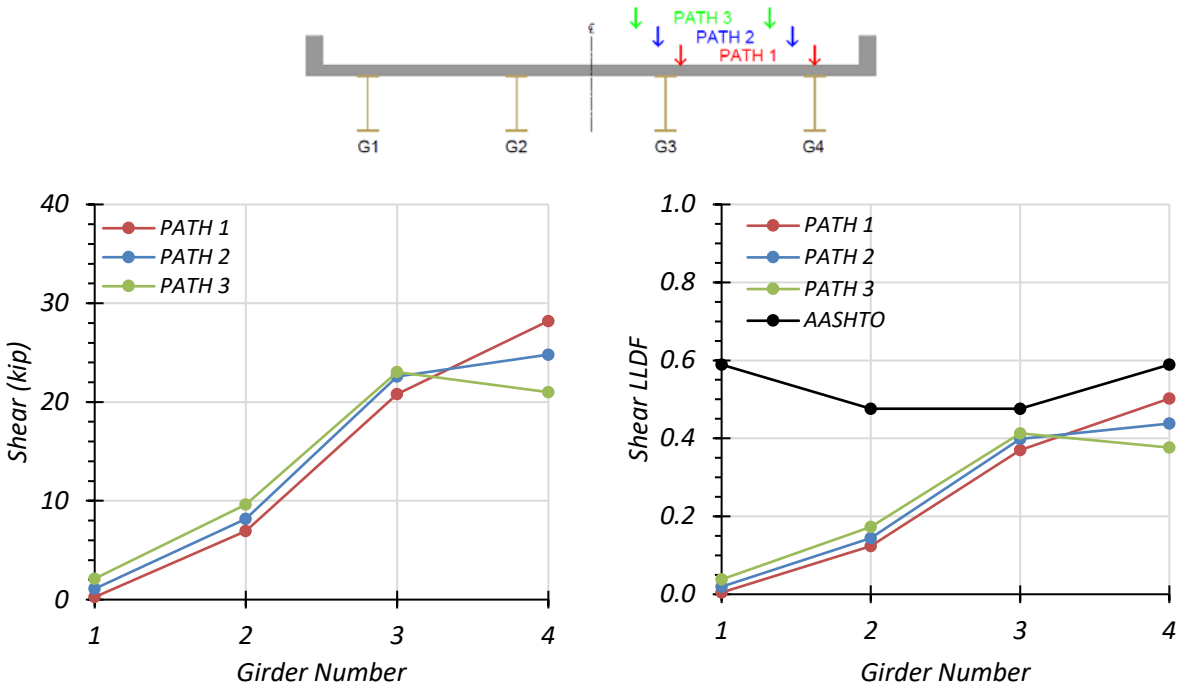

(a) Shear *(b) Shear LLDF*

Figure 6.18. Shear Results for Non-Composite Bridge SC-12 with One-Lane HS-20 Loading

Table 6.21. Maximum Shears for Non-Composite Bridge SC-12 with One-Lane HS-20 Loading

Loading	G1	G2	G3	G4
Path 1	0.3	6.9	20.8	28.2
Path 2	1.1	8.2	22.6	24.8
Path 3	2.1	9.6	23.0	21.0
Note: G = girder, paths indicate transverse loading positions as shown, shears have kip units				

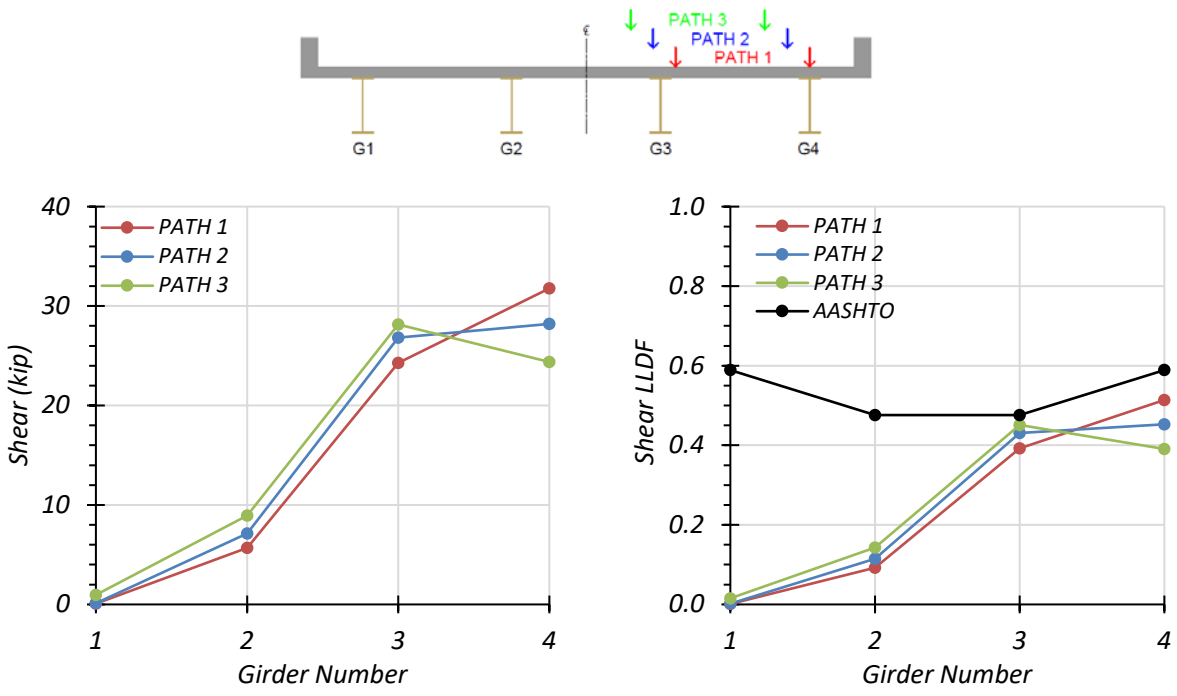

(a) Shear *(b) Shear LLDF*

Figure 6.19. Shear Results for Composite Bridge SC-12 with One-Lane HS-20 Loading

Table 6.22. Maximum Shears for Composite Bridge SC-12 with One-Lane HS-20 Loading

Loading	G1	G2	G3	G4
Path 1	0.1	5.7	24.3	31.8
Path 2	0.1	7.1	26.8	28.2
Path 3	1.0	8.9	28.1	24.4
Note: G = girder, paths indicate transverse loading positions as shown, shears have kip units				

Comparison of governing shear LLDF values computed from FEM results for the composite and non-composite cases reveals that the maximum shear LLDF in an interior girder for the composite bridge is higher than the one for the non-composite bridge with a $g^v_{composite}/g^v_{non-composite}$ ratio of 1.09. The maximum shear LLDF in an exterior girder for the composite bridge is also higher than that for the non-composite bridge with a $g^v_{composite}/g^v_{non-composite}$ ratio of 1.02.

Table 6.23. Governing Shear LLDFs for Bridge SC-12 with One-Lane HS-20 Loading

Type	Girder Location	AASHTO (g^v_{AASHTO})	FEM (g^v_{FEM})	g^v_{AASHTO}/g^v_{FEM}
Non-Composite	Interior	0.476	0.413	1.15
	Exterior	0.589	0.502	1.17
Composite	Interior	0.476	0.451	1.06
	Exterior	0.589	0.514	1.15

6.6.2.4.2. Two-Lane Loading

The same procedure was conducted for two-lane loading. Figure 6.20 shows the individual girder shears and shear LLDF results for the non-composite SM-5 bridge under simulated moving HS-20 loading along three two-lane loading paths. Table 6.24 provides the corresponding maximum shear values of each girder for each loading path. The shear LLDF values are calculated using the estimated shear results from the FEM analysis. Table 6.26 shows the governing shear LLDFs found using the FEM analysis and compares them to the AASHTO LLDF values. Compared to the FEM results, the governing shear LLDF value computed using the approximate equations in the AASHTO Standard Specifications (AASHTO 2002) is slightly conservative for interior girders

with a g^v_{AASHTO}/g^v_{FEM} ratio of 1.04, and is conservative for exterior girders with a g^v_{AASHTO}/g^v_{FEM} ratio of 1.11.

Figure 6.21 shows the individual girder shears and shear LLDF results for the fully composite Bridge SC-12 under simulated moving HS-20 loading along three one-lane loading paths. Table 6.25 provides the corresponding maximum shear values of each girder for each loading path. The shear LLDF values are calculated using the estimated shear results from the FEM analysis. Compared to the FEM results, the governing shear LLDF value computed using the approximate equations in the AASHTO Standard Specifications (AASHTO 2002) is slightly conservative for interior girders with a g^v_{AASHTO}/g^v_{FEM} ratio of 1.02, and is conservative for exterior girders with a g^v_{AASHTO}/g^v_{FEM} ratio of 1.14.

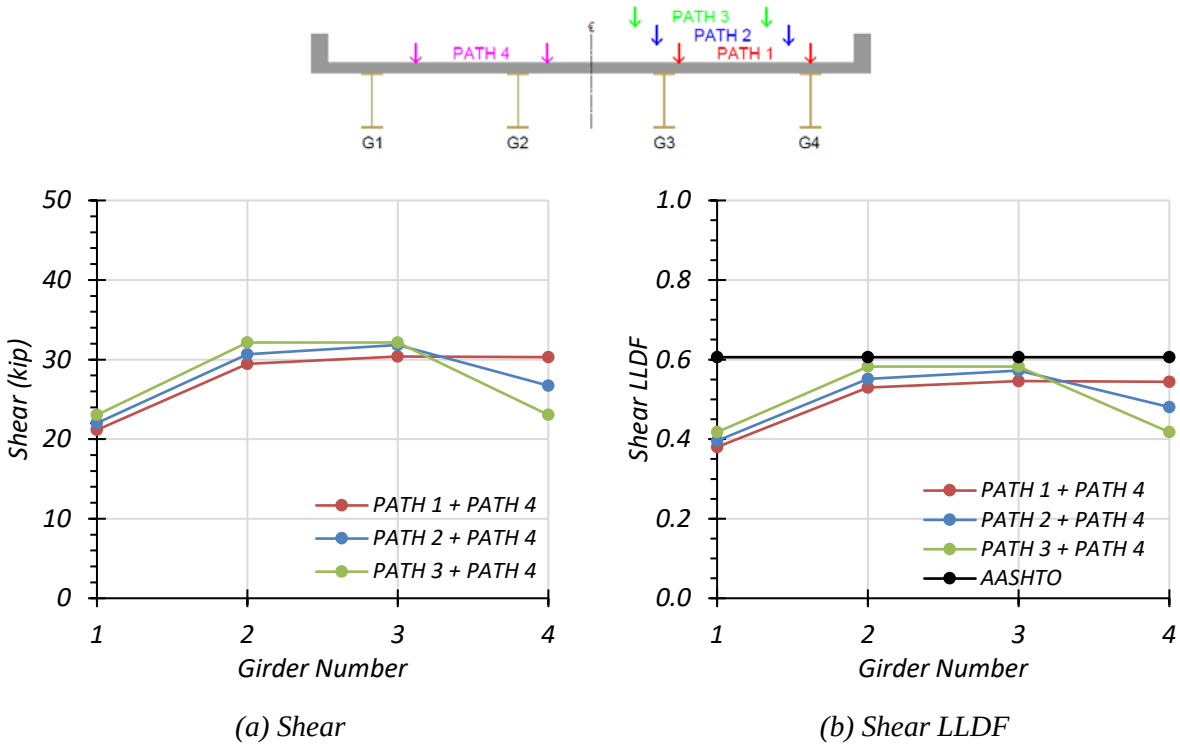

(a) Shear *(b) Shear LLDF*

Figure 6.20. Shear Results for Non-Composite Bridge SC-12 with Two-Lane HS-20 Loading

Table 6.24. Maximum Shears for Non-Composite Bridge SC-12 with Two-Lane HS-20 Loading

Loading	G1	G2	G3	G4
Path 1 + Path 4	21.2	29.5	30.4	30.3
Path 2 + Path 4	22.0	30.7	31.8	26.7
Path 3 + Path 4	23.0	32.1	32.1	23.0
Note: G = girder, paths indicate transverse loading positions as shown, shears have kip units				

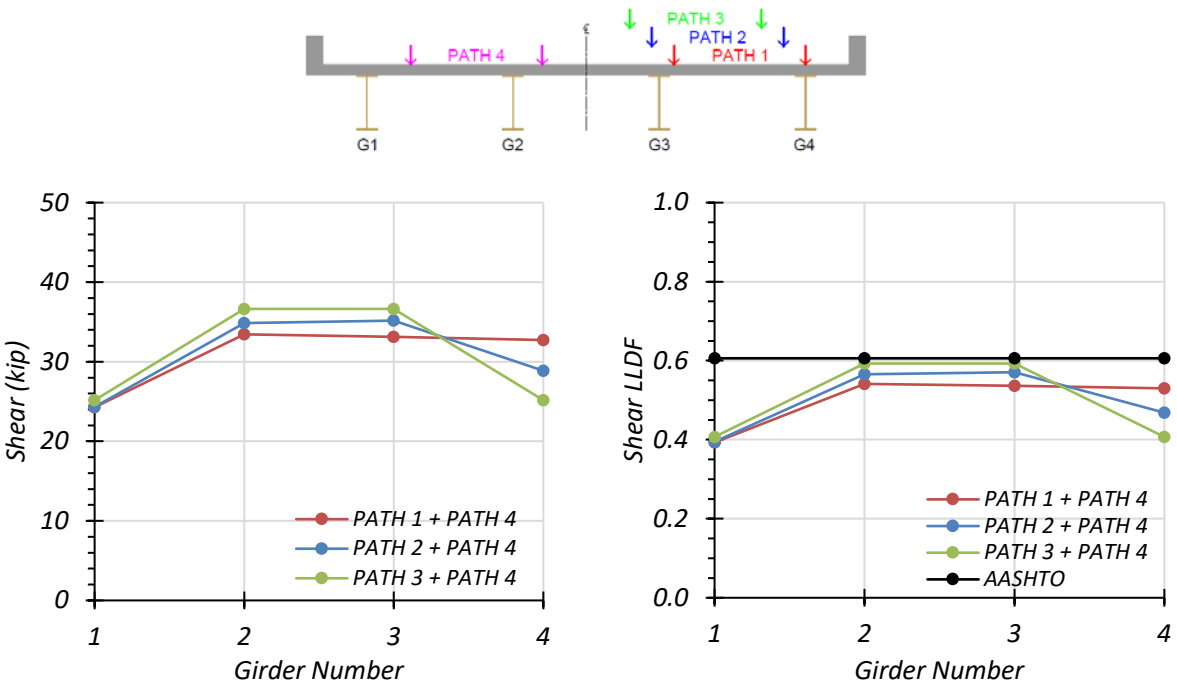

(a) Shear *(b) Shear LLDF*

Figure 6.21. Shear Results for Composite Bridge SC-12 with Two-Lane HS-20 Loading

Table 6.25. Maximum Shears for Composite Bridge SC-12 with Two-Lane HS-20 Loading

Loading	G1	G2	G3	G4
Path 1 + Path 4	24.3	33.4	33.1	32.7
Path 2 + Path 4	24.3	34.9	35.2	28.9
Path 3 + Path 4	25.2	36.6	36.6	25.2
Note: G = girder, paths indicate transverse loading positions as shown, shears have kip units				

Comparison of governing shear LLDF values computed from FEM results for the composite and non-composite cases reveals that the maximum shear LLDF in an interior girder for the composite bridge is higher than the one for the non-composite bridge with a $g^v_{composite}/g^v_{non-composite}$ ratio of 1.02. Whereas, the maximum shear LLDF in an exterior girder for the composite bridge is lower than that for the non-composite bridge with a $g^v_{composite}/g^v_{non-composite}$ ratio of 0.97.

Table 6.26. Governing Shear LLDFs for Bridge SC-12 with Two-Lane HS-20 Loading

Type	Girder Location	AASHTO (g^v_{AASHTO})	FEM (g^v_{FEM})	g^v_{AASHTO}/g^v_{FEM}
Non-Composite	Interior	0.606	0.582	1.04
	Exterior	0.606	0.544	1.11
Composite	Interior	0.606	0.593	1.02
	Exterior	0.606	0.530	1.14

6.6.2.5. Stiffness Adjustment Results

During the analysis of SC-12, it was determined that an additional analysis should be performed considering a reduction of stiffness in the negative moment regions. If the bridge is acting compositely and experiences a large enough negative moment over the interior supports, the concrete deck will experience tension cracking. This will reduce the stiffness of the deck in that region and could possibly influence the distribution of positive and negative moment along the length of the bridge and the LLDFs for each girder. This analysis was only conducted for HS-20 loading, as that is the loading that TxDOT is using to rate this bridge and all of their bridges not design using LRFD.

In order to determine the area in which the stiffness of the deck should be adjusted, the cracking moment of the composite section was determined. The modulus of rupture of concrete was determined using Article 8.15.2.1.1 in the AASHTO Standard Specifications (AASHTO 2002), which is given as follows

$$f_r = 7.5\sqrt{f'_c} \tag{6.1}$$

where,

f_r = Modulus of rupture of concrete (psi)

f'_c = Specified compressive strength of concrete (psi)

Using the modulus of rupture of concrete, the calculated section modulus of the composite section for an interior girder, and the modular ratio, the cracking moment was determined to be approximately 310 kip-ft. Therefore, the stiffness of concrete would need to be adjusted in the regions where the negative moment exceeds a magnitude of 310 kip-ft. Accounting for dead load as well, these regions were determined using the moment diagram for a two-lane HS-20 load case with trucks along Paths 1+4, as this case produced the maximum possible negative moment in an individual girder. Figure 6.22 shows the moment envelope along the bridge length for this load case, considering dead load and live load, as well as the calculated cracking moment in the negative moment region.

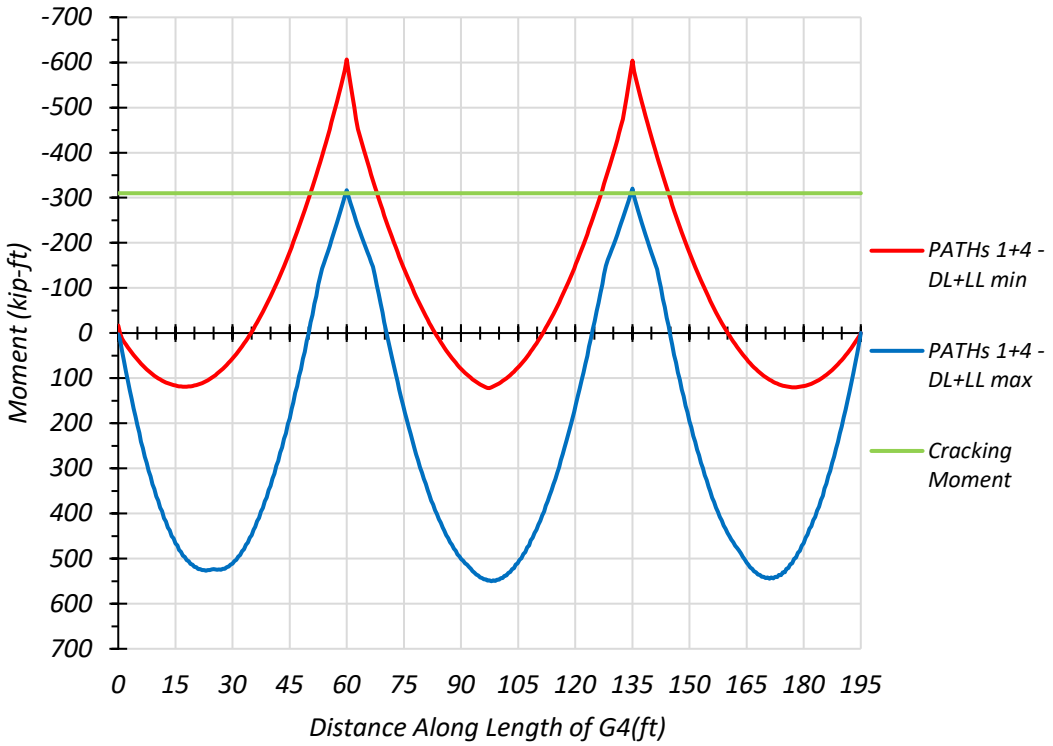

Figure 6.22. Maximum Moment Envelope for SC-12 from HS-20 Loading

Using this moment envelope, the regions where the magnitude of negative moment exceeded the cracking moment was determined to be approximately between 50.5 ft and 68 ft, and between 127 ft and 144.5 ft along the total length of the bridge. The stiffness adjustment was determined by taking the ratio of the area of a cracked element to the area of an uncracked element, considering the 6 in. wide by 6 in. thick elements used in the FEM analysis. The area of an uncracked element is therefore 36 in^2 using the gross concrete area. To determine the area of a cracked element, the amount of steel reinforcement in that element was determined. The construction drawings (TxDOT 2018b) show #5 bars top and bottom, but do not provide a spacing for the longitudinal bars in the deck. Therefore, the spacing of the transverse bars in the deck, given as 12.25 in., was used. Multiplying by the modular ratio, this gives a cracked element area

of 3.04 in^2. Dividing 3.04 by 36 gives a stiffness adjustment ratio of 0.0844. The modulus of elasticity of concrete was multiplied by this ratio in the negative moment regions with a moment demand greater than the cracking moment.

An analysis was conducted using the updated FEM model, and it was determined that the LLDFs for the individual girder did not significantly change due to the stiffness reduction. However, the positive moment and negative moment distribution along the length of the bridge did change. Figure 6.23 shows the moment envelope before the stiffness adjustment, in dashed lines, and after the stiffness adjustment, in solid lines, for exterior girder G4 under HS-20 loading along the Paths 1+4. Figure 6.24 shows the moment envelope before the stiffness adjustment, in dashed lines, and after the stiffness adjustment, in solid lines, for interior girder G3 under HS-20 loading along the Paths 3+4.

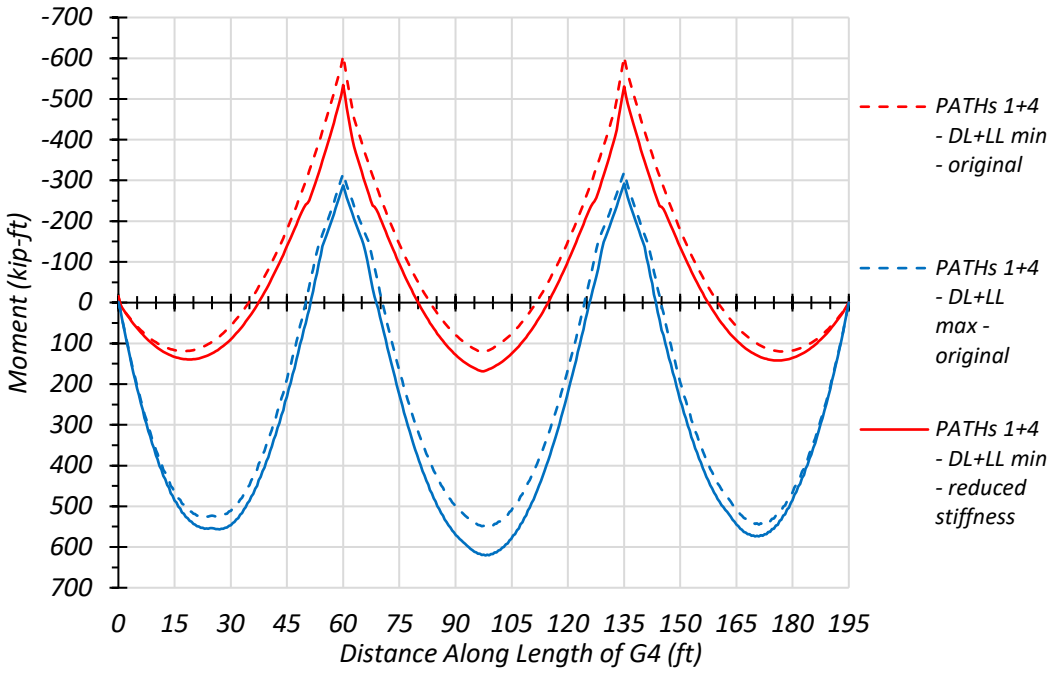

Figure 6.23. Original vs. Reduced Stiffness Moment Envelopes for Exterior Girder

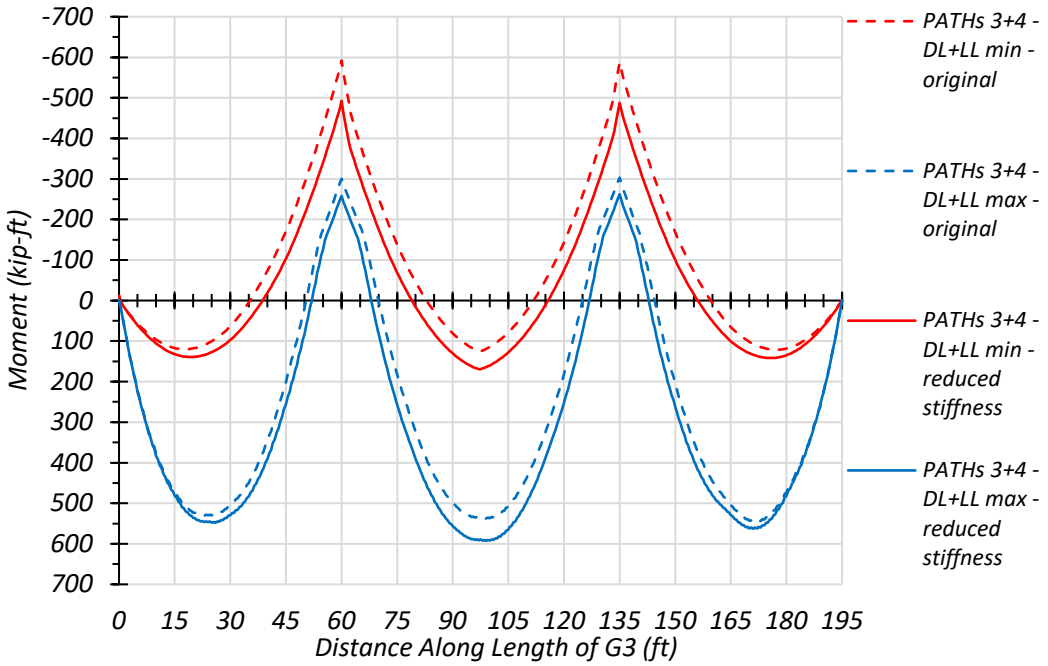

Figure 6.24. Original vs. Reduced Stiffness Moment Envelopes for Interior Girder

The reduction in stiffness of the deck to account for cracking over the negative moment region increased the maximum applied positive moment and decreased the maximum applied negative moment for both the interior and exterior girders. Table 6.27 shows the maximum positive and negative moment values for an interior and exterior girder, as well as the ratio of the original moment using the uncracked deck to the moment calculated considering the reduced deck stiffness due to cracking. This ratio is 0.92 for positive moment and 1.20 for negative moment for an interior girder, while the ratio is 0.89 for positive moment and 1.14 for negative moment for an exterior girder. This analysis has implications on the load rating process because it shows that if the deck in the negative moment region exhibits cracking, then the applied moments used for the rating process could change. During the field testing of Bridge SC-12, the potential impact of deck

cracking in the negative moment region will be explored further if test results confirm that the bridge is acting compositely and that there may be cracking over the interior supports.

Table 6.27. Positive Moment and Negative Moment Changes due to Cracked Deck Section

Girder Location	Maximum Moment Region	Original Moment (kip-ft)	Reduced Stiffness Moment (kip-ft)	Original/Reduced Stiffness Moment
Interior	Positive	545.9	593.0	0.92
	Negative	591.9	492.6	1.20
Exterior	Positive	550.2	620.8	0.89
	Negative	606.5	534.3	1.14

6.6.3. HL-93 Live Load Analysis

Bridge SC-12 was also analyzed using the HL-93 design loading presented in the AASHTO LRFD Specifications (AASHTO 2017). The bridge was analyzed for one-lane and two-lane-loaded cases along four transverse paths as shown in Figure 6.5. Deflection, moment, and shear results were obtained.

6.6.3.1. Deflection Results

Figure 6.25 shows the estimated girder deflection profile envelopes along the full length of the bridge and contours of the half length of the bridge for one-lane HL-93 loading along Path 1 and Path 4 when the bridge is analyzed as fully non-composite. Table 6.28 shows the corresponding positive (downward) and negative (upward) deflections for each girder assuming non-composite action. Load paths 1 and 4 are the only ones shown as these are expected to be the load paths used

in future field load tests, and they were selected to maximize the forces on an interior girder and on an exterior girder.

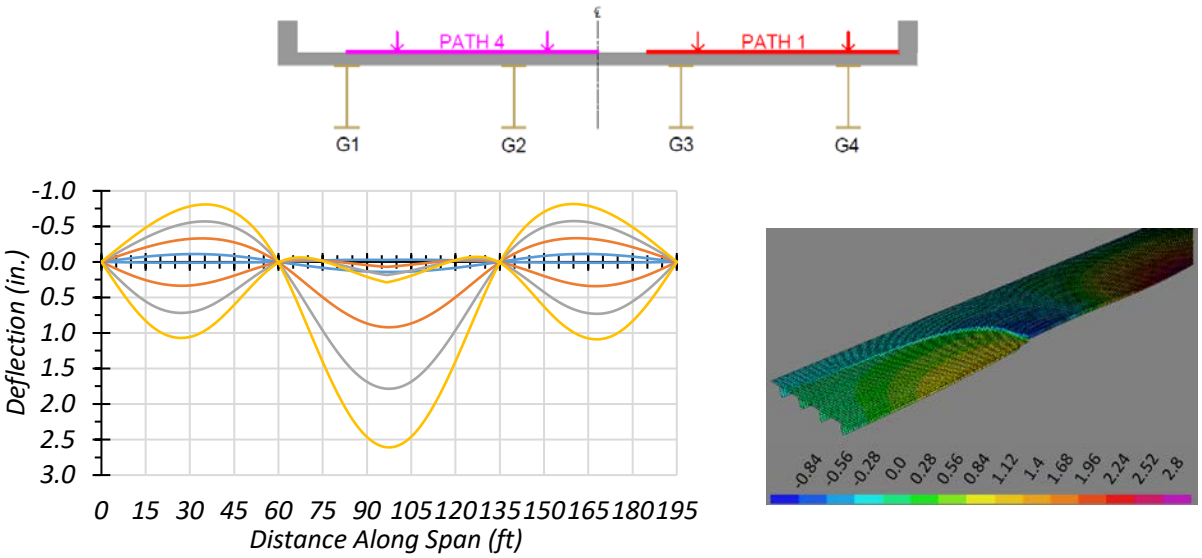

(a) Path 1

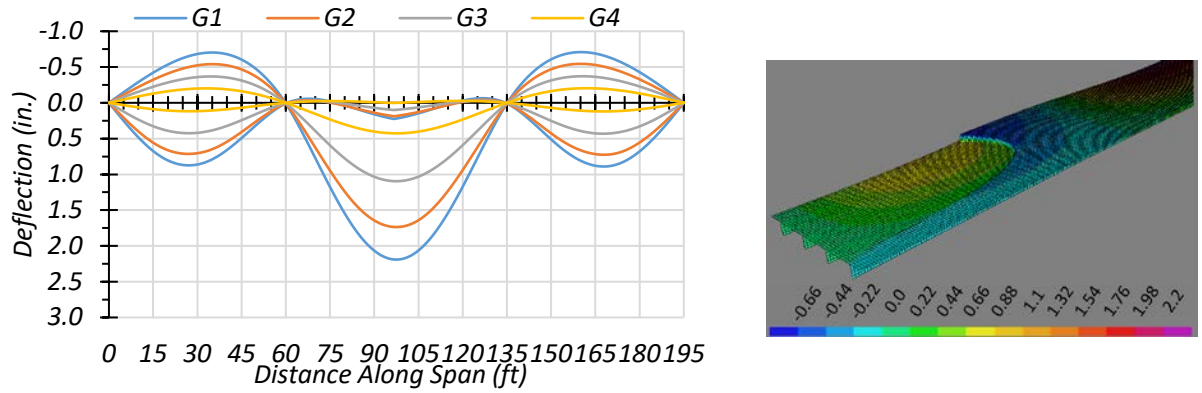

(a) Path 4

Figure 6.25. Deflection Profiles for Non-Composite Bridge SC-12 with HL-93 Loading

Table 6.28. Maximum Deflections for Non-Composite Bridge SC-12 with HL-93 Loading

Loading	Deflection Positive/Negative	G1	G2	G3	G4
Path 1	Positive	0.141	0.920	1.785	2.610
Path 1	Negative	-0.112	-0.334	-0.575	-0.815
Path 4	Positive	2.191	1.736	1.096	0.427
Path 4	Negative	-0.709	-0.544	-0.371	-0.204
Note: G = girder, paths indicate transverse loading positions as shown, deflections have inch units					

Figure 6.26 shows the estimated girder deflection profile envelopes along the full length of the bridge and contours of the half length of the bridge for one-lane HL-93 loading along Path 1 and Path 4 when the bridge is analyzed as fully composite. Table 6.29 shows the corresponding positive (downward) and negative (upward) deflections for each girder assuming fully composite action. Load paths 1 and 4 are the only ones shown as these are expected to be the load paths used in future field load tests, and they were selected to maximize the forces on an interior girder and on an exterior girder.

For both the non-composite and composite cases, the maximum negative deflections were obtained in Girder 4 when the HL-93 truck was run along Path 1. The estimated deflections were 2.61 in. and 1.20 in. for non-composite and composite cases, respectively. This result indicates that the composite bridge is 74 percent stiffer than the non-composite bridge. The maximum deflections obtained when the HL-93 truck was run along Path 4 were in Girder 1 for both the non-composite and composite case. The estimated deflections were 2.19 in. and 0.99 in. for the non-composite and composite cases, respectively, indicating that the composite bridge is 76 percent stiffer than the non-composite bridge. The slightly different values of relative stiffness suggest that the relative girder deflection depends on the location of loading and corresponding load distribution.

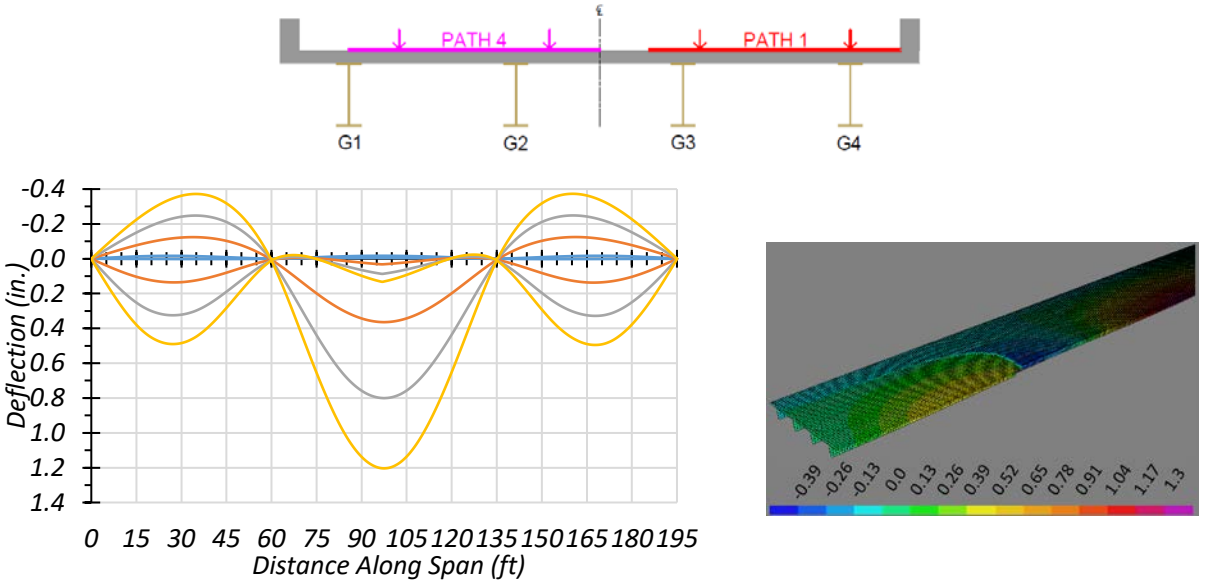

(a) Path 1

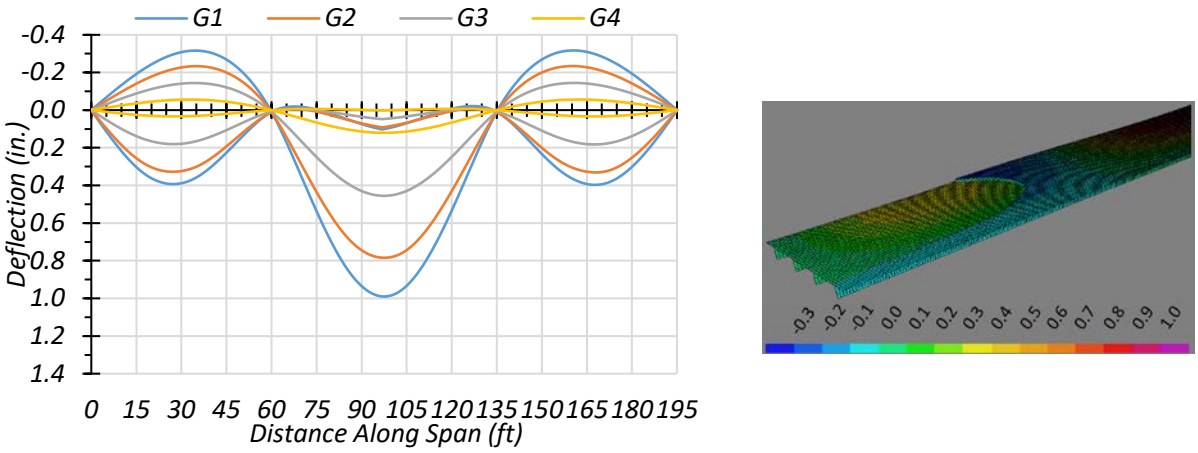

(b) Path 4

Figure 6.26. Deflection Profiles for Composite Bridge SC-12 with HL-93 Loading

Table 6.29. Maximum Deflections for Composite Bridge SC-12 with HL-93 Loading

Loading	Deflection Positive/Negative	G1	G2	G3	G4
Path 1	Positive	0.002	0.364	0.801	1.204
Path 1	Negative	-0.017	-0.125	-0.249	-0.373
Path 4	Positive	0.990	0.784	0.455	0.120
Path 4	Negative	-0.317	-0.234	-0.144	-0.056
Note: G = girder, paths indicate transverse loading positions as shown, deflections have inch units					

6.6.3.2. Positive Moment Results

6.6.3.2.1. One-Lane Loading

Figure 6.27 shows the individual girder positive moment and positive moment LLDF results for the non-composite Bridge SC-12 under simulated moving HL-93 loading along three different one-lane loading paths. Table 6.30 provides the corresponding maximum positive moment values of each girder for each loading path. The positive moment LLDF values are calculated using the estimated positive moment results from the FEM analysis. Table 6.32 shows the governing positive moment LLDFs found using the FEM analysis and compares them to the AASHTO LLDF values. The first AASHTO LLDF value is calculated using the simplified stiffness parameter. The second AASHTO LLDF value is calculated using the analytical stiffness parameter calculated for the specific bridge. Compared to the FEM results, the governing positive moment LLDF value computed using the approximate equation and the simplified stiffness parameter in AASHTO LRFD Specifications (AASHTO 2017) is slightly conservative for interior girders with a $g^m_{AASHTO\_S}/g^m_{FEM}$ ratio of 1.05, and conservative for exterior girders with a $g^m_{AASHTO\_S}/g^m_{FEM}$ ratio of 1.14. Compared to the FEM results, the governing positive moment LLDF value computed using the approximate equations and the analytical stiffness parameter in AASHTO LRFD Specifications (AASHTO 2017) is almost the same for interior girders with a $g^m_{AASHTO\_K}/g^m_{FEM}$ ratio of 1.01, and conservative for exterior girders with a $g^m_{AASHTO\_K}/g^m_{FEM}$ ratio of 1.14.

Figure 6.28 shows the individual girder positive moment and positive moment LLDF results for the fully composite Bridge SC-12 under simulated moving HL-93 loading along the three one-lane loading paths. Table 6.31 provides the corresponding maximum positive moment values of each girder for each loading path. The positive moment LLDF values are calculated using

the estimated positive moment results from the FEM analysis. Compared to the FEM results, the governing positive moment LLDF value computed using the approximate equation and the simplified stiffness parameter in AASHTO LRFD Specifications (AASHTO 2017) is almost the same for interior girders with a $g^m_{AASHTO\_S}/g^m_{FEM}$ ratio of 1.01, and slightly conservative for exterior girder with a $g^m_{AASHTO\_S}/g^m_{FEM}$ ratio 1.10. Compared to the FEM results, the governing positive moment LLDF value computed using the approximate equations and the analytical stiffness parameter in AASHTO LRFD Specifications (AASHTO 2017) is slightly unconservative for interior girders with a $g^m_{AASHTO\_K}/g^m_{FEM}$ ratio of 0.97, while being slightly conservative for exterior girders with a $g^m_{AASHTO\_K}/g^m_{FEM}$ ratio of 1.10.

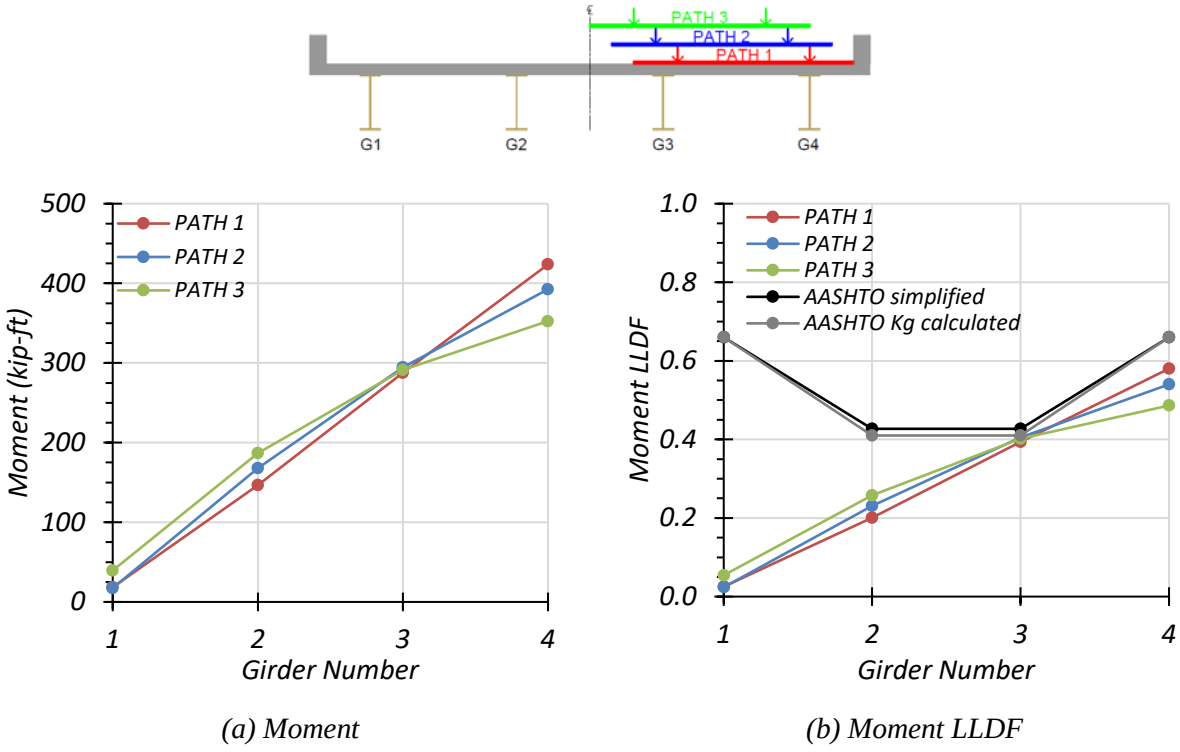

(a) Moment *(b) Moment LLDF*

Figure 6.27. Positive Moment Results for Non-Composite Bridge SC-12 with One-Lane HL-93 Loading

Table 6.30. Maximum Positive Moments for Non-Composite Bridge SC-12 with One-Lane HL-93 Loading

Loading	G1	G2	G3	G4
Path 1	18.4	146.6	287.6	423.7
Path 2	17.4	167.8	294.5	392.6
Path 3	39.4	186.8	291.1	352.6
Note: G = girder, paths indicate transverse loading positions as shown, moments have kip-ft units				

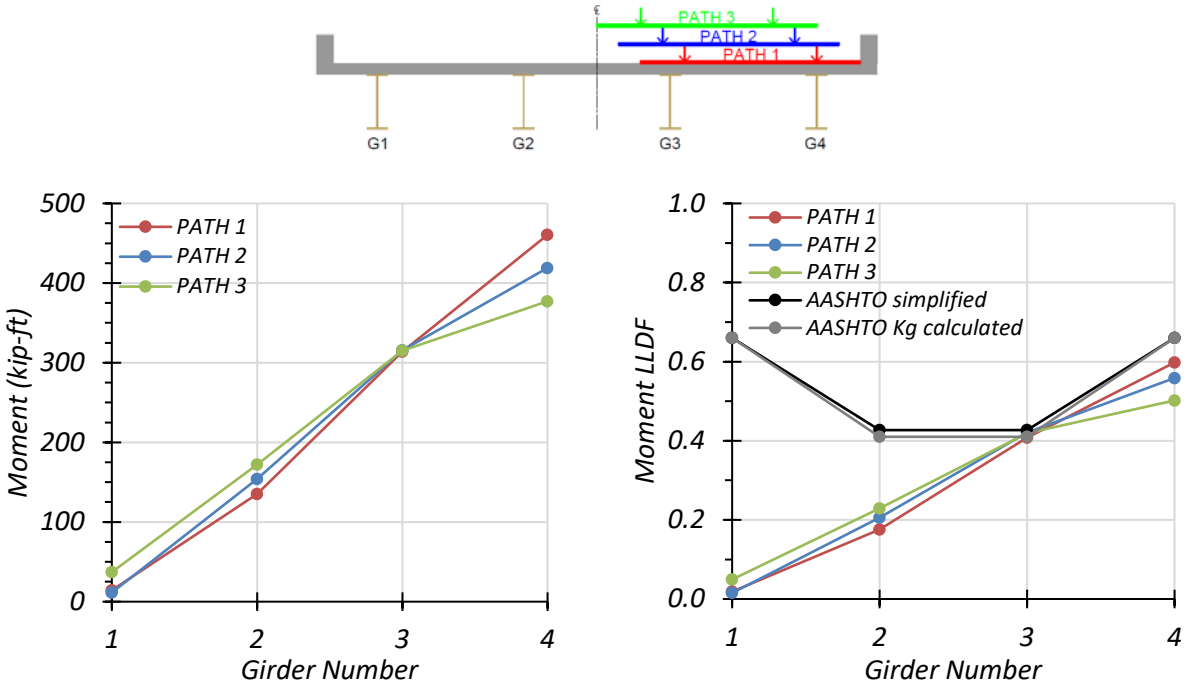

(a) Moment *(b) Moment LLDF*

Figure 6.28. Positive Moment Results for Composite Bridge SC-12 with One-Lane HL-93 Loading

Table 6.31. Maximum Positive Moments for Composite Bridge SC-12 with One-Lane HL-93 Loading

Loading	G1	G2	G3	G4
Path 1	14.3	135.4	313.9	460.5
Path 2	11.4	154.1	315.4	419.0
Path 3	37.1	172.3	315.1	377.1
Note: G = girder, paths indicate transverse loading positions as shown, moments have kip-ft units				

Comparison of governing positive moment LLDF values computed from FEM results for the composite and non-composite cases reveals that the maximum positive moment LLDF in an interior girder for the composite bridge is slightly higher than the one for the non-composite bridge with a $g^m_{composite}/g^m_{non-composite}$ ratio of 1.04. The maximum positive moment LLDF in an exterior girder for the composite bridge is also slightly higher than that for the non-composite bridge with a $g^m_{composite}/g^m_{non-composite}$ ratio of 1.03.

Table 6.32. Governing Positive Moment LLDFs for Bridge SC-12 with One-Lane HL-93 Loading

Type	Girder Location	AASHTO Simplified ($g^m_{AASHTO\_S}$)	AASHTO K_g Calculated ($g^m_{AASHTO\_K}$)	FEM (g^m_{FEM})	$g^m_{AASHTO\_S}/g^m_{FEM}$	$g^m_{AASHTO\_K}/g^m_{FEM}$
Non-Composite	Interior	0.427	0.410	0.405	1.05	1.01
	Exterior	0.660	0.660	0.580	1.14	1.14
Composite	Interior	0.427	0.410	0.421	1.01	0.97
	Exterior	0.660	0.660	0.598	1.10	1.10

6.6.3.2.2. Two-Lane Loading

Figure 6.29 shows the individual girder positive moment and positive moment LLDF results for the non-composite Bridge SC-12 under simulated moving HL-93 loading along three two-lane loading paths. Table 6.33 provides the corresponding maximum positive moment values of each girder for each loading path. The positive moment LLDF values are calculated using the estimated positive moment results from the FEM analysis. Table 6.35 shows the governing positive moment LLDFs found using the FEM analysis and compares them to the AASHTO LLDF values. The first AASHTO LLDF value is calculated using the simplified stiffness parameter. The second AASHTO LLDF value is calculated using the analytical stiffness parameter calculated for the

specific bridge. Compared to the FEM results, the governing positive moment LLDF value computed using the approximate equations and the simplified stiffness parameter in AASHTO LRFD Specifications (AASHTO 2017) is slightly conservative for interior girders with a $g^m_{AASHTO\_S}/g^m_{FEM}$ ratio of 1.10, and conservative for exterior girders with a $g^m_{AASHTO\_S}/g^m_{FEM}$ ratio of 1.18. Compared to the FEM results, the governing positive moment LLDF value computed using the approximate equations and the analytical stiffness parameter in AASHTO LRFD Specifications (AASHTO 2017) is slightly conservative for interior girders with a $g^m_{AASHTO\_K}/g^m_{FEM}$ ratio of 1.05, and conservative for exterior girders with a $g^m_{AASHTO\_K}/g^m_{FEM}$ ratio of 1.18.

Figure 6.30 shows the individual girder positive moment and positive moment LLDF results for the fully composite Bridge SC-12 under simulated moving HL-93 loading along three two-lane loading paths. Table 6.34 provides the corresponding maximum positive moment values of each girder for each loading path. The positive moment LLDF values are calculated using the estimated positive moment results from the FEM analysis. Compared to the FEM results, the governing positive moment LLDF value computed using the approximate equations and the simplified stiffness parameter in AASHTO LRFD Specifications (AASHTO 2017) is slightly conservative for interior girders with a $g^m_{AASHTO\_S}/g^m_{FEM}$ ratio of 1.08, and conservative for exterior girders with a $g^m_{AASHTO\_S}/g^m_{FEM}$ ratio of 1.19. Compared to the FEM results, the governing positive moment LLDF value computed using the approximate equations and the analytical stiffness parameter in AASHTO LRFD Specifications (AASHTO 2017) is slightly conservative for interior girders with a $g^m_{AASHTO\_K}/g^m_{FEM}$ ratio of 1.04, and conservative for exterior girders with a $g^m_{AASHTO\_K}/g^m_{FEM}$ ratio of 1.19.

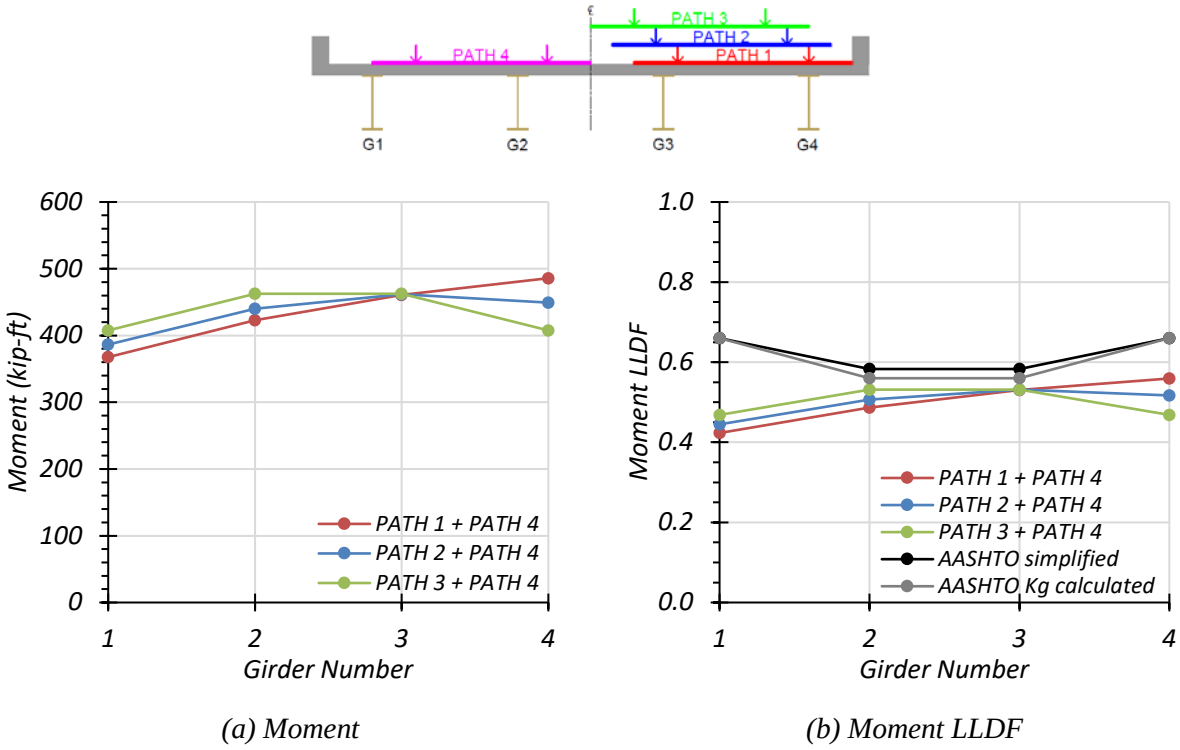

(a) Moment *(b) Moment LLDF*

Figure 6.29. Positive Moment Results for Non-Composite Bridge SC-12 with Two-Lane HL-93 Loading

Table 6.33. Maximum Positive Moments for Non-Composite Bridge SC-12 with Two-Lane HL-93 Loading

Loading	G1	G2	G3	G4
Path 1 + Path 4	367.6	423.0	460.7	485.9
Path 2 + Path 4	386.5	440.1	461.8	449.1
Path 3 + Path 4	407.6	462.5	462.5	407.6
Note: G = girder, paths indicate transverse loading positions as shown, moments have kip-ft units				

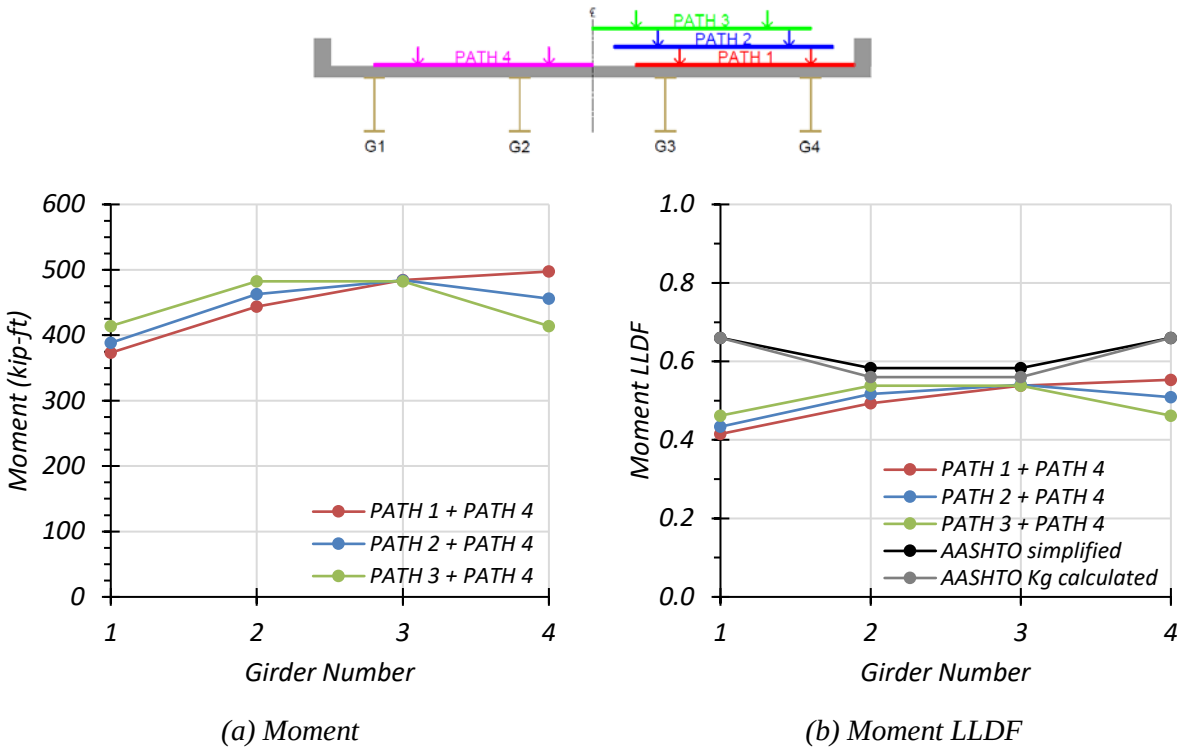

(a) Moment *(b) Moment LLDF*

Figure 6.30. Positive Moment Results for Composite Bridge SC-12 with Two-Lane HL-93 Loading

Table 6.34. Maximum Positive Moments for Composite Bridge SC-12 with Two-Lane HL-93 Loading

Loading	G1	G2	G3	G4
Path 1 + Path 4	373.3	443.6	484.1	497.4
Path 2 + Path 4	388.4	462.9	484.1	456.0
Path 3 + Path 4	414.1	482.4	482.4	414.1
Note: G = girder, paths indicate transverse loading positions as shown, moments have kip-ft units				

Comparison of governing positive moment LLDF values computed from FEM results for the composite and non-composite cases reveals that the maximum positive moment LLDF in both interior and exterior girders for the composite bridge is almost the same as the one for the non-composite bridge with a $g^m_{composite}/g^m_{non-composite}$ ratio of 1.02 and 0.99, respectively.

Table 6.35. Governing Positive Moment LLDFs for Bridge SC-12 with Two-Lane HL-93 Loading

Type	Girder Location	AASHTO Simplified ($g^m_{AASHTO\_S}$)	AASHTO K_g Calculated ($g^m_{AASHTO\_K}$)	FEM (g^m_{FEM})	$g^m_{AASHTO\_S}/g^m_{FEM}$	$g^m_{AASHTO\_K}/g^m_{FEM}$
Non-Composite	Interior	0.583	0.560	0.532	1.10	1.05
	Exterior	0.660	0.660	0.559	1.18	1.18
Composite	Interior	0.583	0.560	0.540	1.08	1.04
	Exterior	0.660	0.660	0.553	1.19	1.19

6.6.3.3. Negative Moment Results

6.6.3.3.1. One-Lane Loading

Figure 6.31 shows the individual girder negative moment and negative moment LLDF results for the non-composite Bridge SC-12 under simulated moving HL-93 loading along three one-lane loading paths. Table 6.36 provides the corresponding maximum negative moment values of each girder for each loading path. The negative moment LLDF values are calculated using the estimated negative moment results from the FEM analysis. Table 6.38 shows the governing negative moment LLDFs found using the FEM analysis and compares them to the AASHTO LLDF values. The first AASHTO LLDF value is calculated using the simplified stiffness parameter. The second AASHTO LLDF value is calculated using the analytical stiffness parameter calculated for the specific bridge. Compared to the FEM results, the governing negative moment LLDF value computed using the approximate equations and the simplified stiffness parameter in AASHTO LRFD Specifications (AASHTO 2017) is slightly conservative for both interior and exterior girders with a $g^m_{AASHTO\_S}/g^m_{FEM}$ ratio of 1.04 and 1.08, respectively. Compared to the FEM results, the governing negative moment LLDF value computed using the approximate equations and the analytical stiffness parameter in AASHTO LRFD Specifications (AASHTO 2017) is almost the

same for interior girders with a $g^m_{AASHTO\_K}/g^m_{FEM}$ ratio of 1.00, and slightly conservative for exterior girders with a $g^m_{AASHTO\_K}/g^m_{FEM}$ ratio of 1.08.

Figure 6.32 shows the individual girder negative moment and negative moment LLDF results for the fully composite Bridge SC-12 under simulated moving HL-93 loading along three one-lane loading paths. Table 6.37 provides the corresponding maximum negative moment values of each girder for each loading path. The negative moment LLDF values are calculated using the estimated negative moment results from the FEM analysis. Compared to the FEM results, the governing negative moment LLDF value computed using the approximate equation and the simplified stiffness parameter in the AASHTO LRFD Specifications (AASHTO 2017) is almost the same for interior girders with a $g^m_{AASHTO\_S}/g^m_{FEM}$ ratio of 0.99, and is slightly conservative for exterior girders with a $g^m_{AASHTO\_S}/g^m_{FEM}$ ratio of 1.07. Compared to the FEM results, the governing negative moment LLDF value computed using the approximate equation and the analytical stiffness parameter in AASHTO LRFD Specifications (AASHTO 2017) is slightly unconservative for interior girders with a $g^m_{AASHTO\_K}/g^m_{FEM}$ ratio of 0.96, and slightly conservative for exterior girders with a $g^m_{AASHTO\_K}/g^m_{FEM}$ ratio of 1.07.

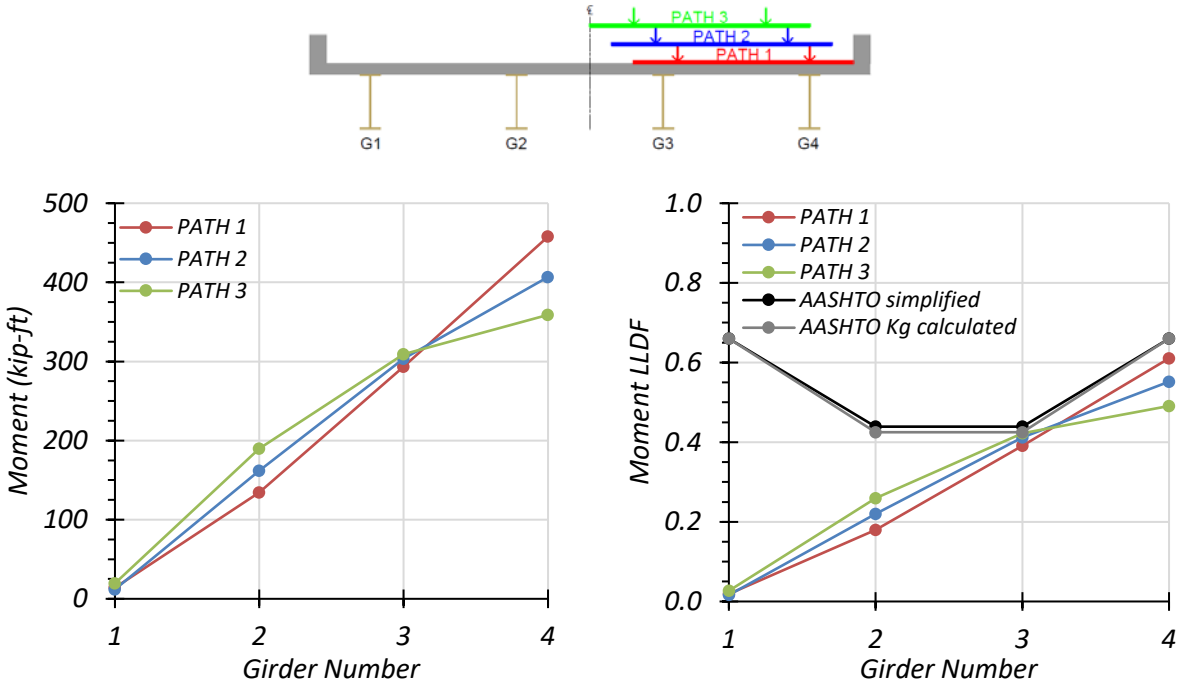

(a) Moment *(b) Moment LLDF*

Figure 6.31. Negative Moment Results for Non-Composite Bridge SC-12 with One-Lane HL-93 Loading

Table 6.36. Maximum Negative Moments for Non-Composite Bridge SC-12 with One-Lane HL-93 Loading

Loading	G1	G2	G3	G4
Path 1	14.1	134.5	293.5	457.8
Path 2	11.9	162.1	303.6	406.8
Path 3	19.6	189.8	309.1	358.9
Note: G = girder, paths indicate transverse loading positions as shown, moments have kip-ft units				

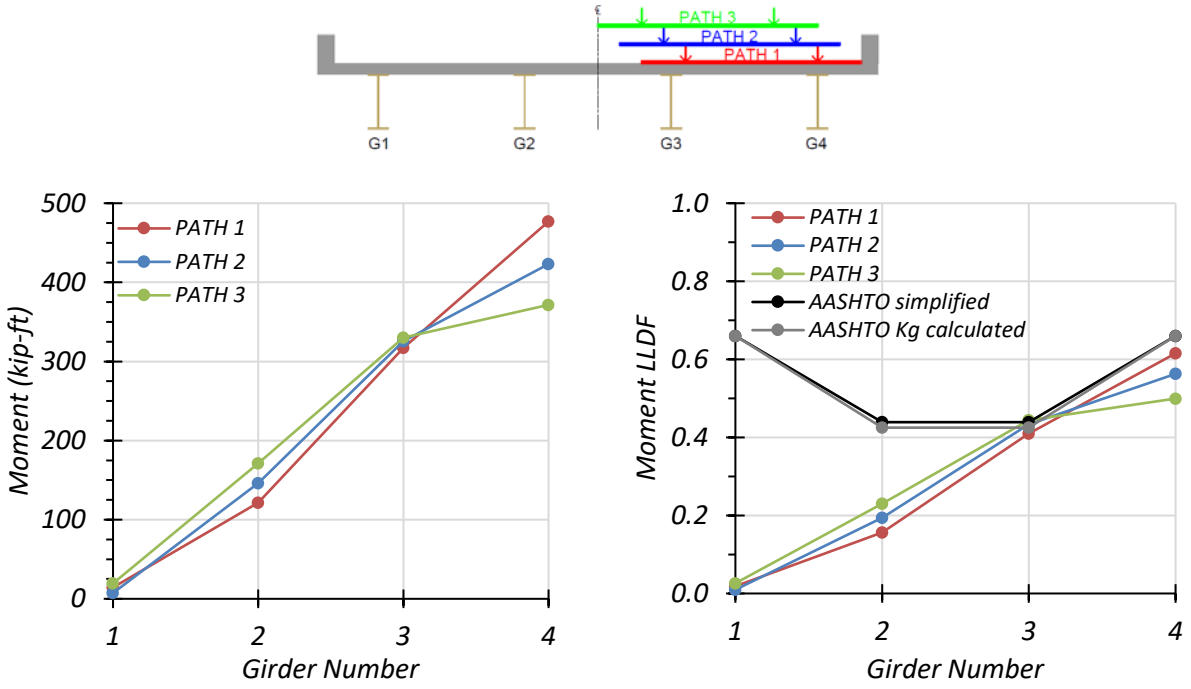

(a) Moment *(b) Moment LLDF*

Figure 6.32. Negative Moment Results for Composite Bridge SC-12 with One-Lane HL-93 Loading

Table 6.37. Maximum Negative Moments for Composite Bridge SC-12 with One-Lane HL-93 Loading

Loading	G1	G2	G3	G4
Path 1	14.4	121.4	317.4	477.0
Path 2	7.3	146.0	325.8	423.1
Path 3	19.5	171.3	330.3	371.5
Note: G = girder, paths indicate transverse loading positions as shown, moments have kip-ft units				

Comparison of governing negative moment LLDF values computed from FEM results for the composite and non-composite cases reveals that the maximum negative moment LLDF in an interior girder for the composite bridge is higher than the one for the non-composite bridge with a $g^m_{composite}/g^m_{non-composite}$ ratio of 1.05. The maximum negative moment LLDF in an exterior

girder for the composite bridge is almost the same as that for the non-composite bridge with a $g^m_{composite}/g^m_{non-composite}$ ratio of 1.01.

Table 6.38. Governing Negative Moment LLDFs for Bridge SC-12 with One-Lane HL-93 Loading

Type	Girder Location	AASHTO Simplified ($g^m_{AASHTO\_S}$)	AASHTO K_g Calculated ($g^m_{AASHTO\_K}$)	FEM (g^m_{FEM})	$g^m_{AASHTO\_S}/g^m_{FEM}$	$g^m_{AASHTO\_K}/g^m_{FEM}$
Non-Composite	Interior	0.439	0.425	0.423	1.04	1.00
	Exterior	0.660	0.660	0.610	1.08	1.08
Composite	Interior	0.439	0.425	0.444	0.99	0.96
	Exterior	0.660	0.660	0.615	1.07	1.07

6.6.3.3.2. Two-Lane Loading

Figure 6.33 shows the individual girder negative moments and negative moment LLDF results for the non-composite Bridge SC-12 under simulated moving HL-93 loading along three two-lane loading paths. Table 6.39 provides the corresponding maximum negative moment values of each girder for each loading path. The negative moment LLDF values are calculated using the estimated negative moment results from the FEM analysis. Table 6.41 shows the governing negative moment LLDFs found using the FEM analysis and compares them to the AASHTO LLDF values. The first AASHTO LLDF value is calculated using the simplified stiffness parameter. The second AASHTO LLDF value is calculated using the analytical stiffness parameter calculated for the specific bridge. Compared to the FEM results, the governing negative moment LLDF value computed using the approximate equations and the simplified stiffness parameter in AASHTO LRFD Specifications (AASHTO 2017) is slightly conservative for interior girders with a $g^m_{AASHTO\_S}/g^m_{FEM}$ ratio of 1.07, and is conservative for exterior girders with a $g^m_{AASHTO\_S}/g^m_{FEM}$ ratio

of 1.18. Compared to the FEM results, the governing negative moment LLDF value computed using the approximate equations and the analytical stiffness parameter in AASHTO LRFD Specifications (AASHTO 2017) is slightly conservative for interior girders with a $g^m_{AASHTO\_K}/g^m_{FEM}$ ratio of 1.04, and is conservative for exterior girders with a $g^m_{AASHTO\_K}/g^m_{FEM}$ ratio of 1.18.

Figure 6.34 shows the individual girder negative moment and negative moment LLDF results for the fully composite Bridge SC-12 under simulated moving HL-93 loading along three two-lane loading paths. Table 6.40 provides the corresponding maximum negative moment values of each girder for each loading path. The negative moment LLDF values are calculated using the estimated negative moment results from the FEM analysis. Compared to the FEM results, the governing negative moment LLDF value computed using the approximate equations and the simplified stiffness parameter in AASHTO LRFD Specifications (AASHTO 2017) is slightly conservative for interior girders with a $g^m_{AASHTO\_S}/g^m_{FEM}$ ratio of 1.06, and conservative for exterior girders with a $g^m_{AASHTO\_S}/g^m_{FEM}$ ratio of 1.20. Compared to the FEM results, the governing negative moment LLDF value computed using the approximate equations and the analytical stiffness parameter in AASHTO LRFD Specifications (AASHTO 2017) is almost the same for interior girders with a $g^m_{AASHTO\_K}/g^m_{FEM}$ ratio of 1.02, and is conservative for exterior girders with a $g^m_{AASHTO\_K}/g^m_{FEM}$ ratio of 1.20.

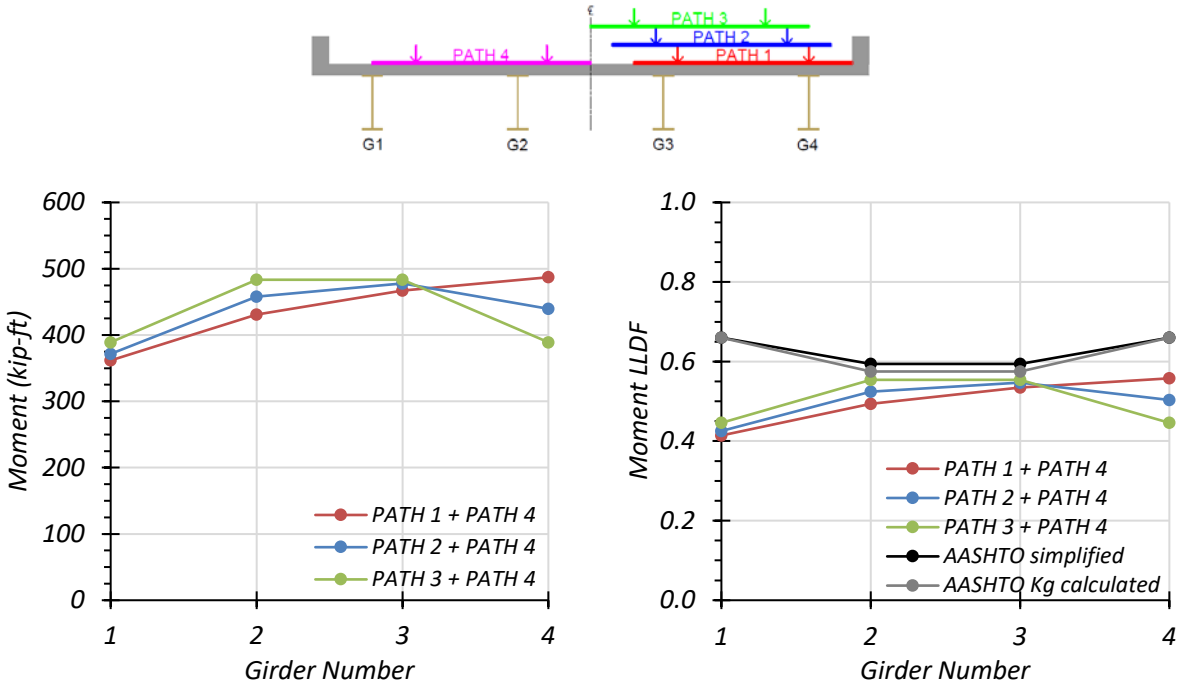

(a) Moment *(b) Moment LLDF*

Figure 6.33. Negative Moment Results for Non-Composite Bridge SC-12 with Two-Lane HL-93 Loading

Table 6.39. Maximum Negative Moments for Non-Composite Bridge SC-12 with Two-Lane HL-93 Loading

Loading	G1	G2	G3	G4
Path 1 + Path 4	361.7	430.9	466.9	487.1
Path 2 + Path 4	371.6	458.1	477.8	439.3
Path 3 + Path 4	389.1	483.4	483.4	389.1
Note: G = girder, paths indicate transverse loading positions as shown, moments have kip-ft units				

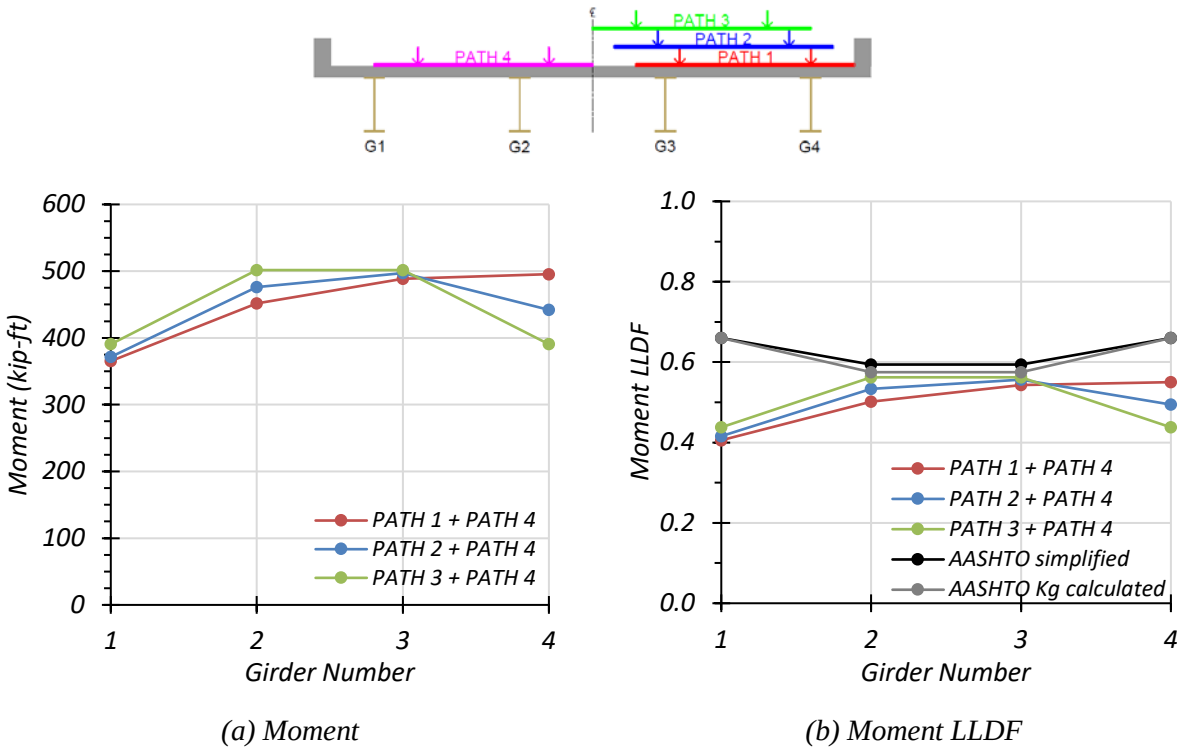

(a) Moment *(b) Moment LLDF*

Figure 6.34. Negative Moment Results for Composite Bridge SC-12 with Two-Lane HL-93 Loading

Table 6.40. Maximum Negative Moments for Composite Bridge SC-12 with Two-Lane HL-93 Loading

Loading	G1	G2	G3	G4
Path 1 + Path 4	365.3	451.7	488.7	495.5
Path 2 + Path 4	371.5	476.3	497.1	441.9
Path 3 + Path 4	390.6	501.6	501.6	390.6
Note: G = girder, paths indicate transverse loading positions as shown, moments have kip-ft units				

Comparison of governing negative moment LLDF values computed from FEM results for the composite and non-composite cases reveals that the maximum negative moment LLDF in an interior and exterior girder for the composite bridge is almost the same as the one for the non-composite bridge with a $g^m_{composite}/g^m_{non-composite}$ ratio of 1.01 and 0.99, respectively.

Table 6.41. Governing Negative Moment LLDFs for Bridge SC-12 with Two-Lane HL-93 Loading

Type	Girder Location	AASHTO Simplified ($g^m_{AASHTO\_S}$)	AASHTO K_g Calculated ($g^m_{AASHTO\_K}$)	FEM (g^m_{FEM})	$g^m_{AASHTO\_S}/g^m_{FEM}$	$g^m_{AASHTO\_K}/g^m_{FEM}$
Non-Composite	Interior	0.594	0.575	0.554	1.07	1.04
	Exterior	0.660	0.660	0.558	1.18	1.18
Composite	Interior	0.594	0.575	0.562	1.06	1.02
	Exterior	0.660	0.660	0.550	1.20	1.20

6.6.3.4. Shear Results

6.6.3.4.1. One-Lane Loading

Figure 6.35 shows the individual girder shears and shear LLDF results for the non-composite Bridge SC-12 under simulated moving HL-93 loading along three different one-lane loading paths. Table 6.42 provides the corresponding maximum shear values of each girder for each loading path. The shear LLDF values are calculated using the estimated shear results from the FEM analysis. Table 6.44 shows the governing shear LLDFs found using the FEM analysis and compares them to the AASHTO LLDF values. Compared to the FEM results, the governing shear LLDF value computed using the approximate equations in AASHTO LRFD Specifications (AASHTO 2017) is conservative for interior girders with a g^v_{AASHTO}/g^v_{FEM} ratio of 1.24, and is slightly conservative for exterior girders with a g^v_{AASHTO}/g^v_{FEM} ratio of 1.07.

Figure 6.36 shows the individual girder shears and shear LLDF results for the fully composite Bridge SC-12 under simulated moving HL-93 loading along three one-lane loading paths. Table 6.43 provides the corresponding maximum shear values of each girder for each loading path. The shear LLDF values are calculated using the estimated shear results from the FEM analysis. Compared to the FEM results, the governing shear LLDF value computed using the

approximate equations in AASHTO LRFD Specifications (AASHTO 2017) is conservative for interior girders with a g^v_{AASHTO}/g^v_{FEM} ratio of 1.16, and is slightly conservative for exterior girders with a g^v_{AASHTO}/g^v_{FEM} ratio of 1.06.

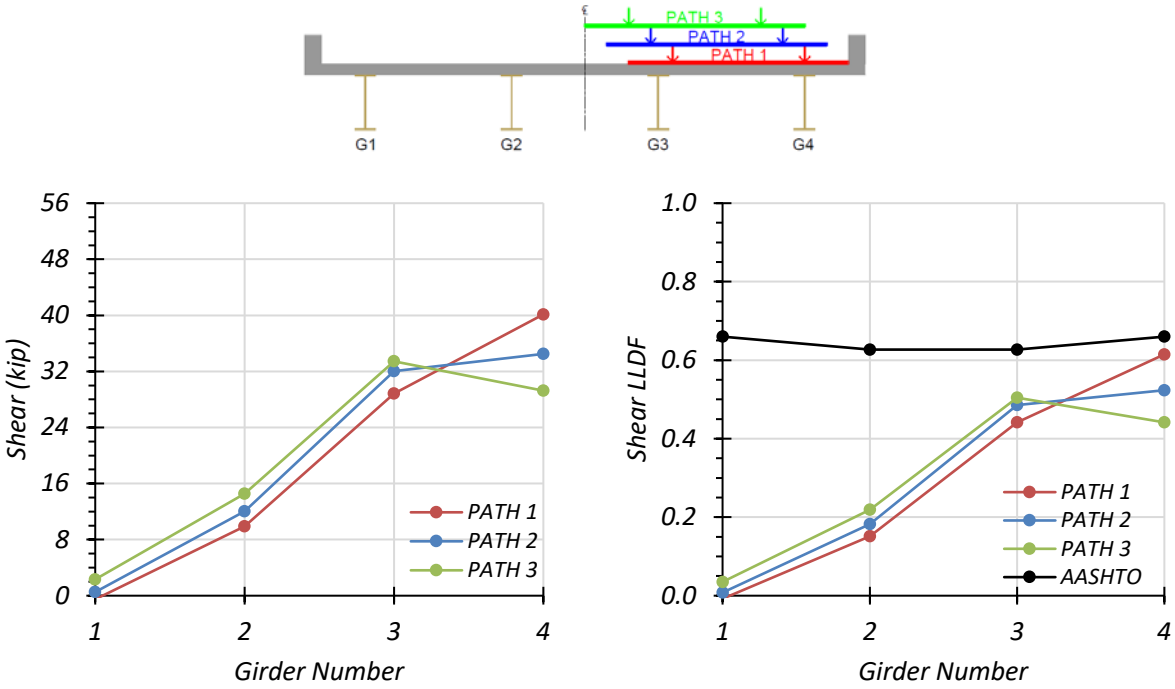

(a) Shear *(b) Shear LLDF*

Figure 6.35. Shear Results for Non-Composite Bridge SC-12 with One-Lane HL-93 Loading

Table 6.42. Maximum Shears for Non-Composite Bridge SC-12 with One-Lane HL-93 Loading

Loading	G1	G2	G3	G4
Path 1	-0.5	9.9	28.8	40.1
Path 2	0.5	12.0	32.0	34.5
Path 3	2.3	14.5	33.4	29.3
Note: G = girder, paths indicate transverse loading positions as shown, shears have kip units				

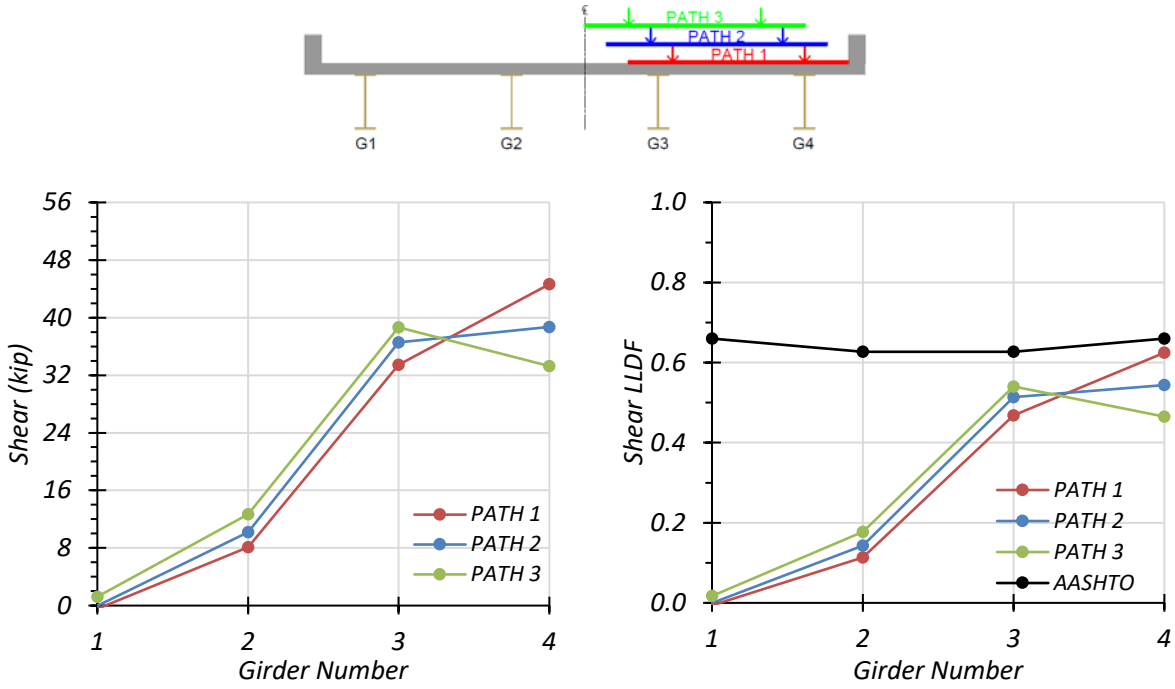

(a) Shear *(b) Shear LLDF*

Figure 6.36. Shear Results for Composite Bridge SC-12 with One-Lane HL-93 Loading

Table 6.43. Maximum Shears for Composite Bridge SC-12 with One-Lane HL-93 Loading

Loading	G1	G2	G3	G4
Path 1	-0.5	8.1	33.4	44.6
Path 2	0.0	10.2	36.5	38.7
Path 3	1.2	12.7	38.6	33.3
Note: G = girder, paths indicate transverse loading positions as shown, shears have kip units				

Comparison of governing shear LLDF values computed from FEM results for the composite and non-composite cases reveals that the maximum shear LLDF in an interior girder for the composite bridge is slightly higher than the one for the non-composite bridge with a $g^v_{composite}/g^v_{non-composite}$ ratio of 1.07. The maximum shear LLDF in an exterior girder for the composite bridge is almost the same as that for the non-composite bridge with a $g^v_{composite}/g^v_{non-composite}$ ratio of 1.02.

Table 6.44. Governing Shear LLDFs for Bridge SC-12 with One-Lane HL-93 Loading

Type	Girder Location	AASHTO (g^v_{AASHTO})	FEM (g^v_{FEM})	g^v_{AASHTO}/g^v_{FEM}
Non-Composite	Interior	0.627	0.504	1.24
	Exterior	0.660	0.615	1.07
Composite	Interior	0.627	0.540	1.16
	Exterior	0.660	0.625	1.06

6.6.3.4.2. Two-Lane Loading

The same procedure was conducted for two-lane loading. Figure 6.37 shows the individual girder shears and shear LLDF results for the non-composite Bridge SC-12 under simulated moving HL-93 loading along the three two-lane loading paths. Table 6.45 provides the corresponding maximum shear values of each girder for each loading path. The shear LLDF values are calculated using the estimated shear results from the FEM analysis. Table 6.47 shows the governing shear LLDFs found using the FEM analysis and compares them to the AASHTO LLDF values. Compared to the FEM results, the governing shear LLDF value computed using the approximate equations in AASHTO LRFD Specifications (AASHTO 2017) is conservative for interior girders with a g^v_{AASHTO}/g^v_{FEM} ratio of 1.20, and is quite conservative for exterior girders with a g^v_{AASHTO}/g^v_{FEM} ratio of 1.32.

Figure 6.38 shows the individual girder shears and shear LLDF results for the fully composite Bridge SC-12 under simulated moving HL-93 loading along three one-lane loading paths. Table 6.46 provides the corresponding maximum shear values of each girder for each loading path. The shear LLDF values are calculated using the estimated shear results from the FEM analysis. Compared to the FEM results, the governing shear LLDF value computed using the

approximate equations in AASHTO LRFD Specifications (AASHTO 2017) is conservative for interior girders with a g^v_{AASHTO}/g^v_{FEM} ratio of 1.20, and is quite conservative for exterior girders with a g^v_{AASHTO}/g^v_{FEM} ratio of 1.34.

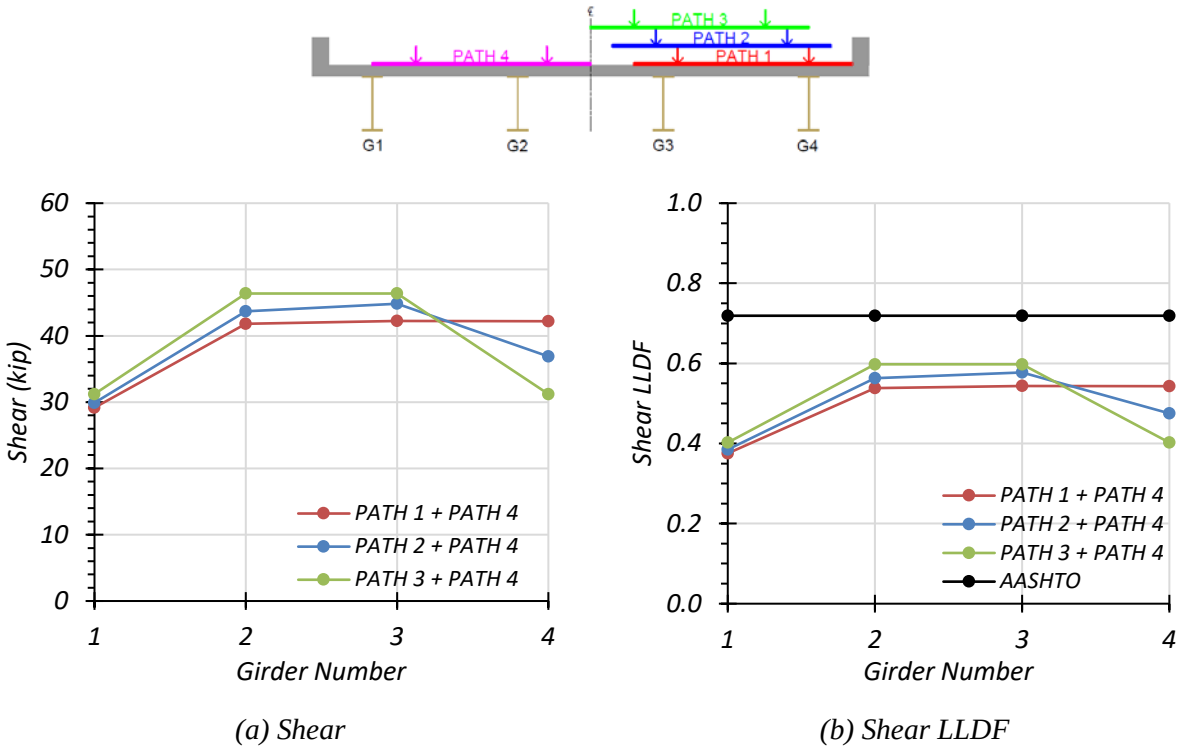

(a) Shear *(b) Shear LLDF*

Figure 6.37. Shear Results for Non-Composite Bridge SC-12 with Two-Lane HL-93 Loading

Table 6.45. Maximum Shear Forces for Non-Composite Bridge SC-12 with Two-Lane HL-93 Loading

Loading	G1	G2	G3	G4
Path 1 + Path 4	29.2	41.8	42.2	42.2
Path 2 + Path 4	29.9	43.7	44.8	36.9
Path 3 + Path 4	31.2	46.4	46.4	31.2
Note: G = girder, paths indicate transverse loading positions as shown, shears have kip units				

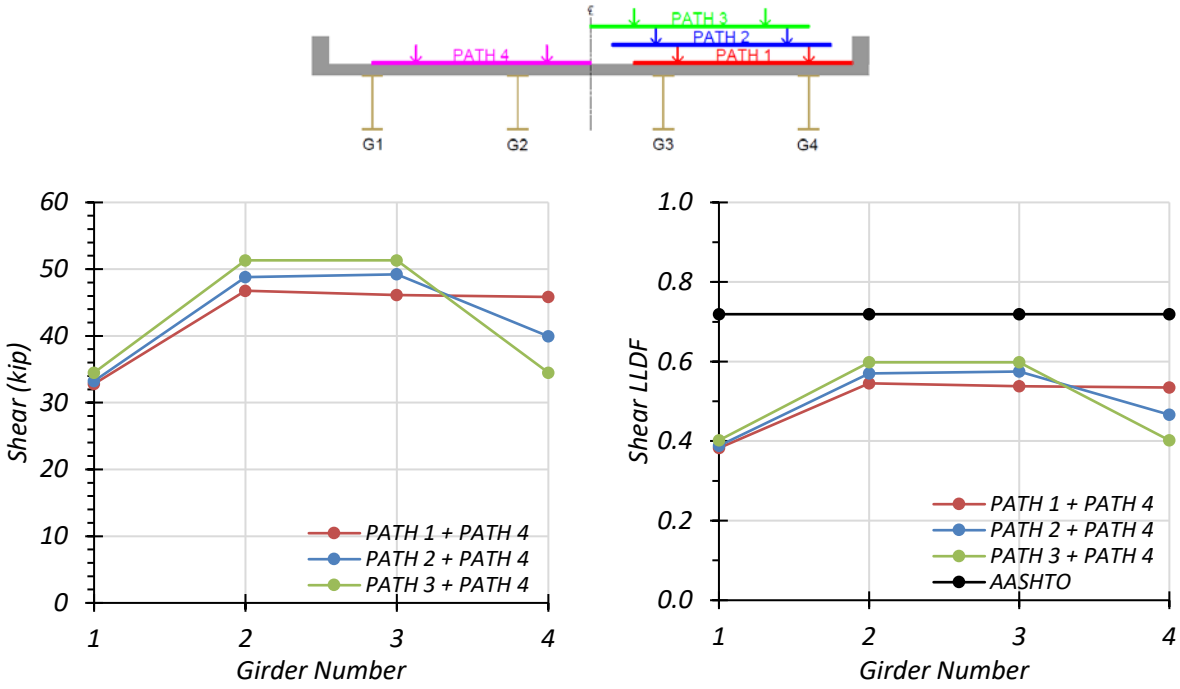

(a) Shear *(b) Shear LLDF*

Figure 6.38. Shear Results for Composite Bridge SC-12 with Two-Lane HL-93 Loading

Table 6.46. Maximum Shear Forces for Composite Bridge SC-12 with Two-Lane HL-93 Loading

Loading	G1	G2	G3	G4
Path 1 + Path 4	32.8	46.8	46.1	45.8
Path 2 + Path 4	33.2	48.8	49.2	39.9
Path 3 + Path 4	34.5	51.3	51.3	34.5
Note: G = girder, paths indicate transverse loading positions as shown, shears have kip units				

Comparison of governing shear LLDF values computed from FEM results for the composite and non-composite cases reveals that the maximum shear LLDF in an interior girder for the composite bridge is the same as the one for the non-composite bridge with a $g^{v}_{composite}/g^{v}_{non-composite}$ ratio of 1.00. Whereas, the maximum shear LLDF in an exterior girder

for the composite bridge is also almost the same as that for the non-composite bridge with a $g^v_{composite}/g^v_{non-composite}$ ratio of 0.99.

Table 6.47. Governing Shear LLDFs for Bridge SC-12 with Two-Lane HL-93 Loading

Type	Girder Location	AASHTO (g^v_{AASHTO})	FEM (g^v_{FEM})	g^v_{AASHTO}/g^v_{FEM}
Non-Composite	Interior	0.719	0.598	1.20
	Exterior	0.719	0.543	1.32
Composite	Interior	0.719	0.598	1.20
	Exterior	0.719	0.535	1.34

6.7. CONCLUSIONS

6.7.1. Live Load Distribution Factors

6.7.1.1. AASHTO Standard Specification LLDFs

The FEM analysis of the selected continuous steel multi-girder bridge has shown that, in general, the current LLDF equations given in the AASHTO Standard Specifications (AASHTO 2002) provide conservative, mostly accurate LLDF values in positive flexure for the selected bridge. The g_{AASHTO}/g_{FEM} ratio for positive flexure ranges from 1.09 to 1.43, with most cases within 0.25 of 1.0. For the negative LLDF values obtained from the FEM analysis produce a very similar result, with the g_{AASHTO}/g_{FEM} ratio ranging from 1.07 to 1.40, with most cases between 0.80 and 1.20. As these results are conservative, but not overly conservative for the most part, possible changes to the LLDFs are not likely to significantly affect HS-20 load ratings of this bridge type.

For the shear LLDF values obtained from the FEM analysis, the g_{AASHTO}/g_{FEM} ratio for ranges from 1.02 to 1.17, producing a lower range of results than for flexure. Again, this result is unlikely to significantly change HS-20 load ratings.

6.7.1.2. AASHTO LRFD Specification LLDFs

The FEM analysis of the selected continuous steel multi-girder bridge has shown that, in general, the current LLDF equations given in the AASHTO LRFD Specifications (AASHTO 2017) provide fairly accurate LLDF values in positive flexure for the selected bridge. The g_{AASHTO}/g_{FEM} ratio for positive flexure using the simplified stiffness parameter ranges from 1.01 to 1.19, and in every case is above 1.0. The g_{AASHTO}/g_{FEM} ratio for positive flexure using the calculated stiffness parameter ranges from 0.97 to 1.19 and is only below 1.0 for one case. A similar trend holds true for negative flexure. The g_{AASHTO}/g_{FEM} ratio for negative flexure using the simplified stiffness parameter ranges from 0.99 to 1.20 and is only below 1.0 for one case. The g_{AASHTO}/g_{FEM} ratio for negative flexure using the calculated stiffness parameter ranges from 0.96 to 1.20 and is only below 1.0 for one case. As these results are accurate for most cases, potential changes to LLDFs are not likely to significantly affect HL-93 load ratings for this bridge type.

For the shear LLDF values obtained from the FEM analysis, the g_{AASHTO}/g_{FEM} ratio for ranges from 1.06 to 1.34, producing slightly conservative results. The LRFR shear LLDFs could possibly be modified in order to increase the LRFR shear RFs of bridges.

6.7.2. Composite Action

When examining the effect of analyzing the bridge as fully composite or fully non-composite with respect to LLDFs, the FEM analysis did not find a significant difference. For the most part, the

LLDFs found were very similar, however, the non-composite bridge seemed to exhibit more uniform LLDF profiles across the bridge transverse section.

When examining HS-20 loading, the $g_{composite}/g_{non-composite}$ ratio for positive flexure ranged from 0.96 to 1.08, the $g_{composite}/g_{non-composite}$ ratio for negative flexure ranged from 0.98 to 1.11, and the $g_{composite}/g_{non-composite}$ ratio for shear ranged from 0.97 to 1.09. The $g_{composite}/g_{non-composite}$ ratio for an interior girder was always above 1.0. For an exterior girder it was always above 1.0 for one-lane loading and below 1.0 for two-lane loading.

When examining HL-93 loading, the $g_{composite}/g_{non-composite}$ ratio for positive flexure ranged from 0.99 to 1.04, the $g_{composite}/g_{non-composite}$ ratio for negative flexure ranged from 0.99 to 1.05, and the $g_{composite}/g_{non-composite}$ ratio for shear ranged from 0.99 to 1.07. The $g_{composite}/g_{non-composite}$ ratio for an interior girder was always above 1.0. For an exterior girder it was always above 1.0 for one-lane loading and below 1.0 for two-lane loading. Between the HS-20 loading and the HL-93 loading, the ratios did not significantly change for the same number of lanes loaded and force being examined.

In terms of LLDFs, composite action does not seem to have a major effect, however, it is known that composite action or partial composite action significantly affects the positive moment capacity of the bridge. This was noticed in the FEM analysis through the stress values computed for the girders. The effect of partial composite action on load rating will be further explored in the next task, where any partial composite measured during field testing will be used to help calibrate the FEM models, which can then be used to develop a more refined load rating of the bridge.

6.7.3. Additional Comments

Additional results reported from the FEM modeling will be used to calibrate the FEM model after field testing is complete. The results presented in this report for deflections and dynamic characteristics will be compared to those found in the field to determine if the girders are acting compositely or non-compositely.

The results of the stiffness adjustment analysis are also useful in identifying the effects of deck cracking on the maximum positive and negative moments that may occur in the actual bridge. If, during testing, the bridge exhibits behavior that indicates a reduced stiffness due to deck cracking, a stiffness reduction could be used in the calibrated FEM model to further investigate the impact on load rating.

7. EXPERIMENTAL TESTING OF BRIDGE SM-5

7.1. INTRODUCTION

Nondestructive load testing of Bridge SM-5 was conducted to gather information about the in-situ behavior of the bridge under vehicular loading. The load test results provide evidence of whether partial composite action or end fixity is present in the structure and measurements of the actual live load distribution between girders. The load test results are also used to update and calibrate the FEM model of the bridge, with which refined analysis is conducted. These results help to determine if the bridge posting can be increased or removed.

Various non-destructive material tests were also performed on Bridge SM-5. Ground Penetrating Radar (GPR) was used to locate steel reinforcing bars in the concrete deck. Ultrasonic Pulse Velocity (UPV) testing, as well as Original Schmidt Hammer and Silver Schmidt Hammer tests, were performed to determine the compressive strength of the concrete deck.

7.2. GENERAL DESCRIPTION OF BRIDGE SM-5

Bridge SM-5 has a deck condition rating of 7 (Good), a superstructure condition rating of 6 (Satisfactory) with 2% beam section loss due to corrosion, and a substructure condition rating of 7 (Good). The steel girders control the rating of the bridge, which has an inventory gross load rating of 17 US tons and an operating gross load rating of 28 US tons. The bridge is posted for a 20,000-pound single axle, a 34,000-pound tandem axle, a 47,000-pound single vehicle, and a 74,000-pound combination vehicle. Table 7.1 shows the posted loads of Bridge SM-5 for different axle and vehicle configurations. Figure 7.1 shows photographs of an elevation view of Bridge SM-5 and a view of the underside of the superstructure. Figure 7.2 shows a transverse section detail of Bridge SM-5.

Table 7.1. Bridge SM-5 Postings

Configuration	Posting (lbs)
Single Axle	20,000
Tandem Axle	34,000
Single Vehicle	47,000
Combination Vehicle	74,000

(a) Elevation view

(b) Underside view

Figure 7.1. Photographs of Bridge SM-5

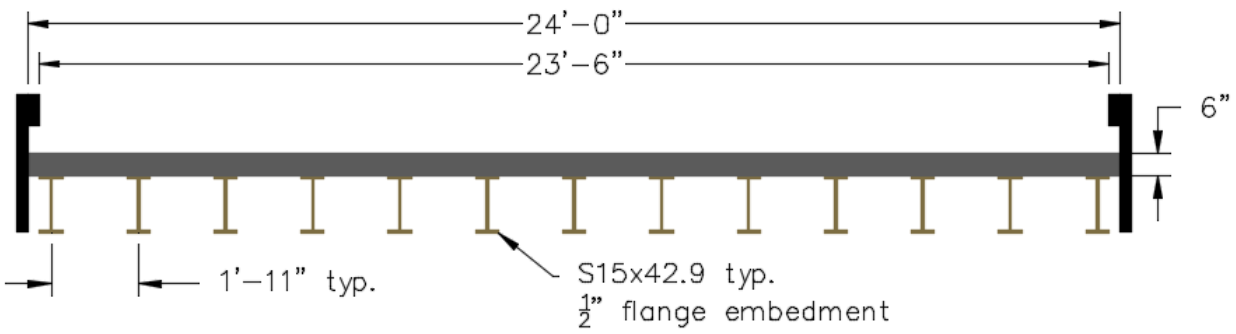

Figure 7.2. Transverse Section of Bridge SM-5 (Adapted from TxDOT 2018b)

7.3. IN-SITU MEASUREMENTS AND OBSERVATIONS

In-situ measurements of the geometric details of the Bridge SM-5 were taken during the field testing. The bridge was measured to be 41'-7" from back wall-to-back wall and the deck was measured to be 24'-0" wide. The abutments were measured as 39'-9" apart (face to face) and approximately a 10 in. length of each girder sat on the concrete abutments, leaving an average gap of approximately 1 in. between the end of the girder and the back wall of the abutment. After taking the simply supported bearing position to be half of the girder bearing length, the center-to-center span length of Bridge SM-5 was determined to be 40'-7" instead of the 40'-2" span length shown in the drawings.

It was also observed that the top flanges of the girders were indeed embedded into the concrete deck, as the drawings show, and that the deck concrete around the embedment exhibited no signs of cracking. This would indicate the potential for composite action between the girders and deck, although the bridge girders were not originally designed as composite members. Figure 7.3 shows a photo taken in the field verifying this observation. The presence of composite action is further evaluated during the load testing.

Figure 7.3. Observation of Girder Flange Embedment with No Signs of Cracking

7.3.1. NDE Results

Four different nondestructive material tests were performed on Bridge SM-5 in order to obtain more information about the concrete deck and steel girder strength. The first test performed was an Ultrasonic Pulse Velocity (UPV) test that measures the time it takes for an ultrasonic wave to travel through a known thickness of concrete. The compressive strength of the concrete can then be estimated based on the measured velocities. For Bridge SM-5, measurements were taken between the bottom and top of the concrete deck, which had a measured thickness of 6.125 in. The wave travel times for the two tests were 31.6 microseconds and 32.4 microseconds. This correlates to an average wave velocity of 4863 m/s. Using this value, the rebound number found using the Original Schmidt Hammer, and the SonReb method equations given in Huang et al. (2011), the concrete compressive strength was found to be 11.3 ksi.

The second NDE material test performed on Bridge SM-5 was the Original Schmidt Hammer. In this test, a device is pushed against the concrete surface and uses the rebound of a spring-loaded mass to estimate the compressive strength of the concrete. For Bridge SM-5, the average rebound value produced by ten Original Schmidt Hammer measurements was 48. Using the conversion chart shown in Figure 7.4, the compressive strength of the deck was determined to be 7.4 ksi.

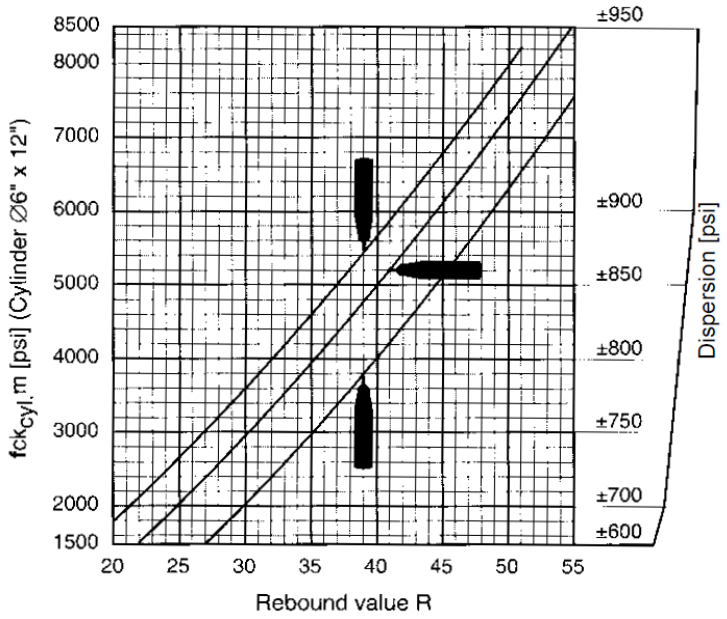

Figure 7.4. Original Schmidt Hammer Conversion Chart (Reprinted from Proceq 2002)

The third NDE test performed on Bridge SM-5 was the Silver Schmidt Hammer. The procedure for performing this test is very similar to that of the Original Schmidt Hammer. For Bridge SM-5, the average Q value produced by ten Silver Schmidt Hammer measurements was 65. Using the conversion chart shown in Figure 7.5, the compressive strength of the deck was determined to be 7.2 ksi.

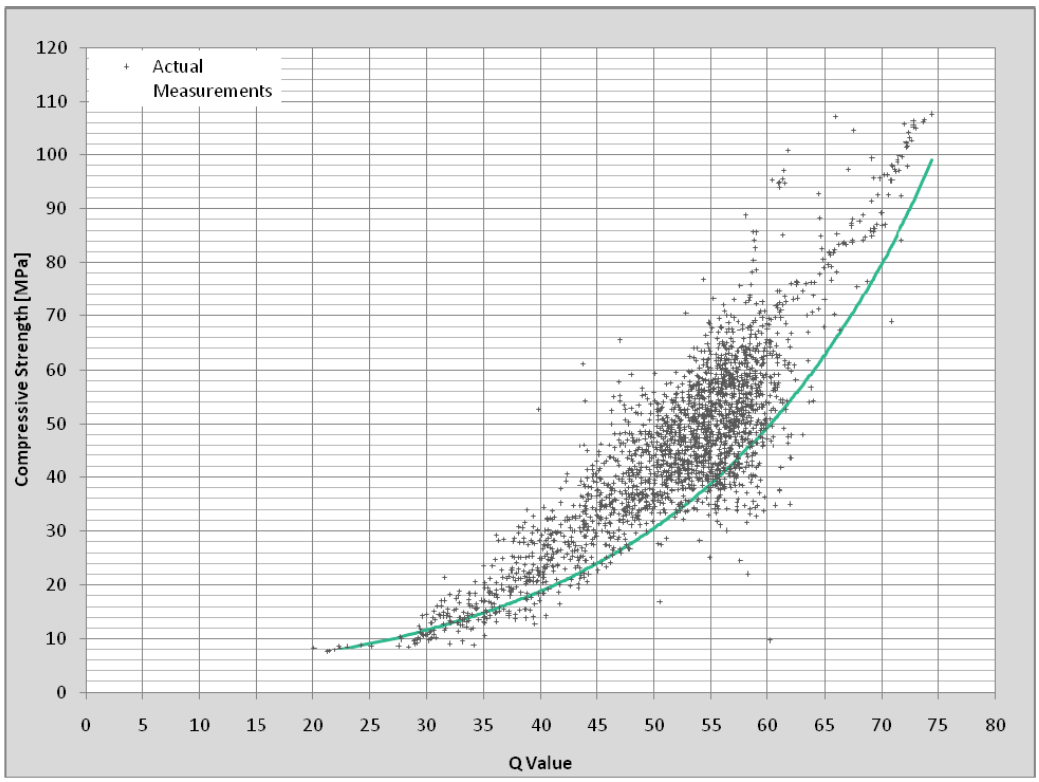

Figure 7.5. Silver Schmidt Hammer Conversion Chart (Reprinted from Proceq 2017)

The fourth NDE test performed on Bridge SM-5 was the use of Ground Penetrating Radar (GPR) in order to determine the spacing of the steel reinforcement in the deck. The GPR device was only run along the underside of deck, as the asphalt layer on the deck prevented it from being used on the top of the deck. Therefore, the spacing of the lower longitudinal bars was determined to be 12 in. and the spacing of the lower transverse bars was determined to be 7.5 in. There are no structural drawings for Bridge SM-5 that show the deck reinforcement; therefore, this information could not be compared.

Out of the three NDE tests performed to measure the compressive strength of the concrete deck, the lowest compressive strength value produced was 7.2 ksi. This value was used in updated

CSiBridge models to perform post-test analysis for comparison of other test values. The measured rebar spacing will also be helpful if an analysis of the concrete deck is performed.

7.4. DATA ACQUISITION AND INSTRUMENTATION FOR BRIDGE SM-5

The instrumentation plan for field testing of Bridge SM-5 was developed based on the objectives of the research project. Three types of instrumentation were used and are shown in Figure 7.8. Strain gauges, string potentiometers, and accelerometers were installed on the bridge to measure its response under the nondestructive vehicular load tests.

7.4.1. Instrumentation Plan for Bridge SM-5

The installed instrumentation and their locations on the bridge were selected in order to obtain specific data to understand the true behavior of the bridge, such as the load sharing between girders, composite action and end fixity, and determine if its posting can be increased or removed.

Figure 7.6 shows the full instrumentation layout for Bridge SM-5, with plan and cross-section views. Figure 7.7 shows the labeling system used for the instrumentation and Table 7.2 shows the instrumentation labels and corresponding DAQ channels.

Strain gauges were installed on the bottom face of the top flange and the top face of the bottom flange as close as possible to the girder web at three longitudinal locations for a selected interior girder and exterior girder. The strain gauges were installed at the midspan location and at an average of 9 in. away from the bearing centerline at each girder end for the selected interior and exterior girders. Several goals were identified in determining the instrumentation types and locations, as follows:

- The strain gauge locations were selected to collect data pertaining to the midspan moments, to determine neutral axis values to check for potential composite action, and to evaluate possible end fixity of the girders.
- The string potentiometer locations were selected to measure midspan deflections and infer experimental LLDFs to compare with the estimated values from the FEM model of Bridge SM-5.
- The accelerometers were selected to collect dynamic property information, allowing for comparison with estimated dynamic properties from the FEM model of the bridge.

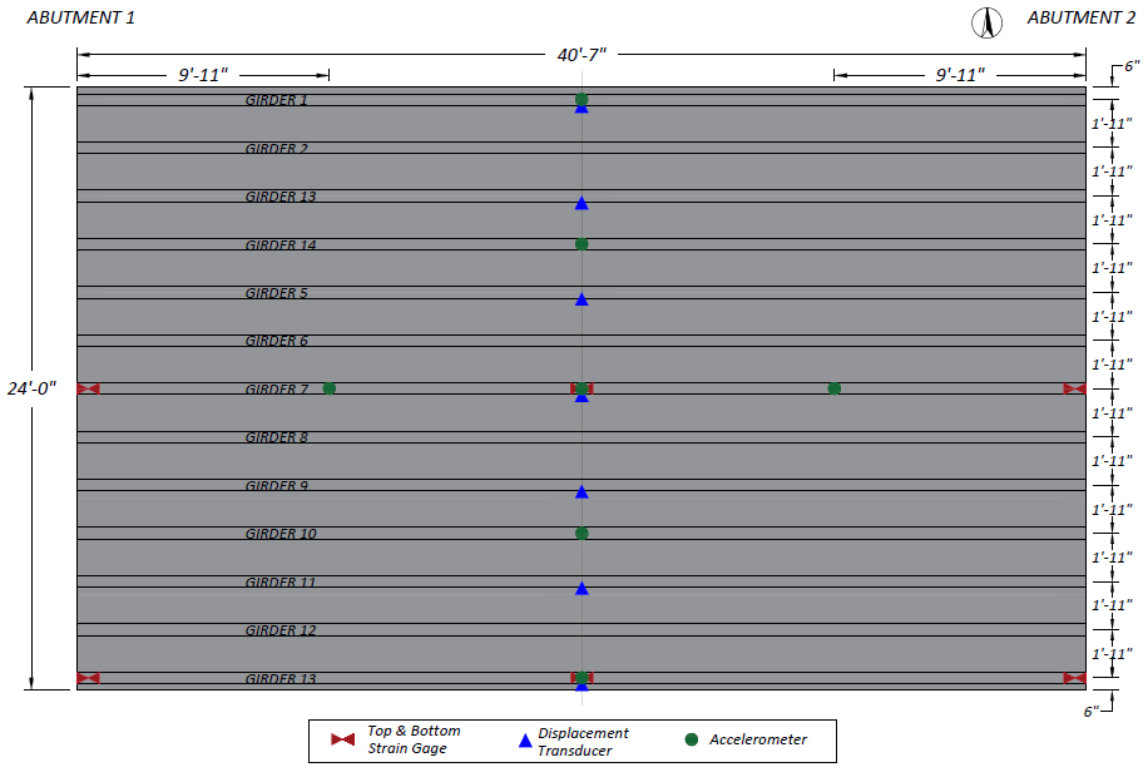

(a) Plan View

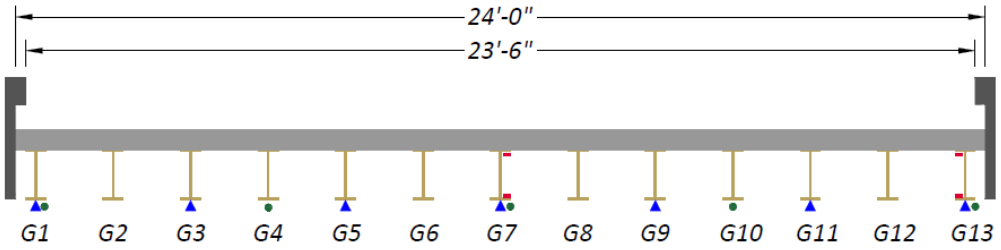

(b) Midspan Section

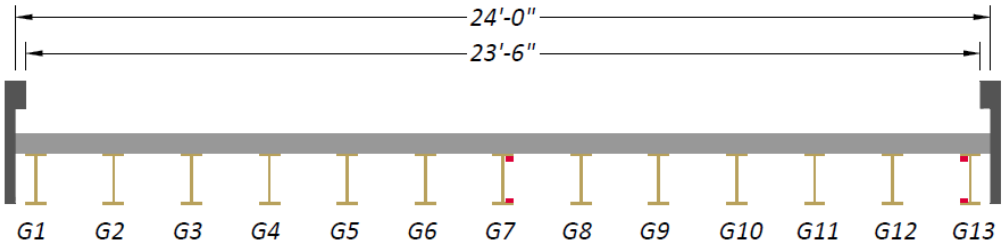

(c) End Section

Figure 7.6. Instrumentation Layout for Bridge SM-5

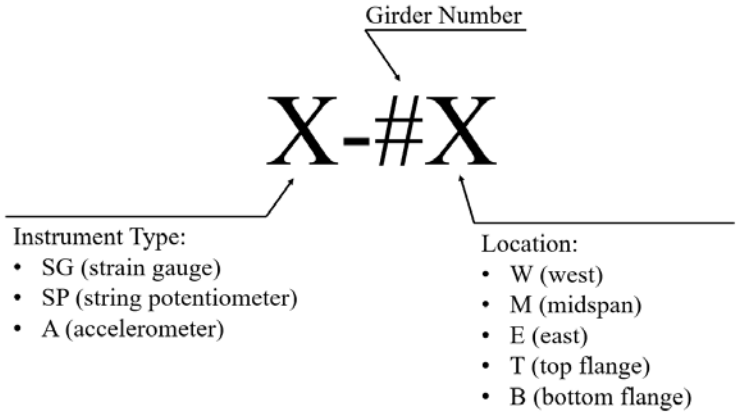

Figure 7.7. Instrumentation Labeling System Used for Bridge SM-5

Table 7.2. Instrumentation Labels for Bridge SM-5

DAQ Box	Channel	Label	Type	DAQ Box	Channel	Label	Type
Strain Book	CH1	SG-13WT	FLA-6	WBK 16-3	CH25	SP-1M	SM1-2
	CH2	SG-13WB	FLA-6		CH26	-	
	CH3	SG-13MT	FLA-6		CH27	-	
	CH4	SG-13MB	FLA-6		CH28	-	
	CH5	SG-13ET	FLA-6		CH29	-	
	CH6	SG-13EB	FLA-6		CH30	-	
	CH7	SG-7WT	FLA-6		CH31	-	
	CH8	SG-7WB	FLA-6		CH32	-	
WBK 16-1	CH9	SG-7MT	FLA-6	WBK 18	CH57	A-13M	4507IEPE
	CH10	SG-7MB	FLA-6		CH58	A-10M	4507IEPE
	CH11	SG-7ET	FLA-6		CH59	A-7M	4507IEPE
	CH12	SG-7EB	FLA-6		CH60	A-4M	4507IEPE
	CH13	-			CH61	A-1M	4507IEPE
	CH14	-			CH62	A-7W	4507IEPE
	CH15	-			CH63	A-7E	4507IEPE
	CH16	-			CH64	-	
WBK 16-2	CH17	-					
	CH18	-					
	CH19	SP-13M	SM1-2				
	CH20	SP-11M	SM1-2				
	CH21	SP-9M	SM1-2				
	CH22	SP-7M	SM1-2				
	CH23	SP-5M	SM1-2				
	CH24	SM-3M	SM1-2				

7.4.2. Data Acquisition System and Instrument Details

7.4.2.1. Data Acquisition System

A total of 24 strain gauges (at 12 measurement locations using half-bridge circuits), seven string potentiometers, and seven accelerometers were installed onto Bridge SM-5. Twenty-six channels were used in the data acquisition system, which consisted of a Measurement Computing StrainBook main DAQ unit and WBK16 extension modules for recording the strain gauge and string potentiometer data, and a WBK18 extension module for recording accelerometer data. Figure 7.8(a) shows the main box and extensions modules of the data acquisition system.

Strainbook WBK16 WBK18

(a) Main Data Acquisition Box and Extension Modules (Reprinted from Measurement Computing 2014)

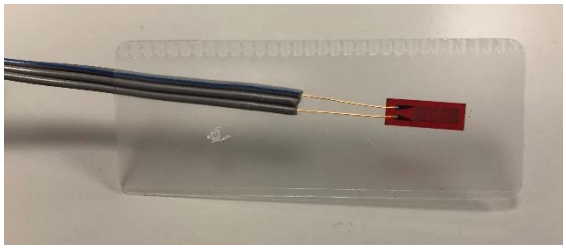

(b) Tokyo Measuring Instruments Lab FLA-6-11-3LJCT Strain Gauges

(c) Celesco SM1-2 String Potentiometer

(d) Brüel & Kjær IEPE Accelerometer

Figure 7.8. Data Acquisition System and Instrumentation

7.4.2.2. Strain Gauges

In order to obtain longitudinal strain data during testing, 24 strain gauges were installed at 12 measurement locations on the steel girders of the bridge. Two strain gauges were installed at each measurement location: a main gauge in the longitudinal direction to obtain longitudinal strain data and a secondary gauge in the transverse direction to compensate for any temperature changes experienced during testing. Figure 7.9 shows a close-up of the installation of the strain gauges. The strain gauges used were selected with ease of installation in mind, as well as the fact that the testing being conducted is short-term and will take place over the span of a couple of hours. Figure

7.8(b) shows the Tokyo Measuring Instruments Lab FLA-6-11-3LJCT strain gauges used during testing.

Figure 7.9. Close-Up of Strain Gauge Installation

7.4.2.3. String Potentiometers

Seven string potentiometers were installed at midspan of every other girder of the 13-girder Bridge SM-5 to obtain girder deflections at midspan. All string potentiometers used were Celesco SM1-2 string potentiometers with a 2.5 in. stroke. Figure 7.8(c) shows the Celesco SM1-2 string potentiometers used during testing.

7.4.2.4. Accelerometers

To obtain dynamic properties of the bridge, such as natural frequency and mode shapes, seven piezoelectric accelerometers were installed on the bridge. Accelerometers were installed at midspan on the bottom of every third girder, as well as at quarter span locations on the bottom of

the middle girder. The accelerometers used were selected because their resonance frequency of 18 kHz is far from the bridge natural frequency and because they are highly sensitive and low in mass and size. Figure 7.8(d) shows the Brüel & Kjær IEPE accelerometers used during testing.

7.5. LOAD TESTING PROCEDURE FOR BRIDGE SM-5

A comprehensive test program was conducted to evaluate the performance and behavior of Bridge SM-5. The test program consisted of two parts: (1) static load tests, which consisted of stop location tests and crawl speed tests, and (2) dynamic load tests. The testing took place on March 7, 2019.

7.5.1. Test Vehicle

The TxDOT Huntsville Maintenance Office provided a Sterling LT 9500 dump truck to be used for the nondestructive load testing of Bridge SM-5. The truck was loaded with asphalt base material such that the rear tandem axles weighed approximately the same as the posted limit of the bridge (posted as 34,000 lb tandem axle). The truck was weighed using portable scales provided by the TxDOT Bryan District Office. The wheel loads, and wheel and axle spacings of the dump truck used for testing are shown in Figure 7.10.

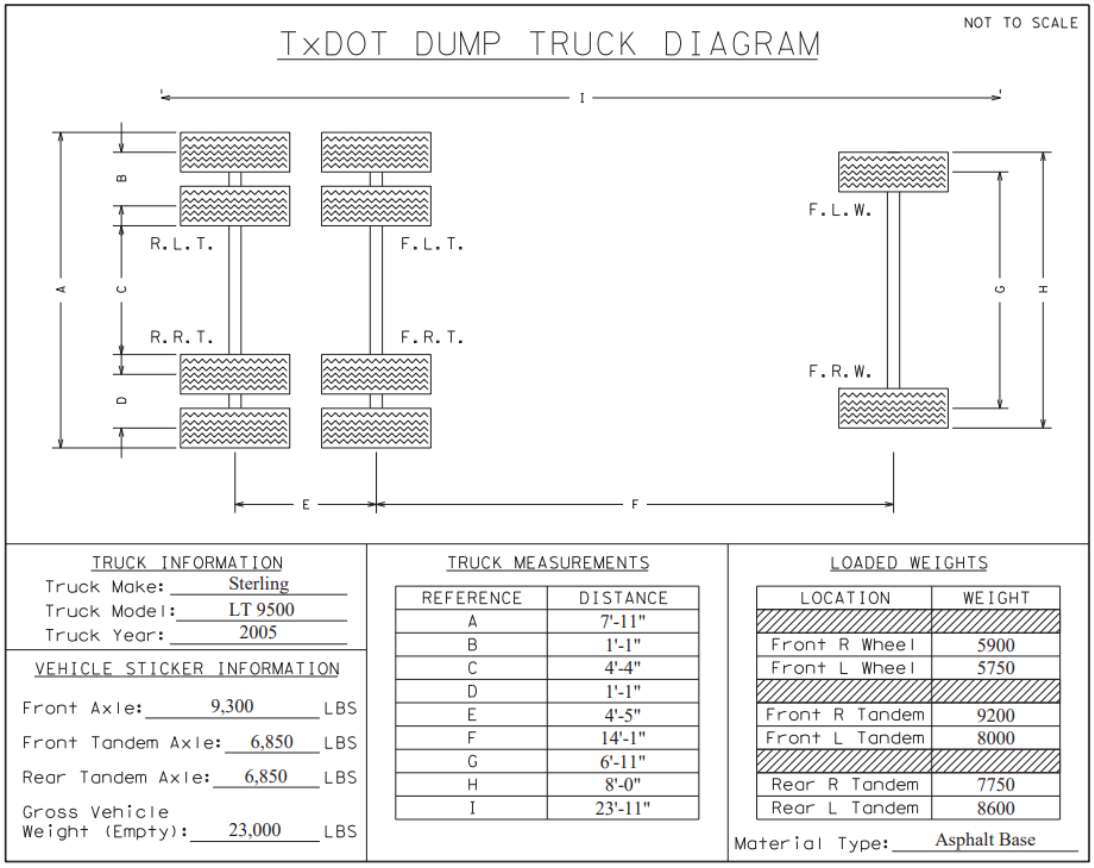

Figure 7.10. Wheel Weights and Spacings of the Loaded Dump Truck

7.5.2. Vehicle Positioning

In order to investigate the transverse load distribution between the bridge girders, three paths were determined that would be used during the testing. The first path, designated Path 1, was at a location such that the centerline of the adjacent rear tires would be 2 ft from the bridge guardrail. The second path, designated Path 2, was in the opposite lane at a location such that the centerline of the adjacent rear tires would be 2 ft from the centerline of the bridge. The third and final path, designated the Middle Path, was at a location such that the truck was straddling the centerline of the bridge. All three testing paths are shown in the bridge cross-section in Figure 7.11.

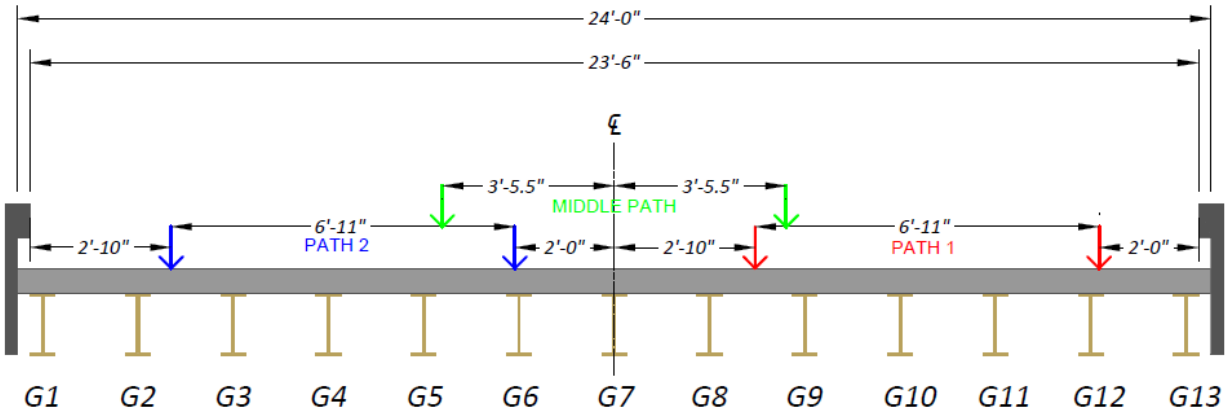

Figure 7.11. Load Test Paths for Bridge SM-5

For the static load tests, it was desired for the truck to be placed approximately at the location at which maximum moment would occur in the girders, as the moment LLDFs are one of the key parameters of interest. Therefore, the truck was placed such that the front axle was 16'-3.5" from the midspan of the bridge, resulting in the rear axles straddling the midspan of the bridge. This longitudinal position was used for the static tests conducted. For the crawl speed tests and the dynamic tests, the truck was run across the bridge without stopping.

7.5.3. Test Protocol

7.5.3.1. Static Tests

Two types of static load tests were performed on Bridge SM-5, stop location tests and crawl speed tests. The stop location load tests began with the truck stopped before entering the bridge to record reference data file that serves as a baseline. The truck then proceeded onto the bridge and was stopped at the longitudinal moment critical position previously described. Once the truck was stopped, data was recorded for a period of approximately five seconds. This procedure was used along each load path. Two different static tests were performed along Path 1 and Path 2: (1) the

truck engine was running, and (2) the truck engine was shut off. For the static test along the Middle Path, the test was performed while the truck engine was shut off. The static test results presented in this chapter are only the ones with the engine shut off. During the static tests in which the engine was running, there is a possibility that due to the truck dynamics with the engine running unwanted vibrations could be introduced in the measurements.

The crawl speed load tests began with the truck stopped before entering the bridge to record a reference data file that serves as a baseline. The truck then proceeded at an idle speed of approximately 2 mph across the full length of the bridge while data was recorded for the entire time. This procedure was used along each load path.

7.5.3.2. Dynamic Tests

The dynamic tests began with the truck stopped at some distance away from the bridge. At this time, a reference data file was recorded. The truck then proceeded at a specific speed across the entire length of the bridge while data was recorded during the passage of the vehicle. This procedure was used along each load path. Two different dynamic tests were performed along Path 1 and Path 2. The first dynamic test was performed at approximately 30 to 35 mph and the second dynamic test was performed at approximately 23 mph. Only one dynamic test was performed along the Middle Path at 35 mph. These speeds were chosen based on a variety of factors including the speed limit of the road (35 mph), the estimated speed at which a heavy vehicle might drive over the bridge, and the comfort level of the truck driver going at certain speeds along the predefined load paths.

7.5.3.3. Impact Tests

In order to obtain more information about the dynamic properties of the bridge, a sledgehammer was used to strike the top of the bridge deck in three different transverse locations (north edge of the bridge, at the centerline of the bridge, and at the south edge of the bridge) at midspan. Although all the instruments were in place while data was being recorded during these three impact tests, only accelerometer measurements were used to identify dynamic characteristics. The impact excitation provides a more accurate way of measuring bridge dynamic characteristics because unlike a vehicle excitation, the impact excitation does not introduce additional mass and dynamic interaction with the bridge. Table 7.3 summarizes all the tests that were performed on Bridge SM-5.

Table 7.3. Test Protocol for Bridge SM-5 Testing

Test Number	Test Location	Test Type
1	Path 1	Static – Stop Location (Engine Running)
2	Path 2	Static – Stop Location (Engine Running)
3	Path 1	Static – Crawl Speed (5 mph)
4	Path 2	Static – Crawl Speed (2 mph)
5	Path 1	Dynamic (30 mph)
6	Path 2	Dynamic (35 mph)
7	Path 1	Dynamic (23 mph)
8	Path 2	Dynamic (22 mph)
9	Path 1	Static – Stop Location (Engine Stopped)
10	Path 2	Static – Stop Location (Engine Stopped)
11	Path 1	Static – Crawl Speed (2 mph)
12	Path 2	Static – Crawl Speed (2 mph)
13	Middle Path	Static – Stop Location (Engine Stopped)
14	Middle Path	Static – Crawl Speed (2 mph)
15	Middle Path	Dynamic (34 mph)
16	North Edge	Sledgehammer
17	Centerline	Sledgehammer
18	South Edge	Sledgehammer

7.5.4. Test Operations

The test program for Bridge SM-5 occurred from March 5, 2019 to March 7, 2019. This includes all instrumentation installation, load testing, and instrumentation removal.

The clearance height of Bridge SM-5 was approximately 14 ft. Therefore, scaffolding platforms were set up below the bridge to provide a working platform for instrumentation installation. To install strain gauges, an approximately 2 in. by 4 in. area at the desired location of the strain gauge was ground using an angle grinder to remove any loosely bonded adherent such as paint, rust, oxides, etc. This location was then sanded using 150 and 220 grit sandpaper to obtain a smooth surface. Conditioner (acetone) was applied repeatedly, and the surface scrubbed with paper towels until a clean tip is no longer discolored by the scrubbing. Liberally applying acetone brings the surface condition back to an optimum alkalinity of 7.0 to 7.5pH for ideal bonding of the glue. The strain gauges were then glued using CN adhesive. Figure 7.12(a) shows an example of installed strain gauges on the girder. String potentiometers were attached to small pieces of 2x4 wood, which were then clamped to the bottom flanges of the girders at the midspan location. The string potentiometers were fixed by attaching fishing wire to metal hooks attached to wooden posts driven into the stream bed. Accelerometers were also attached to the bottom flange of the appropriate girders using magnets. Figure 7.12(b) shows an example of an installed string potentiometer and accelerometer on the bridge.

The load testing took place on March 7, 2019. Traffic control was provided by the TxDOT Bryan District through the Huntsville Maintenance Office while the testing took place. The dump truck was loaded and weighed at the TxDOT Huntsville Maintenance Office in the morning, while members of the research team marked the test paths and the static test stop locations on the bridge using tape and marking spray paint. The previously described tests in the test protocol were performed while data from the installed instruments were recorded during each test period. Once the testing was completed, traffic control ceased, and the instrumentation was removed from the

bridge. Figure 7.13(a) shows the scaffolding setup for instrumentation installation and Figure 7.13(b) shows the test truck on the bridge during a load test.

(a) Installed Strain Gauges at an End Location of a Girder

(b) Installed String Potentiometer and Accelerometer at Midspan of a Girder

Figure 7.12. Installed Instrumentation on Bridge SM-5

(a) Instrumentation of Bridge SM-5

(b) Test Truck at the Stop Location for Path 1

Figure 7.13. Instrumentation and Testing of Bridge SM-5

7.6. TEST RESULTS FOR BRIDGE SM-5

Two types of diagnostic tests were conducted following the guidelines provided in AASHTO MBE (AASHTO 2018): (1) Static Load Tests using stationary loads (avoiding bridge vibrations) to obtain static strains and deflections and infer composite action and LLDFs and (2) Dynamic Load Test with moving loads that excite vibrations in the bridge to measure modes of vibration, frequencies, and dynamic amplification.

The data obtained during testing was compiled, processed, and analyzed. Strains were measured using strain gauges, which allowed stresses to be inferred. Deflections were measured using string potentiometers, which were used to infer transverse load distribution. Accelerations were measured using accelerometers, which were processed to obtain natural frequencies and mode shapes of the bridge. Videos taken during testing were used to determine deflections using computer vision and compared with the string potentiometer measurements. NDE results were also compiled to obtain the in-situ compressive strength of the concrete bridge deck and reinforcement locations in the deck.

7.6.1. Static Load Tests on Bridge SM-5

Two types of static load tests were conducted; (1) stop location tests by parking the vehicle at the moment critical longitudinal position for each selected path on the bridge, and (2) crawl speed tests by moving the truck at low speeds (approximately 2 mph) along the same predefined paths.

7.6.1.1. Strain Measurements and Composite Action

After obtaining strain gauge data from the load testing, the maximum bottom flange strains were plotted along with their corresponding top flange strains at the same time step. In all strain figures shown in this section, the measured strain values are shown by a colored dot symbol. The colored

line connecting two dot symbols represents the strain diagram at this cross-section based on an assumption of plane section remains plane. The blue plot shows the strain results for the west end, the red plot shows the strain results for the east end, and the green plot shows the strain results for the midspan of the girder.

7.6.1.1.1. Interior Girder 7

Figure 7.14 through Figure 7.16 provide plots of the measured strains for interior Girder 7 during static load testing. The strains measured for Girder 7 during the Path 1 static tests are shown in Figure 7.14. Figure 7.14(a) shows the maximum strains observed during the stop location test for Girder 7 at each end of the girder. Figure 7.14(b) shows the maximum strains observed during the stop location test for Girder 7 at midspan. Figure 7.14(c) shows the maximum strains observed during the crawl speed test for Girder 7 at each end of the girder. Figure 7.14(d) shows the maximum strains observed during the crawl speed test for Girder 7 at midspan. The corresponding observed midspan stresses for Girder 7 are 2.14 ksi for the stop location test and 2.10 ksi for the crawl speed test. The observed neutral axis locations at midspan are 13.95 in. from the bottom of the girder for the stop location test and 13.37 in. from the bottom of the girder for the crawl speed test.

The strains measured for Girder 7 during the Path 2 static tests are shown in Figure 7.15. Figure 7.15(a) shows the maximum strains observed during the stop location test for Girder 7 at each end of the girder. Figure 7.15(b) shows the maximum strains observed during the stop location test for Girder 7 at midspan. Figure 7.15(c) shows the maximum strains observed during the crawl speed test for Girder 7 at each end of the girder. Figure 7.15(d) shows the maximum strains observed during the crawl speed test for Girder 7 at midspan. The corresponding observed

midspan stresses for Girder 7 are 2.41 ksi for the stop location test and 2.51 ksi for the crawl speed test. The observed neutral axis locations at midspan are 14.08 in. from the bottom of the girder for the stop location test and 13.77 in. from the bottom of the girder for the crawl speed test.

The strains measured for Girder 7 during the Middle Path static tests are shown in Figure 7.16. Figure 7.16(a) shows the maximum strains observed during the stop location test for Girder 7 at each end of the girder. Figure 7.16(b) shows the maximum strains observed during the stop location test for Girder 7 at midspan. Figure 7.16(c) shows the maximum strains observed during the crawl speed test for Girder 7 at each end of the girder. Figure 7.16(d) shows the maximum strains observed during the crawl speed test for Girder 7 at midspan. The corresponding observed midspan stresses for Girder 7 are 2.96 ksi for the stop location test and 2.95 ksi for the crawl speed test. The observed neutral axis locations at midspan are 15.05 in. from the bottom of the girder for the stop location test and 13.80 in. from the bottom of the girder for the crawl speed test.

For all three paths, there is evidence of restraint at the girder ends causing a negative moment to occur. This is seen by the bottom flange end strain gauges being in compression. Also of note, the measured neutral axes show signs of significant composite behavior occurring. This will be discussed later in this chapter.

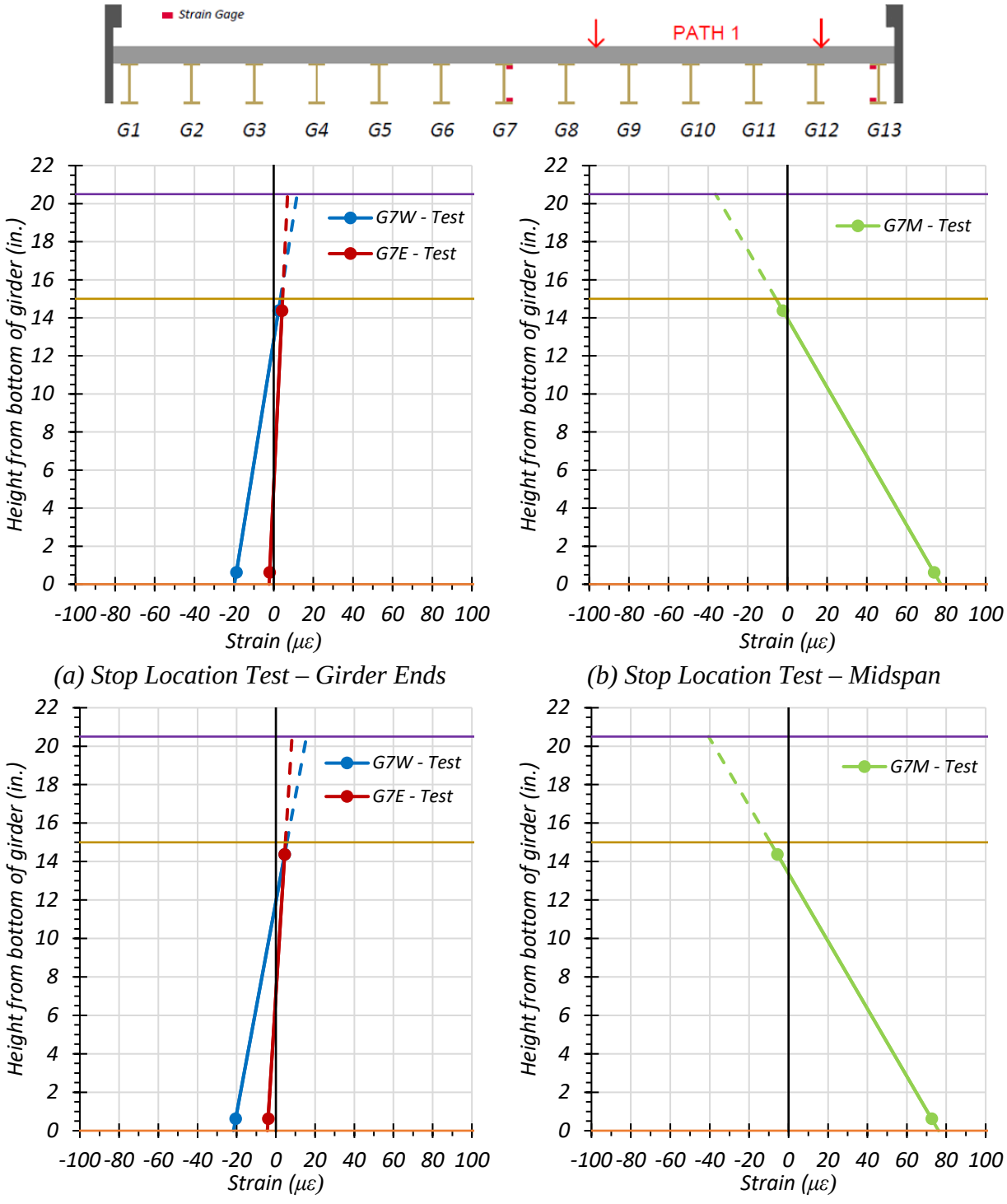

(a) Stop Location Test – Girder Ends

(b) Stop Location Test – Midspan

(c) Crawl Speed Test – Girder Ends

(d) Crawl Speed Test – Midspan

Figure 7.14. Static Strains for Interior Girder 7 – Path 1

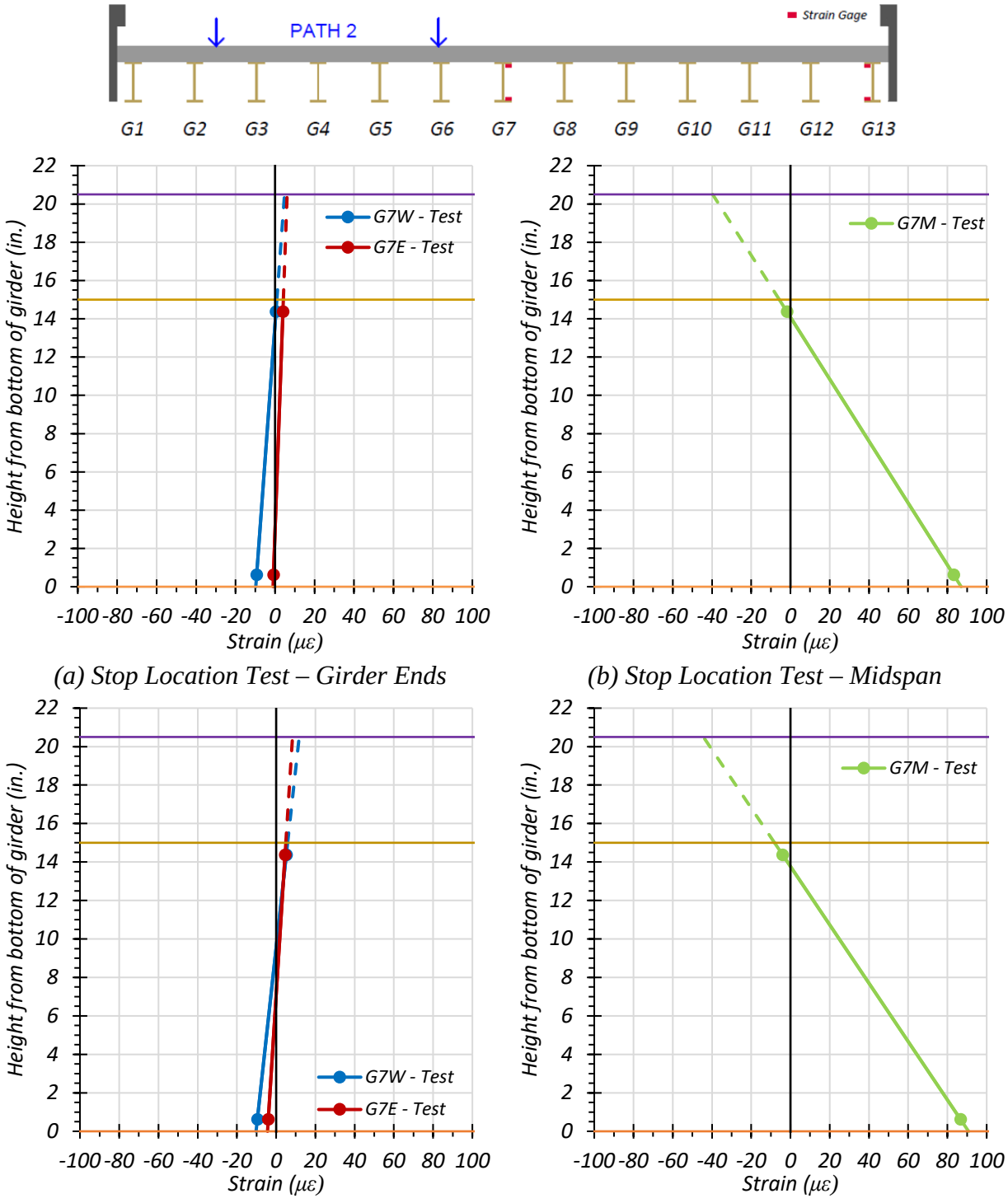

Figure 7.15. Static Strains for Interior Girder 7 – Path 2

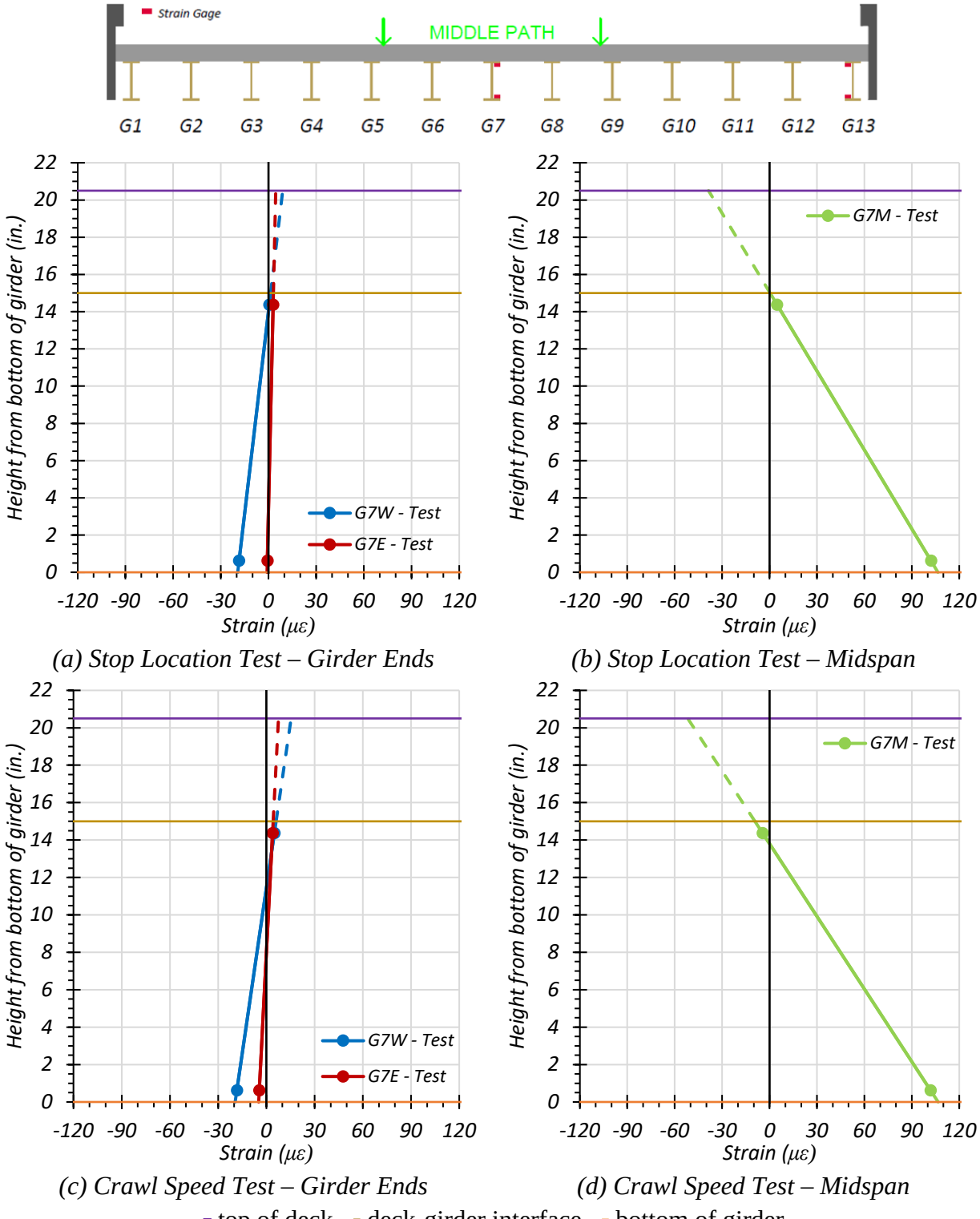

(a) Stop Location Test – Girder Ends

(b) Stop Location Test – Midspan

(c) Crawl Speed Test – Girder Ends

(d) Crawl Speed Test – Midspan

Figure 7.16. Static Strains for Interior Girder 7 – Middle Path

7.6.1.1.2. Exterior Girder 13

Figure 7.17 through Figure 7.19 provide plots of the measured strains for exterior Girder 13 during static load testing. The strains measured for Girder 13 during the Path 1 static tests are shown in Figure 7.17. Figure 7.17(a) shows the maximum strains observed during the stop location test for Girder 13 at each end of the girder. Figure 7.17(b) shows the maximum strains observed during the stop location test for Girder 13 at midspan. Figure 7.17(c) shows the maximum strains observed during the crawl speed test for Girder 13 at each end of the girder. Figure 7.17(d) shows the maximum strains observed during the crawl speed test for Girder 13 at midspan. The corresponding midspan stresses at the bottom flange for Girder 13 are 4.70 ksi for the stop location test and 5.05 ksi for the crawl speed test. The observed neutral axis locations are 13.96 in. from the bottom of the girder for the stop location test and 14.04 in. from the bottom of the girder for the crawl speed test.

The strains measured for Girder 13 during the Path 2 static tests are shown in Figure 7.18. Figure 7.18(a) shows the maximum strains observed during the stop location test for Girder 13 at each end of the girder. Figure 7.18(b) shows the maximum strains observed during the stop location test for Girder 13 at midspan. Figure 7.18(c) shows the maximum strains observed during the crawl speed test for Girder 13 at each end of the girder. Figure 7.18(d) shows the maximum strains observed during the crawl speed test for Girder 13 at midspan. The corresponding observed midspan stresses for Girder 13 are 0.27 ksi for the stop location test and 0.34 ksi for the crawl speed test. The observed neutral axis locations are 12.39 in. from the bottom of the girder for the stop location test and 10.79 in. from the bottom of the girder for the crawl speed test.

The strains measured for Girder 13 during the Middle Path static tests are shown in Figure 7.19. Figure 7.19(a) shows the maximum strains observed during the stop location test for

Girder 13 at each end of the girder. Figure 7.19(b) shows the maximum strains observed during the stop location test for Girder 13 at midspan. Figure 7.19(c) shows the maximum strains observed during the crawl speed test for Girder 13 at each end of the girder. Figure 7.19(d) shows the maximum strains observed during the crawl speed test for Girder 13 at midspan. The corresponding observed midspan stresses for Girder 13 are 1.36 ksi for the stop location test and 1.47 ksi for the crawl speed test. The observed neutral axis locations are 12.70 in. from the bottom of the girder for the stop location test and 13.17 in. from the bottom of the girder for the crawl speed test.

As expected, Girder 13 saw a higher level of stress than Girder 7 during the Path 1 loading, however it saw lower stress levels than Girder 7 during the Path 2 and Middle Path loading. For all three paths, there is also evidence of restraint at the girder ends causing a negative moment to occur. This is seen by the bottom flange end strain gauges being in compression. Also of note, the measured neutral axes show signs of significant composite behavior occurring. This will be discussed later in this chapter.

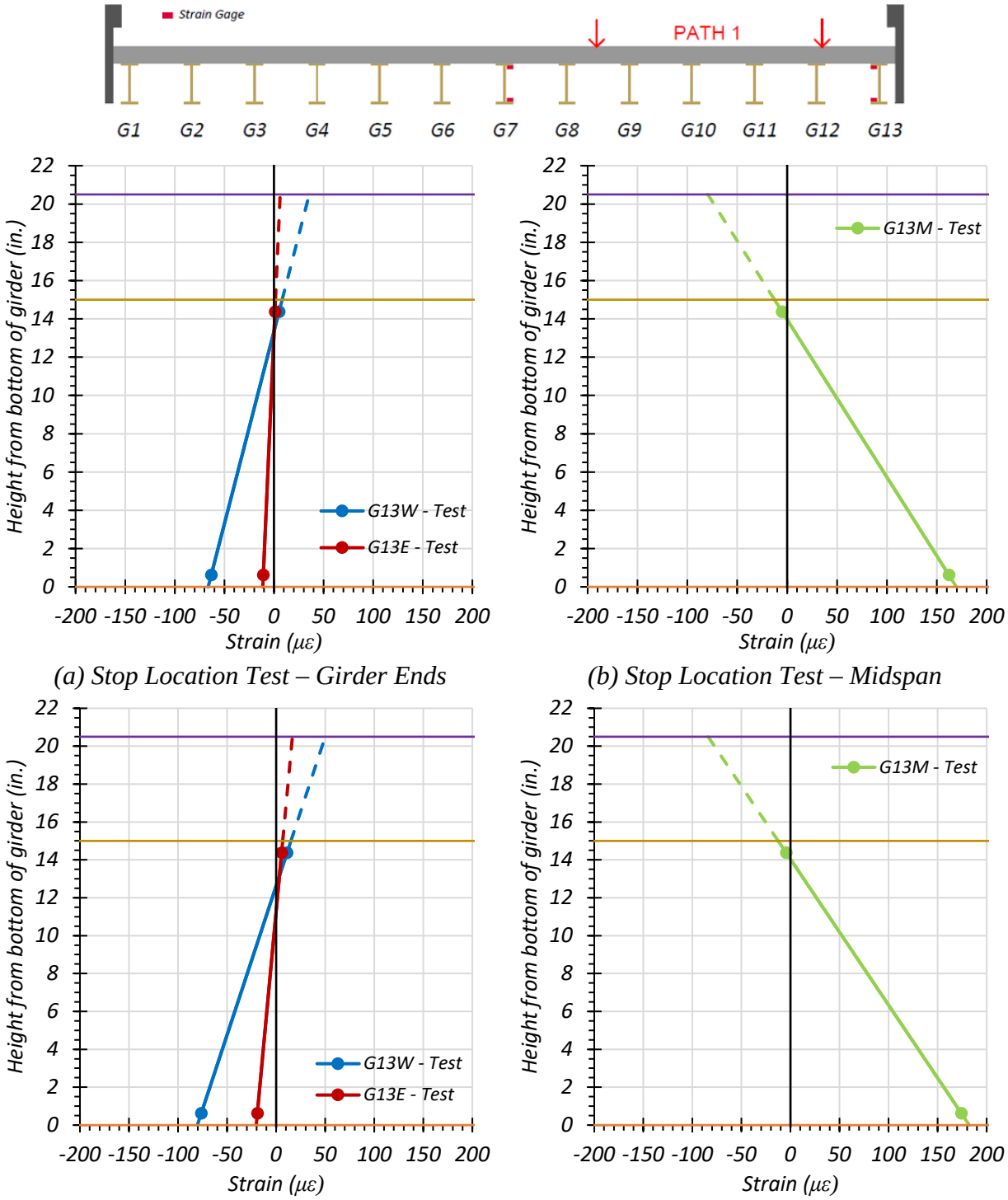

Figure 7.17. Static Strains for Exterior Girder 13 – Path 1

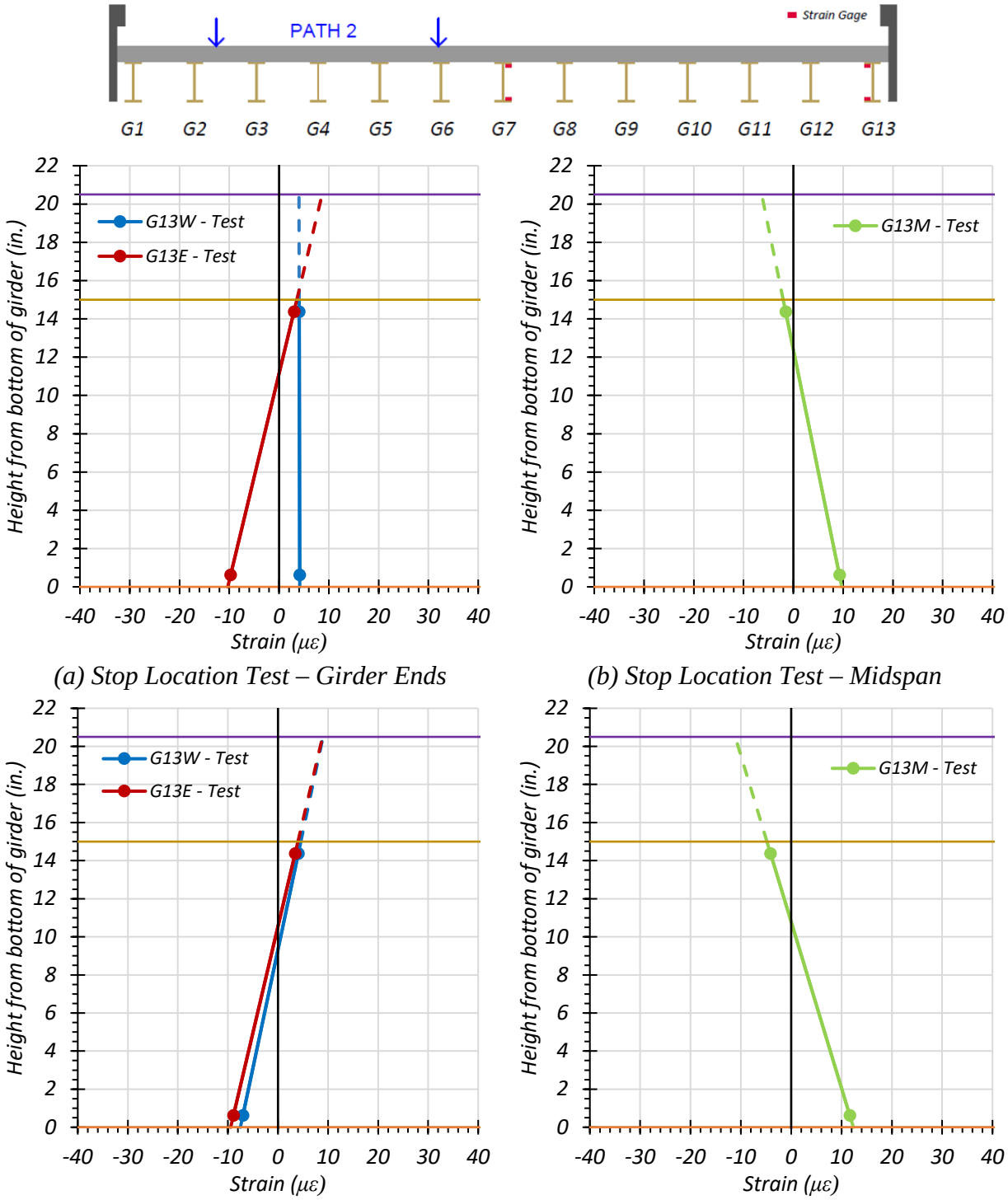

Figure 7.18. Static Strains for Exterior Girder 13 – Path 2

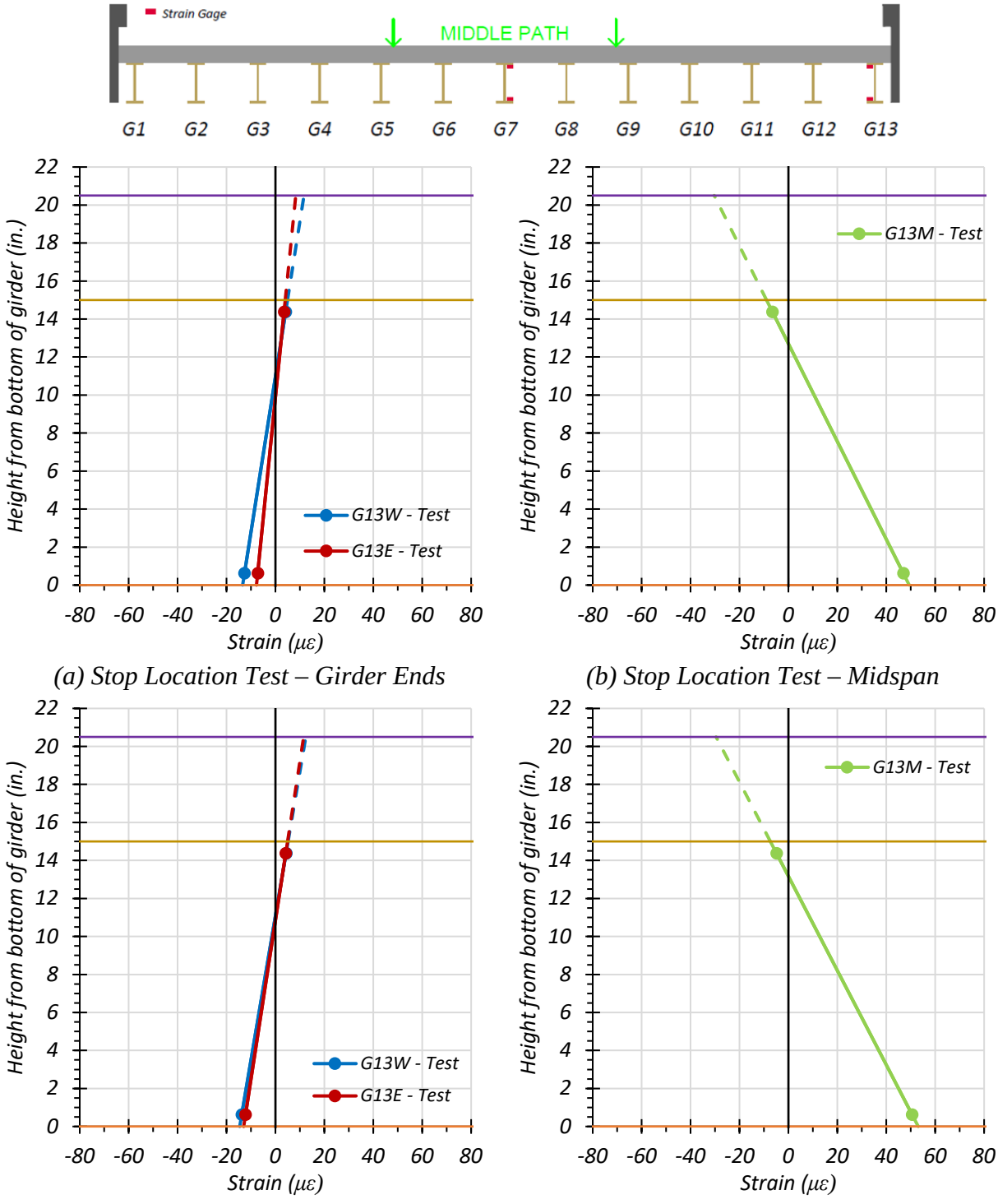

(a) Stop Location Test – Girder Ends

(b) Stop Location Test – Midspan

(c) Crawl Speed Test – Girder Ends

(d) Crawl Speed Test – Midspan

Figure 7.19. Static Strains for Exterior Girder 13 – Middle Path

7.6.1.1.3. Comparison of Measured Strain Results

Table 7.4 and Figure 7.20 show the observed neutral axis locations based on the strain measurements for all static load tests. The average neutral axis locations were 12.84 in. from the bottom of the girder for Girder 13 and 14.00 in. from the bottom of the girder for Girder 7. The test neutral axes tend to be significantly closer to the theoretical composite neutral axis than to the theoretical non-composite neutral axis. This is based on use of the parallel axis theorem using the updated geometric and material properties determined during testing describes in Section 7.3. This includes an f_c' of 7.2 ksi and a corresponding modulus of elasticity of 4836 ksi. The effective deck width used for an interior girder is 23 in. and for an exterior girder is 17.5 in., determined using Article 10.38.3 in the AASHTO Standard Specifications (AASHTO 2002). Reinforcing steel is not included in this calculation. This analysis indicates that Bridge SM-5 is likely has significant horizontal load transfer between the deck and girders and is nearly fully composite.

Table 7.4. Measured Neutral Axis Locations for All Static Load Tests

Test	G7 Neutral Axis Location (in. from bottom of girder)	G13 Neutral Axis Location (in. from bottom of girder)
Path 1 – Stop Location	13.95	13.96
Path 1 – Crawl Speed	13.37	14.04
Path 2 – Stop Location	14.08	12.39
Path 2 – Crawl Speed	13.77	10.79
Middle Path – Stop Location	15.05	12.70
Middle Path – Crawl Speed	13.80	13.17
Theoretical Non-Composite	7.50	7.50
Theoretical Composite	14.28	13.60

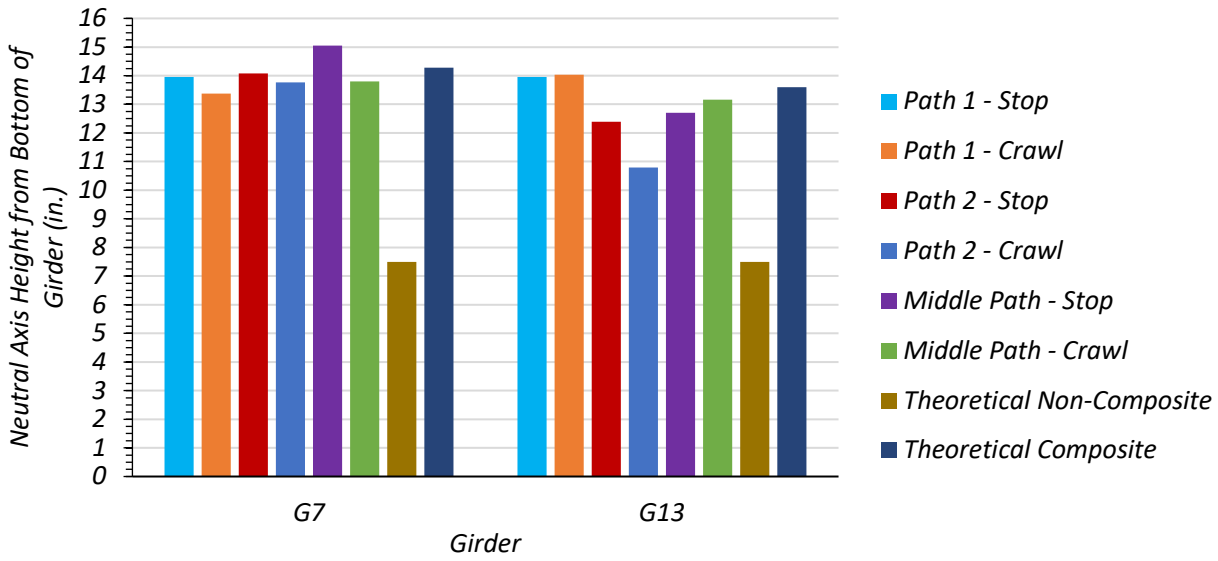

Figure 7.20. Test Neutral Axis Locations

Table 7.5 and Figure 7.21 show the measured bottom flange stress observed during the static load testing. The maximum stress in interior Girder 7 was 3.09 from the Middle Path stop location and crawl speed tests. The maximum stress in exterior Girder 13 was 5.29 ksi from the Path 1 crawl speed test.

Table 7.5. Maximum Static Test Bottom Flange Stresses (ksi)

Load Path	Interior Girder 7		Exterior Girder 13	
	Stop Location Test	Crawl Speed Test	Stop Location Test	Crawl Speed Test
Path 1	2.24	2.21	4.92	5.29
Path 2	2.52	2.63	0.28	0.36
Middle Path	3.09	3.09	1.43	1.54

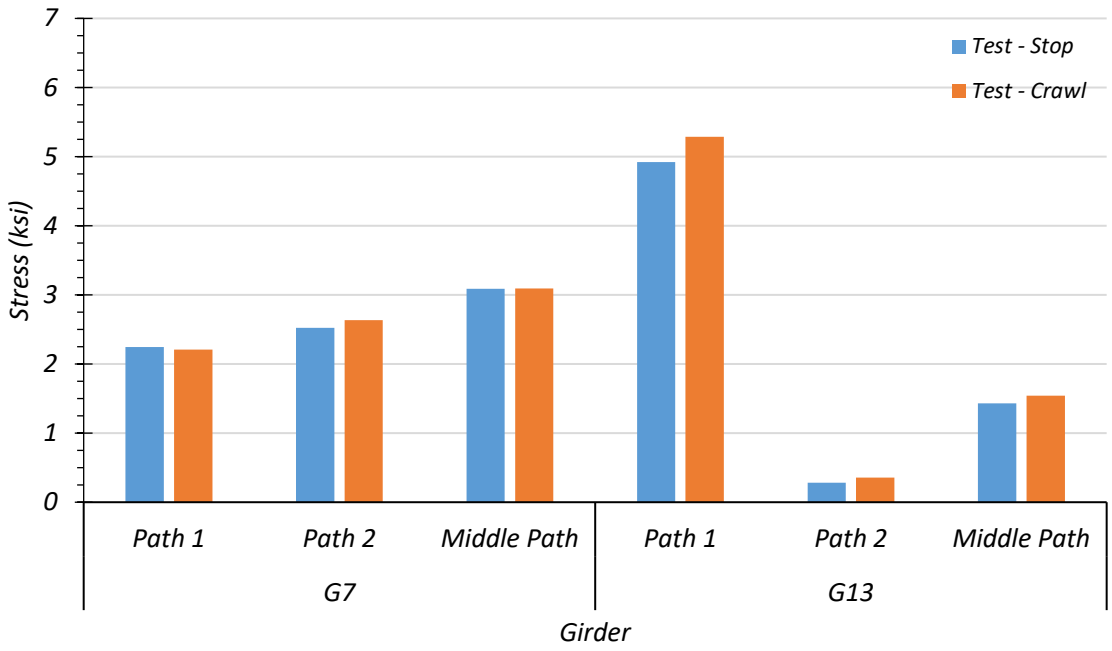

Figure 7.21. Comparison of Maximum Test Bottom Flange Stresses

7.6.1.2. Deflection Measurements and LLDFs

7.6.1.2.1. Path 1 Loading

Table 7.6 shows the measured girder deflections during testing for the stop location test and crawl speed test along Path 1. Deflection data for every other girder was recorded, therefore deflections the intermediate girders have been interpolated. The associated LLDFs, determined using the measured midspan deflections, are also provided.

Table 7.6. Experimental Midspan Deflections and LLDFs for Path 1 Loading

Girder	G1	G2*	G3	G4*	G5	G6*	G7	G8*	G9	G10*	G11	G12*	G13
Stop Location Test Disp. (in.)	-0.009	0.007	0.023	0.045	0.067	0.091	0.114	0.143	0.173	0.195	0.218	0.263	0.307
Stop Location Test LLDF	0.005	0.004	0.014	0.027	0.041	0.055	0.069	0.087	0.104	0.118	0.132	0.159	0.186
Crawl Speed Test Disp. (in.)	-0.013	0.002	0.017	0.040	0.063	0.088	0.112	0.142	0.172	0.197	0.222	0.273	0.324
Crawl Speed Test LLDF	0.008	0.001	0.010	0.024	0.038	0.053	0.068	0.085	0.103	0.118	0.133	0.164	0.195

Note: 1 – G = girder, Disp. = Displacement, * = displacement results have been interpolated using test results
2 – LLDF values are based on the midspan deflections.

Table 7.7 compares the maximum experimental LLDFs based on midspan deflections to those calculated using the AASHTO Standard Specifications, the AASHTO LRFD Specifications using the simplified stiffness parameter, and AASHTO LRFD Specifications using the analytical stiffness parameter (AASHTO 2002; AASHTO 2017). The maximum g_{AASHTO_Std}/g_{test} ratio ranges from 0.84 to 0.94, indicating the AASHTO Standard Specifications estimate is not always conservative. The maximum g_{AASHTO_S}/g_{test} and g_{AASHTO_K}/g_{test} ratios were always above 1.0, ranging from 1.09 to 1.54, indicating conservative estimates of the measured LLDFs.

Table 7.7. LLDF Comparison with AASHTO for Path 1 Loading

Test and Girder Type	AASHTO Standard Specs ($g^m_{AASHTO\_Std}$)	AASHTO LRFD Simplified ($g^m_{AASHTO\_S}$)	AASHTO LRFD K_g Calculated ($g^m_{AASHTO\_K}$)	Test (g^m_{test})	$g^m_{AASHTO\_Std}/g^m_{test}$	$g^m_{AASHTO\_S}/g^m_{test}$	$g^m_{AASHTO\_K}/g^m_{test}$
Stop Location Interior	0.137	0.245	0.212	0.159	0.86	1.54	1.33
Stop Location Exterior	0.174	0.245	0.212	0.186	0.94	1.32	1.14
Crawl Speed Interior	0.137	0.245	0.212	0.164	0.84	1.49	1.29
Crawl Speed Exterior	0.174	0.245	0.212	0.195	0.89	1.26	1.09

Figure 7.22(a) and Figure 7.22(c) show the Path 1 stop location and crawl speed girder deflection profiles. Figure 7.22(b) and Figure 7.22(d) show the Path 1 stop location and crawl speed LLDFs compared to relevant AASHTO values. The governing LLDFs observed during testing are slightly higher than the LLDFs provided by the AASHTO Standard Specifications, and slightly lower than the AASHTO LRFD Specification LLDFs with the analytical stiffness parameter. The measured LLDFs are quite lower than the AASHTO LRFD Specification LLDFs determined using the simplified stiffness parameter.

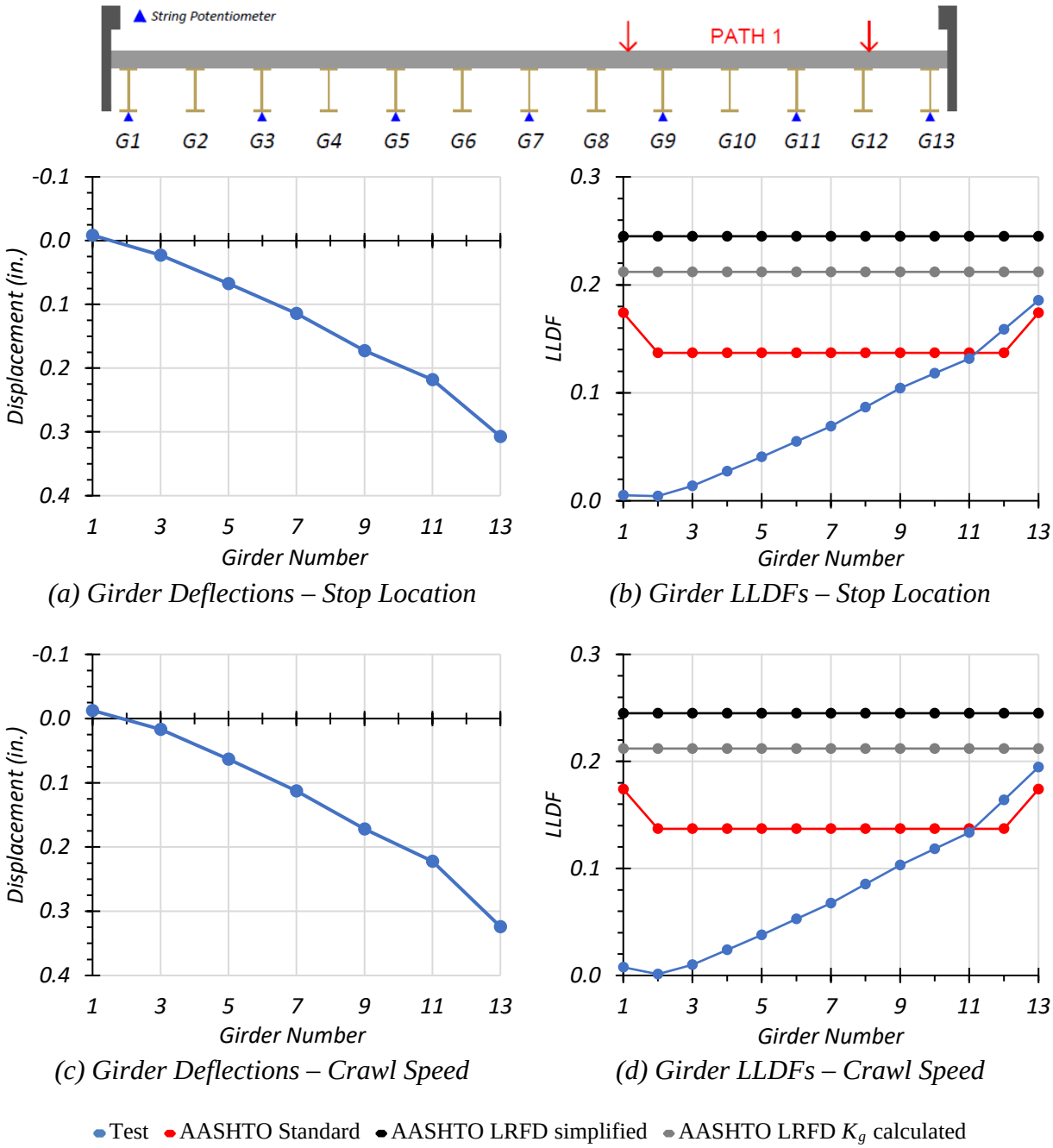

(a) Girder Deflections – Stop Location

(b) Girder LLDFs – Stop Location

(c) Girder Deflections – Crawl Speed

(d) Girder LLDFs – Crawl Speed

Figure 7.22. Static Deflection Results for Path 1 Loading

7.6.1.2.2. Path 2 Loading

Table 7.8 shows the measured girder deflections during testing for the stop location test and crawl speed test along Path 2. Deflection data for every other girder was recorded, therefore deflections the intermediate girders have been interpolated. The associated LLDFs, determined using the measured midspan deflections, are also provided.

Table 7.8. Experimental Midspan Deflections and LLDFs for Path 2 Loading

Girder	G1	G2*	G3	G4*	G5	G6*	G7	G8*	G9	G10*	G11	G12*	G13
Stop Location Test Disp. (in.)	0.212	0.202	0.192	0.179	0.166	0.145	0.124	0.101	0.078	0.056	0.035	0.020	0.006
Stop Location Test LLDF	0.140	0.133	0.127	0.118	0.109	0.096	0.082	0.067	0.051	0.037	0.023	0.013	0.004
Crawl Speed Test Disp. (in.)	0.205	0.197	0.189	0.179	0.168	0.148	0.127	0.104	0.081	0.060	0.039	0.025	0.010
Crawl Speed Test LLDF	0.134	0.129	0.124	0.117	0.110	0.097	0.083	0.068	0.053	0.039	0.026	0.016	0.007
Note: G = girder, Disp. = Displacement, * = displacement results have been interpolated using test results													

Table 7.9 compares the maximum experimental LLDFs based on midspan deflections to those calculated using the AASHTO Standard Specifications, the AASHTO LRFD Specifications using the simplified stiffness parameter, and AASHTO LRFD Specifications using the analytical stiffness parameter (AASHTO 2002; AASHTO 2017). The g_{AASHTO_Std}/g_{test} ratio was always above 1.0, ranging from 1.03 to 1.30, indicating that the AASHTO Standard LLDFs are slightly conservative or conservative for this load path. The g_{AASHTO_S}/g_{test} and g_{AASHTO_K}/g_{test} ratios were also always above 1.0 ranging from 1.51 to 1.90, indicating even more conservative estimates of the measured LLDFs.

Table 7.9. LLDF Comparison with AASHTO for Path 2 Loading

Test and Girder Type	AASHTO Standard Specs ($g^m_{AASHTO\_Std}$)	AASHTO LRFD Simplified ($g^m_{AASHTO\_S}$)	AASHTO LRFD K_g Calculated ($g^m_{AASHTO\_K}$)	Test (g^m_{test})	$g^m_{AASHTO\_Std}/g^m_{test}$	$g^m_{AASHTO\_S}/g^m_{test}$	$g^m_{AASHTO\_K}/g^m_{test}$
Stop Location Interior	0.137	0.245	0.212	0.133	1.03	1.84	1.59
Stop Location Exterior	0.174	0.245	0.212	0.140	1.24	1.75	1.51
Crawl Speed Interior	0.137	0.245	0.212	0.129	1.06	1.90	1.64
Crawl Speed Exterior	0.174	0.245	0.212	0.134	1.30	1.83	1.58

Figure 7.23(a) and Figure 7.23(c) show the Path 2 stop location and crawl speed girder deflection profiles. Figure 7.23(b) and Figure 7.23(d) show the Path 2 stop location and crawl speed LLDFs compared to relevant AASHTO values. The governing LLDFs observed during testing are slightly lower than the LLDFs provided by the AASHTO Standard Specifications. They are significantly lower than the AASHTO LRFD Specification LLDFs with the analytical stiffness parameter and with the simplified stiffness parameter.

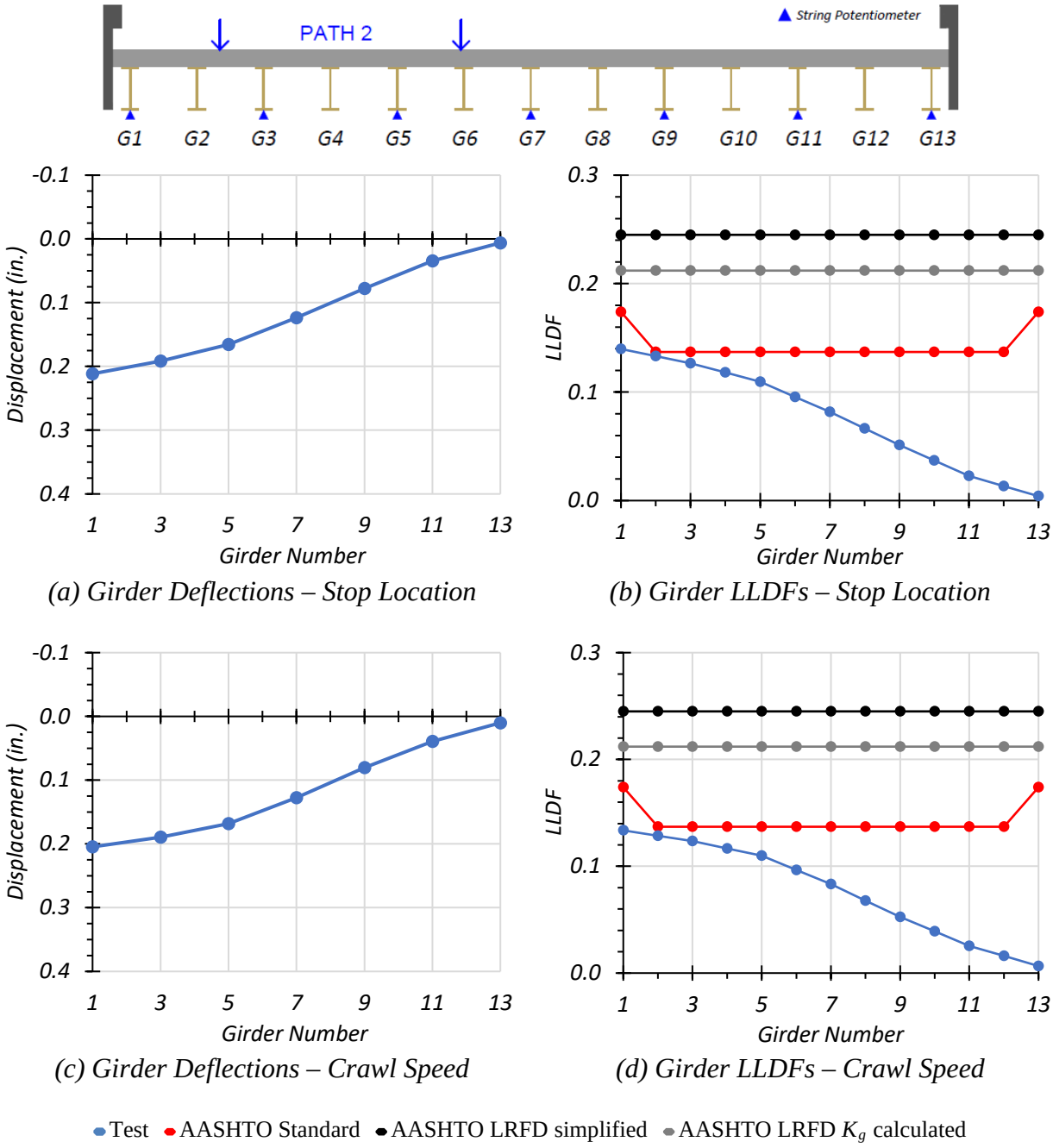

(a) Girder Deflections – Stop Location

(b) Girder LLDFs – Stop Location

(c) Girder Deflections – Crawl Speed

(d) Girder LLDFs – Crawl Speed

Figure 7.23. Static Deflection Results for Path 2 Loading

7.6.1.2.3. Middle Path Loading

Table 7.10 shows the measured girder deflections during testing for the stop location test and crawl speed test along the Middle Path. Deflection data for every other girder was recorded, therefore deflections the intermediate girders have been interpolated. The associated LLDFs, determined using the measured midspan deflections, are also provided.

Table 7.10. Experimental Midspan Deflections and LLDFs for Middle Path Loading

Girder	G1	G2*	G3	G4*	G5	G6*	G7	G8*	G9	G10*	G11	G12*	G13
Stop Location Test Disp. (in.)	0.075	0.089	0.103	0.119	0.134	0.140	0.145	0.142	0.140	0.125	0.109	0.105	0.100
Stop Location Test LLDF	0.049	0.058	0.068	0.078	0.088	0.091	0.095	0.093	0.092	0.082	0.072	0.069	0.066
Crawl Speed Test Disp. (in.)	0.073	0.087	0.102	0.119	0.136	0.141	0.146	0.142	0.139	0.125	0.111	0.107	0.104
Crawl Speed Test LLDF	0.048	0.057	0.066	0.078	0.089	0.092	0.095	0.093	0.091	0.082	0.072	0.070	0.068
Note: G = girder, Disp. = Displacement, * = displacement results have been interpolated using test results													

Table 7.11 compares the maximum experimental LLDFs based on midspan deflections to those calculated using the AASHTO Standard Specifications, the AASHTO LRFD Specifications using the simplified stiffness parameter, and AASHTO LRFD Specifications using the analytical stiffness parameter (AASHTO 2002; AASHTO 2017). The g_{AASHTO_Std}/g_{test} ratio was always above 1.0, ranging from 1.44 to 2.64. The g_{AASHTO_S}/g_{test} and g_{AASHTO_K}/g_{test} ratios were also always above 1.0, ranging from 2.23 to 3.71. In all cases, the AASHTO estimates are conservative relative to the measured LLDFs for the middle path loading.

Table 7.11. LLDF Comparison with AASHTO for Middle Path Loading

Test and Girder Type	AASHTO Standard Specs ($g^m_{AASHTO\_Std}$)	AASHTO LRFD Simplified ($g^m_{AASHTO\_S}$)	AASHTO LRFD K_g Calculated ($g^m_{AASHTO\_K}$)	Test (g^m_{test})	$g^m_{AASHTO\_Std}/g^m_{test}$	$g^m_{AASHTO\_S}/g^m_{test}$	$g^m_{AASHTO\_K}/g^m_{test}$
Stop Location Interior	0.137	0.245	0.212	0.095	1.44	2.58	2.23
Stop Location Exterior	0.174	0.245	0.212	0.066	2.64	3.71	3.21
Crawl Speed Interior	0.137	0.245	0.212	0.095	1.44	2.58	2.23
Crawl Speed Exterior	0.174	0.245	0.212	0.068	2.56	3.60	3.12

Figure 7.24(a) and Figure 7.24(c) show the Middle Path stop location and crawl speed girder deflection profiles. Figure 7.24(b) and Figure 7.24(d) show the Middle Path stop location and crawl speed LLDFs compared to relevant AASHTO values. The governing LLDFs observed during testing are significantly lower when compared to all the LLDFs provided by all three of the AASHTO methods.

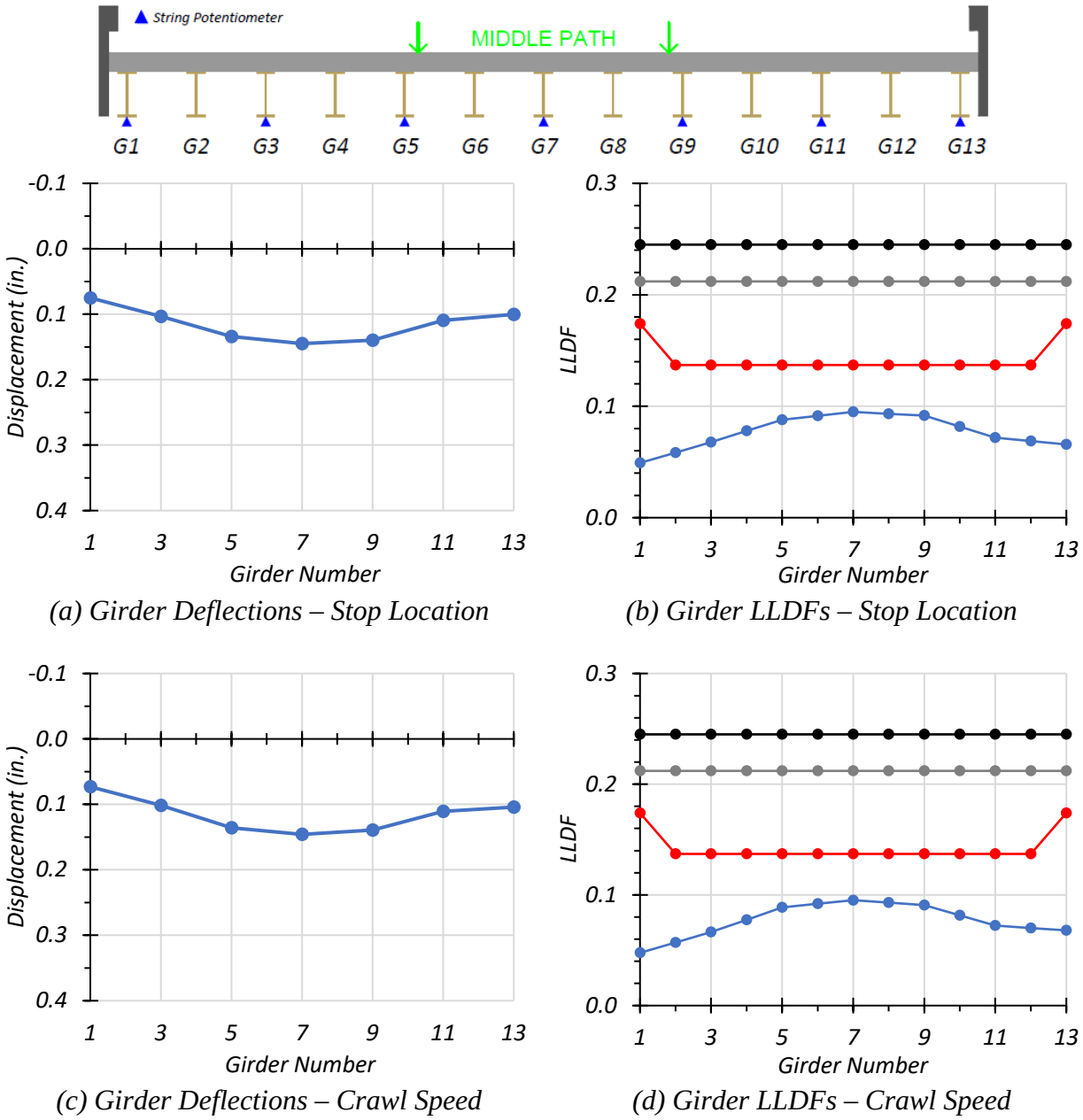

(a) Girder Deflections – Stop Location

(b) Girder LLDFs – Stop Location

(c) Girder Deflections – Crawl Speed

(d) Girder LLDFs – Crawl Speed

Figure 7.24. Static Deflection Results for Middle Path Loading

7.6.1.2.4. Comparison of Results Based on Deflection Measurements

The critical LLDF for an exterior girder was 0.195, which was observed during the crawl speed test along Path 1. This corresponds to a g_{AASHTO}/g_{test} ratio of 0.89 when using the AASHTO Standard Specifications, 1.26 when using the AASHTO LRFD Specifications using the simplified stiffness parameter, and 1.09 when using the AASHTO LRFD Specifications using the analytical stiffness parameter. The critical LLDF for an interior girder was 0.164, which was also observed during the crawl speed test along Path 1. This corresponds to a g_{AASHTO}/g_{test} ratio of 0.84 when using the AASHTO Standard Specifications, 1.32 when using the AASHTO LRFD Specifications using the simplified stiffness parameter, and 1.14 when using the AASHTO LRFD Specifications using the analytical stiffness parameter. During the static load tests along Path 1, the maximum LLDF was 0.186 for stop location test while increasing to 0.195 for the crawl speed test. During the static load tests along Path 2, the maximum LLDF was 0.140 for the stop location test while decreasing to 0.134 for the crawl speed test. During the static load tests along Middle Path, the maximum LLDF of 0.095 for stop location test remained the same for the crawl speed test.

Only the AASHTO Standard Specification LLDFs (AASHTO 2002) produced lower values than the LLDFs observed during field testing. This occurred during Path 1 loading. However, for Path 2 loading and Middle Path loading, the AASHTO Standard Specification LLDFs were conservative. Both LLDF methods in the AASHTO LRFD Specifications (AASHTO 2017) were always conservative for every load case. TxDOT currently uses the AASHTO Standard Specifications to determine LLDFs for Bridge SM-5. As these LLDFs are usually conservative, and only slightly unconservative in some cases, it is unlikely that the LLDFs could be improved for this bridge.

7.6.2. Dynamic Load Tests on Bridge SM-5

7.6.2.1. Dynamic Amplification

7.6.2.1.1. Maximum Girder Strains

From the results of the static and dynamic tests for each path, the increases in strains and deflections at midspan due to the moving vehicle were examined. Figure 7.25, Figure 7.26, and Figure 7.27 show the maximum midspan strains observed for dynamic testing along Path 1, Path 2, and the Middle Path, respectively, plotted with the strains observed for the same alignments (paths) under static loading. Figure 7.28 shows the strain values and compares them to the appropriate static load case.

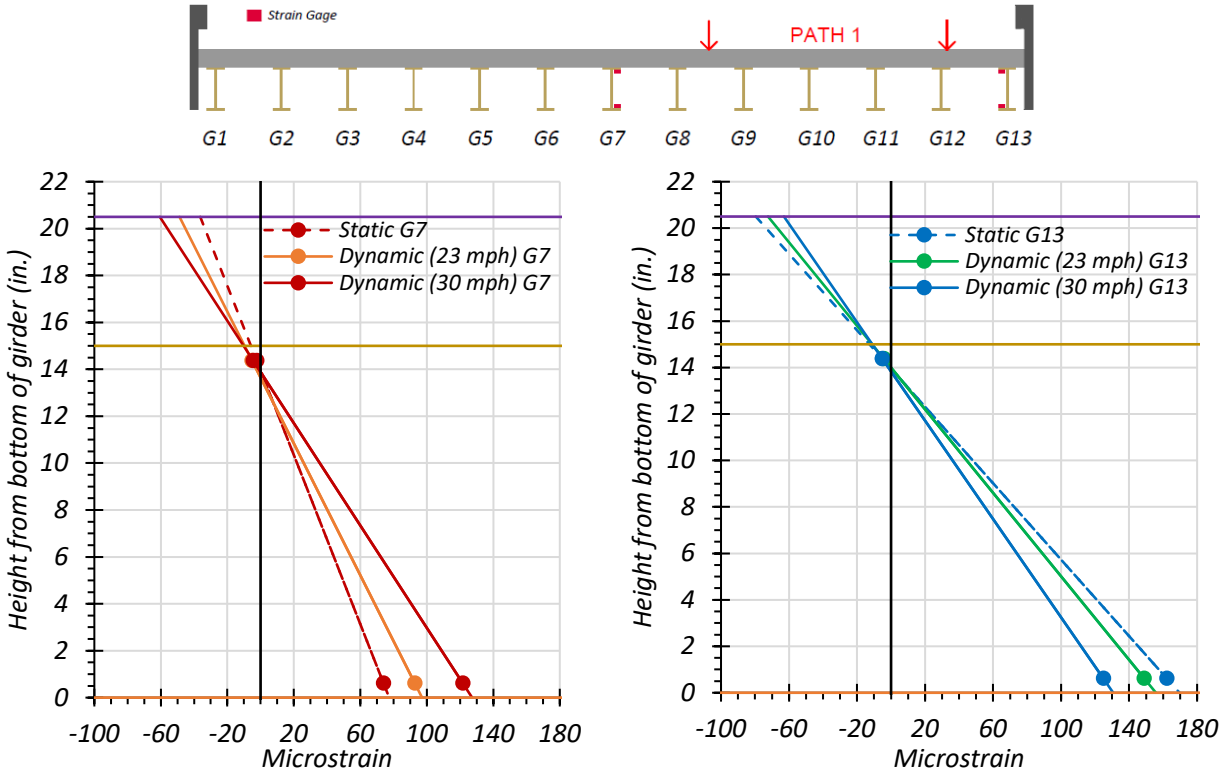

(a) Girder 7 *(b) Girder 13*

Figure 7.25. Maximum Strains for Static and Dynamic Tests for Path 1 Loading

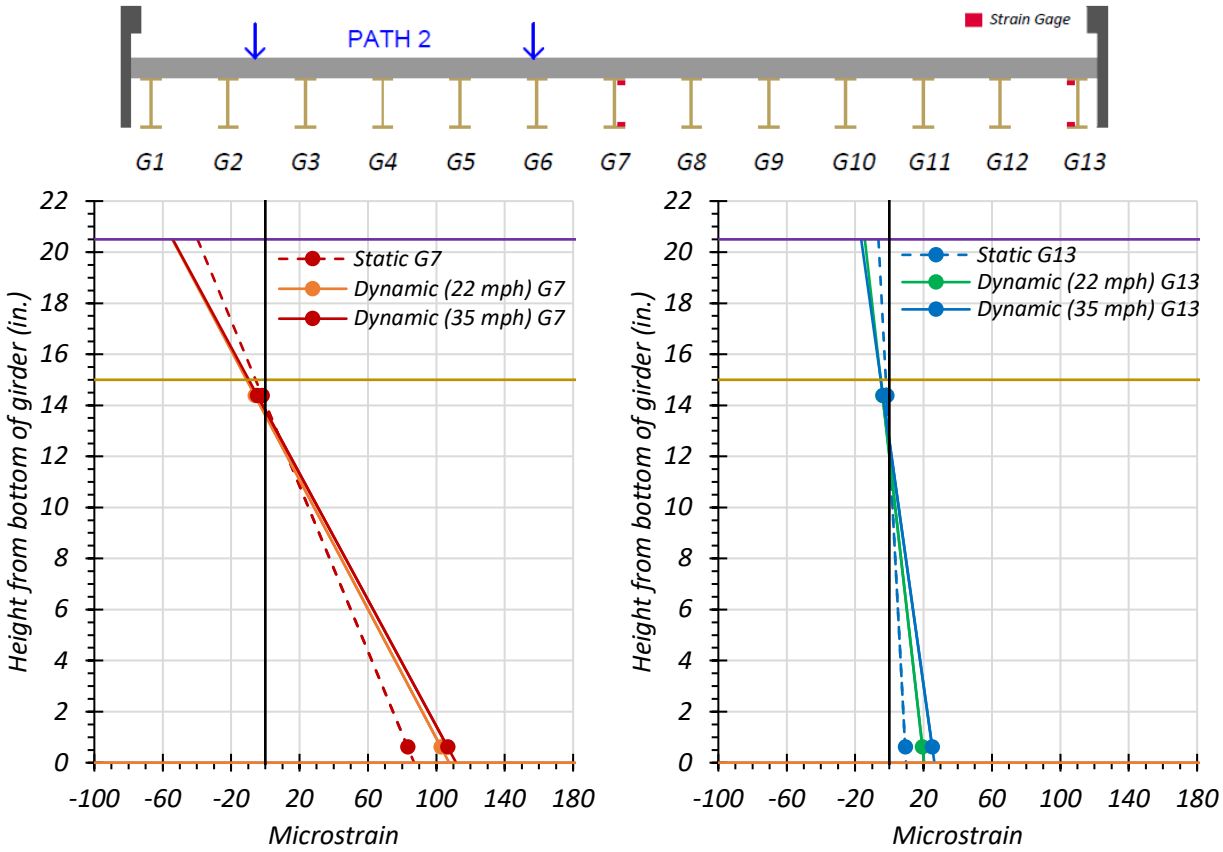

Figure 7.26. Maximum Strains for Static and Dynamic Tests for Path 2 Loading

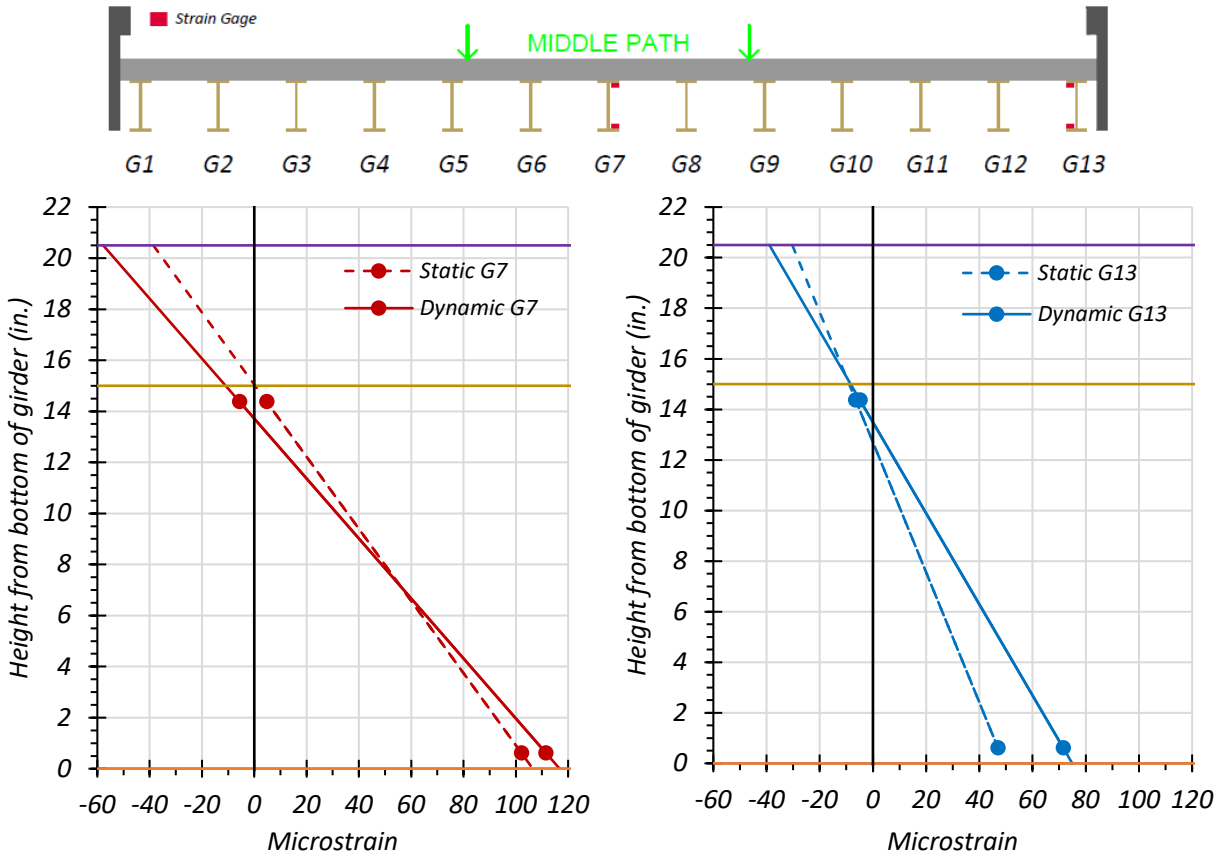

(a) Girder 7 *(b) Girder 13*

Figure 7.27. Maximum Strains for Static and Dynamic Tests for Middle Path Loading

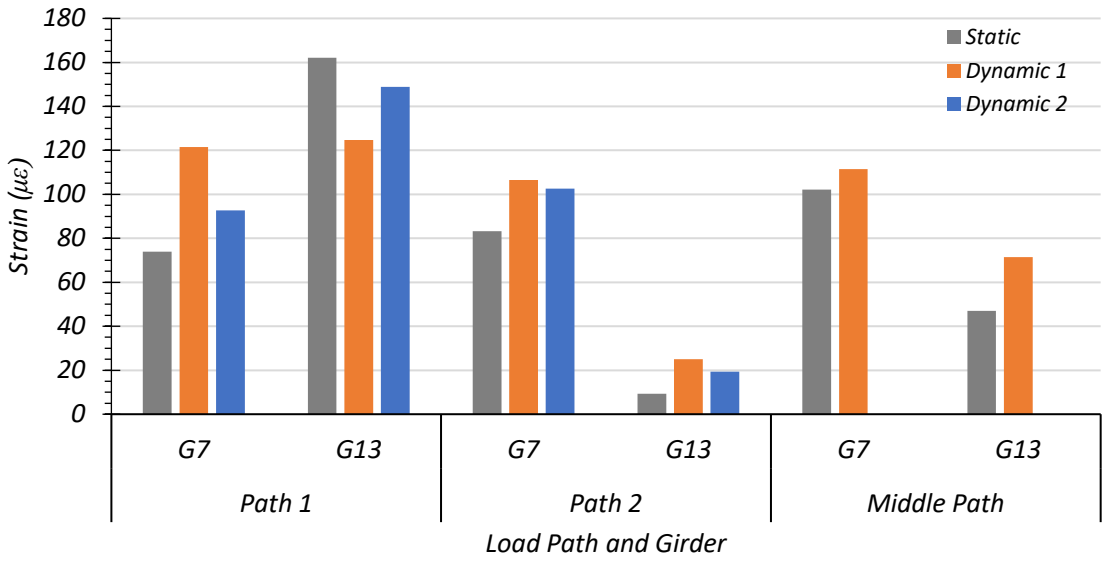

Note:

- *Path 1: Dynamic 1 = 23 mph, Dynamic 2 = 30 mph*
- *Path 2: Dynamic 1 = 22 mph, Dynamic 2 = 35 mph*
- *Middle Path: Dynamic 1 = 34 mph*

Figure 7.28. Comparison of Maximum Strains for Static and Dynamic Tests

The dynamic impact factor given by the AASHTO Standard Specifications for this bridge is 30 percent, while the AASHTO LRFD Specifications specifies an impact factor of 33 percent. The average dynamic impact factor for all girders based on the strain values observed during testing was 45 percent, indicating that for this bridge the dynamic impact factor can be higher than specified by AASHTO. However, this result could be misleading. If a girder experiences a very low amount of strain under static loading, a small increase in strain under dynamic loading could cause a large percent difference to occur. This is the case for Girder 13 under Path 2 loading. It sees an increase in strain from 9.24 microstrain during static loading to 25.06 microstrain during Dynamic 1 loading. That corresponds to a 171 percent difference in strain, however, 25.06 microstrain corresponds to a stress of only 0.73 ksi. Such a large percent difference for a girder that is carrying very little load significantly skews the average dynamic factor in this case.

When examining only Girder 7, which is not skewed by having small strain increases on top of small static strain values, the average dynamic amplification is 30.1 percent. This is almost the same as the AASHTO specified values. When examining Girder 13 under Path 1 loading, its controlling load case, the dynamic strain decreases by 8.2 percent for Dynamic 1 and 23.0 percent for Dynamic 2. Removing the cases that are insignificant for load rating gives values for dynamic amplification that are much more typical.

The dynamic effect seems to be more significant for an interior girder, as shown by the large dynamic increases in Girder 7 under Path 1 and Path 2 loading. Although Girder 13 experienced larger strains during load testing, this girder had a decrease in maximum strain during dynamic loading. As load Path 1 was quite close to the guardrail, the driver might not have felt comfortable or been able to drive along Path 1 perfectly at higher speeds.

7.6.2.1.2. Maximum Girder Deflections at Midspan

Figure 7.29, Figure 7.30, and Figure 7.31 show the girder deflection time histories for the dynamic load cases along Path 1, Path 2, and the Middle Path, respectively, for each dynamic loading test. Table 7.12 provides the maximum measured girder deflections for the stop location load case and for each dynamic load case. Figure 7.32 shows the static and dynamic maximum deflection values and compares them. Figure 7.33 shows the measured deflections for each dynamic load cases as a ratio to the stop location deflection.

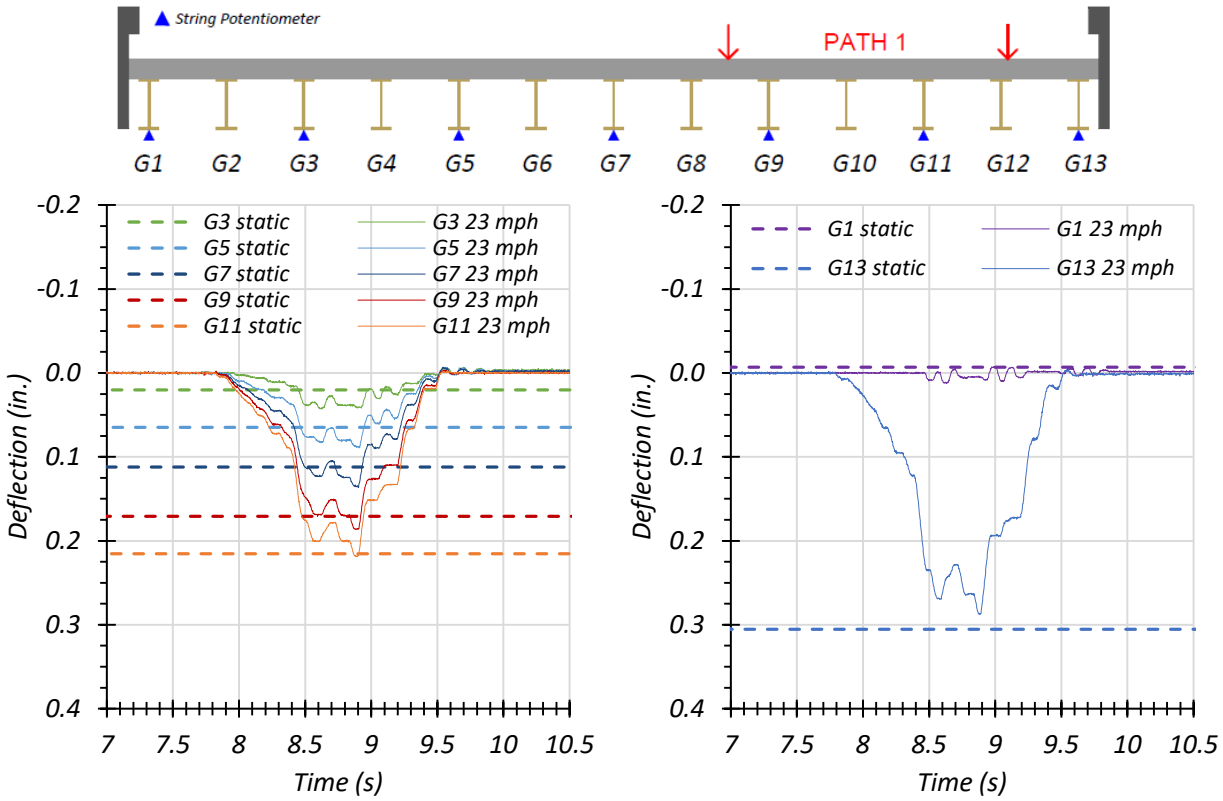

(a) Deflection Time Histories – Dynamic (23 mph)

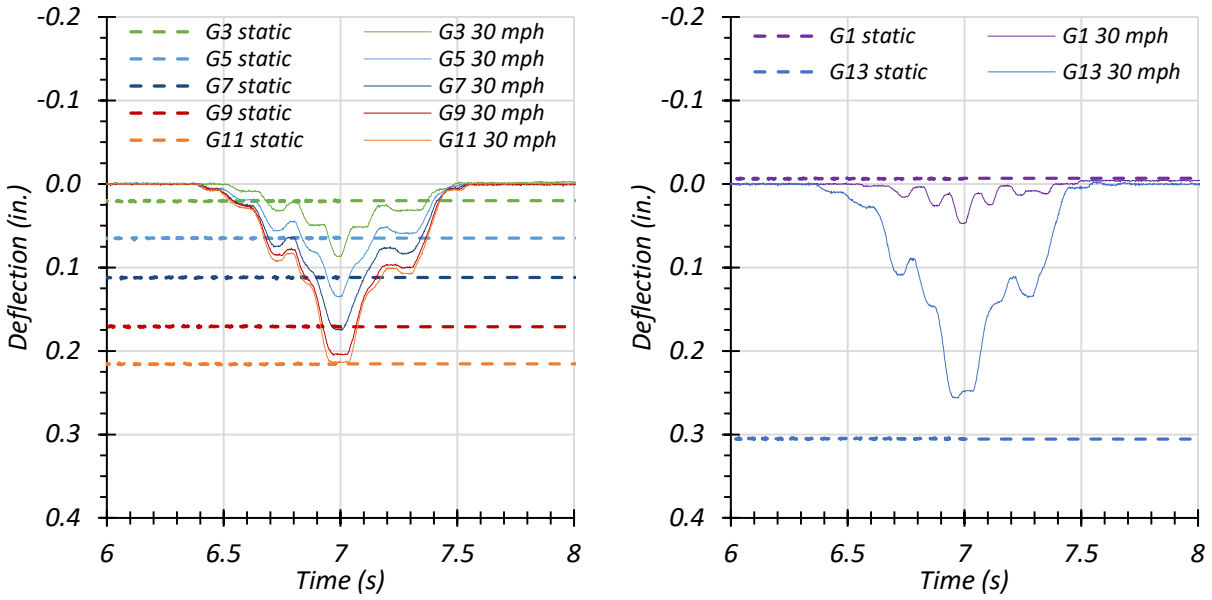

(b) Deflection Time Histories – Dynamic (30 mph)

Figure 7.29. Midspan Deflections for Static and Dynamic Tests for Path 1 Loading

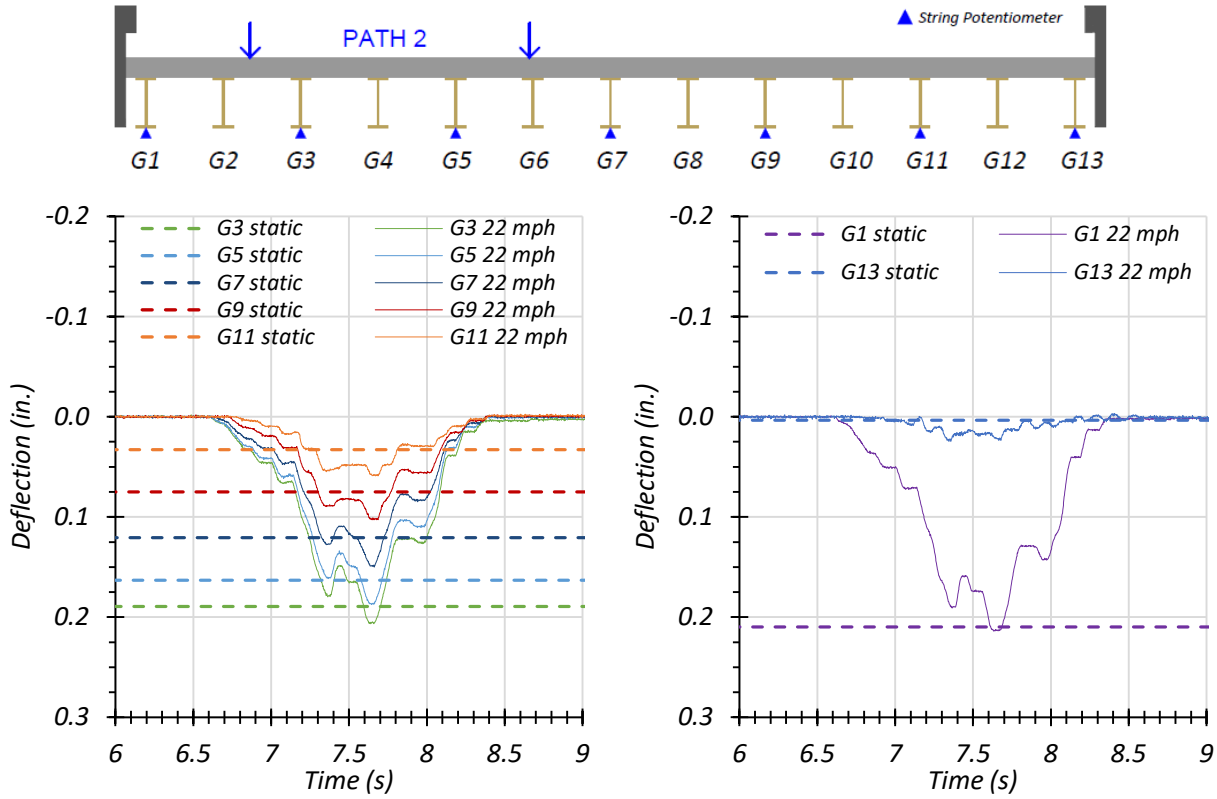

(a) Deflection Time Histories – Dynamic (22 mph)

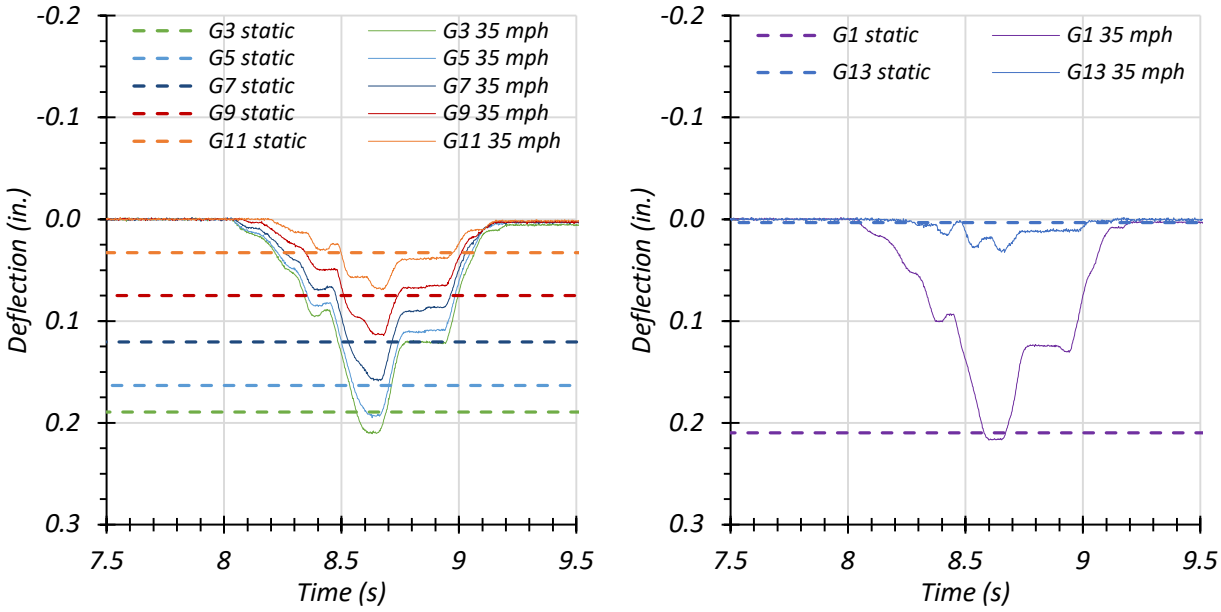

(b) Deflection Time Histories – Dynamic (35 mph)

Figure 7.30. Midspan Deflections for Static and Dynamic Tests for Path 2 Loading

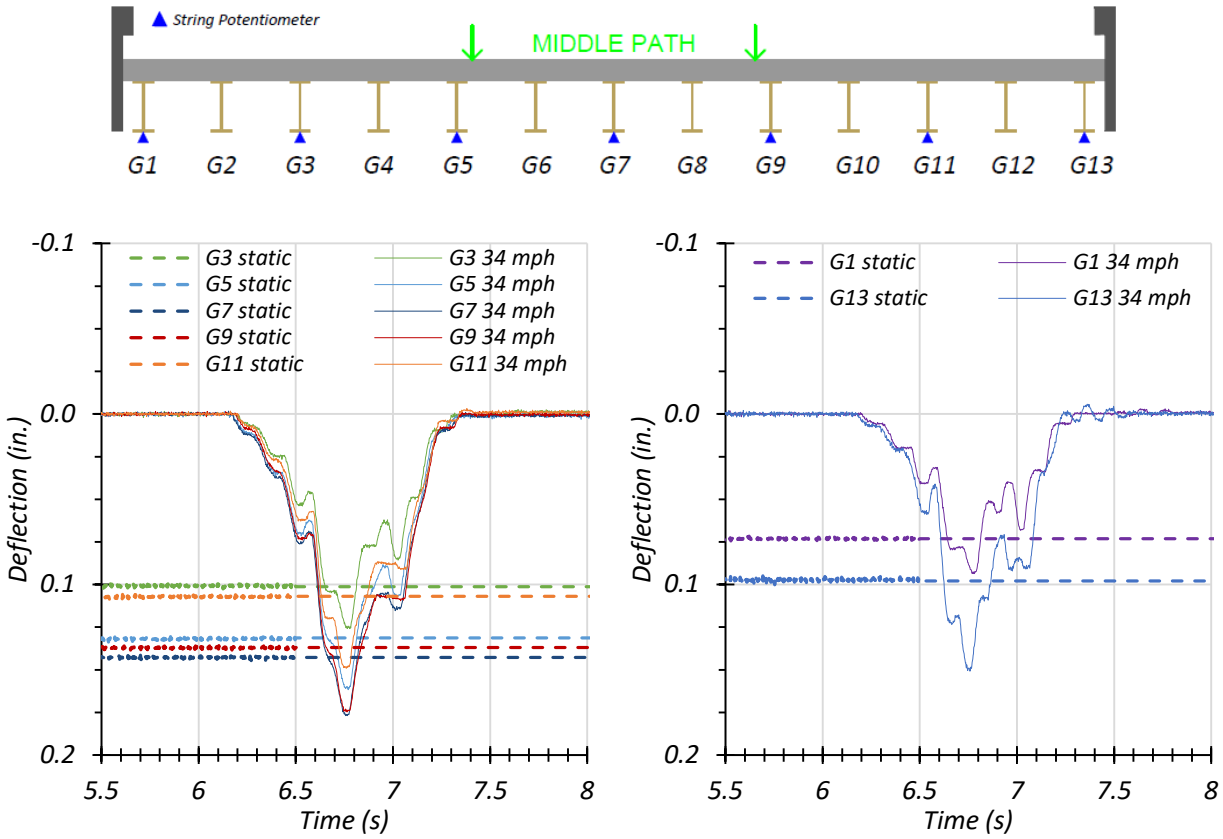

Figure 7.31. Midspan Deflections for Static and Dynamic (34 mph) Tests for Middle Path Loading

Table 7.12. Maximum Midspan Deflections for Static and Dynamic Tests

Load Scenario	Girder Displacement (in.)						
	G1	G3	G5	G7	G9	G11	G13
Path 1 Static	-0.009	0.023	0.067	0.114	0.173	0.218	0.307
Path 1 Dynamic (23 mph)	0.012	0.043	0.089	0.137	0.186	0.219	0.288
Path 1 Dynamic (30 mph)	0.048	0.087	0.135	0.175	0.205	0.214	0.257
Maximum Dynamic Amplification	**659%**	**280%**	**101%**	**53.5%**	**18.8%**	**0.4%**	**-6.4%**
Path 2 Static	0.212	0.192	0.166	0.124	0.078	0.035	0.006
Path 2 Dynamic (22 mph)	0.214	0.207	0.188	0.150	0.103	0.059	0.024
Path 2 Dynamic (35 mph)	0.217	0.211	0.195	0.159	0.114	0.069	0.033
Maximum Dynamic Amplification	**2.5%**	**9.9%**	**17.7%**	**28.5%**	**46.9%**	**101%**	**428%**
Middle Static	0.075	0.103	0.134	0.145	0.140	0.109	0.100
Middle Dynamic (34 mph)	0.094	0.126	0.162	0.177	0.175	0.149	0.151
Maximum Dynamic Amplification	**24.7%**	**22.0%**	**20.5%**	**22.2%**	**25.0%**	**36.3%**	**50.3%**

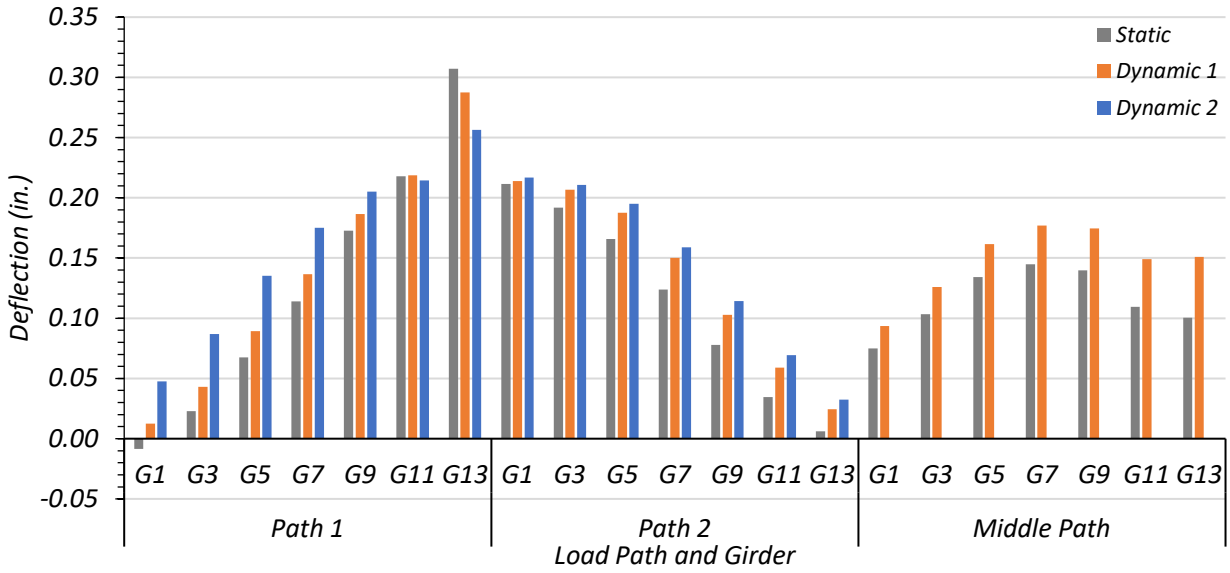

Note:

- *Path 1: Dynamic 1 = 23 mph, Dynamic 2 = 30 mph*
- *Path 2: Dynamic 1 = 22 mph, Dynamic 2 = 35 mph*
- *Middle Path: Dynamic 1 = 34 mph*

Figure 7.32. Comparison of Maximum Midspan Deflections for Static and Dynamic Tests

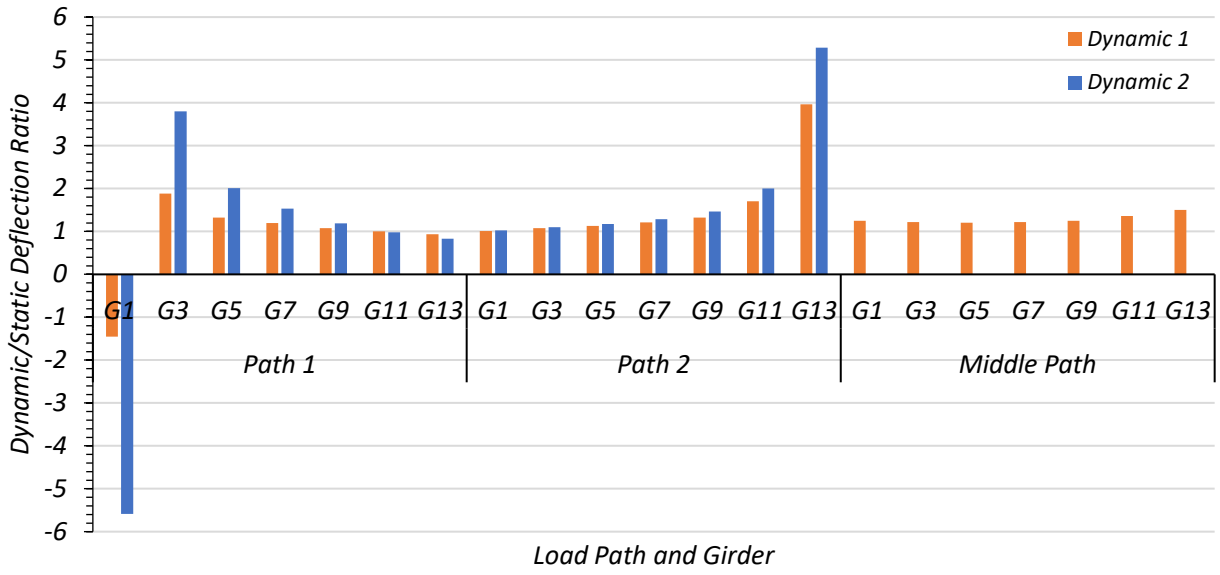

Note:

- *Path 1: Dynamic 1 = 23 mph, Dynamic 2 = 30 mph*
- *Path 2: Dynamic 1 = 22 mph, Dynamic 2 = 35 mph*
- *Middle Path: Dynamic 1 = 34 mph*

Figure 7.33. Maximum Midspan Dynamic Deflections to Static Deflections Ratios

The dynamic impact factor given by the AASHTO Standard Specifications for this bridge is 30 percent, while the dynamic impact factor given by the AASHTO LRFD Specifications is 33 percent. The average dynamic impact factor for all girders based on the deflection values observed during testing was 78 percent. However, this result could be misleading, as many girders had very minimal static deflections. A small numerical increase in deflection would cause a large increase percent difference between the static and dynamic case. This is this case for many of the girders that were on the opposite side of the bridge from the testing load case, meaning they were experiencing minimal amounts of load and therefore would not be controlling. For example, during Path 2 loading, the controlling Girder based on LLDFs was found to be Girder 1. It experienced a stop location deflection of 0.212 in. and a maximum dynamic deflection of 0.217 in. during Dynamic 2. This corresponds to a dynamic amplification of 2.5 percent. On the opposite side of

the bridge, Girder 1 experiences a stop location deflection of 0.006 in. and a maximum dynamic deflection of 0.033 in. during Dynamic 2. This corresponds to a dynamic amplification of 428 percent. This large value puts more weight on the dynamic amplification of a girder that is not controlling, and significantly skews the average dynamic amplification value.

When examining only Girder 7, which is not skewed by having small deflection increases on top of small static deflection values, the average dynamic amplification is 29.1 percent. This is almost the same as the AASHTO specified values. The average dynamic amplification under Middle Path loading for the seven girders whose deflections were measured was 28.7 percent, slightly under the AASHTO values. When examining Girder 13 under Path 1 loading, its controlling load case, the dynamic strain decreases by 6.4 percent for Dynamic 1 and 16.5 percent for Dynamic 2. Removing the cases that are insignificant for load rating gives values for dynamic amplification that are much more typical.

During Path 1 loading, the maximum percent increase in deflection for Girder 7 was 53.5 percent during Dynamic 2 loading. The maximum percent increase in deflection in Girder 13 was -6.4 percent during Dynamic 1 loading.

During Path 2 loading, the maximum percent increase in deflection for Girder 7 was 28.5 percent during Dynamic 2 loading. The maximum percent increase in deflection in Girder 13 was 428.3 percent during Dynamic 2 loading, however, it is worth noting that Girder 13 experiences very minimal deflection during Path 2 loading, which may explain the large dynamic effect.

During Middle Path loading, the maximum percent increase in deflection for Girder 7 was 22.2 percent during Dynamic 1 loading. The maximum percent increase in deflection in Girder 13 was 50.3 percent during Dynamic 1 loading.

In conclusion, Figure 7.32 and Figure 7.33 show that while large dynamic amplifications are possible, for the girders that are most heavily loaded along a particular path, the dynamic amplifications are close to the AASHTO values, and sometime even below them. In some cases, the most heavily loaded girders actually feel a decrease in effect under dynamic loading.

7.6.2.2. Dynamic Characteristics of the Bridge

Data obtained from the accelerometers during dynamic tests and the sledgehammer tests was filtered and a fast Fourier transform (FFT) was performed. This allowed for determination of the first three natural frequencies of the bridge as 7.57 Hz, 9.03 Hz, and 17.58 Hz. For each natural frequency, the amplitude and phase angle of each accelerometer was used to develop the mode shape. Figure 7.34 shows a longitudinal section and a transverse section at midspan of the mode shape produced by the first natural frequency of Bridge SM-5. Figure 7.35 shows a longitudinal section and a transverse section at midspan of the mode shape produced by the second natural frequency of the bridge. Figure 7.36 shows a longitudinal section and a transverse section at midspan of the mode shape produced by the third natural frequency of the bridge.

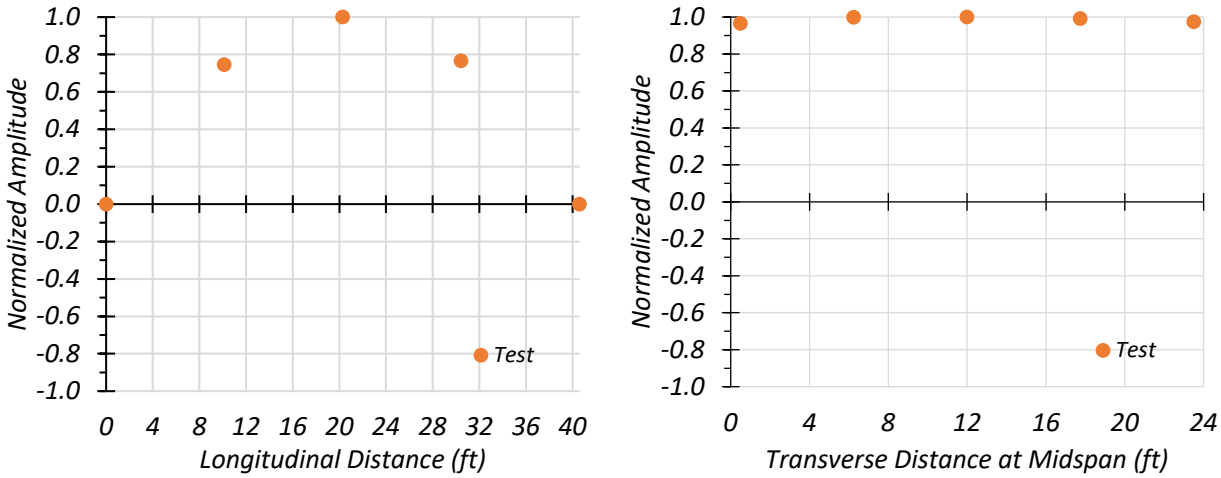

(a) Longitudinal Section *(b) Transverse Section*

Figure 7.34. First Mode Shape of Bridge SM-5 (f_1 = 7.57 Hz)

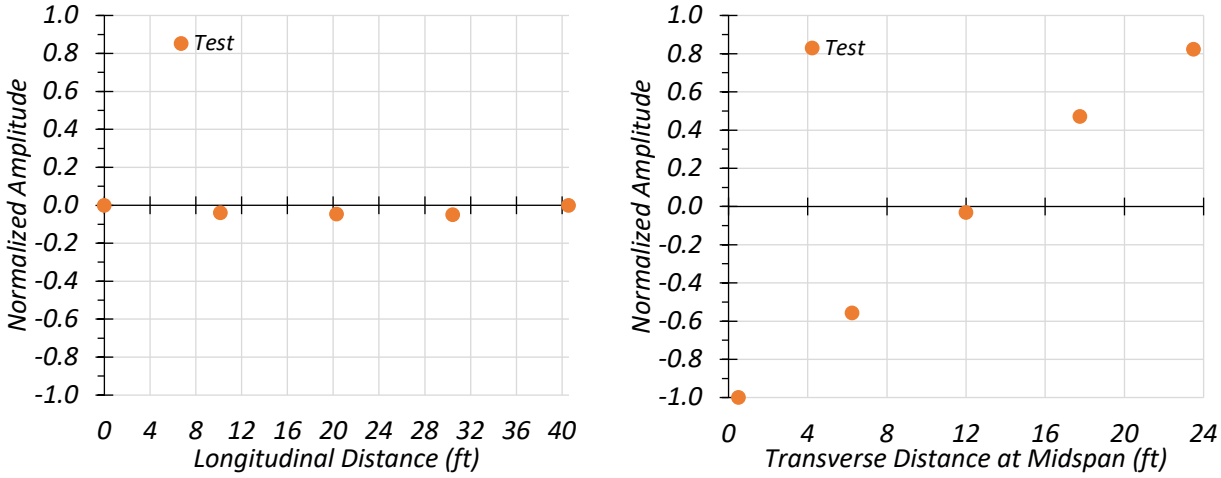

(a) Longitudinal Section *(b) Transverse Section*

Figure 7.35. Second Mode Shape of Bridge SM-5 (f_2 = 9.03 Hz)

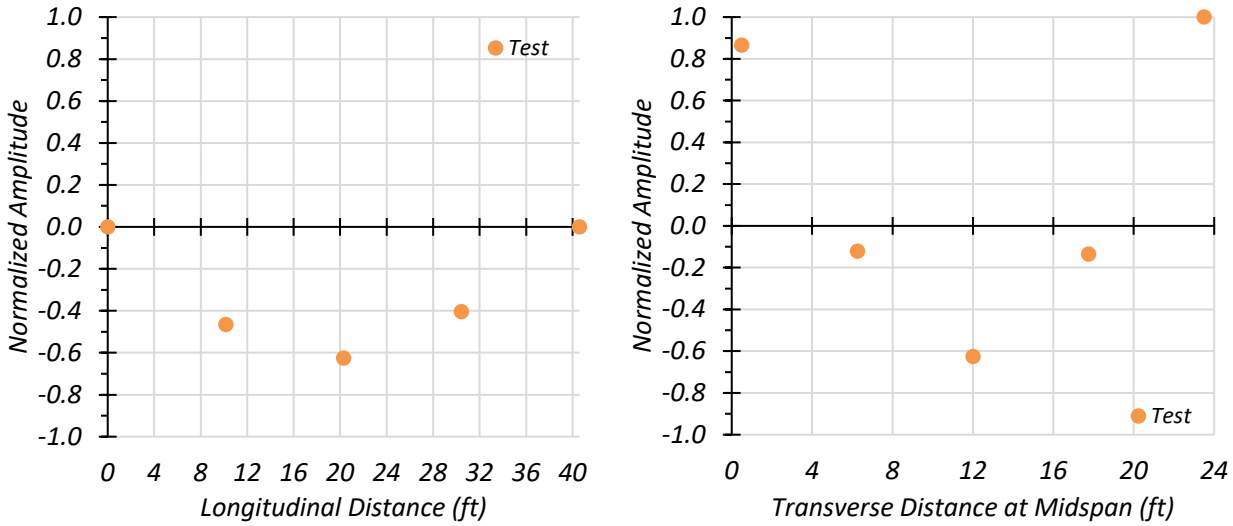

(a) Longitudinal Section *(b) Transverse Section*

Figure 7.36. Third Mode Shape of Bridge SM-5 (f_3 = 17.58 Hz)

7.6.3. Computer Vision

During testing, a handheld video camera was set up on a tripod on the side of the bridge near exterior Girder 13. The camera had a frame size of 1280 pixels by 720 pixels and a sampling frequency of 30 Hz. It was placed near the midspan of the bridge so that the girders were perpendicular to the camera's line of sight. Each load test was recorded, and computer vision was used on each Path 1 load test to measure the deflection experienced in Girder 13.

The computer vision algorithm compares the sub window of the initial frame in the video to the same sub window in the following frames of the video. The user selects the pixel width and height of this initial sub window. The user also defines a reference distance which the algorithm corresponds to a number of pixels. The algorithm then finds the location of the displaced sub window in the frames following the initial frame. The algorithm finds the minimum sum of the squared difference between the location of the first sub window and the location of the subsequent

sub window, therefore calculating the displacement of the objects in the original sub window. A lowpass Butterworth filter was used to smooth the deflection signal output by the program. For all load cases, a 25 pixel by 25 pixel sub window was used for computer vision.

The results from the computer vision were compared with the deflections recorded by the string potentiometer on Girder 13. For Bridge SM-5, computer vision was performed on three of the six Path 1 tests. The three tests for which computer vision was performed include: (1) Test 1 – Path 1 – Static with the Engine Running, (2) Test 3 – Path 1 – Crawl at 5 mph, and (3) Test 7 – Path 1 – Dynamic at 23 mph.

Figure 7.37 shows the deflection over time using computer vision and the deflection measured with the Girder 13 string potentiometer for the Path 1 static load test with the engine running. The cutoff frequency used for filtering was 0.75 Hz. The maximum deflection given by the string potentiometer is 0.307 in., while the maximum deflection given by computer vision is 0.248 in. Computer vision underestimated the deflection value by 0.059 in. and had a percent difference with the string potentiometer of 21.3 percent.

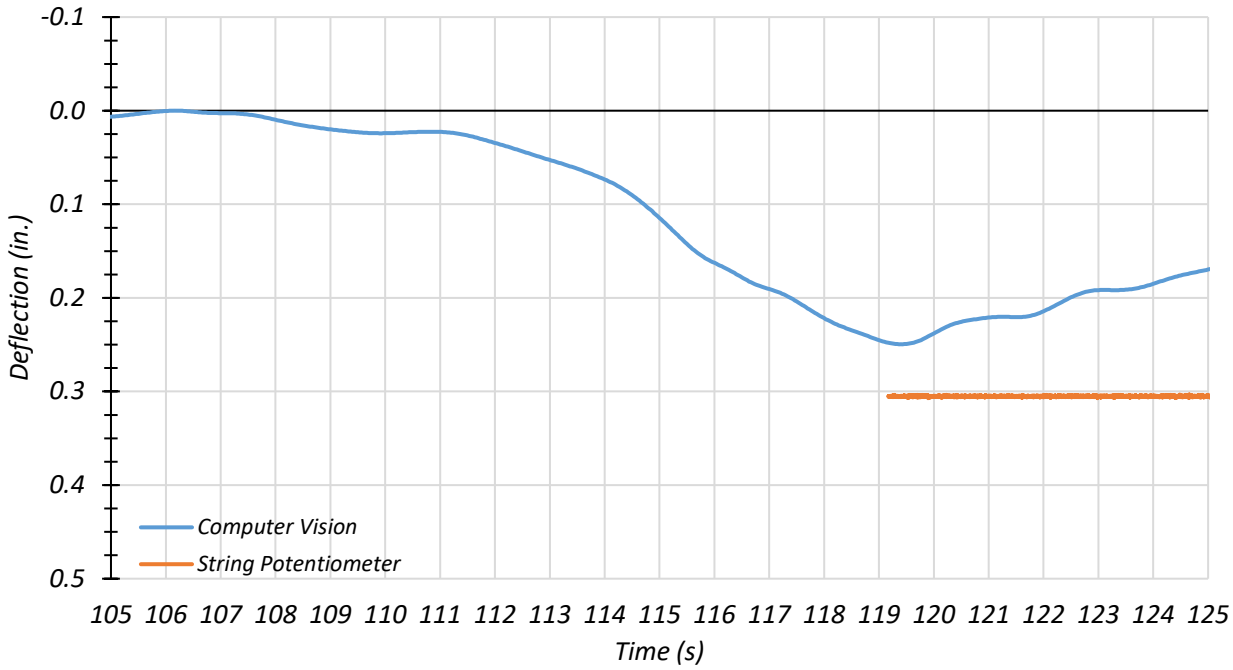

Figure 7.37. Girder 13 Midspan Deflections for Path 1 – Static with Engine Running Test

Figure 7.38 shows the deflection over time using computer vision and from the Girder 13 string potentiometer for the Path 1 crawl speed test at 5 mph. The cutoff frequency used for filtering was 0.75 Hz. The maximum deflection given by the string potentiometer is 0.299 in., while the maximum deflection given by computer vision is 0.298 in. Computer vision underestimated the deflection value by 0.001 in. and had a percent difference with the string potentiometer of 0.3 percent. Computer vision matched the string potentiometer measurements very well for this load test.

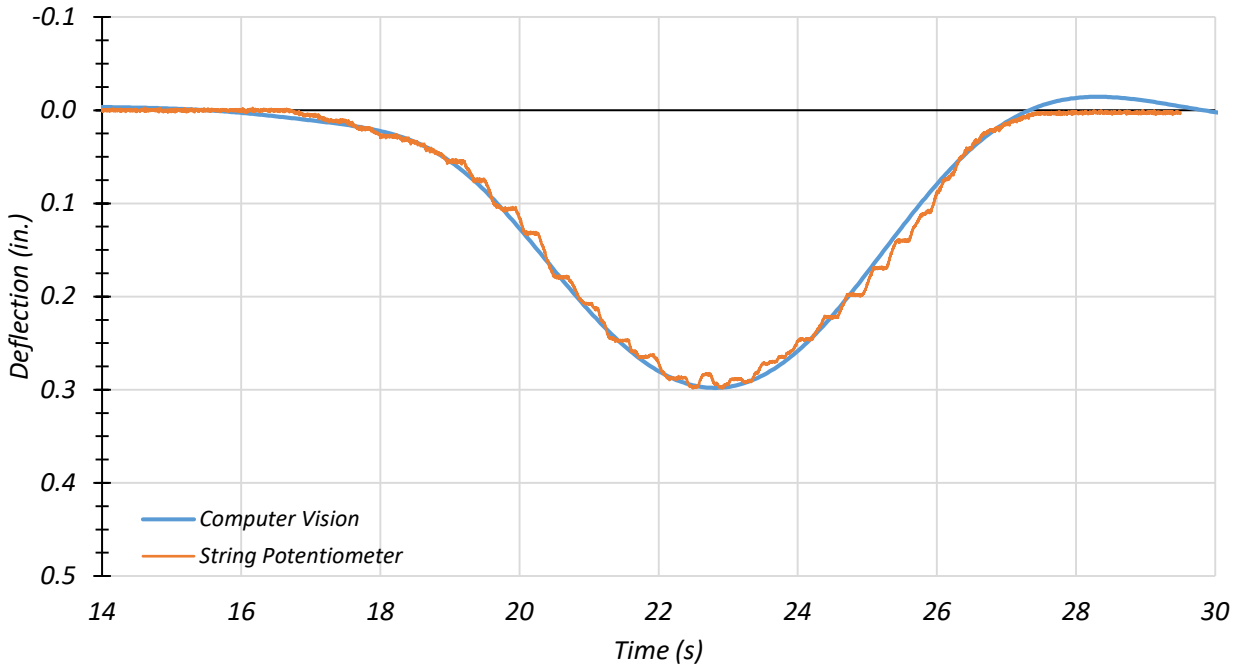

Figure 7.38. Girder 13 Midspan Deflections for Path 1 – Crawl Speed Test at 5 mph

Figure 7.39 shows the deflection over time using computer vision and from the Girder 13 string potentiometer for the Path 1 dynamic test at 23 mph. The cutoff frequency used for filtering was 1.5 Hz. The maximum deflection given by the string potentiometer is 0.288 in., while the maximum deflection given by computer vision is 0.265 in. Computer vision underestimated the deflection value by 0.023 in. and had a percent difference with the string potentiometer of 8.3 percent. Computer vision matched the string potentiometer reasonably well for this test.

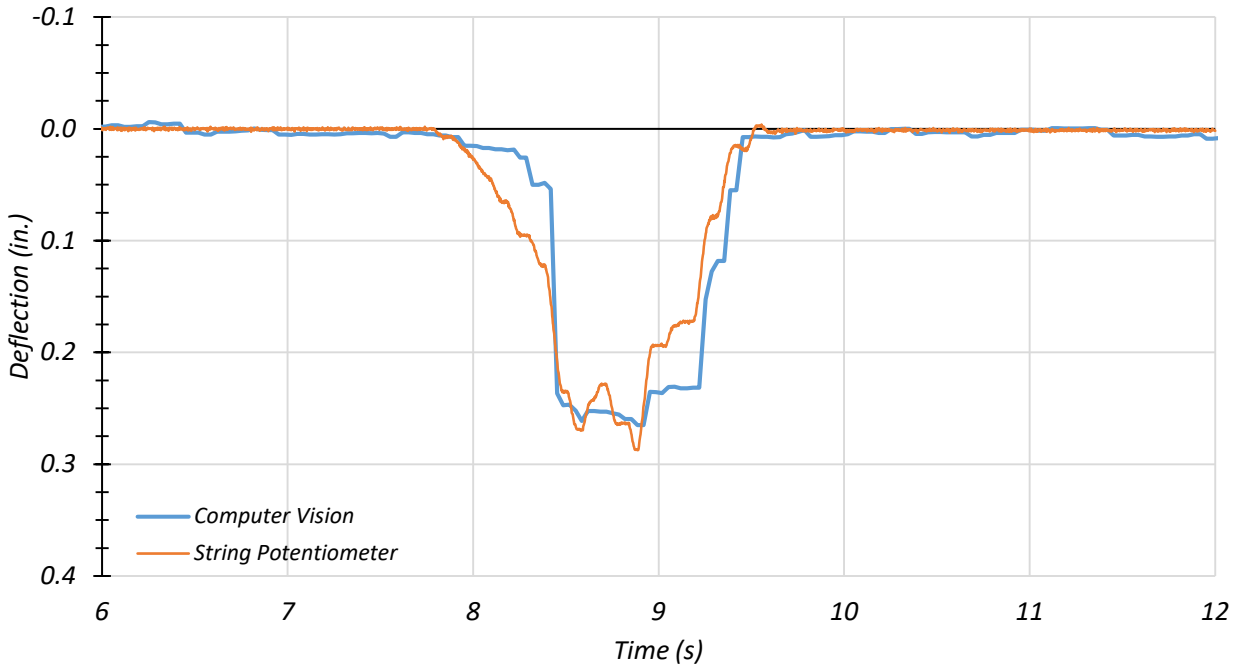

Figure 7.39. Girder 13 Midspan Deflections for Path 1 – Dynamic Test at 23 mph

The testing of Bridge SM-5 indicated that computer vision has the potential to be used to provide deflections during bridge load testing without the need for targets. It could be used to confirm that a bridge is behaving compositely when estimated composite and non-composite deflections are known. For future bridge tests in this report, computer vision is used, as well. The process of using computer vision was improved based on the lessons learned from the first test, such as camera resolution and camera placement.

7.7. FEM MODEL UPDATING AND CALIBRATION

7.7.1. General

Following the load testing, the original FEM model developed for SM-5 was modified to evaluate appropriate modeling parameters based on a comparison to the test results. The models are described first and then compared to the corresponding field measurements in Section 7.6.

7.7.1.1. Modulus of Elasticity

Before the FEM model was updated, a sensitivity study was performed to understand the effect of changes in the modulus of elasticity of concrete on the model analysis. Table 7.13 shows the effect of changing the modulus of elasticity value on the modal frequencies of the bridge, and the midspan deflection, end 1 curvature, and end 2 curvature of the girders. Figure 7.40 shows this change for each output parameter graphically. Of note, the original modulus of elasticity value used during Task 4 of this project was 2850 ksi, corresponding to concrete with an f_c' of 2.5 ksi. This is closest to the modulus of elasticity value of 3000 examined in the sensitivity study. The modulus of elasticity determined from NDE field measurements was 4836 ksi, corresponding to concrete with an f_c' of 7.2 ksi. This is closest to the modulus of elasticity value of 5000 examined in the sensitivity study.

Table 7.13. Effect of Modulus of Elasticity Value on Selected FEM Results

MOE (ksi)	Modal Frequency (Hz)		Midspan Deflection (in.)		End 1 Curvature		End 2 Curvature	
	1st Mode	2nd Mode	G7	G13	G7	G13	G7	G13
3000	11.83	12.31	0.064	0.107	7.02E-06	1.14E-05	7.72E-06	1.27E-05
4000	12.23	12.82	0.059	0.099	6.64E-06	1.10E-05	7.37E-06	1.24E-05
5000	12.51	13.22	0.055	0.094	6.34E-06	1.07E-05	7.09E-06	1.21E-05
6000	12.74	13.55	0.052	0.09	6.14E-06	1.05E-05	6.89E-06	1.18E-05

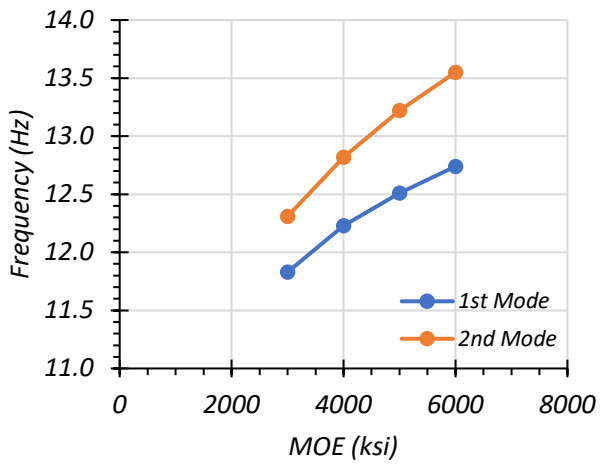

(a) Effect on Modal Frequency

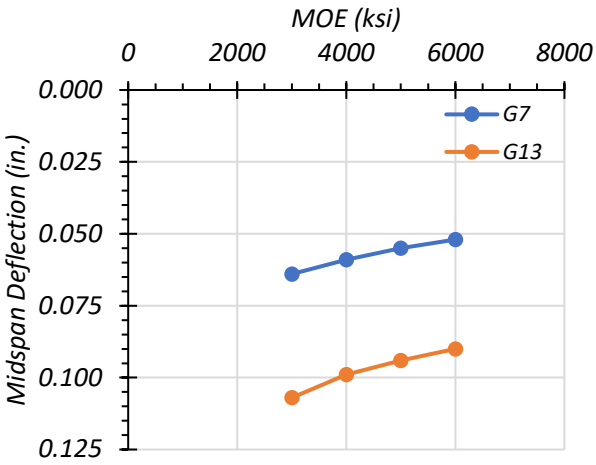

(b) Effect on Midspan Deflection

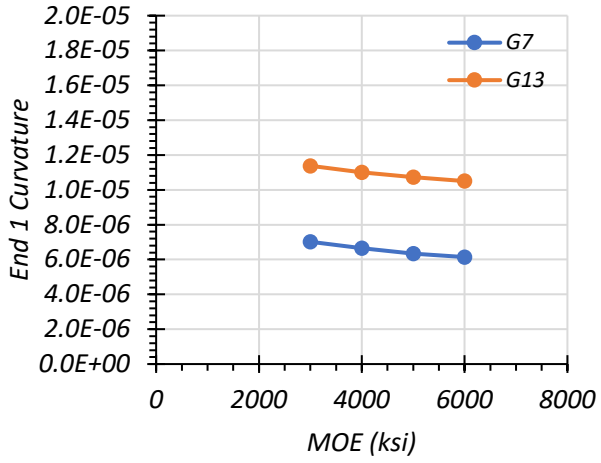

(c) Effect on End 1 Curvature

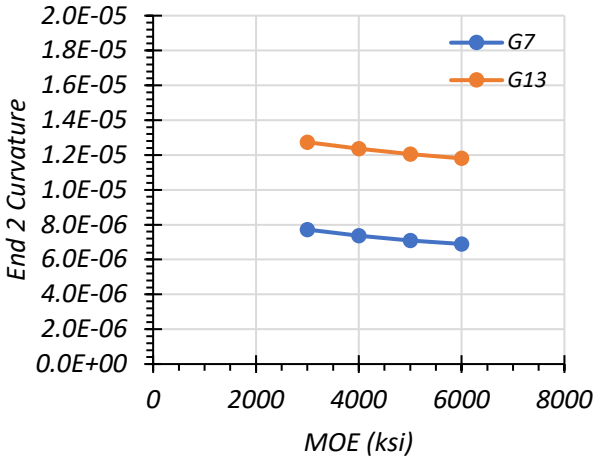

(d) Effect on End 2 Curvature

Figure 7.40. Effect of Modulus of Elasticity Value on Selected FEM Results

7.7.2. Updated FEM Models

Two FEM models were developed based on the original FEM model for Bridge SM-5. The original model was modified to reflect the updated dimensions and in situ concrete compressive strength discussed in Section 7.3. Two FEM models were developed: (1) an updated model assuming no composite action between the steel girders and concrete deck, and (2) an updated model assuming fully composite action between the girders and deck. Both models assume roller boundary conditions at both ends of every girder, except for one end of a single girder that has a pinned support to resist any lateral forces.

The two updated models use the field measured dimensions of the bridge. This includes changing the centerline to centerline of bearing span length from 40'-2" given in the inspection reports to 40'-7" measured in the field. These models also use the minimum f_c' of 7.2 ksi found using the NDE tests described in Subsection 7.3.1. This is an increase in f_c' from the 2.5 ksi used in load rating calculations, based on the age of the bridge, when the concrete deck strength is unknown (TxDOT 2018a). The increase in f_c' corresponds to an increase in computed concrete modulus of elasticity from 2850 ksi to 4836 ksi. Table 7.14 shows the results from the fully composite and fully non-composite simply supported FEM models with updated geometric and material properties, along with selected field-testing results. It can be seen that the test results tend to be closer to the fully composite updated FEM model. The modal frequencies and midspan deflections are closer to the composite case but can be matched more closely. Some end restraint was observed during field testing as well, which is not accounted for in the updated FEM models. It is important to note that TxDOT currently assumes fully non-composite action when load rating bridges without shear studs, such as Bridge SM-5.

Table 7.14. Selected FEM Results for Updated FEM Models

Model	Modal Frequency (Hz)		Midspan Deflection (in.)		End 1 Curvature		End 2 Curvature	
	1st Mode	2nd Mode	G7	G13	G7	G13	G7	G13
Non-Composite	3.78	4.87	0.349	0.627	0.00E+00	0.00E+00	0.00E+00	0.00E+00
Composite	6.28	7.17	0.131	0.245	0.00E+00	0.00E+00	0.00E+00	0.00E+00
Field Test	7.57	9.03	0.145	0.307	1.50E-06	5.41E-06	3.01E-07	9.02E-07

7.7.3. Model Calibration Process

In addition to the two models discussed above, a third FEM model was developed for Bridge SM-5 that took into account the measured end fixity and composite action observed during testing. The goal of the development of this calibrated FEM model was to create a model that more closely represents the measured bridge response. The calibrated model also uses the updated geometric properties and concrete modulus of elasticity as described in the previous section.

With respect to support conditions, the vertical translational degree of freedom is fully restrained at all girder ends for the model, as there are no bearing pad present at the abutments. Partial end fixity was created in the model by including horizontal springs at the nodes located at the bottom flange of each girder and at the deck nodes. Horizontal springs were also added between the bottom surface of the deck and the top girder flanges at each common node location to model partial composite action.

Based on the load tests, five main input parameters were identified to study their effect on the FEM results. These parameters were the interior girder end spring stiffness on the first abutment, the exterior girder end spring stiffness on the first abutment, the interior girder end spring stiffness on the second abutment, the exterior girder end spring stiffness on the second

abutment, and the spring stiffness for partial composite action. Initially the spring stiffness value required for each parameter was set as fully fixed, and the value required for the springs to be fully free were found. Then, each individual parameter was methodically changed while keeping all of the other parameters the same in order to see the effect of that parameter on the FEM results. Based on this parametric study, a spring stiffness value was chosen for each input parameter to begin the process of refining the final calibrated model.

7.7.4. Calibrated FEM Model Results

7.7.4.1. End 1 Interior Girder Stiffness Spring

The first parameter identified for calibration was the longitudinal support spring stiffness in translation for each interior girder at abutment (end) 1.

Table 7.15 shows the effect of changing the end 1 interior girder spring stiffness value on the modal frequencies of the bridge, the midspan deflections of middle girder G7 and exterior girder G13, along with the end 1 and end 2 curvatures of girders G7 and G13. Figure 7.41 shows this change for each output parameter graphically. The Girder 13 results are obtained from the Path 1 stop location load test, Girder 7 results are obtained from the Middle Path stop location load test, and the test modal frequencies are obtained from the sledgehammer test at midspan along the centerline of the bridge. When considering the end 1 interior girder stiffness spring, the desired test result for matching is the G7 end 1 curvature. Based on the sensitivity study, the spring stiffness value that most closely does this is 500 kip/in.

Table 7.15. Effect of End 1 Interior Girder Stiffness Value on Selected FEM Results

Stiffness Value (kip/in.)	Modal Frequency (Hz)		Midspan Deflection (in.)		End 1 Curvature (in^{-1})		End 2 Curvature (in^{-1})	
	1st Mode	2nd Mode	G7	G13	G7	G13	G7	G13
0	10.71	12.67	0.069	0.098	4.01E-07	1.36E-05	7.92E-06	1.20E-05
500	11.33	12.96	0.063	0.094	**1.78E-06**	1.26E-05	7.45E-06	1.17E-05
5000	12.78	13.76	0.052	0.085	4.64E-06	1.04E-05	6.57E-06	1.08E-05
10,000	13.09	13.96	0.050	0.083	5.14E-06	9.90E-06	6.39E-06	1.07E-05
20,000	13.28	14.09	0.049	0.082	5.44E-06	9.58E-06	6.29E-06	1.06E-05
40,000	13.39	14.17	0.048	0.081	5.62E-06	9.43E-06	6.24E-06	1.05E-05
Test	7.57	9.03	0.145	0.307	**1.50E-06**	5.41E-06	3.01E-07	9.02E-07

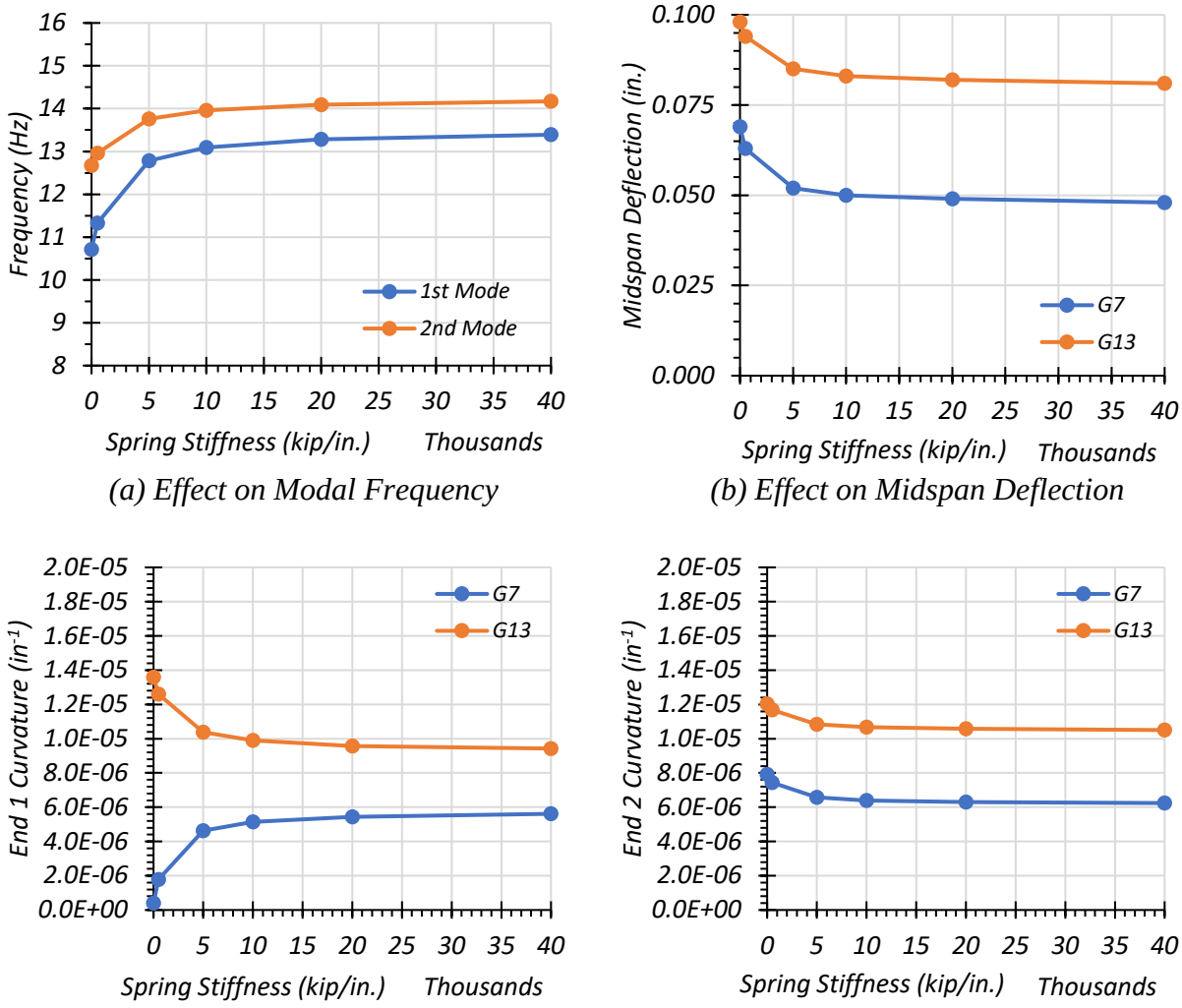

(a) Effect on Modal Frequency

(b) Effect on Midspan Deflection

(c) Effect on End 1 Curvature

(d) Effect on End 2 Curvature

Figure 7.41. Effect of End 1 Interior Girder Stiffness Value on Selected FEM Results

7.7.4.2. End 1 Exterior Girder Stiffness Spring

The second parameter identified for calibration is the longitudinal support spring stiffness in translation for an exterior girder at end 1. Table 7.16 shows the effect of changing the end 1 exterior girder spring stiffness value on the modal frequencies of the bridge, the midspan deflections of middle girder G7 and exterior girder G13, along with the end 1 and end 2 curvatures of girders G7

and G13. Figure 7.42 shows this change for each output parameter graphically. The Girder 13 results are obtained from the Path 1 stop location load test, Girder 7 results are obtained from the Middle Path stop location load test, and the test modal frequencies are obtained from the sledgehammer test at midspan along the centerline of the bridge. When considering the end 1 exterior girder stiffness spring, the test results desired to match was the G13 end 1 curvature. Based on the sensitivity study, the spring stiffness value providing the best match is 2500 kip/in.

Table 7.16. Effect of End 1 Exterior Girder Stiffness Value on Selected FEM Results

Stiffness Value (kip/in.)	Modal Frequency (Hz)		Midspan Deflection (in.)		End 1 Curvature (in^{-1})		End 2 Curvature (in^{-1})	
	1st Mode	2nd Mode	G7	G13	G7	G13	G7	G13
0	13.08	13.40	0.048	0.090	5.62E-06	8.27E-07	6.24E-06	1.14E-05
2500	13.25	13.80	0.049	0.085	5.62E-06	**5.89E-06**	6.24E-06	1.08E-05
3000	13.26	13.83	0.049	0.085	5.62E-06	6.27E-06	6.24E-06	1.08E-05
5000	13.30	13.94	0.049	0.084	5.62E-06	7.22E-06	6.24E-06	1.07E-05
10,000	13.35	14.05	0.048	0.083	5.62E-06	8.27E-06	6.24E-06	1.06E-05
20,000	13.38	14.12	0.048	0.082	5.62E-06	9.00E-06	6.24E-06	1.05E-05
40,000	13.39	14.17	0.048	0.081	5.62E-06	9.43E-06	6.24E-06	1.05E-05
Test	7.57	9.03	0.145	0.307	1.50E-06	**5.41E-06**	3.01E-07	9.02E-07

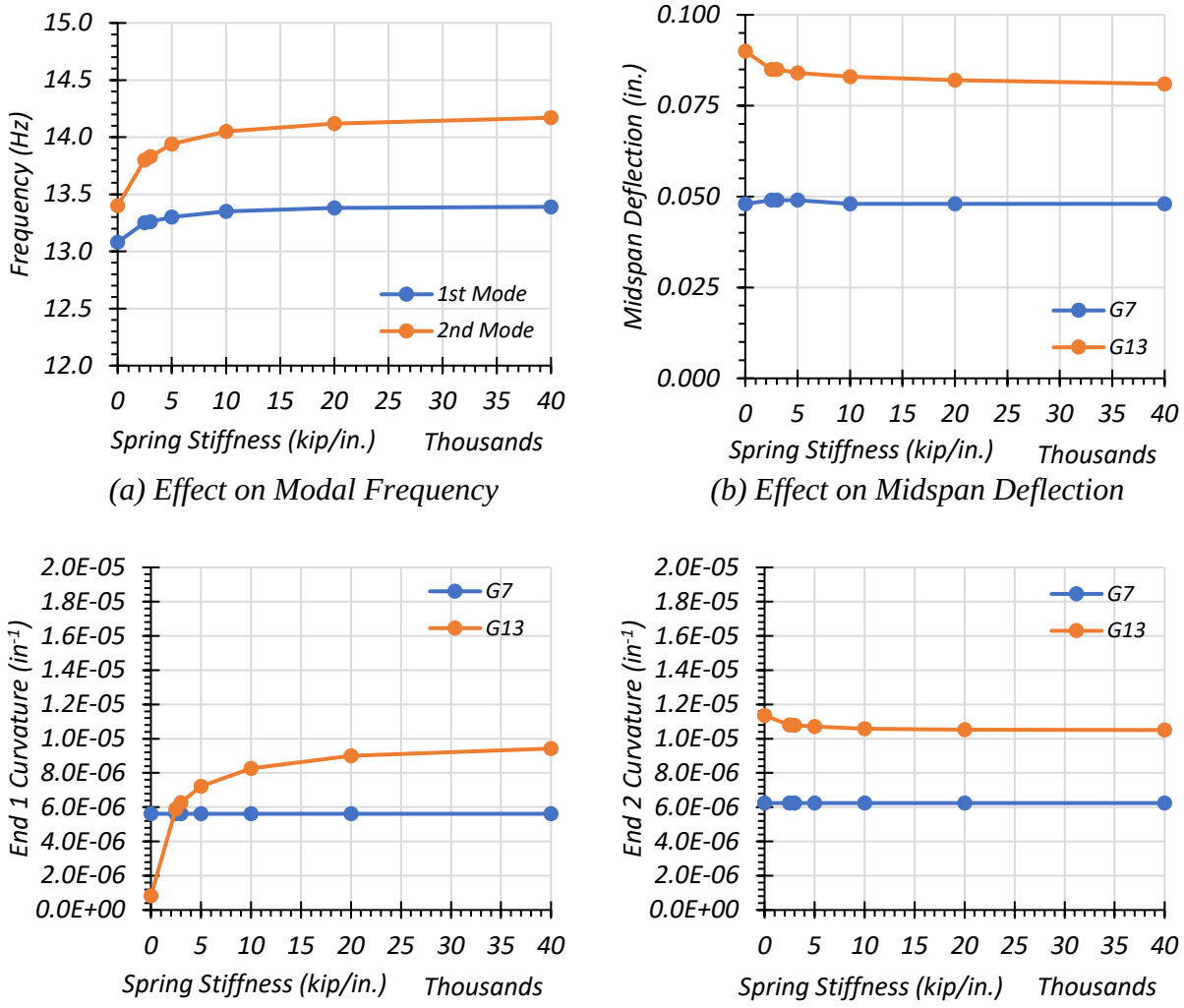

(a) Effect on Modal Frequency

(b) Effect on Midspan Deflection

(c) Effect on End 1 Curvature

(d) Effect on End 2 Curvature

Figure 7.42. Effect of End 1 Exterior Girder Stiffness Value on Selected FEM Results

7.7.4.3. End 2 Interior Girder Stiffness Spring

The third parameter identified for calibration was the longitudinal support spring stiffness in translation for an interior girder at end 2. Table 7.17 shows the effect of changing the end 2 interior girder spring stiffness value on the modal frequencies of the bridge, and the midspan deflection, and end 1 and end 2 curvatures of the girders. Figure 7.43 shows this change for each output

parameter graphically. The Girder 13 results are obtained from the Path 1 stop location load test, Girder 7 results are obtained from the Middle Path stop location load test, and the test modal frequencies are obtained from the sledgehammer test at midspan along the centerline of the bridge. When considering the end 2 interior girder stiffness spring, the test results desired to match was the G7 end 2 curvature. Based on the sensitivity study, the spring stiffness value providing the closest match is 0 kip/in. As this result corresponds to a fully free spring condition, only two iterations of the sensitivity study were performed.

Table 7.17. Effect of End 2 Interior Girder Stiffness Value on Selected FEM Results

Stiffness Value (kip/in.)	Modal Frequency (Hz)		Midspan Deflection (in.)		End 1 Curvature (in^{-1})		End 2 Curvature (in^{-1})	
	1st Mode	2nd Mode	G7	G13	G7	G13	G7	G13
0	10.71	12.67	0.072	0.101	7.55E-06	1.12E-05	**5.26E-07**	1.53E-05
40,000	13.39	14.17	0.048	0.081	5.62E-06	9.43E-06	6.24E-06	1.05E-05
Test	7.57	9.03	0.145	0.307	1.50E-06	5.41E-06	**3.01E-07**	9.02E-07

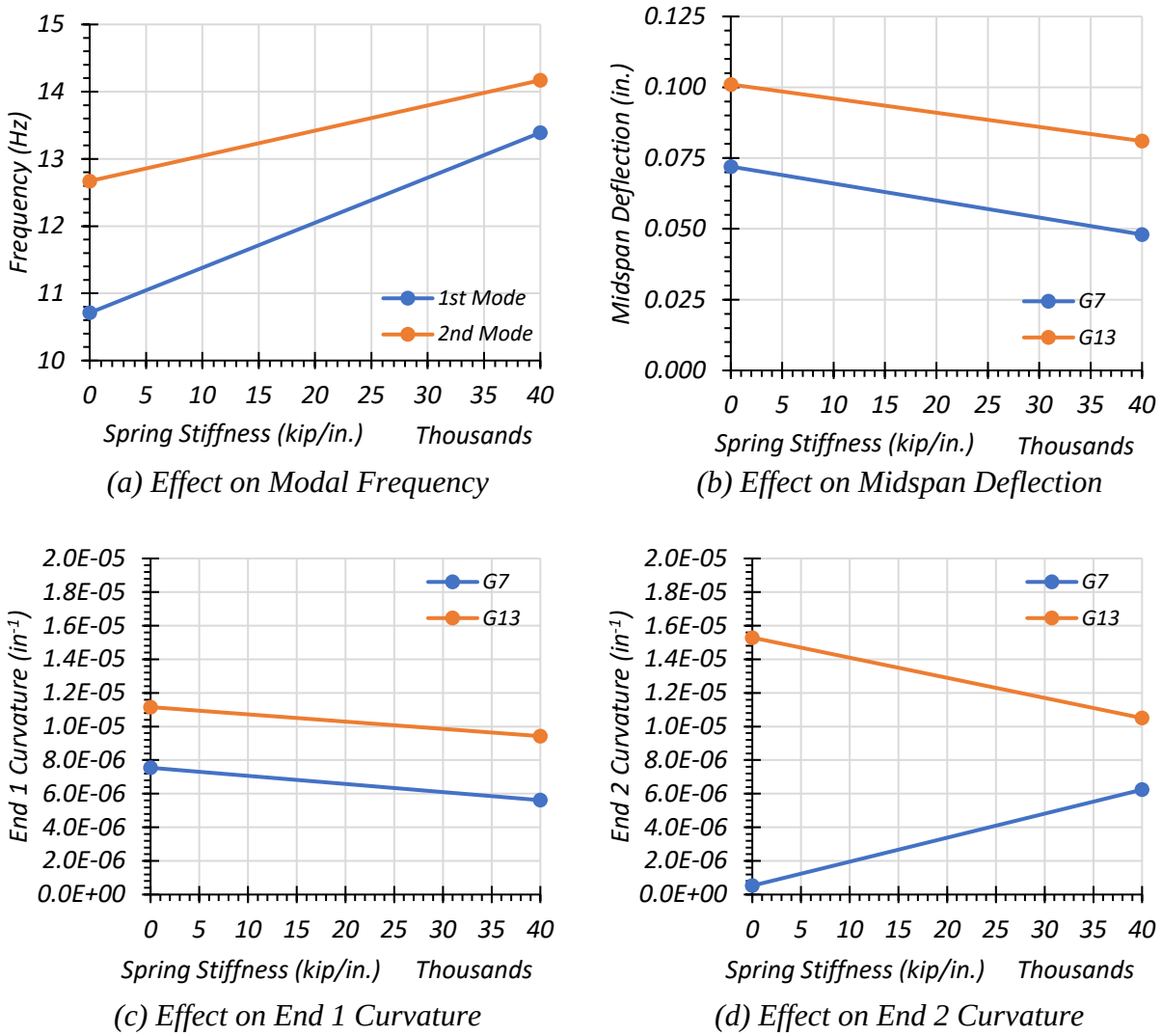

(a) Effect on Modal Frequency

(b) Effect on Midspan Deflection

(c) Effect on End 1 Curvature

(d) Effect on End 2 Curvature

Figure 7.43. Effect of End 2 Interior Girder Stiffness Value on Selected FEM Results

7.7.4.4. End 2 Exterior Girder Stiffness Spring

The fourth parameter identified for calibration was the longitudinal support spring stiffness in translation for an exterior girder at end 2. Table 7.18 shows the effect of changing the end 2 exterior girder spring stiffness value on the modal frequencies of the bridge, and the midspan deflection, and end 1 and end 2 curvatures of the girders. Figure 7.44 shows this change for each output

parameter graphically. The Girder 13 results are obtained from the Path 1 stop location load test, Girder 7 results are obtained from the Middle Path stop location load test, and the test modal frequencies are obtained from the sledgehammer test at midspan along the centerline of the bridge. When considering the end 2 exterior girder stiffness spring, the test results desired to match was the G13 end 2 curvature. Based on the sensitivity study, the spring stiffness value that the spring stiffness value providing the closest match is 0 kip/in.

Table 7.18. Effect of End 2 Exterior Girder Stiffness Value on Selected FEM Results

Stiffness Value (kip/in.)	Modal Frequency (Hz)		Midspan Deflection (in.)		End 1 Curvature (in^{-1})		End 2 Curvature (in^{-1})	
	1st Mode	2nd Mode	G7	G13	G7	G13	G7	G13
0	13.08	13.40	0.048	0.091	5.54E-06	1.02E-05	6.09E-06	**1.43E-06**
100	13.09	13.43	0.048	0.091	5.62E-06	1.01E-05	6.24E-06	2.41E-06
500	13.14	13.53	0.048	0.089	5.62E-06	1.00E-05	6.24E-06	3.46E-06
5000	13.30	13.94	0.048	0.084	5.62E-06	9.63E-06	6.24E-06	8.00E-06
10,000	13.35	14.05	0.048	0.083	5.62E-06	9.53E-06	6.24E-06	9.22E-06
20,000	13.38	14.12	0.048	0.082	5.62E-06	9.45E-06	6.24E-06	1.00E-05
40,000	13.39	14.17	0.048	0.081	5.62E-06	9.43E-06	6.24E-06	1.05E-05
Test	7.57	9.03	0.145	0.307	1.50E-06	5.41E-06	3.01E-07	**9.02E-07**

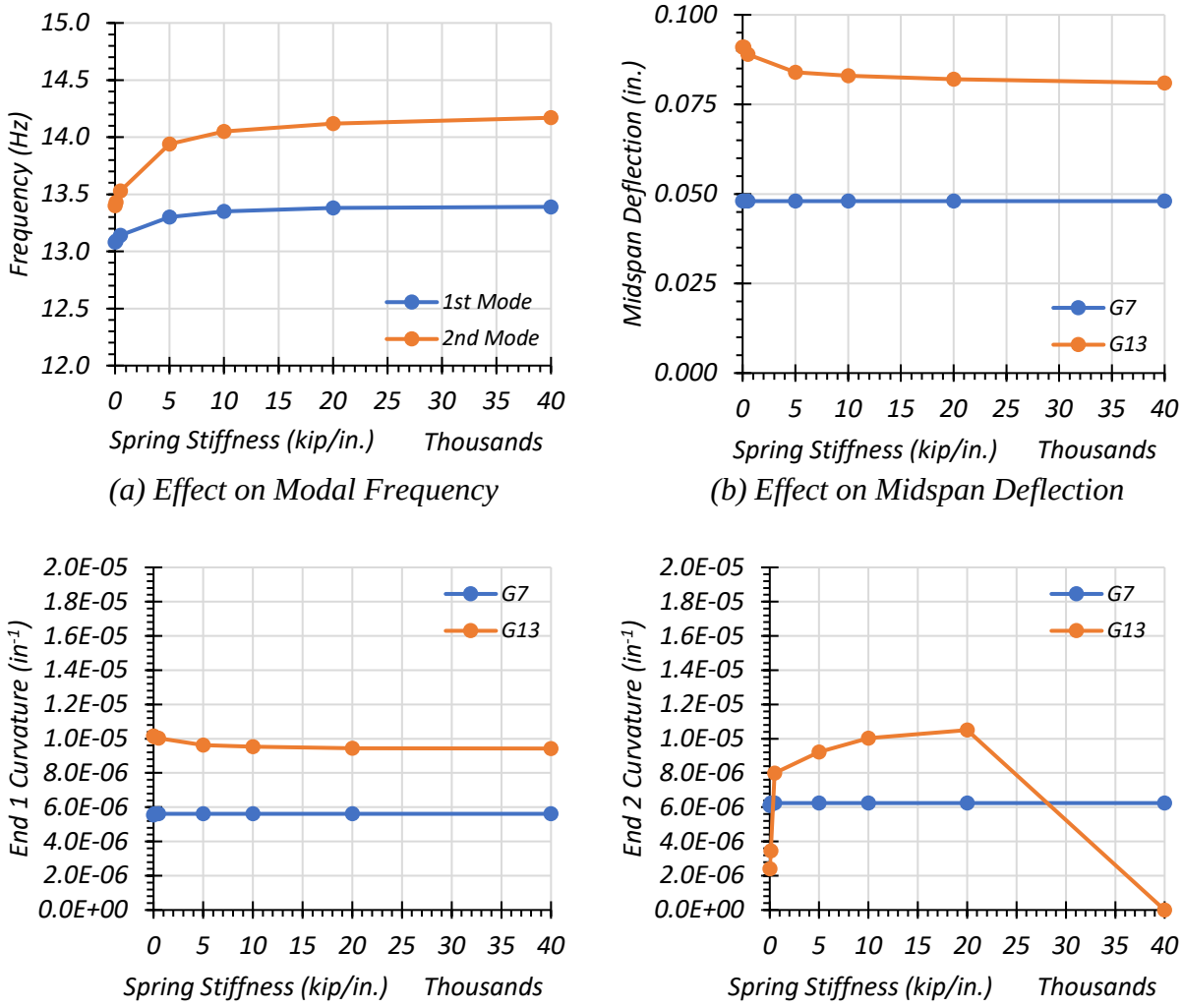

(a) Effect on Modal Frequency

(b) Effect on Midspan Deflection

(c) Effect on End 1 Curvature

(d) Effect on End 2 Curvature

Figure 7.44. Effect of End 2 Exterior Girder Stiffness Value on Selected FEM Results

7.7.4.5. Composite Spring Stiffness

The fifth parameter identified for calibration was the composite spring stiffness between the deck and the girders. Table 7.19 shows the effect of changing the composite spring stiffness value on the modal frequencies of the bridge, and the midspan deflection, end 1 curvature, and end 2 curvature of the girders. Figure 7.45 shows this change for each output parameter graphically. The

Girder 13 results are obtained from the Path 1 stop location load test, Girder 7 results are obtained from the Middle Path stop location load test, and the test modal frequencies are obtained from the sledgehammer test at midspan along the centerline of the bridge.

It is important to note that before performing the composite spring sensitivity analysis, stiffness values were chosen for the springs at the ends of the girders. These values were selected based on the results of the sensitivity study that most closely matched the test results. These values were 500 kip/in. for the end 1 interior girders, 3000 kip/in. for the end 1 exterior girders, 0 kip/in. for the end 2 interior girders, and 100 kip/in. for the end 2 exterior girders. The reason 100 kip/in. was chosen for the end 2 exterior girders was to provide a close match to the bottom flange strain measured in the girder. These values were all kept constant while performing the composite spring sensitivity analysis. Of note, a partial composite spring stiffness value of zero would be fully non-composite (10 was used because modal results cannot be obtained when the stiffness value is zero). Full composite is represented by an infinite spring stiffness.

Table 7.19. Effect of Composite Spring Stiffness Value on Selected FEM Results

Stiffness Value (kip/in.)	Modal Frequency (Hz)		Midspan Deflection (in.)		End 1 Curvature (in^{-1})		End 2 Curvature (in^{-1})	
	1st Mode	2nd Mode	G7	G13	G7	G13	G7	G13
10	5.07	6.65	0.154	0.274	9.12E-06	2.42E-05	4.54E-06	9.88E-06
100	6.77	7.86	0.148	0.264	8.00E-06	2.21E-05	4.24E-06	9.35E-06
250	6.93	8.09	0.141	0.251	7.32E-06	2.08E-05	3.76E-06	8.47E-06
500	7.14	8.31	0.134	0.237	6.62E-06	1.91E-05	3.21E-06	7.34E-06
1000	7.41	8.60	0.125	0.219	5.19E-06	1.72E-05	2.01E-06	5.89E-06
2500	7.78	9.01	0.115	0.197	4.46E-06	1.51E-05	1.73E-06	4.44E-06
7500	8.12	9.38	0.106	0.180	3.58E-06	1.35E-05	1.15E-06	3.36E-06
15,000	8.24	9.52	0.103	0.174	3.16E-06	1.29E-05	7.77E-07	2.96E-06
30,000	8.31	9.60	0.102	0.171	3.13E-06	1.26E-05	9.02E-07	2.91E-06
Infinite	8.39	9.70	0.100	0.167	2.98E-06	1.23E-05	8.77E-07	2.48E-06
Test	7.57	9.03	0.145	0.307	1.50E-06	5.41E-06	3.01E-07	9.02E-07

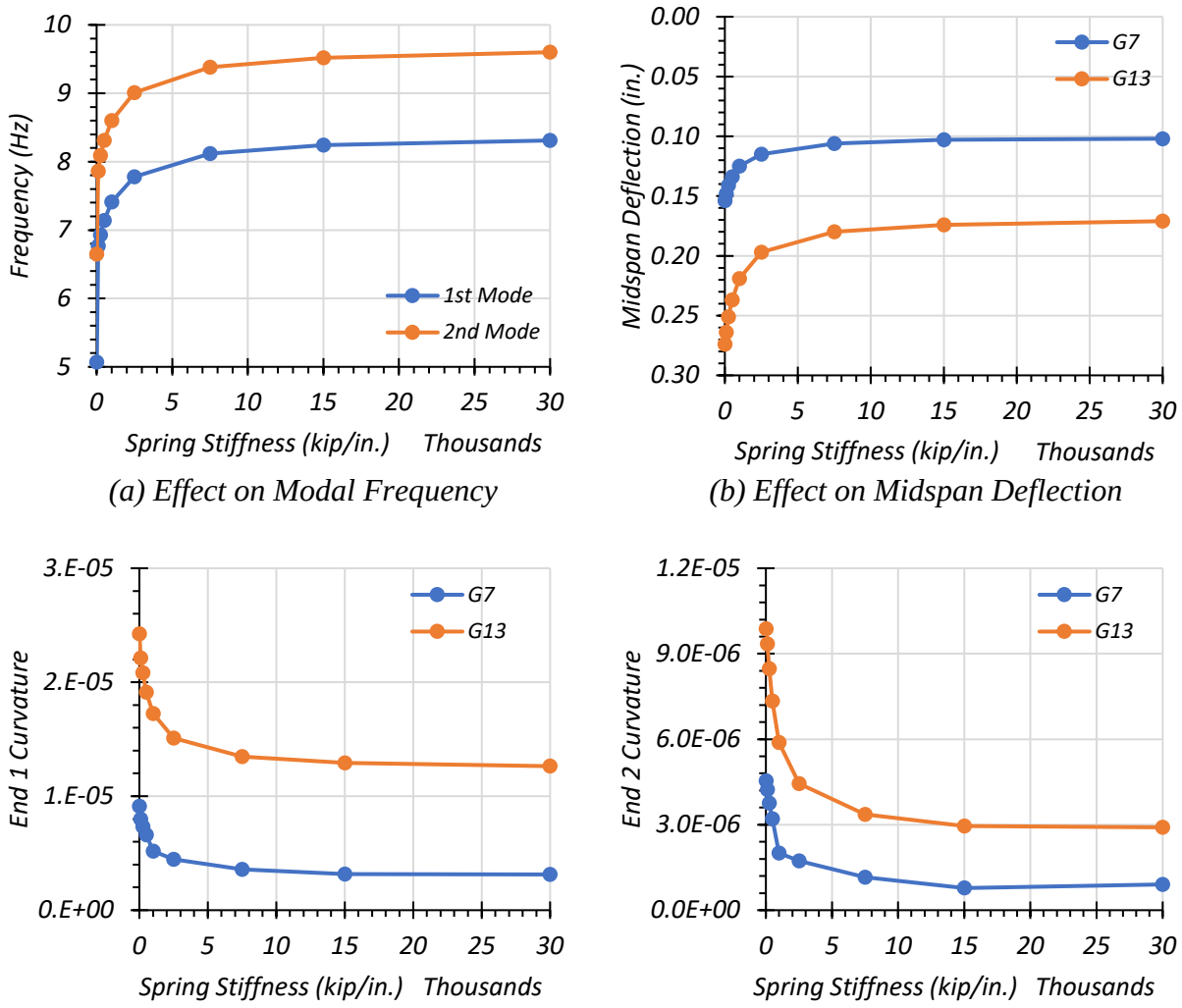

(a) Effect on Modal Frequency

(b) Effect on Midspan Deflection

(c) Effect on End 1 Curvature

(d) Effect on End 2 Curvature

Figure 7.45. Effect of Composite Spring Stiffness Value on Selected FEM Results

7.7.4.6. Final Calibration

Based on the results of the individual sensitivity studies, values were selected for each parameter to begin the final model calibration. In the refinement of the final calibrated model, each input parameter was slightly adjusted in order to get as close as possible to representing the test results. During the refinement process a small amount of horizontal stiffness in the transverse direction at

the bearing supports was added to the springs to achieve a closer match with the test results. The longitudinal stiffness of the springs attached to the deck nodes was also reduced to half of that attached to the bottom flange nodes for the same reason, and this could help if there is more restraint in the bottom of the girders than in the deck for the in situ bridge. Table 7.20 shows the selected spring stiffness values for all parameters in the final calibrated Bridge SM-5 model.

Table 7.20. Selected Spring Stiffness Parameters for Bridge SM-5 Calibration (kip/in.)

Partial Composite	End 1 Longitudinal Bottom		End 2 Longitudinal Bottom		End 1 Transverse		End 2 Transverse		End 1 Longitudinal Top		End 2 Longitudinal Top	
	G7	G13	G7	G13	G7	G13	G7	G13	G7	G13	G7	G13
7500	500	1500	0	50	50	150	250	150	250	750	0	25

Figure 7.46 shows the calibrated model with the end fixity springs and the horizontal deck partial composite springs. Table 7.21 shows the output for selected major parameters for the calibrated FEM model and for the field tests performed on Bridge SM-5. It is important to note that the Girder 13 results come from the Path 1 stop location load case and that the Girder 7 results come from the Middle Path stop location load case. This calibrated model was also used in comparison with the field test results.

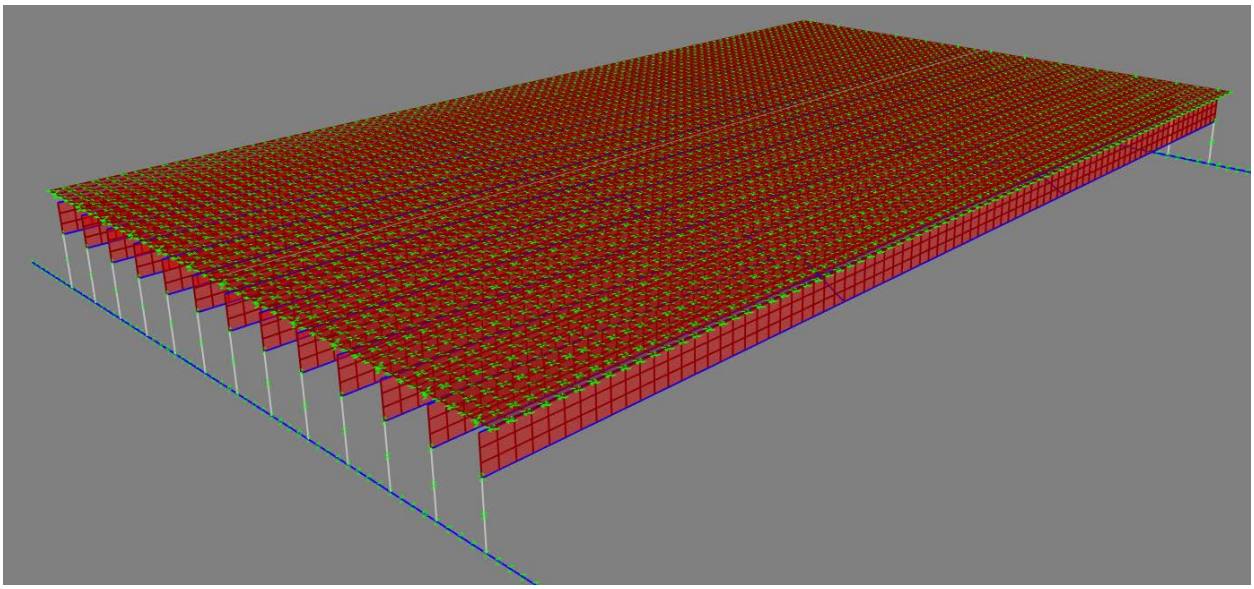

Figure 7.46. Calibrated FEM Model for Bridge SM-5

Table 7.21. Results of SM-5 Model Calibration

Analyzed Parameter	Calibrated FEM Output		Test Result		Updated FEM Composite with End Fixity Output	
	G7	G13	G7	G13	G7	G13
Midspan Deflection (in.)	0.148	0.271	0.145	0.307	0.127	0.230
End 1 Bottom Flange Strain (με)	-19.0	-64.1	-19.3	-66.2	-20.7	-68.6
End 2 Bottom Flange Strain (με)	-2.1	-10.7	-1.0	-11.4	-2.1	-10.0
End 1 Top Flange Strain (με)	1.4	7.2	1.4	8.3	1.2	4.5
End 2 Top Flange Strain (με)	0.0	0.0	3.1	1.0	0.0	0.0
Midspan Bottom Flange Strain (με)	88.6	156.6	102.1	162.1	85.3	151.9
First Modal Frequency (Hz)	6.54		7.57		7.03	
Second Modal Frequency (Hz)	7.78		9.03		7.48	

Because Bridge SM-5 was observed to be acting almost fully composite in the field, a final FEM model was created with the same support conditions as the calibrated model, but with fully fixed composite springs. This was done to observe if a fully composite model with end fixity would also produce results comparable to the test data. These results are included in Table 7.21. It can be seen

that while the end strains and midspan strains matched fairly well with the test results, the midspan deflections are further away from the test results than the calibrated model deflections. The Girder 13 deflection in the fully composite, end fixity model is 28.7 percent different than the test deflections. For this reason, the calibrated model with end fixity and slightly partial composite action was used from this point on.

7.7.5. Dynamic Characteristics of the Bridge

Data obtained from the accelerometers during dynamic tests and the sledgehammer tests was filtered and a fast Fourier transform (FFT) analysis was performed. This allowed for determination of the first three natural frequencies of the bridge as 7.57 Hz, 9.03 Hz, and 17.58 Hz. For each natural frequency, the amplitude and phase angle of each accelerometer was used to develop the mode shape. These modes shapes obtained from testing were compared to the mode shapes obtained from the calibrated FEM model. Figure 7.47 shows a longitudinal section and a transverse section at midspan of the mode shape produced by the first natural frequency of Bridge SM-5. Figure 7.48 shows a longitudinal section and a transverse section at midspan of the mode shape produced by the second natural frequency of the bridge. Figure 7.49 shows a longitudinal section and a transverse section at midspan of the mode shape produced by the third natural frequency of the bridge. In some cases, the magnitudes of the mode shapes produced by the calibrated FEM model are slightly different from the test mode shapes. However, in general, the calibrated model does a reasonably good job of predicting the mode shape.

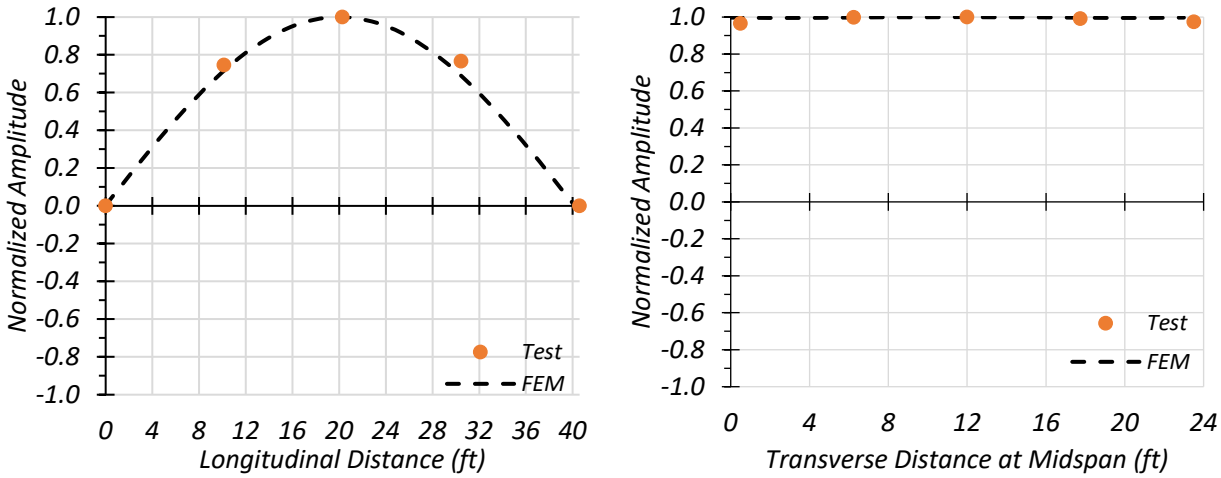

(a) Longitudinal Section *(b) Transverse Section*

Figure 7.47. Comparison of First Mode Shape of Bridge SM-5

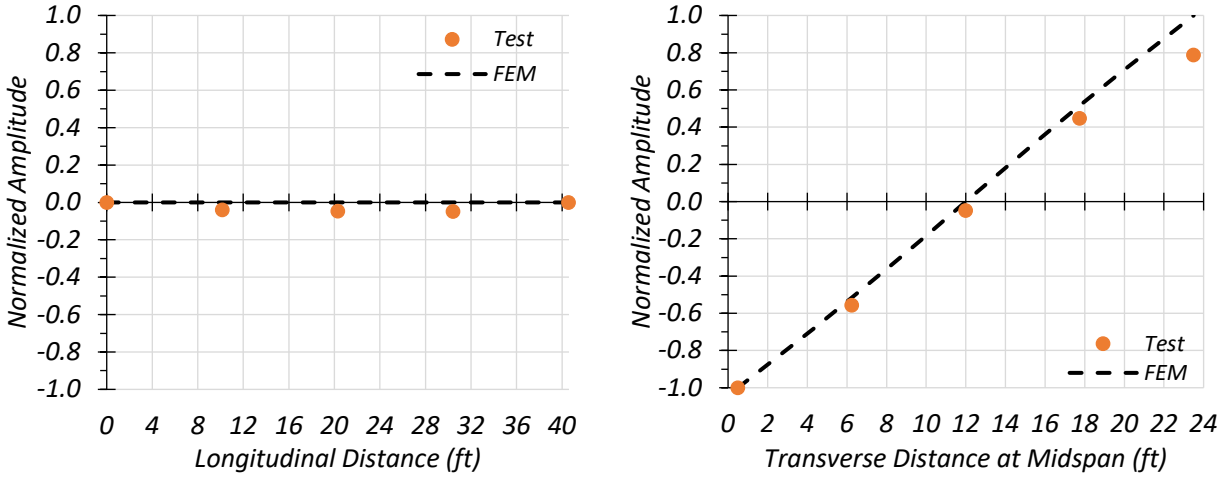

(a) Longitudinal Section *(b) Transverse Section*

Figure 7.48. Comparison of Second Mode Shape of Bridge SM-5

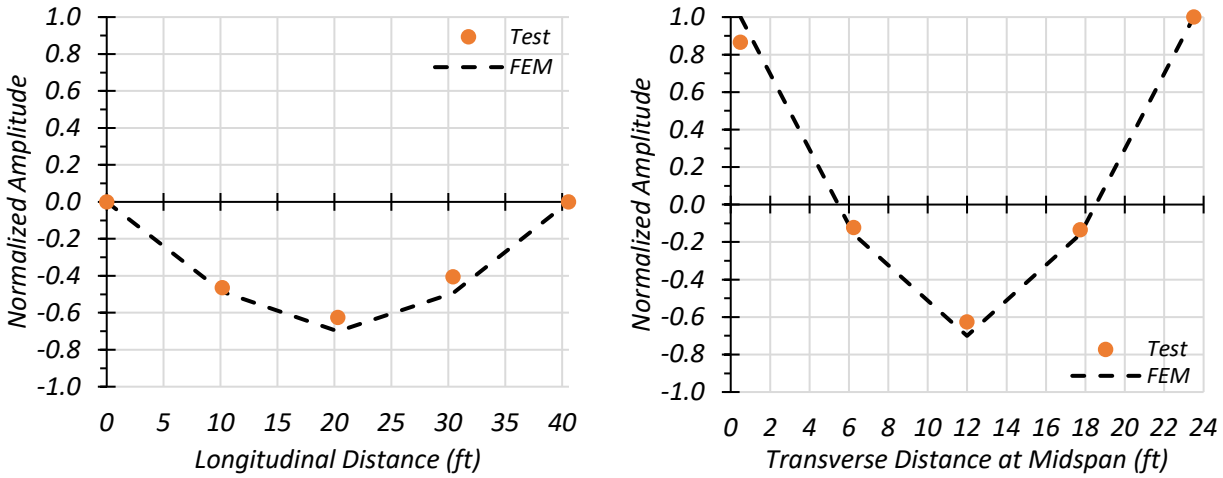

(a) Longitudinal Section *(b) Transverse Section*

Figure 7.49. Comparison of Third Mode Shape of Bridge SM-5

The natural frequencies of Bridge SM-5 observed during testing were compared to the natural frequencies produced by FEM. Table 7.22 shows the test and FEM natural frequencies. The frequencies observed during testing are much closer to those of the composite FEM bridge than those of the non-composite FEM bridge. They are also closer to the calibrated FEM model frequencies than to the updated composite FEM frequencies, but only slightly.

Table 7.22. Bridge SM-5 Test and FEM Natural Frequencies for First Two Mode Shapes

Frequency	Test (Hz)	Updated FEM Composite (Hz)	Updated FEM Non-Composite (Hz)	Calibrated FEM (Hz)
1st Natural Frequency	7.57	6.44	3.83	6.54
2nd Natural Frequency	9.03	7.45	5.10	7.78

7.8. COMPARISON OF TEST RESULTS AND FEM PREDICTIONS

7.8.1. Comparison of Static Load Tests

7.8.1.1. Strain Measurements and Composite Action

Composite action can be determined by reviewing the strain diagrams over the section depth. Some information is available from the measured results to evaluate the composite behavior between the concrete deck and steel girders. A number of strain plots are provided in this section, where the measured strain values are shown by a colored dot symbol. The colored line connecting two dot symbols represents the strain diagram at this cross-section based on the plane sections remains plane assumption. The dashed colored line represents the extrapolation of the observed strain diagram assuming composite action, as it was observed that the deck and girder exhibited significant composite action. The black and grey dotted lines show the composite and non-composite strain diagrams obtained from the updated FEM models, and the purple dotted line shows the strain diagram obtained from the calibrated FEM model. The blue plot shows the strain results for the west end, the red plot shows the strain results for the east end, and the green plot shows the strain results for the midspan of the girder.

7.8.1.1.1. Interior Girder 7

Figure 7.50 through Figure 7.52 provide plots of the measured strains for interior Girder 7 during static loading testing and compares the midspan strain diagram to those obtained through the updated and calibrated FEM models. The strains measured for Girder 7 during the Path 1 static tests are shown in Figure 7.50 and compared with values obtained from the FEM updated and calibrated models. Figure 7.50(a) shows the maximum strains observed during the stop location

test for Girder 7 at each end of the girder. Figure 7.50(b) shows the FEM comparison for the stop location test for Girder 7 at midspan. Figure 7.50(c) shows the maximum strains observed during the crawl speed test for Girder 7 at each end of the girder. Figure 7.50(d) shows the FEM comparison for the crawl speed test for Girder 7 at midspan.

The strains measured for Girder 7 during the Path 2 static tests are shown in Figure 7.51 and compared with values obtained from the FEM updated and calibrated models. Figure 7.51(a) shows the maximum strains observed during the stop location test for Girder 7 at each end of the girder. Figure 7.51(b) shows the FEM comparison for the stop location test for Girder 7 at midspan. Figure 7.51(c) shows the maximum strains observed during the crawl speed test for Girder 7 at each end of the girder. Figure 7.51(d) shows the FEM comparison for the crawl speed test for Girder 7 at midspan.

The strains measured for Girder 7 during the Middle Path static tests are shown in Figure 7.52 and compared with values obtained from the FEM updated and calibrated models. Figure 7.52(a) shows the maximum strains observed during the stop location test for Girder 7 at each end of the girder. Figure 7.52(b) shows the FEM comparison for the stop location test for Girder 7 at midspan. Figure 7.52(c) shows the maximum strains observed during the crawl speed test for Girder 7 at each end of the girder. Figure 7.52(d) shows the FEM comparison for the crawl speed test for Girder 7 at midspan.

Both the calibrated FEM model and the updated fully composite FEM model strain diagrams at midspan compare well with the midspan strain diagram observed during testing. Either model would likely be a good candidate to use to conduct a load rating analysis. The updated fully composite FEM model tends to be slightly closer to the test value when looking at bottom flange

strain, however it is also important to note that the calibrated FEM model does take into account the fixity at the ends of the girders and the updated fully composite FEM model does not.

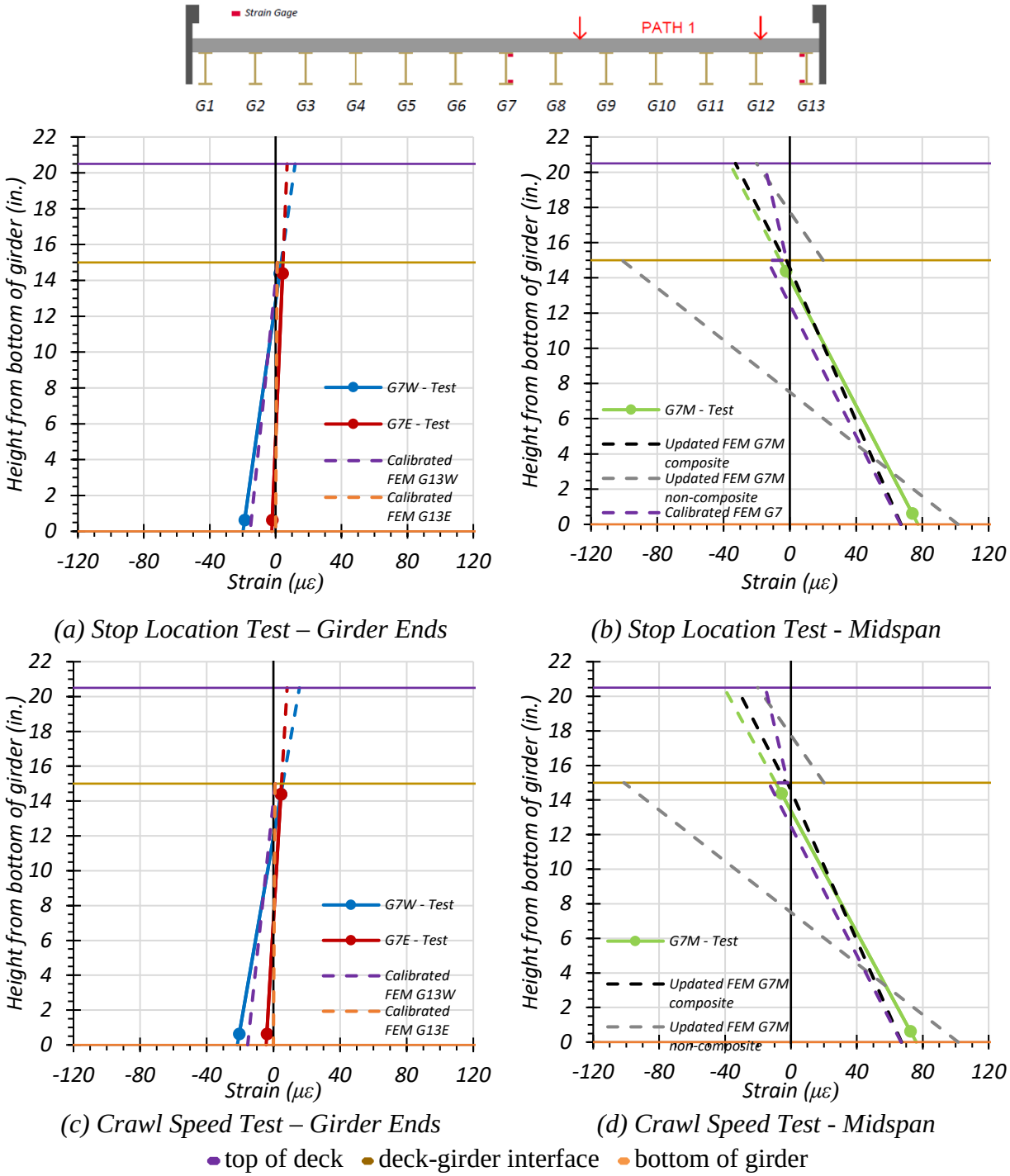

(a) Stop Location Test – Girder Ends

(b) Stop Location Test - Midspan

(c) Crawl Speed Test – Girder Ends

(d) Crawl Speed Test - Midspan

Figure 7.50. Comparison of Static Strains for Girder 7 – Path 1

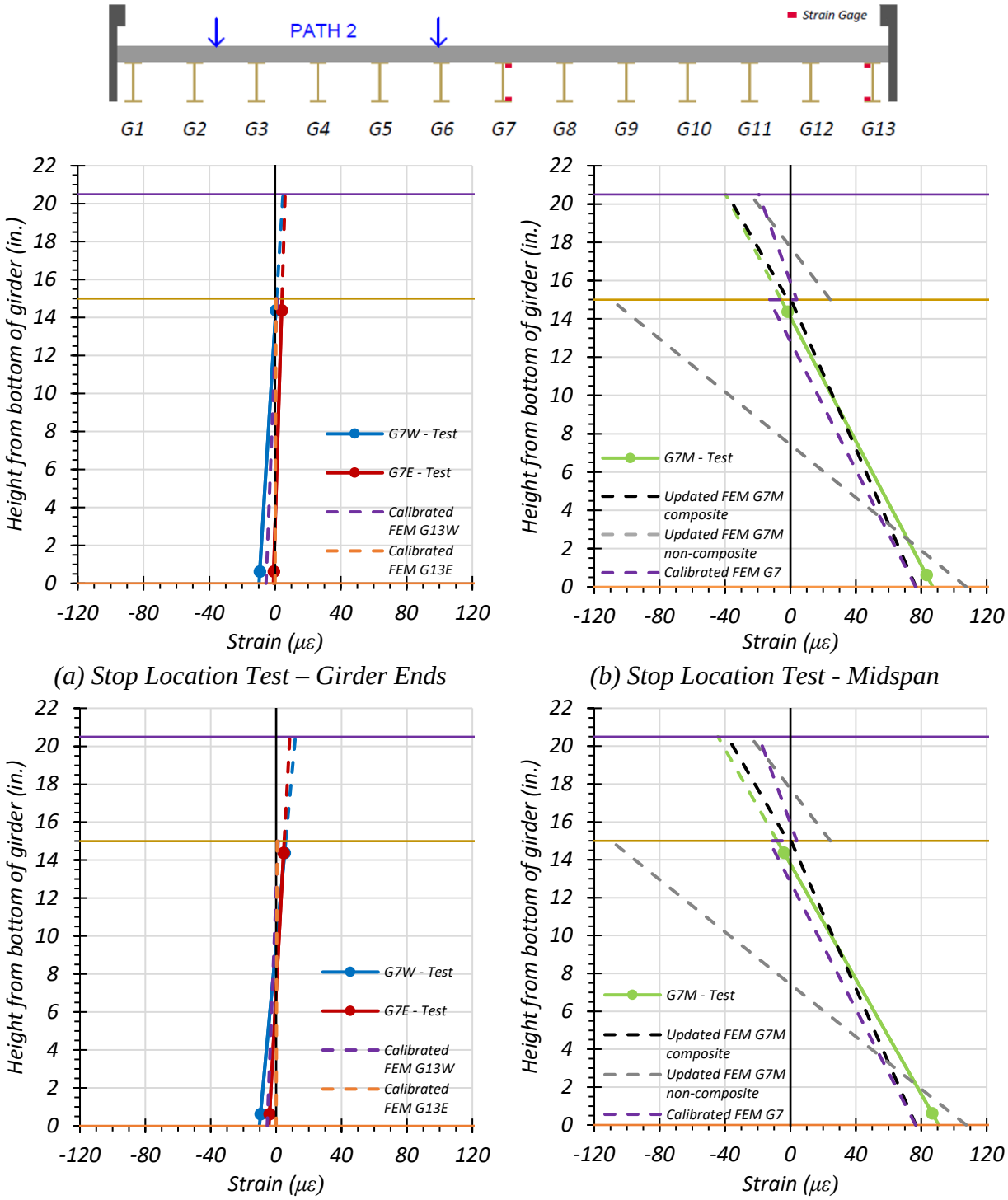

(a) Stop Location Test – Girder Ends

(b) Stop Location Test - Midspan

(c) Crawl Speed Test – Girder Ends

(d) Crawl Speed Test - Midspan

top of deck deck-girder interface bottom of girder

Figure 7.51. Comparison of Static Strains for Girder 7 – Path 2

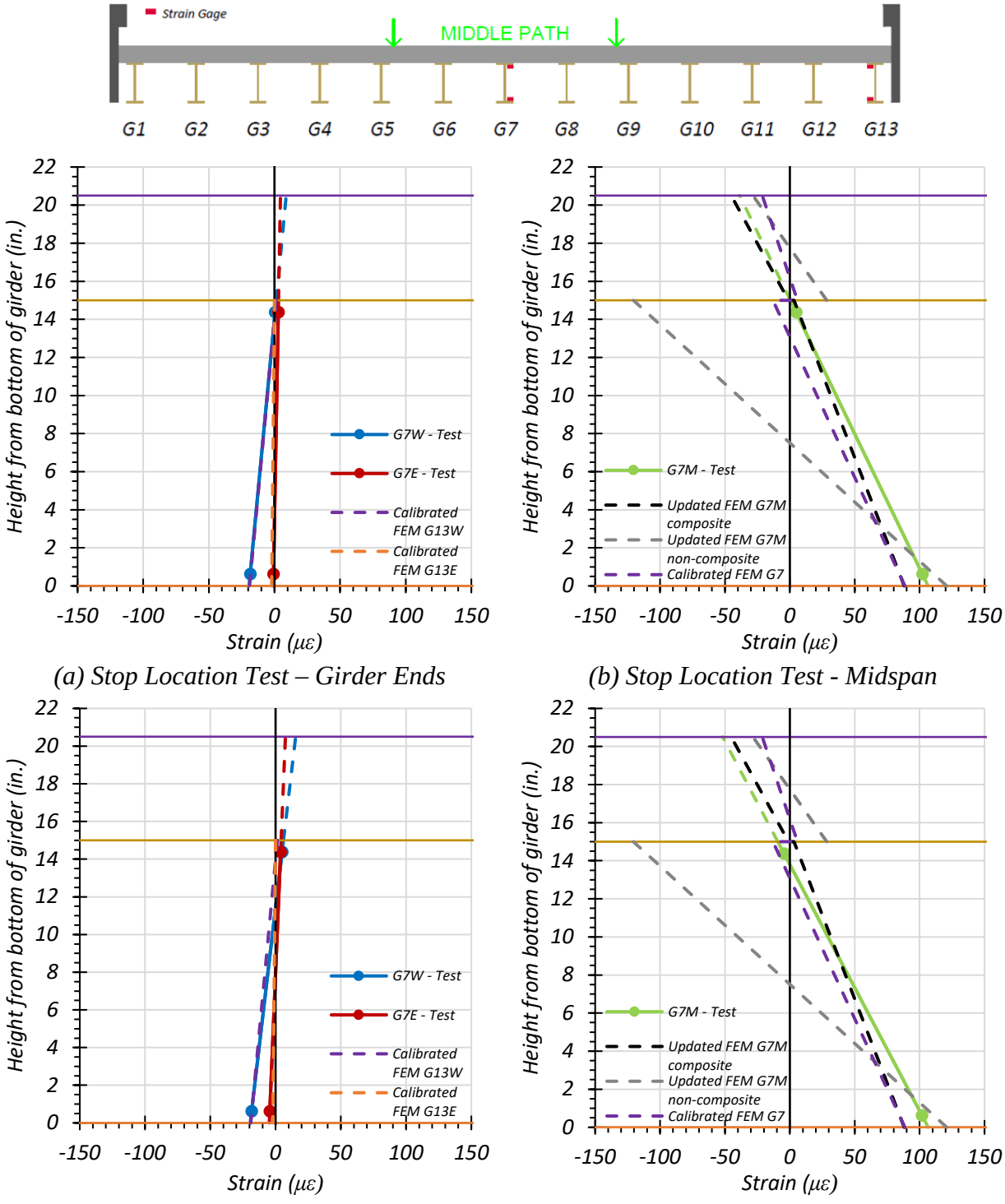

(a) Stop Location Test – Girder Ends

(b) Stop Location Test - Midspan

(c) Crawl Speed Test – Girder Ends

(d) Crawl Speed Test - Midspan

Figure 7.52. Comparison of Static Strains for Girder 7 – Middle Path

7.8.1.1.2. Exterior Girder 13

Figure 7.53 through Figure 7.55 provide plots of the measured strains for exterior Girder 13 during static loading testing and compares the midspan strain diagram to those obtained through the updated and calibrated FEM models. The strains measured for Girder 13 during the Path 1 static tests are shown in Figure 7.53 and compared with values obtained from the FEM updated and calibrated models. Figure 7.53(a) shows the maximum strains observed during the stop location test for Girder 13 at each end of the girder. Figure 7.53(b) shows the FEM comparison for the stop location test for Girder 13 at midspan. Figure 7.53(c) shows the maximum strains observed during the crawl speed test for Girder 13 at each end of the girder. Figure 7.53(b) shows the FEM comparison for the crawl speed test for Girder 13 at midspan.

The strains measured for Girder 13 during the Path 2 static tests are shown in Figure 7.54 and compared with values obtained from the FEM updated and calibrated models. Figure 7.54(a) shows the maximum strains observed during the stop location test for Girder 13 at each end of the girder. Figure 7.54(b) shows the FEM comparison for the stop location test for Girder 13 at midspan. Figure 7.54(c) shows the maximum strains observed during the crawl speed test for Girder 13 at each end of the girder. Figure 7.54(d) shows the FEM comparison for the crawl speed test for Girder 13 at midspan.

The strains measured for Girder 13 during the Middle Path static tests are shown in Figure 7.55 and compared with values obtained from the FEM updated and calibrated models. Figure 7.55(a) shows the maximum strains observed during the stop location test for Girder 13 at each end of the girder. Figure 7.55(b) shows the FEM comparison for the stop location test for Girder 13 at midspan. Figure 7.55(c) shows the maximum strains observed during the crawl speed

test for Girder 13 at each end of the girder. Figure 7.55(d) shows the FEM comparison for the crawl speed test for Girder 13 at midspan.

Both the calibrated FEM model and the updated fully composite FEM model strain diagrams at midspan compare well with the midspan strain diagram observed during testing. Either model would likely be a good candidate to use to conduct a load rating analysis. The updated fully composite FEM model tends to be slightly closer to the test value when looking at bottom flange strain, however it is also important to note that the calibrated FEM model does take into account the fixity at the ends of the girders and the updated fully composite FEM model does not.

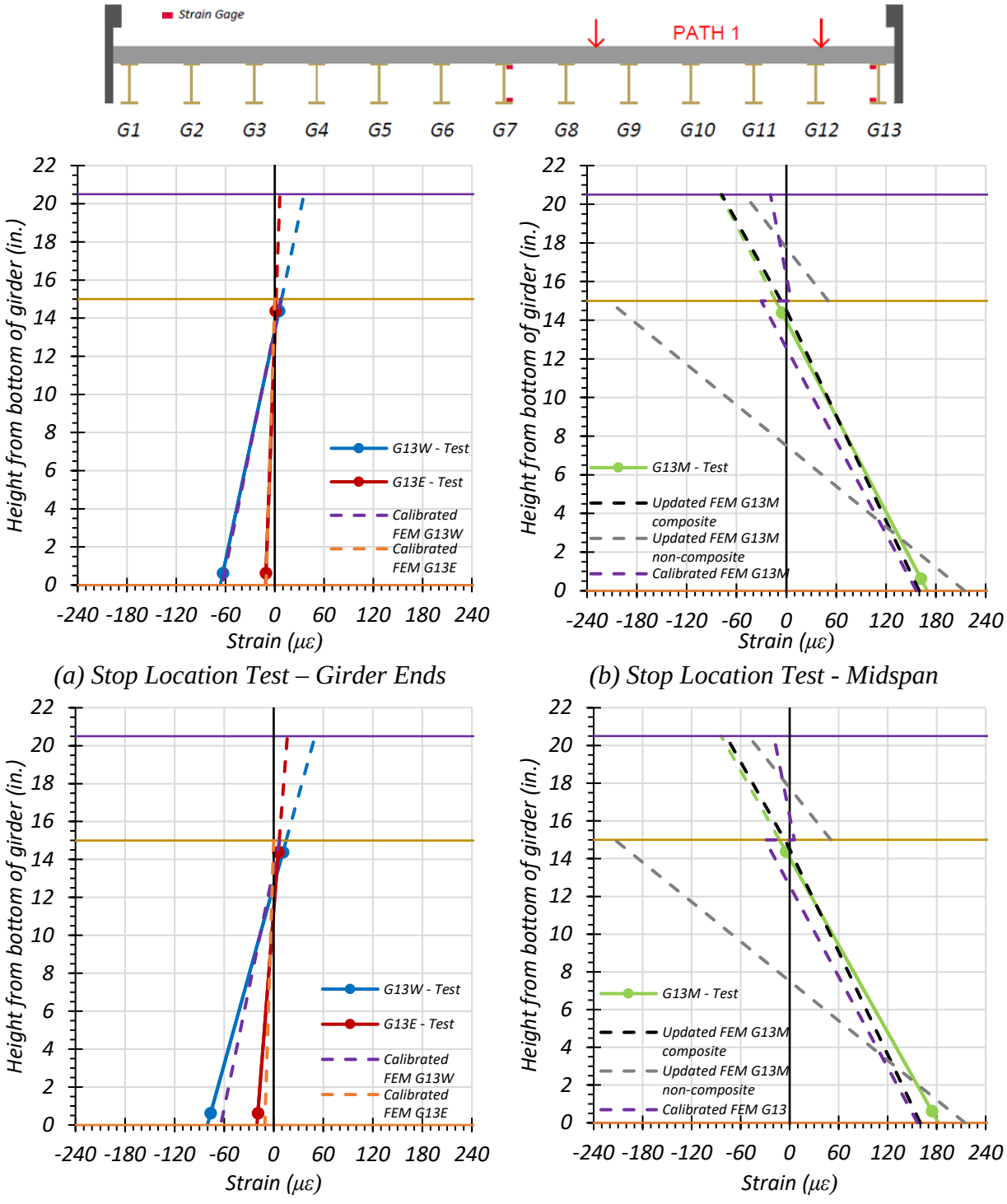

(a) Stop Location Test – Girder Ends

(b) Stop Location Test - Midspan

(c) Crawl Speed Test – Girder Ends

(d) Crawl Speed Test - Midspan

Figure 7.53. Comparison of Static Strains for Girder 13 – Path 1

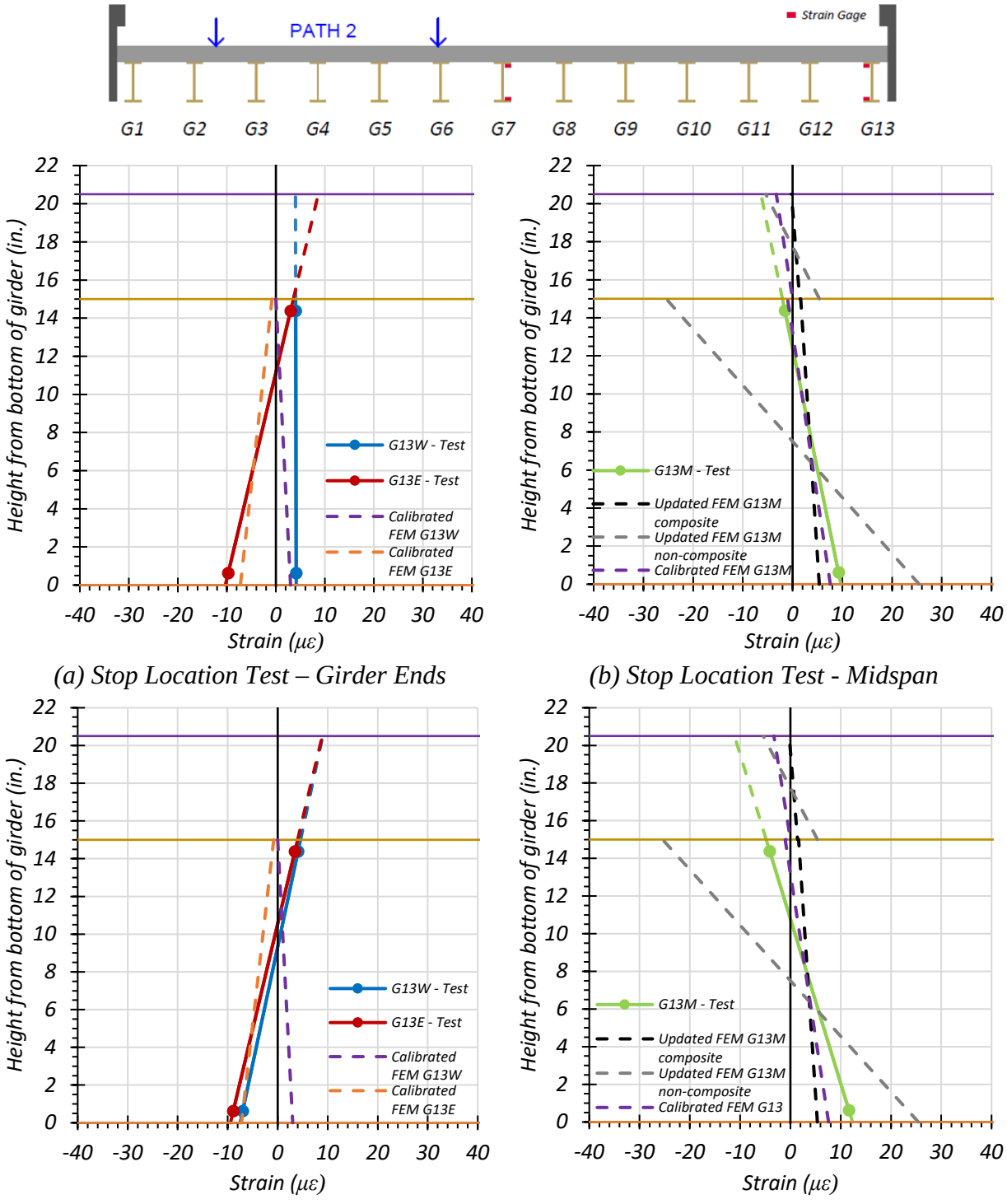

(a) Stop Location Test – Girder Ends

(b) Stop Location Test - Midspan

(c) Crawl Speed Test – Girder Ends

(d) Crawl Speed Test - Midspan

Figure 7.54. Comparison of Static Strains for Girder 13 – Path 2

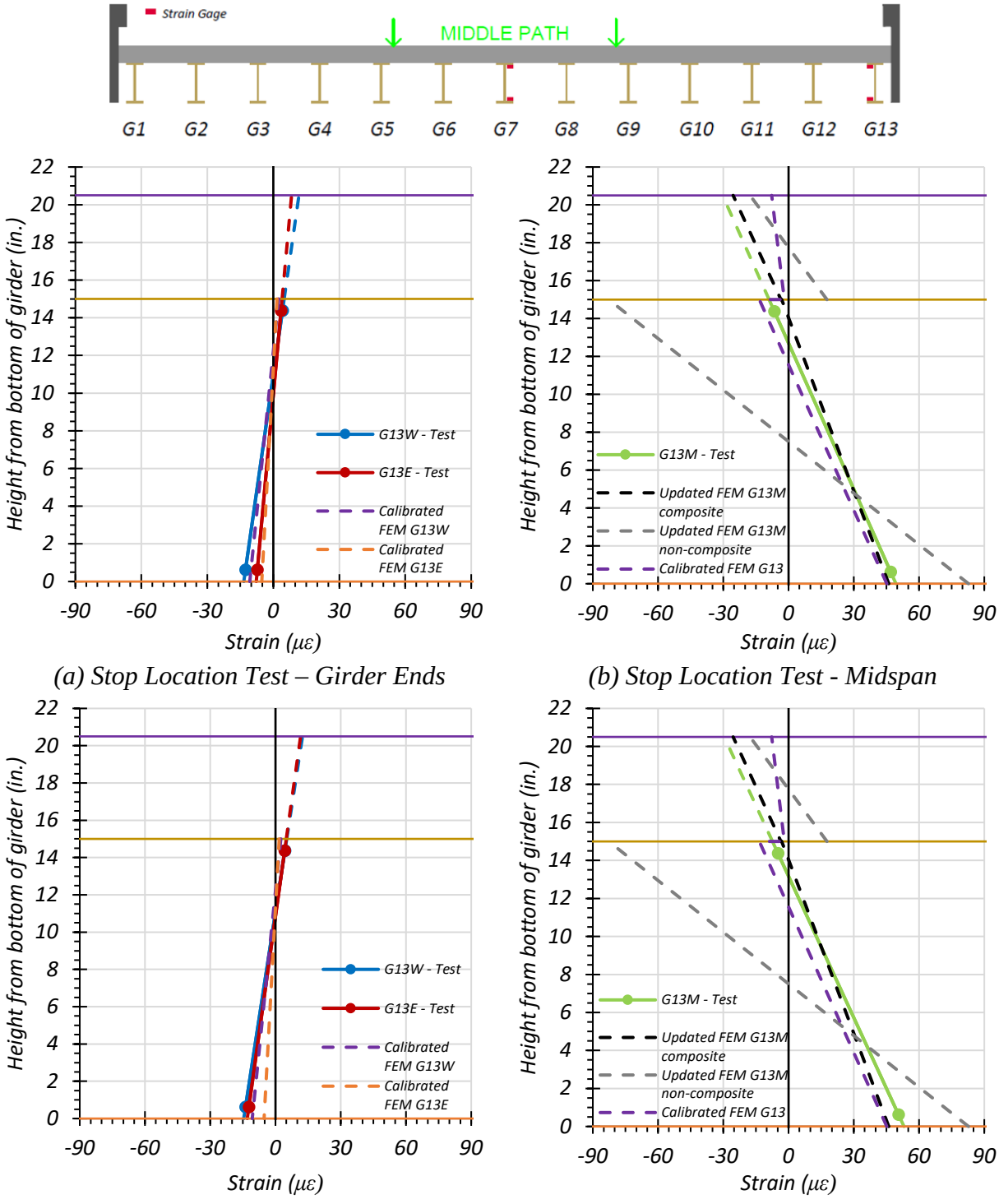

(a) Stop Location Test – Girder Ends

(b) Stop Location Test - Midspan

(c) Crawl Speed Test – Girder Ends

(d) Crawl Speed Test - Midspan

top of deck deck-girder interface bottom of girder

Figure 7.55. Comparison of Static Strains for Girder 13 – Middle Path

7.8.1.1.3. Comparison of Results based on Measured Strains

The neutral axis locations of Girder 13 and Girder 7 observed during the load tests were compared with the theoretical neutral axis locations calculated using the FEM strain predictions. Table 7.23 shows the neutral axis locations measured for all static load tests and for the three FEM models. Figure 7.56 compares the test neutral axis locations with the non-composite and composite neutral axis locations obtained from FEM. As the test neutral axis locations are very close to the FEM composite neutral axis locations, Bridge SM-5 is expected to act as almost fully composite.

Table 7.23. Measured and FEM Neutral Axis Locations for All Static Load Tests

Test	G7 Neutral Axis Location (in. from bottom of girder)	G13 Neutral Axis Location (in. from bottom of girder)
Path 1 – Stop Location	13.95	13.96
Path 1 – Crawl Speed	13.37	14.04
Path 2 – Stop Location	14.08	12.39
Path 2 – Crawl Speed	13.77	10.79
Middle Path – Stop Location	15.05	12.70
Middle Path – Crawl Speed	13.80	13.17
Theoretical Non-Composite	7.50	7.50
Theoretical Composite	14.28	13.60
FEM Non-Composite	7.50	7.50
FEM Composite	14.83	14.51
FEM Calibrated	13.07	12.56

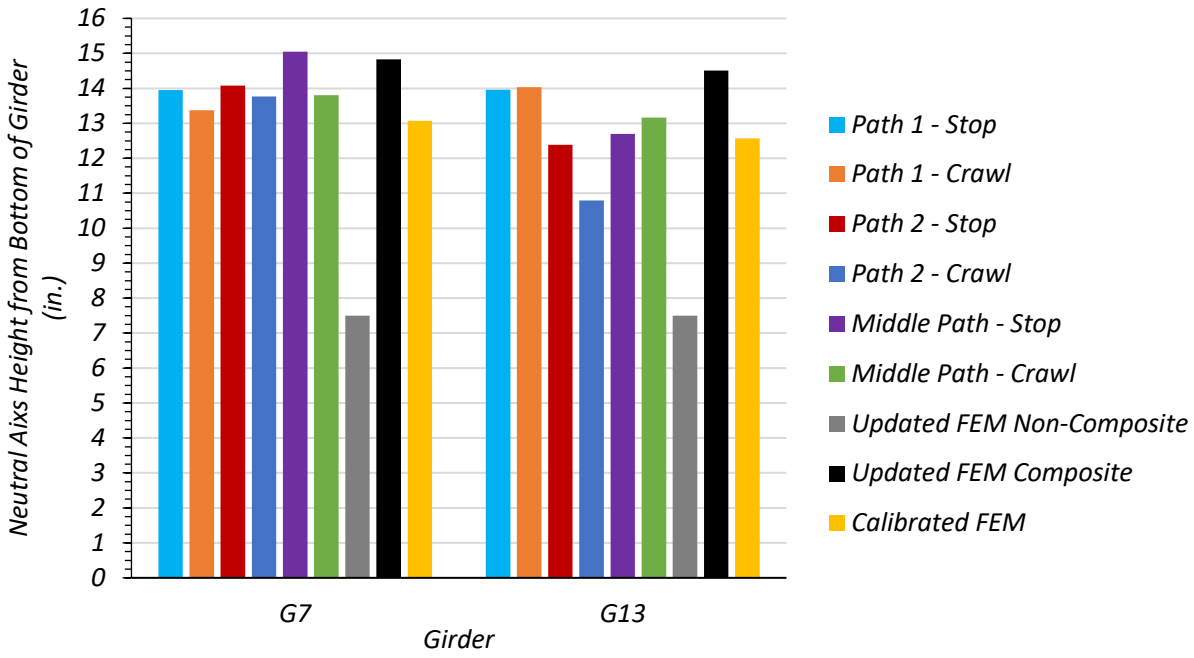

Figure 7.56. Test and FEM Neutral Axis Locations

The maximum bottom flange stresses of Girder 7 and Girder 13 observed during static load tests along each path were compared with the theoretical maximum bottom flange stresses calculated by FEM. Only the stop location tests were used for comparison because CSiBridge performs a step-by-step analysis. Therefore, it would be inappropriate to include dynamic effects in the comparison. Table 7.24 shows the measured bottom flange stress during testing and the FEM non-composite and composite bottom flange stresses for Girder 7. Table 7.25 shows the measured bottom flange stress during testing and the FEM non-composite and composite bottom flange stresses for Girder 13. Figure 7.57 compares the test results with the FEM results. As the measured bottom flange stresses are close to the expected composite bottom flange stresses for most load cases, Bridge SM-5 is expected to be acting at least partially composite.

Table 7.24. Maximum Bottom Flange Stresses from Test and FEM for Girder 7

Load Path	Stop Location Test	Crawl Speed Test	Updated FEM Non-Composite	Updated FEM Composite	Calibrated FEM
Path 1	2.24	2.21	2.94	1.95	1.94
Path 2	2.52	2.63	3.12	2.23	2.22
Middle Path	3.09	3.09	3.51	2.56	2.57

Notes:
1. All stress values are in ksi units.
2. FEM results correspond to the same vehicle longitudinal position as the stop location tests.

Table 7.25. Maximum Bottom Flange Stresses from Test and FEM for Girder 13

Load Path	Stop Location Test	Crawl Speed Test	Updated FEM Non-Composite	Updated FEM Composite	Calibrated FEM
Path 1	4.92	5.29	6.22	4.64	4.54
Path 2	0.28	0.36	0.74	0.16	0.22
Middle Path	1.43	1.54	2.40	1.34	1.31

Notes:
1. All stress values are in ksi units.
2. FEM results correspond to the same vehicle longitudinal position as stop location tests.

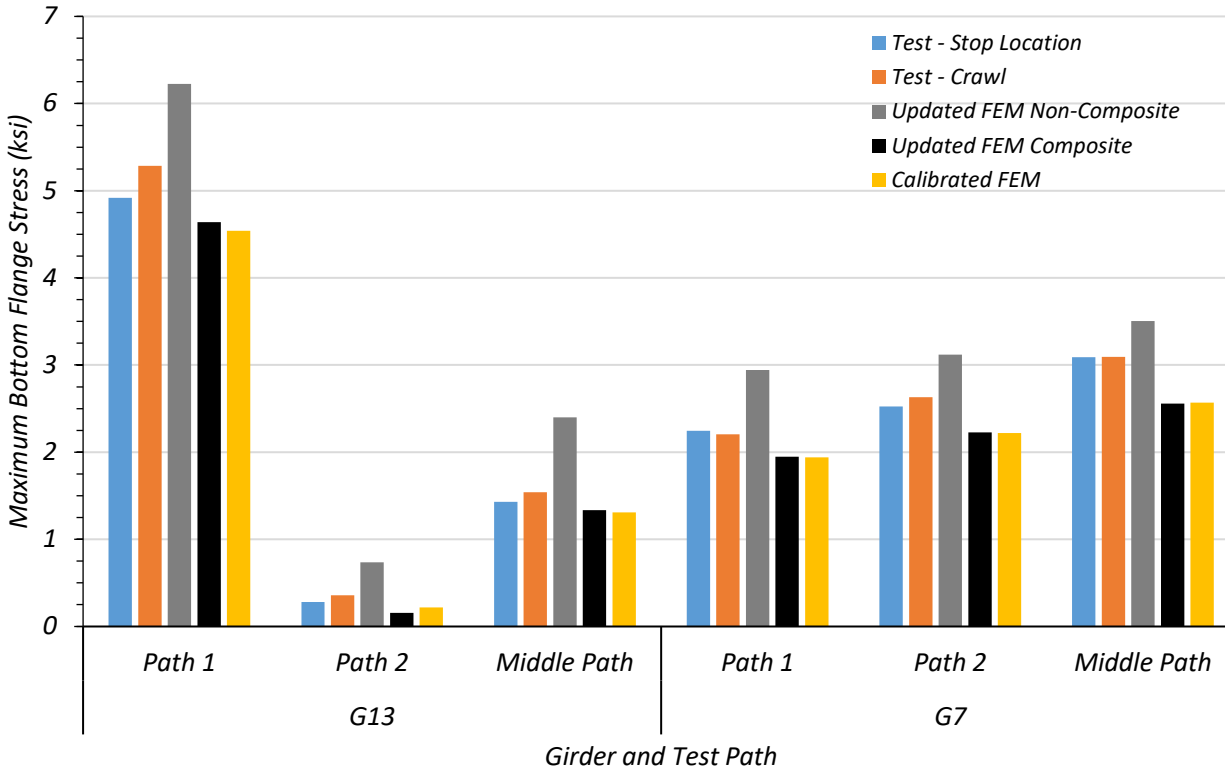

Figure 7.57. Comparison of Maximum Bottom Flange Stresses from Test and FEM

The observed bottom flange stresses tend to match better with the updated composite FEM model and the calibrated FEM model than with the updated non-composite FEM model for most load cases. On average, the updated non-composite FEM model overestimates the bottom flange stress by 34.3 percent.

7.8.1.2. Deflection Measurements and LLDFs

7.8.1.2.1. Path 1 Loading

Table 7.26 shows the measured girder deflections during testing for the stop location test and crawl speed test along Path 1. Deflection data for every other girder was recorded, therefore deflections corresponding to the intermediate girders have been interpolated. The girder displacements

determined by the calibrated, updated non-composite, and updated composite FEM models are also shown.

Table 7.26. Experimental and FEM Deflections for Path 1 Loading

Girder	G1	G2*	G3	G4*	G5	G6*	G7	G8*	G9	G10*	G11	G12*	G13
Updated FEM Non-Composite Disp. (in.)	0.047	0.084	0.121	0.164	0.206	0.256	0.306	0.361	0.415	0.467	0.518	0.573	0.627
Updated FEM Composite Disp. (in.)	-0.007	0.009	0.025	0.044	0.062	0.085	0.107	0.131	0.155	0.177	0.198	0.222	0.245
Calibrated FEM Disp. (in.)	-0.004	0.013	0.031	0.051	0.072	0.096	0.121	0.148	0.173	0.197	0.221	0.246	0.271
Stop Location Test Disp. (in.)	-0.009	0.007	0.023	0.045	0.067	0.091	0.114	0.143	0.173	0.195	0.218	0.263	0.307
Crawl Speed Test Disp. (in.)	-0.013	0.002	0.017	0.040	0.063	0.088	0.112	0.142	0.172	0.197	0.222	0.273	0.324
Note: 1 – G = girder, Disp. = Displacement, * = displacement results have been interpolated using test results													

Table 7.27 compares the test LLDFs determined using deflection to those obtained by the deflections of the updated non-composite, updated composite, and calibrated FEM models. The updated composite and calibrated FEM models do a better job of estimating the LLDFs than the updated non-composite model.

Table 7.27. FEM Displacement LLDF Comparison with Test for Path 1 Loading

Test and Girder Type	Updated Non-Composite FEM LLDF (g_{NC})	Updated Composite FEM LLDF (g_C)	Calibrated FEM LLDF (g_{cal})	Test (g_{test})	g_{NC}/g_{test}	g_C/g_{test}	g_{cal}/g_{test}
Stop Location Interior	0.138	0.153	0.150	0.159	0.87	0.96	0.94
Stop Location Exterior	0.151	0.169	0.166	0.186	0.81	0.91	0.89
Crawl Speed Interior	0.138	0.153	0.150	0.164	0.84	0.93	0.91
Crawl Speed Exterior	0.151	0.169	0.166	0.195	0.91	0.87	0.85

Figure 7.58(a) and Figure 7.58(c) show the Path 1 stop location and crawl speed deflections compared to non-composite, composite, and calibrated values obtained from FEM analysis. Figure 7.58(b) and Figure 7.58(d) show the Path 1 stop location and crawl speed LLDFs compared to relevant AASHTO values as well as values obtained from calibrated FEM model deflection results and moment results. Table 7.28 shows the test LLDF values, the displacement and moment LLDF values obtained from the calibrated FEM model, and the LLDF values found using all three AASHTO methods. The test and calibrated model LLDFs are all significantly lower than the prescribed AASHTO LLDF values. Using the test deflection values to obtain LLDFs slightly overestimates the LLDF for Girder 13 during Path 1 loading when compared to the calibrated FEM moment LLDFs.

Table 7.28. Experimental, FEM, and AASHTO LLDFs for Path 1 Loading

Girder	G1	G2*	G3	G4*	G5	G6*	G7	G8*	G9	G10*	G11	G12*	G13
Stop Location Test Disp. LLDF	0.005	0.004	0.014	0.027	0.041	0.055	0.069	0.087	0.104	0.118	0.132	0.159	0.186
Crawl Speed Test Disp. LLDF	0.008	0.001	0.010	0.024	0.038	0.053	0.068	0.085	0.103	0.118	0.133	0.164	0.195
Calibrated FEM Disp. LLDF	0.002	0.008	0.019	0.031	0.044	0.059	0.074	0.090	0.106	0.120	0.135	0.150	0.166
Calibrated FEM Moment LLDF	0.001	0.008	0.018	0.028	0.041	0.055	0.073	0.094	0.111	0.122	0.136	0.155	0.159
AASHTO Standard LLDF	0.174	0.137	0.137	0.137	0.137	0.137	0.137	0.137	0.137	0.137	0.137	0.137	0.174
AASHTO LRFD LLDF using simplified stiffness	0.245	0.245	0.245	0.245	0.245	0.245	0.245	0.245	0.245	0.245	0.245	0.245	0.245
AASHTO LRFD LLDF using analytical stiffness	0.212	0.212	0.212	0.212	0.212	0.212	0.212	0.212	0.212	0.212	0.212	0.212	0.212
Note: 1 – G = girder, Disp. = Displacement, * = displacement results have been interpolated using test results													

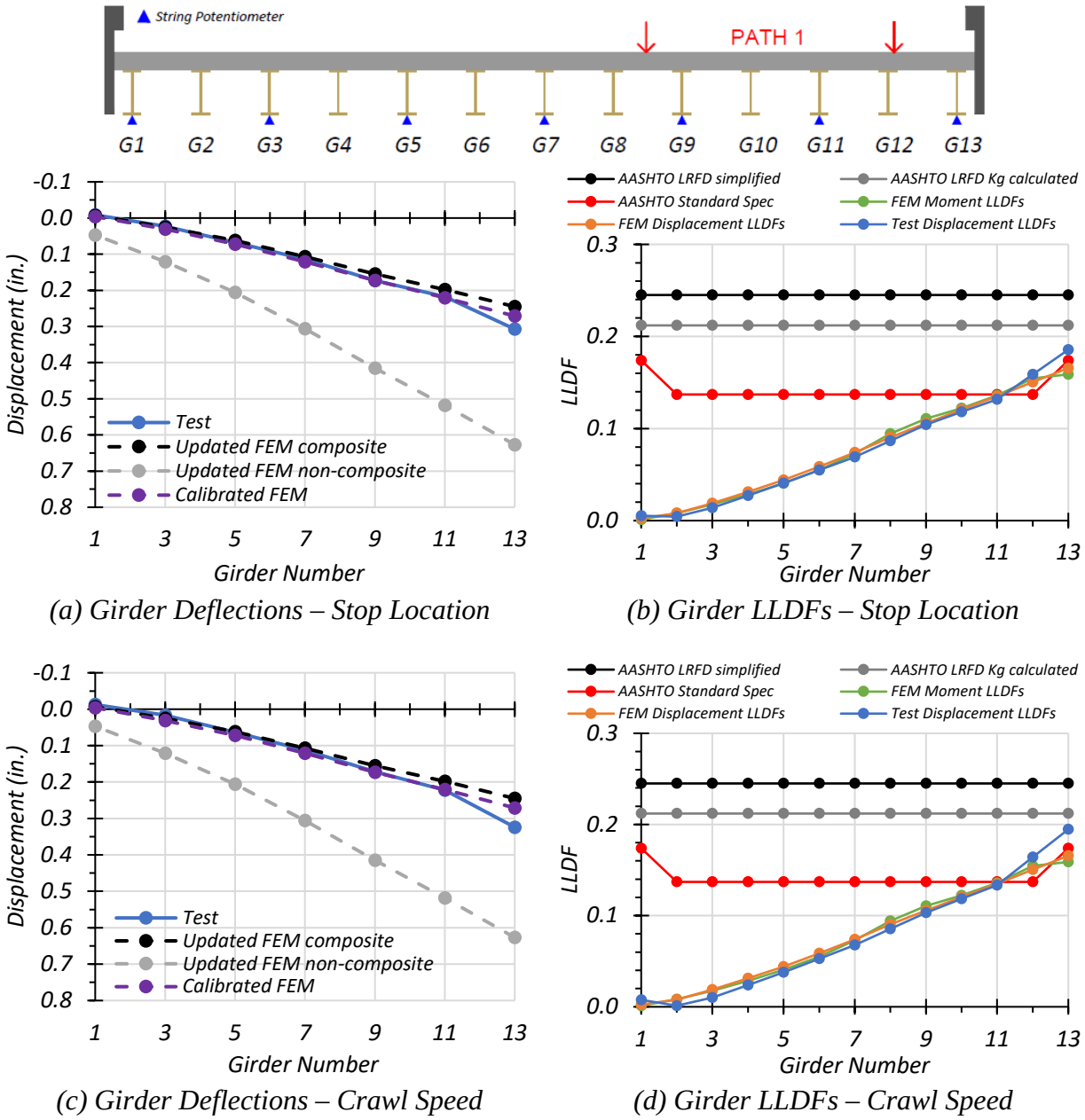

Figure 7.58. Comparison of Static Deflection Results for Path 1 Loading

7.8.1.2.2. Path 2 Loading

Table 7.29 shows the measured girder deflections during testing for the stop location test and crawl speed test along Path 2. Deflection data for every other girder was recorded, therefore deflections

corresponding to the intermediate girders have been interpolated. The girder displacements determined by the calibrated, updated non-composite, and updated composite FEM models are also shown.

Table 7.29. Experimental and FEM Deflections for Path 2 Loading

Girder	G1	G2*	G3	G4*	G5	G6*	G7	G8*	G9	G10*	G11	G12*	G13
Updated FEM Non-Composite Disp. (in.)	0.543	0.510	0.477	0.441	0.404	0.363	0.321	0.277	0.232	0.193	0.153	0.118	0.082
Updated FEM Composite Disp. (in.)	0.206	0.194	0.181	0.166	0.151	0.133	0.115	0.095	0.075	0.057	0.039	0.023	0.007
Calibrated FEM Disp. (in.)	0.229	0.216	0.202	0.186	0.170	0.152	0.131	0.108	0.086	0.066	0.046	0.028	0.011
Stop Location Test Disp. (in.)	0.212	0.202	0.192	0.179	0.166	0.145	0.124	0.101	0.078	0.056	0.035	0.020	0.006
Crawl Speed Test Disp. (in.)	0.205	0.197	0.189	0.179	0.168	0.148	0.127	0.104	0.081	0.060	0.039	0.025	0.010
Note: 1 – G = girder, Disp. = Displacement, * = displacement results have been interpolated using test results													

Table 7.30 compares the test LLDFs determined using deflection to those obtained by the deflections of the updated non-composite, updated composite, and calibrated FEM models. The updated composite and calibrated FEM models do a better job of estimating the LLDFs than the updated non-composite FEM model, however, the calibrated FEM model seems to do the best job.

Table 7.30. FEM Displacement LLDF Comparison with Test for Path 2 Loading

Test and Girder Type	Updated Non-Composite FEM LLDF (g_{NC})	Updated Composite FEM LLDF (g_C)	Calibrated FEM LLDF (g_{cal})	Test (g_{test})	g_{NC}/g_{test}	g_C/g_{test}	g_{cal}/g_{test}
Stop Location Interior	0.124	0.134	0.132	0.133	0.93	1.01	0.99
Stop Location Exterior	0.132	0.143	0.140	0.140	0.94	1.02	1.00
Crawl Speed Interior	0.124	0.134	0.132	0.129	0.94	1.04	1.02
Crawl Speed Exterior	0.132	0.143	0.140	0.134	0.99	1.07	1.04

Figure 7.59(a) and Figure 7.59(c) show the Path 2 stop location and crawl speed deflections compared to non-composite, composite, and calibrated values obtained from FEM analysis. Figure 7.59(b) and Figure 7.59(d) show the Path 2 stop location and crawl speed LLDFs compared to relevant AASHTO values as well as values obtained from calibrated FEM deflection results and moment results. Table 7.31 shows the test LLDF values, the displacement and moment LLDF values obtained from the calibrated FEM model, and the LLDF values found using all three AASHTO methods. The test and calibrated model LLDFs are all significantly lower than the prescribed AASHTO LLDF values. Using the test deflection values to obtain LLDFs slightly overestimates the LLDF for Girder 1 during Path 2 loading when compared to the calibrated FEM moment LLDFs.

Table 7.31. Experimental, FEM, and AASHTO LLDFs for Path 2 Loading

Girder	G1	G2*	G3	G4*	G5	G6*	G7	G8*	G9	G10*	G11	G12*	G13
Stop Location Test Disp. LLDF	0.140	0.133	0.127	0.118	0.109	0.096	0.082	0.067	0.051	0.037	0.023	0.013	0.004
Crawl Speed Test Disp. LLDF	0.134	0.129	0.124	0.117	0.110	0.097	0.083	0.068	0.053	0.039	0.026	0.016	0.007
Calibrated FEM Disp. LLDF	0.140	0.132	0.124	0.114	0.104	0.093	0.080	0.066	0.053	0.040	0.028	0.017	0.007
Calibrated FEM Moment LLDF	0.127	0.135	0.128	0.116	0.109	0.100	0.084	0.065	0.050	0.037	0.026	0.016	0.007
AASHTO Standard LLDF	0.174	0.137	0.137	0.137	0.137	0.137	0.137	0.137	0.137	0.137	0.137	0.137	0.174
AASHTO LRFD LLDF using simplified stiffness	0.245	0.245	0.245	0.245	0.245	0.245	0.245	0.245	0.245	0.245	0.245	0.245	0.245
AASHTO LRFD LLDF using analytical stiffness	0.212	0.212	0.212	0.212	0.212	0.212	0.212	0.212	0.212	0.212	0.212	0.212	0.212
Note: 1 – G = girder, Disp. = Displacement, * = displacement results have been interpolated using test results													

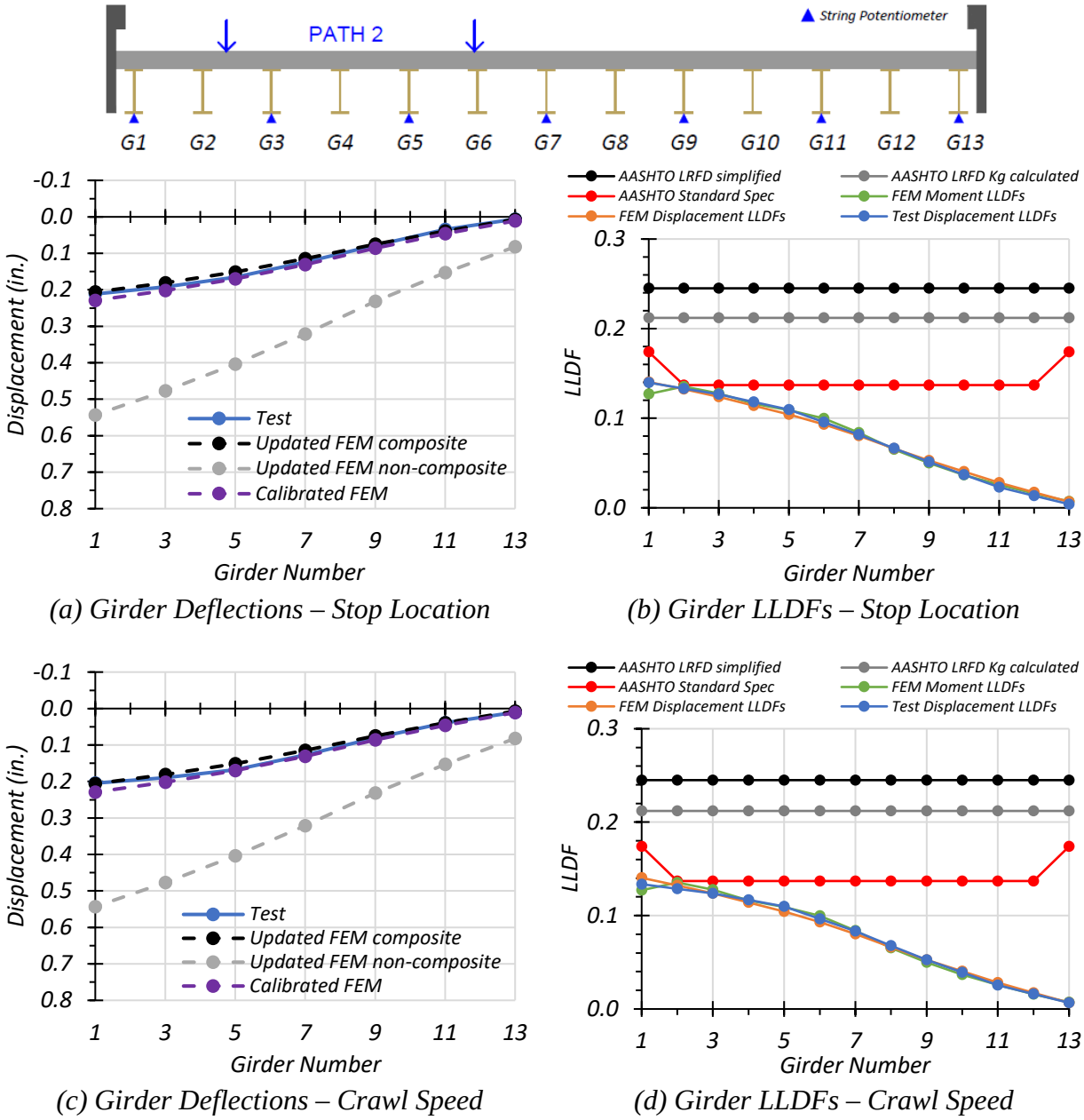

(a) Girder Deflections – Stop Location

(b) Girder LLDFs – Stop Location

(c) Girder Deflections – Crawl Speed

(d) Girder LLDFs – Crawl Speed

Figure 7.59. Comparison of Static Deflection Results for Path 2 Loading

7.8.1.2.3. Middle Path Loading

Table 7.32 shows the measured girder deflections during testing for the stop location test and crawl speed test along the Middle Path. Deflection data for every other girder was recorded, therefore

deflections corresponding to the intermediate girders have been interpolated. The girder displacements determined by the calibrated, updated non-composite, and updated composite FEM models are also shown.

Table 7.32. Experimental and FEM Deflections for Middle Path Loading

Girder	G1	G2*	G3	G4*	G5	G6*	G7	G8*	G9	G10*	G11	G12*	G13
Updated FEM Non-Composite Disp. (in.)	0.267	0.285	0.303	0.321	0.338	0.344	0.349	0.344	0.338	0.321	0.303	0.285	0.267
Updated FEM Composite Disp. (in.)	0.083	0.094	0.105	0.115	0.125	0.128	0.131	0.128	0.125	0.115	0.105	0.094	0.083
Calibrated FEM Disp. (in.)	0.095	0.106	0.119	0.131	0.141	0.147	0.148	0.147	0.141	0.131	0.119	0.106	0.095
Stop Location Test Disp. (in.)	0.075	0.089	0.103	0.119	0.134	0.140	0.145	0.142	0.140	0.125	0.109	0.105	0.100
Crawl Speed Test Disp. (in.)	0.073	0.087	0.102	0.119	0.136	0.141	0.146	0.142	0.139	0.125	0.111	0.107	0.104
Note: 1 – G = girder, Disp. = Displacement, * = displacement results have been interpolated using test results													

Table 7.33 compares the test LLDFs determined using deflection to those obtained by the deflections of the updated non-composite, updated composite, and calibrated FEM models. The updated non-composite FEM model seems to do a better job of estimating the LLDFs than the updated composite and calibrated FEM models.

Table 7.33. FEM Displacement LLDF Comparison with Test for Middle Path Loading

Test and Girder Type	Updated Non-Composite FEM LLDF (g_{NC})	Updated Composite FEM LLDF (g_C)	Calibrated FEM LLDF (g_{cal})	Test (g_{test})	g_{NC}/g_{test}	g_C/g_{test}	g_{cal}/g_{test}
Stop Location Interior	0.086	0.092	0.091	0.095	0.91	0.97	0.96
Stop Location Exterior	0.066	0.058	0.058	0.066	1.00	0.88	0.88
Crawl Speed Interior	0.086	0.092	0.091	0.095	0.91	0.97	0.96
Crawl Speed Exterior	0.066	0.058	0.058	0.068	0.97	0.85	0.85

Figure 7.60(a) and Figure 7.60(c) show the Middle Path stop location and crawl speed deflections compared to non-composite, composite, and calibrated values obtained from FEM analysis. Figure 7.60(b) and Figure 7.60(d) show the Middle Path stop location LLDFs compared to relevant AASHTO values as well as values obtained from calibrated FEM deflection results and moment results. Table 7.34 shows the test LLDF values, the displacement and moment LLDF values obtained from the calibrated FEM model, and the LLDF values found using all three AASHTO methods. The test and calibrated model LLDFs are all significantly lower than the prescribed AASHTO LLDF values.

Table 7.34. Experimental, FEM, and AASHTO LLDFs for Middle Path Loading

Girder	G1	G2*	G3	G4*	G5	G6*	G7	G8*	G9	G10*	G11	G12*	G13
Stop Location Test Disp. LLDF	0.049	0.058	0.068	0.078	0.088	0.091	0.095	0.093	0.092	0.082	0.072	0.069	0.066
Crawl Speed Test Disp. LLDF	0.048	0.057	0.066	0.078	0.089	0.092	0.095	0.093	0.091	0.082	0.072	0.070	0.068
Calibrated FEM Disp. LLDF	0.058	0.065	0.073	0.081	0.087	0.090	0.091	0.090	0.087	0.081	0.073	0.065	0.058
Calibrated FEM Moment LLDF	0.046	0.059	0.070	0.084	0.095	0.098	0.097	0.098	0.095	0.084	0.070	0.059	0.046
AASHTO Standard LLDF	0.174	0.137	0.137	0.137	0.137	0.137	0.137	0.137	0.137	0.137	0.137	0.137	0.174
AASHTO LRFD LLDF using simplified stiffness	0.245	0.245	0.245	0.245	0.245	0.245	0.245	0.245	0.245	0.245	0.245	0.245	0.245
AASHTO LRFD LLDF using analytical stiffness	0.212	0.212	0.212	0.212	0.212	0.212	0.212	0.212	0.212	0.212	0.212	0.212	0.212
Note: 1 – G = girder, Disp. = Displacement, * = displacement results have been interpolated using test results													

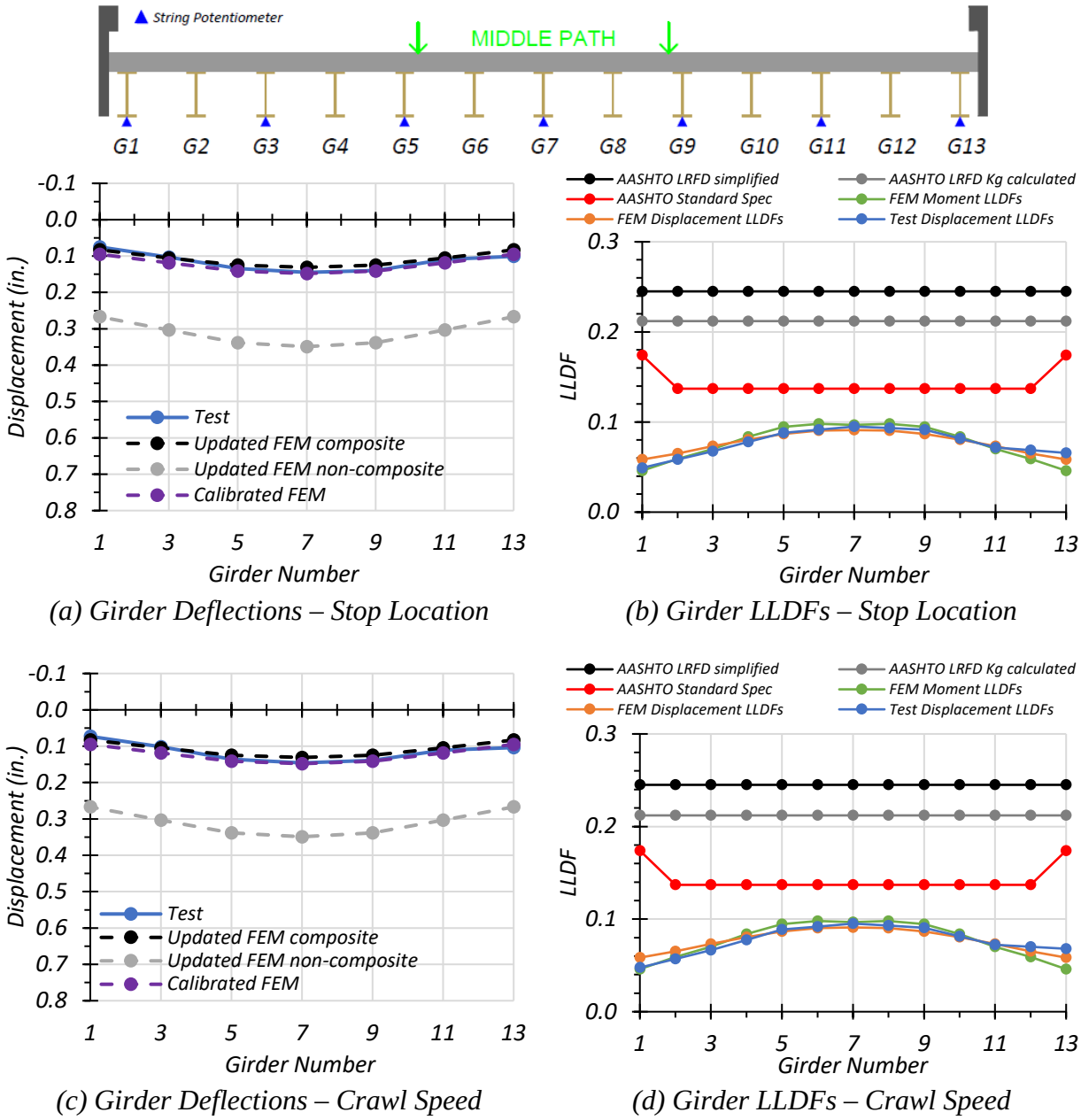

(a) Girder Deflections – Stop Location

(b) Girder LLDFs – Stop Location

(c) Girder Deflections – Crawl Speed

(d) Girder LLDFs – Crawl Speed

Figure 7.60. Comparison of Static Deflection Results for Middle Path Loading

7.9. SUMMARY AND FINDINGS

7.9.1. Live Load Distribution Factors

7.9.1.1. General Findings

LLDF values computed using FEM deflection results and FEM moment results were compared to ensure that the values obtained using midspan deflection data obtained from testing could be used to calculate experimental LLDFs. The FEM values using both displacements and moments were found to be very close, thus LLDF values were determined for each load test based on the maximum midspan deflections.

For the Path 1 load cases, the g_{AASHTO}/g_{Test} ratio for ranges from 0.86 to 0.94 when considering the AASHTO Standard Specifications, from 1.26 to 1.54 when considering the simplified stiffness AASHTO LRFD Specifications, and from 1.09 to 1.33 when considering the analytical stiffness AASHTO LRFD Specifications (AASHTO 2002; AASHTO 2017). While the AASHTO Standard Specifications produce unconservative results for Path 1 loading, they are not very unconservative. This would likely be made up for within other conservative areas of the load rating process. The LLDFs produced by the AASHTO LRFD Specifications are always conservative, however, using the analytical stiffness parameter does produce some LLDF values that are close to the test values.

For the Path 2 load cases, the g_{AASHTO}/g_{Test} ratio for ranges from 1.03 to 1.30 when considering the AASHTO Standard Specifications, from 1.75 to 1.90 when considering the simplified stiffness AASHTO LRFD Specifications, and from 1.51 to 1.64 when considering the analytical stiffness AASHTO LRFD Specifications (AASHTO 2002; AASHTO 2017). In all three methods of determining LLDFs AASHTO is conservative for Path 2 loading. The AASHTO

Standard Specifications are the least conservative however, producing values close to the test values at times.

For the Middle Path load cases, the g_{AASHTO}/g_{Test} ratio for ranges from 1.44 to 2.64 when considering the AASHTO Standard Specifications, from 2.58 to 3.71 when considering the simplified stiffness AASHTO LRFD Specifications, and from 2.23 to 3.21 when considering the analytical stiffness AASHTO LRFD Specifications (AASHTO 2002; AASHTO 2017). In all three methods of determining LLDFs AASHTO is very conservative for Middle Path loading. No LLDF determined by AASHTO is close to the test value.

Of note, the close girder spacing of Bridge SM-5 (23") deems it out of range for use of the AASHTO LRFD Specification LLDF equations, which require a minimum spacing of 42". However, for the sake of comparison they are included in this study. The AASHTO LRFD Specifications indicate that a refined analysis should be performed for girder spacings that are less than the minimum (AASHTO 2017).

TxDOT currently uses the AASHTO Standard Specification LLDFs for load rating of this bridge type and age. Based on the LLDF results observed from load testing, the LLDFs obtained through the AASHTO Standard Specifications provide an appropriate level of conservatism for most scenarios, without being overly conservative. Therefore, a significant reduction in LLDFs is not available for this particular bridge; thus, this is not an area identified for potentially increasing the load rating of Bridge SM-5 or similar bridges of this type.

7.9.1.2. Consideration of Moment of Inertia Difference Between Girders

When calculating the LLDFs obtained from the displacements observed during testing, a more accurate method would be to consider the difference in moment of inertia between an interior

girder and an exterior girder in the case that the moments of inertia are different. Updated LLDFs can be developed for each girder by taking the deflection multiplied by the moment of inertia of an individual girder, and dividing by the sum of the deflection multiplied by the moment of inertia for all girders. Equation (7.1) shows the equation used to obtain an LLDF through this method.

$$LLDF_i = \frac{\Delta_i I_i}{\sum(\Delta_i I_i)} \tag{7.1}$$

where:

$LLDF_i$ = Live load distribution factor for an individual girder

Δ_i = Deflection of the individual girder (in.)

I_i = Moment of inertia of the individual girder (in^4)

Bridge SM-5 has the same steel section for interior and exterior girders (S15x42.9), so under fully non-composite action only the deflection terms impact the LLDFs as the moment of intertia terms cancel. However, under fully composite action, which the measurements for Bridge SM-5 support, the interior girders and exterior girders have different moments of inertia due to different effective deck widths (23" for interior girders and 17.5" for exterior girders). The fully composite interior girder was found to have a moment of inertia of 1329 in^4 and the exterior girder was found to have a moment of inertia of 1231 in^4.

Considering the controlling stop location load case for Girder 13, along Path 1, and using the procedure described above, new LLDFs were developed. The controlling interior girder, Girder 12, experienced a 1.3 percent increase in LLDF from 0.159 to 0.161. The controlling exterior girder, Girder 13, experienced a 6.7 percent decrease in LLDF from 0.186 to 0.174. Table

7.35 and Figure 7.61 show the LLDFs developed using this method compared to LLDFs determined through the calibrated FEM model displacements, the calibrated FEM model moments, the AASHTO Standard Specifications, the AASHTO LRFD Specifications using the simplified stiffness parameter, and the AASHTO LRFD Specifications using the analytical stiffness parameter (AASHTO 2002; AASHTO 2017).

Table 7.35. Bridge SM-5 LLDF Comparison Considering Difference in Inertia

Selected Girder LLDFs for Various Methods	Interior Girder 12	Exterior Girder 13
Test Displacement Considering Inertia Difference	0.161	0.174
Test Displacement without Considering Inertia Difference	0.159	0.186
Calibrated FEM Displacements	0.150	0.166
Calibrated FEM Moments	0.160	0.161
AASHTO Standard Specifications	0.137	0.174
AASHTO LRFD Specifications – Simplified	0.245	0.245
AASHTO LRFD Specifications – Analytical	0.212	0.212

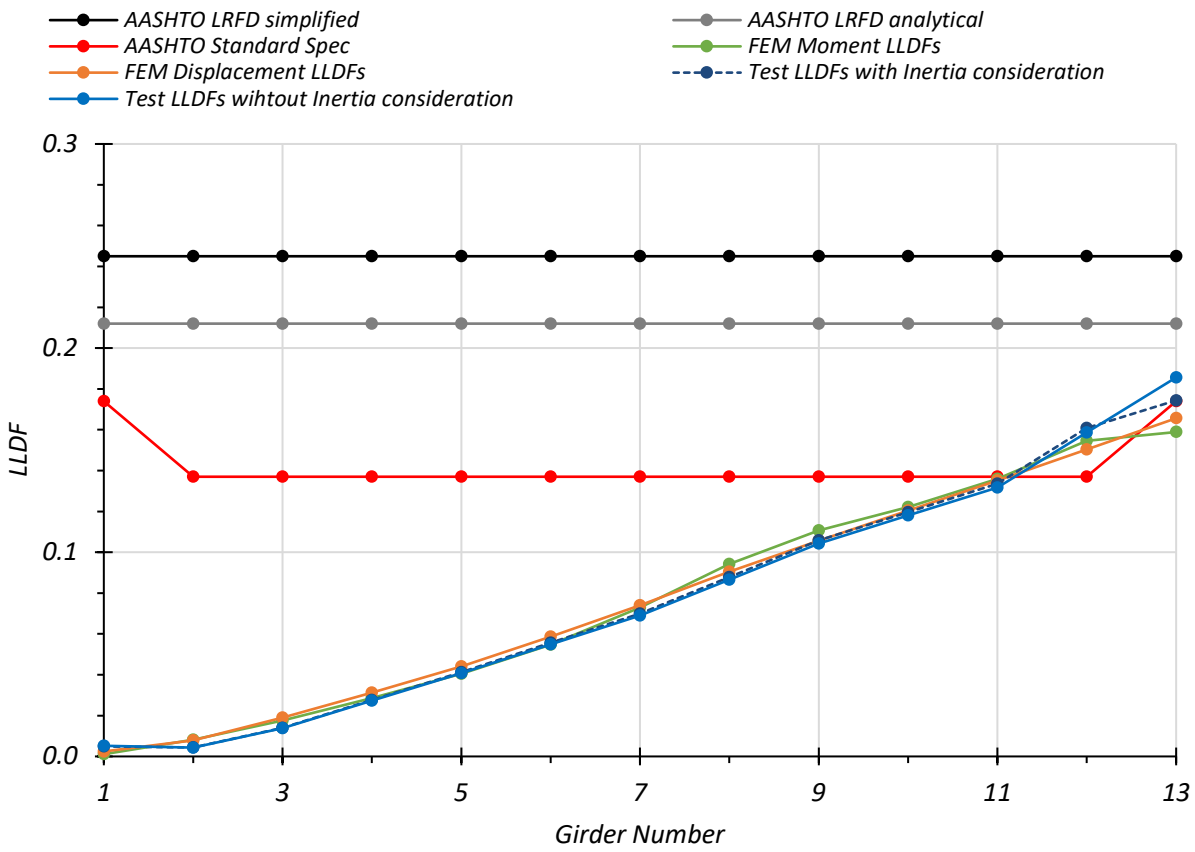

Figure 7.61. Bridge SM-5 LLDF Comparison Considering Difference in Inertia

The consideration of the moment of inertia difference between interior and exterior girders does not cause a significant change in the calculated LLDFs for Bridge SM-5. This is due to the fact that the composite interior and exterior girders do not have a significant difference in moment of inertia. The LLDFs calculated without consideration of inertia difference are slightly more conservative and both methods do a good job of matching the LLDF results from FEM displacements and FEM moments. Both results also match closely to the LLDFs given by the AASHTO Standard Specifications (AASHTO 2002). Furthermore, under the initial conservative assumption made during the basic load rating analysis that Bridge SM-5 is non-composite, there would be no difference in the moment of inertia between interior and exterior girders. Therefore,

the LLDFs would be calculated based only on displacements. Without conducting a field test, it is difficult to ensure that a bridge exhibits composite behavior. For these reasons, the LLDFs were kept as calculated throughout this chapter, and the difference in moment of inertia between interior and exterior girders under composite action was not considered. However, it is noted that to bound the possible LLDFs when considering the presence of partial of full composite action, one can consider both the fully non-composite case and the fully composite case.

7.9.2. Composite Action

A large amount of information was obtained from the load tests that suggests Bridge SM-5 is acting as nearly fully composite under the test truck loading. The girder flanges of this bridge are embedded into the concrete deck, therefore suggesting the potential for composite action. From the strain gauges attached to the top and bottom flanges of the girders, a strain diagram of an interior and exterior girder was constructed for each load test. Although in some cases the neutral axis shown by these diagrams are slightly lower than that expected for fully composite action, in every case the neutral axis is significantly higher than that expected for non-composite section. It was also determined that, in general, the neutral axis was closer to the fully composite value when the truck was near the girder.

The bottom flange stresses obtained from testing were compared to the expected non-composite and composite bottom flange stresses from FEM analysis. For all load tests the measured bottom flange stresses were close to the ones obtained from FEM composite model, while being significantly different than the stress values obtained from FEM non-composite model.

The deflection data obtained during the load testing was compared to estimated girder deflection values from FEM considering both non-composite and composite action. In general, the

girder deflection profiles seen in the field were much closer to those of the composite FEM model, and in some cases the two almost matched.

Bridge SM-5 is acting as nearly fully composite under live load based on four observations: (1) the top flanges are embedded into the deck slab and there are no signs of cracking between the girder flanges and deck, (2) the neutral axis locations, (3) the bottom flange stresses, and (4) the girder deflections. Based on a fully composite section assumption, the RFs calculated for Bridge SM-5 in Task 3 were re-analyzed and compared. Table 7.36 shows the Strength I RFs calculated for Bridge SM-5 using the ASR, LFR, and LRFR rating methods considering the fully composite action observed during load tests. The table compares the updated RFs to those calculated in Task 3 of this project and to the current TxDOT RFs. It is important to note that for the ASR ratings, the dead load stresses used are non-composite stresses. When using the LFR method, which is the method currently used by TxDOT to rate this bridge, the consideration of composite action would allow the posting of this bridge to be removed, per TxDOT's on-system load rating flowchart (TxDOT 2018a), shown in Figure 3.2. For an almost fully composite girder, as used in the calibrated FEM model, the capacity and load rating would be slightly reduced. However, this would not be expected to significantly affect the load posting determined through TxDOT's previously mentioned flowchart.

For the ASR fully composite RF, the capacity stress was 18.15 ksi for Inventory and 24.75 for Operating, the dead load stress was 7.72 ksi, the superimposed dead load stress was 0.77 ksi, and the live load stress was 13.11 ksi. For the LFR fully composite RF, the moment capacity was 284.6 kip-ft, the dead load moment was 43.3 kip-ft, and the live load moment was 102.4 kip-ft. For the LRFR fully composite region RF, the moment capacity was 284.6 kip-ft, the dead load moment was 43.3 kip-ft, and the live load moment was 207.4 kip-ft.

Table 7.36. Comparison of Interior Girder Bridge SM-5 Composite RFs to Non-Composite RFs for Strength I

Method	TxDOT RF		Basic Rating RF		Composite RF		Composite RF/ TxDOT RF		Composite RF/ Basic Rating RF	
	Inv.	Oper.	Inv.	Oper.	Inv.	Oper.	Inv.	Oper.	Inv.	Oper.
ASR	-	-	0.46	0.78	0.74	1.24	-	-	1.61	1.59
LFR	0.47	0.79	0.48	0.81	**0.99**	**1.65**	2.11	2.09	2.06	2.04
LRFR	-	-	0.28	0.37	0.60	0.78	-	-	2.14	2.11
Note: TxDOT and Task 3 RFs are calculated for a non-composite section										

7.9.3. Stresses

The maximum bottom flange stresses experienced during loading were quite minimal. The maximum bottom flange stress for Girder 7 was 3.69 ksi from Test 5. The maximum bottom flange stress for Girder 13 was 5.29 ksi from Test 11. Considering non-composite action, the estimated dead load bottom flange stresses obtained from the calibrated FEM model are 8.53 ksi for Girder 7 and 9.24 ksi for Girder 13.

An ASR load rating can be performed for Bridge SM-5 using this information and the yield strength of 33 ksi prescribed by the AASHTO MBE (AASHTO MBE 2018). Equation (7.2) shows the ASR RF equation with the variables defined as well. The capacity, dead load effect, and live load effect are in terms of stresses.

$$RF = \frac{C - A_1 D}{A_2 L(1 + I)} \tag{7.2}$$

where:

RF = Rating Factor for the live load carrying capacity

C = Capacity of the member = 0.55*F_y for Inventory, 0.75*F_y for Operating

D = Dead load effect on the member (computed as 10.53 ksi for Girder 7 and 11.24 ksi for Girder 13 for the non-composite section)

L = Live load effect on the member (determined from test as 3.69 ksi for Girder 7 and 5.29 ksi for Girder 13)

I = Impact factor to be used with the live load effect = 0.3

A_1 = Factor for dead loads = 1.0

A_2 = Factor for live load = 1.0

Table 7.37 shows the calculated RFs for Bridge SM-5 using the measured test information and the ASR method. It is important to note that these RFs are for the test vehicle, which was almost exactly at the posted limit, not for the design HS-20 truck. It is also important to note that this only considers one truck on the bridge, which is marked as two lanes.

Table 7.37. Bridge SM-5 Calculated ASR RF for Test Vehicle Using Measured Results

Girder	Maximum Measured Live Load Stress from Static Load Tests (ksi)	Inventory RF	Operating RF
Interior G7	3.69	2.01	3.38
Exterior G13	5.29	1.30	2.26

7.9.4. Model Calibration and Update

Using the calibrated FEM model of Bridge SM-5, analysis was performed for the HS-20 design vehicle under two-lane loading. This is the vehicle used in the ASR and LFR rating methods, which

TxDOT uses to perform load ratings of bridges not designed using LRFR (TxDOT 2018a). The maximum dead load bottom flange stresses considering non-composite action were found to be 8.53 ksi for Girder 7 and 9.24 ksi for Girder 13. Using the calibrated model, the maximum live load bottom flange stress on Girder 7 is 9.08 ksi, and the maximum live load bottom flange stress on Girder 13 is 9.22 ksi. With these results, an ASR load rating was performed for Bridge SM-5 for the HS-20 live load.

Table 7.38 shows the ASR HS-20 two-lane RFs for Girder 7 and Girder 13 using the analysis results from the calibrated FEM model. These RFs for Bridge SM-5 allow its posting to be removed based on the TxDOT on-system load posting flowchart (TxDOT 2018a).

Table 7.38. Bridge SM-5 Calculated ASR HS-20 RFs Using Calibrated FEM Model Results

Girder	Inventory RF	Operating RF
Interior G7	0.81	1.37
Exterior G13	0.74	1.29

LFR Strength I RFs can also be developed using the calibrated FEM model of Bridge SM-5. The capacity found using a fully composite section, which Bridge SM-5 was found to essentially be, is 284.6 kip-ft for Girder 7 and 277.0 kip-ft for Girder 13. The capacity was calculated using LFD procedures provided in the AASHTO Standard Specifications (AASHTO 2002). The non-composite dead load moments were found to be 47.1 kip-ft on Girder 7 and 50.9 kip-ft on Girder 13. Using the calibrated FEM model, the controlling live load moments were found to be 62.8 kip-ft on Girder 7 and 59.1 kip-ft on Girder 13 for two-lane HS-20 load paths. Using these results, an LFR load rating was performed for Bridge SM-5 for the HS-20 live load. Equation (7.3)

shows the LFR RF equation with the variables defined as well. The capacity, dead load effect, and live load effect are moment values.

$$RF = \frac{C - A_1 D}{A_2 L(1 + I)} \tag{7.3}$$

where:

RF = Rating Factor for the live load carrying capacity

C = Capacity of the member (computed to be 284.6 kip-ft for Girder 7 and 277.0 kip-ft for Girder 13)

D = Dead load effect on the member (computed to be 57.1 kip-ft for Girder 7 and 60.9 kip-ft for Girder 13)

L = Live load effect on the member (computed to be 62.8 kip-ft for Girder 7 and 59.1 kip-ft for Girder 13)

I = Impact factor to be used with the live load effect = 0.3

A_1 = Factor for dead loads = 1.3

A_2 = Factor for live load = 2.17 for Inventory, 1.3 for Operating

Table 7.39 shows the LFR Strength I HS-20 two-lane RFs for Girder 7 and Girder 13 using the analysis results from the calibrated FEM model. These RFs for Bridge SM-5 allow its posting to be removed based on the TxDOT on-system load posting flowchart (TxDOT 2018a), shown in Figure 3.2.

Table 7.39. Bridge SM-5 Calculated LFR Strength I HS-20 RFs Using Calibrated FEM Model Results

Girder	Inventory RF	Operating RF
Interior G7	1.19	1.98
Exterior G13	1.19	1.98

8. EXPERIMENTAL TESTING OF BRIDGE SC-12

8.1. INTRODUCTION

Nondestructive load testing of Bridge SC-12 was conducted to gather information about the in-situ behavior of the bridge under vehicular loading. The load test results provide evidence of whether partial composite action is present in the structure, and measurements of the actual live load distribution between girders. Field measured geometric details and nondestructive material testing results were used for FEM model updating, and the load test results were used to calibrate the FEM model of the bridge, with which refined analysis is conducted. These results help to determine if the bridge posting can be increased or removed.

Various non-destructive material tests were performed on Bridge SC-12. Ground Penetrating Radar (GPR) was used to locate steel reinforcing bars in the concrete deck. Ultrasonic Pulse Velocity (UPV) testing, as well as Original Schmidt Hammer and Silver Schmidt Hammer tests were performed to determine the compressive strength of the concrete deck.

8.2. GENERAL DESCRIPTION OF BRIDGE SC-12

Bridge SC-12 has a deck condition rating of 6 (Satisfactory), a superstructure condition rating of 7 (Good) without beam section loss due to corrosion, and a substructure condition rating of 7 (Good). The girder flexure controls the rating of the bridge, which has an inventory rating of 19 US tons and an operating rating of 32 US tons. Table 8.1 shows the posted loads of bridge SC-12 for different axle and vehicle configurations. Figure 8.1 shows an elevation view of bridge SC-12 and a view of the underside of the superstructure. Figure 8.2 shows transverse section details of Bridge SC-12.

Table 8.1. Bridge SC-12 Postings

Configuration	Posting (lbs)
Single Axle	20,000
Tandem Axle	34,000
Single Vehicle	58,000
Combination Vehicle	75,000

(a) Elevation view

(b) Underside view

Figure 8.1. Photographs of Bridge SC-12

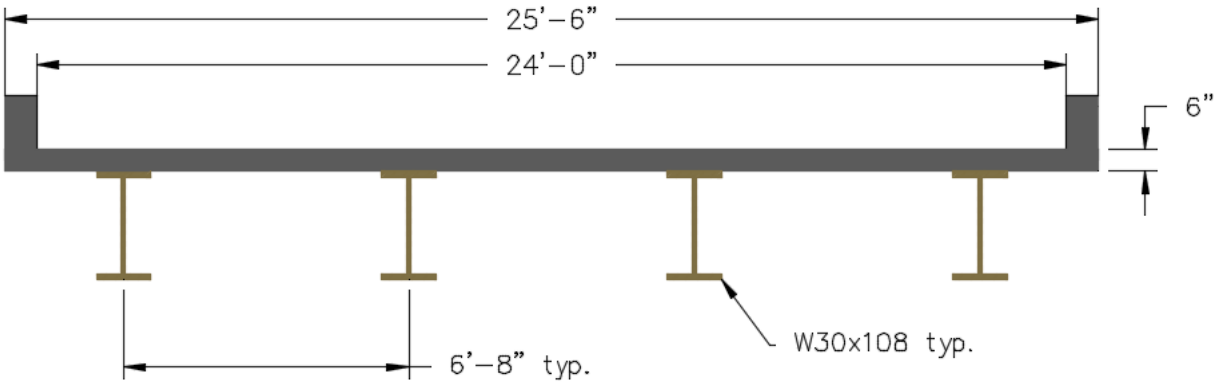

Figure 8.2. Bridge SC-12 Transverse Section (Adapted from TxDOT 2018b)

8.3. IN-SITU MEASUREMENTS AND OBSERVATIONS

In-situ measurements of the geometric details of Bridge SC-12 were taken during the field testing. The only geometric measurement that disputed the measurements given in the as-built drawings was the concrete deck thickness. This is given as 6 in. in the drawings, however, the thickness was measured as 5.75 in. in the field. Therefore, the deck thickness was changed to 5.75 in. in future FEM models.

Three different nondestructive material tests were also performed on Bridge SC-12 in order to obtain more information about the concrete deck. The first test performed was an Ultrasonic Pulse Velocity (UPV) test that measures the time it takes for an ultrasonic wave to travel through a known thickness of concrete. The compressive strength of the concrete can then be estimated based on the measured velocities. For Bridge SC-12, this was performed on both the slab and the curb. The measured wave velocities were 4092 m/s for the slab and 3874 m/s for the curb. Using this value, the rebound number found using the Original Schmidt Hammer, and the SonReb

equations given in Huang et al. (2011), the concrete compressive strength was found to be 6.3 ksi for the slab and 6.9 ksi for the curb.

The second NDE material test performed on Bridge SC-12 was the Original Schmidt Hammer. In this test, a device is pushed against the concrete surface and uses the rebound of a spring-loaded mass to estimate the compressive strength of the concrete. For Bridge SC-12, this was also performed for both the slab and the curb. The average rebound value produced by ten Original Schmidt Hammer measurements was 43.6 for the slab and 48.7 for the curb. Using the conversion chart shown in Figure 8.3, the compressive strength of the slab was determined to be 6.4 ksi and the compressive strength of the curb was determined to be 7.8 ksi.

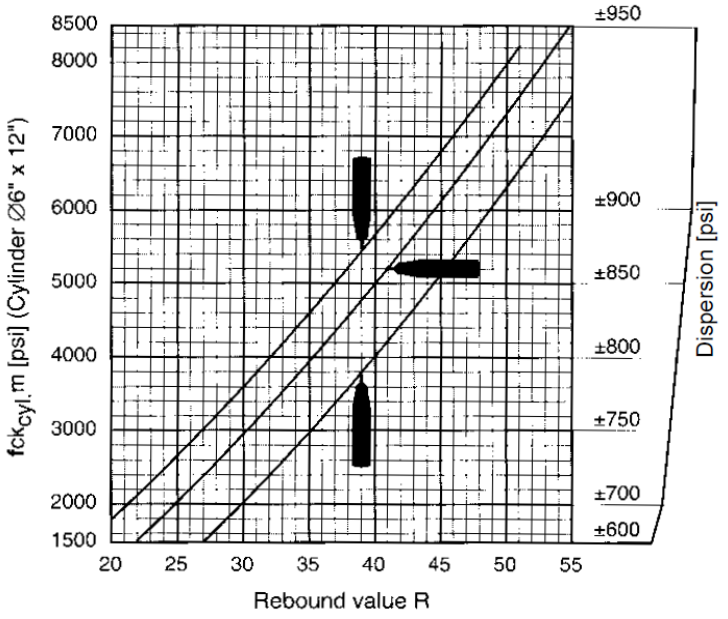

Figure 8.3. Original Schmidt Hammer Conversion Chart (Reprinted from Proceq 2002)

The third NDE test performed on Bridge SC-12 was the Silver Schmidt Hammer test. The procedure for performing this test is very similar to that of the Original Schmidt Hammer. For Bridge SC-12, the average Q value produced by ten Silver Schmidt Hammer measurements was

54 for the slab and 67 for the curb. Using the conversion chart shown in Figure 8.4, these results correspond to a compressive strength of 6.25 ksi for the slab and 10.75 ksi for the curb.

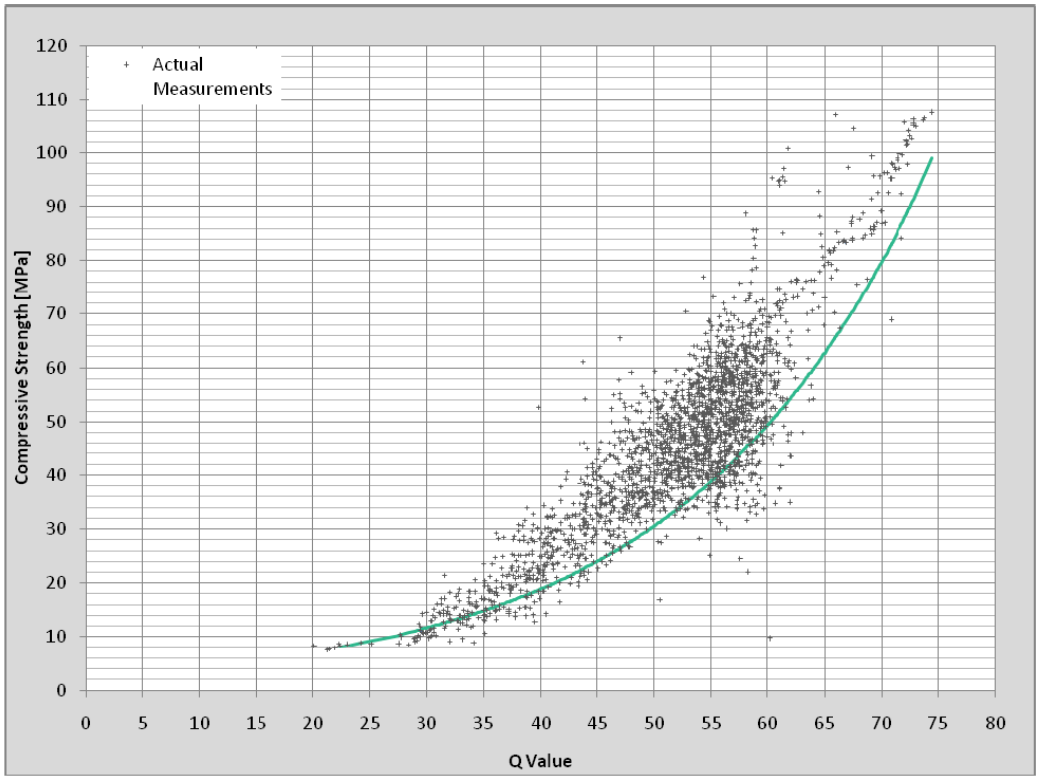

Figure 8.4. Silver Schmidt Hammer Conversion Chart (Reprinted from Proceq 2017)

Of the three NDE tests performed to measure the compressive strength of the concrete deck, the lowest compressive strength value produced was 6.25 ksi. This value was used in updated FEM models to perform post-test analysis for comparison of other test values.

8.4. DATA ACQUISITION AND INSTRUMENTATION OF BRIDGE SC-12

The instrumentation plan for field testing of Bridge SC-12 was developed based on the objectives of the research project. Three types of instrumentation including strain gauges, string

potentiometers, and accelerometers were installed on the bridge to measure its response during the load tests. Figure 8.5 and Figure 8.6 show the detailed instrumentation plan for Bridge SC-12.

8.4.1. Instrumentation Plan for Bridge SC-12

The installed instrumentation and their locations on the bridge were selected in order to obtain specific data to understand the behavior of the bridge, such as the load sharing between girders, composite action, and to determine if the bridge posting can be increased or removed.

Figure 8.5 shows the plan views of the full instrumentation layout for Bridge SC-12 and Figure 8.6 shows cross section views. Figure 8.7 shows the labeling system used for the instrumentation and Table 8.2 shows the data acquisition system instrumentation labels and corresponding DAQ channels.

Strain Gauges were installed on the bottom face of the top flange and the top face of the bottom flange as close as possible to the girder web at three longitudinal locations for an interior girder and an exterior girder. The strain gauges were installed at the midspan location of the main span (Span 2), at 0.4L away from the west abutment for the end span (Span 1), and at an average of 5 in. away from the bearing centerline adjacent to the interior pier for the selected interior and exterior girders. This was done to infer moments within the spans and over the interior support. Several goals were identified in determining the instrumentation types and locations, as follows:

- The strain gauge locations were selected to collect data pertaining to the midspan moments and to determine neutral axis values to check for potential composite action.
- The string potentiometer locations were selected to measure midspan deflections and infer experimental LLDFs to compare with the estimated values from the FEM model of Bridge SC-12.

- The accelerometer locations were selected to collect bridge vibration data, allowing for comparison with estimated dynamic properties from the FEM model of the bridge.

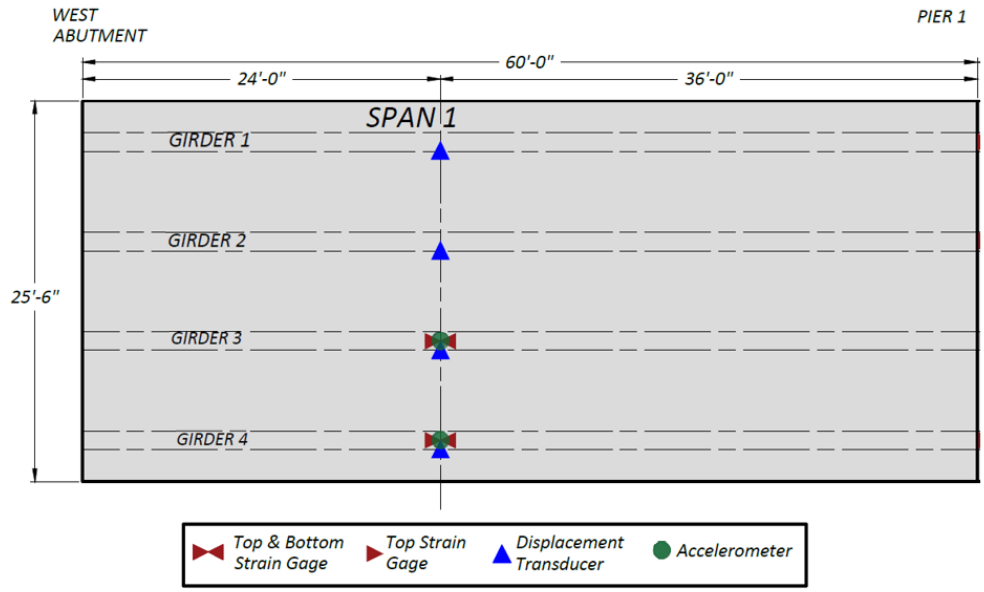

(a) End Span Plan View

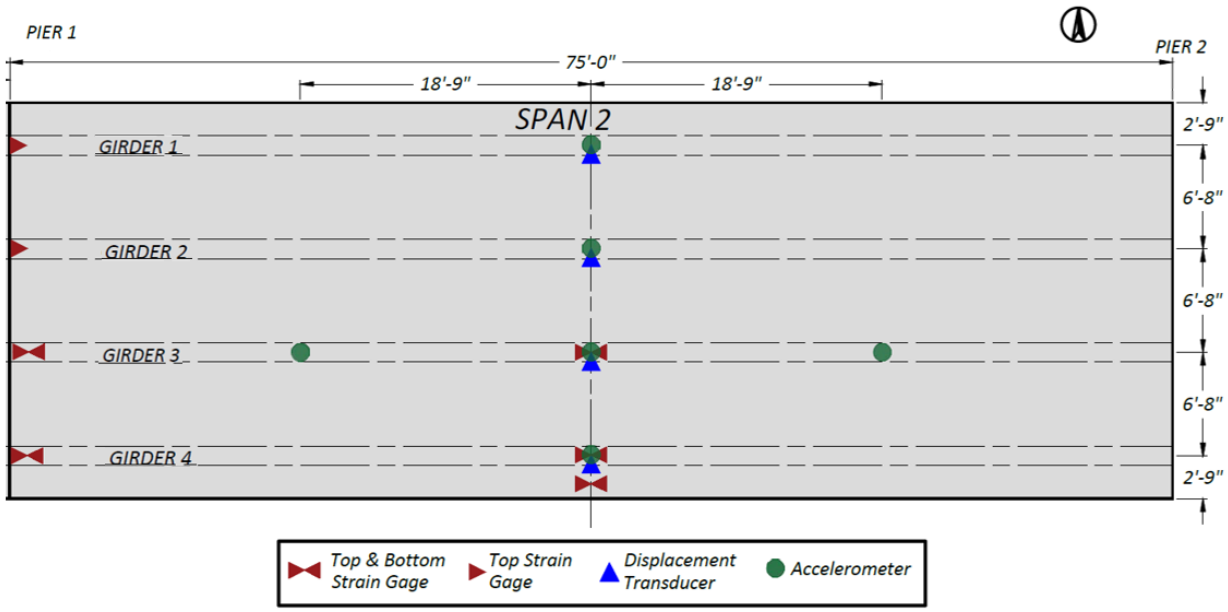

(b) Main Span Plan View

Figure 8.5. Plan View Instrumentation Layout for Bridge SC-12

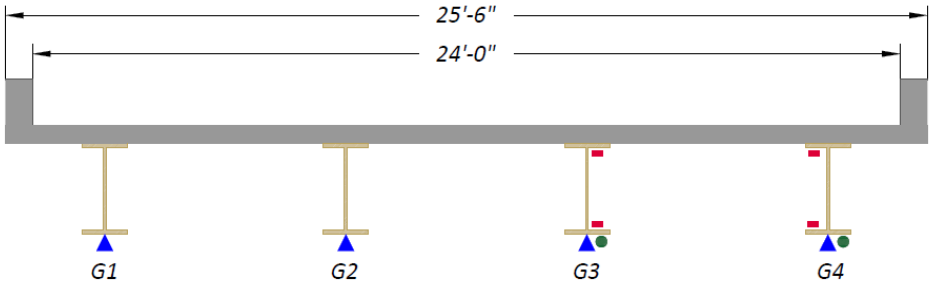

(a) End Span – Section at 0.4L

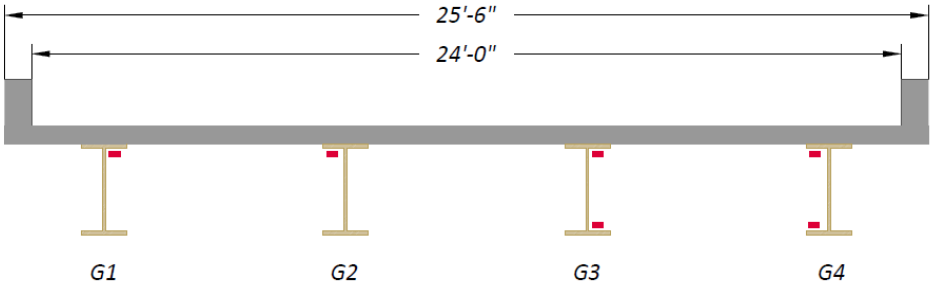

(b) Main Span – Section Adjacent to Interior Pier

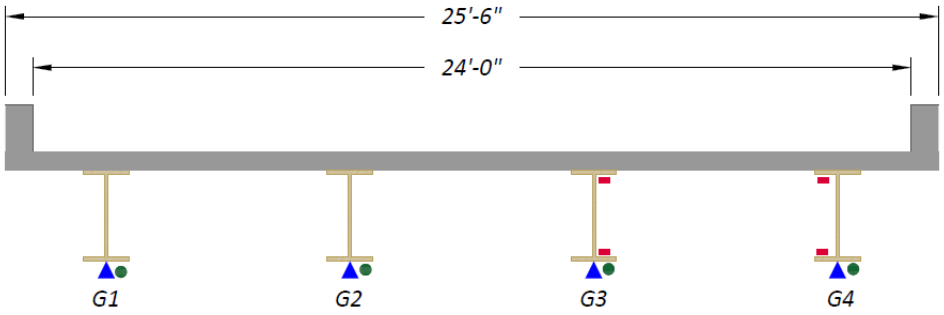

(c) Main Span - Midspan Section

Figure 8.6. Section View Instrumentation Layout for Bridge SC-12

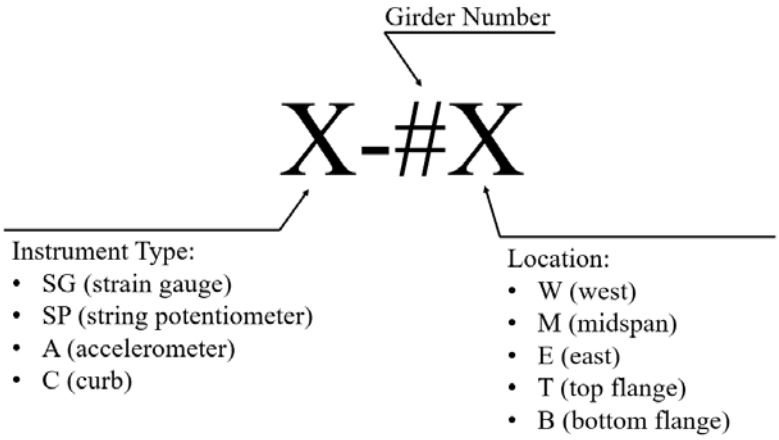

Figure 8.7. Instrumentation Labeling System Used for Bridge SC-12

Table 8.2. Instrumentation Labels for Bridge SC-12

DAQ Box	Channel	Label	Type	DAQ Box	Channel	Label	Type
Strain Book	CH1	SG-4WT	FLA-6	WBK 16-3	CH25	SP-2Mend	SM1-2
	CH2	SG-4WB	FLA-6		CH26	SP-1Mend	SM1-2
	CH3	SG-4MT	FLA-6		CH27	-	
	CH4	SG-4MB	FLA-6		CH28	-	
	CH5	SG-4MTend	FLA-6		CH29	-	
	CH6	SG-4MBend	FLA-6		CH30	-	
	CH7	SG-3WT	FLA-6		CH31	-	
	CH8	SG-3WB	FLA-6		CH32	-	
WBK 16-1	CH9	SG-3MT	FLA-6	WBK 18	CH57	A-4M	4507IEPE
	CH10	SG-3MB	FLA-6		CH58	A-3M	4507IEPE
	CH11	SG-3MTend	FLA-6		CH59	A-2M	4507IEPE
	CH12	SG-3MBend	FLA-6		CH60	A-1M	4507IEPE
	CH13	SG-2WT	FLA-6		CH61	A-3E	4507IEPE
	CH14	SG-1WT	FLA-6		CH62	A-3W	4507IEPE
	CH15	SG-CMT	PL-60		CH63	A-4Mend	4507IEPE
	CH16	SG-CMB	PL-60		CH64	A-3Mend	4507IEPE
WBK 16-2	CH17	-					
	CH18	-					
	CH19	SP-4M	SM1-2				
	CH20	SP-3M	SM1-2				
	CH21	SP-2M	SM1-2				
	CH22	SP-1M	SM1-2				
	CH23	SP-4Mend	SM1-2				
	CH24	SM-3Mend	SM1-2				

8.4.2. Data Acquisition System and Instrument Details

8.4.2.1. Data Acquisition System

A total of 32 strain gauges (at 16 measurement locations using half-bridge circuits), eight string potentiometers, and eight accelerometers were installed onto Bridge SC-12. Thirty-two channels were used in the data acquisition system, which consisted of a Measurement Computing StrainBook main DAQ unit and WBK16 extension modules for recording the strain gauge and string potentiometer data, and a WBK18 extension module for recording accelerometer data. Figure 7.8(a) shows the main box and extensions modules of the data acquisition system.

8.4.2.2. Strain Gauges

In order to obtain longitudinal strain data during load testing, 28 Tokyo Measuring Instruments Lab FLA-6-11-3LJCT strain gauges were installed at 14 locations on the steel girders of the bridge. Two strain gauges were installed at each measurement location: a main gauge in the longitudinal direction to obtain longitudinal strain data and a secondary gauge in the transverse direction to compensate for any temperature changes experienced during testing. Figure 8.8 shows a close-up photograph of an installed quarter bridge strain gauge couple. The strain gauges used were selected with ease of installation in mind, as well as the fact that the testing being conducted takes place over the span of a couple of hours. Figure 8.9 shows the strain gauges used during testing. Four Tokyo Measuring Instruments Lab PL-60-11-3LJCT-F concrete strain gauges were used only at two locations, on the curb and at the top of the deck.

Figure 8.8. Close-Up of Strain Gauge Installation

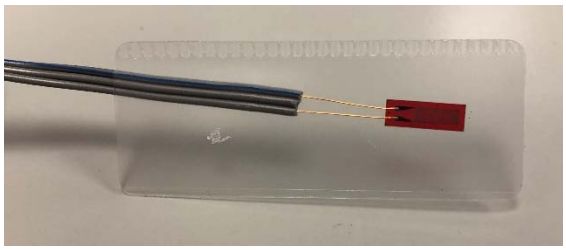

(a) Tokyo Measuring Instruments Lab FLA-6-11-3LJCT Steel Strain Gauge

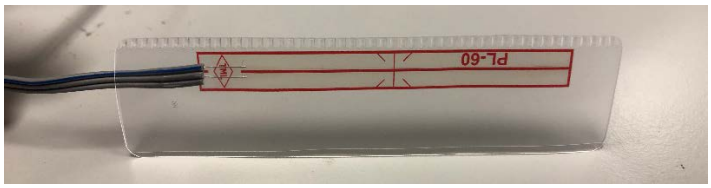

(b) Tokyo Measuring Instruments Lab PL-60-11-3LJCT-F Concrete Strain Gauge

Figure 8.9. Strain Gauges Used During Testing

8.4.2.3. String Potentiometers

A total of eight Celesco SM1-2 string potentiometers, four at midspan of every girder in the main span and another four at the moment critical position (0.4*L* away from the abutment) in one end

span, were installed to obtain girder deflections. All string potentiometers used were Celesco SM1-2 string potentiometers with a 2.5 in. stroke. Figure 7.8(c) shows the string potentiometers used during testing.

8.4.2.4. Accelerometers

To obtain dynamic properties of the bridge, such as natural frequency and mode shapes, eight Brüel & Kjær IEPE piezoelectric accelerometers were installed on the bridge. Accelerometers were installed in the main span at midspan on the bottom of every girder, as well as at quarter span locations on the bottom of the third girder. They were installed at 40 percent of the span length in one end span on the bottom of the third and fourth girders. The accelerometers used were selected because their resonance frequency of 18 kHz is much higher than the bridge natural frequency and because they are highly sensitive and low in mass and size. Figure 7.8(d) shows the accelerometers used during testing.

8.5. LOAD TESTING PROCEDURE FOR BRIDGE SC-12

A comprehensive test program was conducted to evaluate the performance and behavior of Bridge SC-12. The test program consisted of two parts: (1) static load tests, which consisted of stop location tests and crawl speed tests, and (2) dynamic load tests. The testing took place on June 20, 2019.

8.5.1. Test Vehicle

The TxDOT Lampasas Maintenance Office provided an International F-7100 dump truck to be used for the nondestructive testing of Bridge SC-12. It was loaded with asphalt base material such that the rear tandem axles weighed approximately the same as the posted limit of the bridge (posted

as 34,000 lb tandem axle). The truck was weighed using portable scales provided by the Texas Department of Public Safety. The wheel loads and wheel and axle spacings of the dump truck used for testing are shown in Figure 8.10.

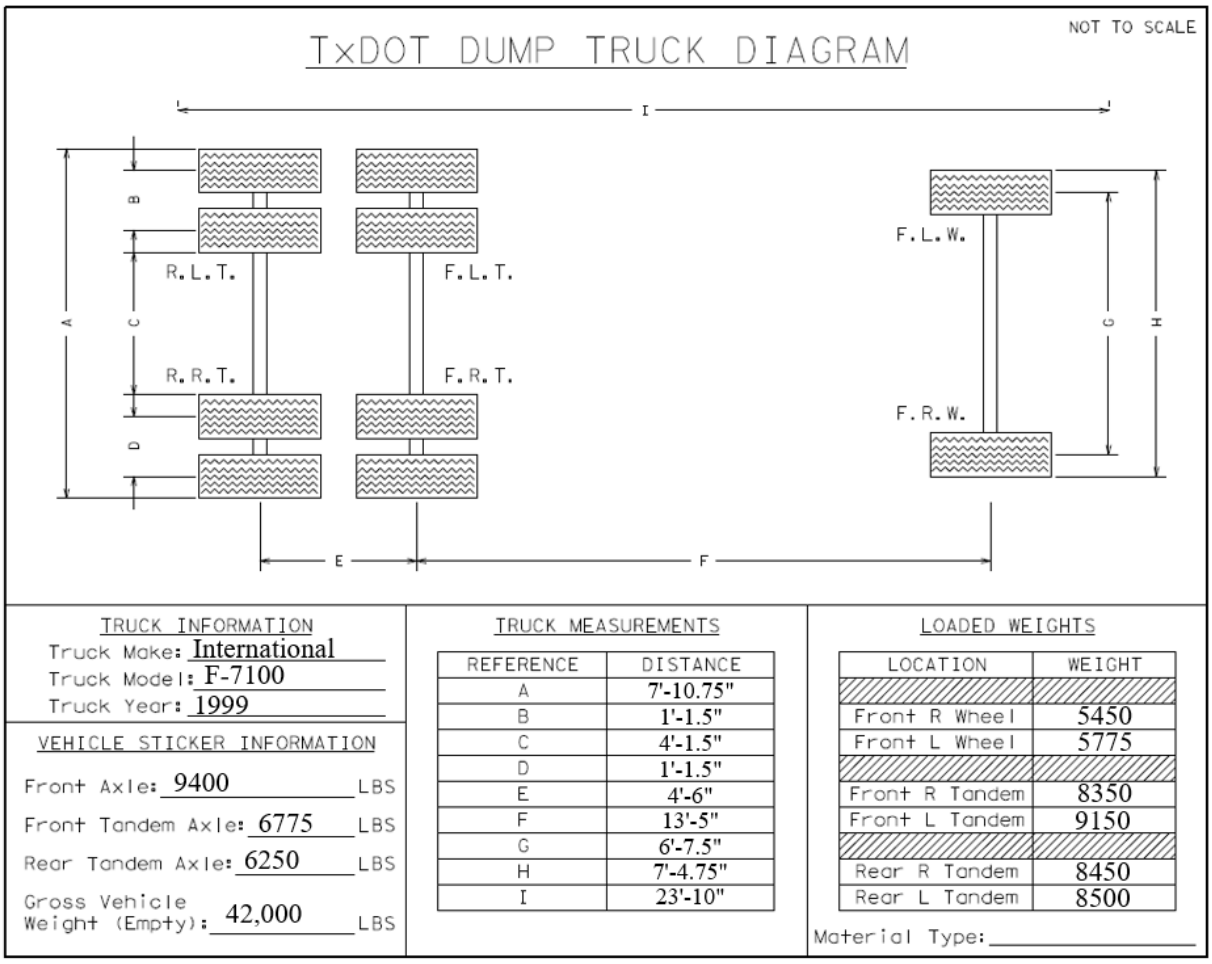

Figure 8.10. Wheel Weights and Spacings of the Loaded Dump Truck

8.5.2. Vehicle Positioning

In order to investigate the transverse load distribution between the bridge girders, three paths were determined that would be used during the testing. The first path, designated Path 1, was at a location such that the centerline of the adjacent rear tires would be 2 ft from the bridge guardrail. The second path, designated Path 2, was in the opposite lane at a location such that the centerline of the adjacent rear tires would be 2 ft from the centerline of the bridge. The third and final path, designated the Middle Path, was at a location such that the truck was straddling the centerline of the bridge. All three testing paths are shown in the bridge cross-section in Figure 8.11.

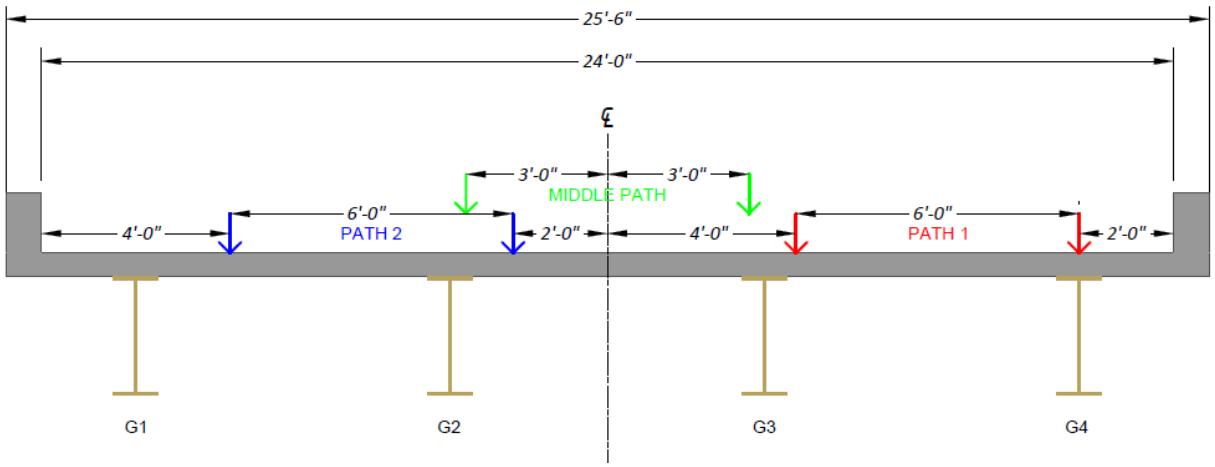

Figure 8.11. Load Test Paths for Bridge SC-12

For the static load tests, it was desired for the truck to be placed approximately at the location at which maximum moment would occur in the girders, as the moment LLDFs are one of the key parameters of interest. There were two stop locations for the static load tests, one for the end span and one for the main span. Therefore, the truck was placed such that the front axle was 13'-5" from the 40 percent span point in the end span, and from midspan in the main span. This

resulted in the first rear axle at either 0.4L and at the midspan, for the end span and main span, respectively. This longitudinal position was used for the static tests conducted. For the crawl speed tests and the dynamic tests, the truck was run completely across the bridge without stopping.

8.5.3. Test Protocol

8.5.3.1. Static Tests

Two types of static load tests were performed on Bridge SC-12, stop location tests and crawl speed tests. The static stop location load tests began with the truck stopped before entering the bridge to record a reference data file that serves as a baseline. The truck then proceeded onto the bridge and was stopped at the longitudinal moment critical position previously described. Once the truck was stopped, data was recorded for a period of approximately five seconds. This procedure was used for each load path. The static stop location tests along Path 1, Path 2, and the Middle Path were conducted at positive moment critical positions of the end span and the main span, resulting in a total of six stop location tests.

The static crawl speed tests began with the truck stopped before entering the bridge to record a reference data file that serves as a baseline. The truck then proceeded at an idle speed of approximately 2 mph across the full length of the bridge while data was recorded for the entire time. This procedure was used along the three previously described transverse load paths.

8.5.3.2. Dynamic Tests

The dynamic tests began with the truck stopped at some distance away from the bridge. At this time, a reference data file was recorded. The truck then proceeded at a specific speed across the entire length of the bridge while data was recorded during the passage of the vehicle. This

procedure was used along each load path. Two different dynamic tests were performed along Path 1 and Path 2. The first dynamic test was performed at approximately 30 mph and the second dynamic test was performed at 37 mph to 44 mph. Three dynamic tests were performed along the Middle Path at 30 mph, 44 mph, and 57 mph. These speeds were chosen based on a variety of factors including the speed limit of the road (60 mph), the estimated speed at which a heavy vehicle might drive over the bridge, and the comfort level of the truck driver going at certain speeds along the load paths.

8.5.3.3. Impact Tests

In order to obtain more information about the dynamic properties of the bridge, a sledgehammer was used to strike the top of the bridge deck in nine different locations. The sledgehammer tests were performed at 40 percent of span length away from the abutment for the end span, and at midspan and quarter span for the main span. The sledgehammer tests were performed at three transverse positions at each of these longitudinal positions: at the north edge, centerline, and south edge of the bridge. Although all the instruments were in place while data was being recorded during these three impact tests, only accelerometer measurements were used to identify dynamic characteristics. The impact excitation may provide a more accurate way of measuring bridge dynamic characteristics because unlike a vehicle excitation, the impact excitation does not introduce additional mass and dynamic interaction with the bridge. Table 8.3 summarizes all the tests that were performed on Bridge SC-12.

Table 8.3. Test Protocol for Bridge SC-12 Testing

Test Number	Test Location	Test Type
1	Path 1 – Span 1	Static – Stop Location (Engine Off)
2	Path 1 – Span 2	Static – Stop Location (Engine Off)
3	Path 1	Static – Crawl (2 mph)
4	Path 1	Dynamic (30 mph)
5	Path 1	Dynamic (37 mph)
6	Path 2 – Span 1	Static – Stop Location (Engine Off)
7	Path 2 – Span 2	Static – Stop Location (Engine Off)
8	Path 2	Static – Crawl (2 mph)
9	Path 2	Dynamic (29 mph)
10	Path 2	Dynamic (44 mph)
11	Middle Path – Span 1	Static – Stop Location (Engine Off)
12	Middle Path – Span 2	Static – Stop Location (Engine Off)
13	Middle Path	Static – Crawl (2 mph)
14	Middle Path	Dynamic (30 mph)
15	Middle Path	Dynamic (44 mph)
16	Middle Path	Dynamic (57 mph)
17	Span 1 – North Edge	Sledgehammer
18	Span 1 – Centerline	Sledgehammer
19	Span 1 – South Edge	Sledgehammer
20	Span 2 – Midspan – North Edge	Sledgehammer
21	Span 2 – Midspan – Centerline	Sledgehammer
22	Span 2 – Midspan – South Edge	Sledgehammer
23	Span 2 – Quarter span – North Edge	Sledgehammer
24	Span 2 – Quarter span – Centerline	Sledgehammer
25	Span 2 – Quarter span – South Edge	Sledgehammer

8.5.4. Test Operations

The test program for bridge SC-12 was conducted from June 18, 2019 to June 20, 2019. This includes all instrumentation installation, load testing, and instrumentation removal.

The clearance height of Bridge SC-12 was found to be approximately 26 ft. Therefore, three-story scaffolding platforms were set up below the bridge to provide a working platform for

instrumentation installation. To install strain gauges, an approximately 2 in. by 4 in. area at the desired location of the strain gauge was ground using an angle grinder to remove any loosely bonded adherent such as paint, rust, oxides, etc. This location was then sanded using 150 and 220 grit sandpaper to obtain a smooth surface. Conditioner (acetone) was applied repeatedly, and the surface scrubbed with paper towels until a clean tip is no longer discolored by the scrubbing. Liberally applying acetone brings the surface condition back to an optimum alkalinity of 7.0 to 7.5 pH for ideal bonding of the glue. The strain gauges were then glued using CN adhesive. Figure 8.12(a) shows an example of installed strain gauges on the girders. String potentiometers were attached to either wood posts or small pieces of wood, which were attached to rocks in the streambed or glued to the sloped abutment, respectively. Figure 8.12(c) shows the installation of the string potentiometers in the streambed and on the abutment. The string potentiometers were fixed by attaching fishing wire to metal hooks attached to the girders using magnets. Accelerometers were attached to the bottom flange of the appropriate girders using magnets. Figure 8.12(b) shows an example of an installed accelerometer and string potentiometer on a girder.

The load testing took place on June 20, 2019. Traffic control was provided by the TxDOT Brownwood District office while the testing took place. The dump truck was loaded and weighed at the TxDOT Lampasas Maintenance Office in the morning, while members of the research team marked the test paths and the static test stop locations on the bridge using chalk. The previously described tests in the test protocol were performed while data from the installed instruments were recorded during each test period. Once the testing was completed, the instrumentation was removed from the bridge, and traffic control ceased. Figure 8.13(a) shows the scaffolding setup

for instrumentation installation and Figure 8.13(b) shows the test truck on the bridge during a load test.

(a) Example of Installed Strain Gauges

(b) Example of Installed Accelerometer

(c) Example of an Installed String Potentiometer

Figure 8.12. Installed Instrumentation on Bridge SC-12

(a) Instrumentation of Bridge SC-12

(b) Test Truck at the Stop Location for Path 2 – Span 1

Figure 8.13. Instrumentation and Testing of Bridge SC-12

8.6. TEST RESULTS FOR BRIDGE SC-12

Two types of diagnostic tests were conducted following the guidelines provided in AASHTO MBE (AASHTO 2018): (1) Static Load Tests using stationary loads (avoiding bridge vibrations) to obtain static strains and deflections and infer composite action and LLDFs, and (2) Dynamic Load Tests with moving loads that excite vibrations in the bridge to measure modes of vibration, frequencies, and dynamic amplification.

The data obtained during testing were compiled, processed, and analyzed. Strains were measured using strain gauges, which allowed stresses to be inferred. Deflections were measured using string potentiometers, which were used to infer transverse load distribution. Accelerations were measured using accelerometers, which were processed to obtain natural frequencies and mode shapes of the bridge. Videos taken during testing were used to determine deflections using computer vision and compared with the string potentiometer measurements. NDE results were also compiled to obtain in situ compressive strength of the concrete bridge deck.

As Bridge SC-12 is three-span continuous, the strain measurements and deflection measurements are presented in two sections: (1) examining end Span 1 data while Span 1 is loaded and (2) examining main Span 2 data while Span 2 is loaded. The stop location test data shown is that of the same span in which the truck is loaded. The crawl test data shown is the maximum recorded result when the truck is on the specified span.

8.6.1. Static Load Tests on Bridge SC-12 Span 1

Two types of static load tests were conducted: (1) stop location tests by parking the vehicle at moment critical longitudinal position in each span for each selected path on the bridge, and (2)

crawl speed tests by moving the truck at low speeds (approximately 2 mph) along the same predefined paths.

8.6.1.1. Strain Measurements and Composite Action

After obtaining strain gauge data from the load testing, the maximum bottom flange strains were plotted along with their corresponding top flange strains at the same moment in time. In all strain figures, the measured strain values are shown by a colored dot symbol. The colored line connecting two dot symbols represents the strain diagram at this cross-section based on the plane section remains plane assumption. The blue plot shows the strain results for the pier location, the red plot shows the strain results for Span 1, and the green plot shows the strain results for Span 2. It is important to note that all strain values were taken at the same point in time as the maximum bottom flange strain value for the span being considered.

8.6.1.1.1. Interior Girder 3

Figure 8.14 through Figure 8.16 provide plots of the measured strains for interior Girder 3 during static load testing. The strains measured for Girder 3 during the Path 1 – Span 1 static tests are shown in Figure 8.14. Figure 8.14(a) shows the maximum strains observed during the stop location test for Girder 3 adjacent to the interior pier and midspan of Span 2. Figure 8.14(b) shows the maximum strains observed during the stop location test for Girder 3 at 0.4*L* of Span 1. Figure 8.14(c) shows the maximum strains observed during the crawl speed test for Girder 3 adjacent to the interior pier and midspan of Span 2. Figure 8.14(d) shows the maximum strains observed during the crawl speed test for Girder 3 at 0.4*L* of Span 1. The corresponding observed Span 1 stresses for Girder 3 are 4.49 ksi for the stop location test and 4.42 ksi for the crawl speed

test. The observed neutral axis locations at midspan are 17.77 in. from the bottom of the girder for the stop location test and 17.34 in. from the bottom of the girder for the crawl speed test.

The strains measured for Girder 3 during the Path 2 – Span 1 static tests are shown in Figure 8.15. Figure 8.15(a) shows the maximum strains observed during the stop location test for Girder 3 adjacent to the interior pier and midspan of Span 2. Figure 8.15(b) shows the maximum strains observed during the stop location test for Girder 3 at 0.4*L* of Span 1. Figure 8.15(c) shows the maximum strains observed during the crawl speed test for Girder 3 adjacent to the interior pier and midspan of Span 2. Figure 8.15(d) shows the maximum strains observed during the crawl speed test for Girder 3 at 0.4*L* of Span 1. The corresponding observed midspan stresses for Girder 3 are 2.23 ksi for the stop location test and 2.07 ksi for the crawl speed test. The observed neutral axis locations at midspan are 20.10 in. from the bottom of the girder for the stop location test and 20.51 in. from the bottom of the girder for the crawl speed test.

The strains measured for Girder 3 during the Middle Path static tests are shown in Figure 8.16. Figure 8.16(a) shows the maximum strains observed during the stop location test for Girder 3 adjacent to the interior pier and midspan of Span 2. Figure 8.16(b) shows the maximum strains observed during the stop location test for Girder 3 at 0.4*L* of Span 1. Figure 8.16(c) shows the maximum strains observed during the crawl speed test for Girder 3 adjacent to the interior pier and midspan of Span 2. Figure 8.16(d) shows the maximum strains observed during the crawl speed test for Girder 3 at 0.4*L* of Span 1. The corresponding observed midspan stresses for Girder 3 are 3.59 ksi for the stop location test and 3.66 ksi for the crawl speed test. The observed neutral axis locations at midspan are 18.28 in. from the bottom of the girder for the stop location test and 17.61 in. from the bottom of the girder for the crawl speed test.

The live load stress levels for interior Girder 3 when locating the test truck on the three considered paths are relatively low. In addition, the neutral axis locations based on the strain measurements over the section depth at $0.4L$ of Girder 3 indicate that partial composite action between the girder and concrete deck could be taking place. In Span 2, a small negative moment is occurring in Girder 3, and the neutral axis is higher than the theoretical non-composite neutral axis of 14.9 in. from the bottom of the girder.

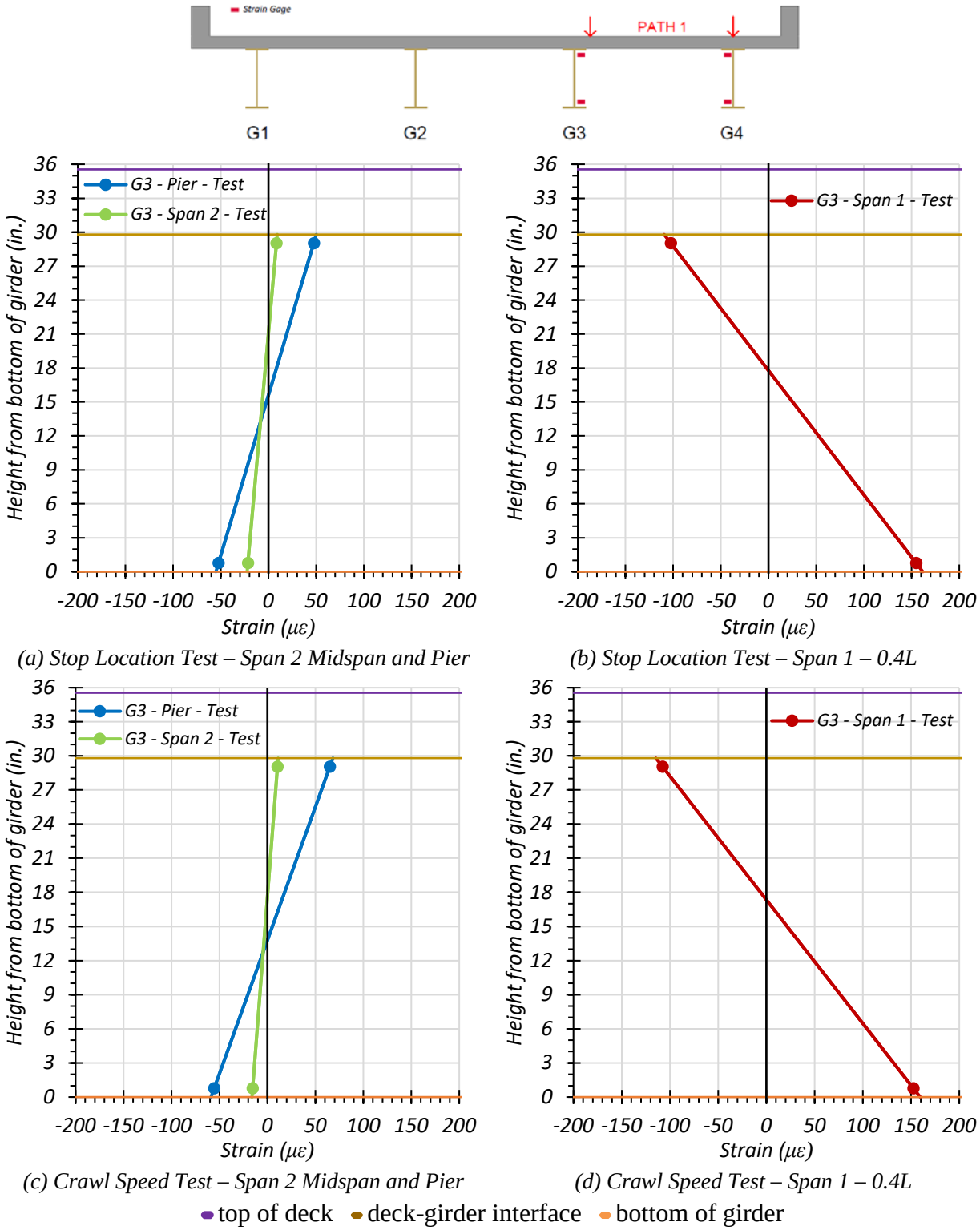

Figure 8.14. Static Strains for Interior Girder 3 – Path 1 – Span 1

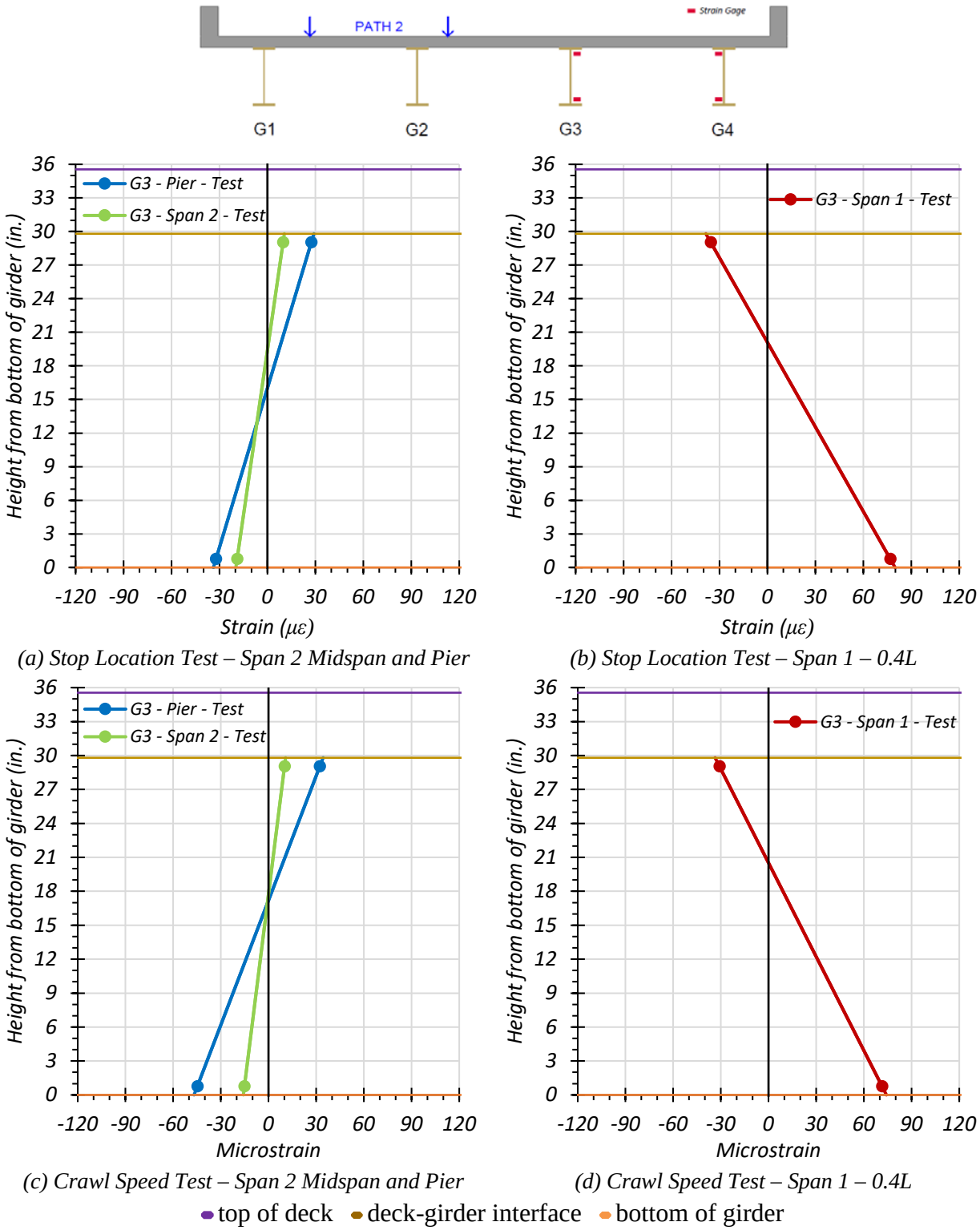

(a) Stop Location Test – Span 2 Midspan and Pier

(b) Stop Location Test – Span 1 – 0.4L

(c) Crawl Speed Test – Span 2 Midspan and Pier

(d) Crawl Speed Test – Span 1 – 0.4L

Figure 8.15. Static Strains for Interior Girder 3 – Path 2 – Span 1

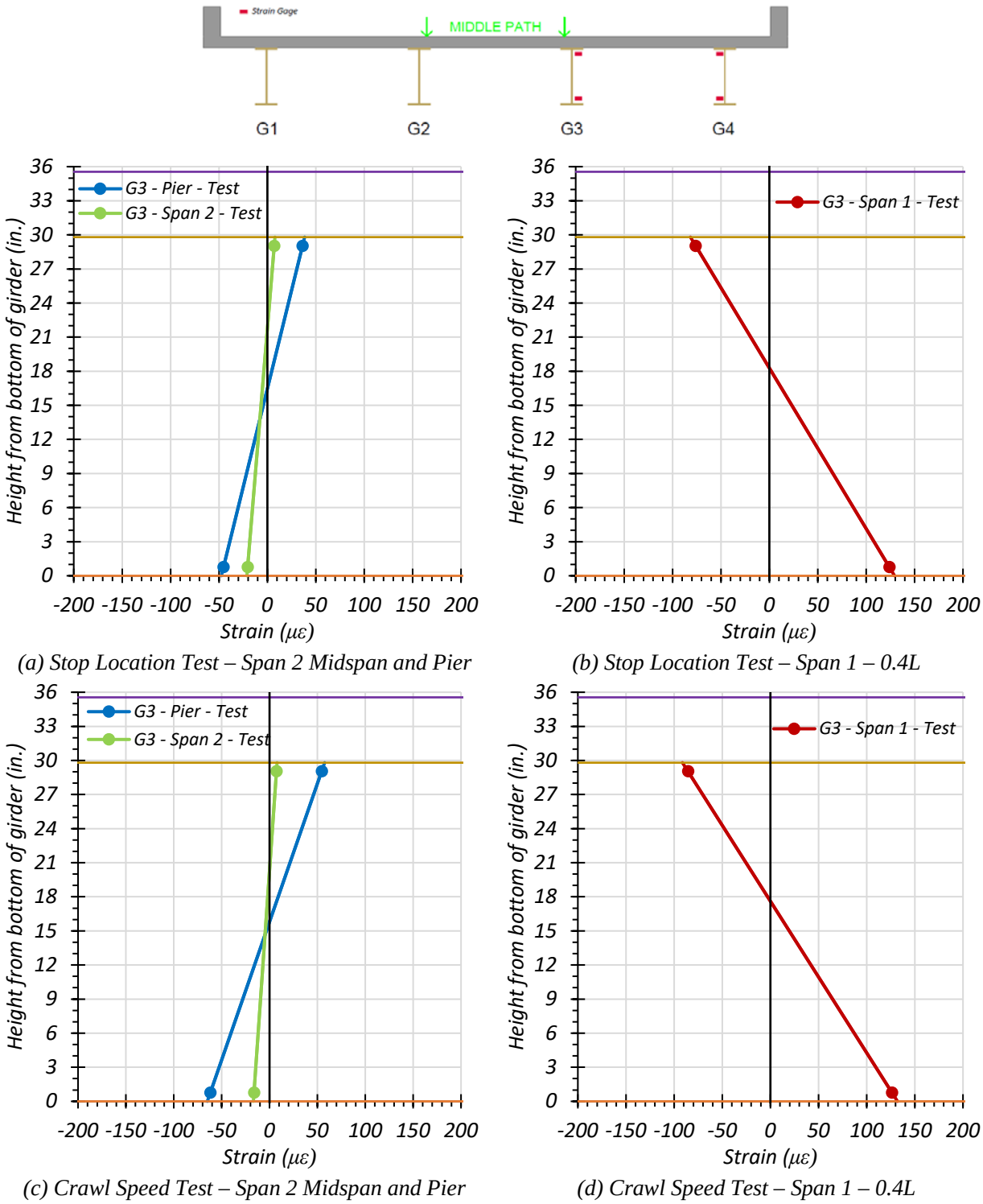

(a) Stop Location Test – Span 2 Midspan and Pier

(b) Stop Location Test – Span 1 – 0.4L

(c) Crawl Speed Test – Span 2 Midspan and Pier

(d) Crawl Speed Test – Span 1 – 0.4L

Figure 8.16. Static Strains for Interior Girder 3 – Middle Path – Span 1

8.6.1.1.2. Exterior Girder 4

Figure 8.17 through Figure 8.19 provide plots of the measured strains for exterior Girder 4 during static load testing. The strains measured for Girder 4 during the Path 1 – Span 1 static tests are shown in Figure 8.17. Figure 8.17(a) shows the maximum strains observed during the stop location test for Girder 4 at the midspan of Span 2 and adjacent to the interior pier. Figure 8.17(b) shows the maximum strains observed during the stop location test for Girder 4 at 0.4*L* of Span 1. Figure 8.17(c) shows the maximum strains observed during the crawl speed test for Girder 4 at the midspan of Span 2 and adjacent to the pier. Figure 8.17(d) shows the maximum strains observed during the crawl speed test for Girder 4 at 0.4*L* of Span 1. The corresponding observed Span 1 stresses for Girder 4 are 5.28 ksi for the stop location test and 5.34 ksi for the crawl speed test. The observed neutral axis locations at 0.4*L* are 17.42 in. from the bottom of the girder for the stop location test and 17.41 in. from the bottom of the girder for the crawl speed test.

The strains measured for Girder 4 during the Path 2 – Span 1 static tests are shown in Figure 8.18. Figure 8.18(a) shows the maximum strains observed during the stop location test for Girder 4 adjacent to the interior pier and midspan of Span 2. Figure 8.18(b) shows the maximum strains observed during the stop location test for Girder 4 at 0.4*L* of Span 1. Figure 8.18(c) shows the maximum strains observed during the crawl speed test for Girder 4 adjacent to the interior pier and midspan of Span 2. Figure 8.18(d) shows the maximum strains observed during the crawl speed test for Girder 4 at 40 percent point of Span 1. The corresponding observed stresses for Girder 4 are 0.67 ksi for the stop location test and 0.43 ksi for the crawl speed test. The observed neutral axis locations at 0.4*L* are 16.50 in. from the bottom of the girder for the stop location test and 15.22 in. from the bottom of the girder for the crawl speed test.

The strains measured for Girder 4 during the Middle Path static tests are shown in Figure 8.19. Figure 8.19(a) shows the maximum strains observed during the stop location test for Girder 4 adjacent to the interior pier and midspan of Span 2. Figure 8.19(b) shows the maximum strains observed during the stop location test for Girder 4 at 0.4*L* of Span 2. Figure 8.19(c) shows the maximum strains observed during the crawl speed test for Girder 4 adjacent to the interior pier and midspan of Span 2. Figure 8.19(d) shows the maximum strains observed during the crawl speed test for Girder 4 at 0.4*L* of Span 1. The corresponding observed stresses for Girder 4 are 2.00 ksi for the stop location test and 2.05 ksi for the crawl speed test. The observed neutral axis locations at 0.4*L* are 17.65 in. from the bottom of the girder for the stop location test and 16.53 in. from the bottom of the girder for the crawl speed test.

The live load stress levels for interior Girder 4 when locating the test truck on the three considered paths are relatively low. In addition, the neutral axis locations based on the strain measurements over the section depth at 0.4*L* of Girder 4 indicate that partial composite action between the girder and concrete deck could be taking place. In Span 2, a small negative moment is occurring in Girder 4, and the neutral axis is higher than the theoretical non-composite neutral axis of 14.9 in. from the bottom of the girder.

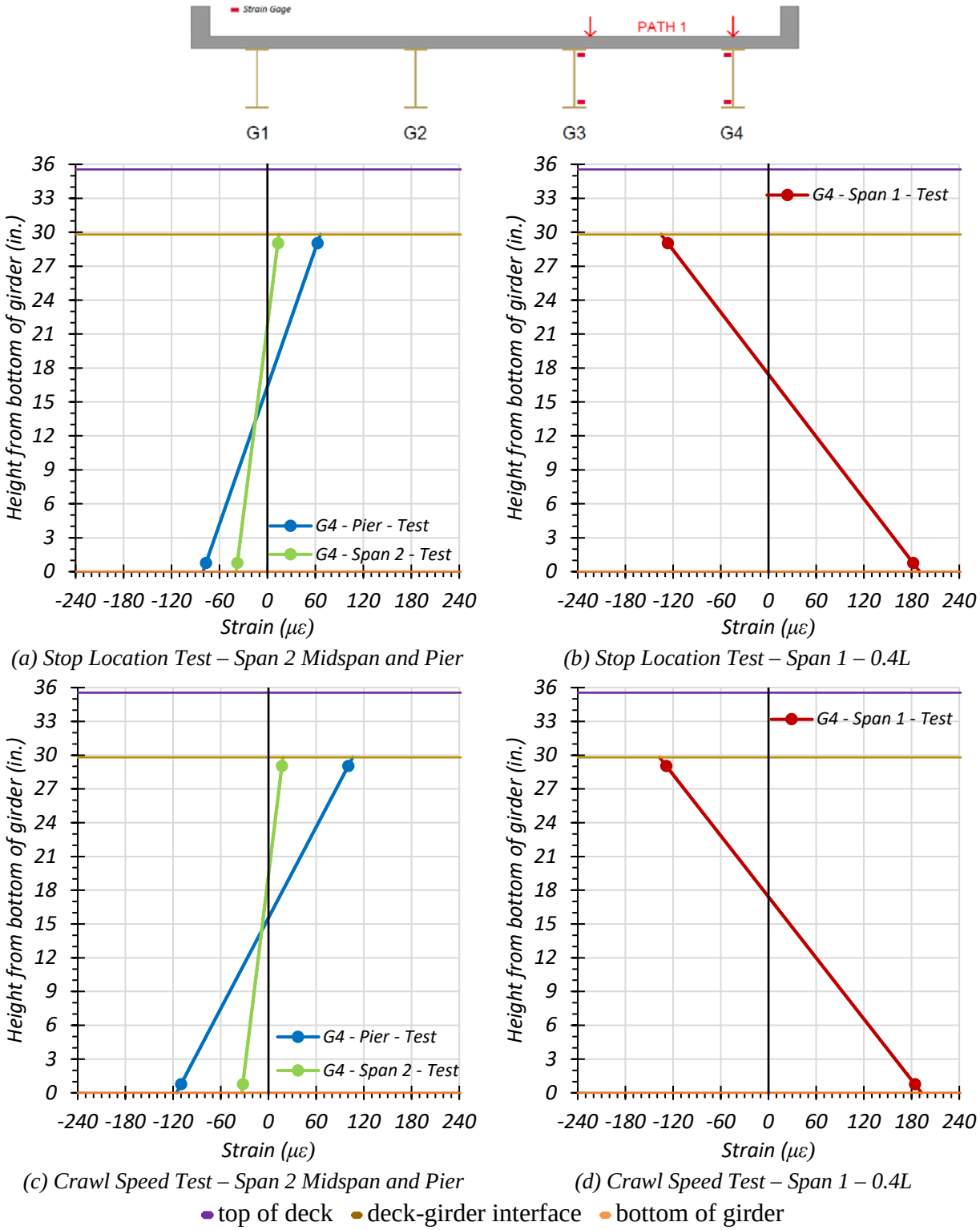

(a) Stop Location Test – Span 2 Midspan and Pier

(b) Stop Location Test – Span 1 – 0.4L

(c) Crawl Speed Test – Span 2 Midspan and Pier

(d) Crawl Speed Test – Span 1 – 0.4L

Figure 8.17. Static Strains for Exterior Girder 4 – Path 1 – Span 1

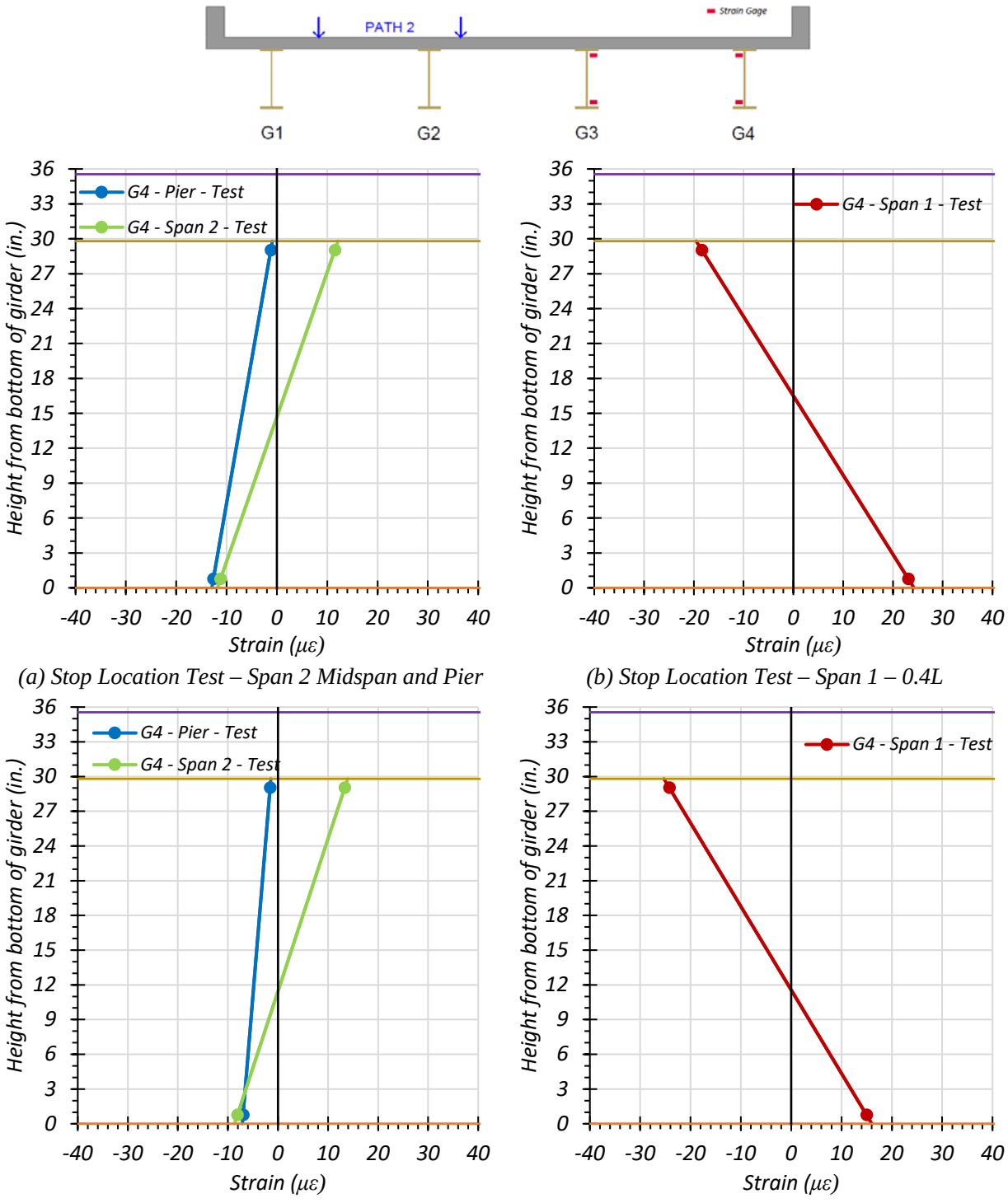

(a) Stop Location Test – Span 2 Midspan and Pier

(b) Stop Location Test – Span 1 – 0.4L

(c) Crawl Speed Test – Span 2 Midspan and Pier

(d) Crawl Speed Test – Span 1 – 0.4L

top of deck deck-girder interface bottom of girder

Figure 8.18. Static Strains for Exterior Girder 4 – Path 2 – Span 1

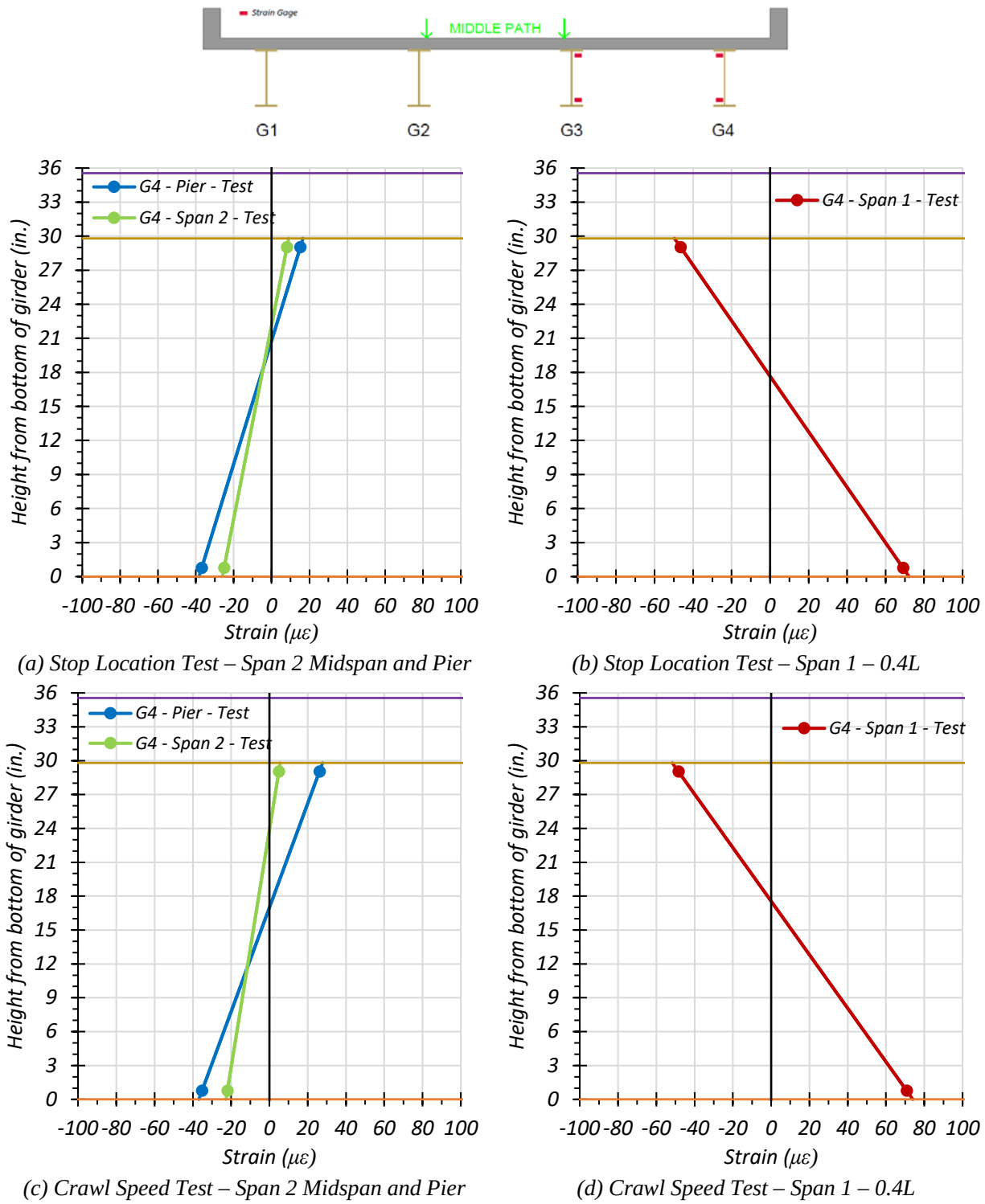

(a) Stop Location Test – Span 2 Midspan and Pier

(b) Stop Location Test – Span 1 – 0.4L

(c) Crawl Speed Test – Span 2 Midspan and Pier

(d) Crawl Speed Test – Span 1 – 0.4L

Figure 8.19. Static Strains for Exterior Girder 4 – Middle Path – Span 1

8.6.1.1.3. Comparison of Measured Strain Results

Table 8.4 and Figure 8.20 show the neutral axis locations measured for all static load tests in Span 1. The average test neutral axis was 18.60 in. from the bottom of the girder for Girder 3 and 16.79 in. from the bottom of the girder for Girder 4. The neutral axis values based on the strain measurements tend to increase as the loading on the girder increases. The measured values from the test truck loading indicate neutral axis values between the theoretical composite and the theoretical non-composite neutral axes. The theoretical values are based on the parallel axis theorem using the updated geometric material properties determined during testing. This includes an f_c' of 6.25 ksi and a corresponding concrete modulus of elasticity of 4506 ksi. The effective deck width used for the interior girder and exterior girder is 5'-9" in., determined using Article 10.38.3 in the AASHTO Standard Specifications (AASHTO 2002). Reinforcing steel is not included in this calculation. The results show that Bridge SC-12 is likely providing some degree of partial composite action between the steel girders and concrete deck for positive bending.

In negative bending, the theoretical non-composite neutral axis is the same as the theoretical non-composite axis in positive bending, 14.90 in. from the bottom of the girder. The theoretical composite neutral axis will be influenced by the presence of reinforcing steel in the deck. The longitudinal reinforcement in the deck is unknown, so for this calculation transverse bar sizes of #5 bars and spacing of 12.25” was used. This was also detailed in Task 4 of this project as well. The theoretical composite neutral axis in negative bending is also shown in Table 8.4.

Table 8.4. Measured Neutral Axis Locations for All Span 1 Static Load Tests

Test	G3 Neutral Axis Location (in. from bottom of girder)	G4 Neutral Axis Location (in. from bottom of girder)
Path 1 – Stop Location	17.77	17.42
Path 1 – Crawl Speed	17.34	17.41
Path 2 – Stop Location	20.10	16.50
Path 2 – Crawl Speed	20.51	15.22
Middle Path – Stop Location	18.28	17.65
Middle Path – Crawl Speed	17.61	16.53
Theoretical Non-Composite	14.90	14.90
Theoretical Composite – Positive Bending	26.11	26.11
Theoretical Composite – Negative Bending	16.66	16.66

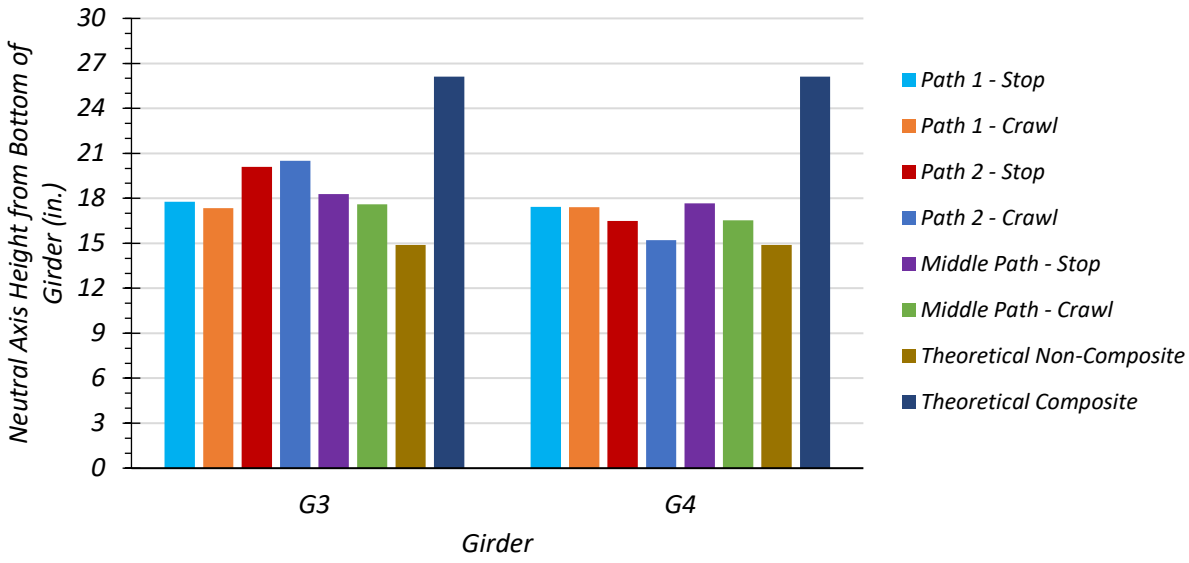

Figure 8.20. Test Neutral Axis Locations for Span 1 Loading

Table 8.5 and Figure 8.21 show the maximum bottom flange stresses observed during Span 1 testing inferred from the measured strains and an assumed elastic modulus for the steel of 29,000 ksi. The maximum tension stress in Girder 4 was 5.58 ksi from the Path 1 crawl speed test. The maximum tension stress in Girder 3 was 4.69 ksi from the Path 1 stop location test.

Table 8.5. Maximum Static Test Bottom Flange Stresses (ksi) for Span 1 Loading

Load Path	Interior Girder 3		Exterior Girder 4	
	Stop Location Test	Crawl Speed Test	Stop Location Test	Crawl Speed Test
Path 1	4.69	4.63	5.52	5.58
Path 2	2.32	2.15	0.70	0.59
Middle Path	3.75	3.83	2.09	2.22

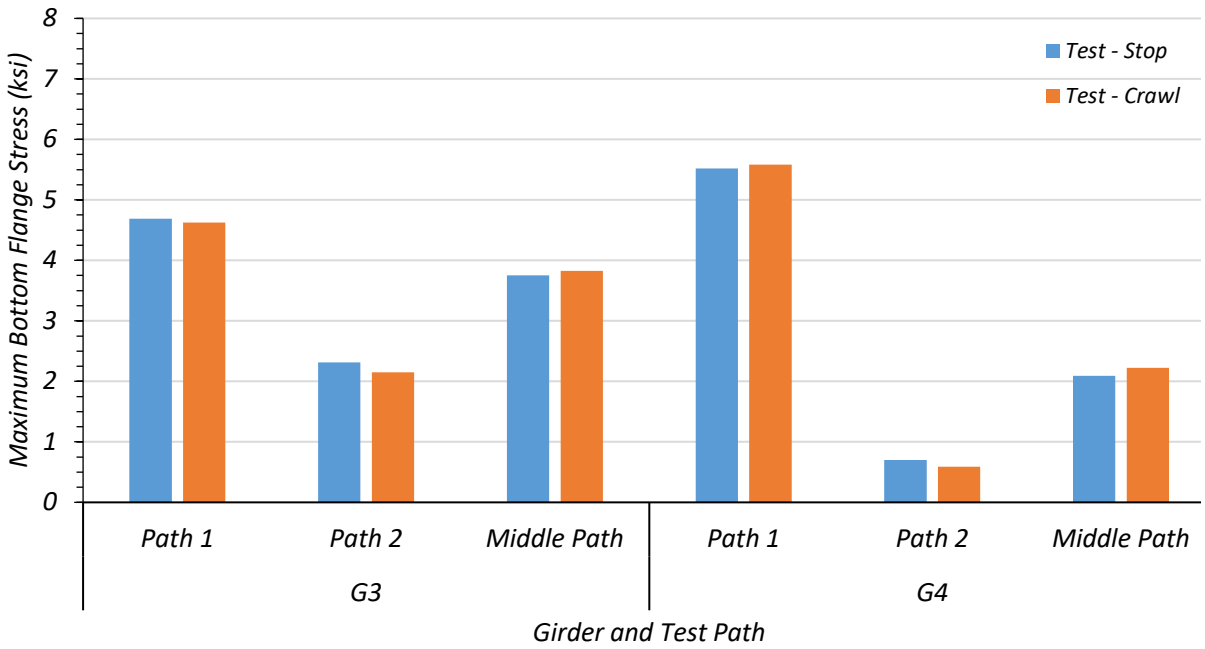

Figure 8.21. Comparison of Maximum Test Bottom Flange Stresses for Span 1 Loading

8.6.1.2. Deflection Measurements and LLDFs

8.6.1.2.1. Path 1 Loading

Table 8.6 shows the measured girder deflections at 0.4*L* during testing for the stop location test and crawl speed test along Path 1 – Span 1. The associated LLDFs, determined using the measured deflections at 0.4*L*, are also provided.

Table 8.6. Experimental Deflections and LLDFs for Path 1 – Span 1 Loading

Description	G1	G2	G3	G4
Stop Location Test Disp. (in.)	0.023	0.176	0.351	0.485
Stop Location Test LLDF	0.023	0.170	0.339	0.468
Crawl Speed Test Disp. (in.)	0.016	0.167	0.342	0.481
Crawl Speed Test LLDF	0.016	0.166	0.340	0.478
Note: 1 – G = girder, Disp. = Displacement 2 – LLDF values are based on 0.4*L* deflections.				

Table 8.7 compares the maximum experimental LLDFs based on deflections at 0.4*L* to those calculated using the AASHTO Standard Specifications, the AASHTO LRFD Specifications determined using the simplified stiffness parameter, and AASHTO LRFD Specifications determined using the analytical stiffness parameter (AASHTO 2002; AASHTO 2017). The maximum g_{AASHTO_Std}/g_{test} ratios are above 1.0, ranging from 1.22 to 1.40. The maximum g_{AASHTO_S}/g_{test} ratios are above 1.0, ranging from 1.32 to 1.41. The maximum g_{AASHTO_K}/g_{test} ratios are also above 1.0, ranging from 1.29 to 1.41. This indicates all three AASHTO methods to determine LLDFs are conservative for Path 1 – Span 1 loading.

Table 8.7. LLDF Comparison with AASHTO for Path 1 – Span 1 Loading

Test and Girder Type	AASHTO Standard Specs ($g^m_{AASHTO\_Std}$)	AASHTO LRFD Simplified ($g^m_{AASHTO\_S}$)	AASHTO LRFD K_g Calculated ($g^m_{AASHTO\_K}$)	Test (g^m_{test})	$g^m_{AASHTO\_Std}/g^m_{test}$	$g^m_{AASHTO\_S}/g^m_{test}$	$g^m_{AASHTO\_K}/g^m_{test}$
Stop Location Interior	0.476	0.452	0.442	0.339	1.40	1.33	1.30
Stop Location Exterior	0.589	0.660	0.660	0.468	1.26	1.41	1.41
Crawl Speed Interior	0.476	0.452	0.442	0.340	1.40	1.33	1.30
Crawl Speed Exterior	0.589	0.660	0.660	0.478	1.23	1.38	1.38

Figure 8.22(a) and Figure 8.22(c) show the Path 1 – Span 1 stop location and crawl speed test girder deflection profiles at 0.4*L*. Figure 8.22(b) and Figure 8.22(d) show the Path 1 – Span 1 stop location and crawl speed measured LLDFs compared to relevant AASHTO values. The governing LLDFs observed during testing are lower than the LLDFs provided by the AASHTO Standard Specifications, the AASHTO LRFD Specification LLDFs using the simplified stiffness parameter, and the AASHTO LRFD Specification LLDFs using the analytical stiffness parameter.

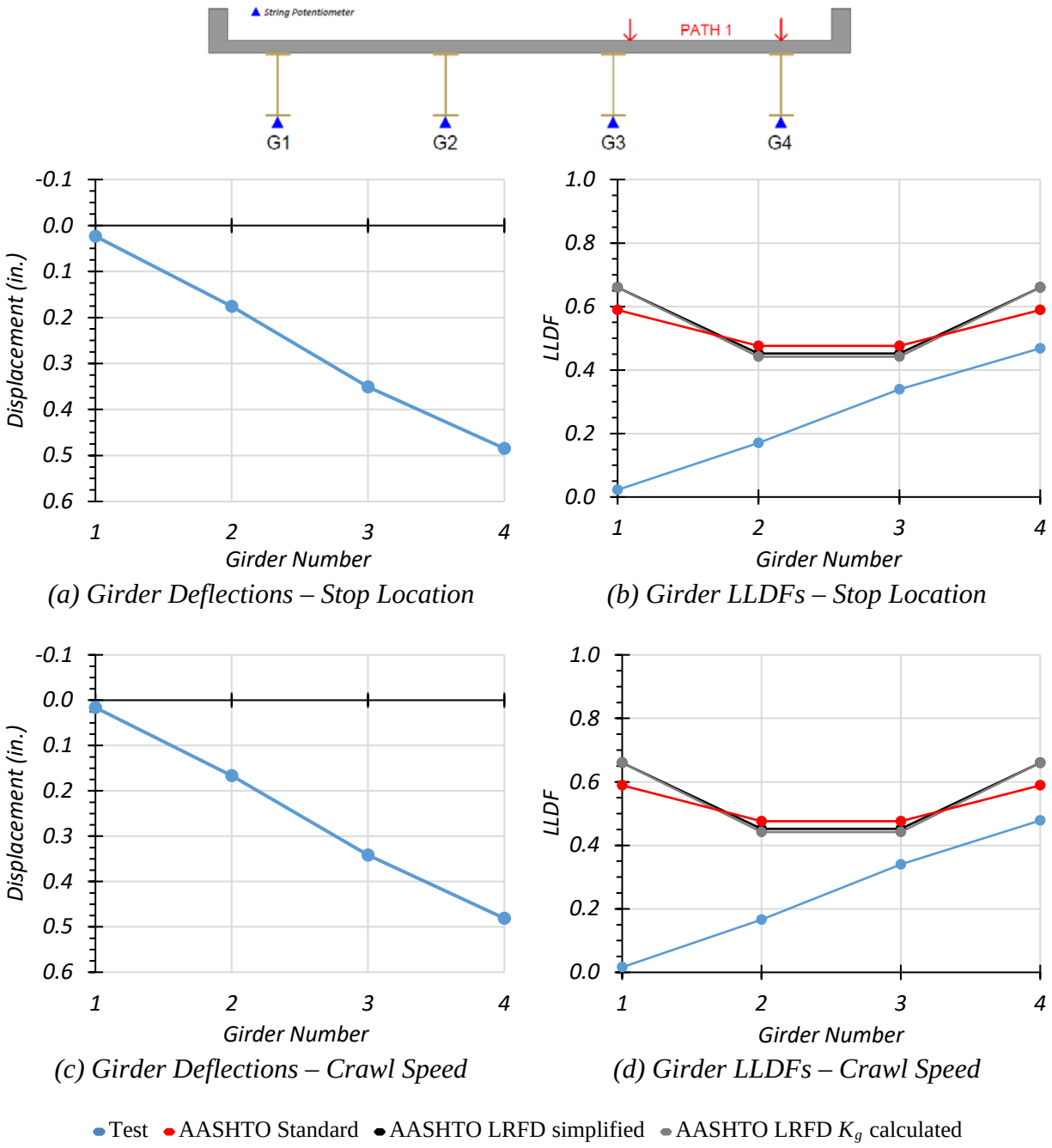

(a) Girder Deflections – Stop Location

(b) Girder LLDFs – Stop Location

(c) Girder Deflections – Crawl Speed

(d) Girder LLDFs – Crawl Speed

Figure 8.22. Static Deflection Results for Path 1 – Span 1 Loading

8.6.1.2.2. Path 2 Loading

Table 8.8 shows the measured girder deflections at 0.4*L* during testing for the stop location test and crawl speed test along Path 2 – Span 1. The associated LLDFs, determined using the measured deflections at 0.4*L*, are also provided.

Table 8.8. Experimental Deflections and LLDFs for Path 2 – Span 1 Loading

Description	G1	G2	G3	G4
Stop Location Test Disp. (in.)	0.422	0.340	0.198	0.075
Stop Location Test LLDF	0.408	0.328	0.192	0.072
Crawl Speed Test Disp. (in.)	0.413	0.322	0.182	0.061
Crawl Speed Test LLDF	0.423	0.329	0.186	0.063
Note: 1 – G = girder, Disp. = Displacement 2 – LLDF values are based on 0.4*L* deflections.				

Table 8.9 compares the test LLDFs to those calculated using the AASHTO Standard Specifications, AASHTO LRFD Specifications determined using the simplified stiffness parameter, and AASHTO LRFD Specifications determined using the analytical stiffness parameter (AASHTO 2002; AASHTO 2017). The maximum g_{AASHTO_Std}/g_{test} ratios are above 1.0, ranging from 1.39 to 1.45. The maximum g_{AASHTO_S}/g_{test} ratios are above 1.0, ranging from 1.37 to 1.62. The maximum g_{AASHTO_K}/g_{test} ratios are also above 1.0, ranging from 1.34 to 1.62. This indicates all three AASHTO methods to determine LLDFs are conservative for Path 2 – Span 1 loading.

Table 8.9. LLDF Comparison with AASHTO for Path 2 – Span 1 Loading

Test and Girder Type	AASHTO Standard Specs ($g^m_{AASHTO\_Std}$)	AASHTO LRFD Simplified ($g^m_{AASHTO\_S}$)	AASHTO LRFD K_g Calculated ($g^m_{AASHTO\_K}$)	Test (g^m_{test})	$g^m_{AASHTO\_Std}/g^m_{test}$	$g^m_{AASHTO\_S}/g^m_{test}$	$g^m_{AASHTO\_K}/g^m_{test}$
Stop Location Interior	0.476	0.452	0.442	0.328	1.45	1.38	1.35
Stop Location Exterior	0.589	0.660	0.660	0.408	1.44	1.62	1.62
Crawl Speed Interior	0.476	0.452	0.442	0.329	1.45	1.37	1.34
Crawl Speed Exterior	0.589	0.660	0.660	0.423	1.39	1.56	1.56

Figure 8.23(a) and Figure 8.23(c) show the Path 2 – Span 1 stop location and crawl speed test girder deflection profiles at 0.4*L*. Figure 8.23(b) and Figure 8.23(d) show the Path 2 – Span 1 stop location and crawl speed LLDFs compared to relevant AASHTO values. The governing LLDFs observed during testing are significantly lower than the LLDFs provided by the AASHTO Standard Specifications, the AASHTO LRFD Specification LLDFs using the simplified stiffness parameter, and the AASHTO LRFD Specification LLDFs using the analytical stiffness parameter.

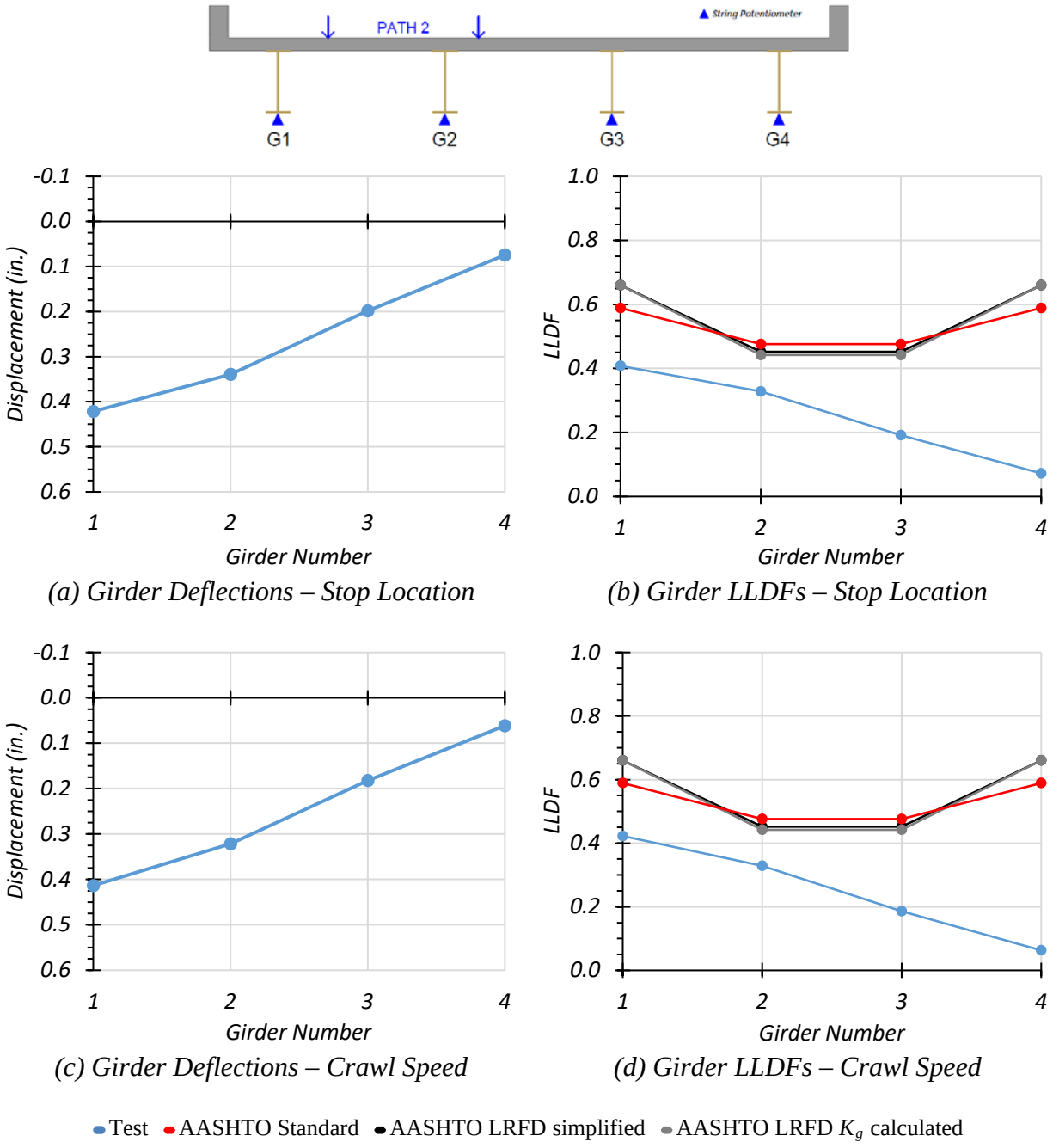

(a) Girder Deflections – Stop Location

(b) Girder LLDFs – Stop Location

(c) Girder Deflections – Crawl Speed

(d) Girder LLDFs – Crawl Speed

Figure 8.23. Static Deflection Results for Path 2 – Span 1 Loading

8.6.1.2.3. Middle Path Loading

Table 8.10 shows the measured girder deflections at 0.4*L* during testing for the Middle Path – Span 1 stop location and crawl speed tests. The associated LLDFs, determined using the measured deflections at 0.4*L* are also provided.

Table 8.10. Experimental Deflections and LLDFs for Middle Path – Span 1 Loading

Description	G1	G2	G3	G4
Stop Location Test Disp. (in.)	0.217	0.286	0.280	0.203
Stop Location Test LLDF	0.220	0.290	0.284	0.205
Crawl Speed Test Disp. (in.)	0.201	0.278	0.280	0.211
Crawl Speed Test LLDF	0.207	0.287	0.289	0.217
Note: 1 – G = girder, Disp. = Displacement 2 – LLDF values are based on 0.4*L* deflections.				

Table 8.11 compares the test LLDFs to those calculated using the AASHTO Standard Specifications, AASHTO LRFD Specifications determined using the simplified stiffness parameter, and AASHTO LRFD Specifications determined using the analytical stiffness parameter (AASHTO 2002; AASHTO 2017). The maximum g_{AASHTO_Std}/g_{test} ratios are above 1.0, ranging from 1.64 to 2.71. The maximum g_{AASHTO_S}/g_{test} ratios are above 1.0, ranging from 1.56 to 3.04. The maximum g_{AASHTO_K}/g_{test} ratios are above 1.0, ranging from 1.52 to 3.04. This indicates all three of the AASHTO methods to determine LLDFs are conservative for Middle Path – Span 1 loading.

Table 8.11. LLDF Comparison with AASHTO for Middle Path – Span 1 Loading

Test and Girder Type	AASHTO Standard Specs ($g^m_{AASHTO\_Std}$)	AASHTO LRFD Simplified ($g^m_{AASHTO\_S}$)	AASHTO LRFD K_g Calculated ($g^m_{AASHTO\_K}$)	Test (g^m_{test})	$g^m_{AASHTO\_Std}/g^m_{test}$	$g^m_{AASHTO\_S}/g^m_{test}$	$g^m_{AASHTO\_K}/g^m_{test}$
Stop Location Interior	0.476	0.452	0.442	0.290	1.64	1.56	1.52
Stop Location Exterior	0.589	0.660	0.660	0.220	2.68	3.00	3.00
Crawl Speed Interior	0.476	0.452	0.442	0.289	1.65	1.56	1.53
Crawl Speed Exterior	0.589	0.660	0.660	0.217	2.71	3.04	3.04

Figure 8.24(a) and Figure 8.24(c) show the Middle Path – Span 1 stop location and crawl speed test girder deflection profiles at 0.4*L*. Figure 8.24(b) and Figure 8.24(d) show the Middle Path – Span 1 stop location and crawl speed LLDFs compared to relevant AASHTO values. The governing LLDFs observed during testing are significantly lower than the LLDFs provided by the AASHTO Standard Specifications, the AASHTO LRFD Specification LLDFs using the simplified stiffness parameter, and the AASHTO LRFD Specification LLDFs using the analytical stiffness parameter.

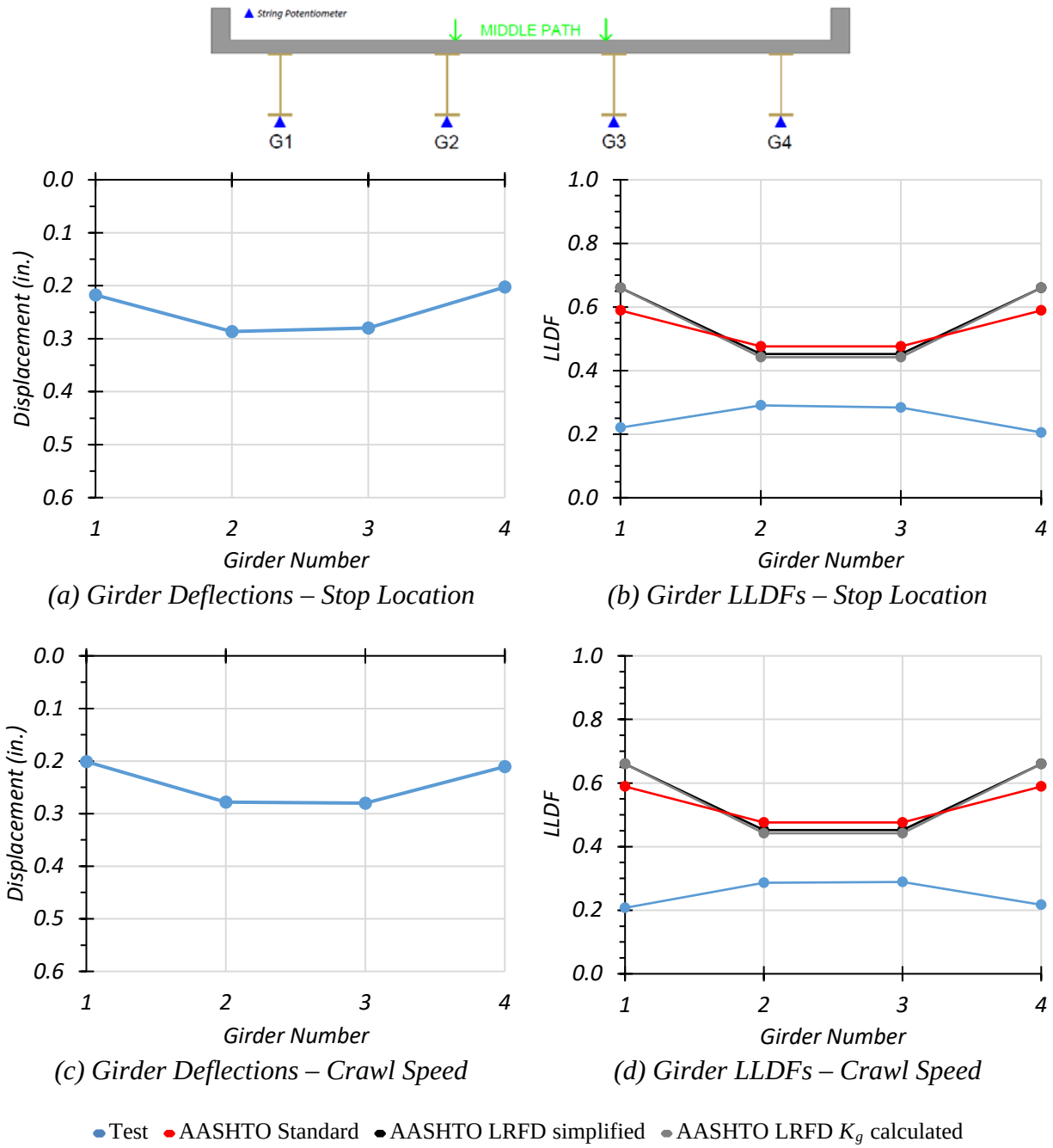

(a) Girder Deflections – Stop Location

(b) Girder LLDFs – Stop Location

(c) Girder Deflections – Crawl Speed

(d) Girder LLDFs – Crawl Speed

Figure 8.24. Static Deflection Results for Middle Path – Span 1 Loading

8.6.1.2.4. Comparison of Results Based on Deflection Measurements

For Span 1 when considering the 0.4*L* location deflections, the critical LLDF for an exterior girder was 0.481, which was observed during the crawl speed test along Path 1. This corresponds to a g_{AASHTO}/g_{test} ratio of 1.22 when using the AASHTO Standard Specifications, 1.37 when using the AASHTO LRFD Specifications determined using the simplified stiffness parameter, and 1.37 when using the AASHTO LRFD Specifications determined using the analytical stiffness parameter. The critical LLDF for an interior girder was 0.342, which was also observed during the crawl speed test along Path 1. This corresponds to a g_{AASHTO}/g_{test} ratio of 1.39 when using the AASHTO Standard Specifications, 1.32 when using the AASHTO LRFD Specifications determined using the simplified stiffness parameter, and 1.29 when using the AASHTO LRFD Specifications determined using the analytical stiffness parameter. During the static load tests along Path 1, the maximum LLDF was 0.461 for stop location test, which increased to 0.481 for the crawl speed test. During the static load tests along Path 2, the maximum LLDF was 0.408 for the stop location test while decreasing to 0.423 for the crawl speed test. During the static load tests along Middle Path, the maximum LLDF of 0.290 for stop location test while decreasing slightly to 0.289 for the crawl speed test.

Overall, none of the AASHTO methods to determine LLDFs produced lower values than the LLDFs observed during Span 1 testing. The AASHTO methods were always conservative for Bridge SC-12, and in most cases by a significant margin. This could possibly be an area through which the load rating for Bridge SC-12 could improve.

8.6.2. Static Load Tests on Bridge SC-12 Span 2

Two types of static load tests were conducted without introducing any dynamic effects: (1) stop location tests by parking the vehicle at moment critical longitudinal position in each span for each selected path on the bridge, and (2) crawl speed tests by moving the truck at low speeds (around 2 mph) along the same predefined paths.

8.6.2.1. Strain Measurements and Composite Action

8.6.2.1.1. Interior Girder 3

Figure 8.25 through Figure 8.27 provide plots of the measured strains for interior Girder 3 during static load testing. The strains measured for Girder 3 during the Path 1 – Span 2 static tests are shown in Figure 8.25. Figure 8.25(a) shows the maximum strains observed during the stop location test for Girder 3 at 0.4*L* of Span 1 and the interior pier. Figure 8.25(b) shows the maximum strains observed during the stop location test for Girder 3 at midspan of Span 2. Figure 8.25(c) shows the maximum strains observed during the crawl speed test for Girder 3 at 0.4*L* of Span 1 and the interior pier. Figure 8.25(d) shows the maximum strains observed during the crawl speed test for Girder 3 at midspan of Span 2. The corresponding observed Span 2 stresses for Girder 3 are 4.50 ksi for the stop location test and 4.47 ksi for the crawl speed test. The observed neutral axis locations at midspan are 19.97 in. from the bottom of the girder for the stop location test and 19.56 in. from the bottom of the girder for the crawl speed test.

The strains measured for Girder 3 during the Path 2 – Span 2 static tests are shown in Figure 8.26. Figure 8.26(a) shows the maximum strains observed during the stop location test for Girder 3 at 0.4*L* of Span 1 and the interior pier. Figure 8.26(b) shows the maximum strains observed during the stop location test for Girder 3 at midspan of Span 2. Figure 8.26(c) shows the

maximum strains observed during the crawl speed test for Girder 3 at 0.4*L* of Span 1 and the interior pier. Figure 8.26(d) shows the maximum strains observed during the crawl speed test for Girder 3 at midspan of Span 2. The corresponding observed midspan stresses for Girder 3 are 2.80 ksi for the stop location test and 2.68 ksi for the crawl speed test. The observed neutral axis locations at midspan are 15.08 in. from the bottom of the girder for the stop location test and 15.32 in. from the bottom of the girder for the crawl speed test.

The strains measured for Girder 3 during the Middle Path static tests are shown in Figure 8.27. Figure 8.27(a) shows the maximum strains observed during the stop location test for Girder 3 at 0.4*L* of Span 1 and the interior pier. Figure 8.27(b) shows the maximum strains observed during the stop location test for Girder 3 at midspan of Span 2. Figure 8.27(c) shows the maximum strains observed during the crawl speed test for Girder 3 at 0.4*L* of Span 1 and the interior pier. Figure 8.27(d) shows the maximum strains observed during the crawl speed test for Girder 3 at midspan of Span 2. The corresponding observed midspan stresses for Girder 3 are 3.86 ksi for the stop location test and 3.86 ksi for the crawl speed test. The observed neutral axis locations at midspan are 15.88 in. from the bottom of the girder for the stop location test and 15.45 in. from the bottom of the girder for the crawl speed test.

The live load stress levels for interior Girder 3 when locating the test truck on the three considered paths are relatively low. In addition, the neutral axis locations based on the strain measurements over the section depth at midspan of Girder 3 indicate that partial composite action between the girder and concrete deck could be taking place. In Span 1, a small negative moment is occurring in Girder 3, and the neutral axis is higher than the theoretical non-composite neutral axis of 14.9 in. from the bottom of the girder.

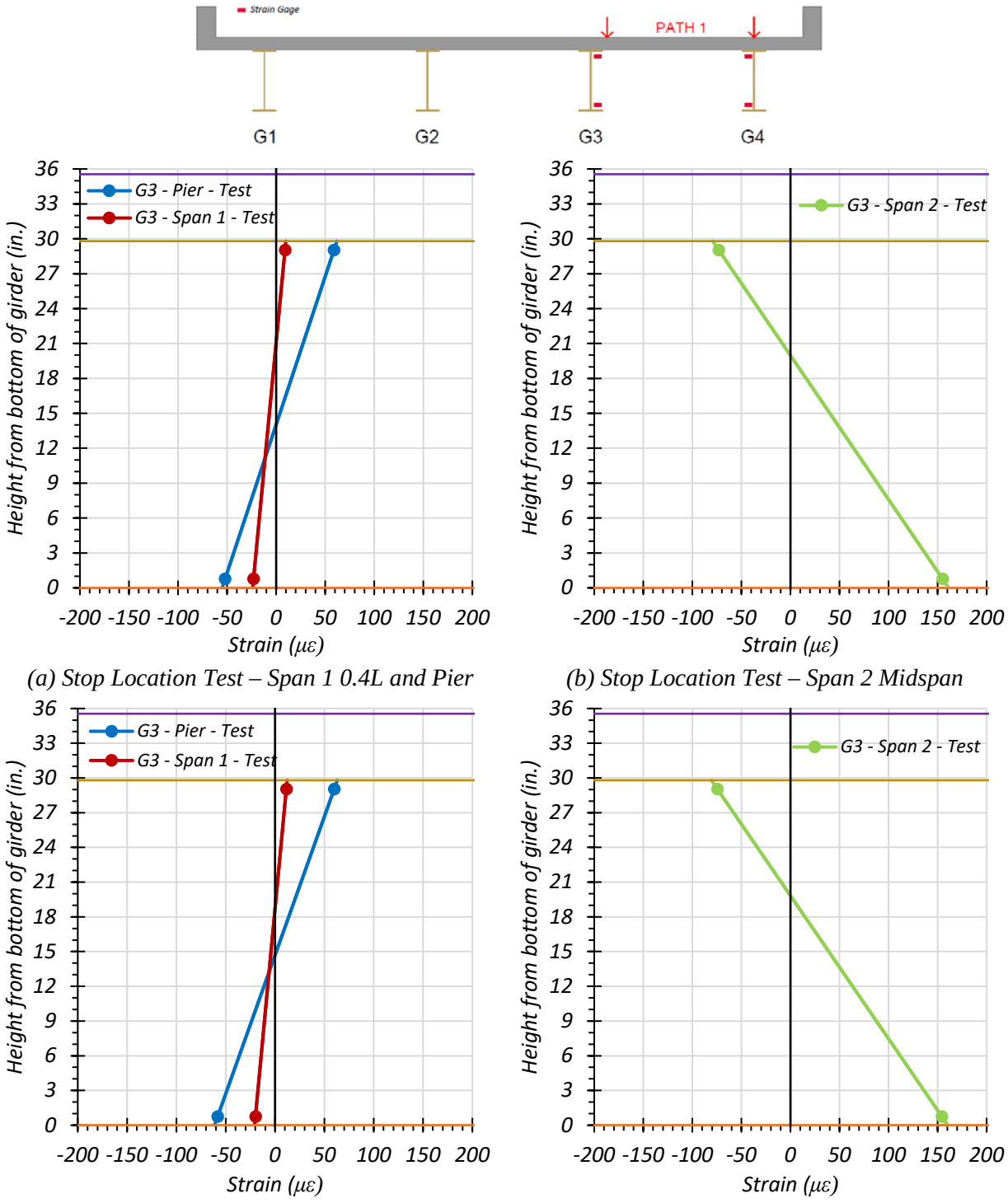

(a) Stop Location Test – Span 1 0.4L and Pier

(b) Stop Location Test – Span 2 Midspan

(c) Crawl Speed Test – Span 1 0.4L and Pier

(d) Crawl Speed Test – Span 2 Midspan

top of deck deck-girder interface bottom of girder

Figure 8.25. Static Strains for Interior Girder 3 – Path 1 – Span 2

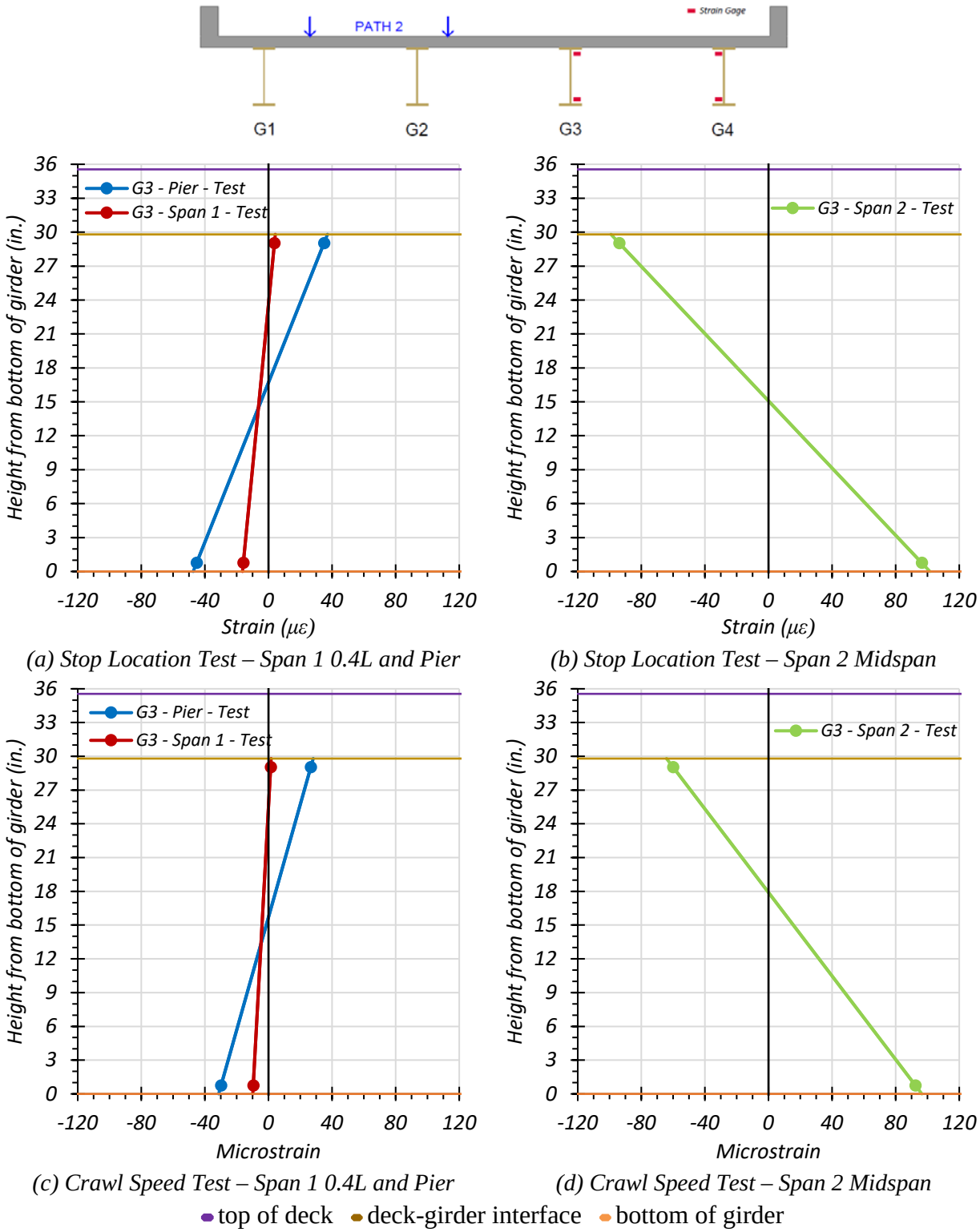

(a) Stop Location Test – Span 1 0.4L and Pier

(b) Stop Location Test – Span 2 Midspan

(c) Crawl Speed Test – Span 1 0.4L and Pier

(d) Crawl Speed Test – Span 2 Midspan

Figure 8.26. Static Strains for Interior Girder 3 – Path 2 – Span 2

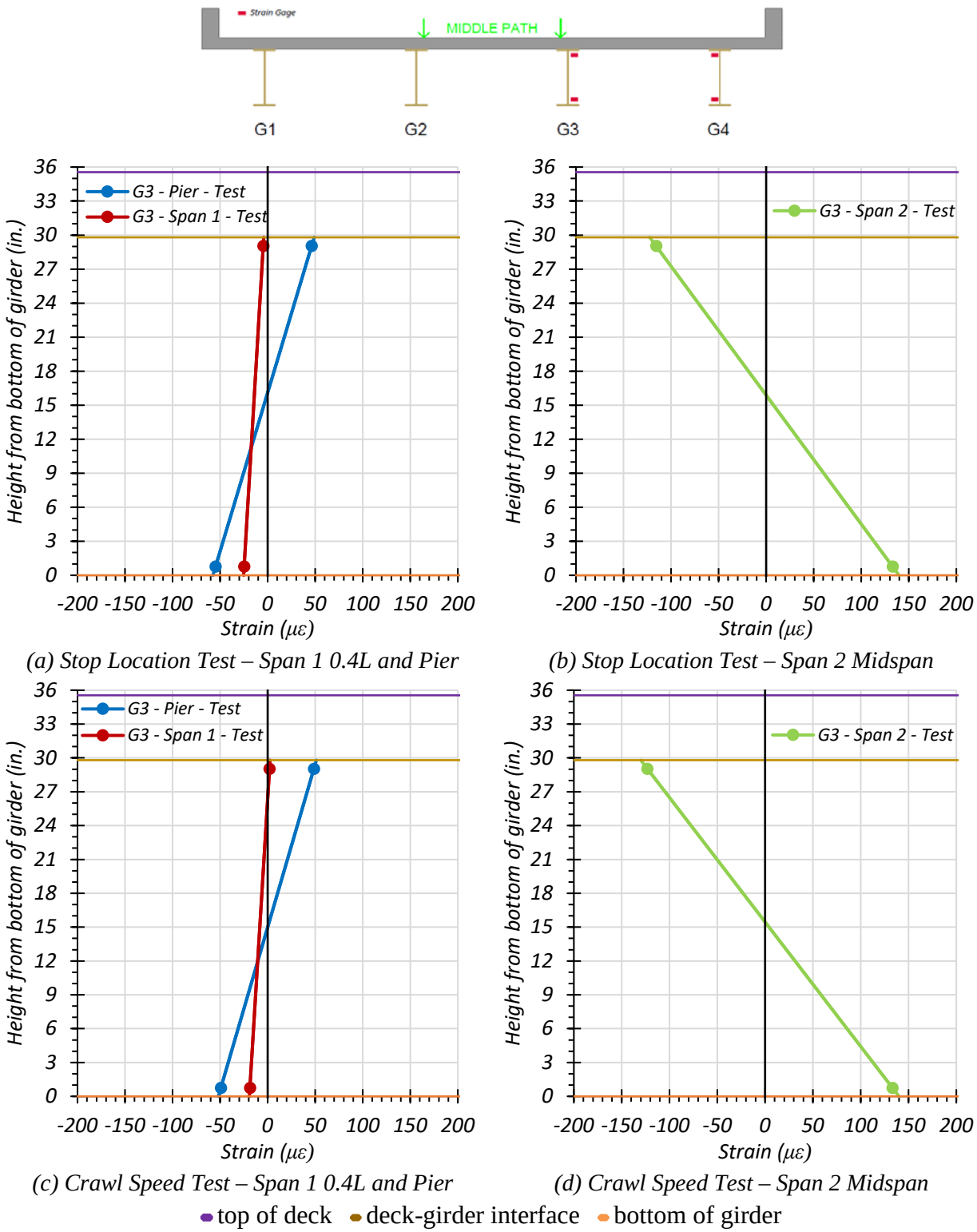

(a) Stop Location Test – Span 1 0.4L and Pier

(b) Stop Location Test – Span 2 Midspan

(c) Crawl Speed Test – Span 1 0.4L and Pier

(d) Crawl Speed Test – Span 2 Midspan

Figure 8.27. Static Strains for Interior Girder 3 – Middle Path – Span 2

8.6.2.1.2. Exterior Girder 4

Figure 8.28 through Figure 8.30 provide plots of the measured strains for exterior Girder 4 during static load testing. The strains measured for Girder 4 during the Path 1 – Span 2 static tests are shown in Figure 8.28. Figure 8.28(a) shows the maximum strains observed during the stop location test for Girder 4 at 0.4*L* of Span 1 and the interior pier. Figure 8.28(b) shows the maximum strains observed during the stop location test for Girder 4 at midspan of Span 2. Figure 8.28(c) shows the maximum strains observed during the crawl speed test for Girder 4 at 0.4*L* of Span 1 and the interior pier. Figure 8.28(d) shows the maximum strains observed during the crawl speed test for Girder 4 at midspan of Span 2. The corresponding observed Span 2 stresses for Girder 4 are 6.61 ksi for the stop location test and 6.82 ksi for the crawl speed test. The observed neutral axis locations at midspan are 19.76 in. from the bottom of the girder for the stop location test and 19.85 in. from the bottom of the girder for the crawl speed test.

The strains measured for Girder 4 during the Path 2 – Span 2 static tests are shown in Figure 8.29. Figure 8.29(a) shows the maximum strains observed during the stop location test for Girder 4 at 0.4*L* of Span 1 and the interior pier. Figure 8.29(b) shows the maximum strains observed during the stop location test for Girder 4 at midspan of Span 2. Figure 8.29(c) shows the maximum strains observed during the crawl speed test for Girder 4 at 0.4*L* of Span 1 and the interior pier. Figure 8.29(d) shows the maximum strains observed during the crawl speed test for Girder 4 at midspan of Span 2. The corresponding observed midspan stresses for Girder 4 are 0.58 ksi for the stop location test and 0.52 ksi for the crawl speed test.

The strains measured for Girder 4 during the Middle Path static tests are shown in Figure 8.30. Figure 8.30(a) shows the maximum strains observed during the stop location test for Girder 4 at 0.4*L* of Span 1 and the interior pier. Figure 8.30(b) shows the maximum strains

observed during the stop location test for Girder 4 at midspan of Span 2. Figure 8.30(c) shows the maximum strains observed during the crawl speed test for Girder 4 at 0.4*L* of Span 1 and the interior pier. Figure 8.30(d) shows the maximum strains observed during the crawl speed test for Girder 4 at midspan of Span 2. The corresponding observed midspan stresses for Girder 4 are 2.72 ksi for the stop location test and 2.68 ksi for the crawl speed test. The observed neutral axis locations at midspan are 34.13 in. from the bottom of the girder for the stop location test and 32.76 in. from the bottom of the girder for the crawl speed test.

The live load stress levels for interior Girder 4 when locating the test truck on the three considered paths are relatively low. In addition, the neutral axis locations based on the strain measurements over the section depth at midspan of Girder 4 indicate that partial composite action between the girder and concrete deck could be taking place. In Span 1, a small negative moment is occurring in Girder 4, and the neutral axis is higher than the theoretical non-composite neutral axis of 14.9 in. from the bottom of the girder.

During Path 2 loading, the strains at the top and bottom of Girder 4 are very similar. It would seem as though the girder is taking a very small amount of almost only axial load. This could be due to the girder receiving very little load during Path 2 loading as the truck is on the other side of the bridge and most load is likely going to Girders 1 and 2.

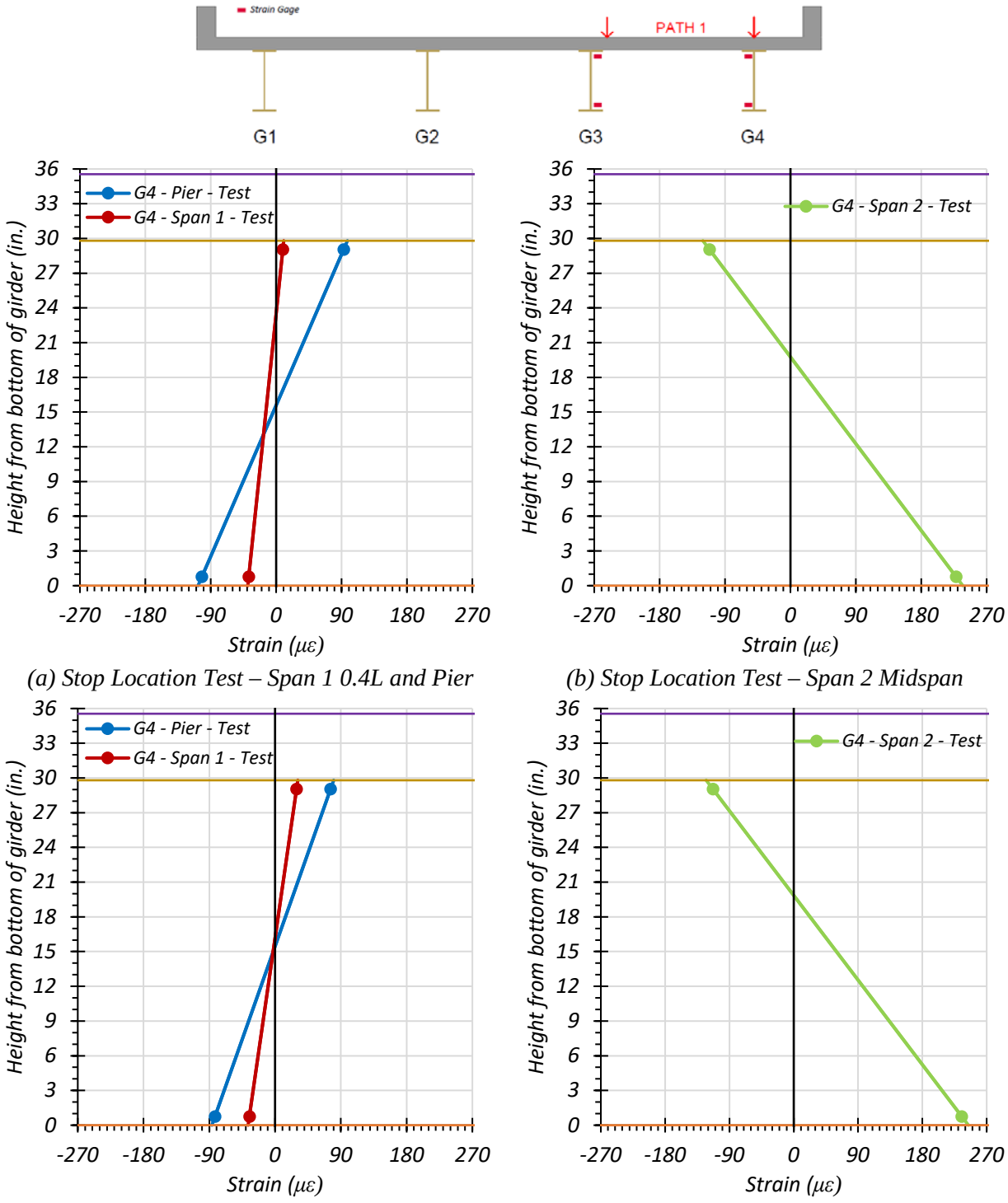

(a) Stop Location Test – Span 1 0.4L and Pier

(b) Stop Location Test – Span 2 Midspan

(c) Crawl Speed Test – Span 1 0.4L and Pier

(d) Crawl Speed Test – Span 2 Midspan

Figure 8.28. Static Strains for Exterior Girder 4 – Path 1 – Span 2

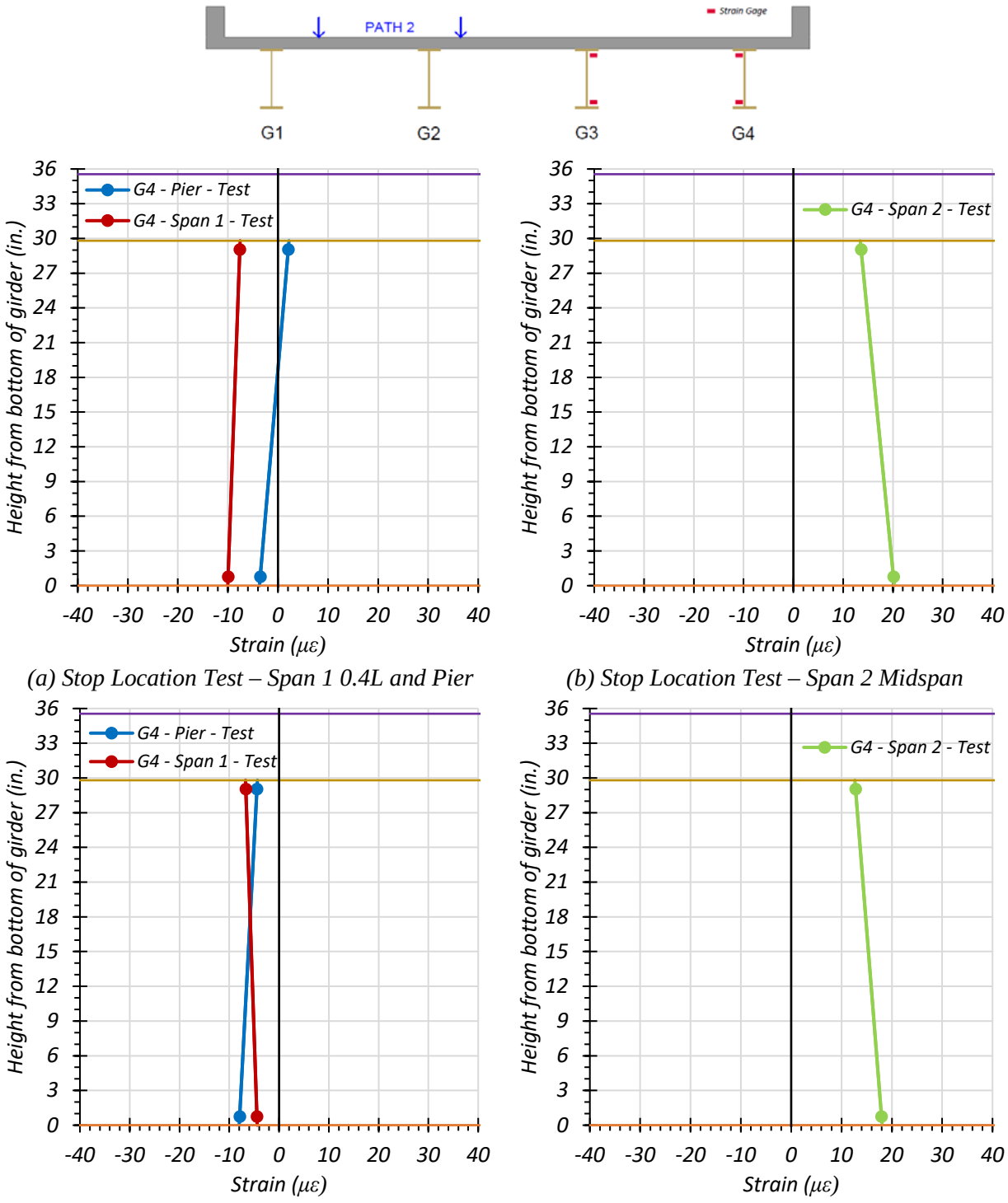

(a) Stop Location Test – Span 1 0.4L and Pier

(b) Stop Location Test – Span 2 Midspan

(c) Crawl Speed Test – Span 1 0.4L and Pier

(d) Crawl Speed Test – Span 2 Midspan

Figure 8.29. Static Strains for Exterior Girder 4 – Path 2 – Span 2

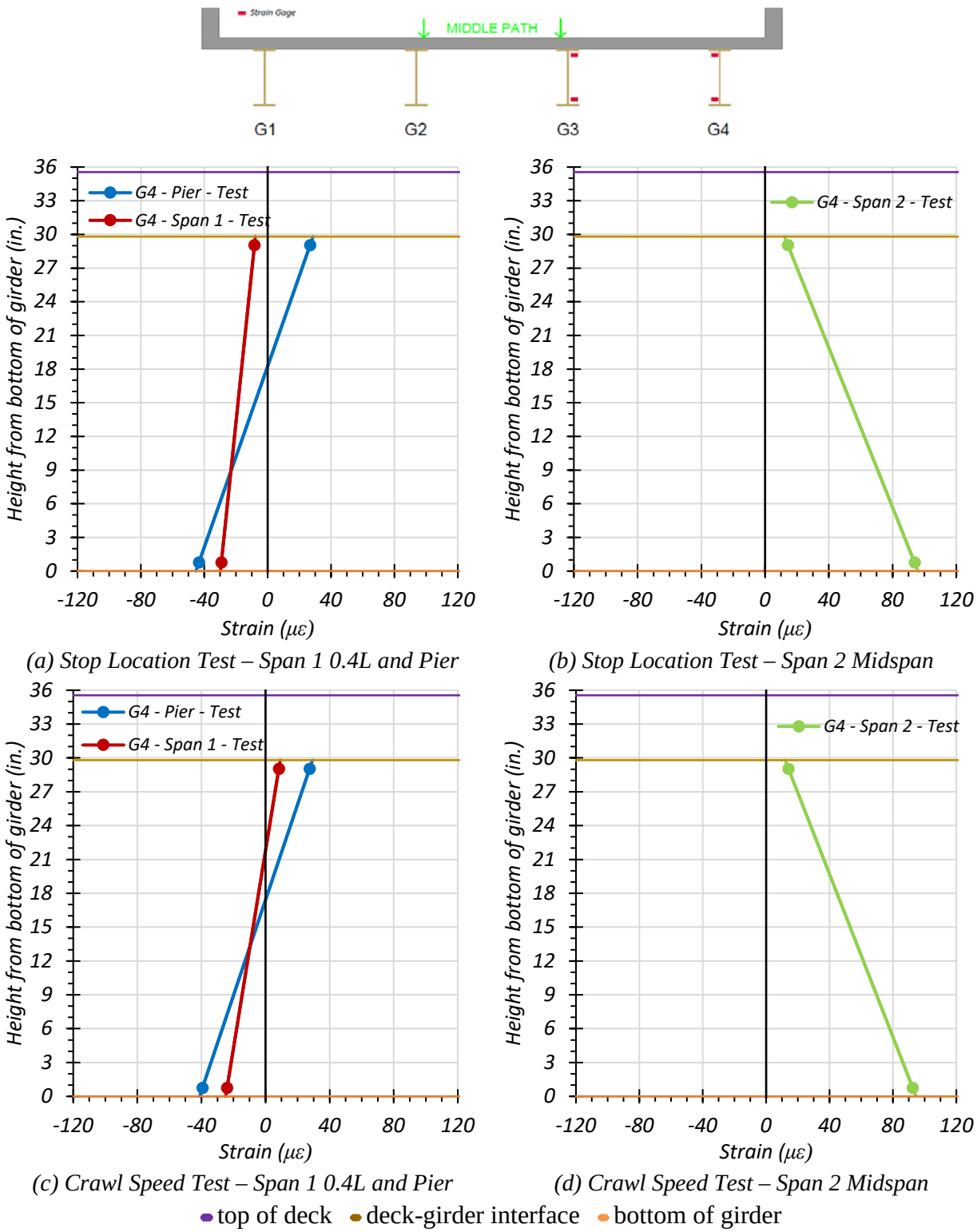

(a) Stop Location Test – Span 1 0.4L and Pier

(b) Stop Location Test – Span 2 Midspan

(c) Crawl Speed Test – Span 1 0.4L and Pier

(d) Crawl Speed Test – Span 2 Midspan

top of deck deck-girder interface bottom of girder

Figure 8.30. Static Strains for Exterior Girder 4 – Middle Path – Span 2

8.6.2.1.3. Comparison of Measured Strain Results

Table 8.12 and Figure 8.31 show the neutral axis locations measured for all static load tests in Span 2. The average test neutral axis value for Girder 3 was 16.88 in. from the bottom of the girder. The test neutral axis that is most meaningful for Girder 4 is 19.76 in. from the bottom of the girder. The neutral axes based on strain measurements during field testing tend to be somewhere in between the theoretical composite and the theoretical non-composite neutral axes, which are based on the parallel axis theorem using the updated geometric material properties determined during testing. This includes an f_c' of 6.25 ksi and a corresponding modulus of elasticity of 4506 ksi. The effective deck width used for an interior girder and for an exterior girder is 69 in., determined using Article 10.38.3 in the AASHTO Standard Specifications (AASHTO 2002). Reinforcing steel is not included in this calculation. This result shows that Bridge SC-12 is likely acting as partially composite. The neutral axis locations observed for Girder 4 under Path 2 loading are quite high. This could be because Girder 4 is receiving very minimal load during Path 2 loading.

Table 8.12. Measured Neutral Axis Locations for All Span 2 Static Load Tests

Test	G3 Neutral Axis Location (in. from bottom of girder)	G4 Neutral Axis Location (in. from bottom of girder)
Path 1 – Stop Location	19.97	19.76
Path 1 – Crawl Speed	19.56	19.85
Path 2 – Stop Location	15.08	88.17
Path 2 – Crawl Speed	15.32	99.15
Middle Path – Stop Location	15.88	34.13
Middle Path – Crawl Speed	15.45	32.76
Theoretical Non-Composite	14.90	14.90
Theoretical Composite – Positive Bending	26.11	26.11
Theoretical Composite – Negative Bending	16.66	16.66

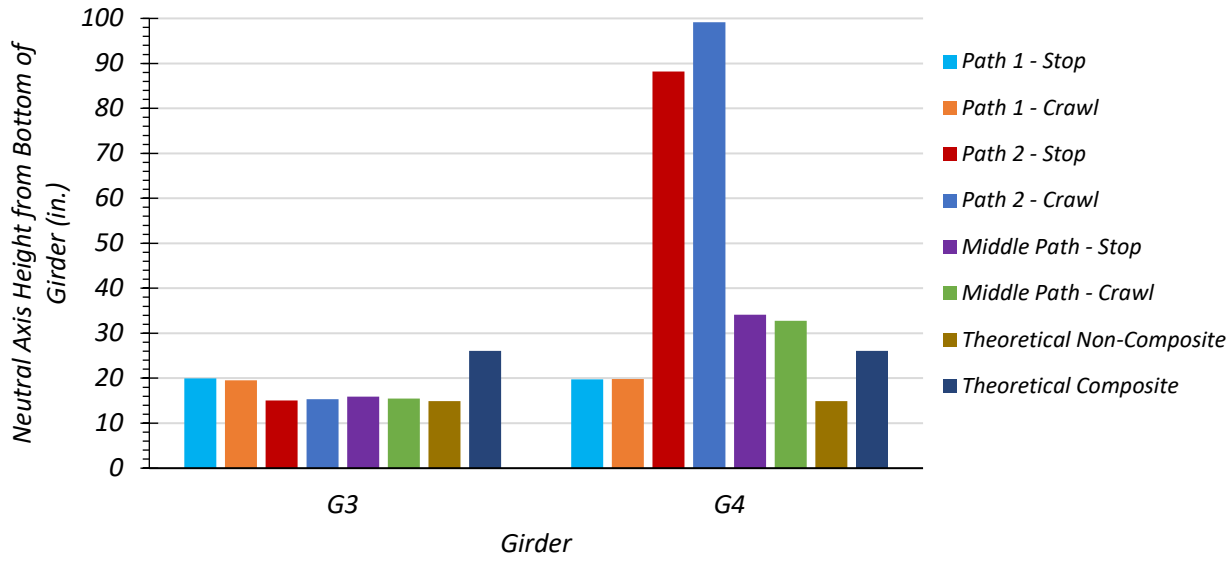

Figure 8.31. Test Neutral Axis Locations for Span 2 Loading

Table 8.13 and Figure 8.32 show the maximum bottom flange stresses observed during Span 2 static testing. The maximum stress in Girder 4 was 7.09 ksi from the Path 1 crawl speed test. The maximum stress in Girder 3 was 4.68 ksi from the Path 1 stop location test. It can be seen that Girder 4 is barely taking any load during the Path 2 load tests, which could explain the unexpectedly high neutral axis values.

Table 8.13. Maximum Test Bottom Flange Stresses (ksi) for Span 2 Loading

Load Path	Interior Girder 3		Exterior Girder 4	
	Stop Location Test	Crawl Speed Test	Stop Location Test	Crawl Speed Test
Path 1	4.68	4.66	6.88	7.09
Path 2	2.94	2.82	0.59	0.52
Middle Path	4.05	4.06	2.78	2.82

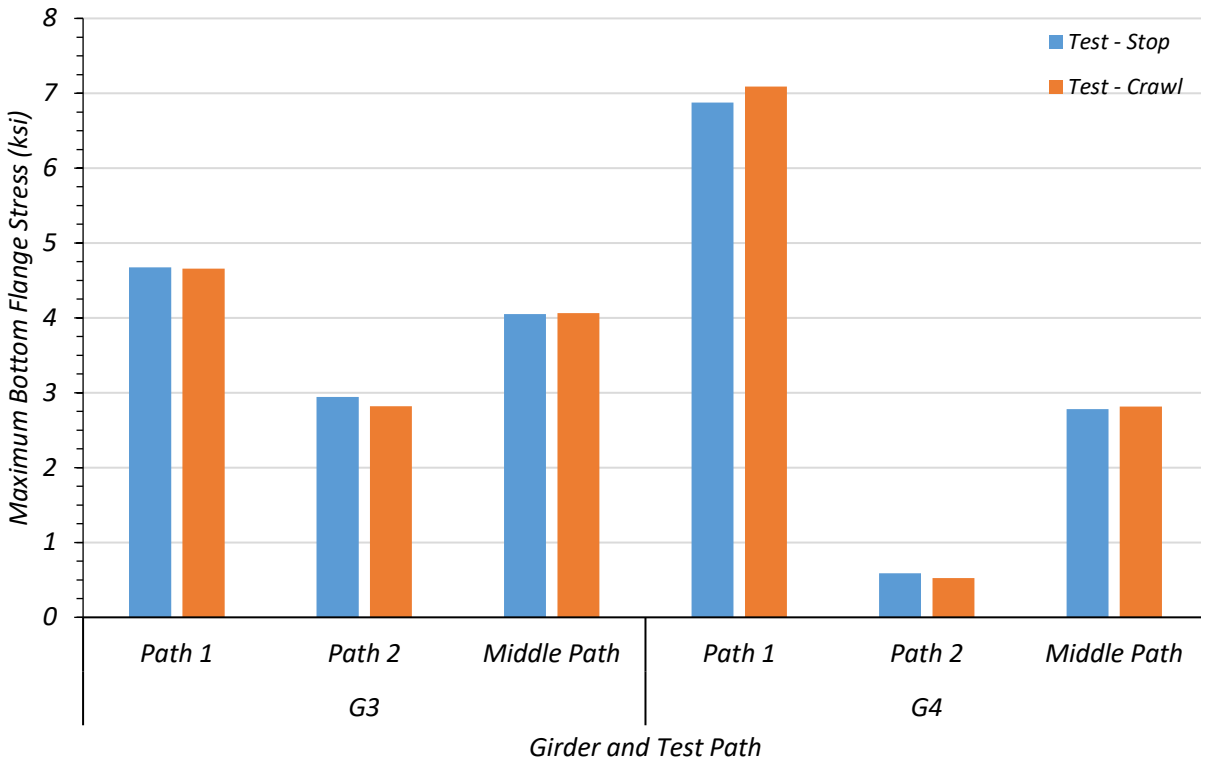

Figure 8.32. Comparison of Test Maximum Bottom Flange Stresses for Span 2 Loading

8.6.2.2. Deflection Measurements and LLDFs

8.6.2.2.1. Path 1 Loading

Table 8.14 shows the measured girder deflections during testing for the stop location test and crawl speed test along Path 1 – Span 2. The associated LLDFs, determined using the measured midspan deflections, are also provided.

Table 8.14. Experimental Midspan Deflections and LLDFs for Path 1 – Span 2 Loading

Girder	G1	G2	G3	G4
Stop Location Test Disp. (in.)	0.049	0.280	0.526	0.755
Stop Location Test LLDF	0.030	0.174	0.327	0.469
Crawl Speed Test Disp. (in.)	0.032	0.260	0.520	0.771
Crawl Speed Test LLDF	0.020	0.164	0.328	0.487
Note: 1 – G = girder, Disp. = Displacement 2 – LLDF values are based on the midspan deflections.				

Table 8.15 compares the test LLDFs to those calculated using the AASHTO Standard Specifications, AASHTO LRFD Specifications determined using the simplified stiffness parameter, and AASHTO LRFD Specifications determined using the analytical stiffness parameter (AASHTO 2002; AASHTO 2017). The maximum g_{AASHTO_Std}/g_{test} ratios are above 1.0, ranging from 1.21 to 1.46. The maximum g_{AASHTO_S}/g_{test} ratios are above 1.0, ranging from 1.30 to 1.41. The maximum g_{AASHTO_K}/g_{test} ratios are above 1.0, ranging from 1.25 to 1.41. This indicates all three of the AASHTO methods to determine LLDFs are conservative for Path 1 – Span 2 loading.

Table 8.15. LLDF Comparison with AASHTO for Path 1 – Span 2 Loading

Test and Girder Type	AASHTO Standard Specs ($g^m_{AASHTO\_Std}$)	AASHTO LRFD Simplified ($g^m_{AASHTO\_S}$)	AASHTO LRFD K_g Calculated ($g^m_{AASHTO\_K}$)	Test (g^m_{test})	$g^m_{AASHTO\_Std}/g^m_{test}$	$g^m_{AASHTO\_S}/g^m_{test}$	$g^m_{AASHTO\_K}/g^m_{test}$
Stop Location Interior	0.476	0.427	0.410	0.327	1.46	1.31	1.25
Stop Location Exterior	0.589	0.660	0.660	0.469	1.26	1.41	1.41
Crawl Speed Interior	0.476	0.427	0.410	0.328	1.45	1.30	1.25
Crawl Speed Exterior	0.589	0.660	0.660	0.487	1.21	1.36	1.36

Figure 8.33(a) and Figure 8.33(c) show the Path 1 – Span 2 stop location and crawl speed test girder deflection profiles. Figure 8.33(b) and Figure 8.33(d) show the Path 1 – Span 2 stop location and crawl speed LLDFs compared to relevant AASHTO values. The governing LLDFs observed during testing are significantly lower than the LLDFs provided by the AASHTO Standard Specifications, the AASHTO LRFD Specification LLDFs using the simplified stiffness parameter, and the AASHTO LRFD Specification LLDFs using the analytical stiffness parameter.

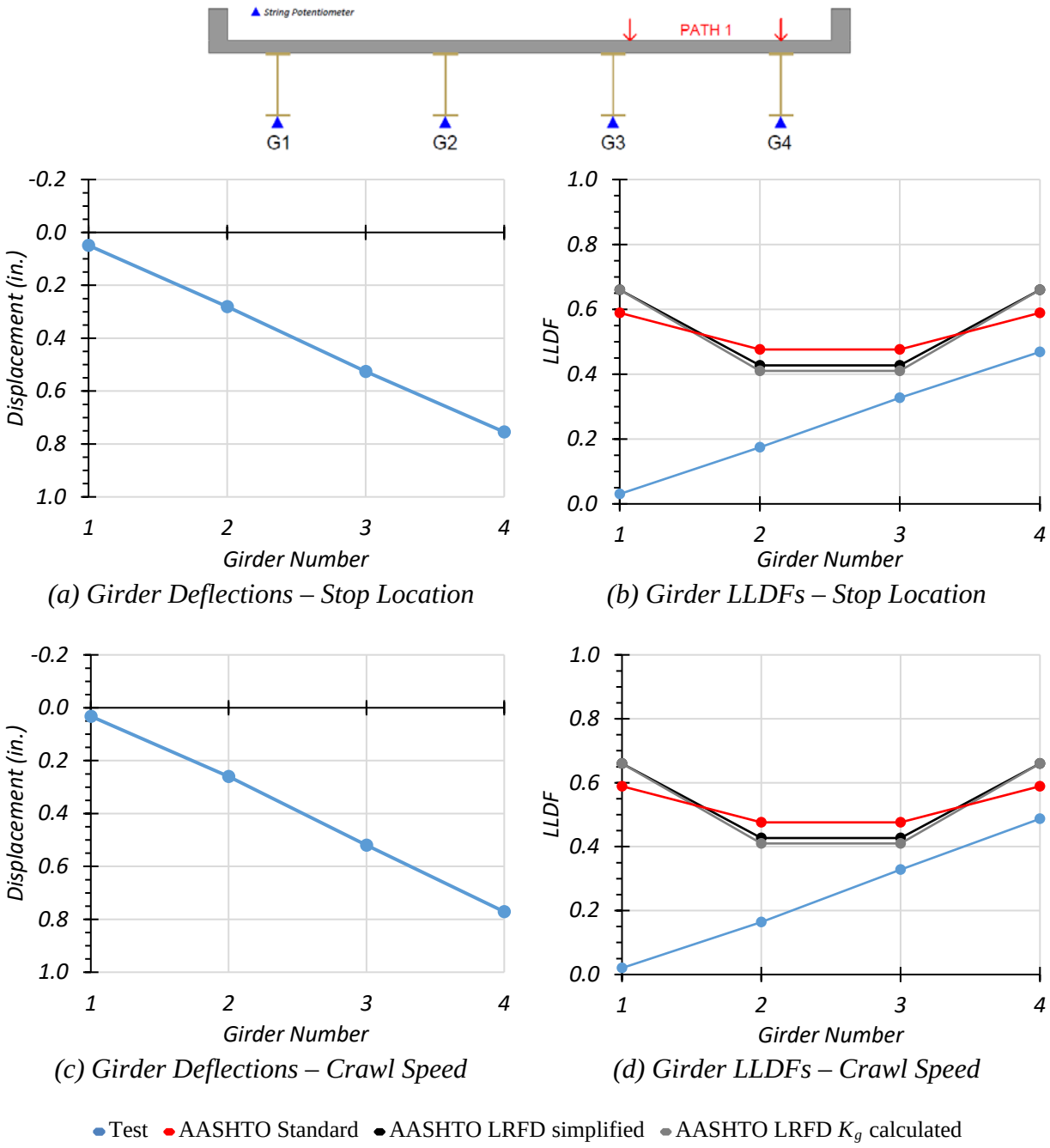

(a) Girder Deflections – Stop Location

(b) Girder LLDFs – Stop Location

(c) Girder Deflections – Crawl Speed

(d) Girder LLDFs – Crawl Speed

Figure 8.33. Static Deflection Results for Path 1 – Span 2 Loading

8.6.2.2.2. Path 2 Loading

Table 8.16 shows the measured girder deflections during testing for the stop location test and crawl speed test along Path 2 – Span 2. The associated LLDFs, determined using the measured midspan deflections, are also provided.

Table 8.16. Experimental Midspan Deflections and LLDFs for Path 2 – Span 2 Loading

Description	G1	G2	G3	G4
Stop Location Test Disp. (in.)	0.692	0.556	0.298	0.077
Stop Location Test LLDF	0.427	0.343	0.184	0.047
Crawl Speed Test Disp. (in.)	0.693	0.537	0.279	0.060
Crawl Speed Test LLDF	0.442	0.342	0.178	0.038
Note: 1 – G = girder, Disp. = Displacement 2 – LLDF values are based on the midspan deflections.				

Table 8.17 compares the test LLDFs to those calculated using the AASHTO Standard Specifications, AASHTO LRFD Specifications determined using the simplified stiffness parameter, and AASHTO LRFD Specifications determined using the analytical stiffness parameter (AASHTO 2002; AASHTO 2017). The maximum g_{AASHTO_Std}/g_{test} ratios are above 1.0, ranging from 1.33 to 1.39. The maximum g_{AASHTO_S}/g_{test} ratios are above 1.0, ranging from 1.24 to 1.55. The maximum g_{AASHTO_K}/g_{test} ratios are above 1.0, ranging from 1.20 to 1.55. This indicates all three of the AASHTO methods to determine LLDFs are conservative for Path 2 – Span 2 loading.

Table 8.17. LLDF Comparison with AASHTO for Path 2 – Span 2 Loading

Test and Girder Type	AASHTO Standard Specs ($g^m_{AASHTO\_Std}$)	AASHTO LRFD Simplified ($g^m_{AASHTO\_S}$)	AASHTO LRFD K_g Calculated ($g^m_{AASHTO\_K}$)	Test (g^m_{test})	$g^m_{AASHTO\_Std}/g^m_{test}$	$g^m_{AASHTO\_S}/g^m_{test}$	$g^m_{AASHTO\_K}/g^m_{test}$
Stop Location Interior	0.476	0.427	0.410	0.343	1.39	1.24	1.20
Stop Location Exterior	0.589	0.660	0.660	0.427	1.38	1.55	1.55
Crawl Speed Interior	0.476	0.427	0.410	0.342	1.39	1.25	1.20
Crawl Speed Exterior	0.589	0.660	0.660	0.442	1.33	1.49	1.49

Figure 8.34(a) and Figure 8.34(c) show the Path 2 – Span 2 stop location and crawl speed test girder deflection profiles. Figure 8.34(b) and Figure 8.34(d) show the Path 2 – Span 2 stop location and crawl speed LLDFs compared to relevant AASHTO values. The governing LLDFs observed during testing are significantly lower than the LLDFs provided by the AASHTO Standard Specifications, the AASHTO LRFD Specification LLDFs using the simplified stiffness parameter, and the AASHTO LRFD Specification LLDFs using the analytical stiffness parameter.

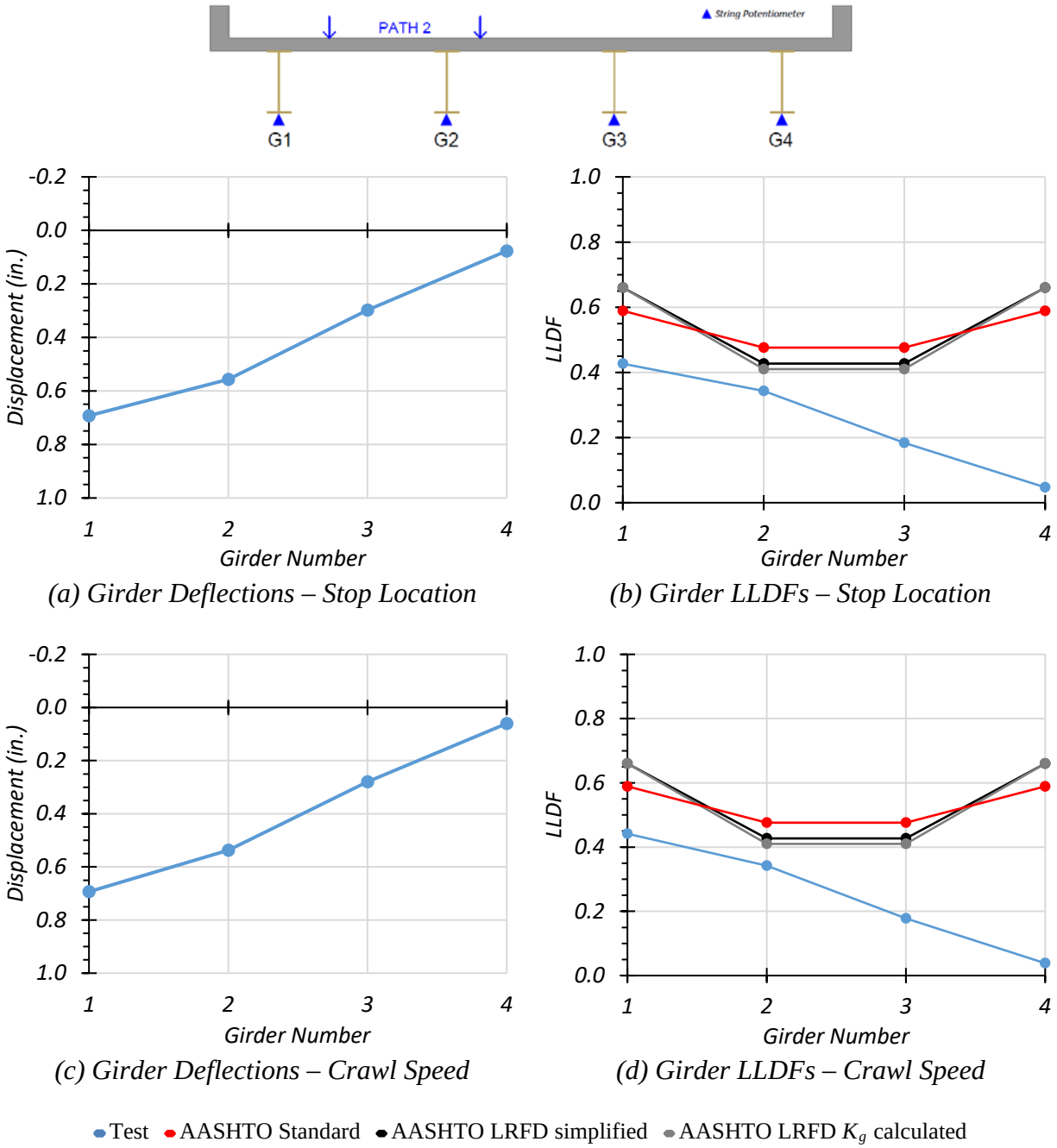

(a) Girder Deflections – Stop Location

(b) Girder LLDFs – Stop Location

(c) Girder Deflections – Crawl Speed

(d) Girder LLDFs – Crawl Speed

Figure 8.34. Static Deflection Results for Path 2 – Span 2 Loading

8.6.2.2.3. Middle Path Loading

Table 8.18 shows the measured girder deflections during testing for the Middle Path – Span 2 stop location test. The associated LLDFs, determined using the measured midspan deflections, are also provided.

Table 8.18. Experimental Midspan Deflections and LLDFs for Middle Path – Span 2 Loading

Description	G1	G2	G3	G4
Stop Location Test Disp. (in.)	0.328	0.457	0.440	0.353
Stop Location Test LLDF	0.208	0.289	0.279	0.224
Crawl Speed Test Disp. (in.)	0.313	0.444	0.436	0.355
Crawl Speed Test LLDF	0.202	0.287	0.281	0.229
Note: 1 – G = girder, Disp. = Displacement 2 – LLDF values are based on the midspan deflections.				

Table 8.19 compares the test LLDFs to those calculated using the AASHTO Standard Specifications, AASHTO LRFD Specifications with the simplified stiffness parameter, and AASHTO LRFD Specifications with the analytical stiffness parameter (AASHTO 2002; AASHTO 2017). The maximum g_{AASHTO_Std}/g_{test} ratios are above 1.0, ranging from 1.65 to 2.63. The maximum g_{AASHTO_S}/g_{test} ratios are above 1.0, ranging from 1.48 to 2.95. The maximum g_{AASHTO_K}/g_{test} ratios are above 1.0, ranging from 1.42 to 2.95. This indicates all three of the AASHTO methods to determine LLDFs are conservative for Middle Path – Span 2 loading.

Table 8.19. LLDF Comparison with AASHTO for Middle Path – Span 2 Loading

Test and Girder Type	AASHTO Standard Specs ($g^m_{AASHTO\_Std}$)	AASHTO LRFD Simplified ($g^m_{AASHTO\_S}$)	AASHTO LRFD K_g Calculated ($g^m_{AASHTO\_K}$)	Test (g^m_{test})	$g^m_{AASHTO\_Std}/g^m_{test}$	$g^m_{AASHTO\_S}/g^m_{test}$	$g^m_{AASHTO\_K}/g^m_{test}$
Stop Location Interior	0.476	0.427	0.410	0.289	1.65	1.48	1.42
Stop Location Exterior	0.589	0.660	0.660	0.224	2.63	2.95	2.95
Crawl Speed Interior	0.476	0.427	0.410	0.287	1.66	1.49	1.43
Crawl Speed Exterior	0.589	0.660	0.660	0.229	2.57	2.88	2.88

Figure 8.35(a) and Figure 8.35(c) show the Middle Path – Span 2 stop location and crawl speed test girder deflection profiles. Figure 8.35(b) and Figure 8.35(d) show the Middle Path – Span 2 stop location and crawl speed LLDFs compared to relevant AASHTO values. The governing LLDFs observed during testing are significantly lower than the LLDFs provided by the AASHTO Standard Specifications, the AASHTO LRFD Specifications LLDFs using the simplified stiffness parameter, and the AASHTO LRFD Specifications LLDFs using the analytical stiffness parameter.

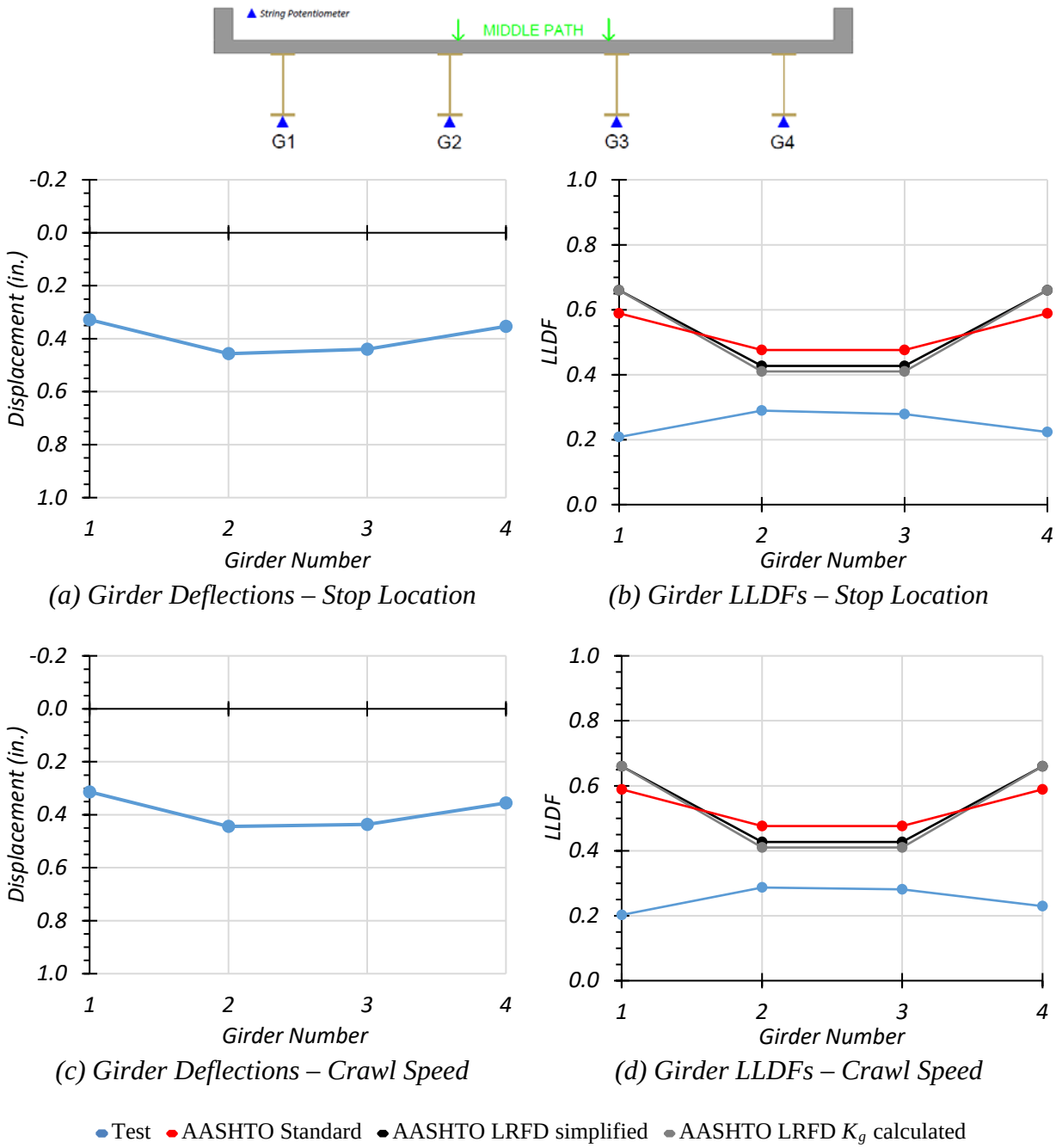

(a) Girder Deflections – Stop Location

(b) Girder LLDFs – Stop Location

(c) Girder Deflections – Crawl Speed

(d) Girder LLDFs – Crawl Speed

Figure 8.35. Static Deflection Results for Middle Path – Span 2 Loading

8.6.2.2.4. Comparison of Results Based on Deflection Measurements

For Span 2 when considering the midspan deflections, the critical LLDF for an exterior girder was 0.487, which was observed during the crawl speed test along Path 1. This corresponds to a g_{AASHTO}/g_{test} ratio of 1.21 when using the AASHTO Standard Specifications, 1.36 when using the AASHTO LRFD Specifications determined using the simplified stiffness parameter, and 1.36 when using the AASHTO LRFD Specifications determined using the analytical stiffness parameter. The critical LLDF for an interior girder was 0.343, observed during the stop location test along Path 2. This corresponds to a g_{AASHTO}/g_{test} ratio of 1.39 when using the AASHTO Standard Specifications, 1.24 when using the AASHTO LRFD Specifications determined using the simplified stiffness parameter, and 1.20 when using the AASHTO LRFD Specifications determined using the analytical stiffness parameter. During the static load tests along Path 1, the maximum LLDF was 0.469 for stop location test while increasing to 0.487 for the crawl speed test. During the static load tests along Path 2, the maximum LLDF was 0.427 for the stop location test while decreasing to 0.442 for the crawl speed test. During the static load tests along Middle Path, the maximum LLDF of 0.289 for stop location test while decreasing slightly to 0.287 for the crawl speed test.

Overall, none of the AASHTO methods to determine LLDFs produced lower values than the LLDFs observed during Span 2 testing. The AASHTO methods were always conservative for Bridge SC-12, and in most cases by a significant margin. This could possibly be an area through which the load rating for Bridge SC-12 could improve.

8.6.3. Pier Location Strains and Negative Moment LLDFS

Using the strain gauges attached to the top flange of each of the four girders at the location adjacent to the interior support within span 2, negative moment region LLDFs were determined. The strains used for the LLDF calculations were taken from the same point in time as when the critical girder felt the maximum effect during the crawl speed test for each loading path. Only the crawl speed test was examined as it is unknown if the stop location test is the truck location that will produce the maximum negative moment. The crawl speed test covers every possible longitudinal location on the bridge, therefore ensuring that the maximum possible negative moment will be experienced.

Table 8.20 shows the measured pier location strains for the Path 1 crawl test. The associated LLDFs, determined using the measured strains, are also provided.

Table 8.20. Pier Location Experimental Strains and LLDFs for Path 1 Crawl Speed Loading

Description	G1	G2	G3	G4
Test Strain (με)	-2.7	25.9	65.2	100.8
Test LLDF	0.014	0.137	0.345	0.533
Note: 1 – G = girder, Disp. = Displacement 2 – LLDF values are based on the top flange strains.				

Table 8.21 compares the test LLDFs to those calculated using the AASHTO Standard Specifications, AASHTO LRFD Specifications determined using the simplified stiffness parameter, and AASHTO LRFD Specifications determined using the analytical stiffness parameter. All three g_{AASHTO}/g_{test} ratios were above 1.0 for both interior and exterior girders. For an interior girder, the g_{AASHTO_Std}/g_{test} ratio of 1.38 was most conservative, while the g_{AASHTO_K}/g_{test} ratio of 1.23 was least conservative. For an exterior girder, the g_{AASHTO_S}/g_{test}

and g_{AASHTO_K}/g_{test} ratios of 1.24 were most conservative, while the g_{AASHTO_Std}/g_{test} ratio of 1.11 was least conservative.

Table 8.21. Negative Moment Region LLDF Comparison with AASHTO for Path 1 Crawl Speed Loading

Girder Type	AASHTO Standard Specs ($g^m_{AASHTO\_Std}$)	AASHTO LRFD Simplified ($g^m_{AASHTO\_S}$)	AASHTO LRFD K_g Calculated ($g^m_{AASHTO\_K}$)	Test (g^m_{test})	$g^m_{AASHTO\_Std}/g^m_{test}$	$g^m_{AASHTO\_S}/g^m_{test}$	$g^m_{AASHTO\_K}/g^m_{test}$
Interior	0.476	0.439	0.425	0.345	1.38	1.27	1.23
Exterior	0.589	0.660	0.660	0.533	1.11	1.24	1.24

Figure 8.36(a) and Figure 8.36(b) show the Path 1 strain values for each girder and the associated LLDFs compared to relevant AASHTO values. The governing LLDFs observed during testing are lower than the LLDFs provided by the AASHTO Standard Specifications, the AASHTO LRFD Specifications LLDFs using the simplified stiffness parameter, and the AASHTO LRFD Specifications LLDFs using the analytical stiffness parameter.

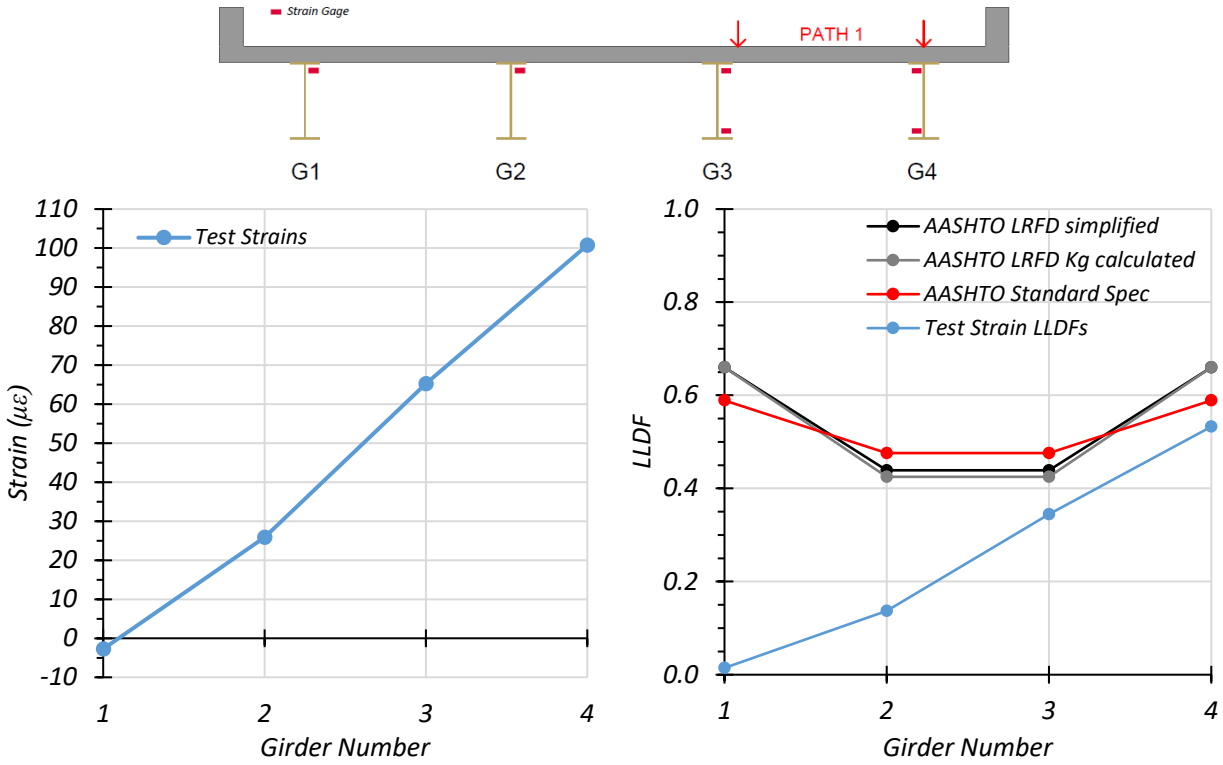

(a) Girder Top Flange Strains *(b) Girder Negative Moment Region LLDFs*

Figure 8.36. Pier Location Results for Path 1 Crawl Speed Loading

Table 8.22 shows the measured pier location strains for the Path 2 crawl test. The associated LLDFs, determined using the measured strains, are also provided.

Table 8.22. Pier Location Experimental Strains and LLDFs for Path 2 Crawl Speed Loading

Description	G1	G2	G3	G4
Test Strain (με)	97.2	70.2	33.1	-3.4
Test LLDF	0.493	0.356	0.168	0.017
Note: 1 – G = girder, Disp. = Displacement 2 – LLDF values are based on the top flange strains.				

Table 8.23 compares the test LLDFs to those calculated using the AASHTO Standard Specifications, AASHTO LRFD Specifications with the simplified stiffness parameter, and

AASHTO LRFD Specifications with the analytical stiffness parameter. All three g_{AASHTO}/g_{test} ratios were above 1.0 for both interior and exterior girders. For an interior girder, the g_{AASHTO_Std}/g_{test} ratio of 1.34 was most conservative, while the g_{AASHTO_K}/g_{test} ratio of 1.19 was least conservative. For an exterior girder, the g_{AASHTO_S}/g_{test} and g_{AASHTO_K}/g_{test} ratios of 1.34 were most conservative, while the g_{AASHTO_Std}/g_{test} ratio of 1.19 was least conservative.

Table 8.23. Negative Moment Region LLDF Comparison with AASHTO for Path 2 Crawl Speed Loading

Girder Type	AASHTO Standard Specs ($g^m_{AASHTO\_Std}$)	AASHTO LRFD Simplified ($g^m_{AASHTO\_S}$)	AASHTO LRFD K_g Calculated ($g^m_{AASHTO\_K}$)	Test (g^m_{test})	$g^m_{AASHTO\_Std}/g^m_{test}$	$g^m_{AASHTO\_S}/g^m_{test}$	$g^m_{AASHTO\_K}/g^m_{test}$
Interior	0.476	0.439	0.425	0.356	1.34	1.23	1.19
Exterior	0.589	0.660	0.660	0.493	1.19	1.34	1.34

Figure 8.37(a) and Figure 8.37(b) show the Path 2 strain values for each girder and the associated LLDFs compared to relevant AASHTO values as well as values. The governing LLDFs observed during testing are significantly lower than the LLDFs provided by the AASHTO Standard Specifications, the AASHTO LRFD Specification LLDFs using the simplified stiffness parameter, and the AASHTO LRFD Specification LLDFs using the analytical stiffness parameter.

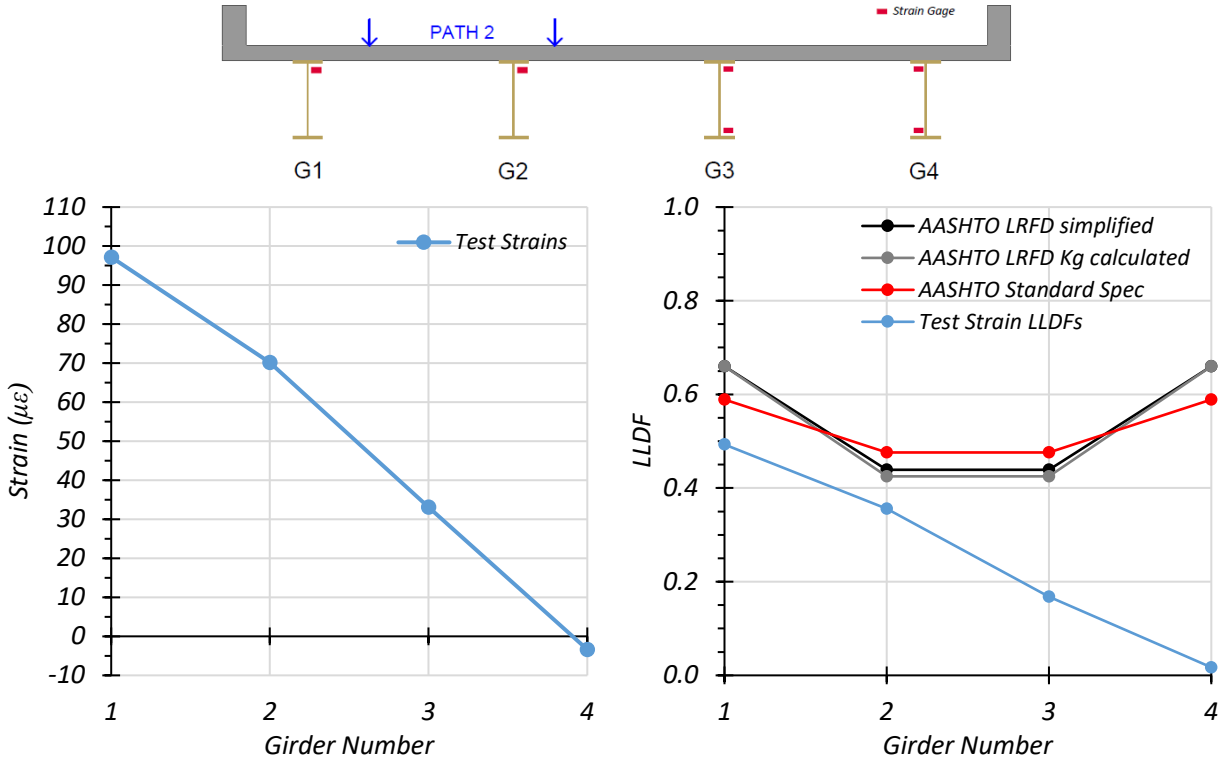

(a) Girder Top Flange Strains *(b) Girder Negative Moment Region LLDFs*

Figure 8.37. Pier Location Results for Path 2 Crawl Speed Loading

Table 8.24 shows the measured pier location strains for the Middle Path crawl test. The associated LLDFs, determined using the measured strains, are also provided.

Table 8.24. Pier Location Experimental Strains and LLDFs for Middle Path Crawl Speed Loading

Description	G1	G2	G3	G4
Test Strain (με)	39.3	55.0	54.6	27.0
Test LLDF	0.223	0.313	0.310	0.154
Note: 1 – G = girder, Disp. = Displacement 2 – LLDF values are based on the top flange strains.				

Table 8.25 compares the test LLDFs to those calculated using the AASHTO Standard Specifications, LRFD Specifications with the simplified stiffness parameter, and LRFD

Specifications with the analytical stiffness parameter. All three g_{AASHTO}/g_{test} ratios were above 1.0 for both interior and exterior girders. For an interior girder, the g_{AASHTO_Std}/g_{test} ratio of 1.52 was most conservative, while the g_{AASHTO_K}/g_{test} ratio of 1.36 was least conservative. For an exterior girder, the g_{AASHTO_S}/g_{test} and g_{AASHTO_K}/g_{test} ratios of 2.96 were most conservative, while the g_{AASHTO_Std}/g_{test} ratio of 2.64 was least conservative.

Table 8.25. Negative Moment Region LLDF Comparison with AASHTO for Middle Path Crawl Speed Loading

Girder Type	AASHTO Standard Specs ($g^m_{AASHTO\_Std}$)	AASHTO LRFD Simplified ($g^m_{AASHTO\_S}$)	AASHTO LRFD K_g Calculated ($g^m_{AASHTO\_K}$)	Test (g^m_{test})	$g^m_{AASHTO\_Std}/g^m_{test}$	$g^m_{AASHTO\_S}/g^m_{test}$	$g^m_{AASHTO\_K}/g^m_{test}$
Interior	0.476	0.439	0.425	0.313	1.52	1.40	1.36
Exterior	0.589	0.660	0.660	0.223	2.64	2.96	2.96

Figure 8.38(a) and Figure 8.38(b) show the Middle Path strain values for each girder and the associated LLDFs compared to relevant AASHTO values as well as values. The governing LLDFs observed during testing are significantly lower than the LLDFs provided by the AASHTO Standard Specifications, the AASHTO LRFD Specification LLDFs using the simplified stiffness parameter, and the AASHTO LRFD Specification LLDFs using the analytical stiffness parameter.

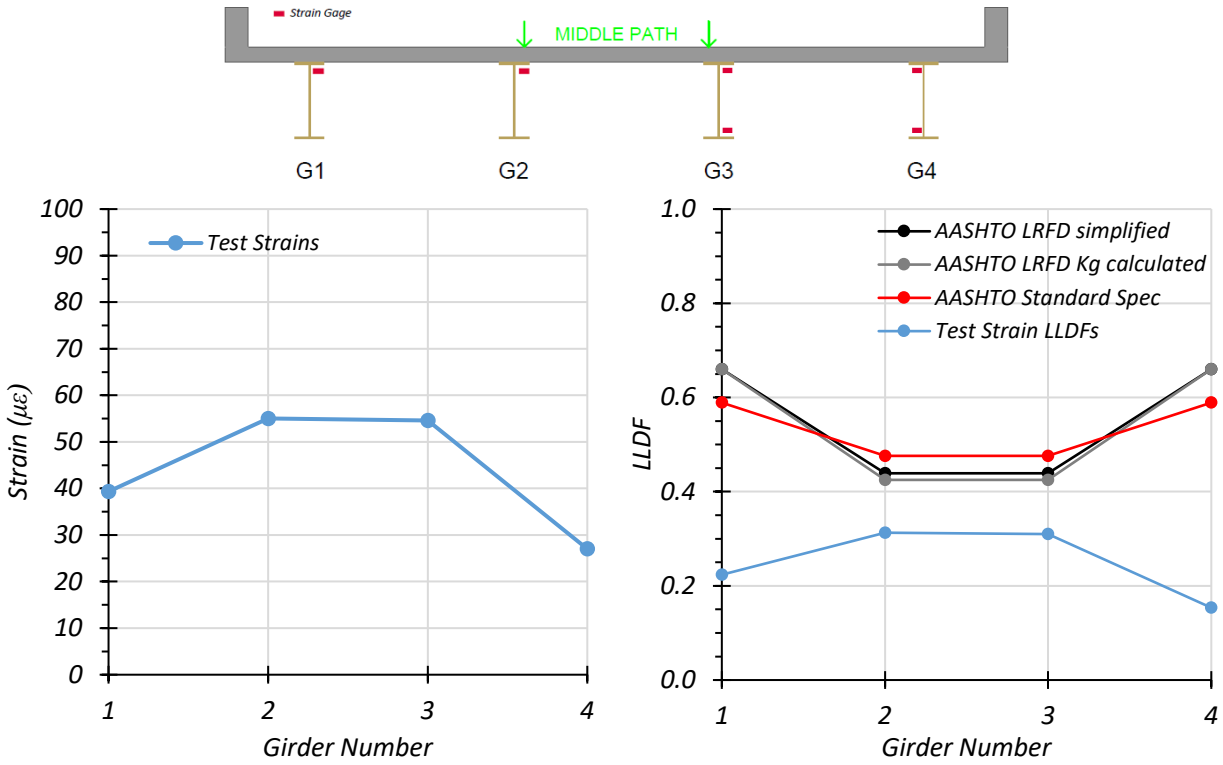

(a) Girder Top Flange Strains *(b) Girder Negative Moment Region LLDFs*

Figure 8.38. Pier Location Results for Middle Path Crawl Speed Loading

In the negative moment region, the critical LLDF for an exterior girder was 0.553 that was observed during the crawl speed test along Path 1. The critical LLDF for an interior girder was 0.356, observed during the crawl speed test along Path 2. These values were less than all of the AASHTO LLDF equations. For the critical interior girder, the g_{AASHTO}/g_{test} ratio was 1.34, 1.23, and 1.19 when considering the AASHTO Standard Specifications, the AASHTO LRFD Specifications with simplified stiffness parameter, and the AASHTO LRFD Specifications with analytical stiffness parameter, respectively. For the critical exterior girder, the g_{AASHTO}/g_{test} ratio was 1.11, 1.24, and 1.24 when considering the AASHTO Standard Specifications, the AASHTO LRFD Specifications with simplified stiffness parameter, and the AASHTO LRFD Specifications with analytical stiffness parameter, respectively.

8.6.4. Curb Strains for Bridge SC-12

Strain gauge data was also obtained from gauges attached to the top of the deck and the top of the curb at midspan of the main span (Span 2). These gauges were used to identify if the curb was taking any load and thereby participating in the resistance. Figure 8.39 shows the maximum compressive strain for the top of the curb observed during the crawl speed test and the corresponding top of deck strain for all three load paths. The data indicates, specifically for Path 1 and Middle Path loading, the curb is participating in the load carrying of the bridge. Therefore, in future FEM models of Bridge SC-12, the curb was included.

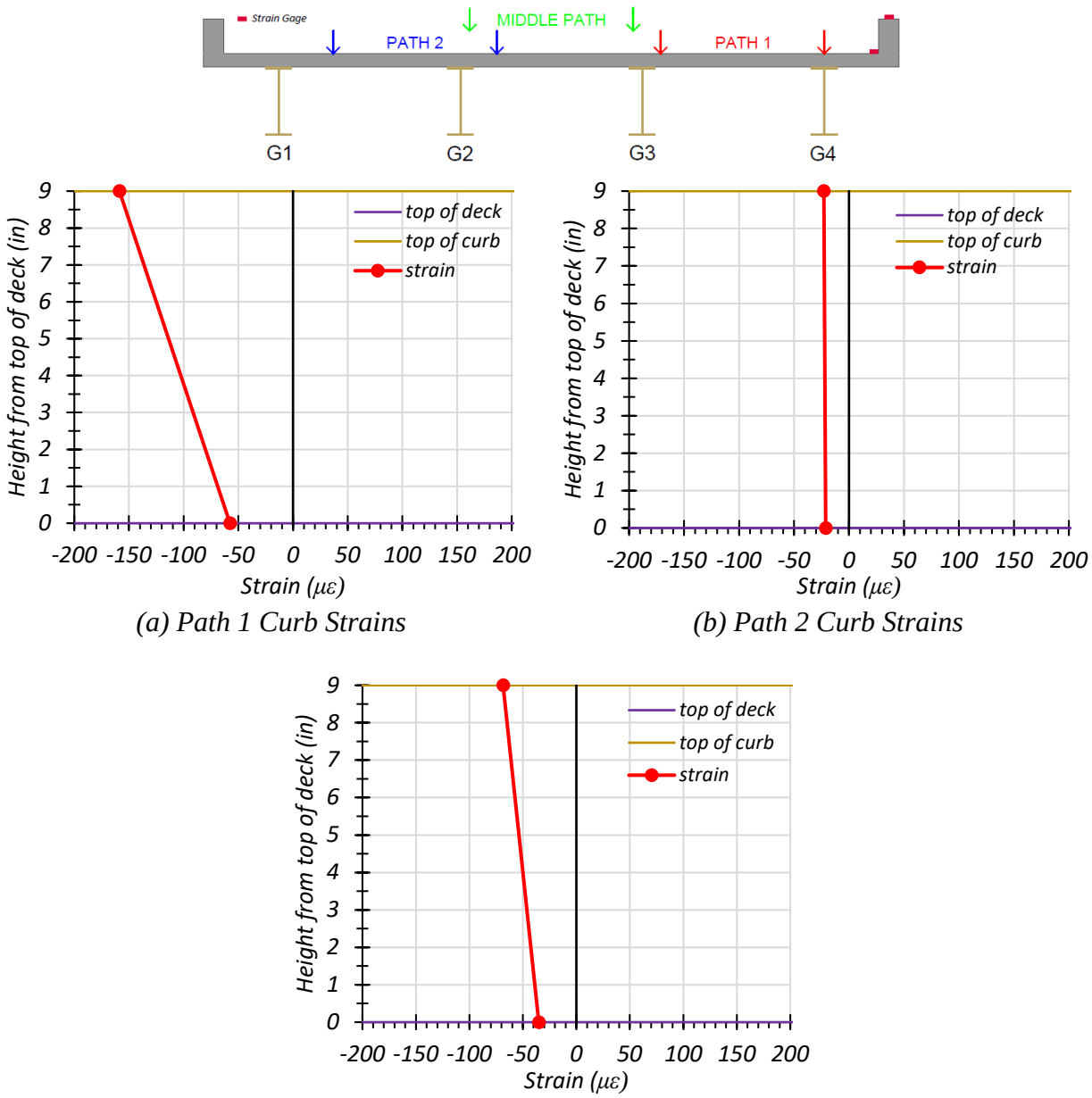

(a) Path 1 Curb Strains

(b) Path 2 Curb Strains

(c) Middle Path Curb Strains

Figure 8.39. Curbs Strains for Loading of All Paths

8.6.5. Dynamic Load Tests on Bridge SC-12

8.6.5.1. Span 1 Dynamic Amplification

8.6.5.1.1. Maximum Girder Strains

From the results of the static and dynamic tests for each path, the increases in strains and deflections due to the moving vehicle were examined. Figure 8.40, Figure 8.41, and Figure 8.42 show the maximum Span 1 dynamic strains observed for Path 1, Path 2, and the Middle Path, respectively, plotted with the static strains observed for those paths. Figure 8.43 shows those strain values and compares them to the appropriate static load case for Span 1.

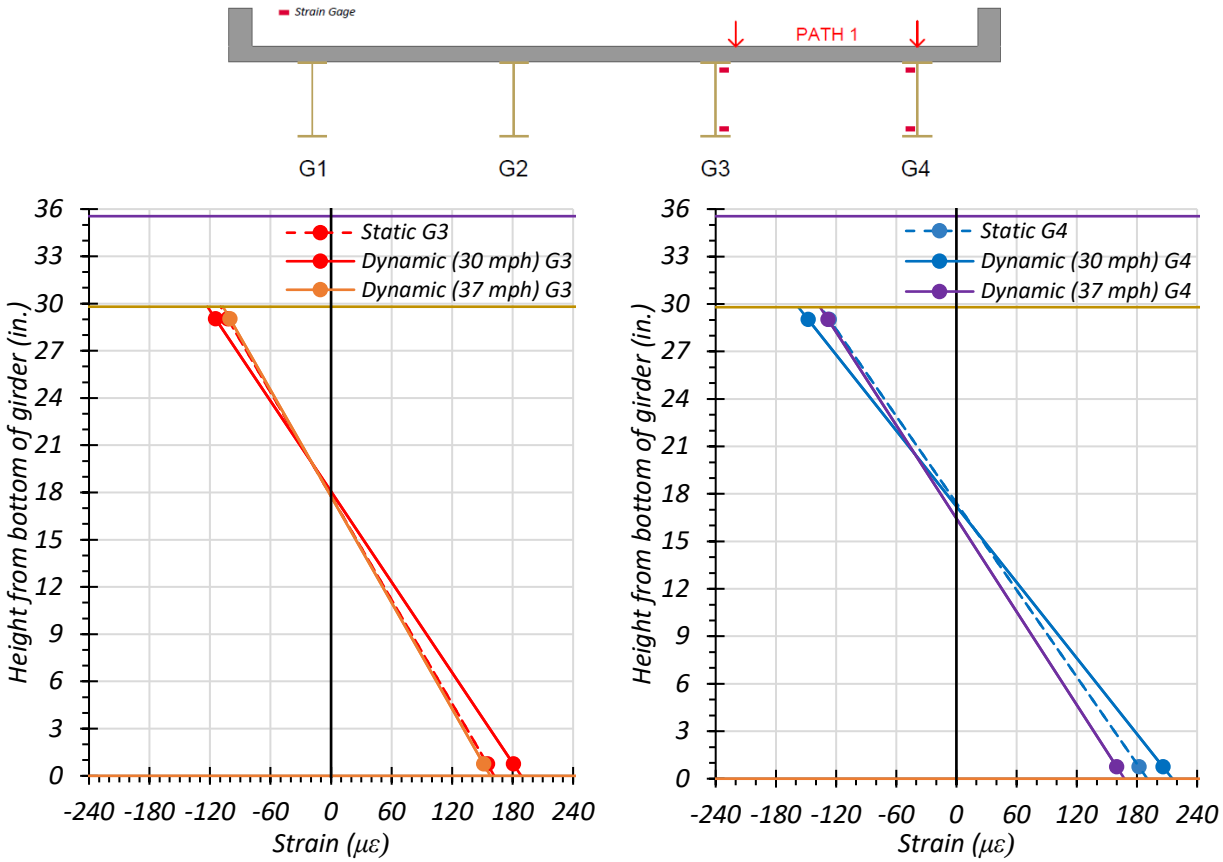

(a) Girder 3 *(b) Girder 4*

top of deck deck-girder interface bottom of girder

Figure 8.40. Maximum Strains for Static and Dynamic Tests for Path 1 – Span 1 Loading

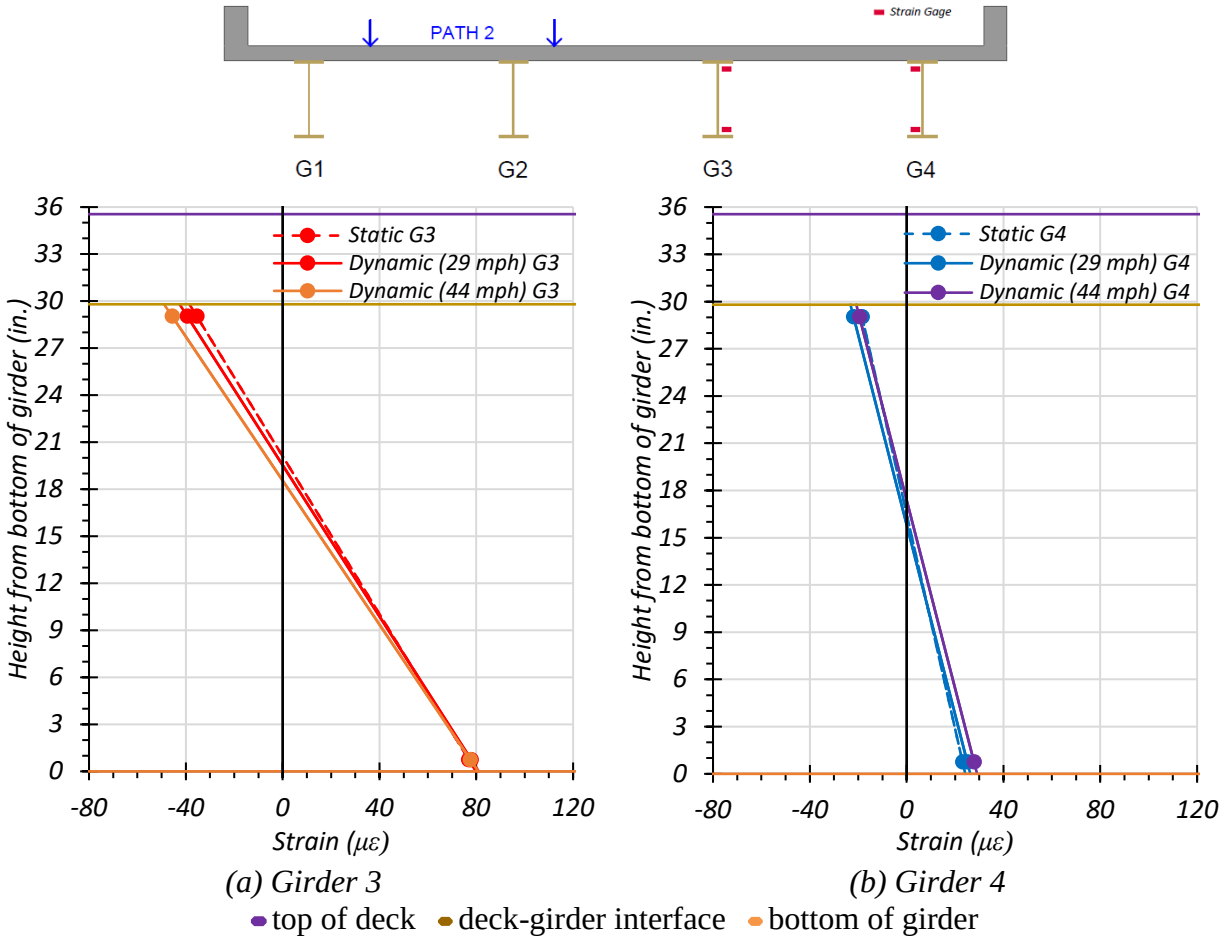

(a) Girder 3 *(b) Girder 4*

top of deck deck-girder interface bottom of girder

Figure 8.41. Maximum Strains for Static and Dynamic Tests for Path 2 – Span 1 Loading

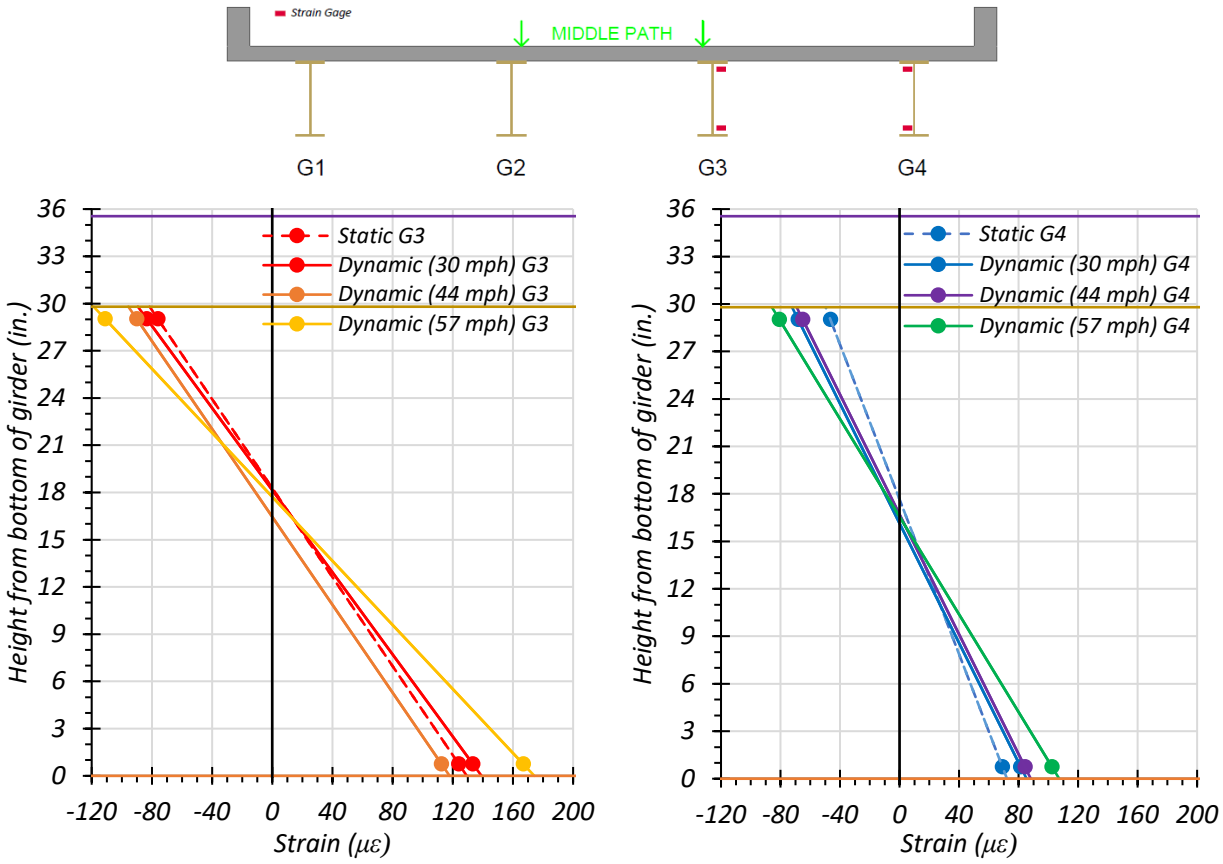

(a) Girder 3 *(b) Girder 4*

top of deck deck-girder interface bottom of girder

Figure 8.42. Maximum Strains for Static and Dynamic Tests for Middle Path – Span 1 Loading

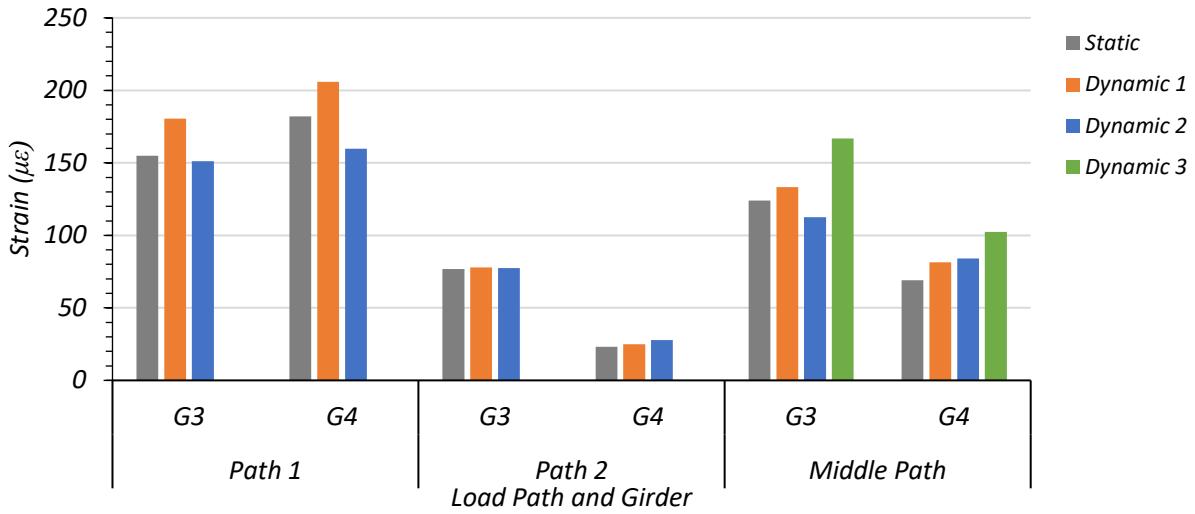

Note:

- *Path 1: Dynamic 1 = 30 mph, Dynamic 2 = 37 mph*
- *Path 2: Dynamic 1 = 29 mph, Dynamic 2 = 44 mph*
- *Middle Path: Dynamic 1 = 30 mph, Dynamic 2 = 44 mph, Dynamic 3 = 57 mph*

Figure 8.43. Comparison of Maximum Bottom Flange Strains for Static and Dynamic Tests in Span 1

The dynamic impact factor given by the AASHTO Standard Specifications for Span 1 of Bridge SC-12 is 27 percent while the dynamic impact factor given by the AASHTO LRFD Specifications for Span 1 is 33 percent. The average dynamic impact factor for all girders for Span 1 based on the strain values observed during testing was 12 percent. The impact factor is more significant for the girders providing the majority of the load resistance. This is seen through the strain increase in Girders 3 and 4 for Dynamic 1 and in Girder 3 for Dynamic 3. However, both Girders 3 and 4 were essentially unaffected by the dynamic impact during Path 2 loading.

8.6.5.1.2. Maximum Girder Deflections

Figure 8.44, Figure 8.45, Figure 8.46, and Figure 8.47 show the Span 1 girder deflection time histories for the dynamic load cases along Path 1, Path 2, and the Middle Path, respectively, for each dynamic loading. Table 8.26 shows the maximum measured girder deflections for the stop

location load case and for each dynamic load case. Figure 8.48 shows the Span 1 static and dynamic maximum deflection values and compares them. Figure 8.49 shows the dynamic effect based on deflection as a ratio to the static deflection.

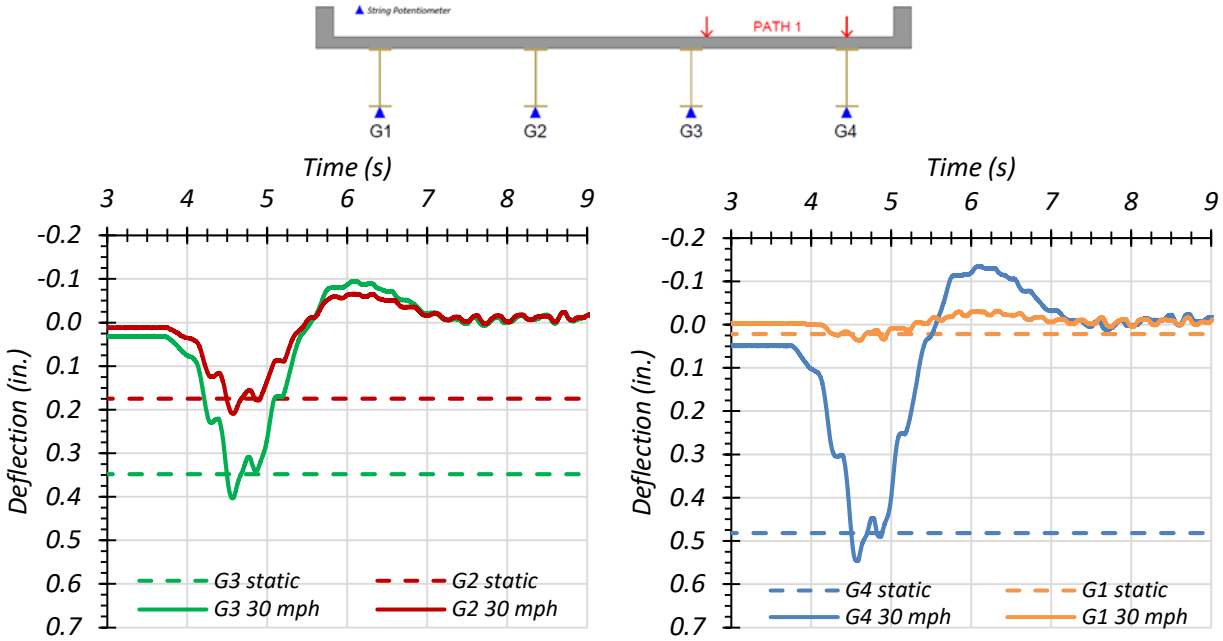

(a) Deflection Time Histories – Dynamic (30 mph)

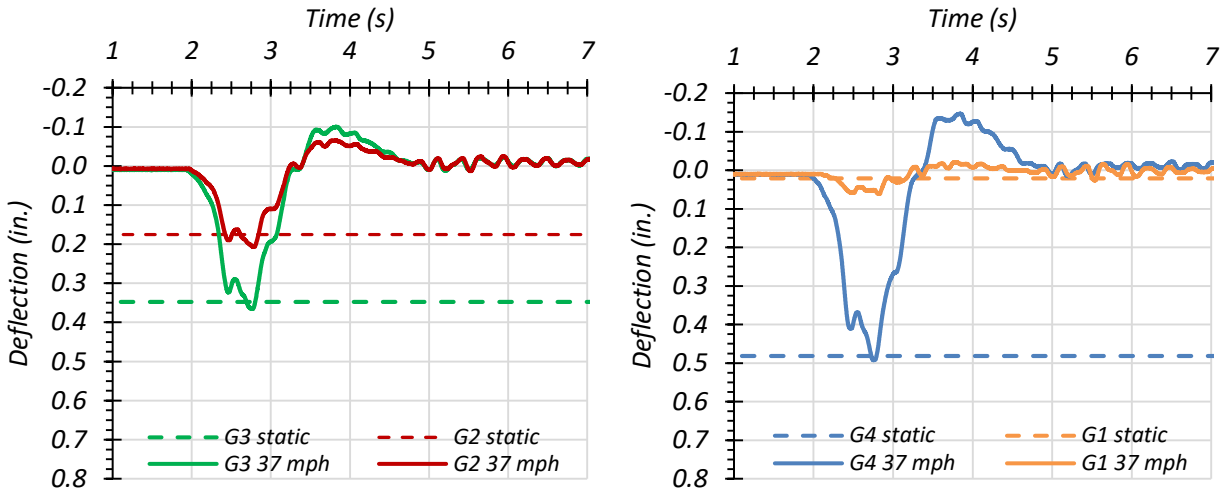

(b) Deflection Time Histories – Dynamic (37 mph)

Figure 8.44. Midspan Deflections for Static and Dynamic Tests for Path 1 – Span 1 Loading

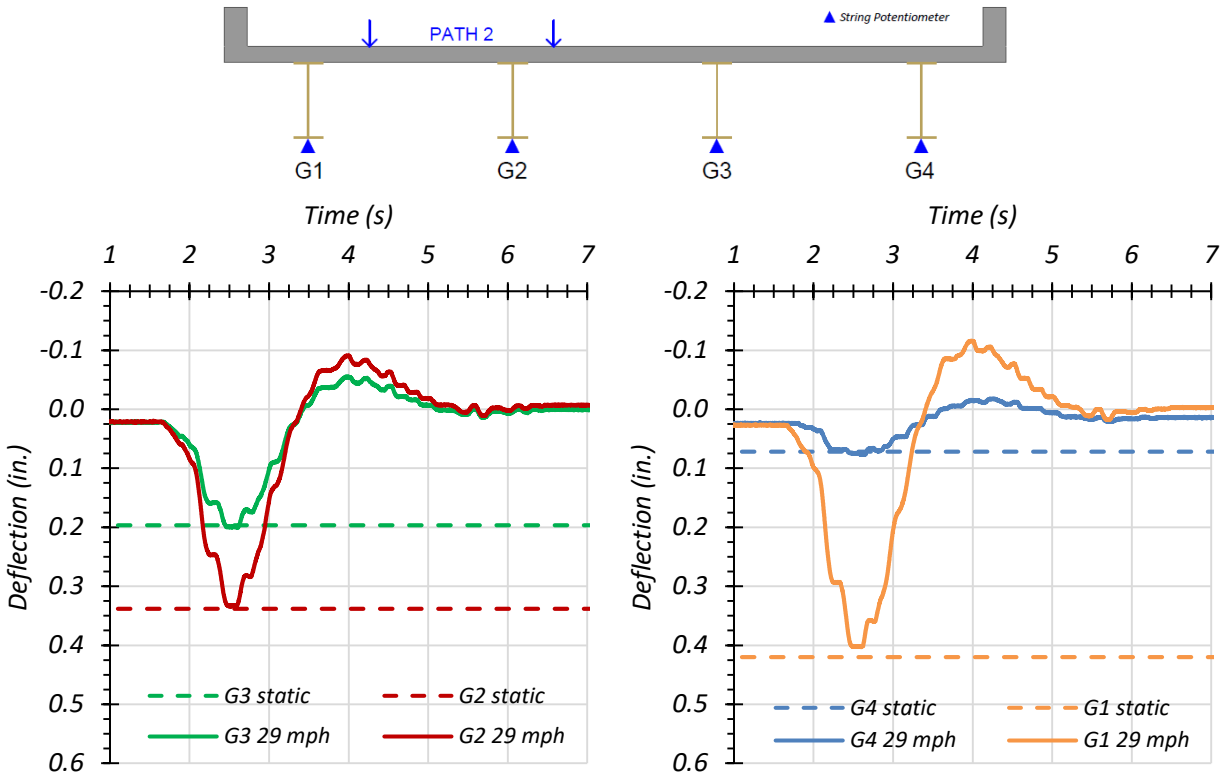

(a) Deflection Time Histories – Dynamic (29 mph)

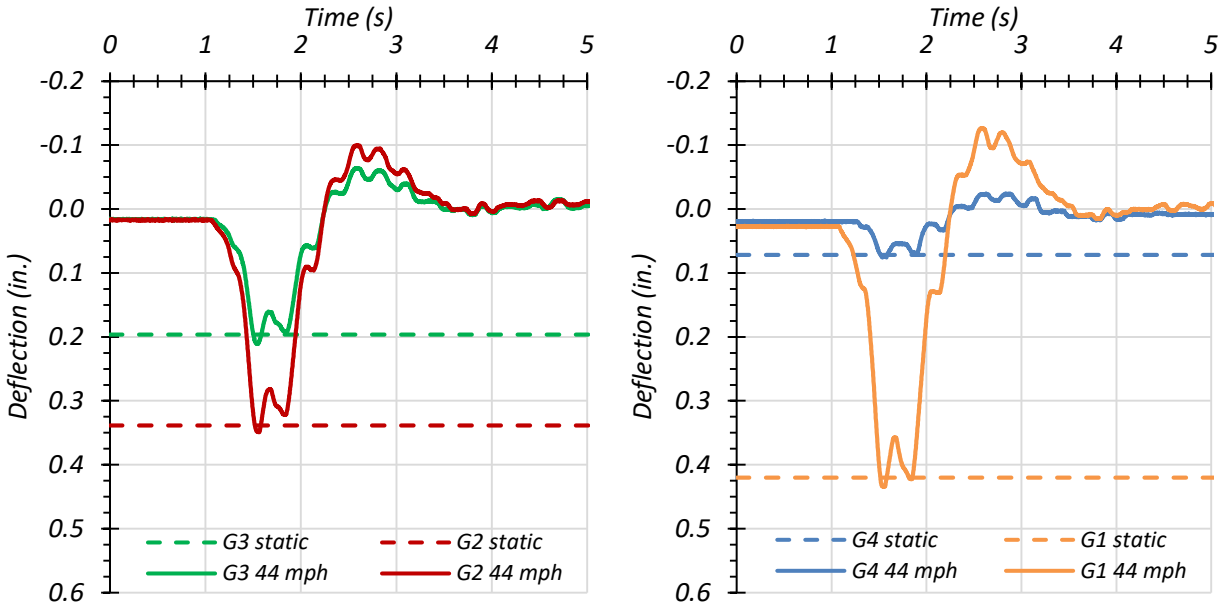

(b) Deflection Time Histories – Dynamic (44 mph)

Figure 8.45. Midspan Deflections for Static and Dynamic Tests for Path 2 – Span 1 Loading

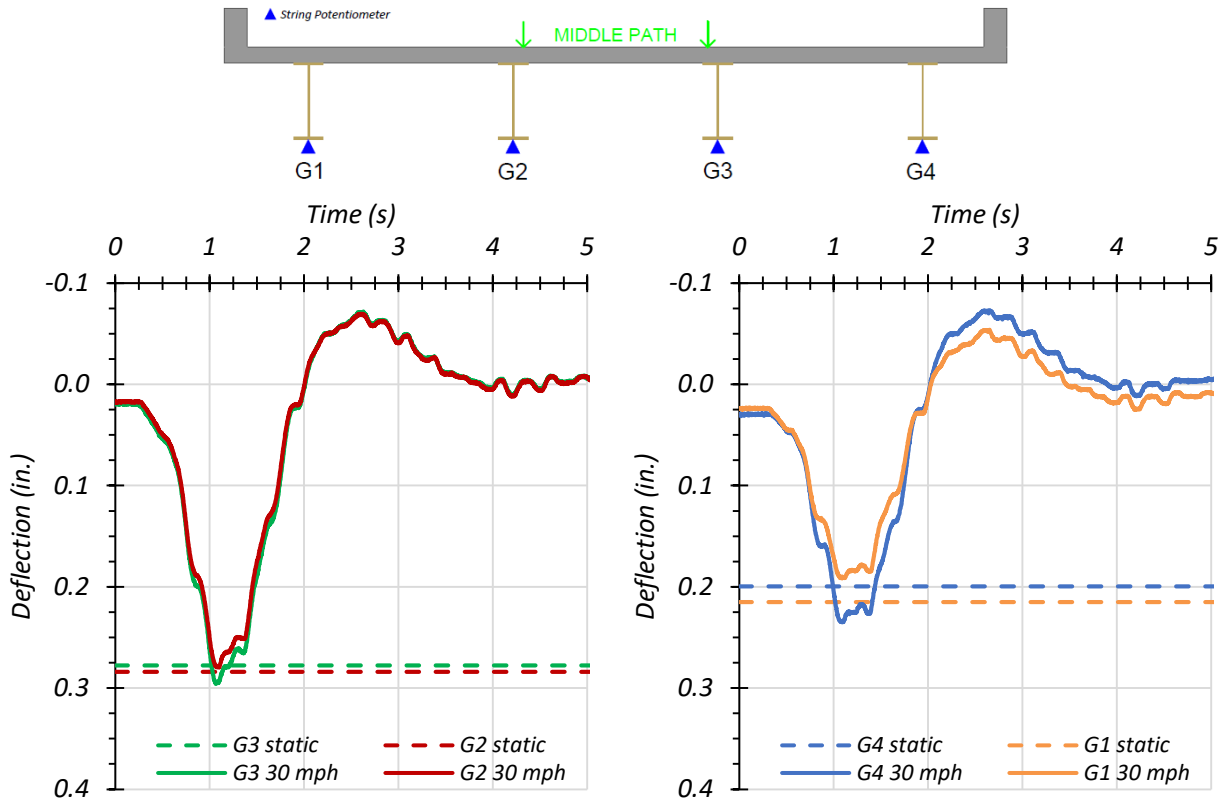

(a) Deflection Time Histories – Dynamic (30 mph)

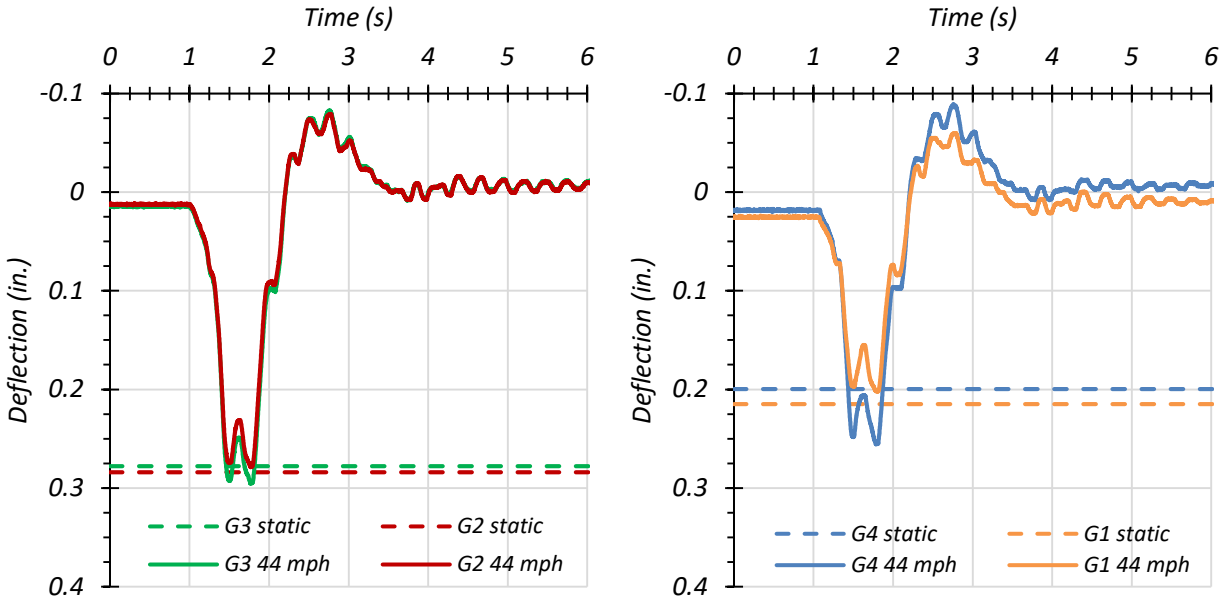

(b) Deflection Time Histories – Dynamic (44 mph)

Figure 8.46. Midspan Deflections for Static and Dynamic Tests for Middle Path – Span 1 Loading

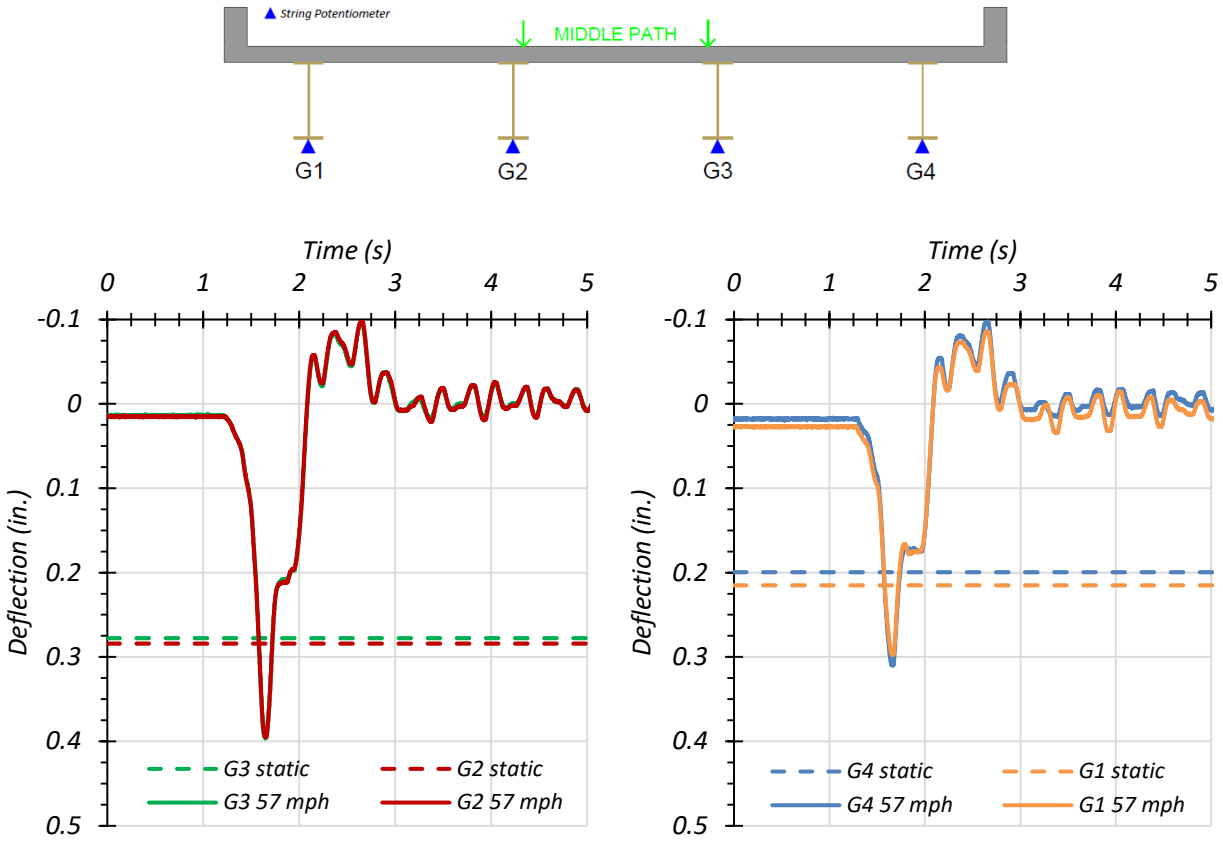

Figure 8.47. Midspan Deflections for Static and Third Dynamic Test for Middle Path – Span 1 Loading

Table 8.26. Maximum Span 1 Deflections for Static and Dynamic Tests

Load Scenario	Girder Displacement (in.)			
	G1	G2	G3	G4
Path 1 Static	0.023	0.176	0.351	0.485
Path 1 Dynamic (30 mph)	0.037	0.209	0.404	0.546
Path 1 Dynamic (37 mph)	0.061	0.207	0.366	0.492
Maximum Dynamic Amplification	**161.4%**	**19.0%**	**15.1%**	**12.8%**
Path 2 Static	0.422	0.340	0.198	0.075
Path 2 Dynamic (29 mph)	0.403	0.334	0.201	0.077
Path 2 Dynamic (44 mph)	0.434	0.349	0.211	0.076
Maximum Dynamic Amplification	**3.0%**	**2.8%**	**6.5%**	**3.7%**
Middle Static	0.217	0.286	0.280	0.203
Middle Dynamic (30 mph)	0.217	0.280	0.296	0.235
Middle Dynamic (44 mph)	0.202	0.279	0.296	0.256
Middle Dynamic (57 mph)	0.298	0.395	0.397	0.310
Maximum Dynamic Amplification	**37.1%**	**38.0%**	**41.8%**	**53.2%**

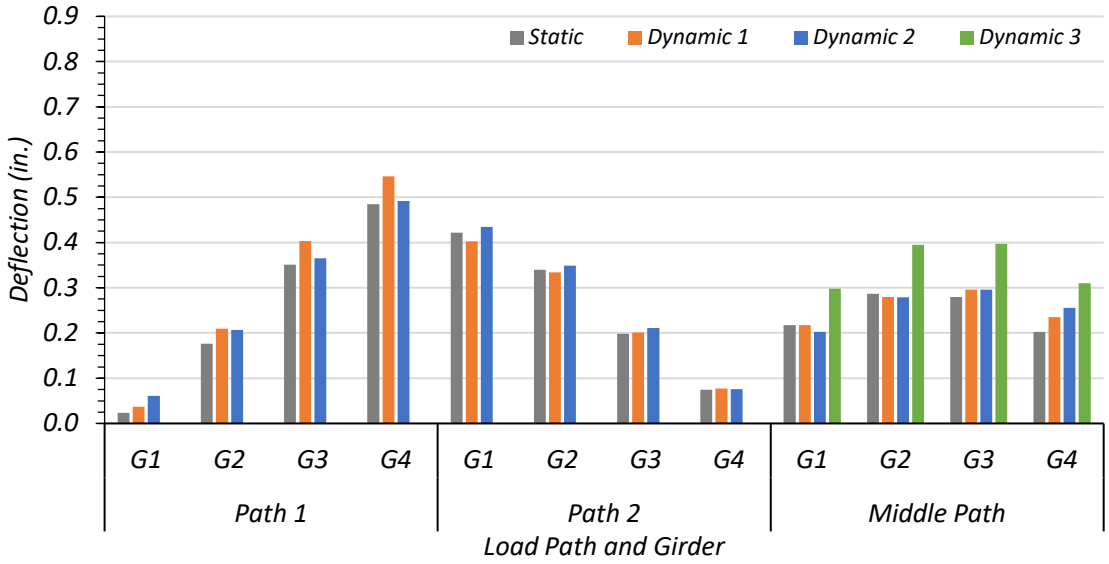

Note:

- *Path 1: Dynamic 1 = 30 mph, Dynamic 2 = 37 mph*
- *Path 2: Dynamic 1 = 29 mph, Dynamic 2 = 44 mph*
- *Middle Path: Dynamic 1 = 30 mph, Dynamic 2 = 44 mph, Dynamic 3 = 57 mph*

Figure 8.48. Comparison of Maximum Span 1 Deflections for Static and Dynamic Tests

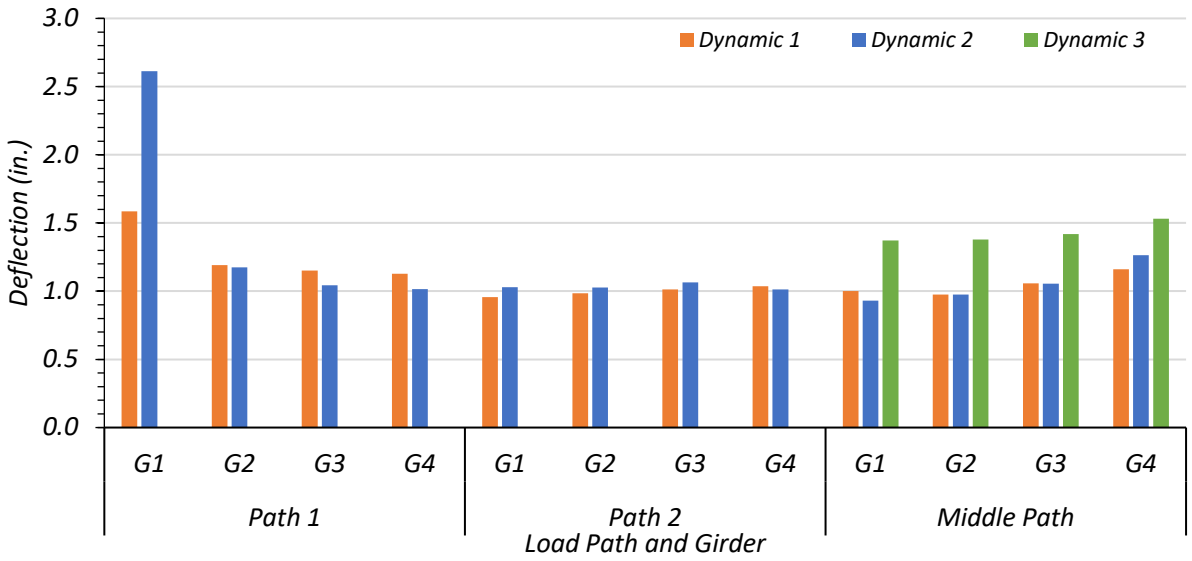

Note:

- *Path 1: Dynamic 1 = 30 mph, Dynamic 2 = 37 mph*
- *Path 2: Dynamic 1 = 29 mph, Dynamic 2 = 44 mph*
- *Middle Path: Dynamic 1 = 30 mph, Dynamic 2 = 44 mph, Dynamic 3 = 57 mph*

Figure 8.49. Ratio of Maximum Span 1 Dynamic Deflection to Static Deflection

The dynamic impact factor given by the AASHTO Standard Specifications for Span 1 of Bridge SC-12 is 27 percent while the dynamic impact factor given by the AASHTO LRFD Specifications for this bridge is 33 percent. The average dynamic impact factor for all girders for Span 1 based on the deflection values observed during testing was 18 percent.

During Path 1 loading, the maximum percent increase in deflection for Girder 3 was 15.1 percent during Dynamic 2 loading. The maximum percent increase in deflection in Girder 4 was 12.8 percent during Dynamic 2 loading.

During Path 2 loading, the maximum percent increase in deflection for Girder 3 was 6.5 percent during Dynamic 2 loading. The maximum percent increase in deflection in Girder 4 was 3.7 percent during Dynamic 1 loading.

During Middle Path loading, the maximum percent increase in deflection for Girder 3 was 41.8 percent during Dynamic 3 loading. The maximum percent increase in deflection in Girder 4 was 53.2 percent during Dynamic 3 loading.

8.6.5.2. Span 2 Dynamic Amplification

8.6.5.2.1. Maximum Girder Strains

From the results of the static and dynamic tests for each path, the increases in strains and deflections due to the moving vehicle were examined. Figure 8.50, Figure 8.51, and Figure 8.52 show the maximum Span 2 dynamic strains observed for Path 1, Path 2, and the Middle Path, respectively, plotted with the static strains observed for those paths. Figure 8.53 shows those strain values and compares them to the appropriate static load case for Span 2.

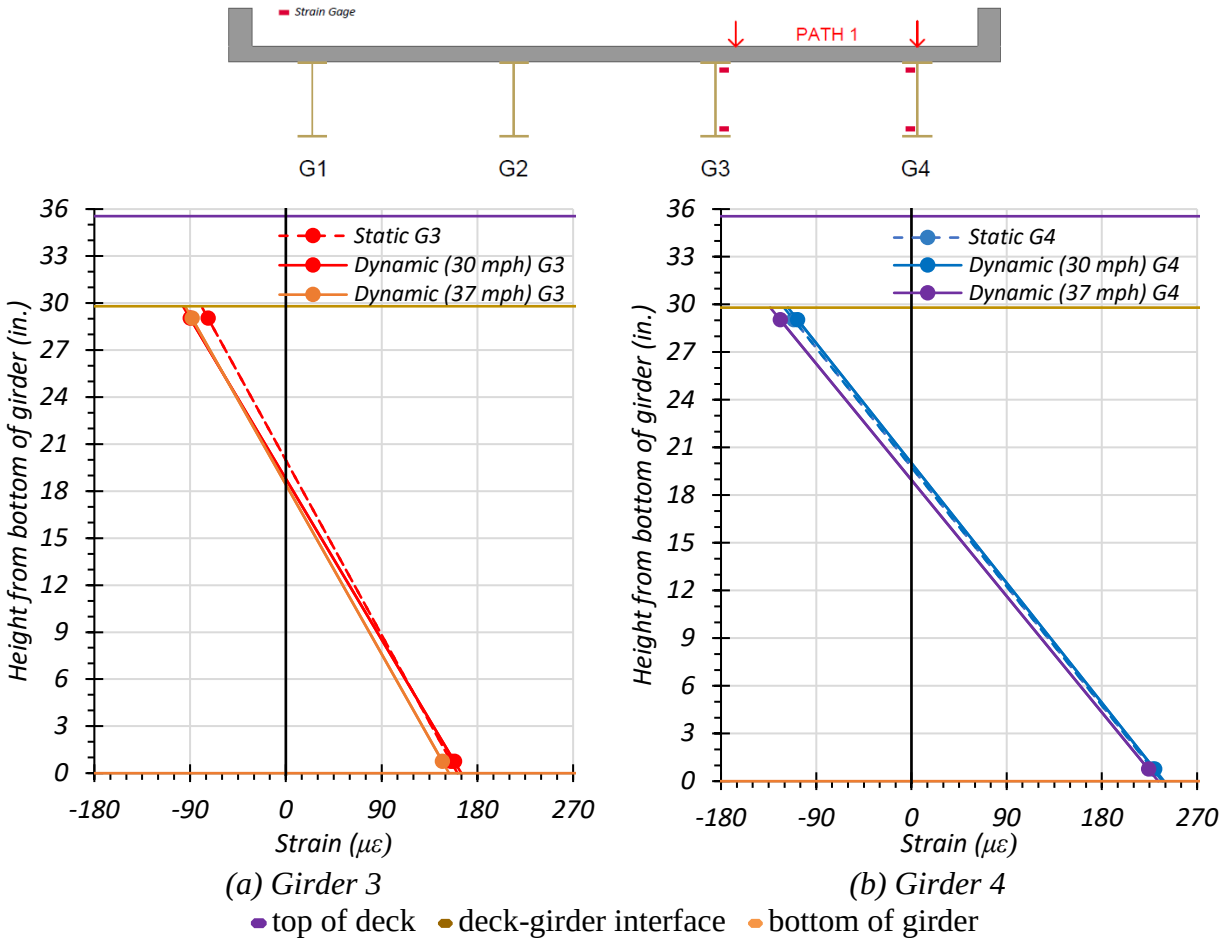

(a) Girder 3 *(b) Girder 4*

Figure 8.50. Maximum Strains for Static and Dynamic Tests for Path 1 – Span 2 Loading

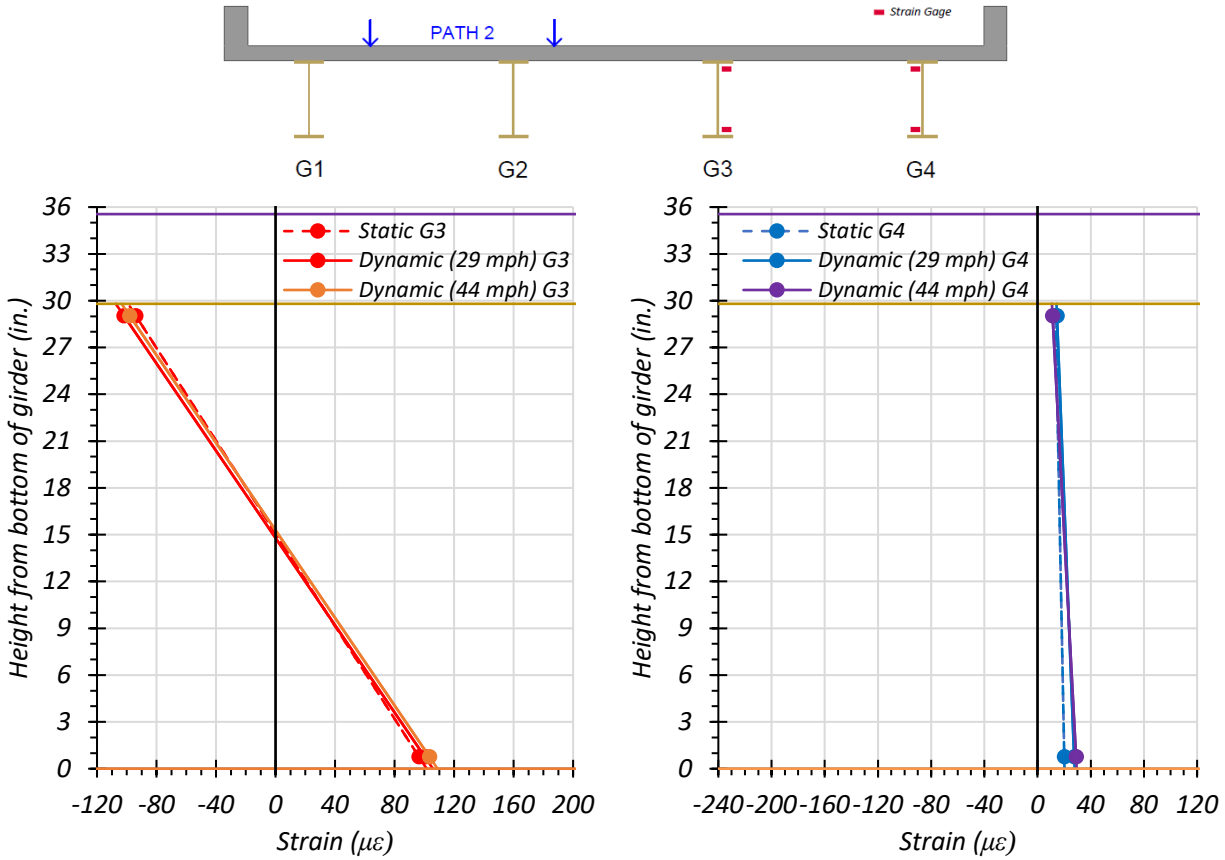

(a) Girder 3 *(b) Girder 4*

top of deck deck-girder interface bottom of girder

Figure 8.51. Maximum Strains for Static and Dynamic Tests for Path 2 – Span 2 Loading

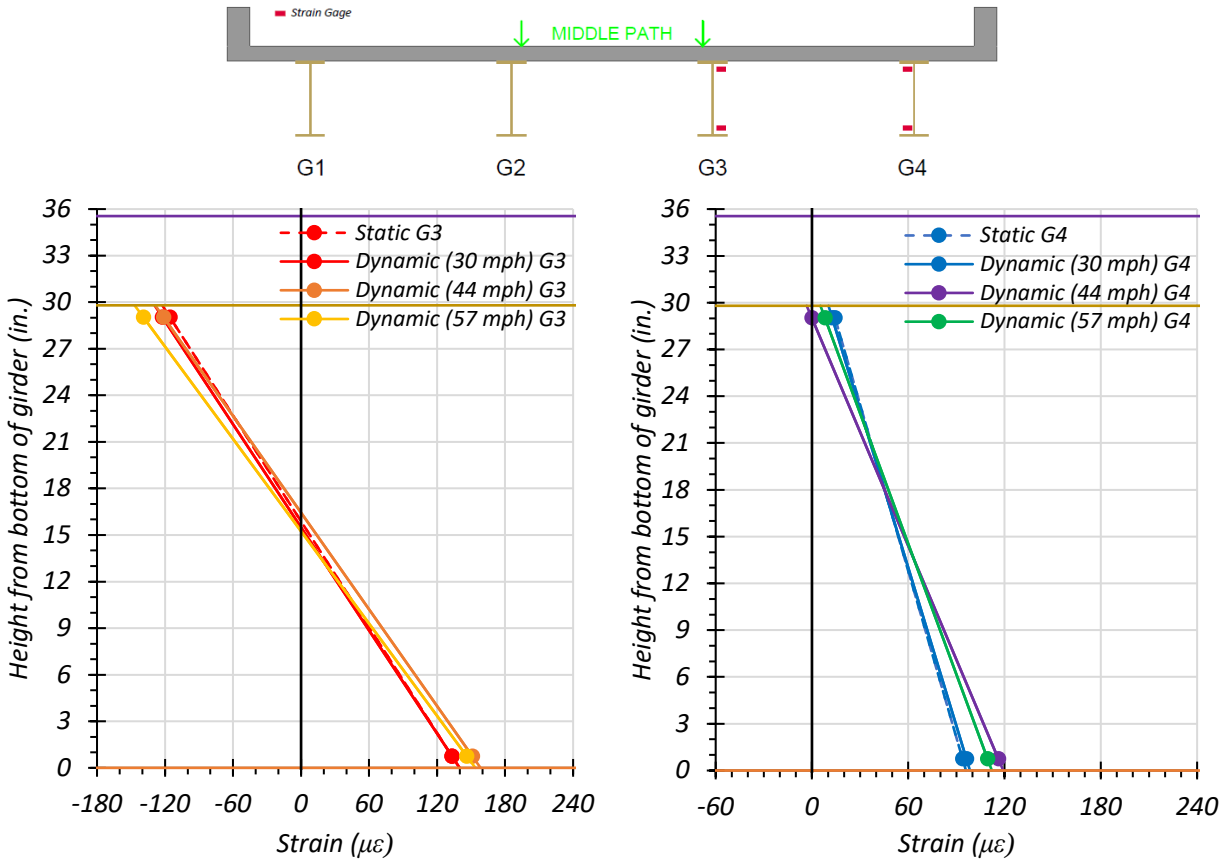

(a) Girder 3 *(b) Girder 4*

top of deck deck-girder interface bottom of girder

Figure 8.52. Maximum Strains for Static and Dynamic Tests for Middle Path – Span 2 Loading

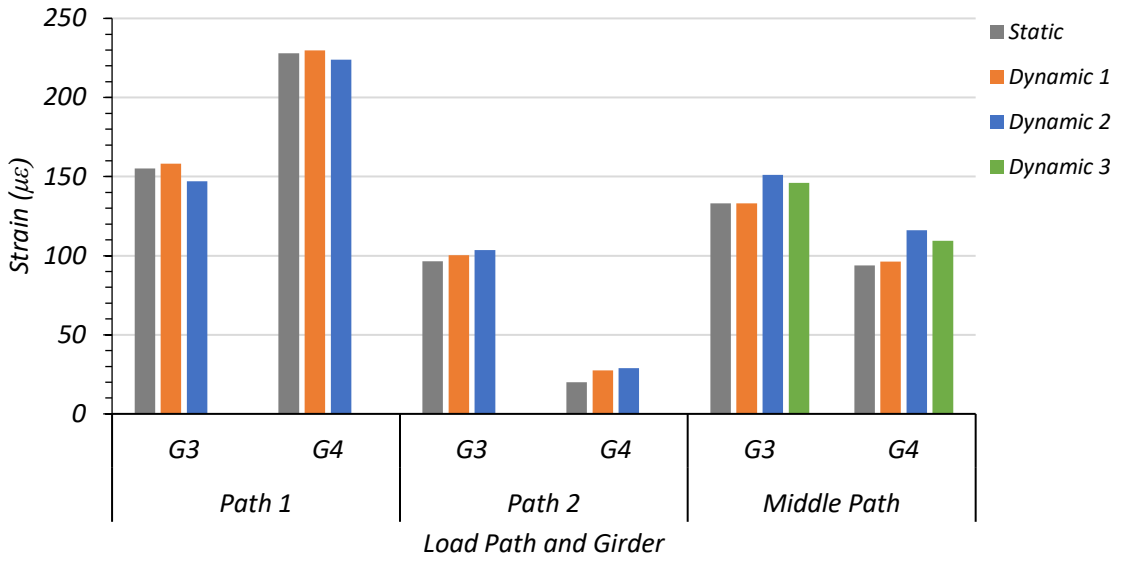

Note:

- *Path 1: Dynamic 1 = 30 mph, Dynamic 2 = 37 mph*
- *Path 2: Dynamic 1 = 29 mph, Dynamic 2 = 44 mph*
- *Middle Path: Dynamic 1 = 30 mph, Dynamic 2 = 44 mph, Dynamic 3 = 57 mph*

Figure 8.53. Comparison of Maximum Bottom Flange Strains for Static and Dynamic Tests in Span 2

The dynamic impact factor given by the AASHTO Standard Specifications for Span 2 of Bridge SC-12 is 25 percent. The dynamic impact factor given by the AASHTO LRFD Specifications for this bridge is 33 percent. The average dynamic impact factor for all girders for Span 2 based on the strain values observed during testing was 11 percent. The dynamic impact factor is less significant for Span 2 than Span 1. Both Path 1 and Path 2 loading produced fairly insignificant dynamic effects for Girder 3 and Girder 4, and in some cases these girders saw decreases in strain under dynamic load. However, the Middle Path loading did produce noticeable dynamic effects on both Girder 3 and 4 for Dynamic 2 and Dynamic 3 loading.

8.6.5.2.2. Maximum Girder Deflections

Figure 8.54, Figure 8.55, Figure 8.56, and Figure 8.57 show the Span 2 girder deflection time histories for the dynamic load cases along Path 1, Path 2, and the Middle Path, respectively, for each dynamic loading. Table 8.27 shows the maximum measured girder deflections for the stop location load case and for each dynamic load case. Figure 8.58 shows the Span 2 static and dynamic maximum deflection values and compares them. Figure 8.59 shows the dynamic effect based on deflection as a ratio to the static deflection.

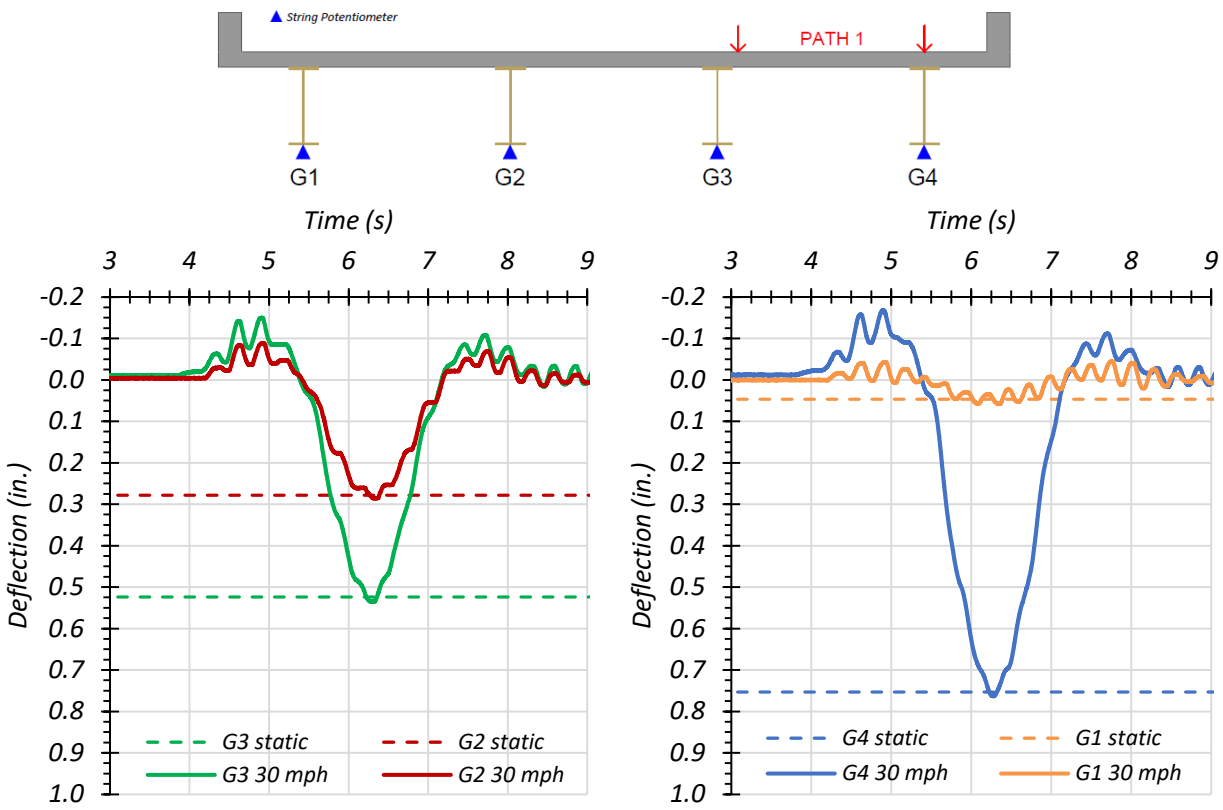

(a) Deflection Time Histories – Dynamic (30 mph)

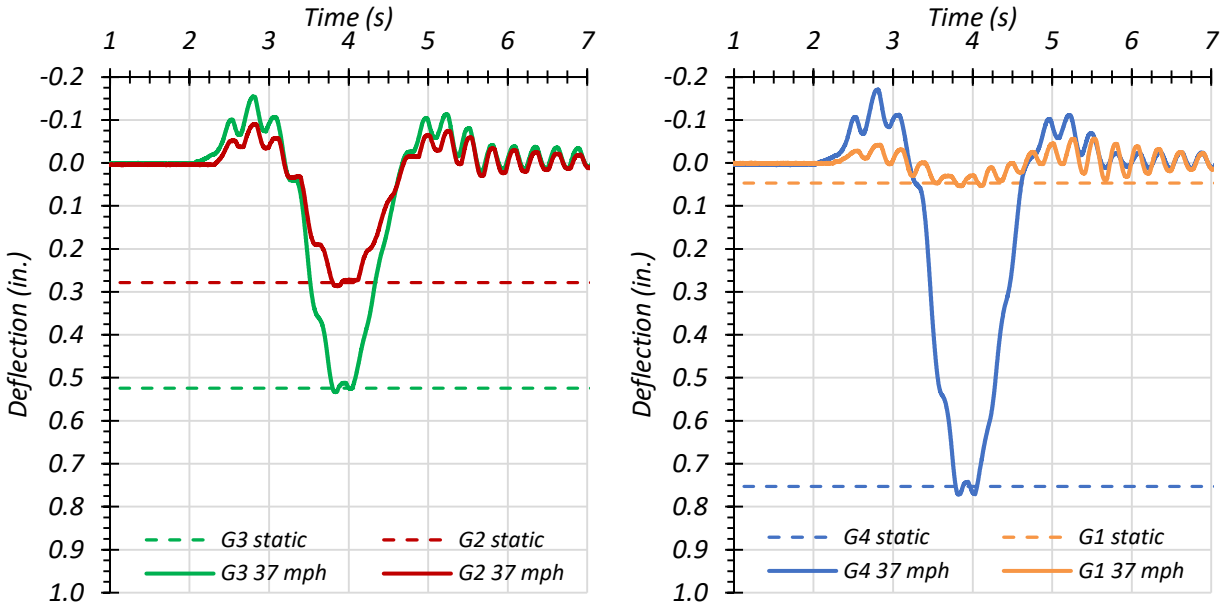

(b) Deflection Time Histories – Dynamic (37 mph)

Figure 8.54. Midspan Deflections for Static and Dynamic Tests for Path 1 – Span 2 Loading

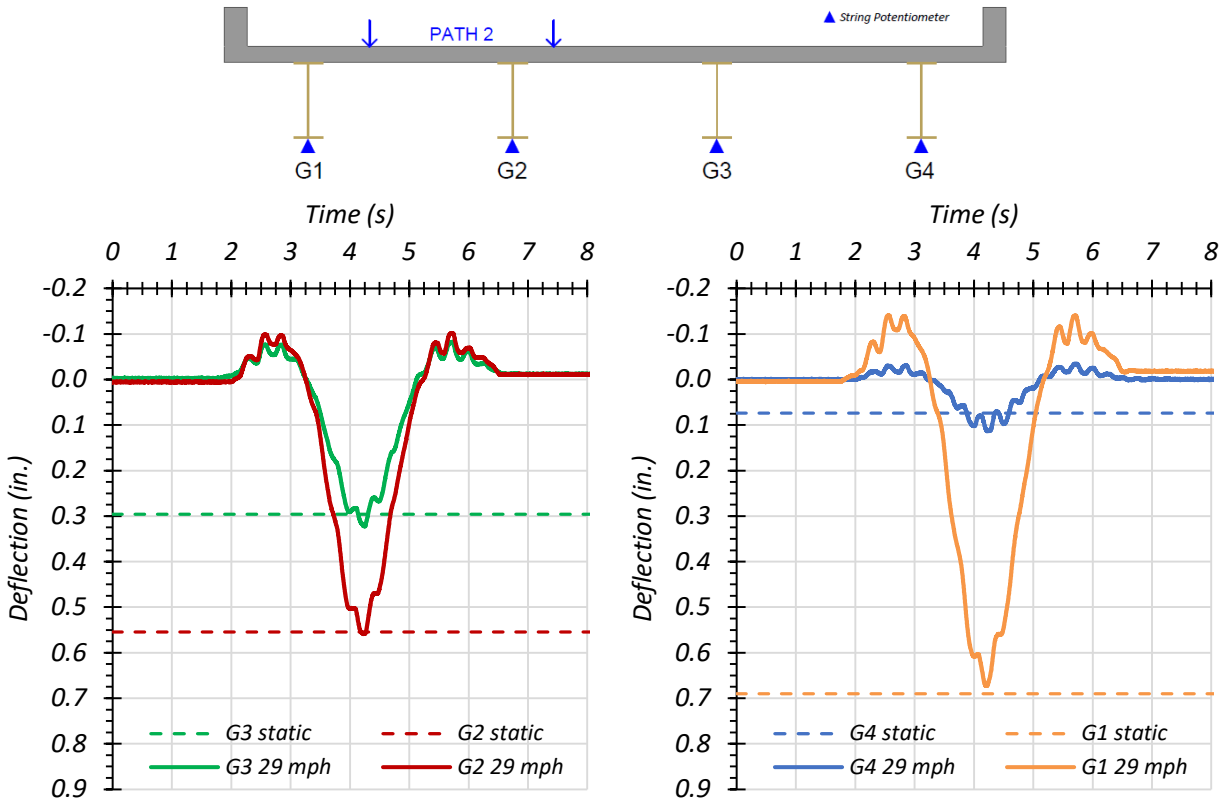

(a) Deflection Time Histories – Dynamic (29 mph)

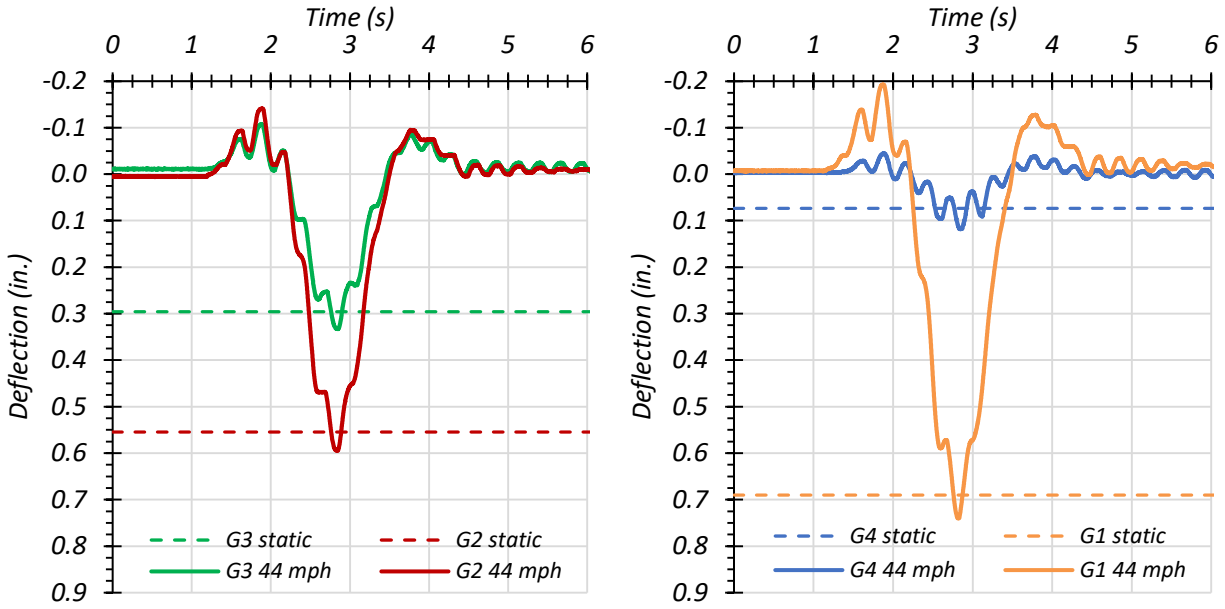

(b) Deflection Time Histories – Dynamic (44 mph)

Figure 8.55. Midspan Deflections for Static and Dynamic Tests for Path 2 – Span 2 Loading

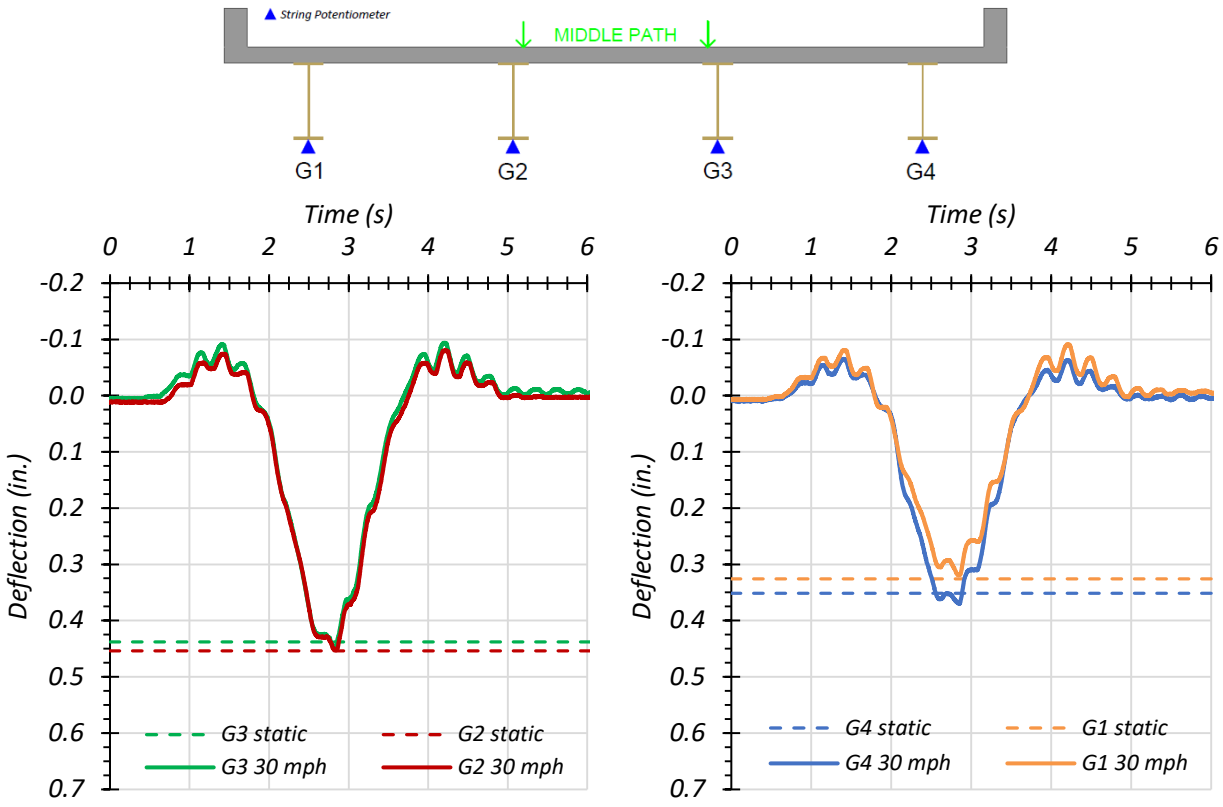

(a) Deflection Time Histories – Dynamic (30 mph)

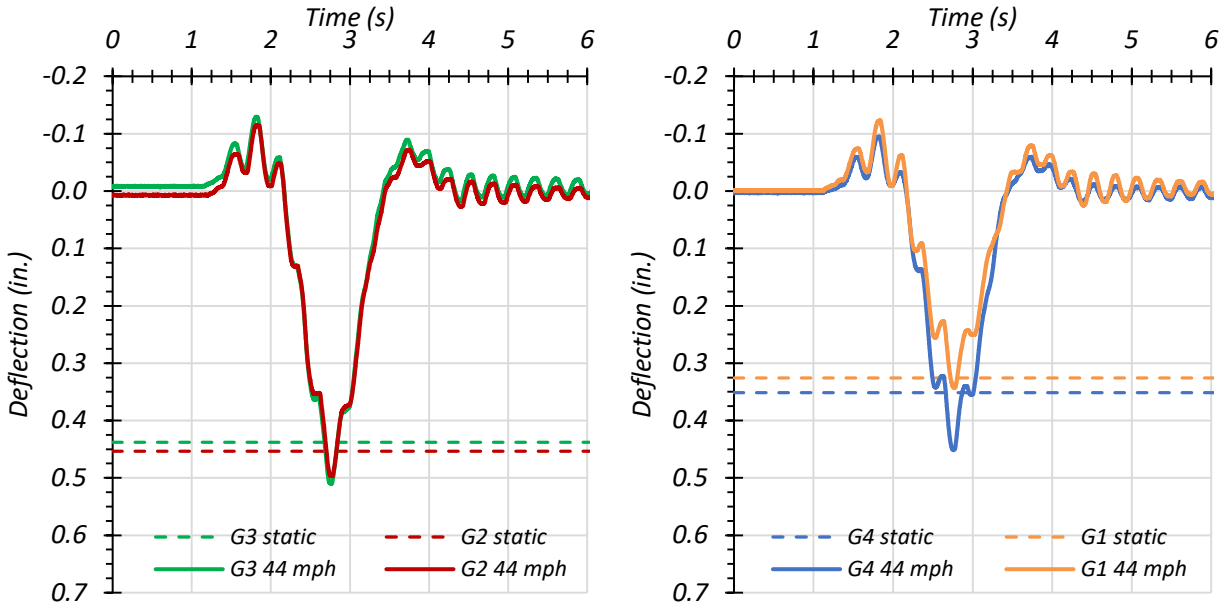

(b) Deflection Time Histories – Dynamic (44 mph)

Figure 8.56. Midspan Deflections for Static and Dynamic Tests for Middle Path – Span 2 Loading

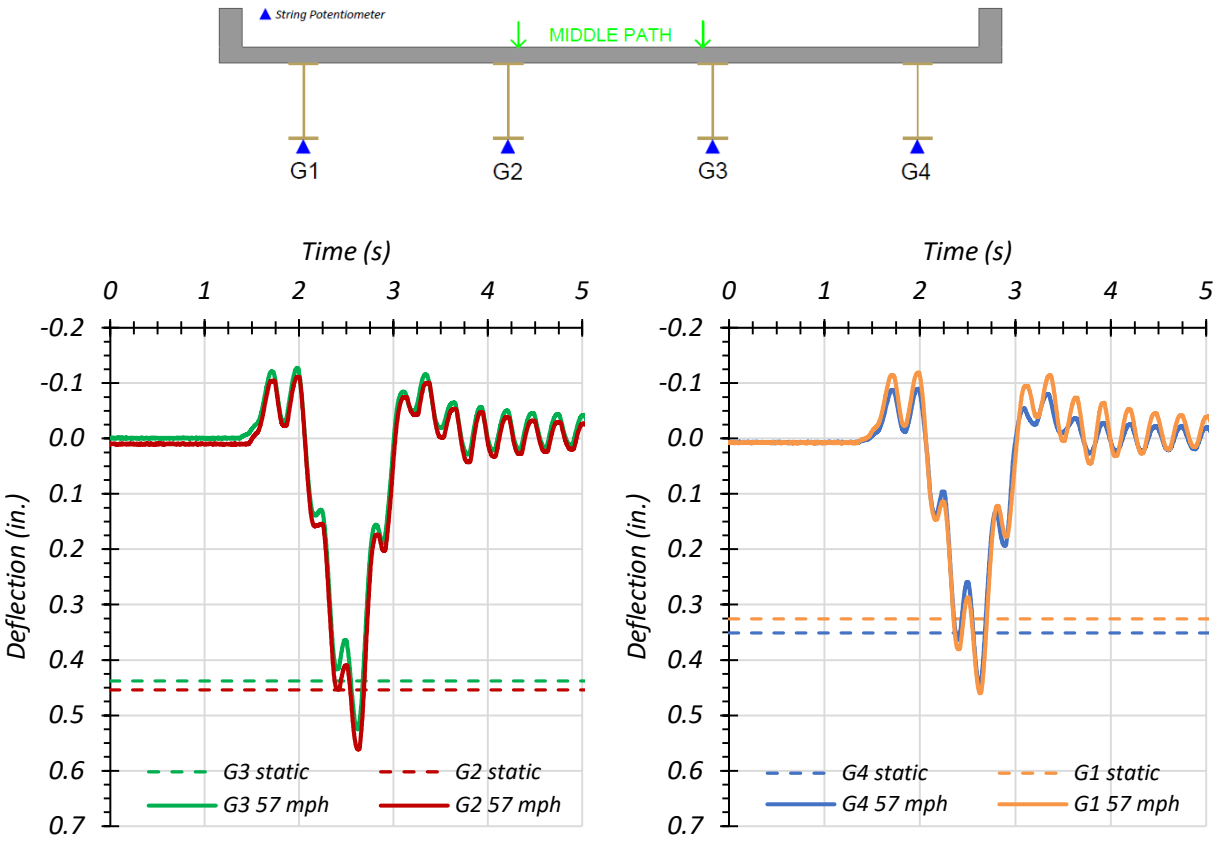

Figure 8.57. Midspan Deflections for Static and Third Dynamic Test for Middle Path – Span 2 Loading

Table 8.27. Maximum Span 2 Deflections for Static and Dynamic Tests

Load Scenario	Girder Displacement (in.)			
	G1	G2	G3	G4
Path 1 Static	0.049	0.280	0.526	0.755
Path 1 Dynamic (30 mph)	0.058	0.286	0.536	0.764
Path 1 Dynamic (37 mph)	0.054	0.287	0.533	0.772
Maximum Dynamic Amplification	**19.0%**	**2.2%**	**1.8%**	**2.3%**
Path 2 Static	0.692	0.556	0.298	0.077
Path 2 Dynamic (29 mph)	0.673	0.559	0.322	0.113
Path 2 Dynamic (44 mph)	0.740	0.595	0.333	0.119
Maximum Dynamic Amplification	**6.9%**	**6.9%**	**11.8%**	**55.1%**
Middle Static	0.328	0.457	0.440	0.353
Middle Dynamic (30 mph)	0.328	0.453	0.446	0.370
Middle Dynamic (44 mph)	0.343	0.497	0.510	0.451
Middle Dynamic (57 mph)	0.460	0.562	0.525	0.444
Maximum Dynamic Amplification	**40.2%**	**23.0%**	**19.4%**	**27.9%**

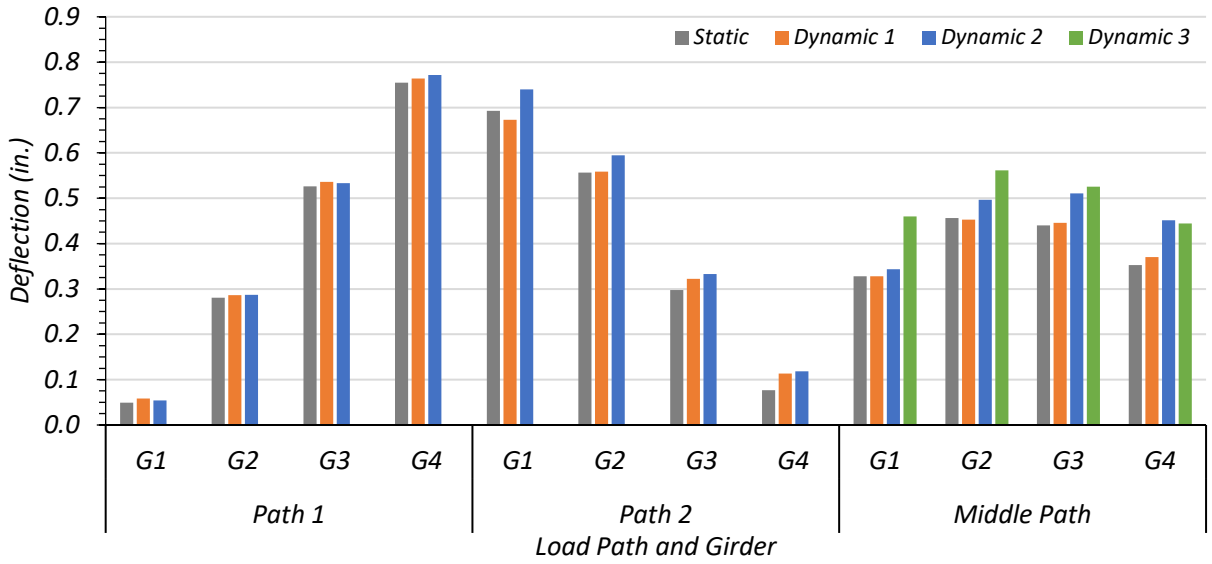

Note:

- *Path 1: Dynamic 1 = 30 mph, Dynamic 2 = 37 mph*
- *Path 2: Dynamic 1 = 29 mph, Dynamic 2 = 44 mph*
- *Middle Path: Dynamic 1 = 30 mph, Dynamic 2 = 44 mph, Dynamic 3 = 57 mph*

Figure 8.58. Comparison of Maximum Span 2 Deflections for Static and Dynamic Tests

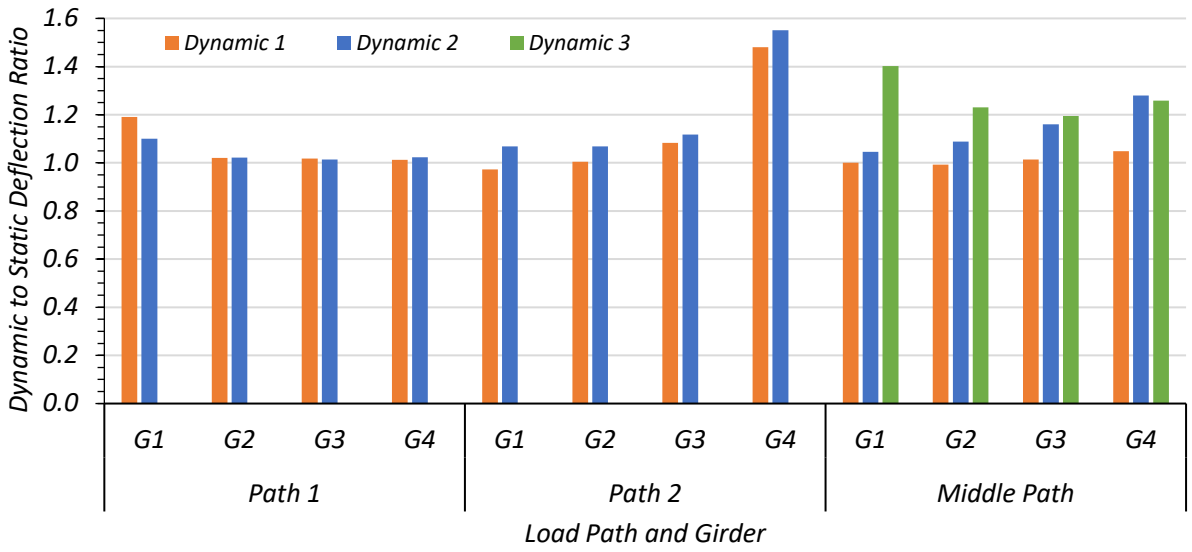

Note:

- *Path 1: Dynamic 1 = 30 mph, Dynamic 2 = 37 mph*
- *Path 2: Dynamic 1 = 29 mph, Dynamic 2 = 44 mph*
- *Middle Path: Dynamic 1 = 30 mph, Dynamic 2 = 44 mph, Dynamic 3 = 57 mph*

Figure 8.59. Ratio of Maximum Span 2 Dynamic Deflection to Static Deflection

The dynamic impact factor given by the AASHTO Standard Specifications for Span 2 of Bridge SC-12 is 25 percent while the dynamic impact factor given by the AASHTO LRFD Specifications for this bridge is 33 percent. The average dynamic impact factor for all girders for Span 2 based on the deflection values observed during testing was 12 percent.

During Path 1 loading, the maximum percent increase in deflection for Girder 3 was 1.8 percent during Dynamic 2 loading. The maximum percent increase in deflection in Girder 4 was 2.3 percent during Dynamic 2 loading.

During Path 2 loading, the maximum percent increase in deflection for Girder 3 was 11.8 percent during Dynamic 1 loading. The maximum percent increase in deflection in Girder 4 was 55.1 percent during Dynamic 2 loading, however, Girder 4 experiences very minimal deflection during Path 2 loading, which may explain the large dynamic effect.

During Middle Path loading, the maximum percent increase in deflection for Girder 3 was 19.4 percent during Dynamic 3 loading. The maximum percent increase in deflection in Girder 4 was 27.9 percent during Dynamic 2 loading.

8.6.5.3. Dynamic Characteristics of the Bridge

Data obtained from the accelerometers during dynamic tests and the sledgehammer tests was filtered and a fast-Fourier transform (FFT) analysis was performed. This allowed for determination of the first two natural frequencies of the bridge as 3.78 Hz and 6.71 Hz. For each natural frequency, the amplitude and phase angle of each accelerometer was used to develop the mode shape. Figure 8.60 shows a cut through the longitudinal centerline of the bridge and a transverse section of both spans for the mode shape produced by the first natural frequency of Bridge SC-12. Figure 8.61 shows a longitudinal section and a transverse section of both spans for the mode shape produced by the second natural frequency of the bridge. Figure 8.62 shows a longitudinal section and a transverse section of both spans for the mode shape produced by the second natural frequency of the bridge.

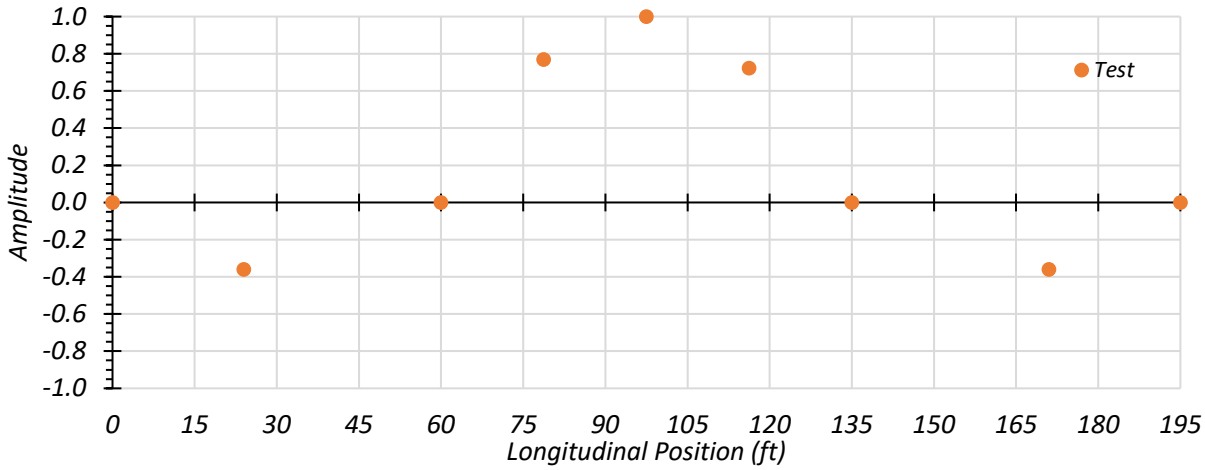

(a) Longitudinal Section

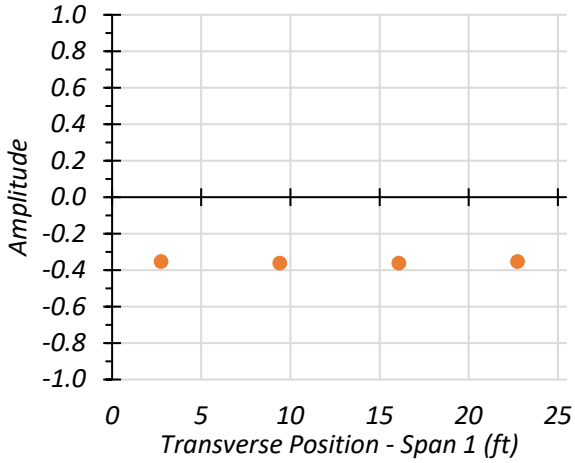

(b) Transverse Section – Span 1

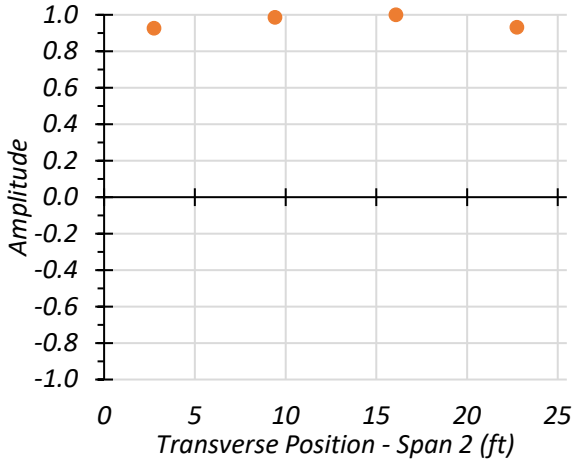

(c) Transverse Section – Span 2

Figure 8.60. First Mode Shape of Bridge SC-12 (f_1 = 3.78 Hz)

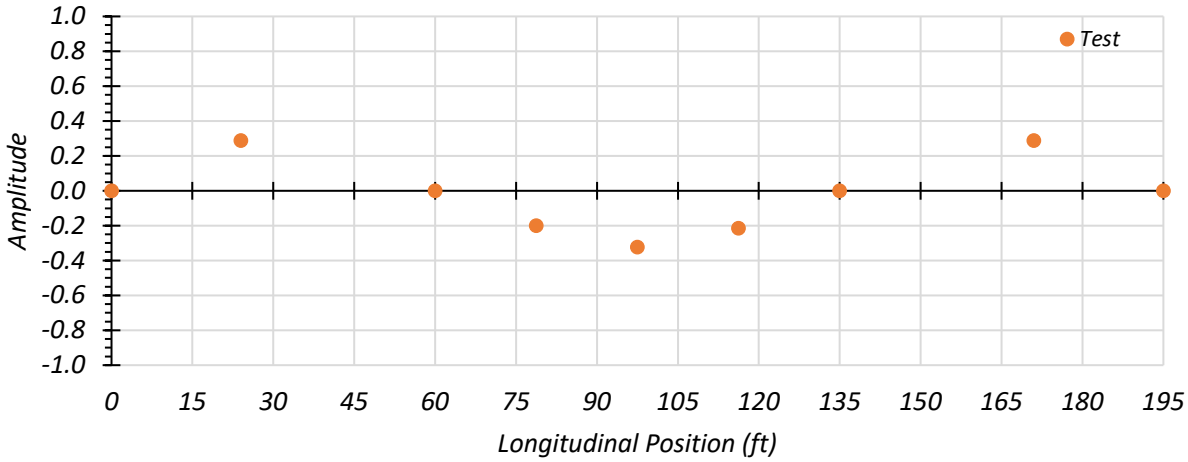

(a) Longitudinal Section

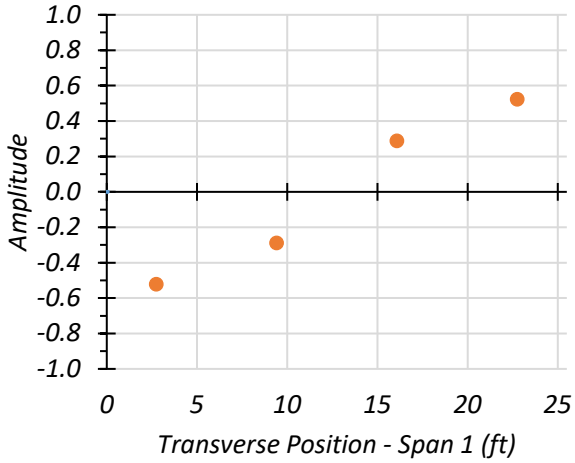

(b) Transverse Section – Span 1

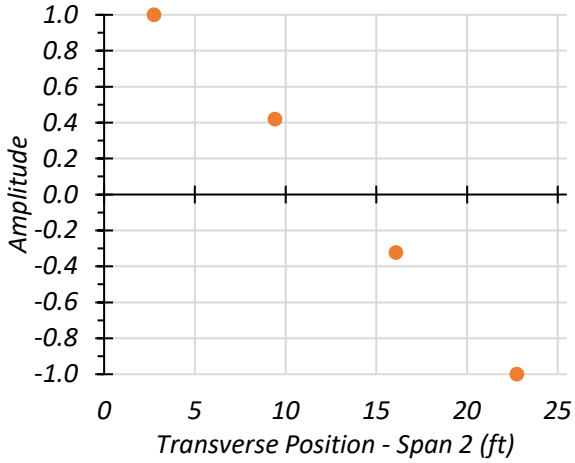

(c) Transverse Section – Span 2

Figure 8.61. Second Mode Shape of Bridge SC-12 (f_2 = 6.71 Hz)

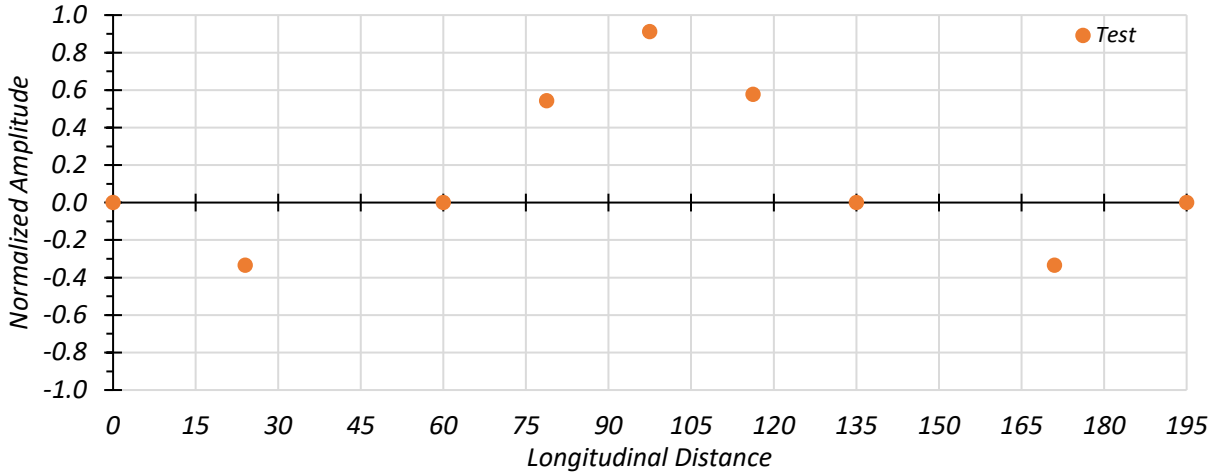

(a) Longitudinal Section

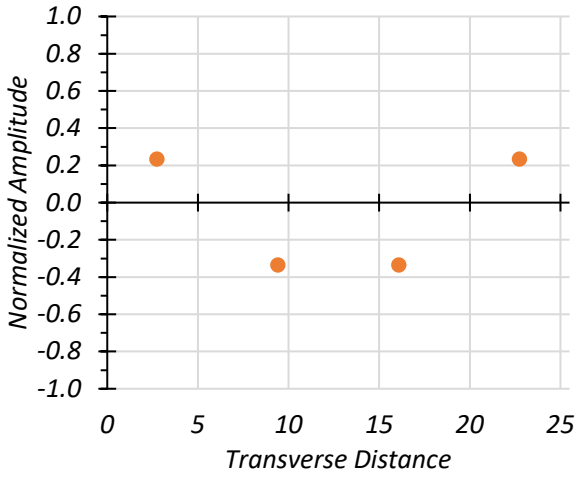

(b) Transverse Section – Span 1

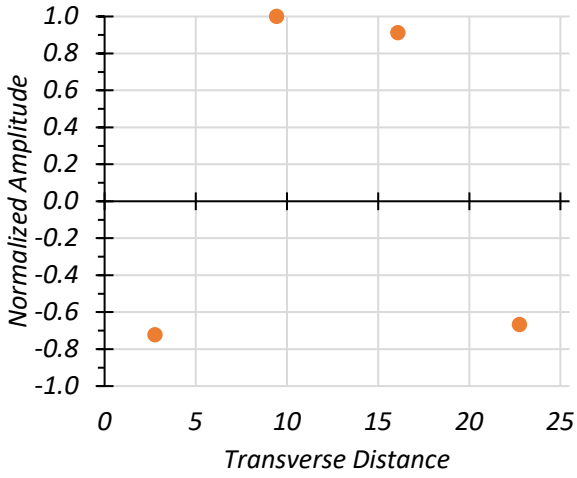

(c) Transverse Section – Span 2

Figure 8.62. Third Mode Shape of Bridge SC-12 (f_3 = 11.23 Hz)

8.6.6. Computer Vision

During testing, a handheld video camera was set up on a tripod on the side of the bridge near exterior Girder 4 at the center of Span 2. The camera had a frame size of 1280 pixels by 720 pixels and a sampling frequency of 30 Hz. An iPhone camera was setup up on a tripod on the side of the

bridge near exterior Girder 1 at 0.4*L* of Span 1. The iPhone camera had a frame size of 3840 pixels by 2160 pixels and a sampling frequency of 60 Hz. The cameras were placed so that the girders were perpendicular to the camera's line of sight. Each load test was recorded, and computer vision was used on each Path 1 load test to measure the deflection experienced in Girder 4, and each Path 2 load test to measure the deflection experienced in Girder 1.

The computer vision algorithm compares the sub window of the initial frame in the video to the same sub window in the following frames of the video. The user selects the pixel width and height of this initial sub window. The user also defines a reference distance which the algorithm corresponds to a number of pixels. The algorithm then finds the location of the displaced sub window in the frames following the initial frame. The algorithm finds the minimum sum of the squared difference between the location of the first sub window and the location of the subsequent sub window, therefore calculating the displacement of the objects in the original sub window. A lowpass Butterworth filter was used to smooth the deflection signal output by the program. For all Path 1 load cases, the handheld video camera was used and a 20 pixel by 20 pixel sub window was used for computer vision. For all Path 2 load cases, the iPhone camera was used and a 100 pixel by 100 pixel sub window was used for computer vision.

The results from the computer vision were compared with the deflections recorded by the corresponding string potentiometers. For Bridge SC-12, computer vision was performed on all five of the Path 1 tests. The algorithm was applied to three of the five Path 2 load tests. The camera drifted slightly while recording, rendering the computer vision ineffective for both Path 2 stop location tests; therefore, those are not included.

8.6.6.1. Maximum Effect Girders

Figure 8.63 shows the Span 2 midspan deflection over time using computer vision and from the Girder 4 string potentiometer for the Path 1 – Span 1 stop location test. The cutoff frequency used for filtering was 0.75 Hz. The maximum deflection given by the string potentiometer is 0.107 in. upwards, while computer vision does not give a result that is meaningful.

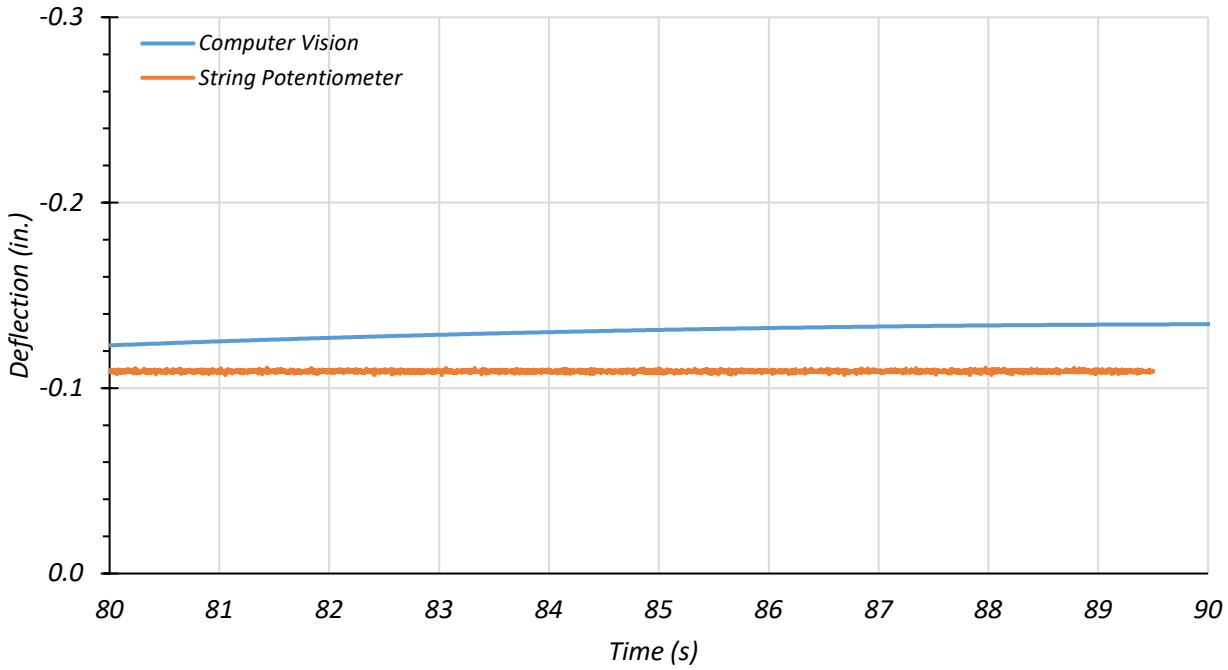

Figure 8.63. Girder 4 – Span 2 Deflections for Path 1 – Span 1 Stop Location

Figure 8.64 shows the Span 2 midspan deflection over time using computer vision and from the Girder 4 string potentiometer for the Path 1 – Span 2 stop location test. The cutoff frequency used for filtering was 0.75 Hz. The maximum deflection given by the string potentiometer is 0.755 in., while the maximum deflection given by computer vision is 0.635 in. Computer vision underestimated the deflection value by 0.120 in. and had a percent difference with the string potentiometer of 17.3 percent.

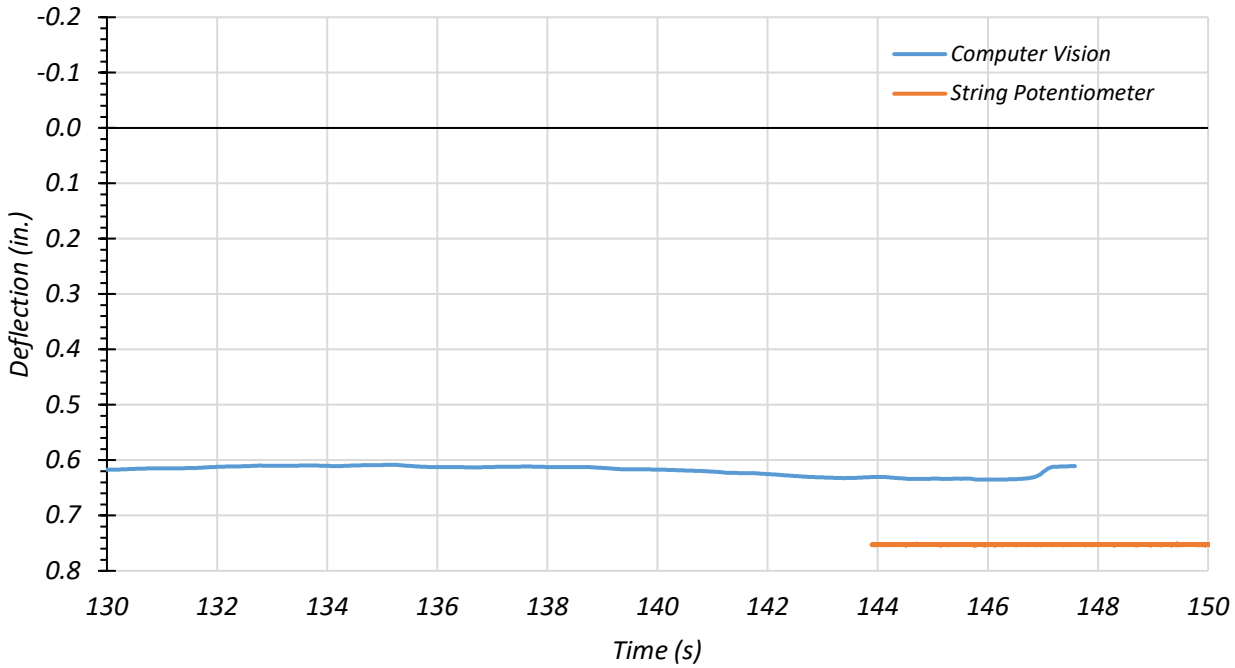

Figure 8.64. Girder 4 – Span 2 Deflections for Path 1 – Span 2 Stop Location

Figure 8.65 shows the Span 2 midspan deflection over time using computer vision and from the Girder 4 string potentiometer for the Path 1 crawl speed test at 2 mph. The cutoff frequency used for filtering was 1.5 Hz. The maximum deflection given by the string potentiometer is 0.771 in., while the maximum deflection given by computer vision is 0.705 in. Computer vision underestimated the deflection value by 0.066 in. and had a percent difference with the string potentiometer of 8.9 percent.

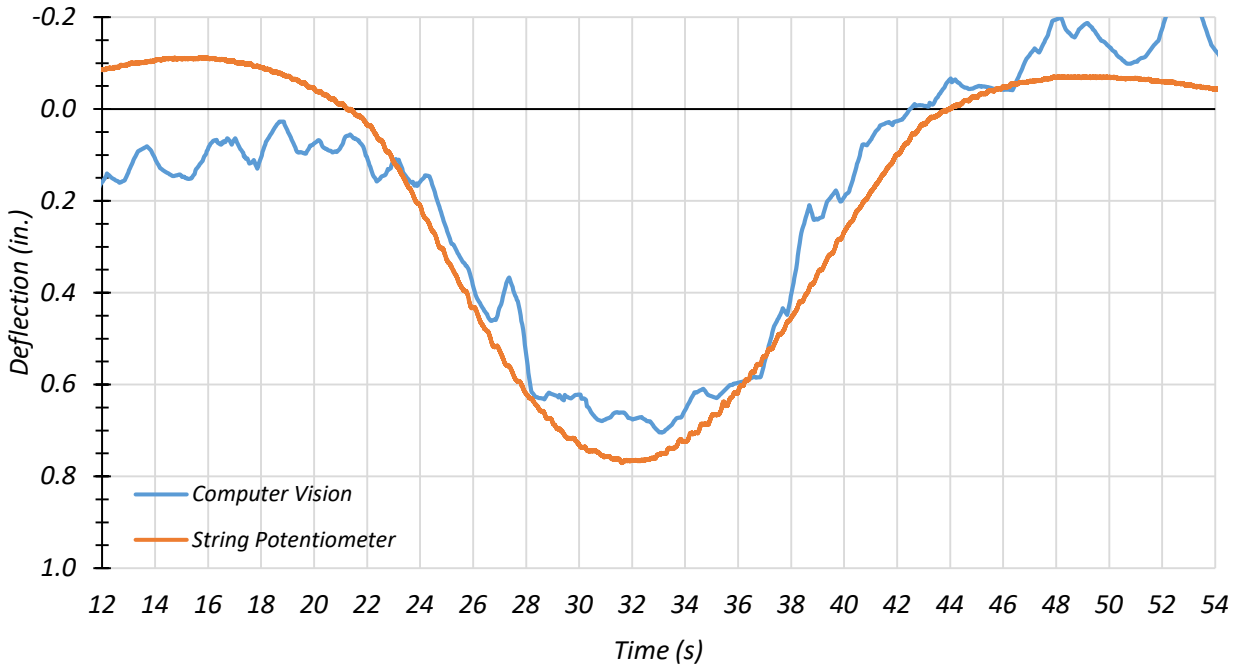

Figure 8.65. Girder 4 – Span 2 Deflections for Path 1 – Crawl Speed Test

Figure 8.66 shows the Span 2 midspan deflection over time using computer vision and from the Girder 4 string potentiometer for the Path 1 dynamic test at 30 mph. The cutoff frequency used for filtering was 1.5 Hz. The maximum deflection given by the string potentiometer is 0.776 in., while the maximum deflection given by computer vision is 0.750 in. Computer vision underestimated the deflection value by 0.026 in. and had a percent difference with the string potentiometer of 3.4 percent. The computer vision deflection value matches the string potentiometer well for this test.

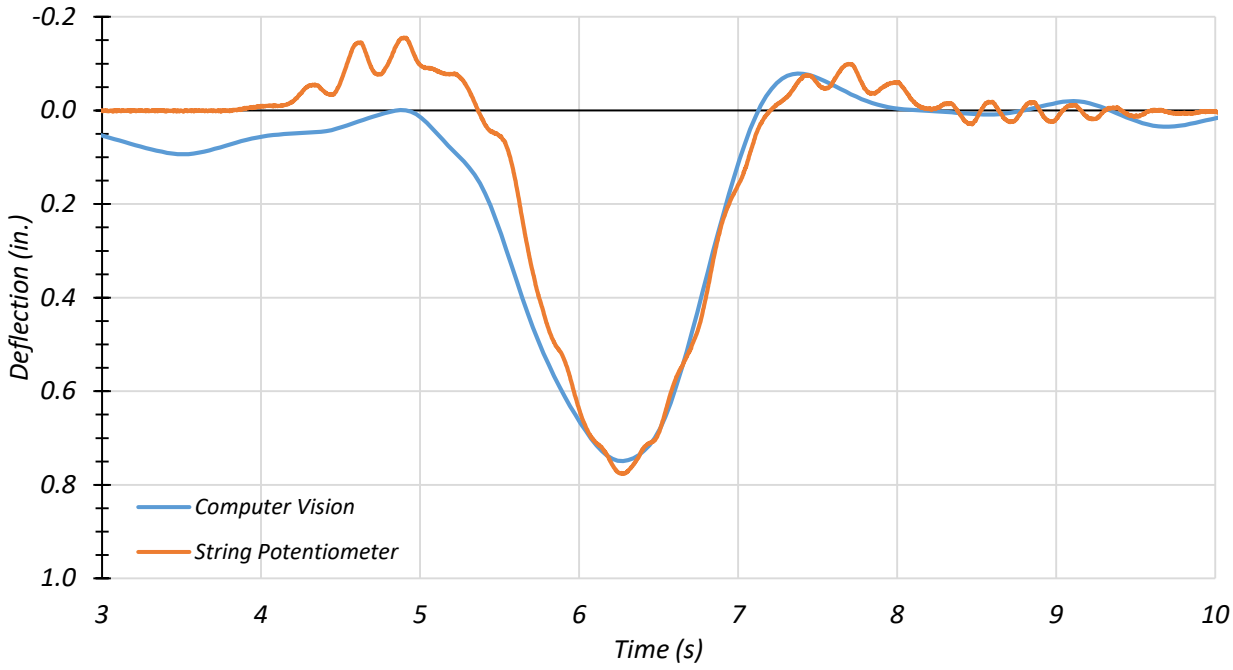

Figure 8.66. Girder 4 – Span 2 Deflections for Path 1 – Dynamic Test at 30 mph

Figure 8.67 shows the Span 2 midspan deflection over time using computer vision and from the Girder 4 string potentiometer for the Path 1 dynamic test at 37 mph. The cutoff frequency used for filtering was 1.5 Hz. The maximum deflection given by the string potentiometer is 0.772 in., while the maximum deflection given by computer vision is 0.617 in. Computer vision underestimated the deflection value by 0.155 in. and had a percent difference with the string potentiometer of 22.3 percent.

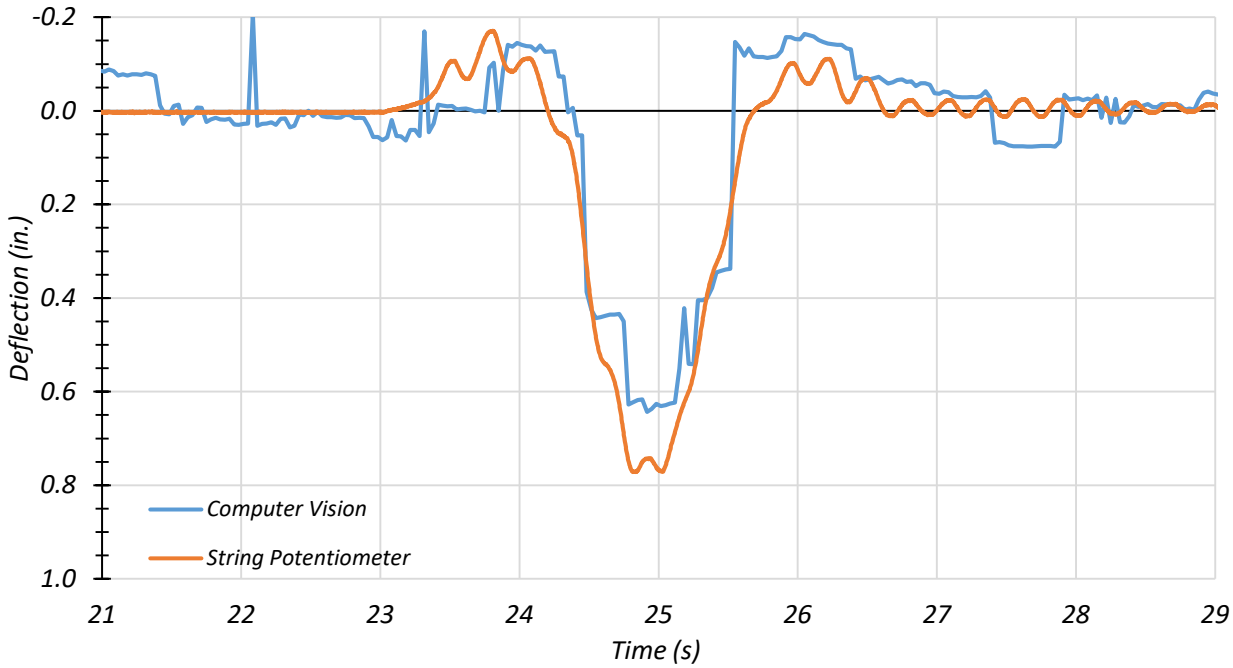

Figure 8.67. Girder 4 – Span 2 Deflections for Path 1 – Dynamic Test at 37 mph

Figure 8.68 shows the Span 1 midspan deflection over time using computer vision and from the Girder 1 string potentiometer for the Path 2 crawl speed test at 2 mph. The cutoff frequency used for filtering was 1.5 Hz. The maximum deflection given by the string potentiometer is 0.413 in., while the maximum deflection given by computer vision is 0.546 in. Computer vision overestimated the deflection value by 0.133 in. and had a percent difference with the string potentiometer of 27.7 percent.

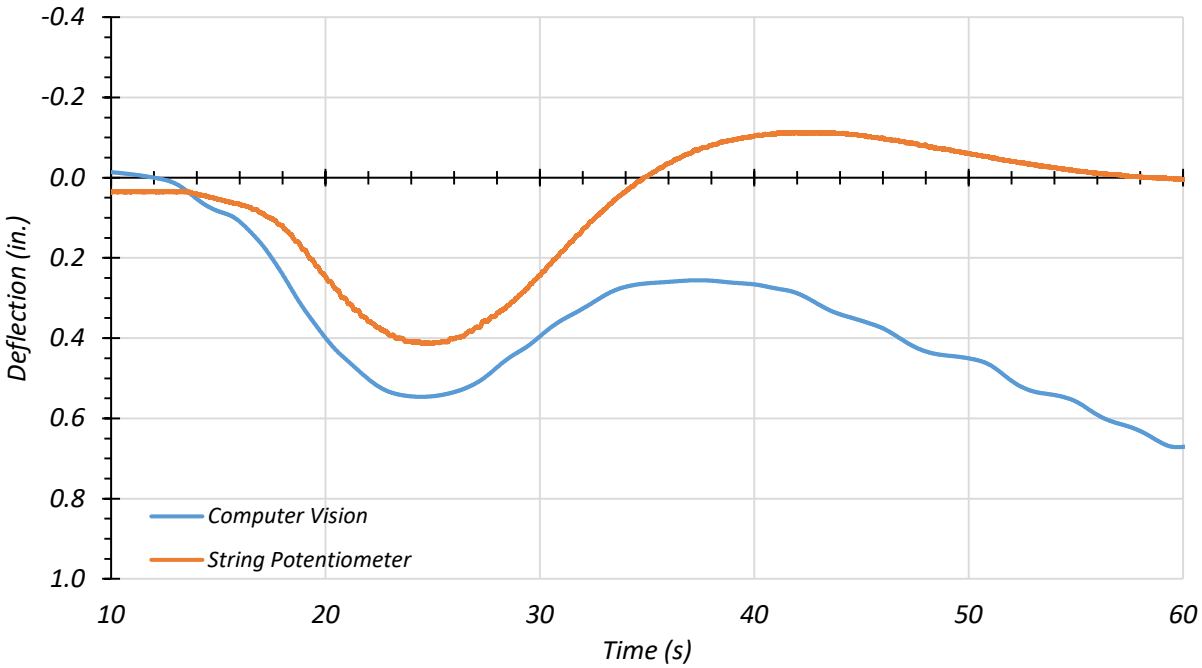

Figure 8.68. Girder 1 – Span 1 Deflections for Path 2 – Crawl Speed Test

Figure 8.69 shows the Span 1 midspan deflection over time using computer vision and from the Girder 1 string potentiometer for the Path 2 dynamic test at 29 mph. The cutoff frequency used for filtering was 0.45 Hz. The maximum deflection given by the string potentiometer is 0.403 in., while the maximum deflection given by computer vision is 0.381 in. Computer vision underestimated the deflection value by 0.022 in. and had a percent difference with the string potentiometer of 5.6 percent. The computer vision deflection value matches the string potentiometer well for this test.

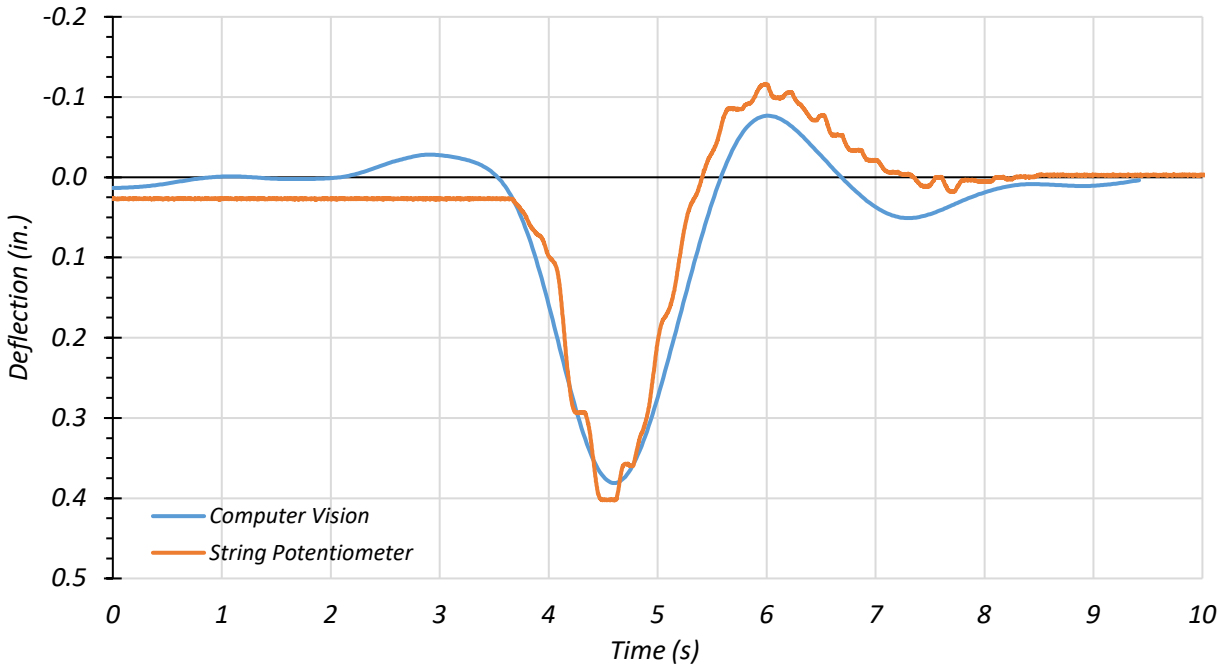

Figure 8.69. Girder 1 – Span 1 Deflections for Path 2 – Dynamic Test at 29 mph

Figure 8.70 shows the Span 1 midspan deflection over time using computer vision and from the Girder 1 string potentiometer for the Path 2 dynamic test at 44 mph. The cutoff frequency used for filtering was 6 Hz. The maximum deflection given by the string potentiometer is 0.434 in., while the maximum deflection given by computer vision is 0.421 in. Computer vision underestimated the deflection value by 0.013 in. and had a percent difference with the string potentiometer of 3.0 percent. The computer vision deflection value matches the string potentiometer well for this test.

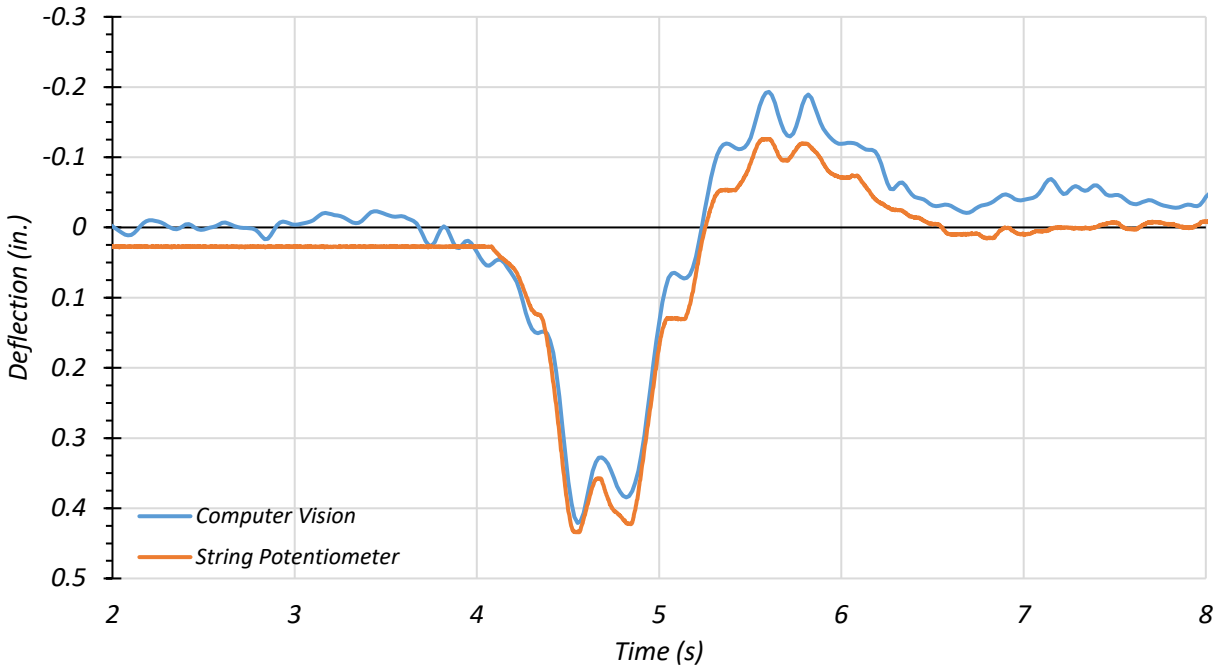

Figure 8.70. Girder 1 – Span 1 Deflections for Path 2 – Dynamic Test at 29 mph

The testing of Bridge SC-12 demonstrates that computer vision has the potential to be used to provide deflections during bridge load testing without the need for targets. More specifically, computer vision seems to be quite accurate for dynamic load tests.

8.6.6.2. Interior Girders

Computer vision was also used to investigate the deflection of the two interior girder during two load tests; (1) the Path 1 dynamic test at 30 mph and (2) the Path 2 dynamic test at 29 mph. Computer vision had difficulty capturing the furthest exterior girder for each test.

Figure 8.71 shows the Span 2 midspan deflection over time using computer vision and from the Girder 3 string potentiometer for the Path 1 dynamic test at 30 mph. The cutoff frequency used for filtering was 3 Hz. The maximum deflection given by the string potentiometer is 0.546 in., while the maximum deflection given by computer vision is 0.513 in. Computer vision underestimated the deflection value by 0.033 in. and had a percent difference with the string potentiometer of 6.2 percent. The computer vision deflection value matches the string potentiometer well for this test.

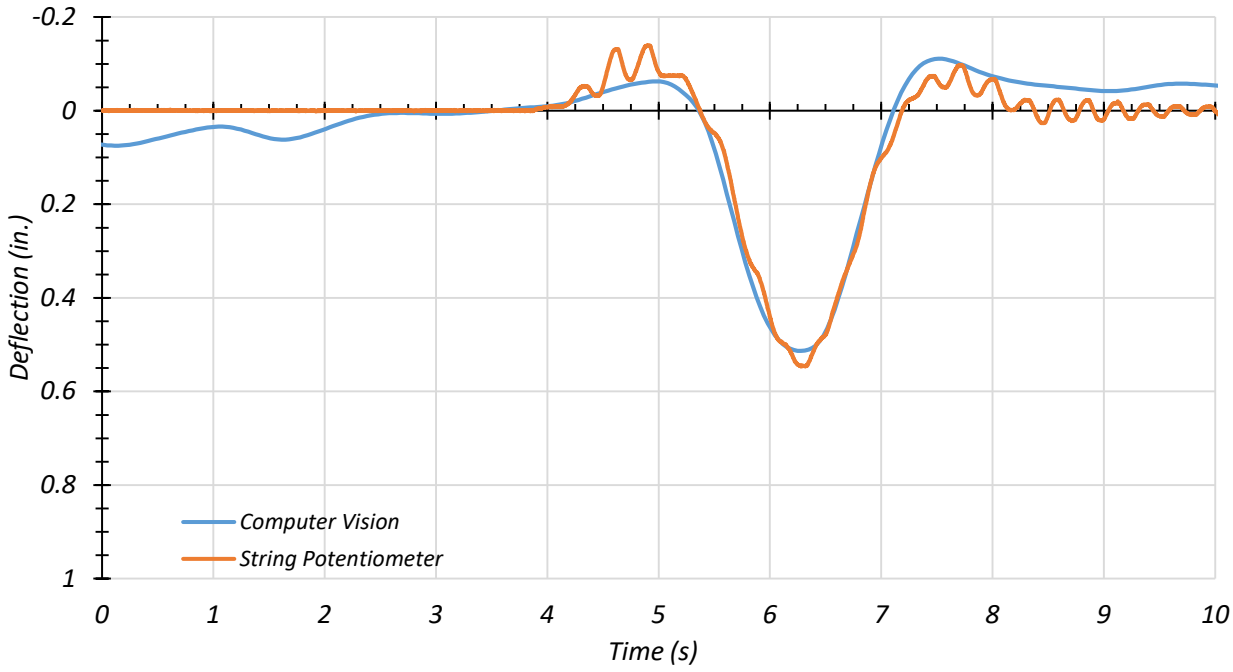

Figure 8.71. Girder 3 – Span 2 Deflections for Path 1 – Dynamic Test at 30 mph

Figure 8.72 shows the Span 2 midspan deflection over time using computer vision and from the Girder 2 string potentiometer for the Path 1 dynamic test at 30 mph. The cutoff frequency used for filtering was 3 Hz. The maximum deflection given by the string potentiometer is 0.290 in., while the maximum deflection given by computer vision is 0.244 in. Computer vision underestimated the deflection value by 0.046 in. and had a percent difference with the string potentiometer of 17.2 percent.

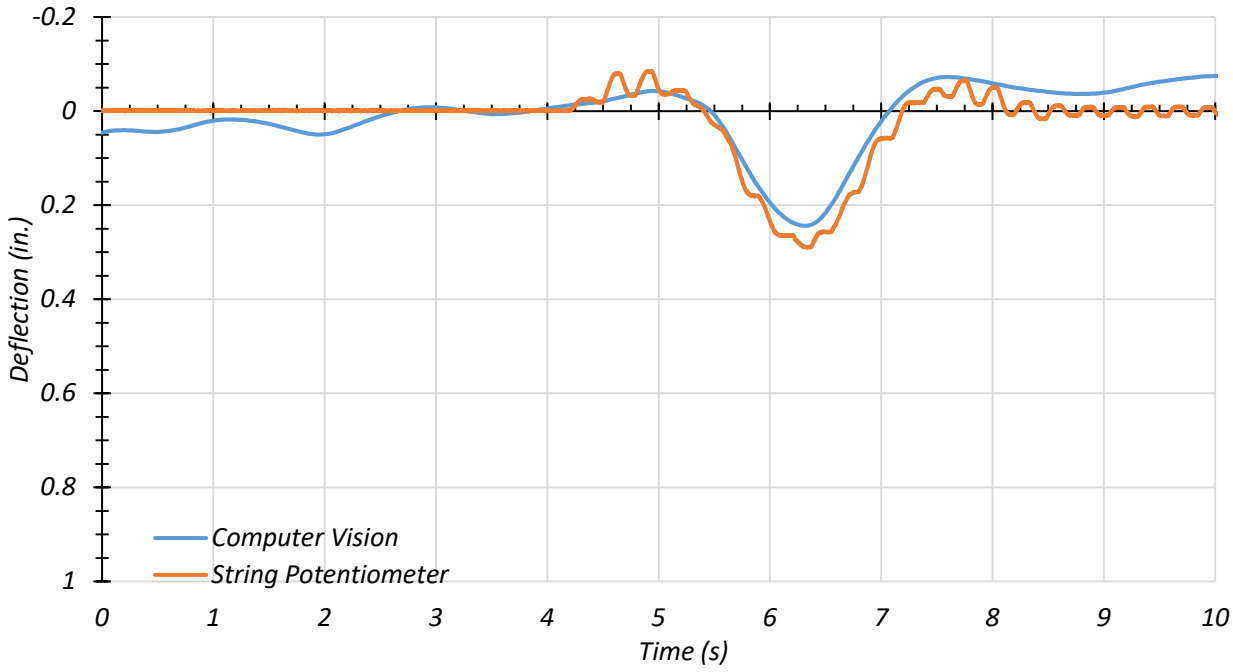

Figure 8.72. Girder 2 – Span 2 Deflections for Path 1 – Dynamic Test at 30 mph

Figure 8.73 shows the Span 1 midspan deflection over time using computer vision and from the Girder 2 string potentiometer for the Path 2 dynamic test at 29 mph. The cutoff frequency used for filtering was 3 Hz. The maximum deflection given by the string potentiometer is 0.334 in., while the maximum deflection given by computer vision is 0.317 in. Computer vision underestimated the deflection value by 0.017 in. and had a percent difference with the string potentiometer of 5.2 percent.

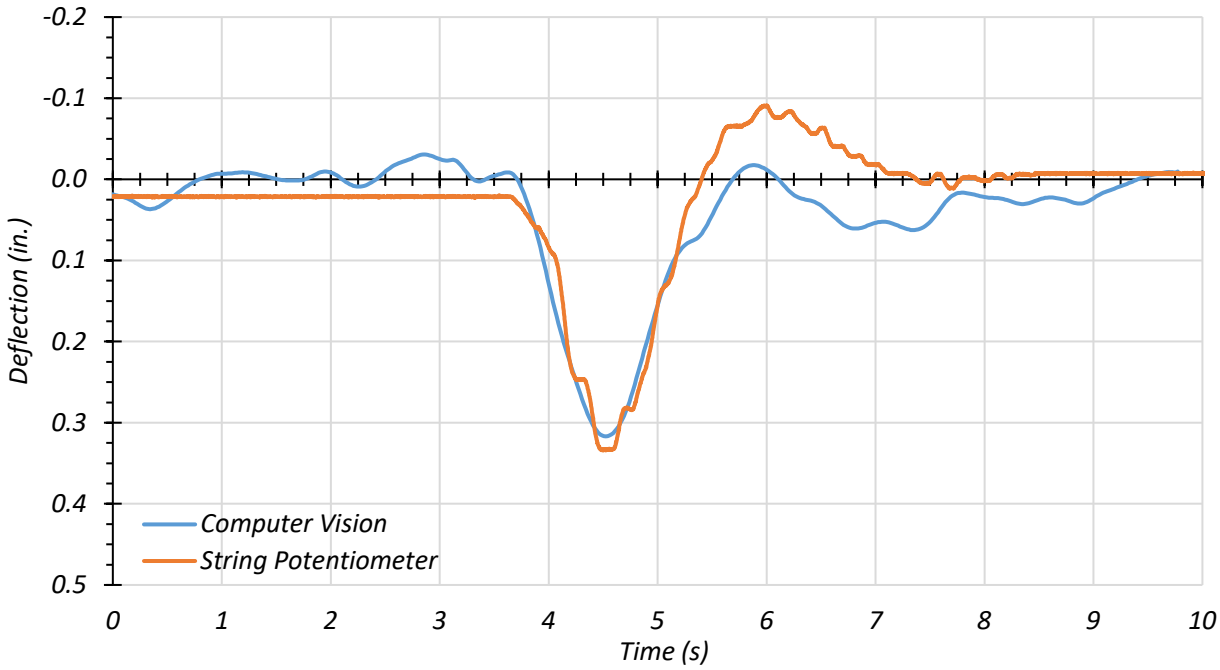

Figure 8.73. Girder 2 – Span 1 Deflections for Path 2 – Dynamic Test at 29 mph

Figure 8.74 shows the Span 1 midspan deflection over time using computer vision and from the Girder 3 string potentiometer for the Path 2 dynamic test at 29 mph. The cutoff frequency used for filtering was 3 Hz. The maximum deflection given by the string potentiometer is 0.201 in., while the maximum deflection given by computer vision is 0.205 in. Computer vision overestimated the deflection value by 0.004 in. and had a percent difference with the string potentiometer of 2.0 percent.

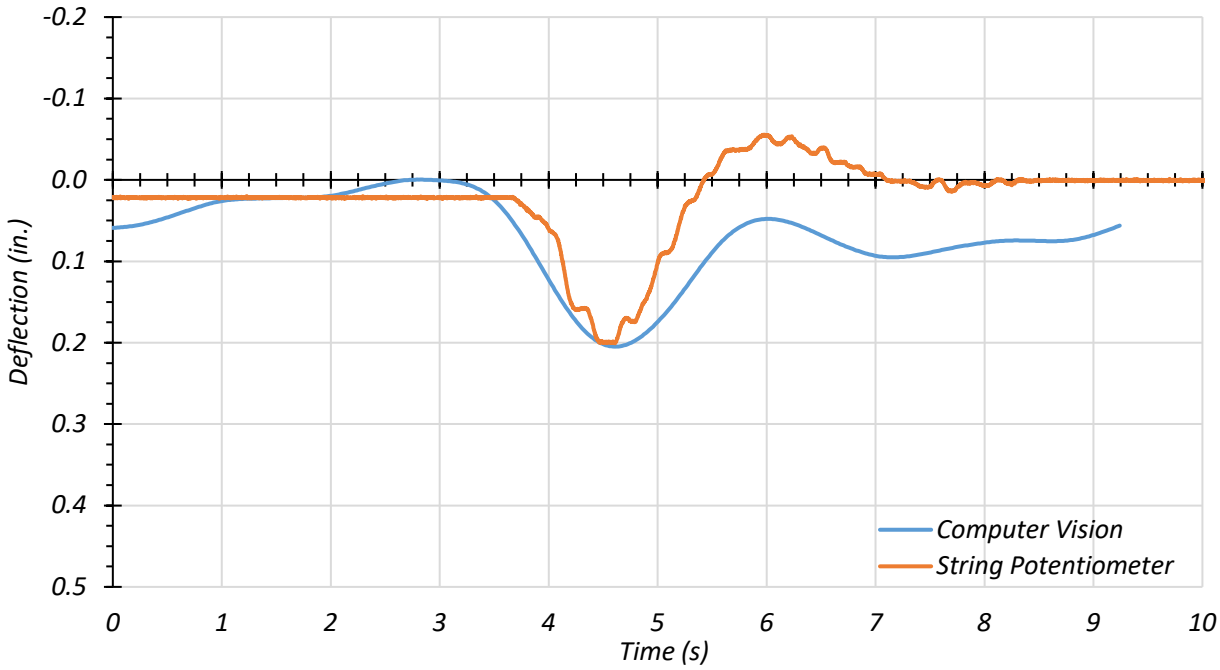

Figure 8.74. Girder 3 – Span 1 Deflections for Path 2 – Dynamic Test at 29 mph

The testing of Bridge SC-12 demonstrates that computer vision has the potential to be used to provide deflections during bridge load testing without the need for targets. This includes capturing the deflections of interior girders. More specifically, computer vision seems to be quite accurate for dynamic load tests.

8.7. FEM MODEL UPDATING AND CALIBRATION

8.7.1. General

Following the load testing, the original FEM model developed for Bridge SC-12 was modified to evaluate appropriate modeling parameters based on a comparison to the test results. The models are described first and then compared to the corresponding field measurements in Section 8.6.

8.7.2. Updated FEM Models

Two FEM models were developed to reflect the updated dimensions and in situ concrete compressive strength discussed in Section 8.3: (1) an updated model assuming no composite action between the steel girders and concrete deck, and (2) an updated model assuming fully composite action between the girders and deck. Both models assume roller boundary conditions at both ends of every girder, except for one end of a single girder that has a pinned support to resist any lateral forces.

The two updated models use the field measured dimensions of the bridge, including changing the deck thickness from the 6 in. given in the as-built drawings to the 5.75 in. measured in the field. These models also use the minimum f_c' of 6.25 ksi found using the NDE tests described in Subsection 8.3. This is an increase in f_c' from the 2.5 ksi that is prescribed by the AASHTO MBE, based on the age of the bridge, when the concrete deck strength is unknown (AASHTO MBE 2018). The increase in f_c' corresponds to an increase in computed concrete modulus of elasticity from 2850 ksi to 4506 ksi. Table 8.28 shows the results from the fully composite and fully non-composite simply supported FEM models with updated material properties, along with selected field-testing results. The results from the field testing seem to show that the bridge is behaving somewhere in between fully composite and fully non-composite. It is worth noting that TxDOT currently assumes fully non-composite behavior to load rate bridges without shears studs, such as this one.

Table 8.28. Selected FEM Results for Updated FEM Models

Model	Modal Frequency (Hz)		Span 1 Deflection (in.)		Span 2 Deflection (in.)		Span 1 Curvature (in^{-1})		Span 2 Curvature (in^{-1})	
	1st Mode	2nd Mode	G3	G4	G3	G4	G3	G4	G3	G4
Non-Composite	3.14	6.07	0.641	0.672	0.672	0.928	2.42E-05	3.65E-05	2.52E-05	3.85E-05
Composite	4.20	6.97	0.236	0.331	0.352	0.495	1.12E-05	1.28E-05	1.15E-05	1.64E-05
Field Test	3.78	6.71	0.351	0.485	0.526	0.755	1.92E-05	2.31E-05	1.70E-05	2.53E-05

8.7.3. Calibrated FEM Model Process

In addition to the two models discussed above, a third FEM model was developed for Bridge SC-12 that took into account the measured composite action observed during testing. The goal in the development of this calibrated FEM model was to create a model that more closely represents the measured bridge response. The calibrated model also uses the updated geometric properties and concrete modulus of elasticity as described in the previous section.

Partial composite action was created in the model by inserting horizontal springs at the nodes between the bottom surface of the deck and the top flanges of the girders. As shown in the original model development, the reduction of stiffness of the concrete deck in the negative moment regions due to cracking can affect the bridge behavior. Although no cracking in the deck was noticed during field testing due to the asphalt overlay, this bridge has been in service for a long period of time. It is expected that the deck is experiencing cracking near the interior supports. For this reason, the stiffness of the deck near the interior supports was reduced in the calibrated FEM model. The procedure for this reduction is explained in the model development for Bridge SC-12 reported earlier.

Initially the horizontal spring stiffness values required for a fully composite structure and a fully non-composite structure were found. Then, the stiffness parameter was methodically increased while keeping all other parameters the same in order to see the effect that partial composite behavior has on the results of the analysis. Based on this parametric study, a spring stiffness value was chosen for each input parameter to begin the process of refining the final calibrated model.

8.7.4. Calibrated FEM Model Results

8.7.4.1. Composite Spring Stiffness

Table 8.29 shows the effect of changing the composite spring stiffness value on the modal frequencies of the bridge, and the Span 1 and Span 2 deflections, and the Span 1 and Span 2 curvatures. Figure 8.75 shows this change for each output parameter graphically. Both Girder 3 and Girder 4 results are obtained from the Path 1 stop location load tests, as these were found to be controlling, and the test modal frequencies are obtained from the sledgehammer test at midspan of Span 2 along the centerline of the bridge.

Table 8.29. Effect of Composite Spring Stiffness Value on Selected FEM Results

Model (kip/in.)	Modal Frequency (Hz)		Span 1 Deflection (in.)		Span 2 Deflection (in.)		Span 1 Curvature (in^{-1})		Span 2 Curvature (in^{-1})	
	1st Mode	2nd Mode	G3	G4	G3	G4	G3	G4	G3	G4
Infinite	4.20	6.97	0.236	0.331	0.352	0.495	1.12E-05	1.28E-05	1.15E-05	1.64E-05
1500	3.84	6.79	0.291	0.391	0.422	0.575	1.44E-05	1.61E-05	1.44E-05	1.98E-05
1000	3.77	6.76	0.303	0.404	0.438	0.592	1.56E-05	1.68E-05	1.57E-05	2.07E-05
500	3.67	6.70	0.325	0.428	0.466	0.624	1.69E-05	1.81E-05	1.73E-05	2.19E-05
250	3.58	6.63	0.347	0.454	0.496	0.660	1.83E-05	1.95E-05	1.86E-05	2.34E-05
150	3.51	6.57	0.364	0.475	0.518	0.690	1.93E-05	2.06E-05	1.96E-05	2.45E-05
5	3.14	6.07	0.641	0.672	0.672	0.928	2.42E-05	3.65E-05	2.52E-05	3.85E-05
Test	3.78	6.71	0.351	0.485	0.526	0.755	1.92E-05	2.31E-05	1.70E-05	2.53E-05

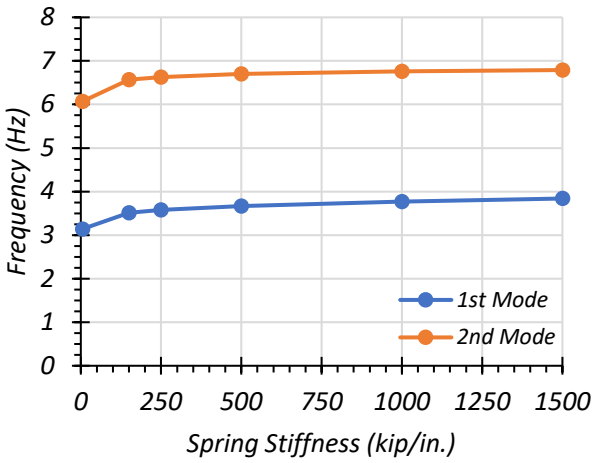

(a) Effect on Modal Frequency

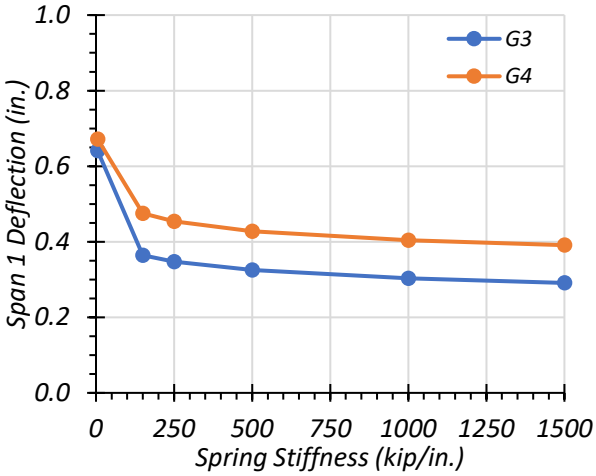

(b) Effect on Span 1 Deflection

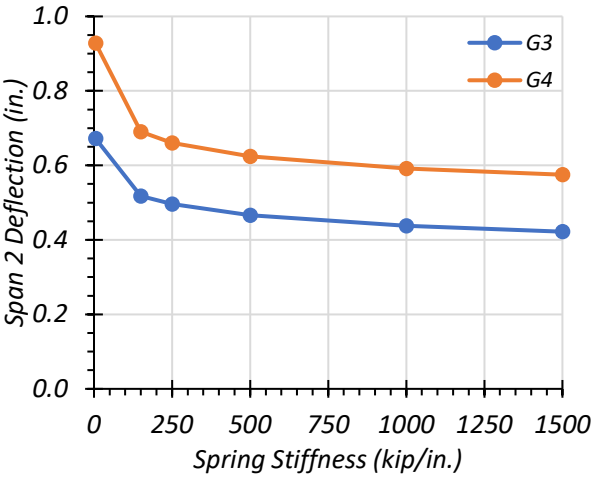

(c) Effect on Span 2 Deflection

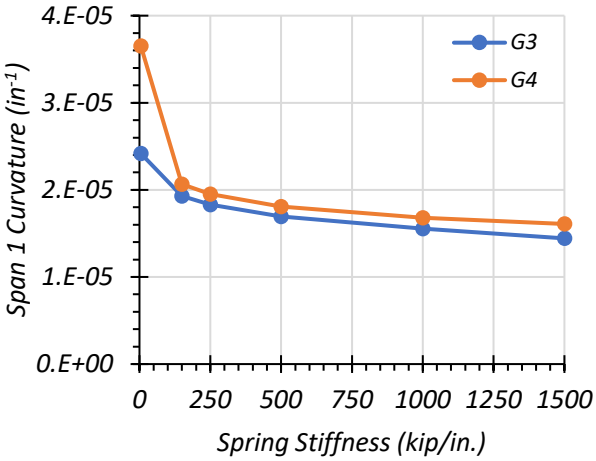

(d) Effect on Span 1 Curvature

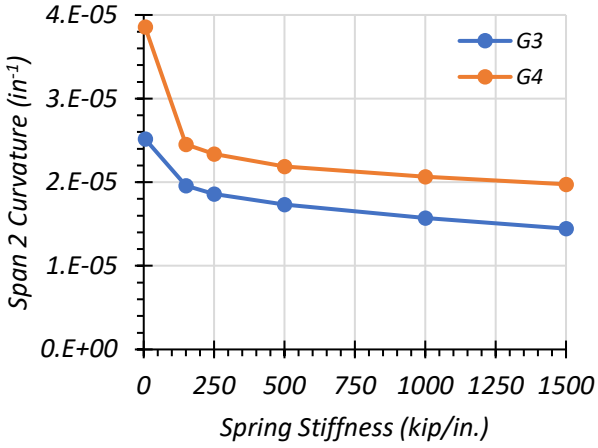

(e) Effect on Span 2 Curvature

Figure 8.75. Effect of Composite Spring Stiffness Value on Selected FEM Results

8.7.4.2. Final Calibration

In the refinement of the final calibrated model, the partial composite spring stiffness was slightly adjusted in order to get as close as possible to representing the test results. In addition, the final calibrated model uses different spring stiffness values for the interior and exterior girders. The stiffness values used in the final model are 200 kip/in. for the interior girders and 100 kip/in. for the exterior girders. Table 8.30 provides the final partial composite horizontal spring stiffness values used for each girder in the calibrated SC-12 model.

Table 8.30. Partial Composite Horizontal Spring Stiffness Values for Calibrated SC-12 Model

Girder	G1	G2	G3	G4
Spring Stiffness (kip/in.)	100	200	200	100

The analysis of the model for each iteration of the calibration process was compared to selected test measurements. Table 8.31 shows the output for selected major parameters for the final calibrated FEM model and for the field tests performed on Bridge SC-12. It is important to note that the results for both girders come from the Path 1 stop location load tests, as that is the controlling load case for both girders. Figure 8.76 shows the final calibrated model with the partial composite horizontal stiffness springs. This calibrated model was also used in comparison with the field test results.

Table 8.31. Results of SC-12 Model Calibration

Parameter	Calibrated FEM Output		Test Result	
	G3	G4	G3	G4
Span 1 Deflection (in.)	0.369	0.490	0.351	0.485
Span 2 Deflection (in.)	0.526	0.720	0.526	0.755
Span 1 Top Flange Strain (με)	-111.6	-99.8	-102.4	-126.9
Span 1 Bottom Flange Strain (με)	150.5	191.3	161.7	190.3
Span 2 Top Flange Strain (με)	-99.1	-104.9	-73.1	-111.4
Span 2 Bottom Flange Strain (με)	163.4	239.9	161.4	237.2
First Modal Frequency	3.50		3.78	
Second Modal Frequency	6.07		6.71	

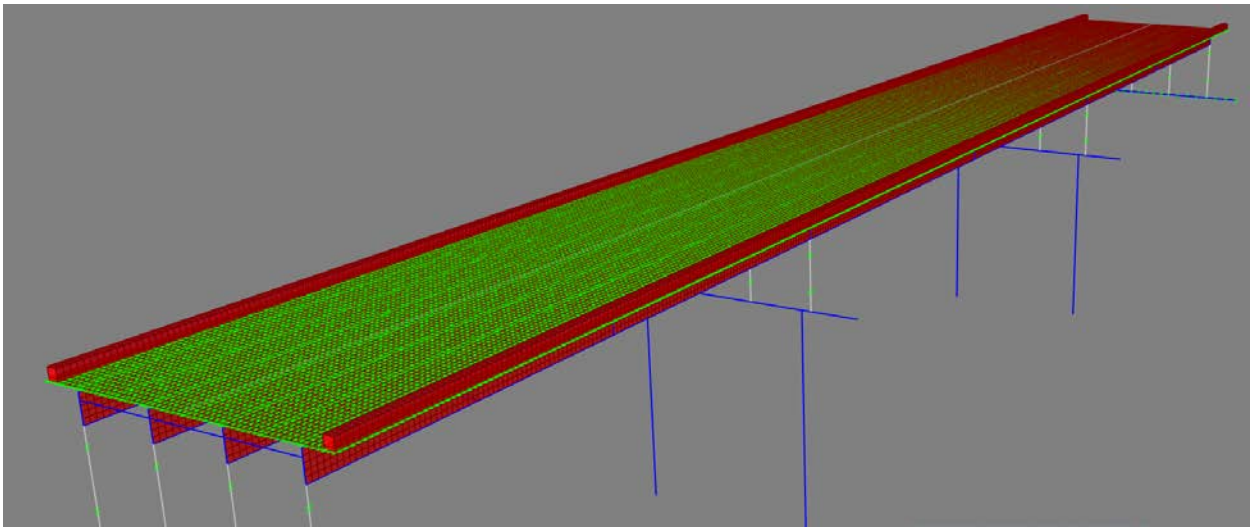

Figure 8.76. Bridge SC-12 Calibrated Model

8.7.5. Dynamic Characteristics of the Bridge

The dynamic characteristics of the bridge were analyzed as part of the model calibration process. Data obtained from the accelerometers during dynamic tests and the sledgehammer tests were filtered and a fast-Fourier transform (FFT) was performed. This allowed for determination of the

first two natural frequencies of the bridge. The calibrated model produced a first modal frequency of 3.50 Hz, compared to a test first modal frequency of 3.78 Hz. The calibrated model produced a second modal frequency of 6.07 Hz, compared to a test first modal frequency of 6.71 Hz. For each natural frequency, the amplitude and phase angle of each accelerometer was used to develop the mode shape. These mode shapes were compared to the calibrated FEM model. Figure 8.77 shows the comparison for a longitudinal section and a transverse section of both spans for the mode shape produced by the first natural frequency of Bridge SC-12. Figure 8.78 shows the comparison for a longitudinal section and a transverse section of both spans for the mode shape produced by the second natural frequency of the bridge. For the third mode shape observed during testing, the modal frequencies presented in the FEM program do not go as high in magnitude. Also, the shape of the third mode seen during testing could not be matched with a mode shape presented by the FEM model. Therefore, it could not be compared. There are some slight differences between magnitudes of the mode shapes developed by the test results to the mode shapes developed by the calibrated FEM model. However, in general, the calibrated model mode shapes fit the test mode shapes well.

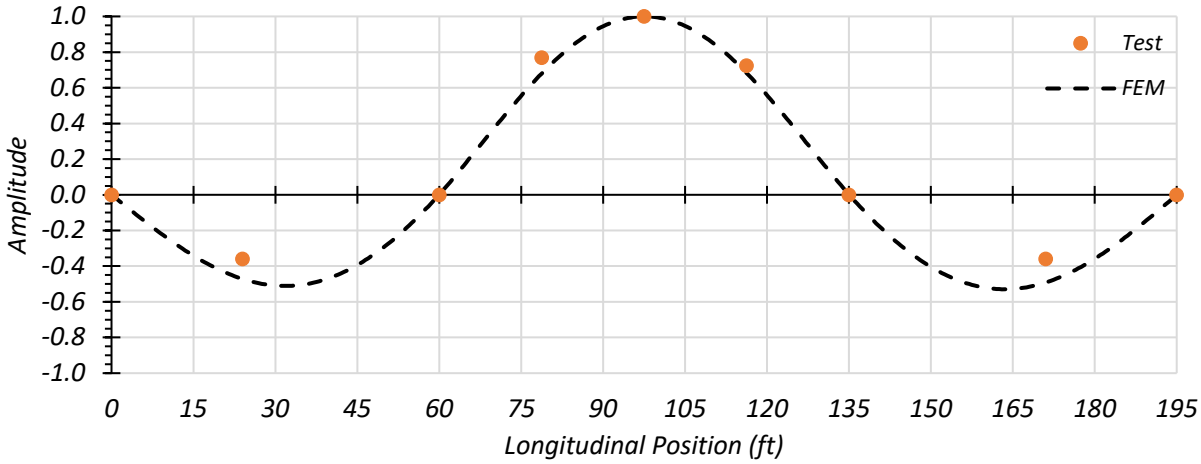

(a) Longitudinal Section

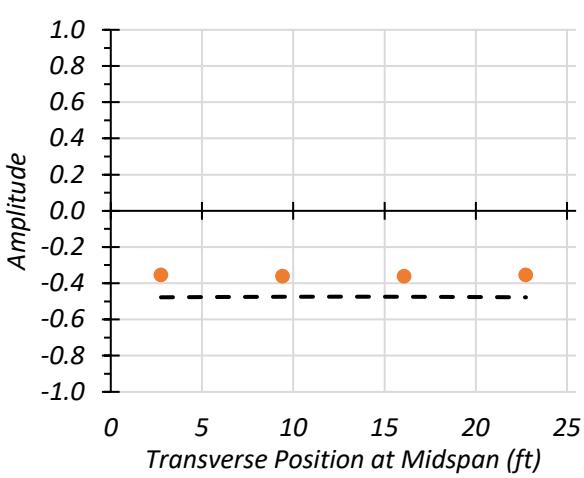

(b) Transverse Section – Span 1

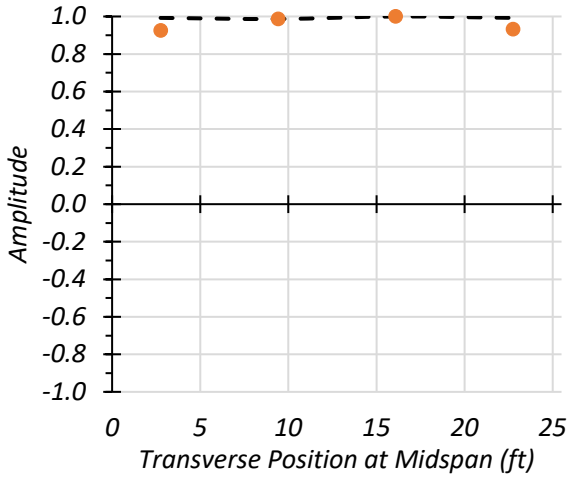

(c) Transverse Section – Span 2

Figure 8.77. Comparison of First Mode Shape of Bridge SC-12

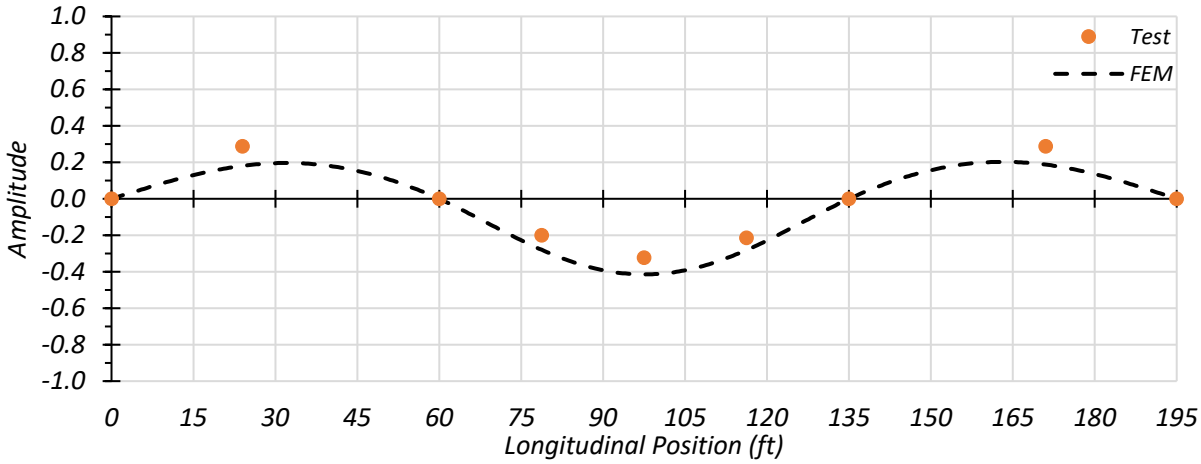

(a) Longitudinal Section

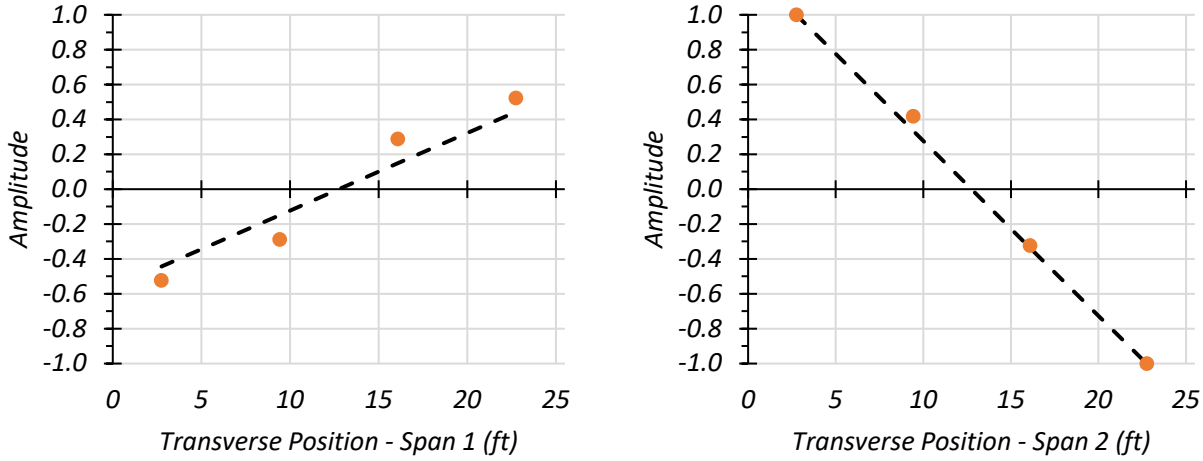

(b) Transverse Section – Span 1

(c) Transverse Section – Span 2

Figure 8.78. Comparison of Second Mode Shape of Bridge SC-12

The natural frequencies of Bridge SC-12 observed during testing were compared to the natural frequencies produced by FEM. Table 8.32 shows the test and FEM natural frequencies. The first natural frequency is close to the calibrated FEM first natural frequency, however, is closer to the first natural frequency of the updated composite FEM model. The test second frequency matches better with the calibrated FEM model second frequency.

Table 8.32. Bridge SM-5 Test and FEM Natural Frequencies for First Two Mode Shapes

Frequency	Test (Hz)	Updated FEM Non-Composite (Hz)	Updated FEM Composite (Hz)	Calibrated FEM (Hz)
1st Natural Frequency	3.78	2.52	3.85	3.50
2nd Natural Frequency	6.71	2.96	8.35	6.07

8.8. COMPARISON OF TEST RESULTS AND FEM PREDICTIONS

8.8.1. Static Load Tests on Bridge SC-12 Span 1

Two types of static load tests were conducted without introducing any dynamic effects: (1) stop location test by parking the vehicle at moment critical longitudinal position in each span for each selected path on the bridge, (2) crawl speed tests by moving the truck at low speeds (around 2 mph) along the same predefined paths.

8.8.1.1. Strain Measurements and Composite Action

Partial composite action can be determined by reviewing the strain diagrams over the section depth. Some information is available from the measured results to evaluate the composite behavior between the concrete deck and steel girders. A number of strain plots are provided in this section, where measured strain values are shown by a colored dot symbol. The colored line connecting two dot symbols represents the strain diagram at this cross-section based on the plane sections remains plane assumption. In the plots for the loaded span, the black and grey dotted lines show the composite and non-composite strain diagrams obtained from the updated FEM models, and the

purple dotted line shows the strain diagram obtained from the calibrated FEM model. The blue plot shows the strain results for the pier location, the red plot shows the strain results for Span 1, and the green plot shows the strain results for Span 2. The orange dotted line and the purple dotted line in figures (a) and (c) represent the calibrated FEM model results for the unloaded span and the pier, respectively.

8.8.1.1.1. Interior Girder 3

Figure 8.79 through Figure 8.81 provide plots of the measured strains for interior Girder 3 during static loading testing and compares the midspan strain diagram to those obtained through the updated and calibrated FEM models. The strains measured for Girder 3 during the Path 1 – Span 1 static tests are shown in Figure 8.79 and compared with values obtained from the FEM updated and calibrated models. Figure 8.79(a) shows the FEM comparison for the stop location test for Girder 3 adjacent to the interior pier and midspan of Span 2. Figure 8.79(b) shows the FEM comparison for the stop location test for Girder 3 at 0.4*L* of Span 1. Figure 8.79(c) shows the FEM comparison for the crawl speed test for Girder 3 adjacent to the interior pier and midspan of Span 2. Figure 8.79(d) shows the FEM comparison for the crawl speed test for Girder 3 at 0.4*L* of Span 1.

The strains measured for Girder 3 during the Path 2 – Span 1 static tests are shown in Figure 8.80 and compared with values obtained from the FEM updated and calibrated models. Figure 8.80(a) shows the FEM comparison for the stop location test for Girder 3 adjacent to the interior pier and midspan of Span 2. Figure 8.80(b) shows the FEM comparison for the stop location test for Girder 3 at 0.4*L* of Span 1. Figure 8.80(c) shows the FEM comparison for the crawl speed test for Girder 3 adjacent to the interior pier and midspan of Span 2. Figure 8.80(d) shows the FEM comparison for the crawl speed test for Girder 3 at 0.4*L* of Span 1.

The strains measured for Girder 3 during the Middle Path static tests are shown in Figure 8.81 and compared with values obtained from the FEM updated and calibrated models. Figure 8.81(a) shows the FEM comparison for the stop location test for Girder 3 adjacent to the interior pier and midspan of Span 2. Figure 8.81(b) shows the FEM comparison for the stop location test for Girder 3 at 0.4*L* of Span 1. Figure 8.81(c) shows the FEM comparison for the crawl speed test for Girder 3 adjacent to the interior pier and midspan of Span 2. Figure 8.81(d) shows the FEM comparison for the crawl speed test for Girder 3 at 0.4*L* of Span 1.

The calibrated model compares well with the Path 1 and Middle Path loading strain diagrams, but not quite as well with the Path 2 loading strain diagram. This is likely due to Girder 3 not receiving much load during Path 2 loading, as the truck is closer to Girders 1 and 2.

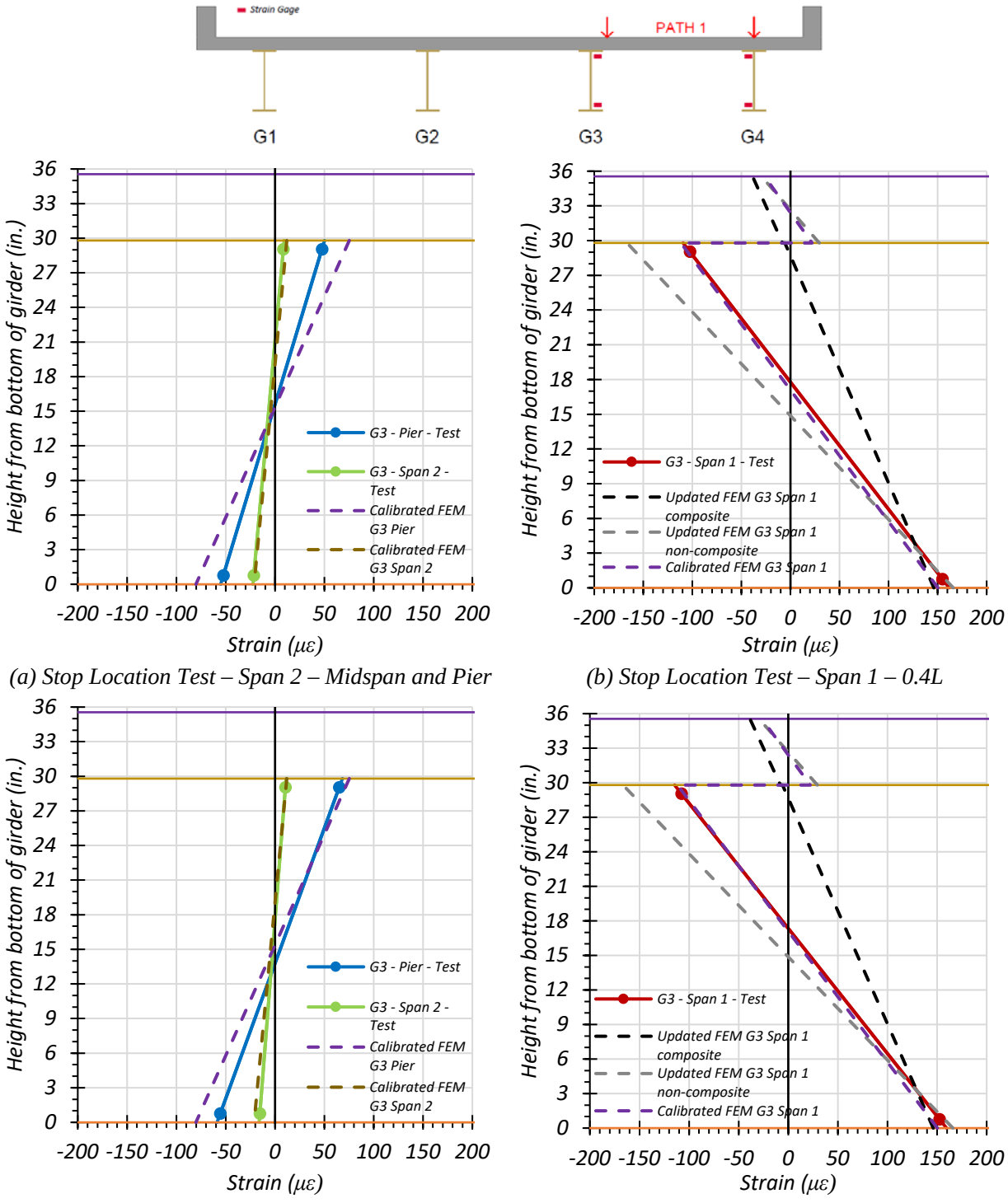

(a) Stop Location Test – Span 2 – Midspan and Pier

(b) Stop Location Test – Span 1 – 0.4L

(c) Crawl Speed Test – Span 2 Midspan and Pier

(d) Crawl Speed Test – Span 1 – 0.4L

Figure 8.79. Comparison of Static Strains for Interior Girder 3 – Path 1 – Span 1

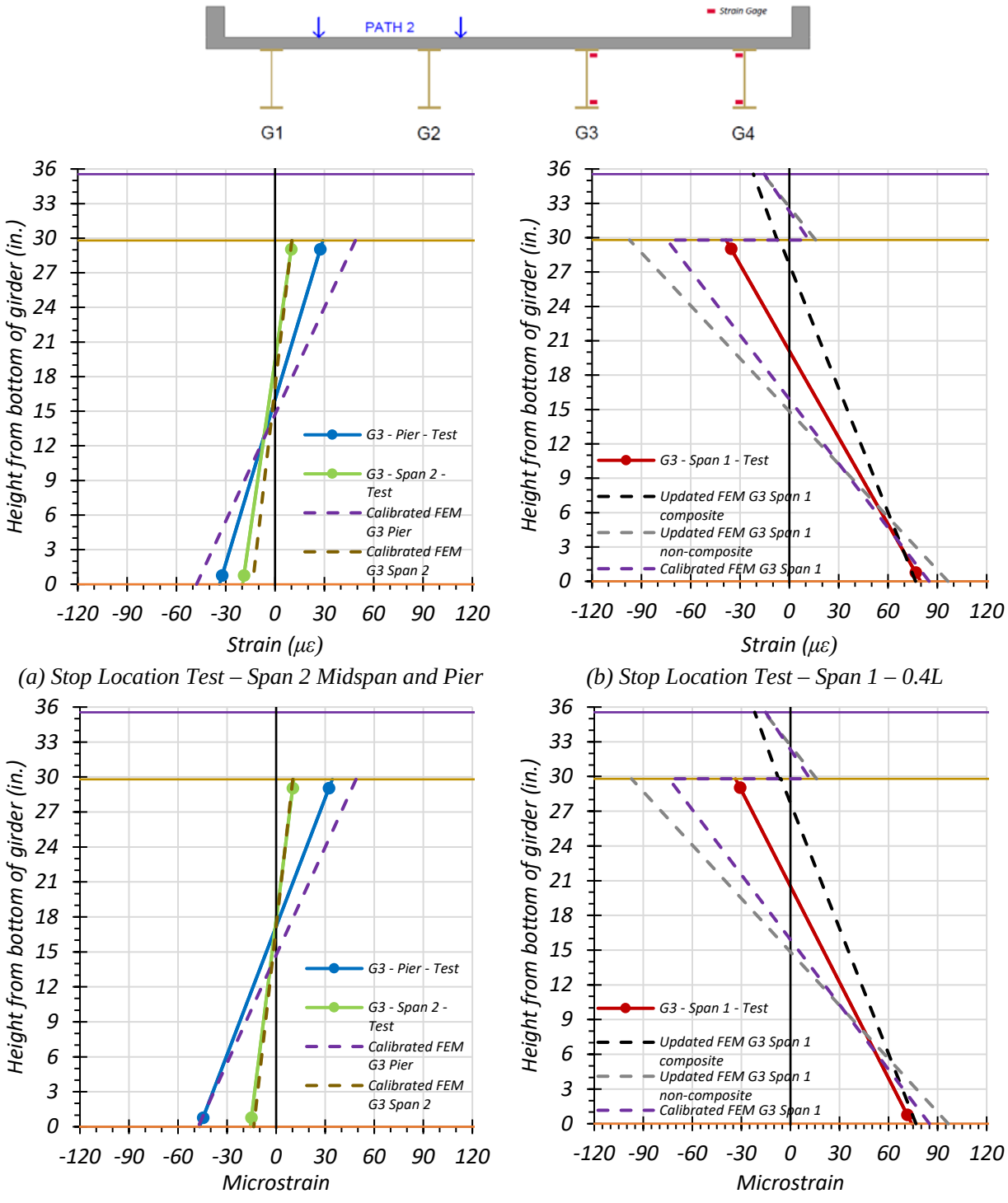

(a) Stop Location Test – Span 2 Midspan and Pier

(b) Stop Location Test – Span 1 – 0.4L

(c) Crawl Speed Test – Span 2 Midspan and Pier

(d) Crawl Speed Test – Span 1 – 0.4L

Figure 8.80. Comparison of Static Strains for Interior Girder 3 – Path 2 – Span 1

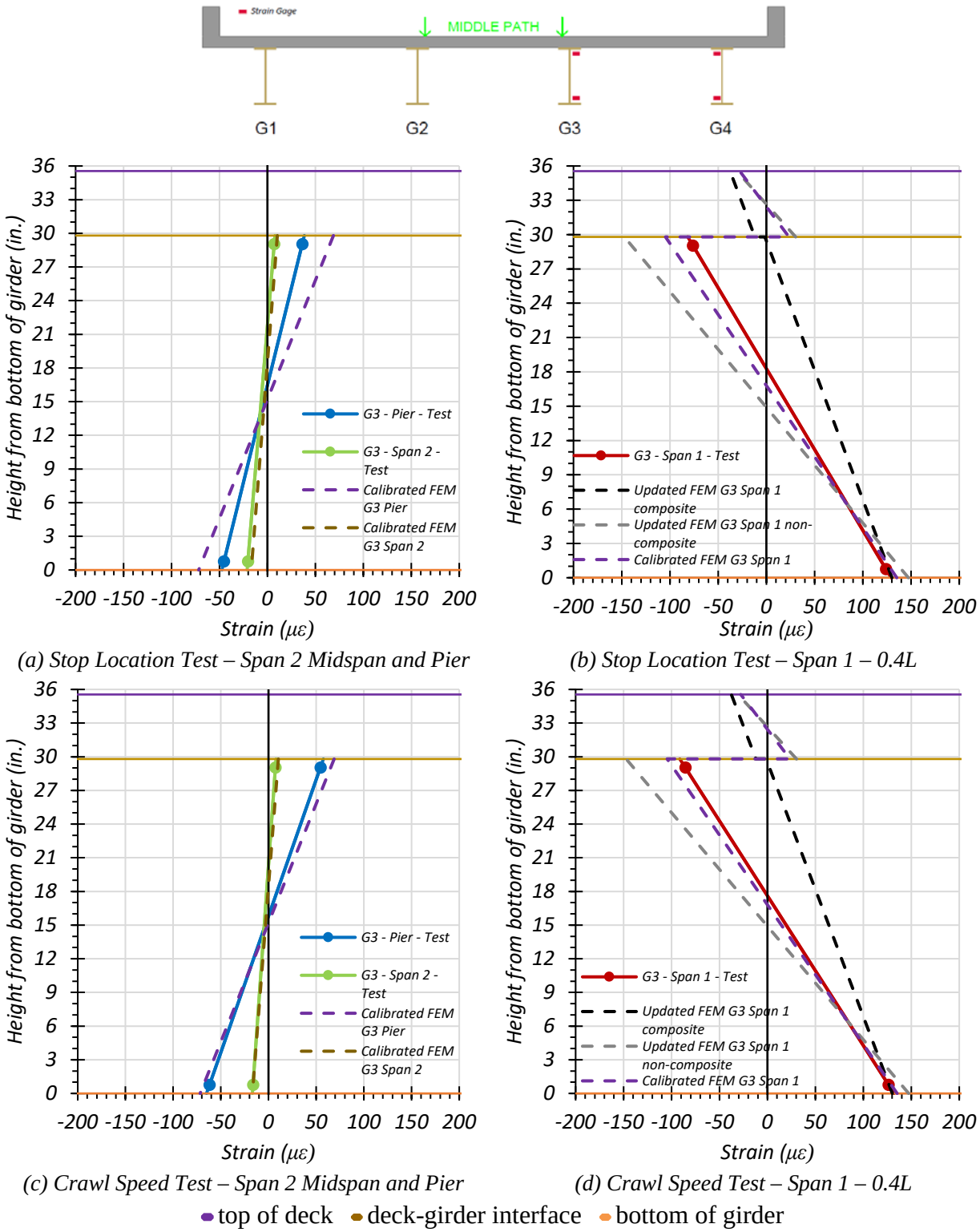

(a) Stop Location Test – Span 2 Midspan and Pier

(b) Stop Location Test – Span 1 – 0.4L

(c) Crawl Speed Test – Span 2 Midspan and Pier

(d) Crawl Speed Test – Span 1 – 0.4L

Figure 8.81. Comparison of Static Strains for Interior Girder 3 – Middle Path – Span 1

8.8.1.1.2. Exterior Girder 4

Figure 8.82 through Figure 8.84 provide plots of the measured strains for exterior Girder 4 during static loading testing and compares the midspan strain diagram to those obtained through the updated and calibrated FEM models. The strains measured for Girder 4 during the Path 1 – Span 1 static tests are shown in Figure 8.82 and compared with values obtained from the FEM updated and calibrated models. Figure 8.82(a) shows the FEM comparison for the stop location test for Girder 4 adjacent to the interior pier and midspan of Span 2. Figure 8.82(b) shows the FEM comparison for the stop location test for Girder 4 at 0.4*L* of Span 1. Figure 8.82(c) shows the FEM comparison for the crawl speed test for Girder 4 adjacent to the interior pier and midspan of Span 2. Figure 8.82(d) shows the FEM comparison for the crawl speed test for Girder 4 at 0.4*L* of Span 1.

The strains measured for Girder 4 during the Path 2 – Span 1 static tests are shown in Figure 8.83 and compared with values obtained from the FEM updated and calibrated models. Figure 8.83(a) shows the FEM comparison for the stop location test for Girder 4 adjacent to the interior pier and midspan of Span 2. Figure 8.83(b) shows the FEM comparison for the stop location test for Girder 4 at 0.4*L* of Span 1. Figure 8.83(c) shows the FEM comparison for the crawl speed test for Girder 4 adjacent to the interior pier and midspan of Span 2. Figure 8.83(d) shows the FEM comparison for the crawl speed test for Girder 4 at 0.4*L* of Span 1.

The strains measured for Girder 4 during the Middle Path static tests are shown in Figure 8.84 and compared with values obtained from the FEM updated and calibrated models. Figure 8.84(a) shows the FEM comparison for the stop location test for Girder 4 adjacent to the interior pier and midspan of Span 2. Figure 8.84(b) shows the FEM comparison for the stop location test for Girder 4 at 0.4*L* of Span 1. Figure 8.84(c) shows the FEM comparison for the

crawl speed test for Girder 4 adjacent to the interior pier and midspan of Span 2. Figure 8.84(d) shows the FEM comparison for the crawl speed test for Girder 4 at 0.4*L* of Span 1.

The calibrated model compares well with the Path 1 loading strain diagrams, but not quite as well with the Path 2 and Middle Path loading strain diagrams. This is likely due to Girder 4 not receiving significant load during Path 2 loading and Middle Path loading, as the truck is closer to Girders 1 and 2 under Path 2 loading, and Girders 2 and 3 under Middle Path loading.

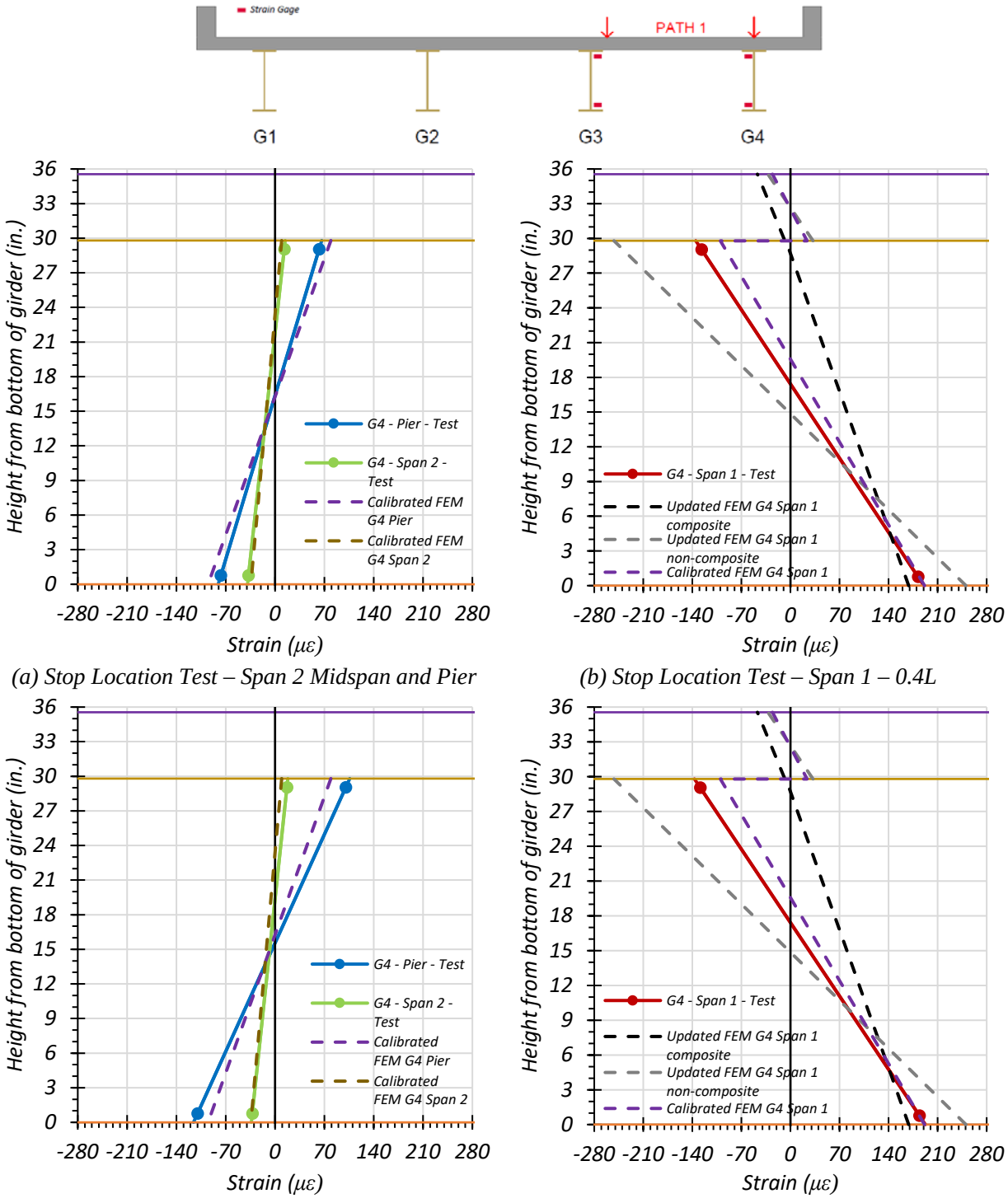

(a) Stop Location Test – Span 2 Midspan and Pier

(b) Stop Location Test – Span 1 – 0.4L

(c) Crawl Speed Test – Span 2 Midspan and Pier

(d) Crawl Speed Test – Span 1 – 0.4L

Figure 8.82. Comparison of Static Strains for Exterior Girder 4 – Path 1 – Span 1

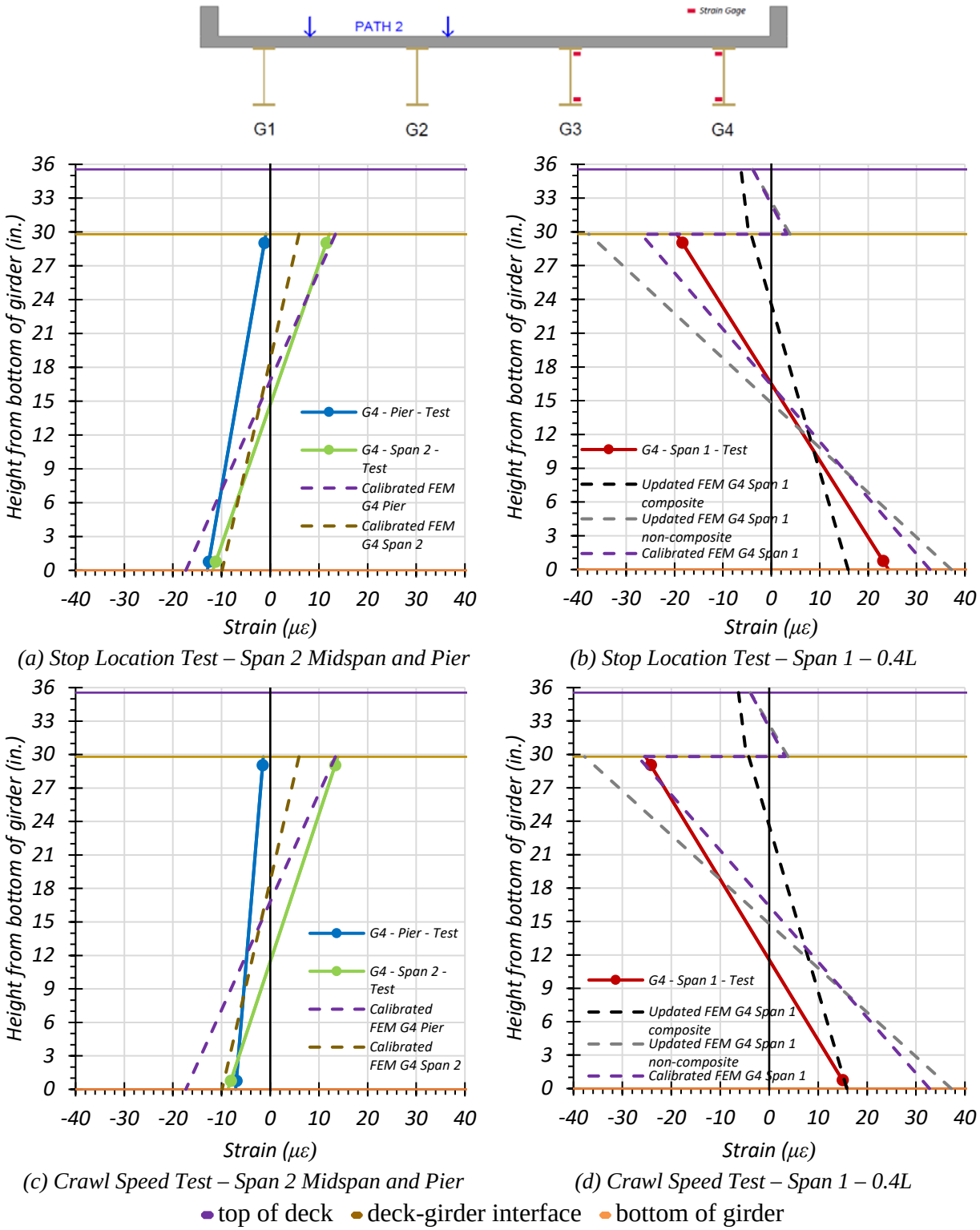

(a) Stop Location Test – Span 2 Midspan and Pier

(b) Stop Location Test – Span 1 – 0.4L

(c) Crawl Speed Test – Span 2 Midspan and Pier

(d) Crawl Speed Test – Span 1 – 0.4L

Figure 8.83. Comparison of Static Strains for Exterior Girder 4 – Path 2 – Span 1

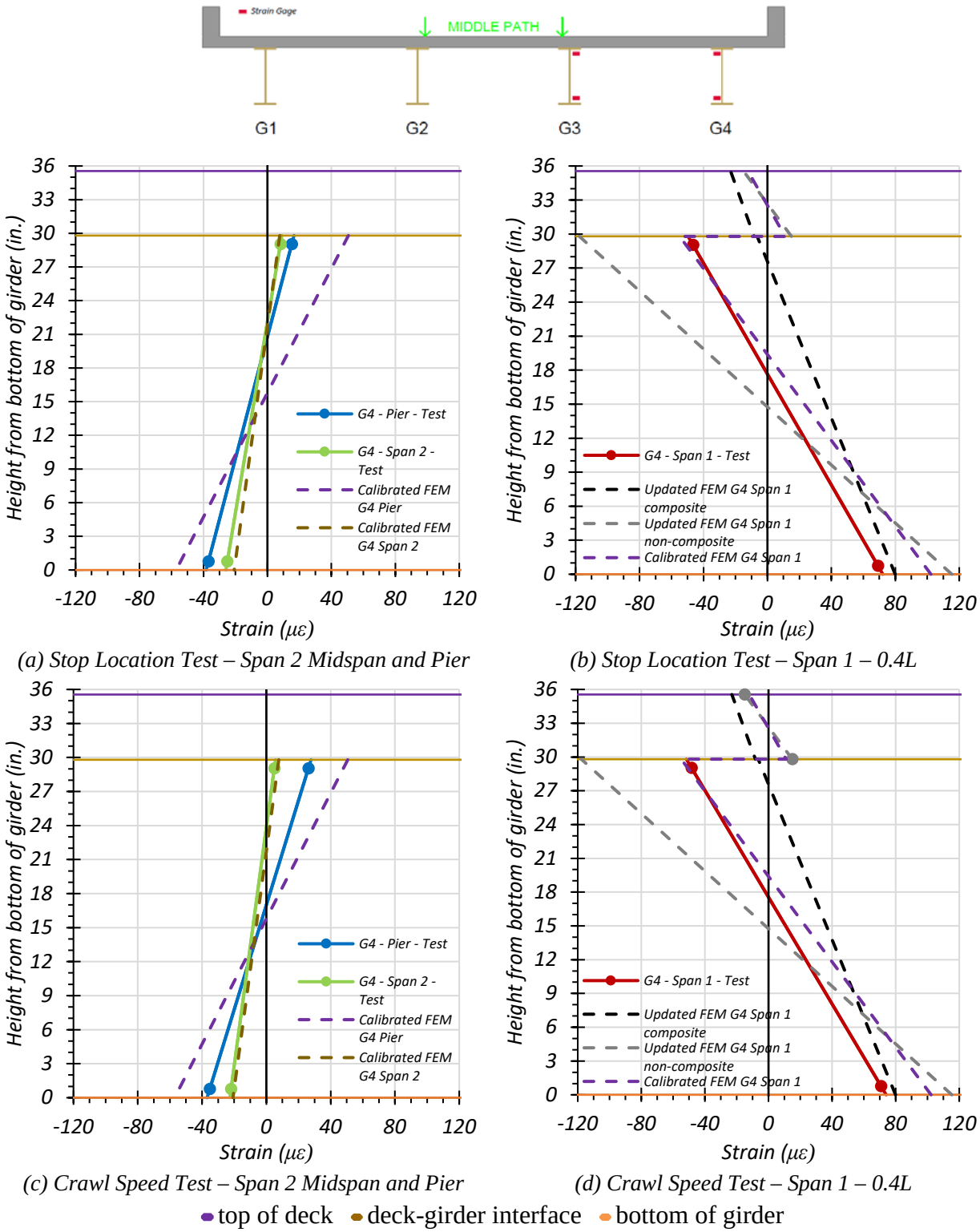

(a) Stop Location Test – Span 2 Midspan and Pier

(b) Stop Location Test – Span 1 – 0.4L

(c) Crawl Speed Test – Span 2 Midspan and Pier

(d) Crawl Speed Test – Span 1 – 0.4L

Figure 8.84. Comparison of Static Strains for Exterior Girder 4 – Middle Path – Span 1

8.8.1.1.3. Comparison of Measured Strain Results

The neutral axis locations of Girder 3 and Girder 4 observed during the load tests were compared with the theoretical neutral axis locations calculated using the FEM strain predictions. Table 8.33 shows the neutral axis locations measured for all static load tests and for the three FEM models. Figure 8.85 compares the test neutral axis locations with the non-composite and composite neutral axis locations obtained from FEM. As the test neutral axis locations are in between the estimated composite neutral axis locations and non-composite neutral axis locations, Bridge SC-12 appears to exhibit partial composite action between the concrete deck and steel girders.

Table 8.33. Measured and FEM Neutral Axis Locations for All Span 1 Static Load Tests Under Positive Bending at 0.4*L* Location

Test	G3 Neutral Axis Location (in. from bottom of girder)	G4 Neutral Axis Location (in. from bottom of girder)
Path 1 – Stop Location	17.77	17.42
Path 1 – Crawl Speed	17.34	17.41
Path 2 – Stop Location	20.10	16.50
Path 2 – Crawl Speed	20.51	15.22
Middle Path – Stop Location	18.28	17.65
Middle Path – Crawl Speed	17.61	16.53
Theoretical Non-Composite	14.90	14.90
Theoretical Composite	26.11	26.11
FEM Non-Composite	14.90	14.90
FEM Composite	28.69	28.73
FEM Calibrated	17.10	19.57

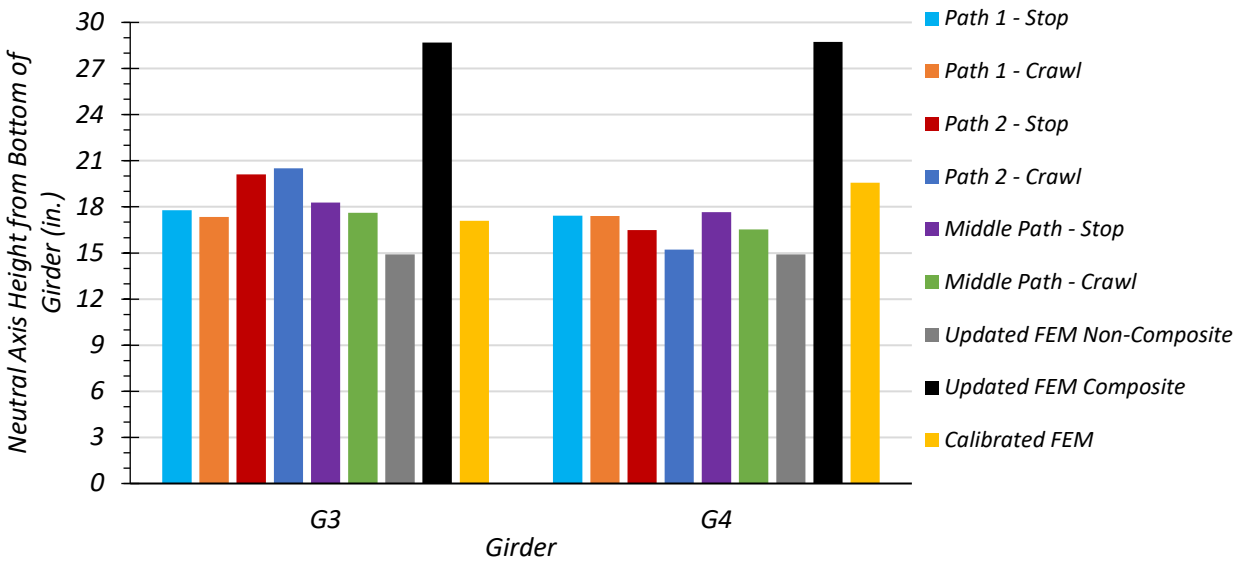

Figure 8.85. Test and FEM Neutral Axis Locations for Span 1 Loading

The maximum bottom flange stresses of Girder 3 and Girder 4 observed during Span 1 static load tests along each path were compared with the theoretical maximum bottom flange stresses calculated by CSiBridge. Only the static tests were used for comparison because CSiBridge performs a multi-step static analysis. Therefore, it would be inappropriate to include dynamic effects in the comparison. Table 8.34 and Table 8.35 show the maximum bottom flange stresses observed during testing and the FEM non-composite, composite, and calibrated bottom flange stresses. Figure 8.86 compares the test results with the FEM results.

Table 8.34. Maximum Girder 3 Bottom Flange Stresses from Test and FEM for Span 1 Loading

Load Path	Stop Location Test	Crawl Speed Test	Updated FEM Non-Composite	Updated FEM Composite	Calibrated FEM
Path 1	4.69	4.63	5.42	4.31	4.77
Path 2	2.32	2.15	3.13	2.19	2.57
Middle Path	3.75	3.83	4.68	3.49	3.91

Notes:
1. All stress values are in ksi units
2. FEM results correspond to the same vehicle longitudinal position as stop location tests

Table 8.35. Maximum Girder 4 Bottom Flange Stresses from Test and FEM for Span 1 Loading

Load Path	Stop Location Test	Crawl Speed Test	Updated FEM Non-Composite	Updated FEM Composite	Calibrated FEM
Path 1	5.52	5.58	7.37	5.74	5.58
Path 2	0.70	0.59	1.2	0.45	0.74
Middle Path	2.09	2.22	3.14	2.23	2.48

Notes:
1. All stress values are in ksi units
2. FEM results correspond to the same vehicle longitudinal position as stop location tests

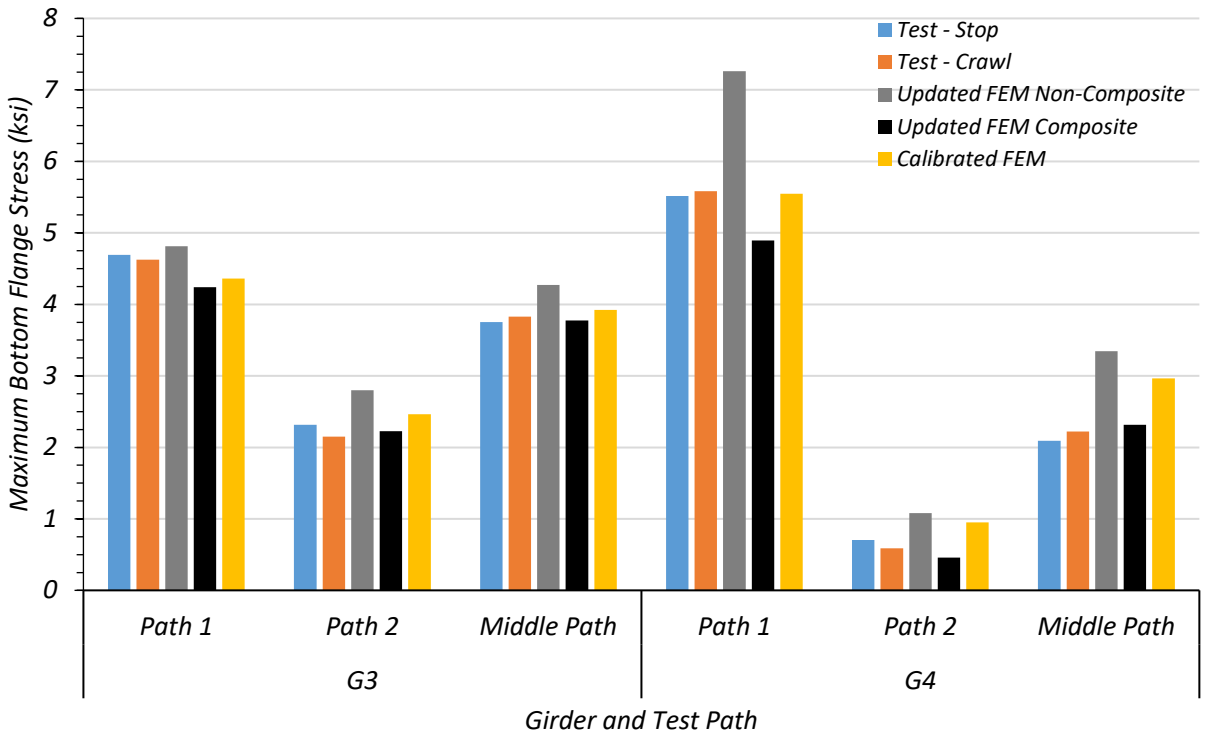

Figure 8.86. Comparison of Maximum Bottom Flange Stresses from Test and FEM for Span 1 Loading

8.8.1.2. Deflection Measurements and LLDFs

8.8.1.2.1. Path 1 Loading

Table 8.36 shows the measured girder deflections during testing for the stop location test and crawl speed test along Path 1 – Span 1. The girder displacements determined by the calibrated, updated non-composite, and updated composite FEM models are also shown.

Table 8.36. Experimental and FEM Deflections for Path 1 – Span 1 Loading

Description	G1	G2	G3	G4
Updated FEM Non-Composite Disp. (in.)	0.062	0.255	0.468	0.641
Updated FEM Composite Disp. (in.)	0.010	0.114	0.236	0.331
Calibrated FEM Disp. (in.)	0.061	0.210	0.369	0.485
Stop Location Test Disp. (in.)	0.023	0.176	0.351	0.485
Crawl Speed Test Disp. (in.)	0.016	0.167	0.342	0.481
Note: 1. G = girder, Disp. = Displacement				

Table 8.37 compares the test LLDFs determined using deflection to those obtained by the deflections of the updated non-composite, updated composite, and calibrated FEM models. All three models do a good job of estimating the LLDF, however the updated composite model is consistently closest to the test results.

Table 8.37. FEM Displacement LLDF Comparison with Test for Path 1 – Span 1 Loading

Test and Girder Type	Updated Non-Composite FEM LLDF (g_{NC})	Updated Composite FEM LLDF (g_C)	Calibrated FEM LLDF (g_{cal})	Test (g_{test})	g_{NC}/g_{test}	g_C/g_{test}	g_{cal}/g_{test}
Stop Location Interior	0.328	0.342	0.328	0.351	0.93	0.97	0.93
Stop Location Exterior	0.450	0.479	0.431	0.485	0.93	0.99	0.89
Crawl Speed Interior	0.328	0.342	0.328	0.342	0.96	1.00	0.96
Crawl Speed Exterior	0.450	0.479	0.431	0.481	0.94	0.99	0.90

Figure 8.87(a) and Figure 8.87(c) show the Path 1 – Span 1 stop location and crawl speed deflections compared to non-composite, composite, and calibrated values obtained from FEM analysis. Figure 8.87(b) and Figure 8.87(d) show the Path 1 – Span 1 stop location and crawl speed

LLDFs compared to relevant AASHTO values as well as values obtained from calibrated FEM deflection results and moment results. Table 8.38 shows the test LLDF values, the displacement and moment LLDF values obtained from the calibrated FEM model, and the LLDF values found using all three AASHTO methods. The test and calibrated model LLDFs are all significantly lower than the prescribed AASHTO LLDF values.

Table 8.38. Experimental, FEM, and AASHTO LLDFs for Path 1 – Span 1 Loading

Description	G1	G2	G3	G4
Stop Location Test Disp. LLDF	0.023	0.170	0.339	0.468
Crawl Speed Test Disp. LLDF	0.016	0.166	0.340	0.478
Calibrated FEM Disp. LLDF	0.054	0.187	0.328	0.431
Calibrated FEM Moment LLDF	0.025	0.155	0.347	0.473
AASHTO Standard LLDF	0.589	0.476	0.476	0.589
AASHTO LRFD LLDF using simplified stiffness	0.660	0.452	0.452	0.660
AASHTO LRFD LLDF using analytical stiffness	0.660	0.442	0.442	0.660

Note:
1. G = girder, Disp. = Displacement

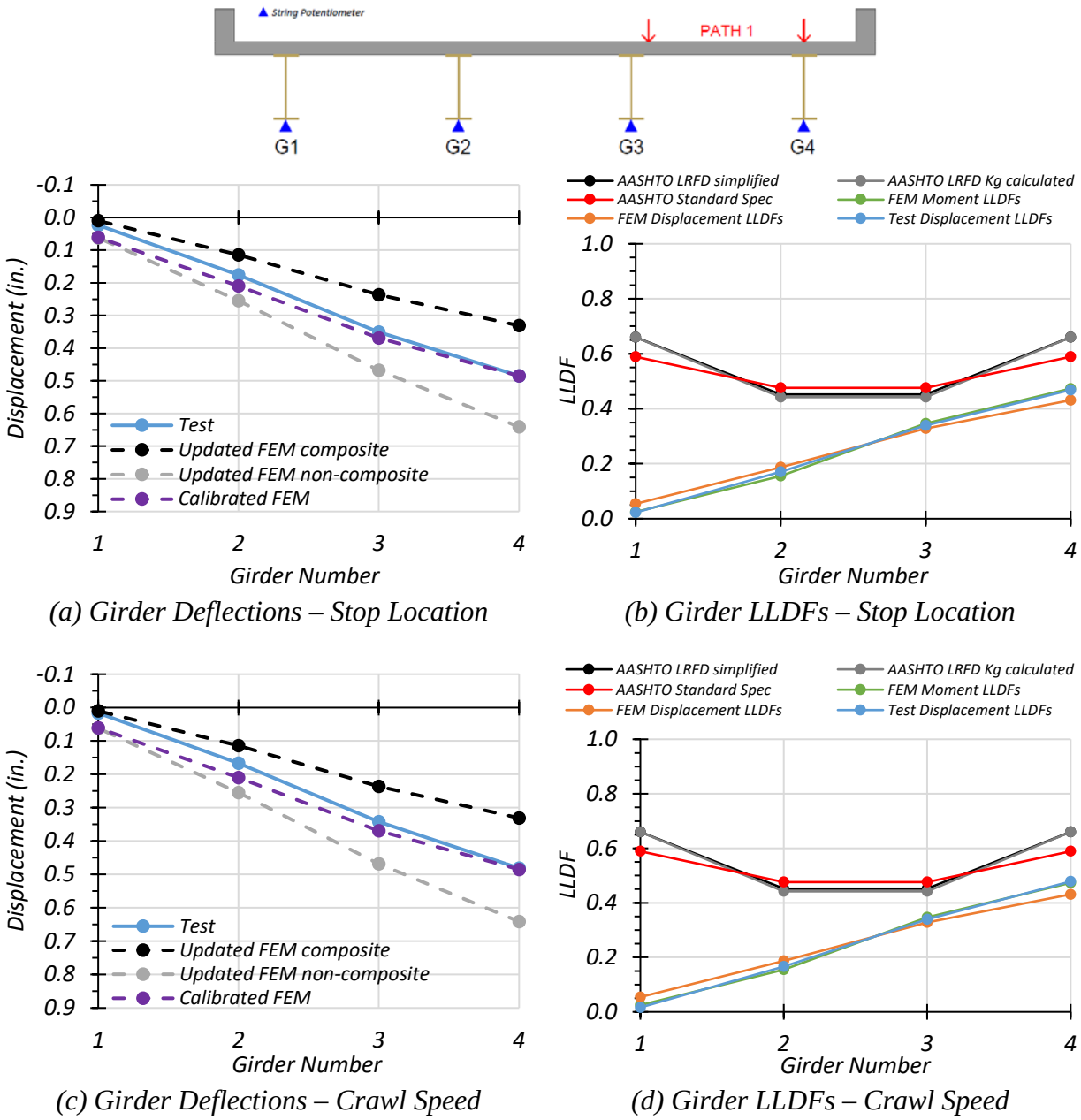

(a) Girder Deflections – Stop Location

(b) Girder LLDFs – Stop Location

(c) Girder Deflections – Crawl Speed

(d) Girder LLDFs – Crawl Speed

Figure 8.87. Comparison of Static Deflection Results for Path 1 – Span 1 Loading

8.8.1.2.2. Path 2 Loading

Table 8.39 shows the measured girder deflections during testing for the stop location test and crawl speed test along Path 2 – Span 1. The girder displacements determined by the calibrated, updated non-composite, and updated composite FEM models are also shown.

Table 8.39. Experimental and FEM Deflections for Path 2 – Span 1 Loading

Description	G1	G2	G3	G4
Updated FEM Non-Composite Disp. (in.)	0.573	0.465	0.288	0.106
Updated FEM Composite Disp. (in.)	0.291	0.236	0.138	0.032
Calibrated FEM Disp. (in.)	0.435	0.369	0.236	0.094
Stop Location Test Disp. (in.)	0.422	0.340	0.198	0.075
Crawl Speed Test Disp. (in.)	0.413	0.322	0.182	0.061
Note: 1. G = girder, Disp. = Displacement				

Table 8.40 compares the test LLDFs determined using deflection to those obtained by the deflections of the updated non-composite, updated composite, and calibrated FEM models. All three models do a good job of estimating the test LLDF, however the calibrated model is somewhat unconservative for the exterior girder.

Table 8.40. FEM Displacement LLDF Comparison with Test for Path 2 – Span 1 Loading

Test and Girder Type	Updated Non-Composite FEM LLDF (g_{NC})	Updated Composite FEM LLDF (g_C)	Calibrated FEM LLDF (g_{cal})	Test (g_{test})	g_{NC}/g_{test}	g_C/g_{test}	g_{cal}/g_{test}
Stop Location Interior	0.325	0.339	0.325	0.328	0.99	1.03	0.99
Stop Location Exterior	0.400	0.418	0.384	0.408	0.98	1.02	0.94
Crawl Speed Interior	0.325	0.339	0.325	0.329	0.99	1.03	0.99
Crawl Speed Exterior	0.400	0.418	0.384	0.423	0.95	0.99	0.91

Figure 8.88(a) and Figure 8.88(c) show the Path 2 – Span 1 stop location and crawl speed deflections compared to non-composite, composite, and calibrated values obtained from FEM analysis. Figure 8.88(b) and Figure 8.88(d) show the Path 2 – Span 1 stop location and crawl speed LLDFs compared to relevant AASHTO values as well as values obtained from calibrated FEM deflection results and moment results. Table 8.41 shows the test LLDF values, the displacement and moment LLDF values obtained from the calibrated FEM model, and the LLDF values found using all three AASHTO methods. The test and calibrated model LLDFs are all significantly lower than the prescribed AASHTO LLDF values.

Table 8.41. Experimental, FEM, and AASHTO LLDFs for Path 2 – Span 1 Loading

Description	G1	G2	G3	G4
Stop Location Test Disp. LLDF	0.422	0.340	0.198	0.075
Crawl Speed Test Disp. LLDF	0.413	0.322	0.182	0.061
Calibrated FEM Disp. LLDF	0.384	0.325	0.208	0.083
Calibrated FEM Moment LLDF	0.414	0.349	0.185	0.053
AASHTO Standard LLDF	0.589	0.476	0.476	0.589
AASHTO LRFD LLDF using simplified stiffness	0.66	0.452	0.452	0.66
AASHTO LRFD LLDF using analytical stiffness	0.66	0.442	0.442	0.66

Note:
1. G = girder, Disp. = Displacement

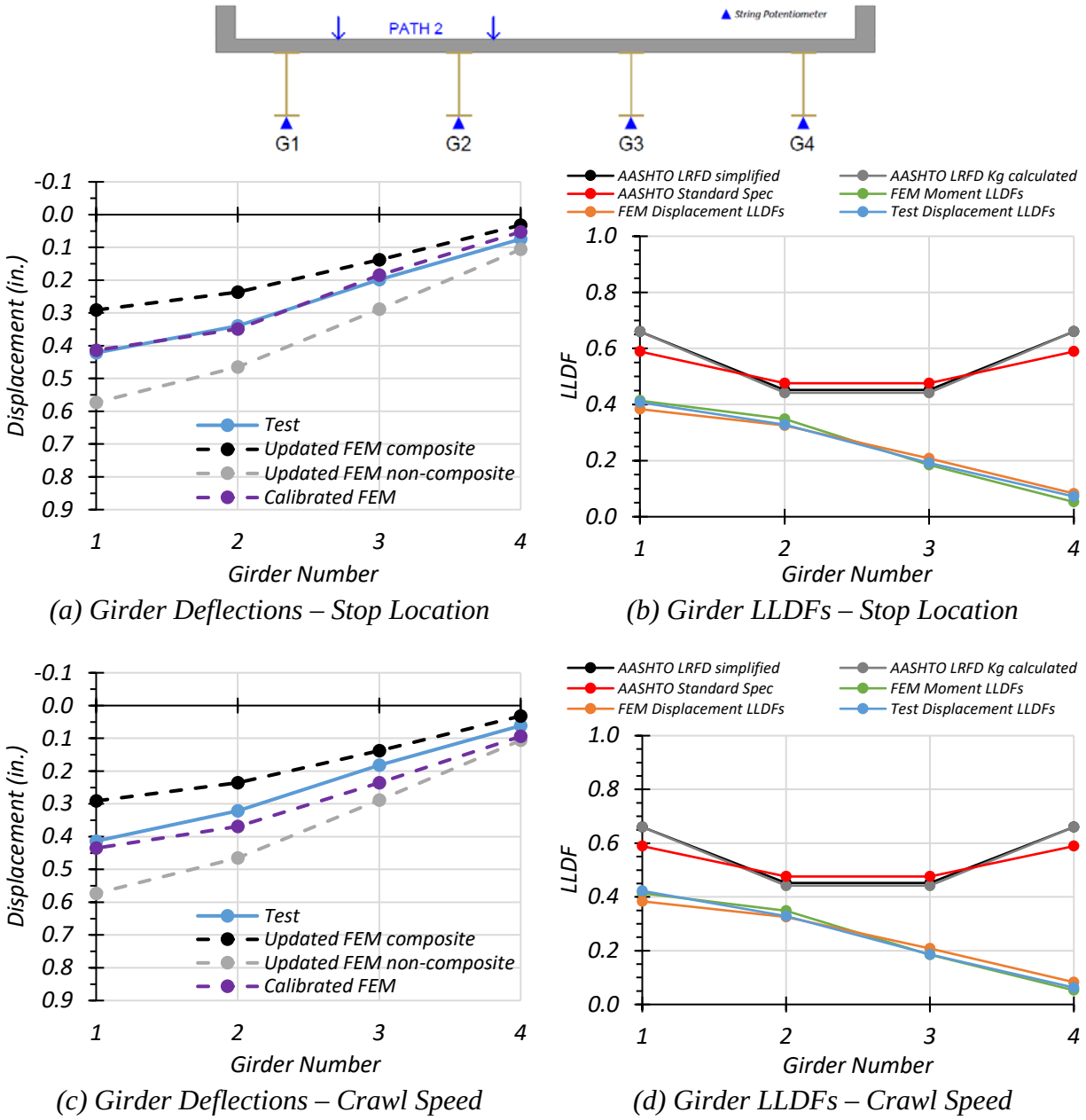

(a) Girder Deflections – Stop Location

(b) Girder LLDFs – Stop Location

(c) Girder Deflections – Crawl Speed

(d) Girder LLDFs – Crawl Speed

Figure 8.88. Comparison of Static Deflection Results for Path 2 – Span 1 Loading

8.8.1.2.3. Middle Path Loading

Table 8.42 shows the measured girder deflections during testing for the Middle Path – Span 1 stop location test. The girder displacements determined by the calibrated, updated non-composite, and updated composite FEM models are also shown.

Table 8.42. Experimental and FEM Deflections for Middle Path – Span 1 Loading

Description	G1	G2	G3	G4
Updated FEM Non-Composite Disp. (in.)	0.314	0.408	0.408	0.314
Updated FEM Composite Disp. (in.)	0.142	0.206	0.206	0.142
Calibrated FEM Disp. (in.)	0.246	0.330	0.330	0.246
Stop Location Test Disp. (in.)	0.217	0.286	0.280	0.203
Crawl Speed Test Disp. (in.)	0.201	0.278	0.280	0.211
Note: 1. G = girder, Disp. = Displacement				

Table 8.43 compares the test LLDFs determined using deflection to those obtained by the deflections of the updated non-composite, updated composite, and calibrated FEM models. All three models do a good job of estimating the test LLDF, however the updated composite model is somewhat unconservative for the exterior girder.

Table 8.43. FEM Displacement LLDF Comparison with Test for Middle Path – Span 1 Loading

Test and Girder Type	Updated Non-Composite FEM LLDF (g_{NC})	Updated Composite FEM LLDF (g_C)	Calibrated FEM LLDF (g_{cal})	Test (g_{test})	g_{NC}/g_{test}	g_C/g_{test}	g_{cal}/g_{test}
Stop Location Interior	0.283	0.296	0.286	0.290	0.98	1.02	0.99
Stop Location Exterior	0.217	0.204	0.214	0.220	0.99	0.93	0.97
Crawl Speed Interior	0.283	0.296	0.286	0.289	0.98	1.02	0.99
Crawl Speed Exterior	0.217	0.204	0.214	0.217	1.00	0.94	0.99

Figure 8.89(a) and Figure 8.89(c) show the Middle Path – Span 1 stop location and crawl speed deflections compared to non-composite, composite, and calibrated values obtained from FEM analysis. Figure 8.89(b) and Figure 8.89(d) show the Middle Path – Span 1 stop location and crawl speed LLDFs compared to relevant AASHTO values as well as values obtained from calibrated FEM deflection results and moment results. Table 8.44 shows the test LLDF values, the displacement and moment LLDF values obtained from the calibrated FEM model, and the LLDF values found using all three AASHTO methods. The test and calibrated model LLDFs are all significantly lower than the prescribed AASHTO LLDF values.

Table 8.44. Experimental, FEM, and AASHTO LLDFs for Middle Path – Span 1 Loading

Description	G1	G2	G3	G4
Stop Location Test Disp. LLDF	0.220	0.290	0.284	0.205
Crawl Speed Test Disp. LLDF	0.207	0.287	0.289	0.217
Calibrated FEM Disp. LLDF	0.214	0.286	0.286	0.214
Calibrated FEM Moment LLDF	0.197	0.303	0.303	0.197
AASHTO Standard LLDF	0.589	0.476	0.476	0.589
AASHTO LRFD LLDF using simplified stiffness	0.66	0.452	0.452	0.66
AASHTO LRFD LLDF using analytical stiffness	0.66	0.442	0.442	0.66

Note:
1. G = girder, Disp. = Displacement

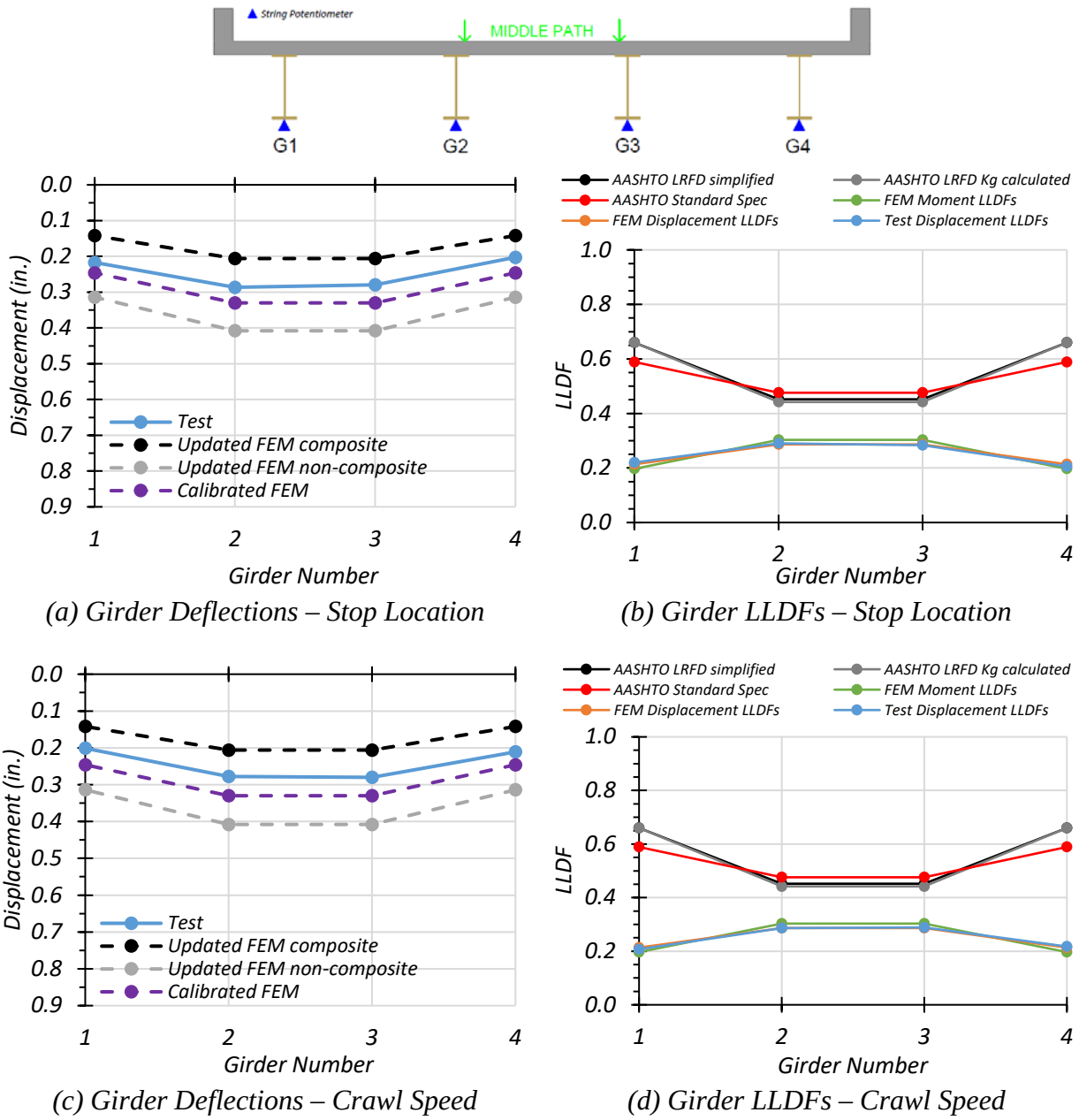

(a) Girder Deflections – Stop Location

(b) Girder LLDFs – Stop Location

(c) Girder Deflections – Crawl Speed

(d) Girder LLDFs – Crawl Speed

Figure 8.89. Comparison of Static Deflection Results for Middle Path – Span 1 Loading

8.8.2. Static Load Tests on Bridge SC-12 Span 2

Two types of static load tests were conducted without introducing any dynamic effects: (1) stop location tests by parking the vehicle at moment critical longitudinal position in each span for each

selected path on the bridge, and (2) crawl speed tests by moving the truck at low speeds (around 2 mph) along the same predefined paths.

8.8.2.1. Strain Measurements and Composite Action

8.8.2.1.1. Interior Girder 3

Figure 8.90 through Figure 8.92 provide plots of the measured strains for interior Girder 3 during static loading testing and compares the midspan strain diagram to those obtained through the updated and calibrated FEM models. The strains measured for Girder 3 during the Path 1 – Span 2 static tests are shown in Figure 8.90 and compared with values obtained from the FEM updated and calibrated models. Figure 8.90(a) shows the FEM comparison for the stop location test for Girder 3 at 0.4*L* of Span 1 and the interior pier. Figure 8.90(b) shows the FEM comparison for the stop location test for Girder 3 at midspan of Span 2. Figure 8.90(c) shows the FEM comparison for the crawl speed test for Girder 3 at 0.4*L* of Span 1 and the interior pier. Figure 8.90(d) shows the FEM comparison for the crawl speed test for Girder 3 at midspan of Span 2.

The strains measured for Girder 3 during the Path 2 – Span 2 static tests are shown in Figure 8.91 and compared with values obtained from the FEM updated and calibrated models. Figure 8.91(a) shows the FEM comparison for the stop location test for Girder 3 at 0.4*L* of Span 1 and the interior pier. Figure 8.91(b) shows the FEM comparison for the stop location test for Girder 3 at midspan of Span 2. Figure 8.91(c) shows the FEM comparison for the crawl speed test for Girder 3 at 0.4*L* of Span 1 and the interior pier. Figure 8.91(d) shows the FEM comparison for the crawl speed test for Girder 3 at midspan of Span 2.

The strains measured for Girder 3 during the Middle Path static tests are shown in Figure 8.92 and compared with values obtained from the FEM updated and calibrated models.

Figure 8.92(a) shows the FEM comparison for the stop location test for Girder 3 at 0.4*L* of Span 1 and the interior pier. Figure 8.92(b) shows the FEM comparison for the stop location test for Girder 3 at midspan of Span 2. Figure 8.92(c) shows the FEM comparison for the crawl speed test for Girder 3 at 0.4*L* of Span 1 and the interior pier. Figure 8.92(d) shows the FEM comparison for the crawl speed test for Girder 3 at midspan of Span 2.

The calibrated model compares well with the Path 1 and Middle Path loading strain diagrams, but not quite as well with the Path 2 loading strain diagram. This is likely due to Girder 3 not receiving much load during Path 2 loading, as the truck is closer to Girders 1 and 2.

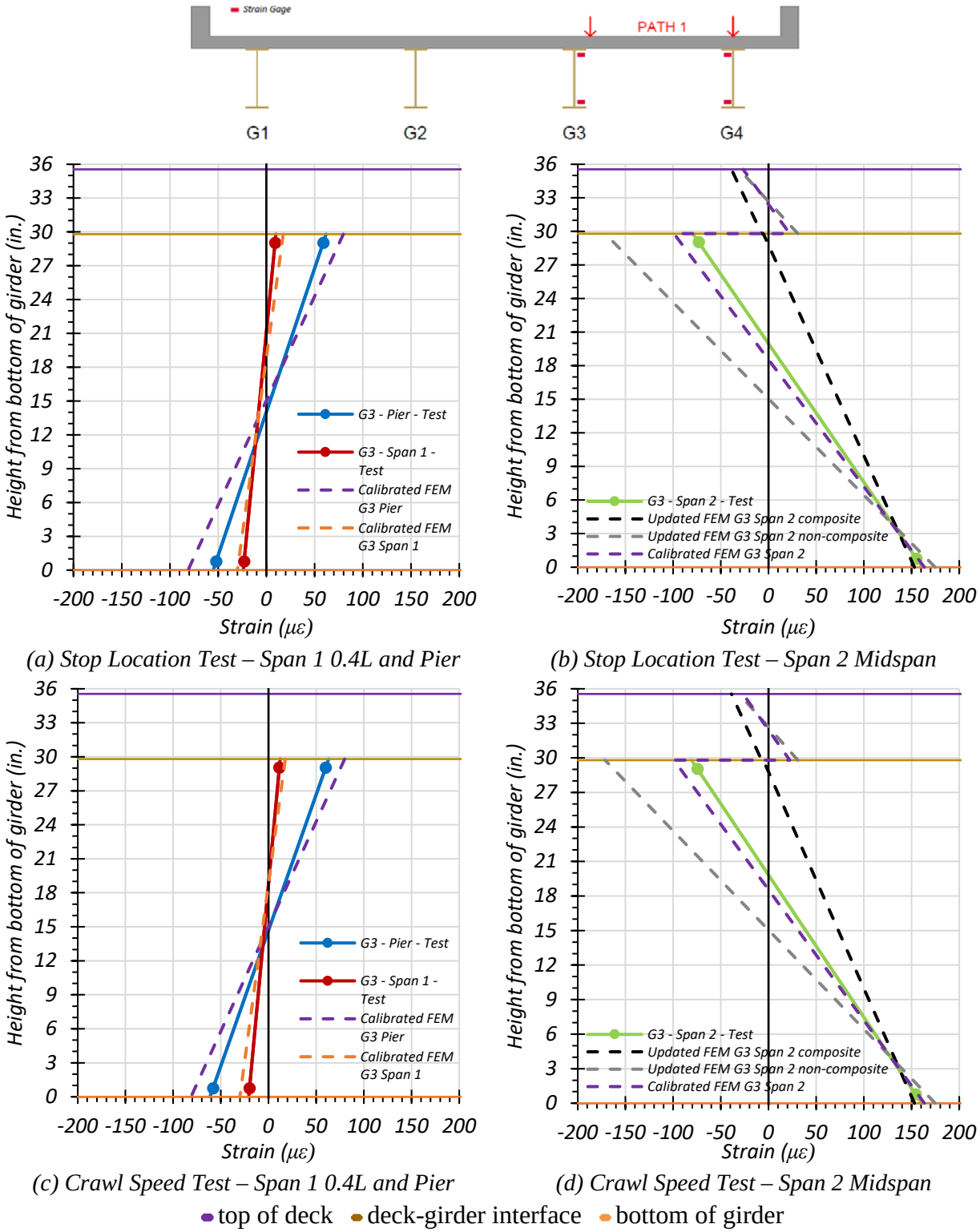

(a) Stop Location Test – Span 1 0.4L and Pier

(b) Stop Location Test – Span 2 Midspan

(c) Crawl Speed Test – Span 1 0.4L and Pier

(d) Crawl Speed Test – Span 2 Midspan

Figure 8.90. Comparison of Static Strains for Interior Girder 3 – Path 1 – Span 2

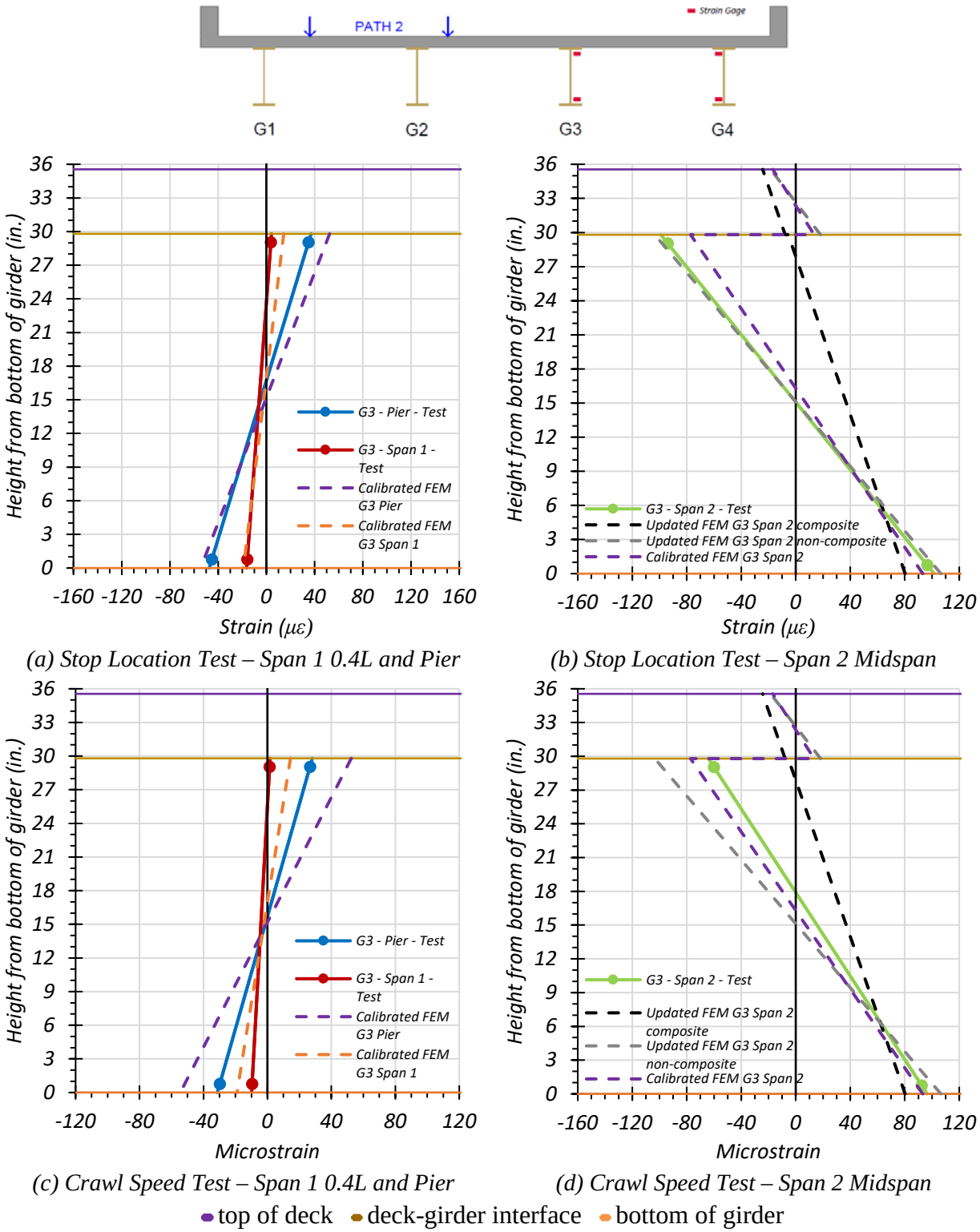

(a) Stop Location Test – Span 1 0.4L and Pier

(b) Stop Location Test – Span 2 Midspan

(c) Crawl Speed Test – Span 1 0.4L and Pier

(d) Crawl Speed Test – Span 2 Midspan

Figure 8.91. Comparison of Static Strains for Interior Girder 3 – Path 2 – Span 2

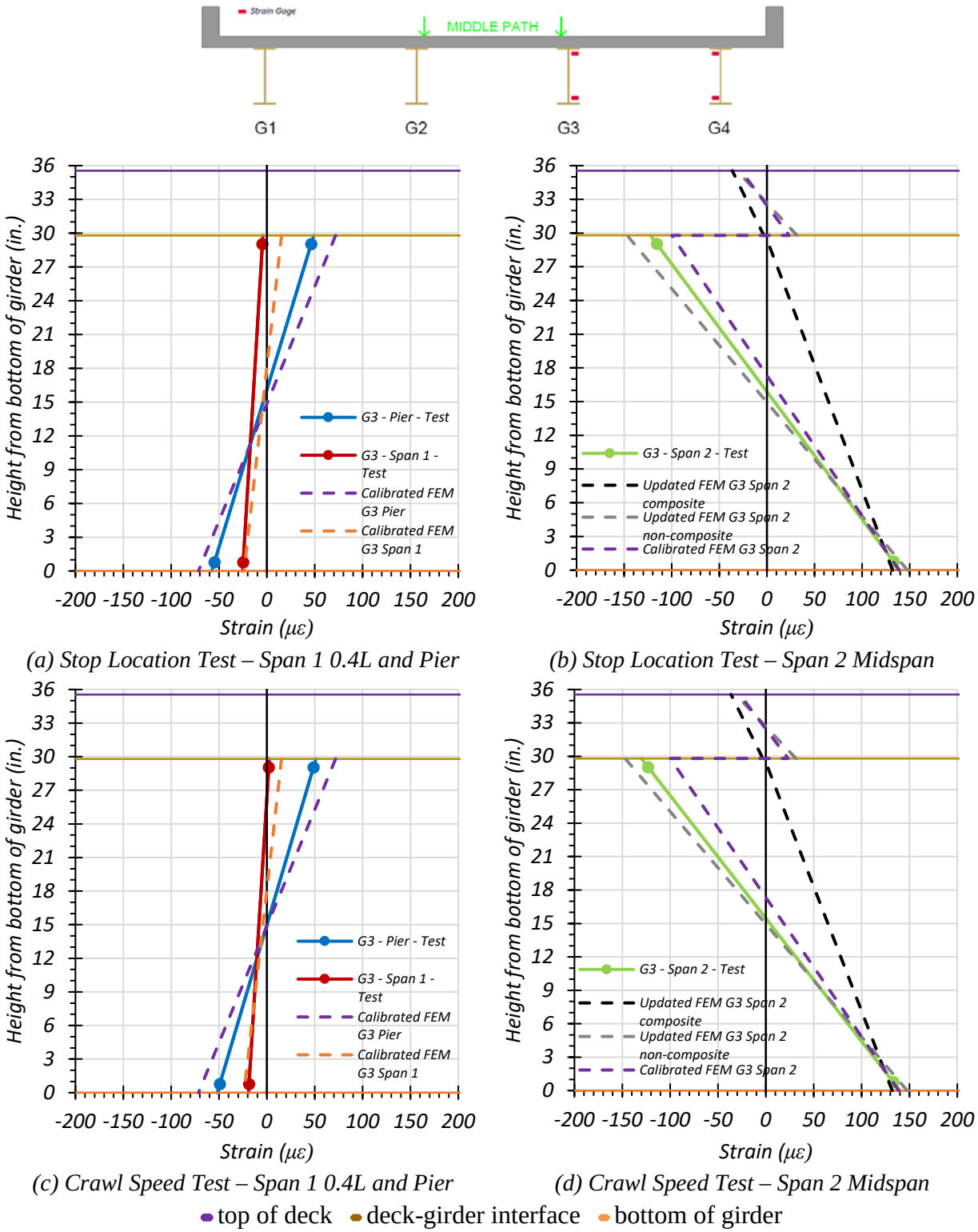

(a) Stop Location Test – Span 1 0.4L and Pier

(b) Stop Location Test – Span 2 Midspan

(c) Crawl Speed Test – Span 1 0.4L and Pier

(d) Crawl Speed Test – Span 2 Midspan

top of deck deck-girder interface bottom of girder

Figure 8.92. Comparison of Static Strains for Interior Girder 3 – Middle Path – Span 2

8.8.2.1.2. Exterior Girder 4

Figure 8.93 through Figure 8.95 provide plots of the measured strains for exterior Girder 4 during static loading testing and compares the midspan strain diagram to those obtained through the updated and calibrated FEM models. The strains measured for Girder 4 during the Path 1 – Span 2 static tests are shown in Figure 8.93 and compared with values obtained from the FEM updated and calibrated models. Figure 8.93(a) shows the FEM comparison for the stop location test for Girder 4 at 0.4*L* of Span 1 and the interior pier. Figure 8.93(b) shows the FEM comparison for the stop location test for Girder 4 at midspan of Span 2. Figure 8.93(c) shows the FEM comparison for the crawl speed test for Girder 4 at 0.4*L* of Span 1 and the interior pier. Figure 8.93(d) shows the FEM comparison for the crawl speed test for Girder 4 at midspan of Span 2.

The strains measured for Girder 4 during the Path 2 – Span 2 static tests are shown in Figure 8.94 and compared with values obtained from the FEM updated and calibrated models. Figure 8.94(a) shows the FEM comparison for the stop location test for Girder 4 at 0.4*L* of Span 1 and the interior pier. Figure 8.94(b) shows the FEM comparison for the stop location test for Girder 4 at midspan of Span 2. Figure 8.94(c) shows the FEM comparison for the crawl speed test for Girder 4 at 0.4*L* of Span 1 and the interior pier. Figure 8.94(d) shows the FEM comparison for the crawl speed test for Girder 4 at midspan of Span 2.

The strains measured for Girder 4 during the Middle Path static tests are shown in Figure 8.95 and compared with values obtained from the FEM updated and calibrated models. Figure 8.95(a) shows the FEM comparison for the stop location test for Girder 4 at 0.4*L* of Span 1 and the interior pier. Figure 8.95(b) shows the FEM comparison for the stop location test for Girder 4 at midspan of Span 2. Figure 8.95(c) shows the FEM comparison for the crawl speed test for

Girder 4 at 0.4*L* of Span 1 and the interior pier. Figure 8.95(d) shows the FEM comparison for the crawl speed test for Girder 4 at midspan of Span 2.

The calibrated model compares well with the Path 1 loading strain diagrams, but not quite as well with the Path 2 and Middle Path loading strain diagrams. This is likely due to Girder 4 not receiving much load during Path 2 loading and Middle Path loading, as the truck is closer to Girders 1 and 2 under Path 2 loading, and Girders 2 and 3 under Middle Path loading.

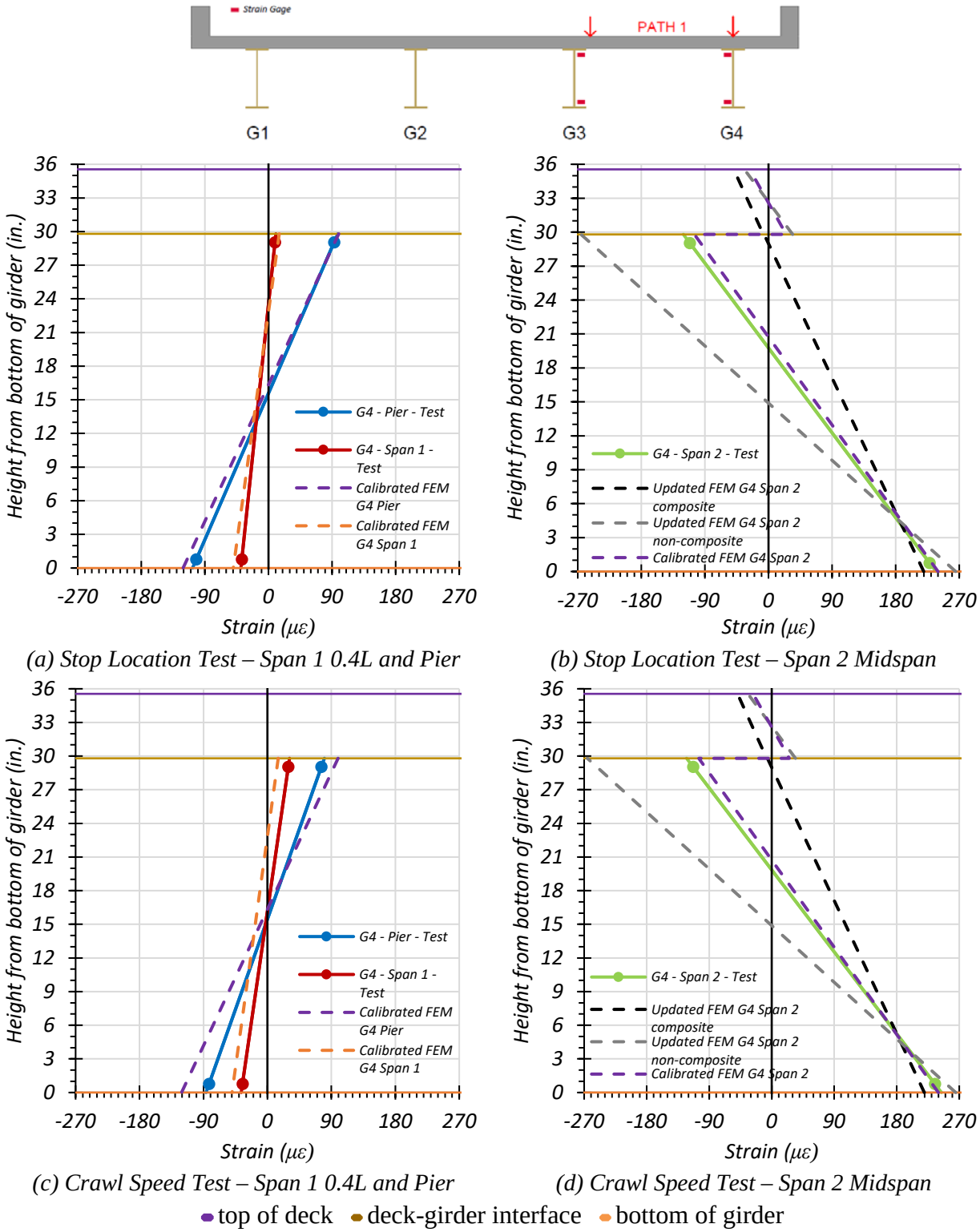

(a) Stop Location Test – Span 1 0.4L and Pier

(b) Stop Location Test – Span 2 Midspan

(c) Crawl Speed Test – Span 1 0.4L and Pier

(d) Crawl Speed Test – Span 2 Midspan

Figure 8.93. Comparison of Static Strains for Exterior Girder 4 – Path 1 – Span 2

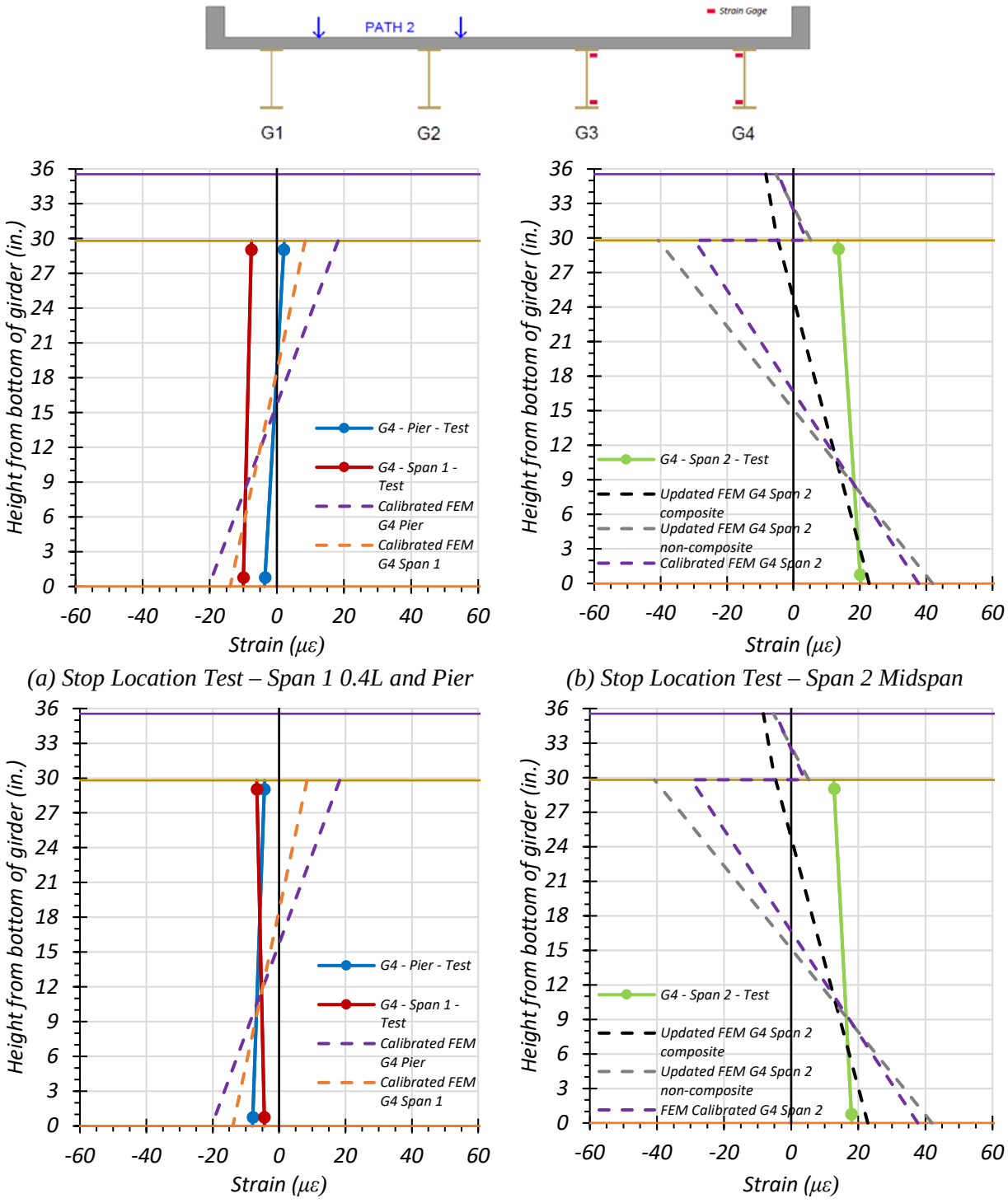

(a) Stop Location Test – Span 1 0.4L and Pier

(b) Stop Location Test – Span 2 Midspan

(c) Crawl Speed Test – Span 1 0.4L and Pier

(d) Crawl Speed Test – Span 2 Midspan

Figure 8.94. Comparison of Static Strains for Exterior Girder 4 – Path 2 – Span 2

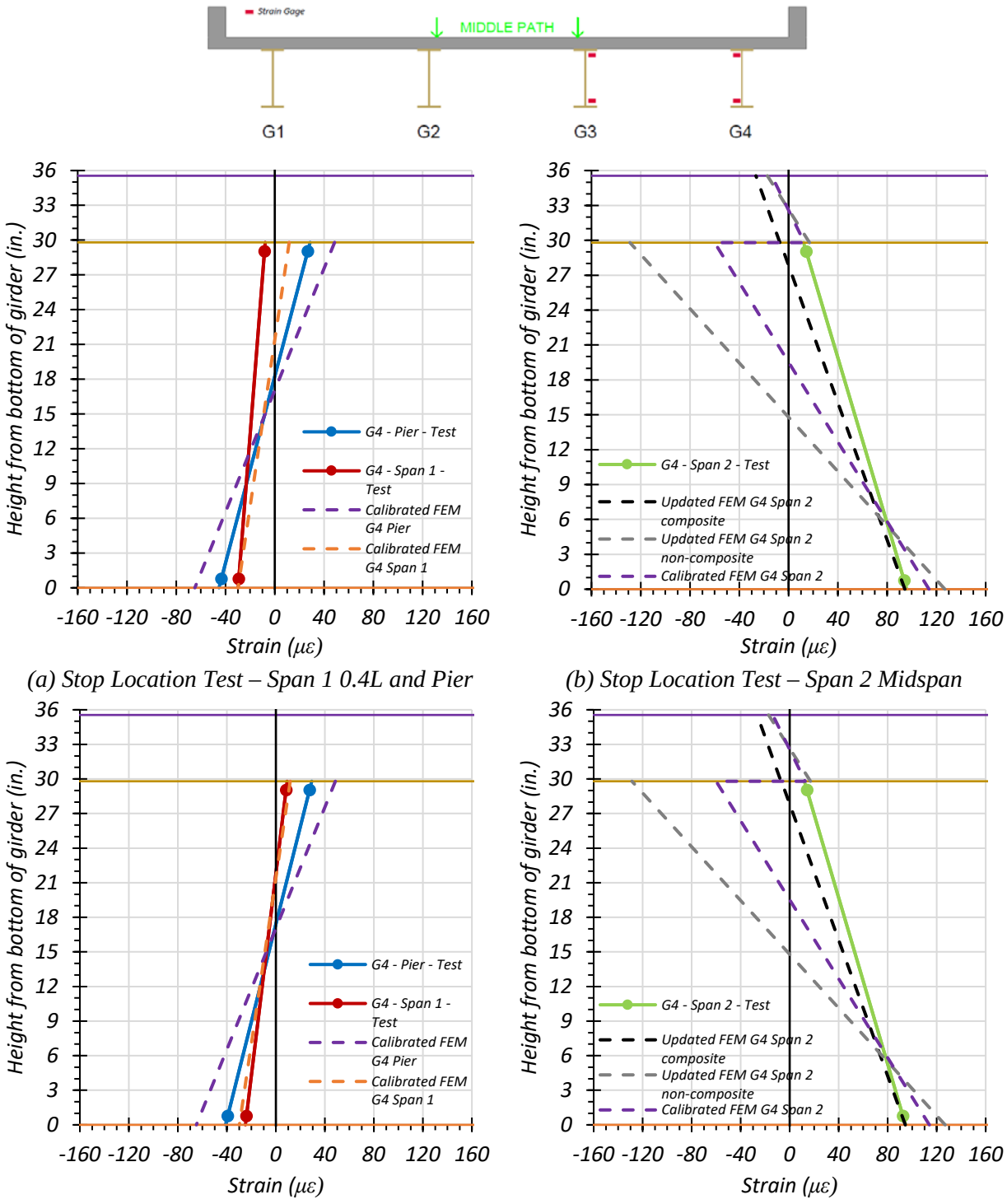

(a) Stop Location Test – Span 1 0.4L and Pier

(b) Stop Location Test – Span 2 Midspan

(c) Crawl Speed Test – Span 1 0.4L and Pier

(d) Crawl Speed Test – Span 2 Midspan

top of deck deck-girder interface bottom of girder

Figure 8.95. Comparison of Static Strains for Exterior Girder 4 – Middle Path – Span 2

8.8.2.1.3. Comparison of Measured Strain Results

The neutral axis locations of Girder 4 and Girder 3 observed during the load tests were compared with the theoretical neutral axis locations calculated using the FEM strain predictions. Table 8.45 shows the neutral axis locations measured for all static load tests and for the three FEM models. Figure 8.96 compares the test neutral axis locations with the non-composite and composite neutral axis locations obtained from FEM. As the test neutral axis locations are in between the estimated composite neutral axis locations and non-composite neutral axis locations, Bridge SC-12 appears to be acting as partially composite.

Table 8.45. Measured and FEM Neutral Axis Locations for All Span 2 Static Load Tests

Test	G3 Neutral Axis Location (in. from bottom of girder)	G4 Neutral Axis Location (in. from bottom of girder)
Path 1 – Stop Location	19.97	19.76
Path 1 – Crawl Speed	19.56	19.85
Path 2 – Stop Location	15.08	88.17
Path 2 – Crawl Speed	15.32	99.15
Middle Path – Stop Location	15.88	34.13
Middle Path – Crawl Speed	15.45	32.76
Theoretical Non-Composite	14.90	14.90
Theoretical Composite	26.11	26.11
FEM Non-Composite	14.90	14.90
FEM Composite	28.79	28.97
FEM Calibrated	18.55	20.73

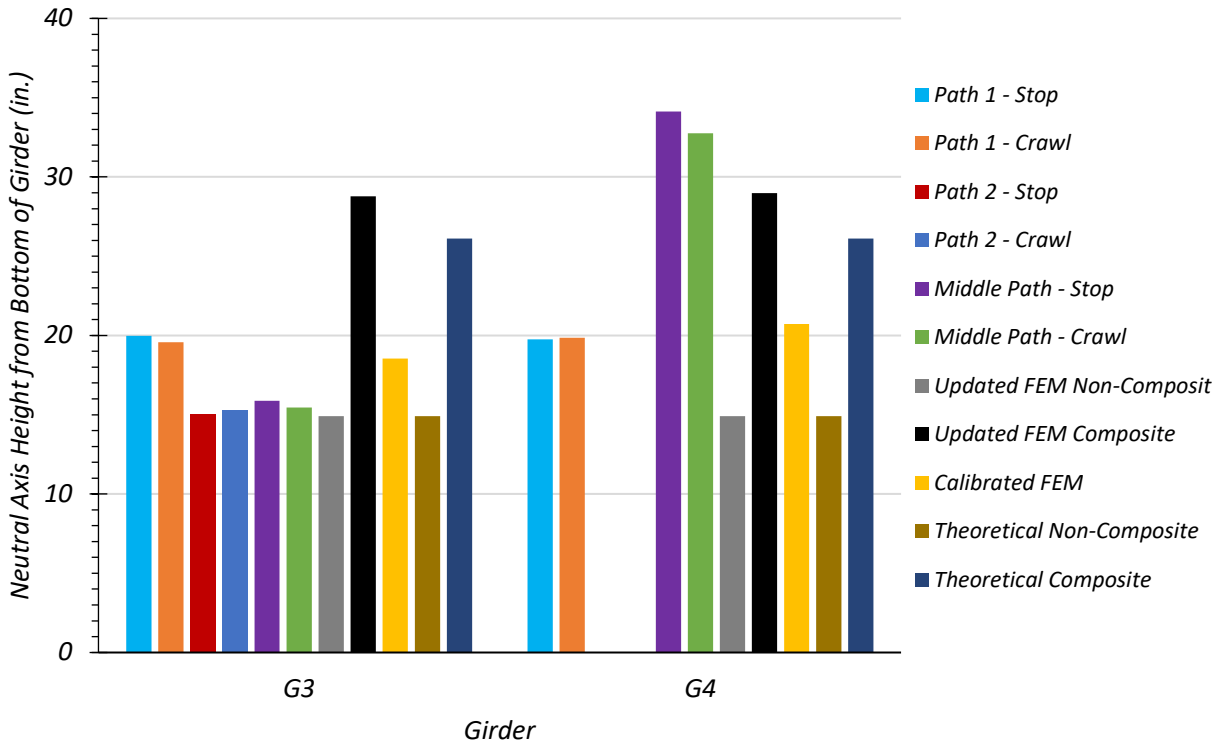

Figure 8.96. Test and FEM Neutral Axis Locations for Span 2 Loading

The maximum bottom flange stresses of Girder 4 and Girder 3 observed during Span 2 static load tests along each path were compared with the theoretical maximum bottom flange stresses calculated by CSiBridge. Only the stop location tests were used for comparison because CSiBridge performs a multi-step static analysis. Therefore, it would be inappropriate to include dynamic effects in the comparison. Table 8.46 and Table 8.47 show the maximum bottom flange stresses observed during testing and the FEM non-composite, composite, and calibrated bottom flange stresses. Figure 8.97 compares the test results with the FEM results. In general, the stresses observed during testing fall in between the expected composite and non-composite stresses.

Table 8.46. Maximum Girder 3 Bottom Flange Stresses from Test and FEM for Span 2 Loading

Load Path	Stop Location Test	Crawl Speed Test	Updated FEM Non-Composite	Updated FEM Composite	Calibrated FEM
Path 1	4.68	4.66	5.59	3.98	4.59
Path 2	2.94	2.82	3.35	2.27	2.90
Middle Path	4.05	4.06	4.77	3.73	4.23

Notes:
1. All stress values are in ksi units
2. FEM results correspond to the same vehicle longitudinal position as stop location tests

Table 8.47. Maximum Girder 4 Bottom Flange Stresses from Test and FEM for Span 2 Loading

Load Path	Stop Location Test	Crawl Speed Test	Updated FEM Non-Composite	Updated FEM Composite	Calibrated FEM
Path 1	6.88	7.09	7.64	6.33	6.85
Path 2	0.59	0.52	1.42	0.59	0.94
Middle Path	2.78	2.82	3.78	2.23	3.10

Notes:
1. All stress values are in ksi units
2. FEM results correspond to the same vehicle longitudinal position as stop location tests

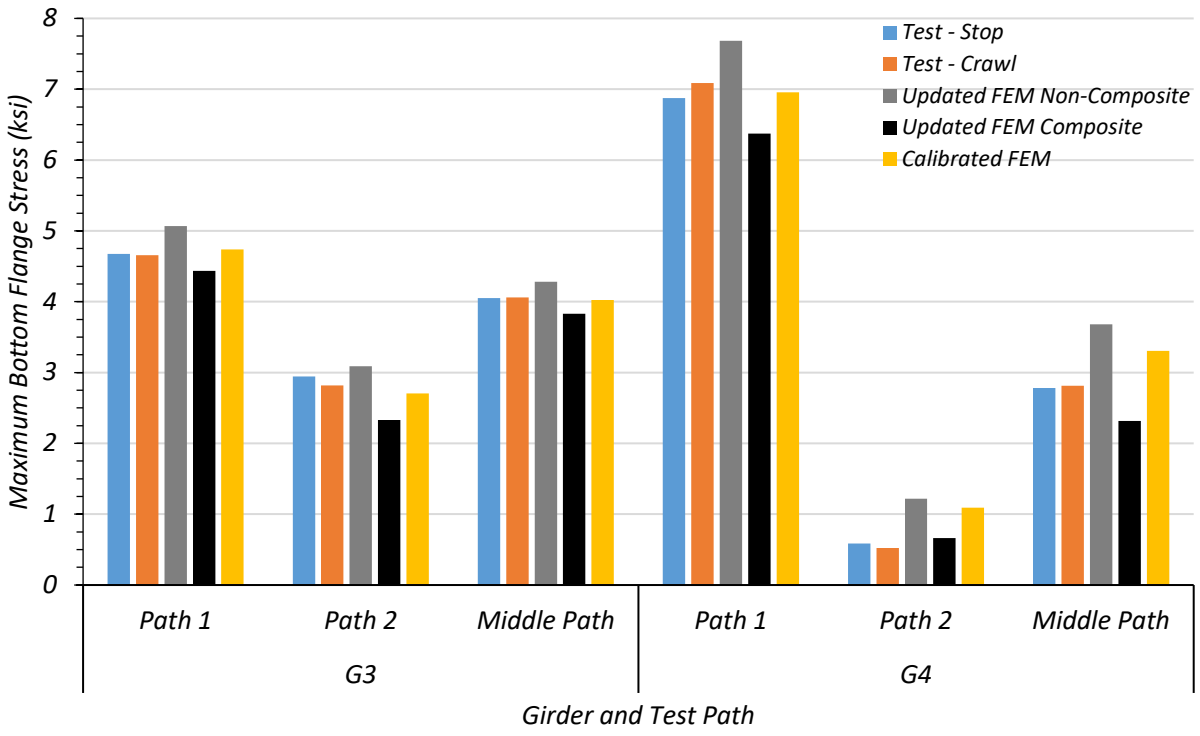

Figure 8.97. Comparison of Maximum Bottom Flange Stresses from Test and FEM for Span 2 Loading

8.8.2.2. Deflection Measurements and LLDFs

8.8.2.2.1. Path 1 Loading

Table 8.48 shows the measured girder deflections during testing for the stop location test and crawl speed test along Path 1 – Span 2. The girder displacements determined by the calibrated, updated non-composite, and updated composite FEM models are also shown.

Table 8.48. Experimental and FEM Deflections for Path 1 – Span 2 Loading

Description	G1	G2	G3	G4
Updated FEM Non-Composite Disp. (in.)	0.098	0.376	0.672	0.928
Updated FEM Composite Disp. (in.)	0.025	0.180	0.352	0.495
Calibrated FEM Disp. (in.)	0.065	0.276	0.511	0.720
Stop Location Test Disp. (in.)	0.049	0.280	0.526	0.755
Crawl Speed Test Disp. (in.)	0.032	0.260	0.520	0.771
Note: 1. G = girder, Disp. = Displacement				

Table 8.49 compares the test LLDFs determined using deflection to those obtained by the deflections of the updated non-composite, updated composite, and calibrated FEM models. All three models do a good job of estimating the LLDF.

Table 8.49. FEM Displacement LLDF Comparison with Test for Path 1 – Span 2 Loading

Test and Girder Type	Updated Non-Composite FEM LLDF (g_{NC})	Updated Composite FEM LLDF (g_C)	Calibrated FEM LLDF (g_{cal})	Test (g_{test})	g_{NC}/g_{test}	g_C/g_{test}	g_{cal}/g_{test}
Stop Location Interior	0.324	0.335	0.325	0.327	0.99	1.02	0.99
Stop Location Exterior	0.447	0.471	0.458	0.469	0.95	1.00	0.98
Crawl Speed Interior	0.324	0.335	0.325	0.328	0.99	1.02	0.99
Crawl Speed Exterior	0.447	0.471	0.458	0.487	0.92	0.97	0.94

Figure 8.98(a) and Figure 8.98(c) show the Path 1 – Span 2 stop location and crawl speed deflections compared to non-composite, composite, and calibrated values obtained from FEM analysis. Figure 8.98(b) and Figure 8.98(d) show the Path 1 – Span 2 stop location and crawl speed LLDFs compared to relevant AASHTO values as well as values obtained from calibrated FEM

deflection results and moment results. Table 8.50 shows the test LLDF values, the displacement and moment LLDF values obtained from the calibrated FEM model, and the LLDF values found using all three AASHTO methods. The test and calibrated model LLDFs are all significantly lower than the prescribed AASHTO LLDF values.

Table 8.50. Experimental, FEM, and AASHTO LLDFs for Path 1 – Span 2 Loading

Description	**G1**	**G2**	**G3**	**G4**
Stop Location Test Disp. LLDF	0.030	0.174	0.327	0.469
Crawl Speed Test Disp. LLDF	0.020	0.164	0.328	0.487
Calibrated FEM Disp. LLDF	0.041	0.176	0.325	0.458
Calibrated FEM Moment LLDF	0.032	0.166	0.335	0.467
AASHTO Standard LLDF	0.589	0.476	0.476	0.589
AASHTO LRFD LLDF using simplified stiffness	0.660	0.427	0.427	0.660
AASHTO LRFD LLDF using analytical stiffness	0.660	0.410	0.410	0.660

Note:
1. G = girder, Disp. = Displacement

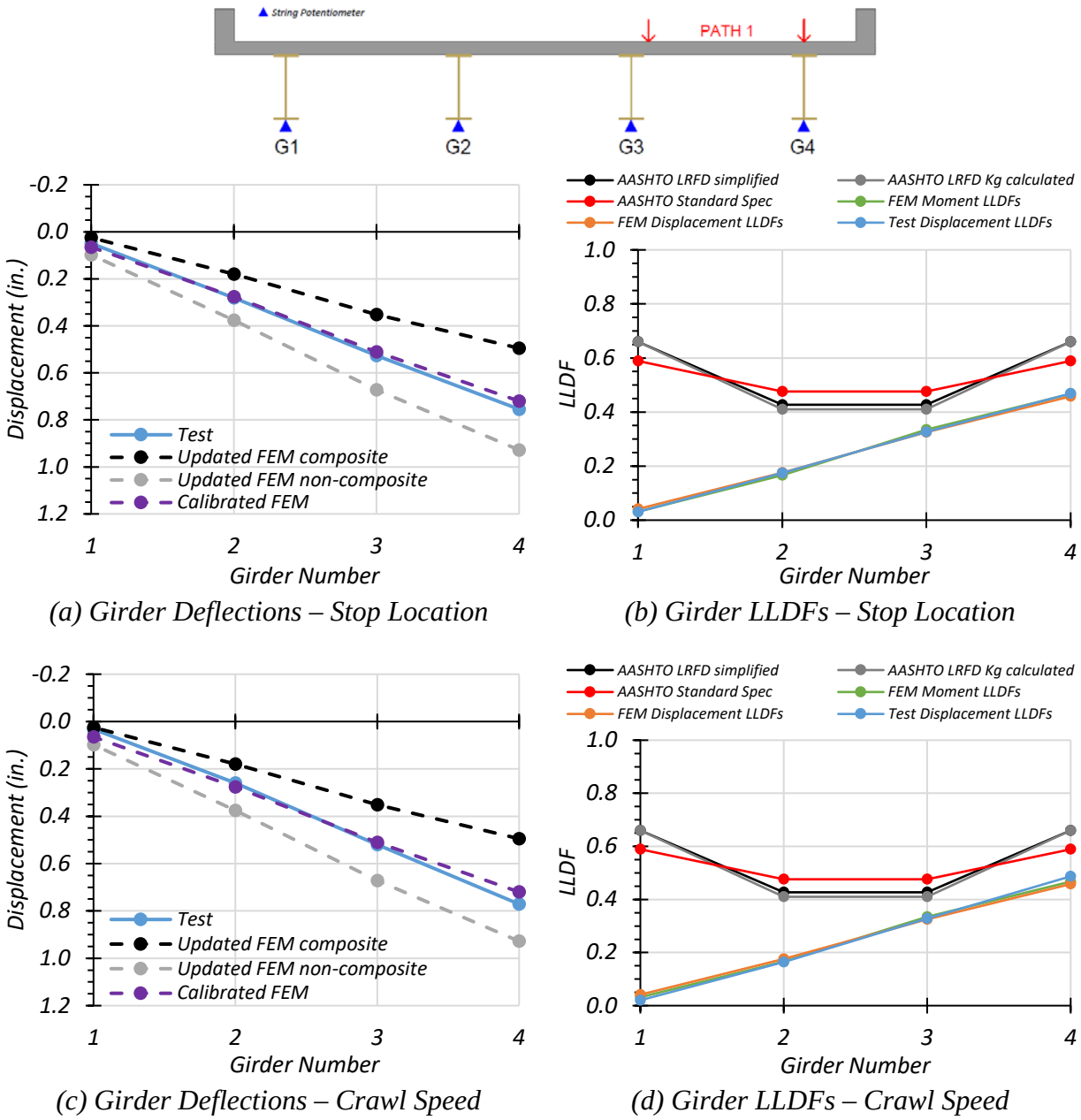

(a) Girder Deflections – Stop Location

(b) Girder LLDFs – Stop Location

(c) Girder Deflections – Crawl Speed

(d) Girder LLDFs – Crawl Speed

Figure 8.98. Comparison of Static Deflection Results for Path 1 – Span 2 Loading

8.8.2.2.2. Path 2 Loading

Table 8.51 shows the measured girder deflections during testing for the stop location test and crawl speed test along Path 2 – Span 2. The girder displacements determined by the calibrated, updated non-composite, and updated composite FEM models are also shown.

Table 8.51. Experimental and FEM Deflections for Path 2 – Span 2 Loading

Description	G1	G2	G3	G4
Updated FEM Non-Composite Disp. (in.)	0.835	0.662	0.418	0.166
Updated FEM Composite Disp. (in.)	0.441	0.347	0.206	0.061
Calibrated FEM Disp. (in.)	0.635	0.520	0.339	0.145
Stop Location Test Disp. (in.)	0.692	0.556	0.298	0.077
Crawl Speed Test Disp. (in.)	0.693	0.537	0.279	0.060
Note: 1. G = girder, Disp. = Displacement				

Table 8.52 compares the test LLDFs determined using deflection to those obtained by the deflections of the updated non-composite, updated composite, and calibrated FEM models. All three models do a good job of estimating the LLDF, however the updated composite model does a slightly better job than the calibrated model and the updated non-composite model.

Table 8.52. FEM Displacement LLDF Comparison with Test for Path 2 – Span 2 Loading

Test and Girder Type	Updated Non-Composite FEM LLDF (g_{NC})	Updated Composite FEM LLDF (g_C)	Calibrated FEM LLDF (g_{cal})	Test (g_{test})	g_{NC}/g_{test}	g_C/g_{test}	g_{cal}/g_{test}
Stop Location Interior	0.318	0.329	0.317	0.343	0.93	0.96	0.92
Stop Location Exterior	0.401	0.418	0.387	0.427	0.94	0.98	0.91
Crawl Speed Interior	0.318	0.329	0.317	0.342	0.93	0.96	0.93
Crawl Speed Exterior	0.401	0.418	0.387	0.442	0.91	0.95	0.88

Figure 8.99(a) and Figure 8.99(c) show the Path 2 – Span 2 stop location and crawl speed deflections compared to non-composite, composite, and calibrated values obtained from FEM analysis. Figure 8.99(b) and Figure 8.99(d) show the Path 2 – Span 2 stop location and crawl speed LLDFs compared to relevant AASHTO values as well as values obtained from calibrated FEM deflection results and moment results. Table 8.53 shows the test LLDF values, the displacement and moment LLDF values obtained from the calibrated FEM model, and the LLDF values found using all three AASHTO methods. The test and calibrated model LLDFs are all significantly lower than the prescribed AASHTO LLDF values.

Table 8.53. Experimental, FEM, and AASHTO LLDFs for Path 2 – Span 2 Loading

Description	G1	G2	G3	G4
Stop Location Test Disp. LLDF	0.427	0.343	0.184	0.047
Crawl Speed Test Disp. LLDF	0.442	0.342	0.178	0.038
Calibrated FEM Disp. LLDF	0.387	0.317	0.207	0.088
Calibrated FEM Moment LLDF	0.415	0.332	0.191	0.063
AASHTO Standard LLDF	0.589	0.476	0.476	0.589
AASHTO LRFD LLDF using simplified stiffness	0.660	0.427	0.427	0.660
AASHTO LRFD LLDF using analytical stiffness	0.660	0.410	0.410	0.660

Note:
1. G = girder, Disp. = Displacement

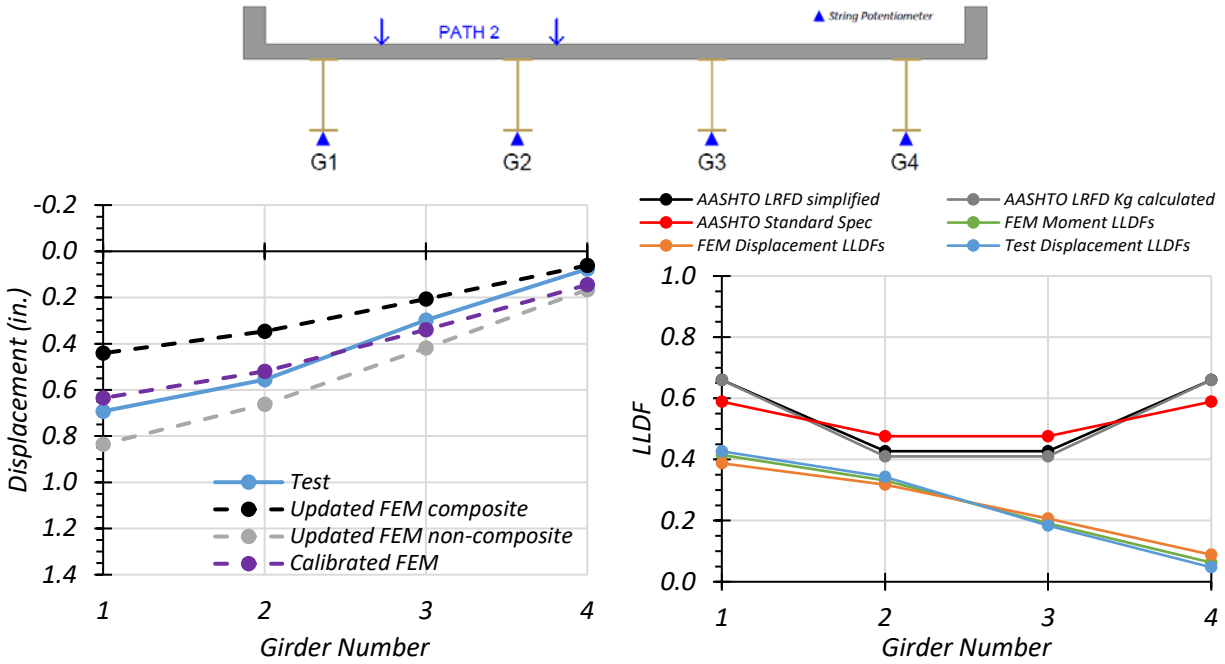

(a) Girder Deflections – Stop Location

(b) Girder LLDFs – Stop Location

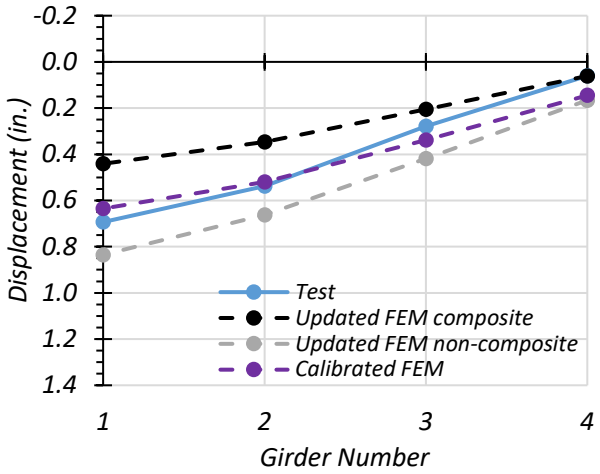

(c) Girder Deflections – Crawl Speed

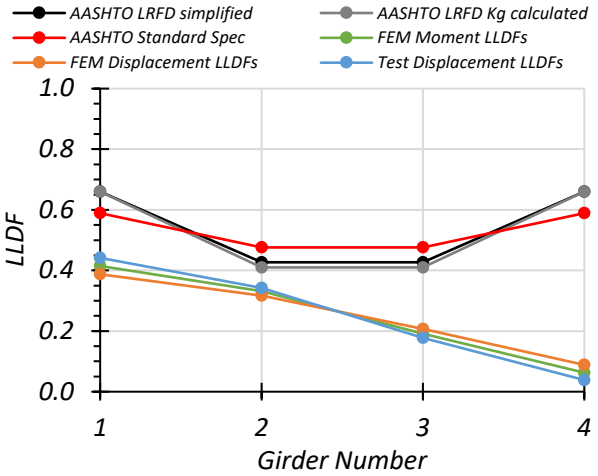

(d) Girder LLDFs – Crawl Speed

Figure 8.99. Comparison of Static Deflection Results for Path 2 – Span 2 Loading

8.8.2.2.3. Middle Path Loading

Table 8.54 shows the measured girder deflections during testing for the Middle Path – Span 2 stop location test. The girder displacements determined by the calibrated, updated non-composite, and updated composite FEM models are also shown.

Table 8.54. Experimental and FEM Deflections for Middle Path – Span 2 Loading

Description	G1	G2	G3	G4
Updated FEM Non-Composite Disp. (in.)	0.474	0.573	0.573	0.474
Updated FEM Composite Disp. (in.)	0.231	0.300	0.300	0.231
Calibrated FEM Disp. (in.)	0.371	0.460	0.460	0.371
Stop Location Test Disp. (in.)	0.328	0.457	0.440	0.353
Crawl Speed Test Disp. (in.)	0.313	0.444	0.436	0.355
Note: 1. G = girder, Disp. = Displacement				

Table 8.55 compares the test LLDFs determined using deflection to those obtained by the deflections of the updated non-composite, updated composite, and calibrated FEM models. All three models do a good job of estimating the LLDF.

Table 8.55. FEM Displacement LLDF Comparison with Test for Middle Path – Span 2 Loading

Test and Girder Type	Updated Non-Composite FEM LLDF (g_{NC})	Updated Composite FEM LLDF (g_C)	Calibrated FEM LLDF (g_{cal})	Test (g_{test})	g_{NC}/g_{test}	g_C/g_{test}	g_{cal}/g_{test}
Stop Location Interior	0.274	0.282	0.277	0.289	0.95	0.98	0.96
Stop Location Exterior	0.226	0.218	0.223	0.224	1.01	0.97	1.00
Crawl Speed Interior	0.274	0.282	0.277	0.287	0.95	0.98	0.97
Crawl Speed Exterior	0.226	0.218	0.223	0.229	0.99	0.95	0.97

Figure 8.100(a) and Figure 8.100(c) show the Middle Path – Span 2 stop location and crawl speed deflections compared to non-composite, composite, and calibrated values obtained from FEM analysis. Figure 8.100(b) and Figure 8.100(d) show the Middle Path – Span 2 stop location and crawl speed LLDFs compared to relevant AASHTO values as well as values obtained from calibrated FEM deflection results and moment results. Table 8.56 shows the test LLDF values, the displacement and moment LLDF values obtained from the calibrated FEM model, and the LLDF values found using all three AASHTO methods. The test and calibrated model LLDFs are all significantly lower than the prescribed AASHTO LLDF values.

Table 8.56. Experimental, FEM, and AASHTO LLDFs for Middle Path– Span 2 Loading

Description	G1	G2	G3	G4
Stop Location Test Disp. LLDF	0.208	0.289	0.279	0.224
Crawl Speed Test Disp. LLDF	0.202	0.287	0.281	0.229
Calibrated FEM Disp. LLDF	0.223	0.277	0.277	0.223
Calibrated FEM Moment LLDF	0.211	0.289	0.289	0.211
AASHTO Standard LLDF	0.589	0.476	0.476	0.589
AASHTO LRFD LLDF using simplified stiffness	0.660	0.427	0.427	0.660
AASHTO LRFD LLDF using analytical stiffness	0.660	0.410	0.410	0.660

Note:
1. G = girder, Disp. = Displacement

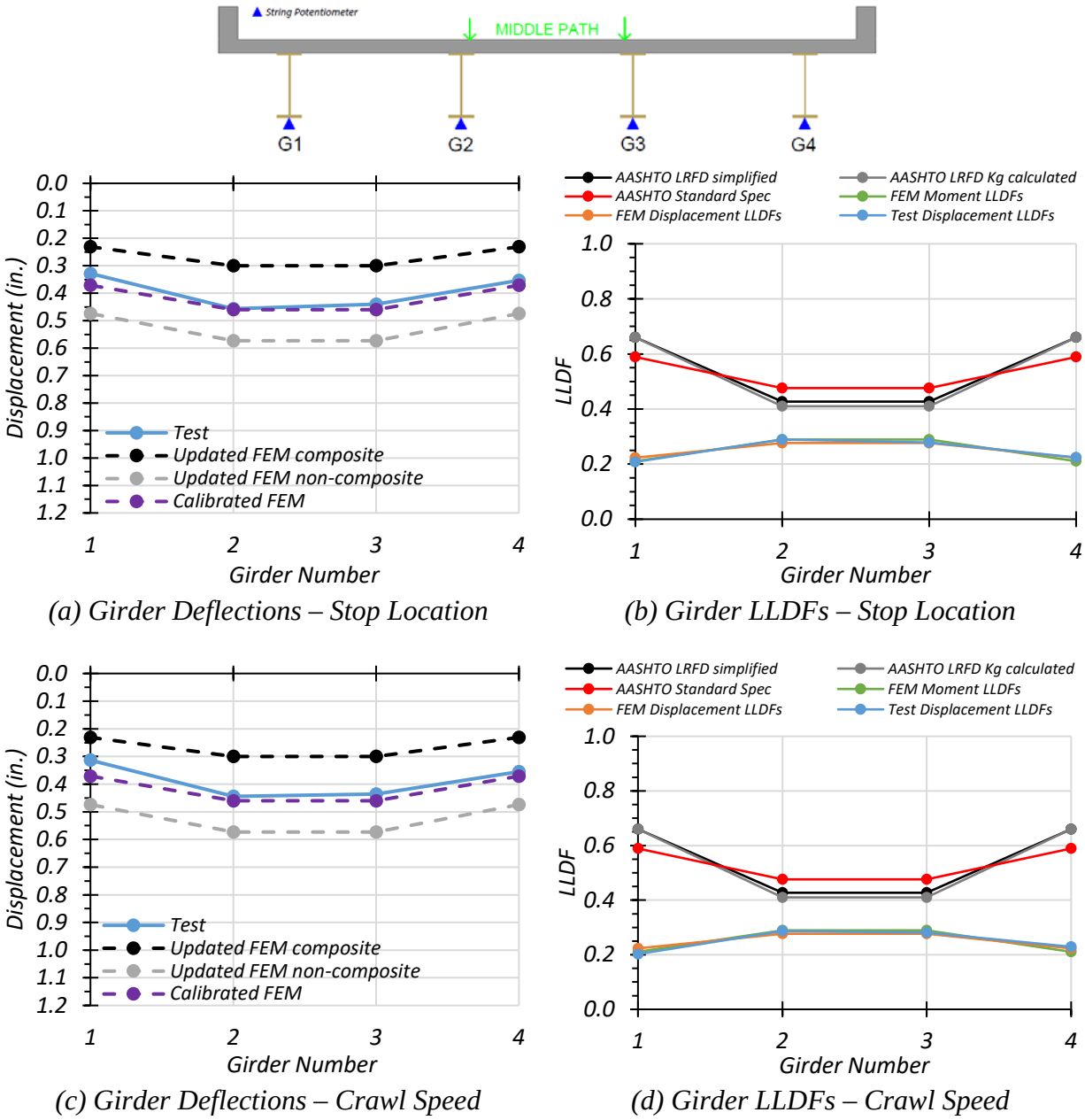

(a) Girder Deflections – Stop Location

(b) Girder LLDFs – Stop Location

(c) Girder Deflections – Crawl Speed

(d) Girder LLDFs – Crawl Speed

Figure 8.100. Comparison of Static Deflection Results for Middle Path – Span 2 Loading

8.9. SUMMARY AND FINDINGS

8.9.1. Live Load Distribution Factors

8.9.1.1. General Findings

LLDF values computed using FEM deflection results and FEM moment results were compared to ensure that the values were close, allowing the deflection data obtained from testing to be used to calculate experimental LLDFs. The FEM values were deemed very close (within 2.0 percent) for the controlling load case, thus LLDF values were determined for each load test based on the maximum span deflections.

For the Path 1 load cases, the g_{AASHTO}/g_{Test} ratio for ranges from 1.21 to 1.46 when considering the AASHTO Standard Specifications, from 1.30 to 1.41 when considering the simplified stiffness AASHTO LRFD Specifications, and from 1.25 to 1.41 when considering the analytical stiffness AASHTO LRFD Specifications (AASHTO 2002; AASHTO 2017). All three AASHTO methods of determining LLDFs for this bridge are significantly conservative for Path 1 loading.

For the Path 2 load cases, the g_{AASHTO}/g_{Test} ratio for ranges from 1.33 to 1.45 when considering the AASHTO Standard Specifications, from 1.24 to 1.62 when considering the simplified stiffness AASHTO LRFD Specifications, and from 1.20 to 1.62 when considering the analytical stiffness AASHTO LRFD Specifications (AASHTO 2002; AASHTO 2017). All three AASHTO methods of determining LLDFs for this bridge are significantly conservative for Path 2 loading.

For the Middle Path load cases, the g_{AASHTO}/g_{Test} ratio for ranges from 1.64 to 2.71 when considering the AASHTO Standard Specifications, from 1.48 to 3.04 when considering the

simplified stiffness AASHTO LRFD Specifications, and from 1.42 to 3.04 when considering the analytical stiffness AASHTO LRFD Specifications (AASHTO 2002; AASHTO 2017). All three AASHTO methods of determining LLDFs for this bridge are significantly conservative for Middle Path loading.

8.9.1.2. Consideration of Moment of Inertia Difference Between Girders

When calculating the LLDFs obtained from the displacements observed during testing, a more accurate method would be to consider the difference in moment of inertia between an interior girder and an exterior girder in the case that the moments of inertia are different. Updated LLDF can be developed for each girder by taking the deflection multiplied by the moment of inertia of an individual girder, and dividing by the sum of the deflection multiplied by the moment of inertia for all girders. Equation (8.1) shows the equation used to obtain an LLDF through this method.

$$LLDF_i = \frac{\Delta_i I_i}{\sum(\Delta_i I_i)} \tag{8.1}$$

where:

$LLDF_i$ = Live load distribution factor for an individual girder

Δ_i = Deflection of the individual girder (in.)

I_i = Moment of inertia of the individual girder (in^4)

Bridge SC-12 has the same steel section for interior and exterior girders (W30x108), so under fully non-composite action only the deflection affects the calculation of the LLDFs. However, under partial composite action, which Bridge SC-12 exhibited based on field testing, the interior girders and exterior girders have different moments of inertia due to different effective deck widths. For

an interior girder, the effective deck width is 72". For an exterior girder, the effective deck width is 56.5" and also includes a 10" wide by 9" tall curb. Bridge SC-12 LLDFs were recompuated based on the field measured displacements, and considering fully composite action to obtain an upper and lower bound for the LLDFs. The fully composite interior girder was found to have a moment of inertia of 11,300 in^4 and the fully exterior girder was found to have a moment of inertia of 13,250 in^4.

Considering the controlling stop location load case for Girder 4, along Path 1 and in Span 2, and using the procedure described above, new LLDFs were developed. The controlling interior girder, Girder 3, experienced an 8.3 percent decrease in LLDF from 0.327 to 0.301. The controlling exterior girder, Girder 4, experienced a 7.6 percent increase in LLDF from 0.469 to 0.506. Table 8.57 and Figure 8.101 show the LLDFs developed using this method compared to LLDFs determined through the calibrated FEM displacements, the calibrated FEM moments, the AASHTO Standard Specifications, the AASHTO LRFD Specifications using the simplified stiffness parameter, and the AASHTO LRFD Specifications using the analytical stiffness parameter (AASHTO 2002; AASHTO 2017).

Table 8.57. Bridge SC-12 LLDF Comparison Considering Difference in Inertia

Selected Girder LLDFs for Various Methods	Interior Girder 3	Exterior Girder 4
Test Displacement Considering Inertia Difference	0.301	0.506
Test Displacement without Considering Inertia Difference	0.327	0.469
Calibrated FEM Displacements	0.325	0.458
Calibrated FEM Moments	0.335	0.467
AASHTO Standard Specifications	0.476	0.589
AASHTO LRFD Specifications – Simplified	0.427	0.660
AASHTO LRFD Specifications – Analytical	0.410	0.660

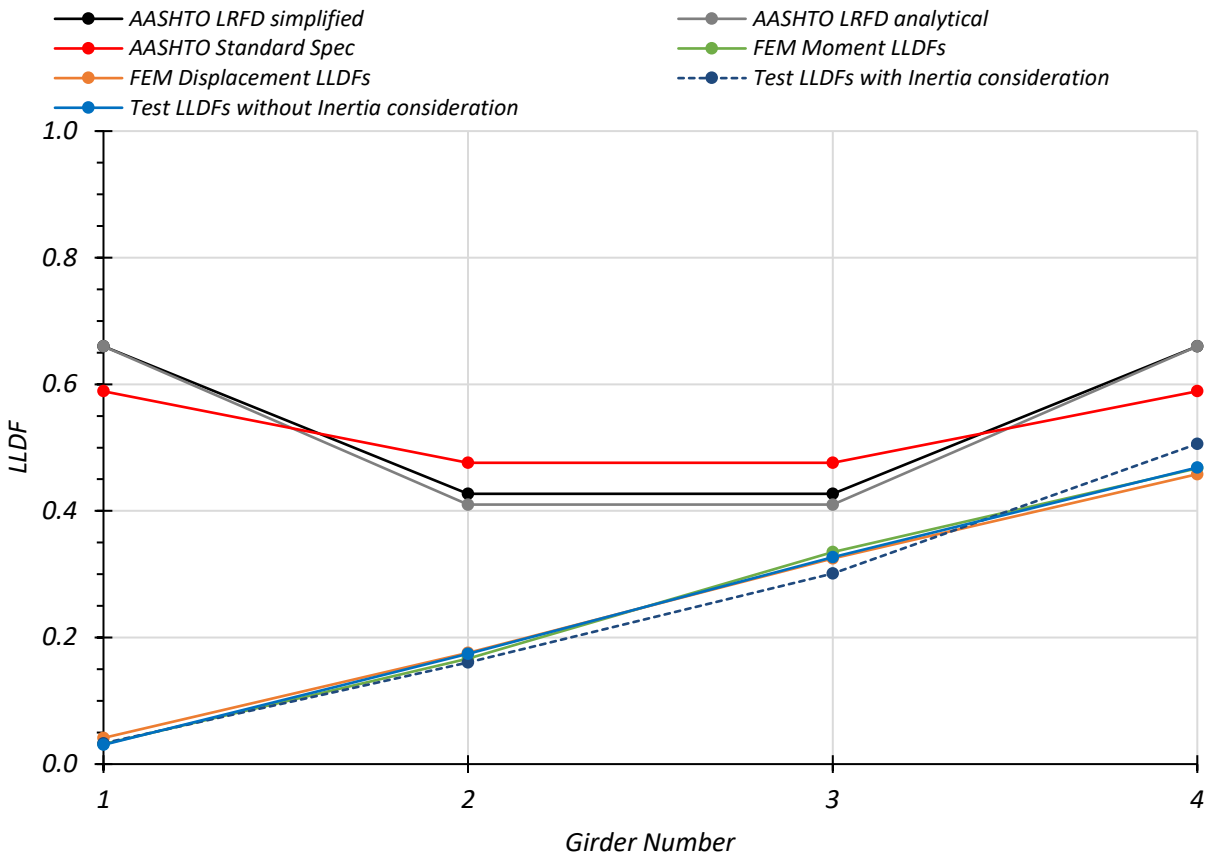

Figure 8.101. Bridge SC-12 – Span 2 LLDF Comparison Considering Difference in Inertia

The consideration of the moment of inertia difference between interior and exterior girders does not cause a significant change in calculated LLDFs for Bridge SC-12. This is because the composite interior and exterior girders do not have a significant difference in the updated moments of inertia. The LLDFs calculated based on displacements alone do a good job of matching the LLDF results from FEM displacements and FEM moments. Both results also remain below the LLDFs given by the AASHTO Standard Specifications (AASHTO 2002), which are proposed to be applied for this bridge. Furthermore, under the initial conservative assumption made during the basic load rating analysis that Bridge SC-12 is non-composite, there would be no difference in the

moment of inertia between interior and exterior girders. Therefore, the LLDFs would be calculated based only on displacements. Without conducting a field test, the presence of partial compositie action cannot be determined. The updated LLDFs were calculated considering the inertia difference based on fully composite action. Therefore, the LLDFs for the partially composite Bridge SC-12 would be between the two values shown based on the test displacements. For these reasons, the LLDFs were kept as calculated throughout this chapter, and the difference in moment of inertia between interior and exterior girders under composite action was not considered further. However, it is noted that to bound the possible LLDFs when considering the presence of partial of full composite action, one can consider both the fully non-composite case and the fully composite case.

8.9.2. Composite Action

Some data obtained during testing suggest Bridge SC-12 is acting as partially composite. From the strain gauges attached to the top and bottom flanges of the girders, a strain diagram of an interior and exterior girder was determined for each load test. The updated non-composite FEM model neutral axis is located 14.9 in. from the bottom of the girder. The updated composite FEM model neutral axis is 28.3 in. from the bottom of the girder for an exterior girder and 28.6 in. from the bottom of the girder for an interior girder. The median test neutral axis was determined to be 18.71 in. from the bottom of the girder for an exterior girder and 17.69 in. from the bottom of the girder for an interior girder, these values lie between the model values determined based on non-composite and fully composite behavior.

The bottom flange stresses obtained from testing were also compared to the expected non-composite and composite bottom flange stresses from the updated FEM analysis. It was found that the stresses also varied between the non-composite and fully composite stress values.

The deflection data obtained during the load testing was compared to the estimated girder deflection values from the FEM model analysis considering both non-composite and fully composite girder behavior. For the Path 1 – Span 2 stop location test, the maximum deflection measured in Girder 4 was 0.755 in., which was between the FEM composite deflection of 0.509 in. and the FEM non-composite deflection of 1.121 in. For the Path 2 – Span 2 stop location test, the maximum deflection measured in Girder 4 was 0.692 in., which was also between the FEM composite deflection of 0.451 in. and the FEM non-composite deflection of 1.007 in. For the Middle Path – Span 2 stop location test, the maximum deflection measured in Girder 4 was 0.457 in., which was again between the FEM composite deflection of 0.291 in. and the FEM non-composite deflection of 0.671 in.

The measured neutral axes during the critical static load tests for Span 2 was 19.77 in. from the bottom of Girder 3 and 19.81 in. from the bottom of Girder 4. The theoretical non-composite neutral axis is 14.90 in. from the bottom of the girder and the theoretical composite neutral axis is 26.11 in. from the bottom of the girder. The neutral axis locations observed during the critical load tests were used in a load rating analysis. As the TxDOT RF for this bridge is found for an interior girder in positive bending, the interior girder positive moment RFs calculated for Bridge SC-12 during the basic load rating were re-analyzed and compared. Table 8.58 shows the Strength I RFs calculated for Bridge SC-12 using the ASR, LFR, and LRFR methods considering the partial composite action observed during load tests. It compares these RFs values to those calculated for an interior girder considering positive bending in the basic load rating analysis and to the current

TxDOT RFs. It is important to note that for the ASR ratings, the dead load stresses are based on the non-composite section. It is also important to note that these results consider all of the same bridge characteristics used in the basic load rating analysis, not any updated parameters from the FEM analysis or from load testing.

For the ASR partial composite, positive moment region RF, the capacity stress was 18.15 ksi for Inventory and 24.75 for Operating, the dead load stress was 5.12 ksi, the superimposed dead load stress was 1.62 ksi, and the live load stress was 16.43 ksi. For the LFR partial composite, positive moment region RF, the moment capacity was 1216 kip-ft, the dead load moment was 172 kip-ft, and the live load moment was 503.1 kip-ft. For the LRFR partial composite, positive moment region RF, the moment capacity was 1216 kip-ft, the dead load moment was 172 kip-ft, and the live load moment was 625.8 kip-ft.

Table 8.58. Comparison of Bridge SC-12 Interior Girder Positive Moment Partial Composite RFs to Non-Composite RFs for Strength I

Method	TxDOT RF		Basic Rating RF		Partial Composite RF		Partial Composite RF/ TxDOT RF		Partial Composite RF/ Basic Rating RF	
	Inv.	Oper.	Inv.	Oper.	Inv.	Oper.	Inv.	Oper.	Inv.	Oper.
ASR	-	-	0.59	0.89	0.70	1.10	-	-	1.19	1.24
LFR	0.55	0.93	0.55	0.92	**1.03**	**1.72**	1.87	1.85	1.87	1.87
LRFR	-	-	0.60	0.78	1.02	1.33	-	-	1.70	1.71
Note: TxDOT and Task 3 RFs are calculated for a non-composite section.										

To determine the ratio of compressive force in the concrete deck for partial composite action to compressive force in the concrete deck for fully composite action, Equation C-I3-4 in the *AISC Steel Construction Manual* (AISC 2013), shown in Equation (8.2), was examined.

$$I_{equiv} = I_s + \sqrt{\frac{\sum Q_n}{C_f}}(I_{tr} - I_s) \quad (8.2)$$

where:

I_{equiv} = Equivalent partial composite moment of inertia = 7271 in^4

I_s = Moment of inertia for the structural steel section = 4460 in^4

I_{tr} = Moment of inertia for the fully composite uncracked transformed section = 10417 in^4

ΣQ_n = Maximum force transferred across the deck-girder interface (kips)

C_f = Compressive force in concrete slab for fully composite beam (kips)

By solving for the $\frac{\sum Q_n}{C_f}$, the ratio of compressive force in the concrete deck for partial composite action to compressive force in the concrete deck for fully composite action can be determined as 0.22. In determining the nominal moment capacity of the partially composite section, the compressive force in the deck was multiplied by this ratio. This produced the same neutral axis location observed during field testing. Then, moments of the components of the cross section were summed about the neutral axis to obtain a nominal moment capacity. The components of the cross-section included the bottom flange in tensions, the web in tension, the web in compression, the top flange in compression, and the part of the concrete deck in compression. It is also worth noting that the partial composite moment capacity was found to be 0.47 of the difference between the non-composite and composite moment capacities, which is the same value as that produce by $\sqrt{\frac{\sum Q_n}{C_f}}$.

8.9.3. Stresses

The maximum bottom flange stresses experienced during static loading were used to perform a stress analysis on the bridge. The maximum bottom flange stress in the positive moment region for Girder 3 was 4.69 ksi from Test 1. The maximum bottom flange stress in the positive moment region for Girder 4 was 7.09 ksi from Test 3. Using the updated FEM model, the estimate non-composite dead load bottom flange stresses in the positive moment region are 6.24 ksi for interior Girder 3 and 7.19 ksi for exterior Girder 4.

The maximum bottom flange stress in the negative moment region for Girder 3 was -2.06 ksi from Test 5. The maximum bottom flange stress in the negative moment region for Girder 4 was -3.42 ksi, also from Test 5. Using the calibrated FEM model, the estimate non-composite dead load bottom flange stresses in the negative moment region are -9.37 ksi for Girder 3 and -10.29 ksi for Girder 4.

An ASR load rating can be performed for Bridge SC-12 using this information and the yield strength of 33 ksi prescribed by the AASHTO MBE (AASHTO MBE 2018). Equation (8.3) shows the ASR RF equation. The capacity, dead load effect, and live load effect are in terms of stresses.

$$RF = \frac{C - A_1 D}{A_2 L(1 + I)} \tag{8.3}$$

where:

RF = Rating Factor for the live load carrying capacity

C = Capacity of the member = 0.55*F_y for Inventory, 0.75*F_y for Operating

D = Dead load effect on the member

L = Live load effect on the member

I = Impact factor to be used with the live load effect = 0.25

A_1 = Factor for dead loads = 1.0

A_2 = Factor for live load = 1.0

Table 8.59 shows the calculated RFs for Bridge SC-12 using the measured test information and the ASR method. It is important to note that these RFs are for a single test vehicle, which was almost exactly at the posted limit, not for the design HS-20 truck. It is also important to note that this only considers one truck on the bridge, which is marked as two lanes.

Table 8.59. Bridge SC-12 Calculated ASR One-Lane Test Vehicle RFs Using Test Results

Girder	Positive Moment Region			Negative Moment Region		
	Maximum Measured Live Load Stress from Static Load Tests (ksi)	**Inventory RF**	**Operating RF**	**Maximum Measured Live Load Stress from Static Load Tests (ksi)**	**Inventory RF**	**Operating RF**
Interior G3	4.69	2.03	3.16	-2.06	3.41	5.97
Exterior G4	7.09	1.24	1.98	-3.42	1.84	3.38

8.9.4. Model Calibration and Update

Using the calibrated FEM model of Bridge SC-12, analysis was performed for the HS-20 design vehicle. This is the vehicle used in the ASR and LFR rating methods, which TxDOT uses to perform load ratings of bridges not designed using LRFR (TxDOT 2018a). The maximum live load bottom flange stress in the positive moment region for interior Girder 3 was 10.31 ksi. The maximum live load bottom flange stress in the positive moment region for exterior Girder 4 was 10.92 ksi. Using the calibrated FEM model, the estimated non-composite dead load bottom flange stresses in the positive moment region are 6.24 ksi for Girder 3 and 7.19 ksi for Girder 4.

The maximum live load bottom flange stress in the negative moment region for Girder 3 was -7.66 ksi. The maximum live load bottom flange stress in the negative moment region for Girder 4 was -8.65 ksi. Using the calibrated FEM model, the estimated non-composite dead load bottom flange stresses in the negative moment region are -9.37 ksi for Girder 3 and -10.29 ksi for Girder 4.

Using these results, an ASR load rating was performed for Bridge SC-12 for the HS-20 live load. Table 8.60 shows the ASR HS-20 RFs for Girder 4 and Girder 3 using the analysis results from the calibrated FEM model. Load Rating using the calibrated FEM model for the HS-20 vehicle would allow the posting of Bridge SC-12 to be removed, per TxDOT's On-System Load Rating flowchart (TxDOT 2018a).

Table 8.60. Bridge SC12 Calculated ASR HS-20 RFs Using Calibrated FEM Model Results

Girder	Positive Moment Region		Negative Moment Region	
	Inventory RF	Operating RF	Inventory RF	Operating RF
Interior G3	0.92	1.44	0.92	1.61
Exterior G4	0.80	1.29	0.73	1.34

LFR Strength I RFs can also be developed using the calibrated FEM model of Bridge SC-12. The positive moment capacity found using a partially composite section with the same neutral axis locations as observed during testing is 1357.0 kip-ft for Girder 3 and 1357.0 kip-ft for Girder 4. The capacity was calculated using LFD procedures provided in the AASHTO Standard Specifications (AASHTO 2002). Using the updated FEM model, the non-composite positive dead load moments were found to be 158.3 kip-ft on Girder 3 and 171.2 kip-ft on Girder 4. Using the calibrated FEM model, the controlling positive live load moments were found to be 290.3 kip-ft on Girder 3 and 299.4 kip-ft on Girder 4 for two-lane HS-20 load paths.

The negative moment capacity found using a non-composite section is -1081.0 kip-ft for Girder 3 and -1081.0 kip-ft for Girder 4. Using the calibrated FEM model, the non-composite negative dead load moments were found to be -306.9 kip-ft on Girder 3 and -337.0 kip-ft on Girder 4. Using the calibrated FEM model, the controlling negative live load moments were found to be -250.9 kip-ft on Girder 3 and -283.3 kip-ft on Girder 4 for two-lane HS-20 load paths.

Using these results, an LFR load rating was performed for Bridge SC-12 for the HS-20 live load. Equation (8.4) shows the LFR RF equation with the variables defined as well. The capacity, dead load effect, and live load effect are moment values.

$$RF = \frac{C - A_1 D}{A_2 L(1 + I)} \tag{8.4}$$

where:

RF = Rating Factor for the live load carrying capacity

C = Capacity of the member

D = Dead load effect on the member

L = Live load effect on the member

I = Impact factor to be used with the live load effect = 0.25

A_1 = Factor for dead loads = 1.3

A_2 = Factor for live load = 2.17 for Inventory, 1.3 for Operating

Table 8.61 shows the LFR Strength I HS-20 two-lane RFs for Girder 3 and Girder 4 using the analysis results from the calibrated FEM model. These RFs for Bridge SM-5 allow its posting to be removed based on the TxDOT on-system load posting flowchart (TxDOT 2018a), shown in Figure 3.2.

Table 8.61. Bridge SC-12 Calculated LFR Strength I HS-20 RFs Using Calibrated FEM Model Results

Girder	Positive Moment Region				Negative Moment Region			
	Capacity (kip-ft)	Live Load Demand (kip-ft)	Inventory RF	Operating RF	Capacity (kip-ft)	Live Load Demand (kip-ft)	Inventory RF	Operating RF
Interior G3	1357.0	290.3	1.46	2.44	-1081.0	-250.9	1.00	1.67
Exterior G4	1357.0	299.4	1.40	2.33	-1081.0	-283.3	0.84	1.40

9. SUMMARY, CONCLUSIONS, AND RECOMMENDATIONS

9.1. SUMMARY

The goal of this study was to provide TxDOT with recommendations to improve the load postings of their steel multi-girder bridges by using refined analysis methods informed by nondestructive load testing for select bridges. A literature review was performed to gain an understanding of the load rating process specified by AASHTO and of the process that TxDOT is currently using to rate and post their bridges. The inventory of posted bridges was also examined to determine the types of steel multi-girder bridges that are most often posted, and therefore provide the most potential benefit from techniques to improve ratings. Based on the literature review, basic load ratings were conducted for a select group of steel simply supported multi-girder bridges and steel continuous multi-girder bridges that were thought to best represent those in the inventory of Texas SSLO bridges. These basic load ratings were used to better understand the load rating process and areas in which there could be room for improvement. Three bridges were selected from this group for modeling using FEM software and for a refined analysis. Live load distribution factors were examined as well as the effect of composite or non-composite action on those LLDFs. The LLDFs were also compared to those obtained using the equations given in the relevant AASHTO guides and specifications. Finally, two bridges, one simply supported and one continuous, were instrumented and load tested in the field. The results of the nondestructive load tests were used to determine the in situ structural behavior of the bridges. They were also used to calibrate the initial FEM models that were developed, which were then used to re-analyze the structures. Using this process, two bridges were examined in depth to assess the potential for a change in their posting status, and recommendations to improve postings for similar bridges were developed.

9.2. CONCLUSIONS AND LOAD RATING RECOMMENDATIONS

9.2.1. Bridge SM-5

Bridge SM-5 is a simply supported steel multi-girder bridge that was designed without shear studs for composite action. The most significant observation for Bridge SM-5 from the field testing was that it is acting as almost fully composite. TxDOT is currently rating this bridge as non-composite as a conservative measure and to be consistent with the design. However, Bridge SM-5 has the top flanges of its steel girders embedded into the concrete deck; and there no signs of deck cracking on the underside that would indicate the occurrence of slippage between the deck and girders. Load testing of Bridge SM-5 showed that the neutral axis locations in the steel girders are very close to the corresponding theoretical composite neutral axis locations. In addition, girder deflections matched almost exactly with the theoretical composite girder deflections obtained from the updated FEM model. Bridge SM-5 also exhibits some end fixity under load. Compressive strains were observed in the bottom flanges at the ends of the two instrumented girders, indicating end restraint. The LLDFs observed during testing of Bridge SM-5 were compared to LLDF values obtained from the AASHTO Standard Specifications and from the AASHTO LRFD Specifications. It was found that, while the AASHTO Standard Specification LLDFs were slightly unconservative for the controlling girder, the difference was not significant and in general they did a good job of estimating the LLDFs of the bridge. The AASHTO LRFD Specification LLDFs tended to be more conservative than the LLDFs observed during testing.

This information was included in a calibrated FEM model of Bridge SM-5, which was used to obtain new RFs using the ASR method, as it originally controlled over the LFR method. Details of this calculation can be seen in Section 7.9.4. The controlling girder found using the model was

an exterior girder, with an ASR Inventory RF of 0.74 and an ASR Operating RF of 1.29 considering two-lane HS-20 loading. Table 9.1 shows the current TxDOT RFs for Bridge SM-5 obtained from the LFR method, the updated RFs based on the calibrated FEM model and compares the two. The updated RFs for Bridge SM-5 allow its posting to be removed based on the TxDOT on-system load posting flowchart (TxDOT 2018a).

Table 9.1. Comparison of Refined ASR RF with TxDOT LFR RF for Bridge SM-5

Rating Factor	TxDOT	Refined	Refined/TxDOT
Inventory	0.47	0.74	1.57
Operating	0.79	1.29	1.63

It is also possible to consider RFs based on adjusting the rating analysis to include the presence of composite action, without the use of a refined model. This can be done using the current LFR rating approach, which is the same method TxDOT uses to rate Bridge SM-5. Table 9.2 shows the RFs obtained by assuming Bridge SM-5 to be fully composite and not changing any other parameter. The LFR method is used for this scenario. These RFs would also allow the posting to be removed for Bridge SM-5 based on the TxDOT on-system load posting flowchart (TxDOT 2018a).

Table 9.2. Comparison of Fully Composite LFR RF with TxDOT LFR RF for Bridge SM-5

Rating Factor	TxDOT	Composite	Composite/TxDOT
Inventory	0.47	1.04	2.21
Operating	0.79	1.74	2.20

9.2.2. Bridge SC-12

During field testing, the continuous steel multi-girder Bridge SC-12 exhibited signs of partial composite action. The neutral axis location was found to be 18.7 in. from the bottom of the girder, compared with FEM composite and non-composite neutral axes of 28.3 and 14.9 in., respectively. The maximum deflection for the critical load case was found to be 0.755 in., compared with FEM composite and non-composite deflections of 0.509 in. and 1.121 in., respectively.

Bridge SC-12 also exhibited LLDFs lower than the values given by the AASHTO codes used for comparison. The maximum interior girder LLDF found during testing was 0.343 in the positive moment region in Span 2, which was found to be the controlling scenario. The maximum exterior girder LLDF found during testing was 0.487 in the positive moment region in Span 2. In comparison, the LLDFs given by the AASHTO Standard Specifications (AASHTO 2002) are 0.476 for the interior girder and 0.589 for the exterior girder. The LLDFs given by the AASHTO LRFD Specifications (AASHTO 2017) using the simplified stiffness parameter are 0.427 for the interior girder and 0.660 for the exterior girder. The LLDFs given by the AASHTO LRFD Specifications (AASHTO 2017) using the analytical stiffness parameter are 0.410 for the interior girder and 0.660 for the exterior girder. The test LLDFs were lower thanall three of the AASHTO values for both interior and exterior girders.

The curb of Bridge SC-12 also showed some strain changes during loading, and was included in the calibrated FEM model. The calibrated model was used to perform a refined analysis of Bridge SC-12 considering partial composite action, actual observed live load distribution, and the load carrying capability of the entire structure instead of just the girders. The ASR method was used to obtain new RFs for Bridge SC-12, as it controlled over the LFR method. Details of this calculation can be seen in Section 8.9.4. The calibrated model gives an ASR Inventory RF of 0.73

and an ASR Operating RF of 1.34 considering two-lane HS-20 loading. Table 9.3 shows the current TxDOT RFs for Bridge SC-12 obtained using the LFR method, the new proposed RFs based on the calibrated FEM model and compares the two. The refined RFs for Bridge SC-12 would allow its posting to be removed based on the TxDOT on-system load posting flowchart (TxDOT 2018a).

Table 9.3. Comparison of Refined ASR RF with TxDOT LFR RF for Bridge SC-12

Rating Factor	TxDOT	Refined	Refined/TxDOT
Inventory	0.55	0.73	1.33
Operating	0.93	1.34	1.44

It is also possible to consider RFs based on adjusting the rating analysis to include the presence of partial composite action, without the use of a refined model. This can be done using the current LFR rating approach, which is the same method TxDOT uses to rate Bridge SC-12. Table 9.4 shows the RFs obtained by assuming Bridge SC-12 to be acting partially composite and not changing any other parameter. The same neutral axis location that was observed during testing was used during load rating calculations. The LFR method is used for this scenario. These RFs would also allow the posting to be removed for Bridge SC-12 based on the TxDOT on-system load posting flowchart (TxDOT 2018a).

Table 9.4. Comparison of Partial Composite LFR RF with TxDOT LFR RF for Bridge SC-12

Rating Factor	TxDOT	Partial Composite	Partial Composite/TxDOT
Inventory	0.55	0.90	1.64
Operating	0.93	1.50	1.61

9.2.3. Refined Analysis

The effect of refined analysis on load ratings was highlighted in this study. Using refined models can provide a more accurate picture of the live load distribution occurring in the bridge and the effect of changes in other parameters on the structure. Using FEM modeling can also provide a more accurate representation of the forces affecting each individual girder under load. It is recommended that TxDOT consider this approach when load rating a bridge whose posting could be more desirable to be removed than a typical bridge. FEM modeling programs exist that enable the user to quickly make a model of a structure and analyze that model in a timely manner.

Refined material properties could also help improve load ratings. For steel bridges, an increase in steel yield strength can greatly increase the capacity. This instrumentation could be invested in as many postings could possibly be improved. In this study, the 28-day concrete compressive strength was determined for the decks of both bridges tested in the field. While compressive strength will likely not help improve the rating of a non-composite structure, an increase in compressive strength could improve the capacity of a composite or partially composite structure.

9.2.4. Live Load Distribution Factors

Currently TxDOT is using the AASHTO Standard Specifications LLDFs when load rating a bridge not designed using LRFD. This study found that the AASHTO Standard Specification LLDFs do a good job of giving values that are conservative in most scenarios, but not overly conservative. In the scenarios in which they are not conservative, they are generally close to the measured LLDF of the bridge. Both methods for finding LLDFs given in the AASHTO LRFD Specifications were found to be almost always conservative and, in most cases, overly conservative. Table 9.5 and

Table 9.6 show the LLDFs found during this study for the three bridges examined in further depth, and compares them to the LLDF values given by the three AASHTO options. It can be seen that the AASHTO Standard Specifications LLDFs provide values that are conservative in most cases, but not overly conservative. TxDOT currently uses the AASHTO Standard Specifications LLDFs when load rating bridges not designed using LRFD, generally for older bridges. Based on the results of this research it is suggested that this practice is appropriate for the considered bridge types.

Table 9.5. Selected Bridge One-Lane LLDF Comparison

Bridge	Girder	Test	AASHTO Standard	AASHTO LRFD with simplified stiffness	AASHTO LRFD with analytical stiffness
SM-5	Interior	0.164	0.137	0.245	0.212
	Exterior	0.195	0.174	0.245	0.212
SC-12	Interior	0.343	0.476	0.427	0.427
	Exterior	0.487	0.589	0.660	0.660
SM-21*	Interior	0.259	0.285	0.345	0.352
	Exterior	0.291	0.364	0.345	0.352
* Bridge SM-21 was not load tested, its test LLDFs come from the FEM analysis in Chapter 5					

Table 9.6. Selected Bridge Two-Lane LLDF Comparison

Bridge	Girder	Test	AASHTO Standard	AASHTO LRFD with simplified stiffness	AASHTO LRFD with analytical stiffness
SM-5	Interior	0.180	0.174	0.288	0.250
	Exterior	0.202	0.174	0.288	0.250
SC-12	Interior	0.517	0.606	0.583	0.560
	Exterior	0.534	0.606	0.660	0.660
SM-21*	Interior	0.344	0.364	0.437	0.447
	Exterior	0.294	0.364	0.437	0.447
* Bridge SM-21 was not load tested, its test LLDFs come from the FEM analysis in Chapter 5					

9.2.5. Composite Action

Bridge SM-5 showed clear signs of acting as nearly fully composite if not fully composite. The top flanges of its girders were embedded into the deck, the girder deflection profile matched the FEM composite deflection profile, and its neutral axis was quite close to the theoretical composite neutral axis. Bridge SC-12 showed signs of partial composite action. It did not have embedded flanges, however its neutral axis location and deflection profile showed behavior between composite and non-composite.

Based on these findings, recommendations can be made about the consideration of composite action when load rating bridges not considered by design to be composite. For steel multi-girder bridges in which the top flange is embedded in the deck, the bridge should first be examined during its inspection. The bridge should be checked to see if it is in good overall condition and there are no signs of cracking on the underside of the deck near the girders, indicating it unlikely that slippage is occurring. If this is the case, then it is likely that the presence of full composite action or partial composite action could be used in the load rating analysis. More definitive information could be derived from nondestructive load testing, as discussed below.

For steel multi-girder bridges in which the top flange is not embedded into the deck, some sort of confirmation must occur in order to consider partial composite action. For example, this could consist of attaching a few string potentiometers, using computer vision, or using some other method to obtain girder deflection data while running a truck with known axle weights and configuration across the bridge. The deflection observed could then be compared to theoretical composite and non-composite deflections for that same vehicle in order to determine if partial composite action is occurring, and if so, how much partial composite action can be assumed.

9.2.6. End Fixity

Bridge SM-5 was observed to exhibit partial end fixity under loading. Confirmation that partial end fixity is occurring for other bridges would most likely be obtained by attaching a strain gauge to the bottom flange of a girder at one or both ends. This coupled with visual observations such as rust and deterioration causing locking between the girders and the bearing or tension cracks in the deck near the bridge abutments could provide enough validation that a bridge is experiencing partial end fixity. If this is observed, some judgement by an engineer would be necessary to assess the level of partial fixity to include in the load rating. However, more extensive field testing would provide more reliable quantitative information.

9.2.7. Number of Lanes

The two-lane LLDFs obtained through any of the three AASHTO methods are higher than the one-lane LLDFs. This distributes more load to the critical girder when conducting a load rating. However, many of the bridges in the TxDOT inventory that are posted are in rural settings and have lanes that are quite narrow. For example, Bridge SM-5 is on a road that is near the entrance to a small state park and has a lane width of 11'-9". It is striped as a two-lane bridge; however, these factors make the likelihood that two design trucks will be on the bridge at the same time very small. Engineering judgement could be used to analyze this bridge, and others like it, as one-lane bridges. This is a limited practice that TxDOT already currently uses in some of their load ratings of narrow bridges. When a bridge is being load rated, the geometry, location of the bridge, and type of traffic it may see should be considered. In some cases, if necessary, the middle stripe could be removed, and signs posted warning that a bridge is only one-lane would be required to ensure safety.

9.2.8. Computer Vision

The use of computer vision to observe deflections, especially for dynamic load cases was examined throughout this study. For dynamic load cases, the computer vision method correctly identified the exterior girder deflections within ten percent for all load cases for which computer vision analysis was performed except for one. If used properly, the computer vision method could be a very quick and effective way to obtain girder deflections under load. It is recommended that TxDOT take the information observed through this study into consideration when analyzing and load rating a bridge. Computer vision could be used to obtain evidence of certain bridge behavior that could help improve load ratings, such as to determine the presence of partial or full composite action.

9.3. RECOMMENDATIONS FOR FUTURE WORK

The following recommendations are made to provide potential areas of further study related to the topic of load rating similar bridges:

1. FEM Modeling: In this study, only three bridges were modeled and had refined analysis performed. Analyzing only a few bridges does not necessarily allow for broader, specific generalizations to be made about a large population of bridges. A large study in which tens of bridges are modeled and analyzed could provide useful information about LLDFs for the specific parameters of interest in the bridge inventory. The bridges could be modeled using user friendly software and the effect of bridge geometry, material properties, compositeness, and end fixity on LLDFs could be examined, allowing more generalizations to be made for a population of bridges.
2. Composite Action: One bridge examined in this study was observed exhibiting partial composite action in a deck-girder system that did not have shear studs and would otherwise be

considered non-composite. However, the behavior of one bridge is not enough to make the same assumption about other bridges. An in-depth study could be performed to determine the true extent to which partial composite action is occurring in bridges that have been constructed as non-composite. A large number of bridges could have less detailed and involved load tests performed to observe any partial composite action. If a generalization could be made, the effect of the increased capacity on load ratings would be significant.

3. Steel Yield Strength: This study was unable to determine steel yield strength in the field due to the limited range of the available NDE devices to do so. This potential area of improvement to load ratings should be explored in more depth. If the capacity of many steel multi-girder bridges can be increased by simply performing a NDE test of steel strength, the effect on the load ratings of an inventory of bridges could be beneficial. In addition, access to mill certificate information could also provide the necessary data to update the steel yield strength to the expected value for a given bridge.
4. Computer Vision: This study examined the use of computer vision as a targetless method to determine girder deflections under load. It was generally successful for dynamic load tests and some crawl speed load tests. The computer vision method should undergo further validation. It is potentially a quick, easy, targetless method to partially measure structural response and determine, based on deflections, the presence of composite action.

REFERENCES

AASHO (1970). "Manual for Maintenance Inspection of Bridges, 1970." American Association of State Highway Officials, Washington D.C.

AASHTO (1974). "Manual for Maintenance Inspection of Bridges, 1974." American Association of State Highway and Transportation Officials, Washington D.C.

AASHTO (1978). "Manual for Maintenance Inspection of Bridges, 1978." American Association of State Highway and Transportation Officials, Washington D.C.

AASHTO (1983). "Manual for Maintenance Inspection of Bridges, 1983." American Association of State Highway and Transportation Officials, Washington D.C.

AASHTO (1994). "Guide Specifications for Distribution of Loads for Highway Bridges." American Association of State Highway and Transportation Officials, Washington, DC.

AASHTO (1994). "Manual for Condition Evaluation of Bridges, 1994." American Association of State Highway and Transportation Officials, Washington D.C.

AASHTO (1996). "Standard Specifications for Highway Bridges, 16th Edition." American Association of State Highway and Transportation Officials, Washington D.C.

AASHTO (2002). "Standard Specifications for Highway Bridges, 17th Edition." American Association of State Highway and Transportation Officials, Washington D.C.

AASHTO (2003). "Manual for Condition Evluation and Load and Resistance Factor Rating (LRFR) of Highway Bridges." American Association of State Highway and Transportation Officials, Washington D.C.

AASHTO (2008). "Manual for Bridge Evaluation, 1st Edition." American Association of State Highway and Transportation Officials, Washngton D.C.

AASHTO (2011). "Manual for Bridge Evaluation, 2nd Edition." American Association of State Highway and Transportation Officials, Washngton D.C.

AASHTO (2014). "AASHTO LRFD Bridge Design Specifications." American Association of State Highway and Transportation Officials (AASHTO), Washington, DC.

AASHTO (2017). "AASHTO LRFD Bridge Design Specifications, Eighth Edition." American Association of State Highway and Transportation Officials, Washington D.C.

AASHTO MBE (2011). "Manual for Bridge Evaluation, 2nd Edition." American Association of State Highway and Transportation Officials, Washngton D.C.

AASHTO MBE (2018). "Manual for Bridge Evaluation, 3rd Edition." American Association of State Highway and Transportation Officials, Washington, DC.

AISC (1953). "Historical Record, Dimensions and Properties, Rolled Shapes, Steel & Wrought Iron Beams and Columns." American Institute of Steel Construction, New York.

AISC (2013). "Steel Construction Manual, 14th Edition." American Institute of Steel Construction, United States of America.

American Association of State Highway and Transportation Officials (2002). "Standard Specifications for Highway Bridges, 17th Edition." AASHTO, Washington D.C.

American Association of State Highway and Transportation Officials (2014). "AASHTO LRFD Bridge Design Sepcifications, Seventh Edition." AASHTO, Washington D.C.

ASCE/SEI-AASHTO Ad-Hoc Group On Bridge Inspection, R., Rehabilitation, and Replacement (2009). "White Paper on Bridge Inspection and Rating." *Journal of Bridge Engineering*, 14(1), 1-5.

Barnard, T., Hovell, C. G., Sutton, J. P., Mouras, J. M., Neuman, B. J., Samaras, V. A., Kim, J., Williamson, E. B., and Frank, K. H. (2010). "Modeling the Response of Fracture Critical Steel Box-Girder Bridges." *Report No. FHWA/TX-10/9-5498*, Center for Transportation Research at the Univ. of Texas at Austin, Austin, TX.

Barth, K. (2015). "Design Example 2A: Two-Span Continuous Straight Composite Steel I-Girder Bridge." *Steel Bridge Design Handbook*, Federal Highway Administration, ed., US Department of Transportation.

Bowman, M. D., and Chou, R. (2014). "Review of Load Rating and Posting Procedures and Requirements." Indiana Department of Transportation and Purdue University.

Chajes, M. J. (1997). "Experimental Load Rating of a Posted Bridge." *Journal of Bridge Engineering*, 2(1).

Computers and Structures, I. 2019. CSiBridge, version 20Computers and Structures, Inc, Berkeley, California, USA.

CTC & Associates (2009). "Improved LRFD/LRFR Specifications for Permit and Fatigue Load Trucks." https://rosap.ntl.bts.gov/view/dot/27698

Ellingwood, B. R., O'Malley, C., Wang, N., and Zureick, A.-H. (2009a). "Report of Task 1 - Appraisal of State-of-the-Art of Bridge Condition Assessment." *Condition Assessment of Existing Bridge Structures*, Georgia Institute of Technology.

Ellingwood, B. R., O'Malley, C., Wang, N., and Zureick, A.-H. (2009b). "Report of Task 4 - Development of guidelines for condition assessment, evaluation, and rating of bridges in Georgia." *Condition Assessment of Existing Bridge Structures*, Georgia Institute of Technology.

Ellingwood, B. R., O'Malley, C., Wang, N., and Zureick, A.-H. (2009c). "Report of Tasks 2 and 3 - A Bridge Testing Program." *Condition Assessment of Existing Bridge Structures*, Georgia Institute of Technology.

Federal Highway Administration (2015). "Bridge Formula Weights." US Department of Transportation, ed. https://ops.fhwa.dot.gov/freight/publications/brdg_frm_wghts/

Florida Department of Transportation (2017). "Bridge Load Rating Manual." *Posting Avoidance*, FDOT. https://www.fdot.gov/maintenance/loadrating.shtm

Hearn, G. (2014). "State Bridge Load Posting Processes and Practices." *Synthesis 453*, NCHRP, Washington D.C. http://www.trb.org/Publications/Blurbs/170534.aspx

Huang, Q., Gardoni, P., and Hurlebaus, S. (2011). "Predicting Concrete Compressive Strength Using Ultrasonic Pulse Velocity and Rebound Number." *Materials Journal*, 108(4).

Hueste, M., Mander, J. B., Terzioglu, T., Jiang, D., and Petersen-Gauthier, J. (2015). "Spread Prestressed Concrete Slab Beam Bridges." Texas A&M Transportation Institute.

Hurlebaus, S., Mander, J. B., Terzioglu, T., Boger, N. C., and Fatima, A. (2018). "Fracture Critical Steel Twin Tub Girder Bridges: Technical Report."

Imbsen, R. A., Liu, W. D., Schamber, R. A., and Nutt, R. V. (1987). "Strength evaluation of existing reinforced concrete bridges." *National Cooperative Highway Research Program report ; 292*, Transportation Research Board, National Research Council, Washington, D.C

Indiana Department of Transportation (2016). "INDOT Bridge Inspection Manual." *Part 3 - Load Rating*, INDOT. https://www.in.gov/dot/div/contracts/standards/bridge/inspector_manual/

Iowa Department of Transportation (2013). "Bridge Rating Manual." *General Requirements*. https://siims.iowadot.gov/IowaDOT_BridgeRatingManual.pdf

Kulicki, J. M. (1998). "Development of comprehensive bridge specifications and commentary." *Research results digest ; no. 198*, Transportation Research Board, National Research Council, Washington, D.C.

Lichtenstein, A. G. (1993). "The Silver Bridge Collapse Recounted." *Journal of Performance of Constructed Facilities*, 7(4), 249-261.

Lichtenstein Consulting Engineers (2001). "Manual for Condition Evaluation and Load Rating of Highway Bridges Using Load and Resistance Factor Philosophy." *Contractor's Final Report*Paramus, NJ.

Lwin, M. M. (2006). "Bridge Load Ratings for the National Bridge Inventory." Federal Highway Administration - Office of Bridge Technology, ed., US Department of Transportation.

MassDOT (2013). "LRFD Bridge Manual - Part I." *Chapter 7 - Bridge Load Rating Guidelines*, Massachusetts Department of Transportation.

Measurement Computing (2014). "StrainBook/616." <http://www.mccdaq.com/products/strainbook616.htm>. (July 15, 2014).

Mertz, D. (2015). "Steel Bridge Design Handbook - Load Rating of Steel Bridges." HDR, Inc.

Mertz, D. R. (2005). "Load Rating by Load and Resistance Factor Evaluation Method." National Cooperative Highway Research Program, Transportation Research Board.

Mertz, D. R. (2007). "Simplified live load distribution factor equations." Transportation Research Board, National Research Council, Washington D.C.

Michigan Department of Transportation (2009). "Bridge Analysis Guide, Part 1, 2005 Edition with 2009 Interim Update." Michigan Department of Transportation. https://www.michigan.gov/documents/mdot/MDOT_2009__InterimBridgeAnalysisGuide_Part1_274530_7_608697_7.pdf

Minnesota Department of Transportation (2009). "LRFD Bridge Design." *Chapter 15 - Bridge Load Rating*. https://www.dot.state.mn.us/bridge/datamanagement.html

Mlynarski, M., Wassef, W. G., and Nowak, A. S. (2011). "A comparison of AASHTO bridge load rating methods." Transportation Research Board, National Research Council, Washington D.C.

Moses, F. (2001). "Calibration of load factors for LRFR bridge evaluation." Transportation Research Board, National Research Council, Washington D.C.

Moses, F., and Verma, D. (1987). "Load capacity evaluation of existing bridges." Transportation Research Board, National Research Council, Washington, D.C.

NBI (2016). "National Bridge Inventory (NBI)." Federal Highway Administration, Washington, DC.

New York State Department of Transportation (2005). "Load Rating/Posting Guidelines for State-Owned Highway Bridges." *Engineering Instruction 05-034*. https://www.dot.ny.gov/portal/page/portal/main/business-center/consultants/forms-publications-and-instructions/engineering-information-issuance-system/ei-repository/ei05034.pdf

Newmark, N. M. (1938). *A distribution procedure for the analysis of slabs continuous over flexible beams*, The University of Illinois, Urbana, Illinois.

ODOT (2015). "LRFR Manual." Oregon Department of Transportation, Salem, OR. https://www.oregon.gov/ODOT/Bridge/Pages/Load-Rating.aspx

Pelphrey, J., Higgins, C., Sivakumar, B., Groff, R. L., Hartman, B. H., Charbonneau, J. P., Rooper, J. W., and Johnson, B. V. (2008). "State-specific LRFR live load factors using weigh-in-motion data." *Journal of Bridge Engineering*, 13(4), 339-350.

Pennsylvania Department of Transportation (2010). "Bridge Safety Inspection Manual." *Distribution of Live Loads on Longitudinal Members, Bridge Rating Software*, PennDOT. https://www.dot.state.pa.us/public/PubsForms/Publications/PUB%20238.pdf

Proceq "Original Schmidt Hammer Conversion Chart." Proceq. 2002 http://www.pcte.com.au/images/pdf/Original%20Schmidt%20Hammer/Schmidt-Hammer-Type-N-L-NR-LR-Manual.pdf

Proceq "Silver Schmidt Hammer Conversion Chart." Proceq. 2017 https://www.proceq.com/uploads/tx_proceqproductcms/import_data/files/SilverSchmidt_Operating%20Instructions_English_high.pdf

Puckett, J. A., Huo, S. X., Jablin, M., and Mertz, D. R. (2011). "Framework for Simplified live load distribution-factor computations." *Journal of Bridge Engineering*, 16(6), 777-791.

Quinley, R. (2010). "WIM Data Analyst's Manual." Federal Highway Association, Washington D.C. https://www.fhwa.dot.gov/pavement/wim/pubs/if10018/if10018.pdf

Rhode Island Department of Transportation (2017). "Bridge Load Rating Guidelines." RIDOT. http://www.dot.ri.gov/documents/doingbusiness/RIDOT_LRFR_Guidelines.pdf

RISA Tech, I. 2016. RISA-3D, version 15RISA Tech, Inc.

Ryan, T. W., Mann, J. E., Chill, Z. M., and Ott, B. T. (2012). "Bridge Inspector's Reference Manual." Federal Highway Administration. https://www.dot.state.mn.us/bridge/pdf/insp/birm/birmchapt0-cover.pdf

Shoukry, S. N., William, G. W., Riad, M. Y., and Luo, Y. (2008). "Enhancement of bridge live loads based on West Virginia weigh-in-motion data." *Bridge Structures*, 4(3, 4), 121-133.

TxDOT (2013). "Bridge Inspection Manual." *Ratings and Load Posting*, Texas Department of Transportation. http://onlinemanuals.txdot.gov/manuals/index.html

TxDOT (2018a). "Bridge Inspection Manual." *Ratings and Load Posting*, Texas Department of Transportation. http://onlinemanuals.txdot.gov/txdotmanuals/ins/ins.pdf

TxDOT (2018b). "InspecTech Inspection Records." Bentley Systems.

United States Government (1958). "US Code Title 23 - Highways." United States Government, Washington D.C.

United States Government (2004). "Rules and Regulations." Department of Transportation, ed., Federal Register, 74419.

Utah Department of Transportation (2014). "Bridge Management Manual." *Chapter 4 - Load Rating*, UDOT. https://www.udot.utah.gov/main/f?p=100:pg:0:::1:T,V:4263,

Wisconsin Department of Transportation (2017). "WisDOT Bridge Manual." *Chapter 45 - Bridge Rating*, WisDOT. https://wisconsindot.gov/Pages/doing-bus/eng-consultants/cnslt-rsrces/strct/bridge-manual.aspx

Zokaie, T., Imbsen, R. A., and Osterkamp, T. A. (1991). "Distribution of wheel loads on highway bridges." Transportation Research Board, National Research Council, Washington D.C.